AN EXPERIMENTAL STUDY OF THE RESPONSE OF REINFORCED CONCRETE FRAMES WITH WOOD PANEL INFILLS TO SIMULATED EARTHQUAKES

by

Charles Skehan Kerby

A Thesis

Submitted to the Faculty of Purdue University

In Partial Fulfillment of the Requirements for the degree of

Master of Science in Civil Engineering

Lyles School of Civil Engineering

West Lafayette, Indiana

May 2022

THE PURDUE UNIVERSITY GRADUATE SCHOOL

STATEMENT OF COMMITTEE APPROVAL

Dr. Ayhan Irfanoglu, Chair

Lyles School of Civil Engineering, Purdue University, Structures

Dr. Santiago Pujol

University of Canterbury, New Zealand, Structures

Dr. Jan Olek

Lyles School of Civil Engineering, Purdue University, Materials

Approved by:

Dr. Dulcy Abraham

To my grandparents

Mary and Bob Kerby

Mary K and Chuck Brown

ACKNOWLEDGMENTS

I am grateful to each of my committee members for their support while writing this document: Dr. Santiago Pujol, who provided me my first research opportunity and opened his door to a young student, Dr. Ayhan Irfanoglu, whose advice and lectures built on my passion for civil engineering with every passing day, and Dr. Jan Olek for his consultation and time.

I am grateful to Dr. Jonathan Monical, on whose shoulders my work undoubtably stands. His willing mentorship made my own work orders of magnitude easier. I also thank Dr. Prateek Shah and Dr. William Pollalis, who taught me many a practical lesson about researching efficiently and effectively at Bowen Laboratory. I consider my relation with each of them a lasting friendship. Let my inclusion of each of their well-deserved titles be a testament to their character.

I am grateful to Kevin Brower and Harry Tidrick, the pair of Bowen Laboratory staffers who gave each day working on the lab floor personality with wise advice and wry jokes.

I am grateful for my family, especially my parents, for raising a son capable of completing such a task. Any accolade I have earned is owned in part by them. I dedicated this work to each of my four grandparents, that they might share in my excitement at finishing one chapter of my life and beginning to write the next.

Boiler Up. Hammer Down. Hail Purdue.

TABLE OF CONTENTS

LIST OF TABLES

LIST OF FIGURES

NOMENCLATURE

A_g	Gross Cross-Sectional Area
A_{net}	Net Cross-Sectional Area
APA	American Plywood Association
b	Column Width
d	Column Effective Depth to Longitudinal Reinforcement
DR	Drift Ratio
E_c	Modulus of Elasticity of Concrete
E_m	Modulus of Elasticity of Masonry
E_w	Modulus of Elasticity of Wood
F1	Frame 1
F2	Frame 2
f_c'	Compressive Strength of Concrete Cylinder
f_y	Measured Yield Stress of Steel
f_u	Measured Ultimate Stress of Steel
f_m'	Compressive Strength of Masonry-Mortar Coupon
f_{mortar}'	Compressive Strength of Type-N Mortar
F_{TC}	Time Compression Factor
h_c	Column Clear Height
g	Acceleration due to Gravity
$K_{initial}$	Initial Secant Stiffness of Infilled Frame
K_{sec}	Secant Stiffness of Infilled Frame
n	Number of 3/4” Plywood Panels Forming a Wood Infill Thickness
NS	North-South

P	Applied Load
PEER	Pacific Earthquake Engineering Research Center
PGA	Peak Ground Acceleration
PGD	Peak Ground Displacement
PGV	Peak Ground Velocity
s	Transverse Reinforcement Spacing
SDOF	Single Degree of Freedom
t_{infill}	Infill Thickness
T_{secant}	Period Derived from Secant Stiffness and Effective Mass
T_{PDI}	Period Derived from Phase Difference Index
TC	Time Compression Factor
RSN	Record Sequence Number
R1	Intensity Reference Run Number of a Given Series
-1PB	Wood Infill Thickness Constructed from One 3/4"" Rated Sheathing Panel
-2PB	Wood Infill Thickness Constructed from Two 3/4" Rated Sheathing Panels
-4PB	Wood Infill Thickness Constructed from Four 3/4" Rated Sheathing Panels
-B	Bare Frame, No Retrofits
-C	External Post-Tensioned Clamps Applied to Frame Columns
-M	Masonry Infilled Frame
-S	External Post-Tensioned Clamps Applied Mid-Series

Damaged Frame Series

Referring to the Union of Series F2-C-4PB, F1-C-2PB, and F1-C-1PB

Recast Frame Series

Referring to the Union of Series F2-R-C-4PB, F2-R-C-2PB, F2-R-C-1PB, and F2-R-C

ABSTRACT

Masonry infills historically have increased in-plane stiffness and reduced drift demands of reinforced concrete frames. An inherent risk remains during intense ground motions that unreinforced masonry infills can develop shear cracks, fail out-of-plane, or lead to the formation of captive-column conditions. This study explored the use of full-bay, plywood panel infills in non-ductile reinforced concrete frames as a novel seismic retrofit. Wood infills were constructed from layers of APA 3/4" Rated Sheathing plywood panels. Infills were tested using two single-bay, single-story concrete frames at 1/3 scale, with initial periods between 0.1 and 0.3 seconds once infilled. External post-tensioning was provided to the columns during all series to prevent column shear failure and doubled as dowel connections between the concrete frame and wood panel infill. Test series were performed on a uniaxial earthquake simulator with the frame bay parallel to the direction of ground motion. Wood infills were approximately $0.36 * b$, $0.18 * b$, and $0.09 * b$ thick, where *b* is the column width. Multi-layer infills were screw-laminated via a 6" square grid. Infills were tested in previously damaged and nominally pristine frames.

During similar ground motions, masonry infills reduced the effective period of the pristine bare frame by approximately 50%. In nominally pristine frames, one-panel plywood infills reduced the bare frame period by a maximum of 50%, and two-panel infills by 60%. One and two-panel wood infills reduced drift demands in comparison to the pristine bare frame by a factor of $\frac{1}{\sqrt{2*n}}$ in previously damaged frames and by $\frac{1}{2*n}$ in nominally pristine frame, where *n* is the number of panels of plywood across the infill thickness. There was no extra reduction in drift demands resulting from increasing the wood infill thickness beyond two panels. One-panel wood infills failed via out-of-plane buckling causing splitting at a drift demand of approximately 1.5%.

The results of this study confirm that wood panel infill retrofits are structurally viable alternatives to stiffen non-ductile reinforced concrete frames. Plywood panel infills reduced drift demands more efficiently per unit thickness and unit weight than masonry infills; the resilience and ease of construction of wood infills suggest expanded use should be explored. Experimental study of full-scale wood infills is needed before this retrofit method could become field deployable.

1. INTRODUCTION

In this experimental research the effectiveness of novel wood panel infills in non-ductile reinforced concrete frames was investigated. Masonry-mortar infilled frames are the subject of much current research, both experimental and analytical. Masonry infills have been observed to decrease drift demands but can also fail in brittle manners that decrease drift capacity. It was theorized that a less brittle material that could develop near equivalent stiffness, such as timber, could be an infill alternative. Timber may also be more available, affordable, or sustainable than masonry in regions with abundant wood. For these reasons, an investigation into the effectiveness of timber infill panels used to reduce drift demands in non-ductile reinforced concrete frames was conducted.

Engineered plywood panels are well understood in design as shear wall panels in light frame construction. With design controlled by nailing schedules, the load capacity of the wood panels is never achieved. If wood shear panels were coupled with reinforced concrete frames, the high capacities of concrete frames would not require connection schedules designed to fail before the plywood approached ultimate strength. Plywood is weaker but more widely available than structurally bonded mass timber elements which require custom fabrication. Thus, plywood panel infills were chosen to form the timber infills in this study.

The success of infills as seismic retrofits will be studied based on reduction of drift demands. Infills imitate the behavior of shear walls, limiting drift through high relative stiffness relative to that of a bare frame.

1.1 Scope

This program produced data from seven series of single bay, single story frame dynamic tests at the Bowen Laboratory for Large Scale Civil Engineering Research at Purdue University in West Lafayette, Indiana, USA. The first six test series were completed with infilled bays, and the final series tested a bare frame. Frames were subjected to North-South histories of the 1940 El Centro Earthquake, compressed in time and linearly scaled in amplitude.

Each series expanded upon the work completed by Monical (2022) on masonry infilled frames. Inheriting the reinforced concrete frames and experimental design used by Monical, the

opportunity for comparison of bare, masonry infilled, and wood infilled frame response to simulated earthquakes was uniquely prepared. Relative performance of wood infills was discerned from comparison of data collected in 14 frame-infill configurations and 273 simulated ground motions combined from this experimental program and Monical's experimental program.

The importance of connection schedules in wood panel design is undeniable, but not within the scope of this study. For example, wood shear panel design tables list capacities as a direct function of the nail schedule used at panel edges and on interior studs (AWC, 2017). The wood infills designed here interacted with the frame via bearing edge-joints and dowel-type connections, avoiding typical failure modes of nail pullout or fatigue. Similarly, no interior panel splices or framing studs were required to span the 1/3 scale frame bay. This study focused on the performance of the wood panel(s) alone and the interactions between infill and concrete frame. The discussion presented here intends to act as an exploratory look into the possibility of using wood panel infills in reinforced concrete frames to reduce drift demands.

Without framing studs, infills of varying thickness were formed via screw lamination. Lamination of wood shear panels by nail or screw on the same side of a stud line is uncommon but not unheard of. The APA allows designers to treat a two-panel nail or screw lamination (dubbed "Double-Sheathed Shear Walls") as a single shear panel with double the capacity in design given the requirements of technical topics report TT-115 are met (APA, 2016). These requirements include details for connection (3" diameter washers used at all anchor bolts), edge spaces (base layer 1" minimum edge distance), and panel arrangements (no interior panel joints overlapping). Lamination of more than two panels is not permitted in design by the APA but was explored in this program to compare response of wood and masonry infills of equivalent net thickness.

Infills can be qualified as "participating" or "non-participating" (The Masonry Society, 2016). A non-participating infill is designed with edge gaps a minimum of 3/8" wide between infill boundary and surrounding frame and is not analyzed as a part of the lateral load resisting system. If the isolation joints are non-compliant, the infill defaults to a participating infill. As will be explained, wood infills in reinforced concrete frames in current European design practice are nearly exclusively non-participating. The experimental design presented here does not default into the category of participating infills, but rather intentionally induced bearing between frame and infill to study participating wood panel infills under dynamic loadings.

Inspiration for testing wood infills within concrete frames was drawn from personal communications between Dr. M. Maeda of Tohoku University, Japan and Dr. S. Pujol of the University of Canterbury, New Zealand.

1.2 Literature Review

There has been limited experimental work completed to-date studying the interaction of participating wood infills in reinforced concrete frames in North America. Relevant works studying both wood and masonry infills are reviewed to compare between these two infill materials.

1.2.1 Non-participating Wood-Panel Infills

Eriksson (2003) described industry practice for non-participating wood infill panels in concrete frames across Europe (mainly in Nordic countries) and select regions of Asia. Wood sheathing panels are commonly used as exterior walls of mid-rise residential construction. In the Netherlands, 50% of new construction at the time of report publication consisted of timber infilled concrete frames. Standard practice connected the wood panels on the interior face of the bay with steel angles at the top and bottom of the bay. Breather membranes along vertical edges were fitted for seal and gaps filled with mineral wool insulation. Bearing forces are thus not induced across the breather membranes.

Blaylock (2012) tested the lateral effects of non-participating wood infills in reinforced concrete frames matching those described by Eriksson. A reinforced concrete frame with a single 16’ x 8’ bay was infilled with four 0.5” thick Oriented Strand Boards (OSB) and 0.62” drywall sheathing. The infill was connected to studs placed every 24” on center by 6d nails at 6” at edges and 12” in the infill center. Tests were performed under a static loading regime calibrated to simulate service and ultimate wind loadings, both in-plane and out-of-plane. Gaps ranging from 0.24” to 1.26” were maintained between the infill edge and concrete faces and were filled with expanding insulating foam. Wood shims were inserted between the lower frame beam and infill bottom edge. The infilled deformed to a maximum of 0.18“ diagonally during bi-directional in-plane sway tests. Insulation foam was cited as a likely variable explaining the maximum 13% underestimation or 9% overestimation of observed stiffness values from SAP2000 linear elastic

models. It was concluded that current design assumptions for in-plane infill response do not account for evident load transfer from concrete frames to wood infills through edge-bearing.

1.2.2 Participating Cross-Laminated Timber (CLT) Infills

Stazi et al. (2019) completed an experimental and numerical study on CLT panels as reinforced concrete frame infills. CLT panels are a form of mass timber formed from layered wood laminated with structural adhesive, seismically stronger and more durable than plywood panels. Square CLT panels constructed from C24 Red Spruce boards were 3.94" thick and 35.4" in diagonal were tested in diagonal compression tests until failure. The in-plane modulus of elasticity of the CLT was 1031 ksi and the shear modulus was 100 ksi. Peak loads were between 81 kips and 90 kips for unconfined and panels confined with metal shoes respectively. All panels displayed linear, brittle behavior in diagonal compression tests, with residual strength about 70% of the peak load. 3-ply CLT panels were found to be stiffer in shear than 5-ply CLT panels. CLT panels were next modeled as infills in single-story, single-bay reinforced concrete frame. Under the assumptions of perfect bonding between frame and CLT infill and linear panel response, a global lateral stiffness 7 times higher and a peak lateral force 4 times higher than equivalently modeled RC frame with traditional masonry infill were found.

1.2.3 Research on External Post-Tensioned Transverse Reinforcement

Skillen (2020) tested two 18"x18" concrete columns with similar longitudinal ($\rho = 2\%$) and shear reinforcement detailing ($\rho_{tr} = 0.1\%$, s = 12"). Both specimens were axially loaded to a constant 150 kips. Column C1 had external post-tensioned transverse reinforcement ("clamps") while C2 did not. The external clamps resisted in-plane shear through two ½" diameter threaded rods, tightened to approximately 70 ksi against A36 3"x5" angles snug to each column corner. C1 did not fail in shear due to confinement of diagonal shear cracks by the external clamps, and sustained drift ratios up to 7% without loss of axial or lateral load capacity. Without external clamps, C2 failed in shear at a drift ratio of 1.5%. It was concluded that external clamps did not increase column strength or plastic moment capacity, but did increase column drift capacity and ductility. The findings of this experimental program were supported in results produced by Monical (2022).

1.2.4 Research on Participating Masonry Infills

Marinkovic & Butenweg (2019) tested single-story, 105.5" x 96.9" single-bay traditional masonry infills and vertically decoupled infills in reinforced concrete frames with 9.84" square columns. The novel vertical decoupling system tested was specially designed to reduce the rate of stiffness decay of unreinforced masonry infills. Specimens were cyclically loaded to in-plane drift ratios of 3.5% under a total axial load of 90 kip. The in-plane secant stiffness of the traditional infill reduced from an initial peak 423.3 $\frac{kip}{in}$ to less than 144.2 $\frac{kip}{in}$, (27% of the $K_{initial}$) by a drift ratio of 0.5%. The novel decoupling system decreased rate of in-plane secant stiffness decay, while also reducing the initial system in-plane stiffness to 81.9 $\frac{kip}{in}$.

Van & Lau (2021) tested single-story, single-bay bare and masonry infilled frames under monotonic and cyclic loadings up to approximately 4% and 2% peak drift ratios respectively. Cyclic loadings of infilled frames caused peak strength to occur at drift ratios 40-50% smaller than monotonic loading. A constant 8.1 kip vertical load was applied to the frames. The in-plane lateral stiffness of three of the four masonry infilled frames fell below one-third the initial lateral stiffness, ranging from 97 $\frac{kip}{in}$ to 148.4 $\frac{kip}{in}$, at a peak drift ratio of 0.5%. The conclusion that abrupt damage and loss of lateral stiffness occurs after the development of the first cracks in the masonry infills was reached via development of degradation curves of system secant stiffness.

Monical (2022) compiled the experimental results of 13 experimental programs dating from 1994 to 2020 studying the seismic response of bare and masonry infilled single-bay, single-story frames, in addition to designing and completing an experimental program studying two single-story, single-bay reinforced concrete frames dynamically tested via earthquake simulation. The frames constructed by Monical had 8"x8" columns with a clear height of 40" between heavily reinforced beams (120"x20"x8"). Shear reinforcement consisted of four 3/8" ties in each column. External clamps similar to those tested by Skillen (2020) were applied and tightened to 40 ksi bar stress after initial bare frame tests to avoid column shear failure. The frame top beam was connected rigidly to a concrete block weighing 44,500 pounds that swung freely during dynamic tests. Masonry infills were constructed from clay bricks 7/5/8"x3-5/8"x2-1/4" and mortar mix ($f'_m \approx 2800\ psi$) that filled the single 64"x40" bay. Monical concluded that drift demands in tests with full-bay masonry infills were no larger than one-third demands of matching bare frames.

Further detail on Monical's work will be provided throughout this study, as data from Monical's experimental program are commonly reproduced, with permission (Appendix F).

2. EXPERIMENTAL PROGRAM

An experimental program was developed to study the seismic response reinforced concrete frames with wood panel infills in comparison to those with unreinforced masonry infills. The primary experimental program consisted of seven infilled frame configurations subjected to earthquake simulations. Supplemental to these tests, a series of supplementary 4-point bending tests were performed to determine the Modulus of Elasticity (E_w) of the wood infills. This section briefly explains the design of the program. Detailed descriptions are given in Appendix A.

The experimental program was competed in two parts. First, test frames were inherited in a severely damaged state from the experimental program completed by Monical (2022). The damaged frames were retrofitted with wood infills of varying thickness and dynamically tested. Prior to each test series of a damaged frame, mortar repairs of loose column concrete were completed. The second part of the experimental program began with a repair of one of the test frames. This repair consisted of removing and recasting the concrete of all column ends, returning the frame to a nominally pristine condition. The repaired frame was then infilled and dynamically tested with wood panels of varying thicknesses like those in the first half of the study.

2.1.1 Series Naming Convention

Series in this program are named following the style of "F*x*-*y*-*z*". "F*x*" represents the ID number of the frame being tested (i.e., F1- or F2-). "-*y*-*z"* represent modifiers listed in the table below, summarizing both the naming modifiers developed for this experimental program and those developed by Monical (2022). A combination of modifiers denotes all listed conditions were applicable to the frame prior to the start of the test series.

Table of Series Naming Modifiers

-B	Bare frame, no Retrofit
-R	Frame Columns previously Recast
-C	Post-tensioned External Transverse Reinforcement (clamps) applied
-M	Unreinforced Masonry Infill
-1PB, -2PB, -4PB	Wood Infill, and the Number of 3/4" Boards Forming the full Infill Thickness (e.g. -2PB = "2 plywood board thickness Wood Infill")
-S	Clamps applied mid-series after formation of large shear cracks at column bases (see Table 3-7)
-10, -20, -40, -60, -80, -100	Linear Percent Scaling of Ground Motion (e.g., -60 = 60% ground motion intensity)

2.2 Series Design and Setup

Dynamic tests of infilled frames were performed using the earthquake simulator at Bowen Lab for Large Scale Civil Engineering Research. Specifications of the earthquake simulator are described by Sozen (1969). Dynamic testing consisted of a base motion parallel to the length of the frame (Figure 2-1 and Figure 2-2). Base motions simulated the North-South record of the 1940 El Centro Earthquake obtained from PEER (Ancheta et al., 2014), compressed in time by a factor of 2 and linearly scaled in amplitude by a factor of 1.9. Target ground motion parameters, acceleration and displacement histories, and spectra of the target displacement history are provided in Table 2-1 and Figure 2-3 to Figure 2-6 respectively. Spectra were plotted at a 2% damping ratio based on analysis completed by Monical. Base displacement histories were linearly scaled from the target ground motion to 10%, 20%, 40%, 60%, 80%, or 100%. Test series began with two motions at each intensity from 10% upwards, halting the increase of intensity either once a 100% motion was performed twice or the approximate 70-kip yield limit of the servoram to platform

connection was approached. A varying pattern of runs of descending intensity were performed after the peak motion during some series (see Section 3.1).

Test series with wood infills were performed immediately after the termination of the experimental program completed by Monical (2022) using a pair of test frames inherited directly from Monical's experiments, named Frame 1 and Frame 2. Both frames had incurred severe damage during Monical's test series and were tested in a damaged state during the first three test series with wood infills (Series F2-C-4PB, F1-C-2PB, and F1-C-1PB). Prior to the start of each test series, loose column concrete near beam-column joints was repaired with type-N mortar ($f'_{mortar} \approx 1700\,psi$). Mortar repairs provided an even surface for bearing of external post-tensioned reinforcement and infill edges. After Series F1-C-1PB, Frame 2 had column concrete removed by jackhammer and recast near each joint, returning Frame 2 to a nominally pristine state for the remaining series (F2-R-C-4PB, F2-R-C-2PB, F2-R-C-1PB, and F2-R-C).

Each test frame had identical dimensions and reinforcement. Two beams 120"x72"x20" in dimension flanked two columns with a 40" clear height (Figure 2-7). Inherited frame concrete had a measured 6"x12" cylinder 28-day compressive strength of $f'_c = 3800\,psi$ (Table A-1). The measured Modulus of Elasticity of the concrete was $E_c = 3{,}200\,ksi$. Frames were cast and cured on their west faces (as tested in-plane) before being righted and raised onto the simulator platform for testing. Columns were 8"x8" square in cross section and formed a single bay 64" long by 40" high. Column longitudinal reinforcement consisted of four 5/8" diameter bars, $d = 6\,in$ on all sides. The longitudinal reinforcement ratio was $\rho = \frac{4\,bars * 0.31\,in^2}{64\,in^2} = 1.9\%$. Column ties were 3/8" diameter and were spaced at $s = 6\,in$ with 90 degree hooks on each end (Figure 2-8). The transverse reinforcement ratio was $\rho_{tr} = 0.45\%$. Uniaxial tension tests were performed on four longitudinal bars by Monical (2022) measured bar yield stress and strength at $f_y = 63\,ksi$ and $f_u = 99\,ksi$ (Figure 2-9). Uniaxial tension tests of four ties by Monical (2022) measured tie yield stress and strength at $f_y = 70\,ksi$ and $f_u = 97\,ksi$ (Figure 2-10).

2.2.1 Inherited Condition of Frame 1

Frame 1 had undergone 56 in-plane and 22 out-of-plane runs and had a 3/8" residual in-plane drift towards the South prior to its first test series with wood infill. Spalling was most severe at column bases and was concentrated below the location of the first external post-tensioning

device, 3” above the joint (Figure 2-11). All columns had large flexural cracks both at the joint face and approximately away 3” from the joint face. Smaller flexural cracks at mid-height of the columns had formed. Local crumbling of concrete often occurred beneath contact surfaces of external post-tensioned clamps. Flexural cracks were no wider than 0.005”. In-plane inclined shear cracks of widths between 0.01” and 0.075” were present near column ends.

2.2.2 Inherited Condition of Frame 2

Frame 2 had undergone 97 in-plane and 0 out-of-plane runs and had a 1/8” residual in-plane drift towards the South prior to its first test with wood infill. Severe flexural cracking had occurred at each column-joint face. Concrete spalling at column bases was more severe than in Frame 1 and reached up to the location of the third external post-tensioning device, 9” above the joint (Figure 2-12). Longitudinal reinforcement was exposed in the south column but had not buckled. Inclined cracks on the south column, east face, were as large as 0.1”. Thin flexural cracks near column mid-height were present. Figure 2-13 shows the extent of spalled column concrete and a photograph of the mortar repairs performed prior to Series F2-C-4PB.

Before the final four test series performed on Frame 2 (F2-R-C-4PB, F2-R-C-2PB, F2-R-C-1PB, F2-R-C), column concrete near the joints was removed and recast to create nominally pristine frame conditions. Column concrete was removed by jackhammer from the joint face to two inches beyond the farthest inclined shear crack in the column. 11” of concrete was removed from the tops of both columns. 15” of concrete were removed from the northern column base and 13” from the southern column base (Figure 2-14). High strength ready-mix concrete was mixed with additives increasing cold joint bond strength and cast to reform the columns. Standard 4”x8” cylinders were cast and tested in compression and split tensile tests with each mix (Table A-3 and Table A-4). On the first testing day of Series F2-R-C-4PB (25 days post cast), the measured compressive strength of the new concrete was $f_c' = 5290\,psi$ and the measured split tensile strength was $f_t' = 555\,psi$. Figure 2-15 displays Frame 2 after column ends were recast and formwork stripped. Appendix C provides a more detailed description of mix details and the recasting process.

2.2.3 Instrumentation

Instruments measured displacements of the frame and simulator platform, tri-axis accelerations at frame beam corners, load between the suspended mass and frame top beam, and strains on the servoram connection to the simulation platform (Figure 2-16). Data were collected during runs at 1000 Hz using a National Instruments data acquisition system (DAQ). Two optical tracking systems (Optotrack and Optitrack) recorded tri-axis displacements of targets on the infill, frame, and test setup hardware independently of the National Instruments DAQ. Calibration data and range of performance of all sensors are provided in Appendix B.

Linear Variable Differential Transformers (LVDTs) measured the in-plane displacement of the frame foundation beam top, top beam soffit, and top beam top (Figure 2-17), the in-plane displacement of the servoram (Figure 2-18), and vertical deflections of the simulator platform (Figure 2-20). Story drift was calculated as the average displacement of the top beam in-plane LVDTs minus the displacement of the foundation beam LVDT. Drift ratio was calculated by dividing the story drift by 50", the height from the top of the foundation beam to the centerline of the top beam. Micro-electro-mechanical-system ADXL and piezoelectric PCB accelerometers collected tri-axial acceleration data at each end of the frame foundation and top beams. A load cell built into the dual-swivel link between frame and external suspended mass measured applied lateral forces to the frame top beam. Forces were also derived from readings of the strain gages on the servoram to simulator platform flexure link.

2.2.4 Effective Mass Breakdown and Connection

The test specimen represented a single degree-of-freedom (SDOF) dynamic system with a total effective mass of 49 kips (Table 2-2). Frame columns did not support the weight of the external mass, only approximately 2 kips per column from self-weights of the frame and connection hardware. The mass of the wood infills was neglected, as the mass of the masonry infills was neglected by Monical (2022). Most of the seismic mass was provided by a 14' x 5' x 4' heavily reinforced concrete block positioned adjacent to the south end of the simulator platform, suspended from an overhead crane approximately 35' above the center of mass of the concrete block (Figure 2-19). A dual-swivel link assembled by Monical (2022) connected the block to the frame top beam (Figure 2-21). Deformations across this dual-swivel link were tracked using the

optical tracking system Optitrack to confirm that the external mass and frame top beam underwent similar displacements during test runs. A breakdown of the components of the dual-swivel link can be found in Appendix A.

The dual-swivel link was connected to a pair of MC18x58 channels confining the frame top beam at its north end. The channels were attached to the frame top beam via a slip-critical connection of fourteen 1" diameter high-strength threaded rods passing through the confining channels and top beam near midspan, exerting a total confining force of 300 kips. Adjustable bolts bore on angles attached to confining channels at the northern end of the top beam to prevent slip (Figure A-18 (a)). At the south end, a load cell assembly within the dual-swivel link bore on stiffened angles via a 2" threaded rod (Figure A-18 (b)).

To prepare the mass for a ground motion, one of Bowen Lab's Dearborn Crane and Engineering Co. 30-ton overhead cranes was aligned above the center of mass of the concrete block. The external mass was suspended such that its center of mass was aligned in-plane with the center of the frame top beam and was directly beneath the crane head. Out-of-plane motion (East-West) of the external mass was controlled with four vertical steel tubes. Teflon pads on tube faces nearest the hanging mass reduced friction when rubbing occurred (Figure 2-19). Prior to each run, bracing was tightened to within ½" of the aligned mass. When not suspended, the mass was supported at the corners by hydraulic jacks that prevented the block from lowering and loading the frame (Figure 2-19).

The nature of the hanging external mass removed cumulative drift from relevance to this study. Gravity pulled the suspended mass towards a stable equilibrium directly beneath the crane head after each run. As a result, the frame returned to near the same ending drift as its starting position while attached to the suspended mass, on average within 0.01".

2.2.5 Frame Connection to Simulator Platform

Figure 2-22 provides a labeled elevation of all connection components between the frame, simulator platform, and external mass.

Ten 1/2" diameter threaded rods tied into the simulator platform every 12" and attached the frames to the simulator platform. Rods passed through holes cut in the exterior flanges of W18x65 sections flanking the frame foundation beam in-plane. Above the W-Sections, the rods passed between pairs of 3" steel channels fitted through the infill bay. The threaded rods were

tightened to approximately 10 kips via ¾" nuts on the tops of the channels. The total force connecting the frame to the simulator platform was approximately 220 kips.

MC18x58 channels were tightened to the North and South edge of the simulator platform perpendicular to the direction of in-plane ground motion. Adjustable bolts were tightened against the channels over the width of the foundation beam to prevent slip (Figure 2-23). The in-plane W-sections flanking the foundation beam also contacted the out-of-plane channels via two adjustable bolts per bottom flange end.

2.2.6 Infill and Retrofit Design

The single 64"x40" rectangular bay within Frames 1 and 2 was filled by lateral-load participating plywood infills. Wood infills were constructed in 1PB (0.70" net thickness, 1-panel), 2PB (1.41", 2-panel), and 4PB (2.81", 4-panel) thicknesses. Edge gaps between infill and frame were a maximum of 1/4" wide, depending on the uneven geometry of the damaged column concrete. Edge gap width was precisely monitored during construction due to the sensitivity of infilled frame response to edge gap (Fiorato et al., 1970). In Series F2-C-4PB, mortar was pushed into edge gaps and cured for 14 days to form the bearing edge-joint. In all other test series, wooden shims were driven from alternating sides by hammer and glued to form the edge-joint.

Wood infills were constructed from 6-ply Douglas-Fir / Southern Pine Rated Sheathing plywood panels, rated APA PS1-09 bond category and 23/32 performance category (Figure 2-24). The panels did not meet the requirements for an APA Structural-I rating, the rating for shear panels with higher racking strength designated for use seismic areas. Infills were constructed such that exterior ply grains were parallel to the direction of in-plane motion according to APA D5150 (Figure 2-25). Panels were cut to fill the single bay according to Figure 2-27 and Figure 2-28. The infill was centered within the thickness of the columns. During series with 2PB or 4PB infills, panels were laminated into screw-laminated infills[1] using a 6" x 6" grid of screws driven into infills from alternating east-west faces. The first screw was located 6" up from the bottom of the bay and 8" away from the nearest column face. 4PB infills were laminated with 3", 9d construction screws. 2PB infills were laminated with 1.5", 8d construction screws.

[1] The "screw-laminated" nomenclature was made in reference to other common names of mass timber construction including CLT (Cross-Laminated Timber), DLT (Dowel-Laminated Timber) and NLT (Nail-Laminated Timber).

Post-tensioned external clamps designed after those used by Skillen (2020) were applied prior to all tests in this program. Clamps were aligned about columns in accordance with Figure 2-29. The clamps consisted of 3"x2"x3/8" A36 angles and 1/2" diameter high strength threaded rods. The stress-strain curves measured from a uniaxial tension test of one high-strength threaded rod is displayed in Figure 2-26, with $f_y = 150\ ksi$ and $f_u = 175\ ksi$. Spacer plates 1/8" thick were added at clamp corners adjacent to the infill to prevent rods from tearing-out of the infill. Clamps were tightened with a calibrated torque-wrench to an estimated bar stress of $40\ ksi$ assuming the full ½" diameter. The estimated total confining pressure at column ends (approximately $470\ psi$) was sufficient to resist the frame base-shear at yield. 1/2" diameter holes were drilled through the wood infills and the clamp rods slid through (see Appendix A: Figure A-11). Nuts were wrench-tightened onto both sides of the infill to brace the infill edges. By passing threaded rods through the infill thickness, the clamps formed a dowel-type connection between columns and wood infills.

2.3 Modulus of Elasticity Four-Point Bending Beam Tests

Four beams 24" long by 6" deep were constructed to find E_w. Beams were constructed with thicknesses and screw-lamination matching the wood infills. The beams were centered on rollers 18" apart beneath a welded 6" steel channel that applied 2 point-loads to the specimens (Figure 2-31 and Figure 2-32) to form a 4-point bending test setup. Two beams had a 2PB infill net thickness (1.41"), and two had 4PB infill net thickness (2.81"). Single 0.70" panels were cut individually then screw laminated to form the beam thickness. This construction method matched the process of infill construction and created incongruities along beam edges between panels and cuts of slightly varying dimension.

Beam tests were performed using Bowen Lab's Baldwin Southwark Tate-Emery Testing Machine. Load data was recorded from the built-in load cell (±10 lbf). The 2PB beams were loaded up to 3.5 kips, and the 4PB beams to 6.0 kips, both at approximately 0.3 kip increments. Deflection data were collected at a 100Hz rate using the Optotrack digital imaging system. Optotrack targets were placed at mid-depth above supports and at midspan, according to Figure 2-33. A reference plane of four targets was constructed adjacent to the beam using a section of HSS for post-processing reference and data transformation. Beam midspan deflections were calculated as the

midspan target's vertical location subtracted from the average of the support target's vertical locations (Appendix A: Figure A-25) and are reported in Appendix A: Table A-8.

The average Modulus of Elasticity of the wood (E_w) during the four-point bending tests was 461 ksi (Figure 2-34), derived from basic mechanics. For reference, this E_w was approximately one third that of the masonry coupons tested by Monical (2022) and half that of a 4" thick, 3-layer CLT panel constructed by Stazi et al. (2019).

3. TEST SERIES HISTORY AND SEISMIC RESPONSE

3.1 Test Series History

The comprehensive test series history and key run parameters are provided in Table 3-1 through Table 3-8 for test series completed by Monical (2022) and Table 3-9 through Table 3-15 for test series completed in this study. Each series performed as a part of this experimental program will be explained sequentially by date of occurrence. 34 runs were performed on Frame 1 and 63 runs on Frame 2 by the writer. The lifetime total number of in-plane runs was 90 for Frame 1 (excluding 22 out-of-plane tests) and 160 for Frame 2. Observations were made after the termination of a given run. Dates of testing and concrete age on the first day of each test series are listed in Table 2-3.

The layouts of optical coordinate-tracking targets (Optitrack and Optotrack) varied by series and were combinations of the following: Optitrack target layout A (Figure 3-1) or B (Figure 3-2) and Optotrack target layout A (Figure 3-3) or B (Figure 3-4). When optical tracking data is used in analysis or discussion, target layouts will be specified. An example photograph of Frame 2 with Optitrack layout B and Optotrack layout B is provided in Figure 3-5.

3.1.1 F2-C-4PB

The first series in this program tested Frame 2 with a 4-panel infill of 2.81" net thickness. Optitrack layout B and Optotrack target layout A were used. The frame underwent two runs at 10%, 20%, 40%, 60%, and 80% intensities on the first day. As noted in Section 2.2.6, the bearing edge-joint was formed with type-N mortar (Figure 3-6). During the 20% intensity run, crumbling of the mortar between frame and infill began at each of the four infill corners. Deterioration of the mortar bearing edge-joint increased during successive runs and allowed the infill to slide within the bay, causing the development of a "pinching" region of the force-drift plots (Figure D-99). Optitrack targets were added in two locations at the top of the wood infill and on the bottom of the frame top beam to measure the sliding (see Figure 3-2). The relative horizontal displacement between these sets of targets defined the amount of infill slip. Slip accounted for an average of 38% of the peak drift during the first day of testing, and reached a maximum of 46% of the peak drift during the second 40% run.

During the first 60% motion, all mortar in the bearing edge-joint crumbled within 6” of the corners (Figure 3-7). Mortar used to repair the columns had spalled off the column bases. Rotations in columns were concentrated at the flexural cracks near the column top and bottom joint faces. Rotations also concentrated at flexural cracks approximately 3” below the top joint face (marked in Figure 3-8 and Figure 3-9). Damage to the infill was limited to a 5” single-ply split at the top of the infill (Figure 3-10). During the 80% motions the peak drift was 0.75” north (1.5%) and the peak lateral force was 44 kips.

On the second day of testing, ground motion intensity decreased from 60% with single repeat runs at each intensity (60%, 40%, 20%, 10%). No prior repairs to frame or infill were performed. No new damage to columns or edge-joints developed resulted from runs of decreasing intensity. At the end of the second day of testing, a third 80% motion was performed. The new peak series drift was 0.84” south (1.68%), and the new peak series force was 45 kips.

On the third testing day, a single fourth 80% run was performed. Two alterations to the frame were made to control sliding between infill and frame. First, the mortar between infill and frame was replaced along the upper edge of the infill. Second, the channel pairs passing through the infill bay as part of the frame-to-platform connection hardware had aluminum spacer plates added to induce bearing between the channels and wood infill (Figure 3-11). The spacer plates restrained the channels from sliding with the infill and secured the infill base into a set position within the bay. Slip was reduced to account for only 19% of the peak drift during this run. The peak drift was 0.6” south (1.2%).

Column base concrete spalled to expose an entire crosstie in the south column (Figure 3-12). Transverse reinforcement had shifted due to the lack of confining concrete. Spalling occurred to 12” from each column base (Figure 3-12). Frame F2 was removed from the simulator after conclusion of the fourth 80% run. The 4PB infill was removed from the frame and preserved for repeat use in recast-frame Series F2-R-C-4PB.

3.1.2 F1-C-2PB

Frame 1 was secured to the simulator platform and attached to the external mass. The 2PB infill was constructed from two new plywood boards with a total net thickness of 1.41”. Optitrack layout A and Optotrack layout A were used. The bearing edge-joint was formed with wood shims (Figure 3-13), a practice that became standard for all remaining test series. The pattern of run

intensities deviated from that used in Series F2-C-4PB after the first 40% run because of out-of-plane motion (East-West) of the frame top beam. Optotrack sensors recorded the out-of-plane motion at larger than 20% of the total in-plane drift. The external mass was realigned and a third 20% motion run was performed. The realignment reduced out-of-plane motion of the frame top beam by half during the repeat 40% base motion (Figure 3-14). Run intensities increased with single repeats after the mass realignment to two 80% motions, then decreased to 10% with single intensity repeats. A third 80% motion was the final run in the series.

Beginning during the second 40% intensity run, shims forming the bearing edge-joint became loose and fell out (Figure 3-15). Damage to the 2PB infill was limited to five small instances of crushing along the infill edges, examples are shown in Figure 3-16. All column repair mortar near beam-column joints crumbled (Figure 3-17). The peak series drift was 0.73" south (1.46%) and the peak series force was 41 kips.

3.1.3 F1-C-1PB

The eastern infill layer from F1-C-2PB was stripped to create a 1PB infill with a net thickness of 0.70". Mortar repairs of loose column concrete were completed near joints. Optitrack layout A and Optotrack layout B were used. The test series ramped up from 10% intensity with a single repeat run at each level (10%, 20%, 40%, 60%, 80%). During the first 60% intensity run, the infill began to bow out-of-plane. The amplitude of infill bowing increased with subsequent runs. Figure 3-18 illustrates the maximum infill bowing amplitude along the northern-most gridline of infill Optotrack targets. Bowing caused most of the shims forming the bearing edge-joint to fall out. Full-thickness cracks in the infill formed at the top-north and bottom-south of the infill during the first 80% intensity run, locations of the largest out-of-plane bowing (Figure 3-19 and Figure 3-20). Failure of the infill occurred as the top beam drifted north in the repeat 80% run via out-of-plane splitting 8" from the north column face (Figure 3-21 and Figure 3-22). A matching spilt partially formed 8" from the south column face. The peak series drift ratio was 1.25" north (2.5%) and the peak series force was 30 kips. Damage to columns included crumbling of all repair mortar and spalling of concrete outside the column core at the column bases (Figure 3-23)[1].

[1]Column damage was less severe in Frame 1 as it had been subjected to less total in-plane ground motions at the end of Series F1-C-1PB than Frame 2 at the end of Series F2-C-4PB.

Optotrack target layout B included a square grid of 20 targets glued to the western face of the wood infill (Figure 3-4). Targets were spaced 10” vertically and 12” horizontally. The first gridline of targets began 8” from the north column face. The target grid was designed to quantify infill deformations at various cross sections. As illustrated in Figure 3-24, the lowest and highest grid targets along the infill centerline and northern edge were chosen to quantify deformations. Gridline deformations were calculated by subtracting the in-plane displacement of the lowest target from the highest target along a given vertical gridline. Dividing by the vertical distance between those targets (approximately 30”) produced a unitless deformation measure. Figure 3-25 plots the difference between the edge and centerline infill deformations during Frame 1 run 103 at 40% intensity. A low intensity base motion was chosen to remove the effects of out-of-plane bowing of the infill. The difference between edge and centerline infill deformations reached a maximum during instances of tension acting on the upper north edge of the infill through the dowel-type clamp connections. The deformation magnification at the infill edge, defined as the ratio of infill deformations at edge and centerline, was approximately 1.25.

After panel failure, the wood infill was cut out using a Sawzall. Small sections remained along each column face, as complete removal of the infill required disassembly of the external clamps. Wood sections approximately 30” high by 3” long remained centered along the column height but avoided contribution to frame flexural stiffness (Figure 3-26). Single runs of Frame 1 with clamps and no-infill at 20%, 40%, 60%, and 80% intensities were performed to measure the stiffness of the bare frame. The peak drift was 1.47” north (2.94%) and the peak load was 20 kips. Frame 1 was removed from the simulator platform; a permanent drift of 7/8” South was recorded after the bare frame was disconnected from external suspended mass, 1/2” larger than inherited.

3.1.4 F2-R-C-4PB

As discussed in Section 2.1.1, portions of the columns of Frame 2 were recast and cured for 7 days under wet burlap, achieving $f_c' \geq 5000\ ksi$ before being lifted onto the earthquake simulator platform. All cracks on the new concrete from shrinkage or transportation were noted. Optitrack layout B and Optotrack layout B were used. The infill preserved from Series F2-C-4PB ($t_{inf} = 2.81$") was built into the frame bay such that differences in response between Series F2-C-4PB and F2-R-C-4PB could be used to estimate the effect of the recast columns on the frame stiffness.

Six days prior to the start of testing, the hydraulic jacks supporting the external mass while not suspended (Figure 2-19 (b)) lost pressure. The external mass dropped approximately 2", exerting an 8.3 kip force on the frame. The 4PB infill had been constructed and the edge bearing edge-joint was formed at the time of loading. The exact duration of loading is unknown but was less than 18 hours. The frame drifted 0.03" (0.06%) south because of this static loading. The mass was lifted and hydraulic jacks repressurized upon discovery. A 0.035" width crack formed partially across the north column base cold joint (Figure 3-27).

This abbreviated test series included two runs at 10%, 20%, and 40% intensities. The test was halted after a hairline crack developed at the north column base and nearly formed across the entire joint face during the 40% runs (Figure 3-28). The 4PB infill sustained no new damage. Comparison to the secant stiffness of the F2-C-4PB series at similar intensities confirmed that the recasting process had succeeded in returning the frame columns to a nominally pristine state with a secant stiffness (K_{sec}) equal to 120 $\frac{kip}{in}$. After the 40% runs, K_{sec} of the recast frame was estimated at 95 $\frac{kip}{in}$. The peak series drift was 0.16" south (0.32%) and the peak series force was 24 kips.

Local infill deformations during Frame 2 run 122 at 40% intensity showed decreased deformation magnification at the infill edge compared to Series F1-C-1PB (Figure 3-29). The deformation magnification due to drifts causing tensile forces at the top of the northern edge of the infill was approximately 1.1.

3.1.5 F2-R-C-2PB

Two new panels were cut to construct a 2PB infill ($t_{inf} = 1.41"$). Because no spalling occurred during the previous series, no repairs were made to the columns. Optitrack layout B and Optotrack layout B were used. The frame was tested from 10% to 80% (10%, 20%, 40%, 60%, 80%) with single repeat runs. Testing was halted as the earthquake simulator load limit was approached, and no 100% intensity runs were performed.

Cracks at all cold joints developed beginning during the first 20% run. During the first 60% run, the crack at the bottom west face of the northern column that had opened during Series F2-R-C-4PB spanned the full column width (Figure 3-30). During the second 80% run, a hairline diagonal shear cracked formed 4" above the northern column base (Figure 3-31) and was the only crack on any of the recast concrete not located directly over a cold joint. Ramp-down runs and

repeats were performed at only 40% and 20% intensities, to preserve the recast concrete for succeeding test series.

The peak series drift was 0.48" (0.96%) south and the peak series force was 56 kips, the largest lateral load developed during this experimental program. Comparison of load cell data with loads derived from strain gages on the servoram link showed no inelastic behavior of the double flexure link between simulator platform and servoram (Figure 3-32). The recast frame stiffness was determined to range from 85 $\frac{kip}{in}$ to 50 $\frac{kip}{in}$ through comparison to Series F2-C-2PB.

Local deformations were studied during Frame 2 run 128 at 40% intensity (Figure 3-33). The only damaged sustained by the infill was a single-ply split between the pair of vertical clamping devices nearest the north column (Figure 3-34). The deformation magnification at the infill edge was approximately 1.4 relative to the infill centerline when the upper portion of the northern infill edge was in tension.

3.1.6 F2-R-C-1PB

As during Series F1-C-1PB, the eastern panel of the Series F2-R-C-2PB infill was removed to create the 1-panel infill for this test ($t_{inf} = 0.70$"). Optitrack layout B and Optotrack layout B were used. This series started at 10% intensity and increased to 100% (10%, 20%, 40%, 60%, 80%, 100%) with repeats at each intensity. Series F2-R-C-1PB was the first test series to simulate a 100% intensity ground motion.

As in Series F1-C-1PB, the 1PB infill bowed out-of-plane beginning during 60% intensity runs. Multiple flexural hairline cracks of recast column concrete formed during the first 80% run. Cracks overlapping the cold joints at both column bases spanned the full column width after the second 80% run. The 1PB infill experienced edge tear-out at the top two clamps on the south column (Figure 3-35). During the 100% intensity runs, large flexural cracks opened at join faces. Diagonal shear cracks formed within each region of recast concrete (Figure 3-36 and Figure 3-37). The infill split near the north edge during the 100% intensity runs as during Series F1-C-1PB. The splitting failure was localized to the upper half of the infill in the vertical compression chord forming during northern drift ratios. The failure formed partially through the infill thickness during the first 100% run (Figure 3-38 and Figure 3-39), and cracked through the entire infill during the repeat 100% run when the top beam first drifted south (Figure 3-40 and Figure 3-41). Local panel

failure caused the infilled frame to remain stiffer than a bare frame alone during the remainder of the repeat 100% intensity run. Force-drift plots marking the instant of infill failure during Series F1-C-1PB and F2-R-C-1PB are provided in Figure 3-42 and Figure 3-43 respectively. Note that plateaus form in both directions in Figure 3-42, as the panel failure was complete. Localized panel failure is denoted in Figure 3-43 by a force plateau forming during instances of positive (southern) drift, which placed the northern infill upper corner in compression and buckled the panel out of plane.

Being the first test series to simulate a 100% scaled input ground motion, a comparison of the earthquake simulator input and output displacements was completed to verify the accuracy of simulation (Figure 3-44). The discrepancy between servoram input commands and output displacements during the simulation was consistently within ±0.005 inches. Also plotted were the displacements of the frame foundation beam LVDT, which had a maximum discrepancy from the input commands of +0.03 inches. Foundation beam displacements exceeded simulator inputs during the largest ground displacements in both directions. Differences between foundation beam displacements and servoram outputs informed the decision that ground motion parameters such as peak ground acceleration, peak ground velocity, and peak ground displacement were to be recorded from the foundation beam LVDT record and not from simulator inputs or outputs.

The peak series drift was 0.97” south (1.94%) after infill failure, and the peak series force was 47 kips. No ramp down tests were performed. Local deformations were studied during Frame 2 run 143 at 40% intensity (Figure 3-45). Deformation was magnified at the infill northern edge by approximately 1.7 during instances of tension acting on the upper northern edge of the infill.

3.1.7 F2-R-C

The recast frame was tested a final time with clamps but no infill (Figure 3-46). This series was performed on the same day as Series F2-R-C-1PB. No rearrangement of the suspended external mass or repairs of loose concrete were performed. Optitrack layout B and Optotrack layout A were used. The series was nominally the same as Series F1-C by Monical: both frames had only external clamps with no infill and had sustained damaged from multiple previous test series. Drift ratios of Series F2-R-C matched those of Series F1-C at similar intensity ground motions, confirming the nominal similitude of frame condition (Figure 3-47). The run intensity history

began with two runs at 10% and increased to 100% with repeat motions (10%, 20%, 40%, 60%, 80%, 100%). No ramp-down intensity runs were performed.

The series peak drift was 1.53” north (3.06%) during the second 100% run and the peak series force was 30 kips during the first 60% run. The plastic load capacity of the frame with post-tensioned clamps was approximately 30 kips. All runs after the first 60% run nearly achieved that same peak load (Figure 3-48). The plastic load capacity of Series F2-R-C was 6 to 8 kips larger than Series F1-C.

4. DISCUSSION OF TEST RESULTS

This section discusses the trends present within and between test series. It also offers comparisons between test series within this study and the test series performed by Monical (2022). In discussion, lateral stiffness will be defined according to either the peak-to-peak secant or instantaneous slope of the force-drift plot as defined in Figure 4-1. In all figures, the following marks will represent each test series:

Series Retrofit	Symbol
Bare Frame	+
Masonry Infill	×
4-panel Wood Infill	○ = damaged frame ● = recast frame
2-panel Wood Infill	△ = damaged frame ▲ = recast frame
1-panel Wood Infill	□ = damaged frame ■ = recast frame

4.1 Force-Drift Response of Wood Infills

4.1.1 Force-Drift Response in Damaged Frames

Force-drift plots from runs of damaged frames series are available in Figure D-99 through Figure D-101. Response was approximately bi-linear. At low drift ratios only the frame was engaged, followed by engagement of both frame and infill after a brief transition region (Figure 4-2). The slope at low displacements matches that of the bare frame stiffness, until the necessary drift is achieved for the wood infill to engage. This bilinear approximation for response of frames with infill agrees with observations made by Fiorato et al. (1970). The initial "slip" region accounts for an average of 30% of the total drift during the 4PB infilled series, the largest of any series. Alterations to the test setup discussed in Section 3.1.1 reduced slip. Force plateaus are visible only in the 80% motions of F1-C-1PB after infill failure (see Figure 3-42). Force-drift responses display a tendency to "wobble" during loading cycles of intense ground motions (most clear in Figure 3-43 during positive drift) resembling a sine wave acting along the secant between origin and peak

load. A similar occurrence is visible during tests on pristine frames (Monical, 2022, Figure 3-4), so the phenomenon is attributed to the test setup and is independent of the infill design.

Figure 4-3 shows the base shear versus drift envelope for all damaged frame series with wood infill. Only in Series F1-C-1PB is a plateau in lateral force visible, starting at a drift ratio between 1.25% and 1.8%. The 4PB and 2PB series envelopes are approximate linear and equivalent, surpassing the masonry envelope beyond 1.0% drift ratios.

4.1.2 Force-Drift Response in Recast Frames

Force-drift response was linear in each of the three repaired frame series (Figure D-102 through Figure D-104). Unloading and loading cycles followed near identical paths on force-drift plots, especially during early cycles of a given ground motion. The base shear versus drift envelopes of the 4PB and 2PB series surpassed the envelope of series with masonry infills beyond a 0.3% drift ratio (Figure 4-4). Beyond drift ratios of 1.0%, the envelope of the recast frame series with 1PB infill surpassed that of series with masonry infill. The recast frame series with 1PB infill experienced panel failure leading to a force plateau at approximately 1.5% drift. Because the infill panel failed locally near the top of the infill bay, the plastic lateral load remained approximately 20 kips higher than that of the bare frame.

4.2 Drift Demands of Wood Infilled Frames

Infill performance is next assessed relative to drift demands from the pristine frame in Series F1-B. Frames with wood infills are categorized by equivalent frame condition (damaged or recast).

4.2.1 Drift Demands Relative to Frames without Infill

Damaged Frame Series Comparison

Drift demands plotted with respect to peak ground velocity (PGV) displayed a strong, positive, linear relationship between peak drift ratio and PGV (Figure 4-5) At a given PGV, the drift demand of a frame with wood infill relative to a pristine bare frame was proportional to the square root of the number of panels forming the infill:

$$DR_{infill,Damaged} = DR_{bare} * \frac{1}{\sqrt{2*n}} \quad \text{(Equation 4-1)}$$

where:

$DR_{infill,Damaged}$ *= Story drift ratio of damaged frame with wood infill (%) at a given PGV*

DR_{bare} *= Pristine, bare frame story drift ratio (%) from Series F1-B at a given PGV*

$n =$ *Number of infill panels (1 or 2)*

Equation 4-1 does not apply to Series F2-C-4PB. The stiffness of the 4PB infill was similar to that of the 2PB infill (see Section 4.2.3) and infill sliding took a large role in the response of the system as discussed in Section 3.1.1. Reduction in bare frame drift demands in the damaged frame series with 4PB infill were equivalent to the reductions seen in damaged frame 2PB series.

Recast Frame Series Comparison

A strong, positive, linear relationship between drift ratio and PGV was also observed during recast frame series with wood infills (Figure 4-6). Force-drift plots from each recast frame series are provided in Figure D-102 through Figure D-104, displaying linear response that delineates near immediate infill engagement within recast frames. The recast concrete created uniform bearing surfaces at infill edges that better engaged the infills, reducing or even eliminating infill slip. Recast frames with wood infills reduced the drift demands of a pristine bare frame approximately according to the following equation:

$$DR_{infill,Pristine} = DR_{bare} * \frac{1}{2*n} \quad \text{(Equation 4-2)}$$

where:

$DR_{infill,Pristine}$ *= Story drift ratio of pristine frame with wood infill (%) at a given PGV*

DR_{bare} *= Pristine, bare frame story drift ratio (%) from Series F1-B at a given PGV*

$n =$ *Number of infill panels (1 or 2)*

The same caveat applied to Equation 4-1 regarding the 4PB series applies here: Series F2-R-C-4PB approximately matched the drift demands of Series F2-R-C-2PB at all PGVs.

The recasting procedure performed on Frame 2 was effective in returning the frame to a nominally pristine condition. The higher strength concrete used to recast portions of the columns increased the peak force the frame could develop from 24 kips to 30 kips (Figure 3-48). At all PGVs the drift ratios of the recast frame without infill (Series F2-R-C) were similar to the original frame in nominally identical condition (Series F1-C) (Figure 3-47). Frame deformability is

arguably more important to discussions of seismic response than strength. Similar drift ratios mean similar stiffnesses of the frames without infill. This similarity of drift demand supports that the recast frame may be discussed as nominally equivalent to a pristine frame.

4.2.2 Drift Demands Relative to Masonry Infilled Frames

The drift demands of frames with wood infill are next discussed relative to drift demands of frames with masonry infill. Test series with wood infills are categorized by net infill thickness.

Drift Demands of Series with 4PB infills

Figure 4-8 displays the peak in-run drift ratio relative to PGV for the damaged and recast frame series with 4PB infills. The net thickness of the 4PB wood infill was 2.81", about 75% of the gross thickness of the masonry infill (3.6") and nearly equivalent to the masonry net thickness (2.7"), which discounted for the hollow portions of the clay bricks. The modulus of elasticity of the 4PB wood infill ($E_w \approx 460\ ksi$) was less than one-third that of the modulus of the masonry infill ($E_m \approx 1400\ ksi$ as estimated by Monical).

At low PGVs, the damaged frame series with 4PB infills decreased bare frame drift demands approximately half as much as the masonry infilled frames. As the ground motion intensity increased, drift demands of Series F2-C-4PB became closer to those of the masonry series but were never equivalent. This can be attributed to slower stiffness decay of the wood infills relative to the masonry, as discussed in Section 4.4. Drift demands measured during Series F2-R-C-4PB were similar to drift demands of frames with masonry infills. While the 4PB infills were near as effective in reducing drift demands as masonry infills, neither 4PB infilled series reduced drift demands significantly more than their 2PB infilled cousins.

Drift Demands of Series with 2PB infills

Series F1-C-2PB reduced the drift demands of the bare frame by approximately one-half (Figure 4-9) at low PGVs, matching the typical reduction of drift demand from Series F2-C-4PB. At PGVs above 6 in/s, drift demands of the damaged frame series with 2PB infill were similar to the highest drift demands observed in frames with masonry infill. Series F2-R-C-2PB reduced drift demands to approximately equal to or below the drift demands of frames with masonry infill.

Beyond the 6 in/s PGV threshold, Series F2-R-C-2PB reduced the drift demand of the bare frame approximately 1.5 times more than frames with masonry infill.

The net thickness of the 2PB infill was half that of the masonry infill, and E_w was less than one-third E_m. A first guess reached by multiplying the modulus of elasticity by net thickness might suggest the masonry infills should have been 6 times stiffer than the 2PB wood infill. Yet no secant stiffness of a masonry infilled series was greater than 4.0 times larger than the stiffness of the damaged frame 2PB series and 2.5 times larger than that of the recast frame 2PB series. This heightened relative stiffness can be attributed the shear and tensile loads that masonry cannot easily carry. The aspect ratio of the test frames increased the relevance of shear to infill behavior. The peak empirical shear strength of type-N mortar was approximately 80 psi from shear coupon tests performed by Monical (2022). The design shear strength for a 3/4" rated sheathing panel ranges from 180 psi to 240 psi based on the quality of the panel (Douglas Fir Plywood Association, 1948) and the USDA working shear stress limit for through-the-thickness shear on American plywood products (Wilson, 1934). These working stress values, while dated, are close to the nominal stress limits for 3/4" rated sheathing panel with 3" edge fastener spacing provided in modern design as 1330 pounds per linear foot of panel, or about 186 psi (NDS, 2015). It is commonly assumed that concrete or mortar can carry no tensile load, a load easily carried by the fibers in wood panels. The conclusion drawn is that the tensile and shear capacities of the mortar were surpassed early during testing, and little stiffness beyond compression stiffness was engaged. In the wood infills, the shear and tensile capacities were rarely surpassed, and the in-plane stiffness of the wood reacting to all three load types contributed to the infill stiffness.

Drift Demands of Series with 1PB infills

The peak drift demands of the damaged frame with 1PB wood infill are plotted on Figure 4-10. The infill failed in the final run of Series F1-C-1PB, as shown by the peak drift demand being near identical to that of a bare frame. There is little to distinguish the drift demands of the damaged and recast frame series with 1PB infill at low PGVs. During the highest intensity ground motions, the damaged frame 1PB series reduced drift demands half as much as the masonry infill, while the recast frame series with 1PB infill reduced drift demands nearly as much as the masonry infill. Considering the net thickness of the 1PB infill was approximately 25% of the masonry infill, equivalent drift reduction is a testament to the efficiency of wood infills and a strong commentary

on the inability of masonry infills to maintain in-plane lateral stiffness beyond drift ratios inducing shear cracks. The observed bowing during both 1PB series is of concern during any full-scale test. Framing and interior connection schedules should be carefully designed during any full-scale test to control bowing behavior and develop the full capacity of the 1PB wood infill.

4.2.3 4-Panel Infill Performance

4PB infills did not reduce drifts more than 2PB infills. The performance of the 4PB infills relative to each of the other infills (1PB, 2PB, and masonry) will be quantified through normalized variables, and a theory explaining the decreased infill efficiency will be offered.

Relative infill efficiency is measurable via the secant stiffness (K_{secant}) during each run normalized by the net thickness of the infill. The net thickness of the masonry infill was taken as 2.71", and as 0.70" times the number of panels forming a given wood infill. Plotting the thickness-normalized stiffness against the peak drift ratio displays the infill efficiency after having sustained a given drift. During damaged frame series (Figure 4-11), 1PB and 2PB infills developed at least equivalent normalized lateral stiffness as masonry infills beyond drift ratios of 0.4%. There is an approximate 10 $\frac{kip}{in}$ decrease in normalized K_{secant} from 1PB to 2PB, though this decrease pales in comparison to the decrease to the thickness-normalized 4PB K_{secant}. At all drift ratios, the normalized K_{secant} of Series F2-C-4PB is at least 30 $\frac{kip}{in}$ lower than the 2PB series, a minimum 50% decrease in stiffness per unit thickness. During recast frame series (Figure 4-12), the 1PB and 2PB series thickness-normalized K_{secant} were at or above the masonry infilled series for all drift ratios. The loss in stiffness from 1PB to 2PB was consistently 25 $\frac{kip}{in}$. The 4PB infill was equivalent to masonry infilled series in normalized K_{secant} above of drift ratios of 0.15%, but again at most 50% of the 1PB and 2PB normalized K_{secant}. Figure 4-11 and Figure 4-12 present wood as a more efficient material per unit thickness at developing lateral stiffness and a more durable material after sustaining high drift ratios than traditional unreinforced masonry. These plots also highlight the diminishing returns of infill laminations beyond two panels in thickness. This second conclusion matches that previously found in terms of drift demands.

The metrics of drift demands and normalized K_{secant} agree that the performance of the 4PB infills was no better than 2PB infills. Both measures could be confounded by differences in drifts prior to infill engagement: the "slip" of infills, an occurrence highlighted during the summary

of Series F2-C-4PB (Section 3.1.1). The region of force-drift plots when infills were not fully engaged will now be removed entirely from discussion to see if the diminishing stiffness returns of 4PB infills remain when the instantaneous peak stiffness is compared. The extreme sensitivity of the load cell made a consistent method for finding instantaneous stiffness from load cell-based force-drift plots unreasonable. Instead, force-drift plots were generated from the frame top beam accelerometer data (units of g) multiplied by the effective mass of 49 kips. The data from ADXLs was trimmed and filtered (see Appendix B.3: Accelerometers) to provide smoothed force-displacement curves, which could be derived to find an approximation of instantaneous stiffness. The procedure performed in each test is illustrated in Figure 4-13. First, any data point occurring at a drift less than 50% of the peak drift was removed such that only points when the infill was fully engaged were studied. Second, points corresponding to unloading cycles were removed. Finally, the slope between points 0.05 seconds apart was calculated and the instantaneous stiffness plotted. The procedure was carried out for all wood infilled series during the first run at 40%, 60%, and 80% intensities.

The results of are summarized in Table 4-1 and Figure 4-14. A 40 $\frac{kip}{in}$ increase in peak instantaneous stiffness existed between Series F1-C-1PB and F1-C-2PB. After recasting, the increase from Series F2-R-C-1PB to F2-R-C-2PB was approximately 60 $\frac{kip}{in}$. Part of this instantaneous stiffness increase came from the recast frame itself (Figure 4-7). There was no large increase in peak in-run instantaneous stiffness from 2PB to 4PB infills during either the damaged or recast frame series.

Observations of drift demands, normalized secant stiffnesses, and peak instantaneous stiffness each support the conclusion that the 4PB infills were no stiffer than 2PB infills during dynamic testing. The question raised is how force was transferred to each panel of a screw laminated infill. Loads can be transferred in plywood panels across plies bonded with adhesive from panel construction, but the screw-lamination pattern used in this experimental program was only sufficient to brace infills against buckling. If each panel forming a multi-layered infill was directly loaded at least at one point, forces were transferred through the intra-ply adhesive. Figure 4-15 shows a section of the ideal shim-based edge connection in a typical 4PB and 2PB construction, with contact areas highlighted. In the 4PB construction, widths of the two center panels did not bear on the columns, while the 2PB bearing edge-joint created contact across the

entire infill edge. As the edge-joint deteriorated with runs of increasing intensity, the force transfer from column to infill only became more inconsistent.

The trend that 4PB thickness infills did not engage each of the four panels equally is supported by plots of load versus midspan deflection from 4-point bending beam tests described in Section 2.3. The flexural stiffness of each beam is defined by the slope of the plot in Figure 4-16. From basic mechanics, doubling the thickness of a rectangular beam should also double the moment of inertia and flexural stiffness. During the 4-point bending tests, 2PB beam data grouped with little scatter at an average flexural stiffness of 115 $\frac{kip}{in}$. In 2PB beams, any eccentric load due to panel edge incongruities would twist the section out of plane until the second panel contacted the roller and was engaged. The slopes of the 4PB specimens did not group, beam 4PB-2 was at 190 $\frac{kip}{in}$ and beam 4PB-1 was at 240 $\frac{kip}{in}$. If each panel thickness delivered about 60 $\frac{kip}{in}$ of flexural stiffness in the 4-point bending test, then specimen 4PB-1 engaged all four panels while 4PB-2 only engaged the three. In determining the contact points on the 4PB beams, edge profiles directly above the roller supports were created with thin metal wires, displaying the bearing edge-joint incongruities that caused uneven loading of the four laminated panels (Figure 4-17). Beam 4PB-1 had one incongruity at roller supports across the full width of the panel. Even edges created contact with all four panels at both roller supports after loads were applied. Beam 4PB-2, which developed the flexural stiffness of approximately three panels, was constructed with uneven edges above both supports as shown by the wire profiles.

Each beam was also backlit using a bright flashlight in both its unloaded and loaded state to confirm contact of panels in all beams (Figure 4-18). Lengths of the beams not contacting the roller allowed the backlight through, while areas contacting the roller appear blacked out. Beams 2PB-1, 2PB-2, and 4PB-1 all deformed at supports to form at least one contact point to each of the panels forming the infill thickness (Figure 4-19 through Figure 4-21). Beam 4PB-2 retained a full-panel thickness that did not contact the roller after loading and thus could not develop the stiffness of the one panel (Figure 4-22). Load flows first to the stiffest resisting member, therefore an open edge-gap between a panel and bearing surface cannot transfer load.

4.2.4 Note on Failures of 1PB Wood Infills

In both 1PB infilled series, infills exhibited brittle failures associated with large out-of-plane bowing (Figure 3-18). Both failures were vertically oriented and located at a distance 8" from the north column edge, in line with the first gridline of screw laminations. The failures did not occur at similar lateral forces or base motion intensities: 30 kips (Series F1-C-1PB at 80% intensity) compared to 47 kips (Series F2-R-C-1PB at 100% intensity). Both failures occurred as the frames exceeded an in-run drift ratio of approximately 1.5% (Figure 3-42 and Figure 3-43).

4.2.5 Local Deformations of Wood Infills

Wood infill deformations caused by frame drifts were distributed non-uniformly. Unlike in masonry infills, the wood infills were loaded in tension via the dowel-type edge connections of clamp rods (see Figure 2-29 (a)). Northern edge infill deformations were studied during four series (F1-C-1PB, F2-R-C-4PB, F2-R-C-2PB, and F2-R-C-1PB). It was observed that drifts inducing tension in the top of northern infill edge magnified infill edge deformations compared to deformations at the infill centerline (Figure 3-25, Figure 3-29, Figure 3-33, and Figure 3-45). Deformation magnification (defined as $\frac{Edge\ Deformation}{Centerline\ Deformation}$) was reduced with increasing infill thickness, decreasing from a magnification of 1.7 during Series F2-R-C-1PB to 1.1 during Series F2-R-C-4PB (Figure 4-23). Shear capacity design tables for plywood panels are rated by edge nailing schedule (APA, 2019), confirming that the critical nature of panel edge behavior is well known. Confirmation of large deformation magnification at edges of a 64"x40" infill purport even greater influence of edge deformations during a full-scale test.

4.3 Infilled Frame Natural Periods

4.3.1 Methods for Estimation of Natural Period

Natural period was estimated two ways: Secant period (T_{secant}) and the Phase Difference Index (PDI) period (T_{PDI}) (Cheng, 2017). T_{secant} was calculated according to the circular natural frequency associated with the secant stiffness (Figure 4-1) and effective mass (Table 2-2), converted to period according to the relation $T_{secant} = 2 * \pi * \sqrt{\frac{mass}{K_{secant}}}$. Secant period describes

the response period during the peak drifts. The PDI method is founded on the basis that the roof and base of a SDOF oscillator will displace in the same direction (phase angle less than 90°) while responding at frequencies below the resonant frequency and will displace in opposite directions (phase angle greater than 90°) during response at frequencies above the resonant frequency. The phase angle is independent of amplitude of motion. The natural frequency of a given system occurs at the frequency where the cosine of the phase angle relating roof and base acceleration histories crosses zero. Using uniaxial in-plane acceleration records from ADXL accelerometers on the top and foundation beams, the phase angle at 100 frequencies between 1 Hz and 10 Hz were plotted using a custom MATLAB function written by Cheng (2017). An example plot of the cosine of the phase angle for Frame 2 Run 130 (Series F2-R-C-2PB) is provided in Figure 4-24, with the zero-crossing point and natural frequency marked. T_{PDI} is defined by the inverse of the zero-crossing period interpolated between the closest frequencies to the crossing. Typical input parameters used for PDI analysis of runs are provided in Table 4-2. T_{secant} and T_{PDI} during the first run at each ground motion intensity for all series are listed in Table 4-3.

Both estimates of period are generally within ±0.05 seconds of each other (Figure 4-25). Six out of thirty-eight data points fall outside this range: three runs of Series F2-C-4PB, two runs of Series F1-M-C, and one run of Series F1-C-1PB. T_{PDI} is greater than T_{secant} in all instances. Infill slip during Series F2-C-4PB (see Section 3.1.1) explains that during response to high intensity ground motions, the infill was not fully engaged and the PDI method was measuring a natural period closer to that of a frame without infill. Alternatively, the secant period considers the peak drift, which is affected by the region of maximum infill engagement. The same logic explains the runs from Series F1-M-C in which $T_{PDI} > T_{secant}$, as the first full width shear crack through infill mortar formed prior to the first run in which T_{PDI} is more than 0.05 seconds larger than T_{secant}. During Series F1-C-1PB, the 1PB infill split through the full thickness during the first drift of the run. As this first drift was the response on which T_{secant} was calculated, it is no surprise that the natural period of the structure during the remainder of the run was much larger. Fourier Spectra were not used in the estimation of natural period due to the repeated smoothing required to determine a natural period from the ratio of roof to base Fourier Spectra amplitudes. Smoothing would have reduced precision of period estimates below that provided by the PDI method. The PDI method provided an estimate of response period from all series with great fidelity beyond the response period during peak load and peak drift as given by T_{secant}. The true behavior of the

infilled frames during ground motions is best represented by some average of the two methods described, as the methods are built on varying assumptions. The response period of frames with wood infills will be discussed in comparison to the pristine bare frame from Series F1-B, and the masonry infilled frame from Series F1-M-C (see Table 4-4).

Damaged Frame Response Periods

The initial T_{PDI} of the damaged frame with 1PB infill was 0.26 seconds, slightly lower than the approximate 0.28 second initial period of the pristine bare frame (Figure 4-26). The response period increased approximately linearly to a maximum of 0.46 seconds during Series F1-C-1PB. The increase in period with ground motion intensity nearly matched the trend found in the pristine bare frame after concrete cracking. As there is no decrease in period associated with the application of external post-tensioned clamps, the single-panel infill retrofit restored the damaged concrete frame to near that of a pristine bare frame, one hallmark of a successful retrofit. The initial period of Series F1-C-2PB was 0.19 seconds, and the maximum period was 0.29 seconds (Figure 4-27). The damaged frame 2PB infill reduced the initial T_{PDI} of the pristine bare frame two-thirds as much as the masonry infill. The 2PB infill was an excellent retrofit to the damaged frame; it was easily constructed, lightweight, and lowered the system natural period. At any given PGV, T_{PDI} of the damaged 2PB series was about 0.08 seconds lower than the damaged 1PB series. The lowest recorded period during Series F2-C-4PB was 0.20 seconds, similar to the two-panel infilled frame (Figure 4-28). The period of the damaged 4PB series matched that of the damaged 1PB series between PGV's of 2 in/sec and 5 in/sec, but plateaued at $T_{PDI} = 0.38\,sec$ as ground motion intensity increased. This increase in period at low PGVs can be attributed to the mortar-filled bearing edge-joint deteriorating and the infill sliding, and the plateau forming as the infill was engaged during large drifts.

All damaged frames with wood infill reduced the initial T_{PDI} below that of a pristine bare frame. The 2PB and 4PB infills reduced the damaged frame initial T_{PDI} about two-thirds as much as a traditional masonry infill.

T_{PDI} and T_{secant} are normalized by the periods of Series F1-B during matching ground motions in Figure 4-29. The discrepancy in shape between the plots in Figure 4-29 is a function of the bare frame T_{PDI} during the lowest intensity motions being about one and a half times larger than T_{secant}. The pair of bare frame period curves converged as PGV increased. Masonry infills

reduced the bare frame T_{PDI} by 60% during low intensity ground motions and 40% during high intensity ground motions (Figure 4-29 (a)). Within a damaged frame, the 2PB infill reduced the bare frame T_{PDI} by approximately 40% during the most intense ground motions, and the 1PB reduced the bare frame T_{PDI} by 15%. The reduction in T_{secant} due to masonry infills was consistently near 50% of the bare frame (Figure 4-29 (c)). Wood infills reduced T_{secant} of the pristine bare frame by up to 40% in 2PB and 4PB test series, and 20% in the 1PB test series. Using both metrics for period, the 2PB infill was only slightly less effective in reducing frame period in a severely damaged frame than a masonry infill in a minorly damaged frame during the most intense ground motions.

Recast Frame Response Periods

The initial periods of Series F2-R-C-1PB, F2-R-C-2PB, and F2-R-C-4PB were approximately 0.19, 0.14, and 0.14 seconds respectively. T_{PDI} increased nearly linearly with respect to PGV in all recast frame series. The 1PB series increased to a maximum period of 0.28 seconds linearly at a PGV of 8.4 in/sec, approximately matching T_{PDI} of the frame with masonry infill (Figure 4-26). A response period at or below 0.20 seconds was maintained during the entirety of Series F2-R-C-2PB (Figure 4-27) and F2-R-C-4PB (Figure 4-28). As in the damaged frame series comparison, there was no additional reduction in T_{PDI} between the 2PB and 4PB infills. Both test series' natural periods were less than the natural period of the masonry-infilled frame above PGVs of 3 in/sec. Masonry infills greatly decreased natural period initially, but mortar failure increased the period during low intensity ground motions, a trend further discussed in Section 4.4.

The reduction in bare frame period provided by infills in nominally pristine frames was equivalent to or greater than that of the masonry infills. All three react frame series with wood infills series reduced T_{PDI} of the bare frame beyond the 40% reduction by masonry infills during the most intense ground motions. There was a 50% reduction with the 1PB infill and a 60% reduction with the 2PB infill (Figure 4-29 (b)). Similar magnitude reductions in T_{secant} occurred (Figure 4-29 (d)), though only the 2PB infill reduced the period of the frame more than the masonry infill.

4.3.2 Note on Displacement Spectra

As the response period of the frames changed, so did the representative point on the linear displacement spectra. Displacement spectra derived from foundation beam measured accelerations during a 100% intensity run are displayed in Figure 4-30. Infilled frame natural periods ranged from 0.1 to 0.3 seconds during all test series excluding Series F1-C-1PB (Section 4.3.1). There exists a nearly linear increase in spectral displacement within this range (Figure 4-30), void of large peaks or valleys. It is therefore unlikely that an infilled frame with a lower period in this range would drift the same amount or more than one with a higher period during similar ground motions.

4.4 Stiffness Decay

K_{sec} was normalized with respect to $K_{initial}$ and plotted against drift ratio in Figure 4-31 for damaged frame series and Figure 4-32 for recast frame series. The stiffness decay rates of masonry-infilled frames (series F1-M-C and F2-M) were by far the fastest of all series studied. The secant stiffness of these series is less than half of $K_{initial}$ at a drift ratio of 0.15%. Beyond drift ratios of 0.35%, after shear cracks had developed either in the frame columns or through the infill mortar, the normalized K_{sec} was $0.3 * K_{initial}$ and plateaued to $0.15 * K_{initial}$. While improved from the masonry infilled frames, the pristine bare frame presents the second fastest decay of lateral stiffness. Half of $K_{initial}$ had decayed by a 0.43% drift, and a plateau forms at $0.15 * K_{initial}$ beyond 2% drift. The rate of decay of the pristine frame was exponential, but less steep than that of the masonry infilled frame. These results agree in trend with the stiffness decay curves presented by Marinkovic & Butenweg (2019) and Van & Lau (2021), though the numerical breakdown of stiffness decay curves are specific to given test setups.

Wood infill series decayed linearly with respect to drift ratio. Below drift ratios of 0.75%, all wood infills maintained a normalized stiffness of approximately $0.7 * K_{initial}$. The only data points that fell below $0.5 * K_{initial}$ occurred during 1PB series after the infills had sustained damage or failed. This drift limit on stiffness decay beyond 50% $K_{initial}$ of is approximately ten times larger than the drift limit for masonry infilled frames, and three times larger than during the bare frame series, highlighting the stability of response provided by wood infills. Linear decay occurred in stark contrast to the bare frame and masonry infills, which decayed exponentially in

all masonry infilled series mentioned in this study (see Section 1.2.4). Rates of stiffness decay for frames with masonry infill were a function of variables such as mortar integrity and masonry unit selection while the wood infills decayed only as the bond between plywood fibers failed. The integrity of the mortar defined the stiffness of the masonry infills in Series F1-M-C and F2-M; as a continuous infill, the plywood panels maintained stiffness better across multiple ground motions at varying intensities.

Normalized stiffness is a valuable tool for discussion of relative infill performance but does not consider differences in true stiffness. The true secant stiffness of all test series at relevant drift ratios is described in Table 4-5. The frame with masonry infill developed by far the highest initial secant stiffness at approximately $500\frac{kips}{in}$. This supports the assumption that prior to incurring damage, frames with masonry infill are far stiffer than those with wood infills. Still, the rapid decay of masonry infill remains clear. At a drift ratio of 0.25% two recast frames with wood infills were equivalently as stiff as the frame with masonry infill. At a 1.0% drift ratio, the frame with masonry infill was less stiff than all recast frames with wood infill and only marginally stiffer than damaged frames with wood infills. Equivalence of secant stiffness supports the observation of similar reduction of drift demands between series with different infills in Section 4.2.

5. CONCLUSIONS

Good seismic response is defined by low drift demands, high drift capacity, and stable response. This study focused on the first criteria: the relative reduction in drift demands of reinforced concrete frames with masonry infills and with wood infills. Frames with masonry infills developed initial stiffnesses higher than frames with wood infills. After the initial stiffness of masonry infills decayed during the most intense simulated ground motions, frames with masonry and wood infills reduced drift demands comparably.

The key conclusions drawn in this study are applied within the following parameters:

PARAMETER	DESCRIPTION
Frame Bay	Rectangular
Infill Shape	Full bay
Frame Initial Period	$0.1 \text{ sec} \leq T_{initial} \leq 1.0\ sec$
Infill Thickness	$t_{infill} > \frac{1}{12} * column\ width$
Infill Material	APA certified Panel(s), Group 1 Plywood
Plywood Performance Category	At least 23/32 Rated Sheathing or equivalent
Plywood Performance Standard	PS 1-09, PRP-108
Plywood Bond Classification	Exterior (C-C sheathing grade), or Exposure 1 without long-term weather/moisture exposure
Infill Panel Continuity	Continuous wood panels without interior splices
Bearing Edge-Joint	Solid and uniform edge-joint, no larger than 3/8" wide

The key conclusions drawn from this experimental program are:

- Per unit net thickness, wood panel infills were more efficient at reducing drift demands than unreinforced masonry infills.

- Bearing at infill edges was critical to the seismic response of wood panel infilled frames. Strains in wood panel infills were concentrated near the columns, and edge connections must be designed with care to prevent local panel failure.

- There were diminishing returns of lateral stiffness from the construction of screw-laminated wood panel infills of increasing thickness with the edge-joints constructed in this test setup. Four-panel infills did not display higher secant or instantaneous lateral stiffnesses than two-panel infills.

- The stiffness decay of wood panel infills was nearly linear with respect to drift demand and slower than the exponential stiffness decay in bare and masonry infilled frames. The drift ratio at which a 50% of the initial system stiffness had decayed was approximately 10 times larger in wood panel infilled frames (1.5%) than masonry infilled frames (0.15%).

- External-post tensioned clamps increased column drift capacity and provided a dowel connection between wood infills and reinforced concrete columns, an advantageous setting in wood panel infill seismic retrofits that allowed coupling of wood and concrete.

- Peak drift demands increased nearly linearly with respect to peak base velocity (PGV) in all test series.

The conclusions drawn are promising with regards to the response of wood panel infills as a retrofit in non-ductile reinforced concrete frames. A full-scale experimental study of the seismic behavior of wood panel infills should be explored.

REFERENCES

Ancheta, T. D., Darragh, R. B., Stewart, J. P., Seyhan, E., Silva, W. J., Chiou, B. S.-J., . . . Donahue, J. L. (2014). *NGA-West2 Database*. Earthquake Spectra, 30(3), 989-1005.

American Wood Council (AWC) (2017) *National Design Specification for Wood Construction.* AWC, Leesburg, VA.

APA (2020). *Panel Design Specification.* Form No. D510. APA – The Engineered Wood Association. Tacoma, WA.

APA (2019). *Engineered Wood Construction Guide*. APA – The Engineered Wood Association. Tacoma, WA.

APA (2016) *Double-Sheathed Shear Walls*. Technical Topics 115. APA – The Engineered Wood Association. Tacoma, WA.

ASTM (2020) *ASTM C39/C39M-20, Standard Test Method for Compressive Strength of Cylindrical Concrete Specimens"* ASTM International, West Conshohocken, PA.

ASTM (2017) *ASTM 4969/C496M-17, Standard Test Method for Splitting Tensile Strength of Cylindrical Concrete Specimens"* ASTM International, West Conshohocken, PA.

AWC (2018) *National Design Specification (NDS) for Wood Construction.* American Wood Council. Leesburg, VA.

Blaylock, Jeffrey R. L. (2012). *Wood Infill Walls in Reinforced Concrete Frame Structures: A Wood/concrete Construction Niche*. The University of Western Ohio. Electronic Thesis and Dissertation Repository. 888. https://ir.lib.uwo.ca/etd/888

Cheng, L. H. (2017). *Phase Difference Index: A Frequency-Domain Analysis Tool for Structural Mode Identification (PhD Thesis).* Purdue University. West Lafayette, IN.

Douglas Fir Plywood Association (1948). *Technical Data on Douglas Fir Plywood for Engineers and Architects.* Tacoma, WA.

Eriksson, E. (2003). *Wood Components in Steel and Concrete Buildings – In-fill Exterior Wall Panels.* Nordic Timber Council. Retrieved from

Fiorato, A. E., Sozen, M. A., & Gamble, W. L. (1970). *An investigation of the interaction of reinforced concrete frames with masonry filler walls.* Technical report no. UILI-ENG70-100, University of Illinois at Urbana-Champaign, Urbana, IL.

Gulkan, P., & Sozen, M. A. (1971). *Response and Energy-Dissipation of Reinforced Concrete Frames Subjected to Strong Base Motions.* Civil Engineering Studies, Structural Research Series, University of Illinois at Urbana-Champaign, Vol. 377, Urbana, IL

Nievinski, F. G. (2022) *subtightplot*. MATLAB Central File Exchange. Htttps://www.mathworks.com/matlabcentral/fileexchange/39664-subtightplot. Retrieved January 5, 2022.

Marinković, M. & Butenweg, C. (2019) *Innovative Decoupling System for the seismic protection of masonry infill walls in Reinforced Concrete Frames.* Engineering Structures. Vol 197.

MATLAB. (2018). *Version 9.5.0 (R2018b).* The MathWorks Inc. Natick, Massachusetts.

Monical, J. (2022). *A Study of the Response of Reinforced Concrete Frames with and without Masonry Infill Walls to Simulated Earthquakes (PhD Thesis).* Purdue University. West Lafayette, IN.

NaturalPoint Inc. (2021) *Optitrack – motion capture systems.* Available at: http://optitrack.com/

NDS - Special Design Provision for Wind and Seismic (2015). American Forest & Paper Association, Inc. & American Wood Council.

Northern Digital, Inc. (2021). *NDI Legacy Products.* Available at: http://www.ndigital.com/products/legacy-products/

Pollalis, W (2021). *Drift Capacity of Reinforced Concrete Walls with Lap Splices (PhD Thesis).* Purdue University. West Lafayette, IN.

Skillen, K. C. (2020). *The Effects of Transverse Reinforcement on the Strength and Deformability of Reinforced Concrete Elements (PhD Thesis).* Purdue University. West Lafayette, IN.

Smith, B. S. (1966), *Behavior of square infilled frames.* Journal of the Structural Division: ASCE 192(1): 381-403.

Sozen, M. A., Otani, S., Gulkan, P., & Nielsen, N. N. (1969). The University of Illinois Earthquake Simulator. *Proceedings of the Fourth World Conference on Earthquake Engineering*, (pp. 139-150). Santiago, Chile.

Stazi, F., Serpilli, M., Maracchini G., & Pavone, A. (2019) *An experimental and numerical study on CLT panels used as infill shear walls for RC buildings retrofit*. Construction and Building Materials, Volume 211 (pp 605-611).

The Masonry Society (2016). *Building Code Requirements and Specification for Masonry Structures.* TMS 402/602. Longmont, CO.

Van, T. C. & Lau, T. L (2021). *Experimental Evaluation of Reinforced Concrete Frames with Unreinforced Masonry Infills under Monotonic and Cyclic Loadings.* International Journal of Civil Engineering. Vol 19. (pp 401-419).

Wilson, T. R. C. (1934). *Guide to the Grading of Structural Timbers and the Determination of Working Stresses.* USDA Miscellaneous Publication 185. United States Department of Agriculture.

TABLES

Table 2-1: Ground Motion Parameters for 100% Intensity NS El Centro Record, Unscaled and Scaled

Record	RSN	Direction	Unscaled					
			PGA (g)	PGV (in/sec)	PGD (in)	time step (sec)		
1940 El Centro	6	NS	0.28	12.2	3.41	0.01		
Record	**RSN**	**Direction**	**Scaled (100% Intensity)**				F_{tc}[1]	**Amplitude Scaling Factor[2]**
			PGA (g)	**PGV (in/sec)**	**PGD (in)**	**time step (sec)**		
1940 El Centro	6	NS	0.53	11.6	1.62	0.005	2.00	1.90

Table 2-2: Effective Mass Breakdown of Frame-External Mass System (In-Plane)

Component	Mass, lbf
RC block (external, suspended mass)	44,500
Hardware	2,500
RC frame (top beam plus half of RC columns)	1,900
Total	48,900

[1] Time compression factor
[2] Amplitude scaled such that target ground motion PGV was below simulator velocity limit (12 in/sec)

Table 2-3: Series Testing Dates and Concrete Age

Specimen	Series	Dates Tested	Original Concrete Age (days)	Recast Concrete Age (days)
F1	F1-B	2020.01.06 - 2020.01.16	129	-
	F1-C	2020.01.19 - 2020.01.20	142	-
	F1-M-C	2020.03.05 - 2020.03.11	188	-
	F1-M-C-OOP	2020.06.18 - 2020.06.25	293	-
	F1-C-2PB	2021.05.05 - 2021.05.06	615	-
	F1-C-1PB	2021.06.01	642	-
F2	F2-C	2020.08.03 - 2020.08-12	339	-
	F2-M	2020.09.07 - 2020.09.08	374	-
	F2-M-C-S	2020.09.11	378	-
	F2-C-S	2020.09.14	381	-
	F2-C-4PB	2021.03.05 - 2021.03.24	554	-
	F2-R-C-4PB	2021.07.12	683	25
	F2-R-C-2PB	2021.07.19	690	32
	F2-R-C-1PB	2021.07.26	697	39
	F2-R-C	2021.07.26	697	39

Table 3-1: Summary of Series F1-B (Monical, 2022)

Frame Run Number	Test ID	PGA[1], g	PGV[2], in/sec	PGD[3], in	Peak in-run drift ratio[4], %	Peak base-shear coefficient[5]
1	F1-B-10-1	0.1	1.3	0.17	0.12	0.15
2	F1-B-10-2	0.1	1.4	0.17	0.13	0.14
3	F1-B-10-3	0.1	1.3	0.18	0.14	0.17
4	F1-B-20-1	0.2	3.0	0.70	0.34	0.27
5	F1-B-10-4	0.1	1.3	0.17	0.25	0.15
6	F1-B-10-5	0.1	1.5	0.18	0.24	0.15
7	F1-B-20-2	0.2	2.2	0.34	0.56	0.33
8	F1-B-40-1	0.3	4.5	0.57	1.10	0.49
9	F1-B-40-2	0.2	4.7	0.68	1.18	0.47
10	F1-B-60-1	0.3	7.1	0.84	1.68	0.49
11	F1-B-60-2	0.4	6.9	0.88	1.93	0.46
12	F1-B-80-1	0.4	8.2	1.11	2.58	0.47
13	F1-B-80-2	0.4	8.1	1.10	2.26	0.44
14	F1-B-40-3	0.2	4.9	0.58	1.37	0.24
15	F1-B-40-4	0.3	5.1	0.61	1.36	0.24

[1] Obtained from measurements of ADXL accelerometers mounted on base of specimen
[2] Obtained from measurements of ADXL accelerometers mounted on base of specimen
[3] Obtained from measurements of LVDT mounted inside servoram driving simulator platform
[4] Obtained from measurements of LVDTs attached to specimen and measured relative to initial position of specimen at beginning of run
[5] Ratio of peak lateral load obtained from measurements of load cell to effective mass of series (49,000 lbf)

Table 3-2: Summary of Series F1-C (Monical, 2022)

Frame Run Number	Test ID	PGA, g	PGV, in/sec	PGD, in	Peak in-run drift ratio, %	Peak Base-shear coefficient
16	F1-C-10-1	0.1	1.4	0.15	0.45	0.07
17	F1-C-10-2	0.1	1.0	0.15	0.45	0.08
18	F1-C-20-1	0.2	2.1	0.32	0.74	0.14
19	F1-C-20-2	0.2	2.4	0.27	0.72	0.14
20	F1-C-40-1	0.3	4.1	0.52	1.54	0.35
21	F1-C-40-2	0.3	4.2	0.62	1.58	0.36
22	F1-C-60-1	0.3	6.6	0.99	2.09	0.46
23	F1-C-60-2	0.3	6.0	0.89	2.15	0.45
24	F1-C-80-1	0.4	7.8	1.15	2.40	0.47
25	F1-C-80-2	0.4	7.8	1.10	2.34	0.45
26	F1-C-100-1	0.5	9.5	1.34	2.91	0.45
27	F1-C-100-2	0.5	9.8	1.32	2.95	0.44
28	F1-C-80-3	0.4	8.1	1.06	2.59	0.42
29	F1-C-80-4	0.4	8.2	1.08	2.58	0.42
30	F1-C-60-3	0.3	6.5	0.77	2.14	0.35
31	F1-C-60-4	0.3	6.7	0.77	2.17	0.35
32	F1-C-40-3	0.3	4.6	0.54	1.45	0.21
33	F1-C-40-4	0.3	4.8	0.56	1.45	0.21
34	F1-C-20-3	0.2	2.5	0.30	0.78	0.09
35	F1-C-20-4	0.2	2.4	0.25	0.79	0.09
36	F1-C-10-3	0.1	1.3	0.18	0.43	0.04
37	F1-C-10-4	0.1	1.3	0.19	0.43	0.04

Table 3-3: Summary of Series F1-M-C (Monical, 2022)

Frame Run Number	Test ID	PGA, g	PGV, in/sec	PGD, in	Peak in-run drift ratio, %	Peak Base-shear coefficient
38	F1-M-C-10-1	0.19	2.0	0.51	0.07	0.27
39	F1-M-C-10-2	0.15	1.8	0.44	0.07	0.27
40	F1-M-C-20-1	0.16	2.9	0.37	0.12	0.39
41	F1-M-C-20-2	0.16	3.0	0.35	0.13	0.33
42	F1-M-C-40-1	0.26	5.9	0.67	0.34	0.52
43	F1-M-C-40-2	0.29	5.4	0.53	0.51	0.63
44	F1-M-C-60-1	0.43	7.7	0.85	0.73	0.71
45	F1-M-C-60-2	0.37	6.9	0.84	0.75	0.74
46	F1-M-C-80-1	0.52	9.6	1.09	1.03	0.88
47	F1-M-C-80-2	0.51	8.2	1.10	1.12	0.86
48	F1-M-C-60-3	0.38	6.5	0.83	0.94	0.58
49	F1-M-C-60-4	0.37	6.5	0.84	0.98	0.61
50	F1-M-C-40-3	0.28	4.5	0.54	0.76	0.35
51	F1-M-C-40-4	0.28	4.6	0.55	0.78	0.36
52	F1-M-C-20-3	0.19	2.5	0.29	0.52	0.17
53	F1-M-C-20-4	0.20	2.6	0.29	0.52	0.18
54	F1-M-C-10-3	0.13	1.4	0.14	0.28	0.06
55	F1-M-C-10-4	0.13	1.4	0.16	0.29	0.06
56	F1-M-C-80-3	0.47	8.4	1.08	1.29	0.77

Table 3-4: Summary of Series F1-M-C-OOP (Monical, 2022)

Frame Run Number	Test ID	PGA, g	PGV, in/sec	PGD, in	Peak in-run drift ratio, %	Peak Base-shear coefficient
57	F1-M-C-OOP-10-1	0.13	1.4	0.15	0.23	0.01
58	F1-M-C-OOP-10-2	0.13	1.4	0.15	0.24	0.02
59	F1-M-C-OOP-20-1	0.18	2.5	0.28	0.45	0.03
60	F1-M-C-OOP-20-2	0.19	2.4	0.27	0.46	0.03
61	F1-M-C-OOP-40-1	0.28	4.8	0.55	0.90	0.06
62	F1-M-C-OOP-40-2	0.28	4.6	0.54	0.96	0.06
63	F1-M-C-OOP-60-1	0.36	7.2	0.84	1.40	0.09
64	F1-M-C-OOP-60-2	0.36	7.0	0.83	1.48	0.09
65	F1-M-C-OOP-80-1	0.42	9.0	1.09	1.69	0.12
66	F1-M-C-OOP-80-2	0.42	9.4	1.11	1.77	0.12
67	F1-M-C-OOP-100-1	0.50	10.8	1.36	2.00	0.14
68	F1-M-C-OOP-100-2	0.49	11.0	1.41	2.02	0.14
69	F1-M-C-OOP-80-3	0.42	9.4	1.20	1.93	0.12
70	F1-M-C-OOP-80-4	0.43	9.2	1.20	1.99	0.13
71	F1-M-C-OOP-60-3	0.34	6.9	0.85	1.67	0.10
72	F1-M-C-OOP-60-4	0.34	6.7	0.81	1.68	0.10
73	F1-M-C-OOP-40-3	0.26	4.6	0.56	1.26	0.07
74	F1-M-C-OOP-40-4	0.26	4.6	0.54	1.27	0.07
75	F1-M-C-OOP-20-3	0.18	2.4	0.28	0.54	0.02
76	F1-M-C-OOP-20-4	0.18	2.4	0.27	0.54	0.02
77	F1-M-C-OOP-10-3	0.11	1.3	0.16	0.25	0.01
78	F1-M-C-OOP-10-4	0.12	1.3	0.14	0.25	0.01

Table 3-5: Summary of Series F2-C (Monical, 2022)

Frame Run Number	Test ID	PGA, g	PGV, in/sec	PGD, in	Peak in-run drift ratio, %	Peak Base-shear coefficient
1	F2-C-RSN6975-PGV2-1	0.08	2.10	0.38	0.10	0.08
2	F2-C-RSN77-PGV2-1	0.09	2.18	0.23	0.13	0.08
3	F2-C-RSN2114-PGV2-1	0.08	1.96	0.37	0.17	0.10
4	F2-C-RSN6-TC4-PGV2-1	0.16	1.71	0.13	0.33	0.19
5	F2-C-RSN6-TC2-PGV2-1	0.13	1.92	0.24	0.37	0.19
6	F2-C-RSN1051-PGV2-1	0.14	2.06	0.21	0.53	0.27
7	F2-C-RSN95-PGV2-1	0.12	1.71	0.26	0.66	0.33
8	F2-C-RSN6975-PGV2-2	0.11	2.21	0.40	0.31	0.11
9	F2-C-RSN77-PGV2-2	0.10	1.92	0.25	0.37	0.15
10	F2-C-RSN2114-PGV2-2	0.10	1.95	0.40	0.45	0.17
11	F2-C-RSN6-TC4-PGV2-2	0.24	2.11	0.14	0.47	0.20
12	F2-C-RSN6-TC2-PGV2-2	0.14	2.09	0.24	0.55	0.26
13	F2-C-RSN1051-PGV2-2	0.13	1.86	0.20	0.76	0.35
14	F2-C-RSN95-PGV2-2	0.11	1.91	0.26	0.60	0.24
15	F2-C-RSN6975-PGV4-1	0.15	3.76	0.77	0.57	0.23
16	F2-C-RSN77-PGV4-1	0.22	3.72	0.47	0.57	0.26
17	F2-C-RSN2114-PGV4-1	0.12	3.76	0.78	0.71	0.30
18	F2-C-RSN6-TC4-PGV4-1	0.42	3.76	0.28	0.75	0.35
19	F2-C-RSN6-TC2-PGV4-1	0.20	3.83	0.47	1.00	0.44
20	F2-C-RSN1051-PGV4-1	0.22	3.67	0.36	1.25	0.48
21	F2-C-RSN95-PGV4-1	0.17	3.42	0.51	1.53	0.46
22	F2-C-RSN6975-PGV4-2	0.19	3.48	0.74	0.81	0.19
23	F2-C-RSN77-PGV4-2	0.15	3.64	0.48	1.06	0.31
24	F2-C-RSN2114-PGV4-2	0.12	3.90	0.77	1.16	0.35
25	F2-C-RSN6-TC4-PGV4-2	0.33	3.75	0.28	1.32	0.43
26	F2-C-RSN6-TC2-PGV4-2	0.26	4.15	0.45	1.47	0.43
27	F2-C-RSN1051-PGV4-2	0.22	4.24	0.38	1.76	0.46
28	F2-C-RSN95-PGV4-2	0.21	3.64	0.52	0.98	0.22
29	F2-C-RSN6975-PGV6-1	0.25	5.32	1.13	1.24	0.29
30	F2-C-RSN77-PGV6-1	0.22	5.41	0.70	1.59	0.41
31	F2-C-RSN2114-PGV6-1	0.15	5.77	1.14	1.69	0.41
32	F2-C-RSN6-TC4-PGV6-1	0.52	5.05	0.38	2.00	0.45
33	F2-C-RSN6-TC2-PGV6-1	0.31	5.30	0.71	2.02	0.44
34	F2-C-RSN1051-PGV6-1	0.43	5.84	0.56	2.35	0.46
35	F2-C-RSN95-PGV6-1	0.30	5.65	0.75	1.79	0.34
36	F2-C-RSN6975-PGV6-2	0.19	5.34	1.13	1.18	0.18
37	F2-C-RSN77-PGV6-2	0.26	5.31	0.70	1.90	0.38

Table 3-5 (continued): Summary of Series F2-C (Monical, 2022)

Frame Run Number	Test ID	PGA, g	PGV, in/sec	PGD, in	Peak in-run drift ratio, %	Peak Base-shear coefficient
39	F2-C-RSN6-TC4-PGV6-2	0.44	5.14	0.37	2.23	0.42
40	F2-C-RSN6-TC2-PGV6-2	0.31	5.49	0.72	1.79	0.36
41	F2-C-RSN1051-PGV6-2	0.43	5.74	0.57	2.78	0.47
42	F2-C-RSN95-PGV6-2	0.26	5.56	0.76	2.04	0.38
43	F2-C-RSN6975-PGV8-1	0.27	6.90	1.52	1.54	0.24
44	F2-C-RSN77-PGV8-1	0.31	6.89	0.93	2.46	0.44
45	F2-C-RSN2114-PGV8-1	0.18	7.35	1.52	2.71	0.43
46	F2-C-RSN6-TC4-PGV8-1	0.58	6.70	0.50	2.96	0.45
47	F2-C-RSN6-TC2-PGV8-1	0.38	7.14	0.94	2.47	0.40
48	F2-C-RSN1051-PGV8-1	0.63	7.75	0.73	3.53	0.47
49	F2-C-RSN95-PGV8-1	0.32	7.23	1.04	2.86	0.40
50	F2-C-RSN6975-PGV8-2	0.31	7.42	1.51	1.70	0.21
51	F2-C-RSN6-TC2-PGV8-2	0.37	7.67	0.93	2.43	0.36
52	F2-C-RSN95-PGV8-2	0.35	7.15	1.04	2.80	0.42
53	F2-C-RSN6975-PGV6-3	0.22	5.94	1.12	1.37	0.18
54	F2-C-RSN6-TC2-PGV6-3	0.35	5.83	0.72	1.73	0.26
55	F2-C-RSN95-PGV6-3	0.30	5.44	0.79	2.30	0.36
56	F2-C-RSN6975-PGV4-3	0.16	4.12	0.75	1.04	0.13
57	F2-C-RSN77-PGV4-3	0.26	3.59	0.47	1.66	0.20
58	F2-C-RSN2114-PGV4-3	0.13	3.83	0.76	1.78	0.22
59	F2-C-RSN6-TC4-PGV4-3	0.37	4.15	0.26	1.69	0.21
60	F2-C-RSN6-TC2-PGV4-3	0.24	4.02	0.47	1.33	0.17
61	F2-C-RSN1051-PGV4-3	0.25	3.62	0.35	2.17	0.29
62	F2-C-RSN95-PGV4-3	0.19	3.57	0.54	1.54	0.21
63	F2-C-RSN6975-PGV2-3	0.09	1.92	0.39	0.68	0.06
64	F2-C-RSN77-PGV2-3	0.14	1.81	0.24	0.93	0.08
65	F2-C-RSN2114-PGV2-3	0.11	1.97	0.38	0.96	0.09
66	F2-C-RSN6-TC4-PGV2-3	0.25	2.55	0.13	0.55	0.05
67	F2-C-RSN6-TC2-PGV2-3	0.14	1.97	0.24	0.86	0.09
68	F2-C-RSN1051-PGV2-3	0.12	1.81	0.18	0.97	0.11
69	F2-C-RSN95-PGV2-3	0.11	1.82	0.27	0.85	0.08

Table 3-6: Summary of Series F2-M (Monical, 2022)

Frame Run Number	Test ID	PGA, g	PGV, in/sec	PGD, in	Peak in-run drift ratio, %	Peak Base-shear coefficient
70	F2-M-10p-1	0.09	1.45	0.13	0.03	0.16
71	F2-M-10p-2	0.10	1.46	0.15	0.04	0.18
72	F2-M-20p-1	0.18	2.69	0.29	0.11	0.28
73	F2-M-20p-2	0.16	2.56	0.28	0.16	0.29
74	F2-M-40p-1	0.24	4.80	0.55	0.38	0.48
75	F2-M-40p-2	0.27	4.82	0.55	0.43	0.53
76	F2-M-60p-1	0.43	7.21	0.82	0.72	0.71
77	F2-M-60p-2	0.38	6.42	0.83	0.82	0.69
78	F2-M-80p-1	0.50	8.42	1.10	1.14	0.75

Table 3-7: Summary of Series F2-M-C-S (Monical, 2022)

Frame Run Number	Test ID	PGA, g	PGV, in/sec	PGD, in	Peak in-run drift ratio, %	Peak Base-shear coefficient
79	F2-M-C-S-10p-1	0.11	1.28	0.17	0.13	0.13
80	F2-M-C-S-20p-1	0.15	2.34	0.30	0.24	0.25
81	F2-M-C-S-40p-1	0.24	4.33	0.54	0.48	0.45
82	F2-M-C-S-60p-1	0.33	6.24	0.84	0.74	0.68
83	F2-M-C-S-80p-1	0.46	8.09	1.06	1.12	0.82
84	F2-M-C-S-80p-2	0.45	8.31	1.08	1.22	0.72

Table 3-8: Summary of Series F2-C-S (Monical, 2022)

Frame Run Number	Test ID	PGA, g	PGV, in/sec	PGD, in	Peak in-run drift ratio, %	Peak Base-shear coefficient
85	F2-C-S-10p-1	0.13	1.31	0.15	0.35	0.04
86	F2-C-S-20p-1	0.22	2.66	0.27	0.72	0.09
87	F2-C-S-40p-1	0.29	4.61	0.54	1.61	0.25
88	F2-C-S-60p-1	0.38	6.70	0.82	2.41	0.38
89	F2-C-S-80p-1	0.43	8.84	1.10	2.84	0.42
90	F2-C-S-100p-1	0.48	10.28	1.35	3.17	0.43
91	F2-C-S-100p-2	0.49	10.32	1.37	3.21	0.41
92	F2-C-S-RSN1051-PGV8-1	0.58	7.01	0.74	3.31	0.42
93	F2-C-S-RSN1051-PGV8-2	0.56	6.94	0.72	3.44	0.41
94	F2-C-S-RSN1051-PGV10-1	0.75	8.31	0.90	4.02	0.43
95	F2-C-S-RSN1051-PGV10-2	0.71	8.36	0.89	3.91	0.42
96	F2-C-S-RSN1051-PGV12-1	0.89	9.25	1.07	4.51	0.42
97	F2-C-S-RSN1051-PGV12-2	0.87	9.26	1.07	4.68	0.40

Table 3-9: Summary of Series F2-C-4PB

Frame Run Number[1]	Test ID	PGA, g	PGV, in/sec	PGD, in	Peak in-run drift ratio, %	Peak Base-shear coefficient
98	F2-C-4PB-10p-1	0.11	1.65	0.16	0.16	0.16
99	F2-C-4PB-10p-2	0.13	1.40	0.14	0.14	0.15
100	F2-C-4PB-20p-1	0.19	2.39	0.27	0.31	0.26
101	F2-C-4PB-20p-2	0.18	2.33	0.50	0.37	0.24
102	F2-C-4PB-40p-1	0.26	4.61	0.55	0.76	0.50
103	F2-C-4PB-40p-2	0.26	4.50	0.55	0.78	0.51
104	F2-C-4PB-60p-1	0.36	6.69	0.87	1.03	0.69
105	F2-C-4PB-60p-2	0.34	6.72	0.83	1.08	0.73
106	F2-C-4PB-80p-1	0.48	8.73	1.09	1.35	0.86
107	F2-C-4PB-80p-2	0.39	9.16	1.10	1.51	0.90
108	F2-C-4PB-60p-3	0.39	7.48	0.86	1.40	0.83
109	F2-C-4PB-60p-4	0.38	7.27	0.81	1.49	0.85
110	F2-C-4PB-40p-3	0.27	5.05	0.53	1.42	0.57
111	F2-C-4PB-40p-4	0.27	4.89	0.56	1.39	0.55
112	F2-C-4PB-20p-3	0.21	2.64	0.28	0.66	0.12
113	F2-C-4PB-20p-4	0.21	2.66	0.29	0.68	0.12
114	F2-C-4PB-10p-3	0.12	1.30	0.15	0.36	0.04
115	F2-C-4PB-10p-4	0.12	1.32	0.15	0.36	0.04
116	F2-C-4PB-80p-3	0.44	9.34	1.12	1.69	0.92
117	F2-C-4PB-80p-4	0.41	8.68	1.12	1.21	0.80

[1]Adding to runs completed by Monical (2022), as listed in Tables 3-1 to 3-8

Table 3-10: Summary of Series F1-C-2PB

Frame Run Number	Test ID	PGA, g	PGV, in/sec	PGD, in	Peak in-run drift ratio, %	Peak Base-shear coefficient
79	F1-C-2PB-10p-1	0.11	1.16	0.15	0.12	0.14
80	F1-C-2PB-10p-2	0.11	1.20	0.16	0.11	0.14
81	F1-C-2PB-20p-1	0.16	2.33	0.31	0.28	0.26
82	F1-C-2PB-20p-2	0.14	2.22	0.31	0.28	0.26
83	F1-C-2PB-40p-1	0.24	4.53	0.62	0.59	0.46
84	F1-C-2PB-20p-3	0.20	2.30	0.30	0.33	0.25
85	F1-C-2PB-40p-2	0.25	4.41	0.58	0.57	0.48
86	F1-C-2PB-60p-1	0.32	6.28	0.84	0.87	0.67
87	F1-C-2PB-60p-2	0.36	6.58	0.84	0.92	0.67
88	F1-C-2PB-80p-1	0.48	8.63	1.08	1.24	0.82
89	F1-C-2PB-80p-2	0.49	8.76	1.14	1.34	0.84
90	F1-C-2PB-60p-3	0.37	6.79	0.84	1.14	0.61
91	F1-C-2PB-60p-4	0.36	6.66	0.84	1.16	0.63
92	F1-C-2PB-40p-3	0.25	4.83	0.58	0.89	0.41
93	F1-C-2PB-40p-4	0.25	4.82	0.55	0.88	0.42
94	F1-C-2PB-20p-4	0.17	2.39	0.28	0.51	0.17
95	F1-C-2PB-20p-5	0.17	2.42	0.30	0.51	0.18
96	F1-C-2PB-10p-3	0.14	1.62	0.21	0.30	0.09
97	F1-C-2PB-10p-4	0.13	1.38	0.15	0.29	0.09
98	F1-C-2PB-80p-3	0.50	8.60	1.12	1.45	0.80

Table 3-11: Summary of Series F1-C-1PB

Frame Run Number	Test ID	PGA, g	PGV, in/sec	PGD, in	Peak in-run drift ratio, %	Peak Base-shear coefficient
99	F1-C-1PB-10p-1	0.14	1.40	0.20	0.17	0.12
100	F1-C-1PB-10p-2	0.14	1.50	0.16	0.18	0.12
101	F1-C-1PB-20p-1	0.19	2.33	0.31	0.36	0.22
102	F1-C-1PB-20p-2	0.19	2.31	0.30	0.37	0.21
103	F1-C-1PB-40p-1	0.30	4.45	0.54	0.78	0.39
104	F1-C-1PB-40p-2	0.27	4.45	0.55	0.80	0.39
105	F1-C-1PB-60p-1	0.36	6.69	0.88	1.22	0.56
106	F1-C-1PB-60p-2	0.35	6.86	0.87	1.35	0.57
107	F1-C-1PB-80p-1	0.48	9.18	1.14	1.79	0.62
108	F1-C-1PB-80p-2	0.50	9.15	1.13	2.50	0.59
109	F1-C-1PB-20p-3*	0.17	2.41	0.28	1.01	0.11
110	F1-C-1PB-40p-3*	0.29	4.71	0.56	1.64	0.21
111	F1-C-1PB-60p-3*	0.36	6.97	0.85	2.16	0.32
112	F1-C-1PB-80p-3*	0.45	9.03	1.10	2.94	0.42

* Infill partially removed after failure during Run 108 (see Figure 3-26)

Table 3-12: Summary of Series F2-R-C-4PB

Frame Run Number[1]	Test ID	PGA, g	PGV, in/sec	PGD, in	Peak in-run drift ratio, %	Peak Base-shear coefficient
118	F2-R-C-4PB-10p-1	0.10	1.59	0.16	0.06	0.14
119	F2-R-C-4PB-10p-2	0.11	1.49	0.16	0.06	0.15
120	F2-R-C-4PB-20p-1	0.15	2.67	0.29	0.12	0.27
121	F2-R-C-4PB-20p-2	0.16	2.78	0.33	0.13	0.28
122	F2-R-C-4PB-40p-1	0.26	4.85	0.58	0.32	0.48
123	F2-R-C-4PB-40p-2	0.24	4.68	0.54	0.32	0.48

[1] Recast procedure of frame F2 completed prior to this series

Table 3-13: Summary of Series F2-R-C-2PB

Frame Run Number	Test ID	PGA, g	PGV, in/sec	PGD, in	Peak in-run drift ratio, %	Peak Base-shear coefficient
124	F2-R-C-2PB-10p-1	0.11	1.43	0.15	0.08	0.15
125	F2-R-C-2PB-10p-2	0.12	1.35	0.16	0.08	0.16
126	F2-R-C-2PB-20p-1	0.17	2.55	0.28	0.16	0.28
127	F2-R-C-2PB-20p-2	0.15	2.48	0.36	0.16	0.28
128	F2-R-C-2PB-40p-1	0.26	4.60	0.60	0.33	0.52
129	F2-R-C-2PB-40p-2	0.26	4.65	0.63	0.33	0.51
130	F2-R-C-2PB-60p-1	0.33	6.92	0.83	0.49	0.72
131	F2-R-C-2PB-60p-2	0.33	7.73	0.88	0.53	0.76
132	F2-R-C-2PB-80p-1	0.51	10.08	1.19	0.80	1.03
133	F2-R-C-2PB-80p-2	0.58	10.26	1.15	0.96	1.14
134	F2-R-C-2PB-40p-3	0.26	4.42	0.65	0.59	0.67
135	F2-R-C-2PB-40p-4	0.24	4.50	0.70	0.59	0.67
136	F2-R-C-2PB-20p-3	0.15	2.23	0.33	0.29	0.33
137	F2-R-C-2PB-20p-4	0.15	2.34	0.38	0.29	0.33

Table 3-14: Summary of Series F2-R-C-1PB

Frame Run Number	Test ID	PGA, g	PGV, in/sec	PGD, in	Peak in-run drift ratio, %	Peak Base-shear coefficient
138	F2-R-C-1PB-10p-1	0.12	1.21	0.17	0.14	0.16
139	F2-R-C-1PB-10p-2	0.13	1.20	0.14	0.14	0.16
140	F2-R-C-1PB-20p-1	0.17	2.31	0.31	0.30	0.31
141	F2-R-C-1PB-20p-2	0.19	2.23	0.29	0.30	0.31
142	F2-R-C-1PB-40p-1	0.25	4.32	0.57	0.65	0.62
143	F2-R-C-1PB-40p-2	0.25	4.20	0.55	0.67	0.65
144	F2-R-C-1PB-60p-1	0.34	6.47	0.87	1.00	0.91
145	F2-R-C-1PB-60p-2	0.31	6.43	0.83	1.05	0.93
146	F2-R-C-1PB-80p-1	0.40	8.44	1.14	1.29	1.06
147	F2-R-C-1PB-80p-2	0.44	9.24	1.03	1.15	0.89
148	F2-R-C-1PB-100p-1	0.46	10.66	1.36	1.43	0.97
149	F2-R-C-1PB-100p-2	0.56	11.02	1.39	1.94	0.89

Table 3-15: Summary of Series F2-R-C

Frame Run Number	Test ID	PGA, g	PGV, in/sec	PGD, in	Peak in-run drift ratio, %	Peak Base-shear coefficient
150	F2-R-C-10p-1	0.11	1.18	0.16	0.39	0.10
151	F2-R-C-10p-2	0.11	1.28	0.14	0.39	0.10
152	F2-R-C-20p-1	0.14	2.29	0.26	0.96	0.25
153	F2-R-C-20p-2	0.14	2.33	0.27	0.97	0.26
154	F2-R-C-40p-1	0.22	5.13	0.57	1.69	0.58
155	F2-R-C-40p-2	0.21	4.72	0.53	1.70	0.58
156	F2-R-C-60p-1	0.30	7.23	0.83	2.16	0.62
157	F2-R-C-60p-2	0.39	7.20	0.80	2.30	0.59
158	F2-R-C-80p-1	0.54	9.04	1.06	2.69	0.61
159	F2-R-C-80p-2	0.42	8.20	1.16	2.83	0.59
160	F2-R-C-100p-1	0.45	9.98	1.42	3.06	0.59
161	F2-R-C-100p-2	0.44	10.17	1.32	2.96	0.56

Table 4-1: Instantaneous Average and Maximum Lateral Stiffness

Series	Run Intensity (%)	Instantaneous Stiffness	
		Mean	Max
F2-C-4PB	40	56	93
F2-C-4PB	60	55	96
F2-C-4PB	80	51	92
F1-C-2PB	40	73	100
F1-C-2PB	60	68	95
F1-C-2PB	80	59	86
F1-C-1PB	40	46	66
F1-C-1PB	60	42	58
F1-C-1PB	80	29	52
F2-R-C-4PB	40	133	178
F2-R-C-2PB	40	141	175
F2-R-C-2PB	60	127	166
F2-R-C-2PB	80	112	145
F2-R-C-1PB	40	83	107
F2-R-C-1PB	60	76	112
F2-R-C-1PB	80	69	93

Table 4-2: Phase Difference Index Input Parameters

Input Parameter	**Value and Units**
Roof Acceleration history	NE top beam ADXL X-axis (g)
Base ADXL Acceleration history	NE Foundation Beam ADXL X-axis (g)
Sample Rate	1000 (Hz)
Minimum Amplitude Filter	0.05 * Max Acceleration (g)
Frequency Range	1 Hz - 10 (Hz)
Number of Narrow Frequency Bands	100
Finite Impulse Response filter order	1500

Table 4-3: Secant and Phase Difference Index Natural Periods, Wood Infills

Frame #	Run #	Series	Intensity (%)	T_{secant} (sec)	T_{PDI} (sec)	$T_{secant} - T_{PDI}$
2	98	F2-C-4PB	10	0.211	0.196	0.015
2	100	F2-C-4PB	20	0.255	0.280	-0.025
2	102	F2-C-4PB	40	0.275	0.356	-0.081
2	104	F2-C-4PB	60	0.276	0.375	-0.100
2	106	F2-C-4PB	80	0.286	0.372	-0.086
1	79	F1-C-2PB	10	0.201	0.185	0.016
1	81	F1-C-2PB	20	0.225	0.212	0.013
1	84	F1-C-2PB	40	0.249	0.255	-0.007
1	86	F1-C-2PB	60	0.249	0.273	-0.024
1	88	F1-C-2PB	80	0.262	0.291	-0.029
1	99	F1-C-1PB	10	0.272	0.256	0.016
1	101	F1-C-1PB	20	0.294	0.285	0.009
1	103	F1-C-1PB	40	0.318	0.345	-0.027
1	105	F1-C-1PB	60	0.337	0.370	-0.033
1	107	F1-C-1PB	80	0.384	0.455	-0.071
2	118	F2-R-C-4PB	10	0.137	0.137	0.000
2	120	F2-R-C-4PB	20	0.152	0.142	0.010
2	122	F2-R-C-4PB	40	0.171	0.168	0.003
2	124	F2-R-C-2PB	10	0.157	0.137	0.020
2	126	F2-R-C-2PB	20	0.164	0.161	0.003
2	128	F2-R-C-2PB	40	0.174	0.167	0.006
2	130	F2-R-C-2PB	60	0.183	0.175	0.008
2	132	F2-R-C-2PB	80	0.193	0.191	0.002
2	138	F2-R-C-1PB	10	0.208	0.190	0.018
2	140	F2-R-C-1PB	20	0.216	0.200	0.016
2	142	F2-R-C-1PB	40	0.225	0.219	0.006
2	144	F2-R-C-1PB	60	0.234	0.233	0.001
2	146	F2-R-C-1PB	80	0.250	0.247	0.003
2	148	F2-R-C-1PB	100	0.278	0.282	-0.004

Table 4-4: Secant and Phase Difference Index Natural Periods, Masonry Infill and Bare Frame

Frame #	**Run #**	**Series**	**Intensity (%)**	T_{secant} **(sec)**	T_{PDI} **(sec)**	$T_{secant} - T_{PDI}$
1	5	F1-B	10	0.284	0.296	-0.012
1	7	F1-B	20	0.282	0.272	0.010
1	8	F1-B	40	0.325	0.320	0.005
1	10	F1-B	60	0.414	0.430	-0.016
1	12	F1-B	80	0.488	0.510	-0.023
1	38	F1-M-C	10	0.105	0.120	-0.015
1	40	F1-M-C	20	0.124	0.138	-0.014
1	42	F1-M-C	40	0.168	0.203	-0.035
1	44	F1-M-C	60	0.207	0.263	-0.056
1	46	F1-M-C	80	0.229	0.294	-0.065

Table 4-5: Secant Stiffnesses of Test Series

		Drift Ratio (%)				
Series Name		initial	0.25	0.50	0.75	1.00
	F1-B	120	75	60	50	40
	F1-M-C	500	180	125	95	80
Damaged Frame Series	F2-C-4PB	110	80	65	65	65
	F1-C-2PB	125	100	90	75	70
	F1-C-1PB	75	60	55	50	45
Recast Frame Series	F2-R-C-4PB	265	190	x	x	x
	F2-R-C-2PB	200	180	150	140	120
	F2-R-C-1PB	120	110	100	95	90

FIGURES

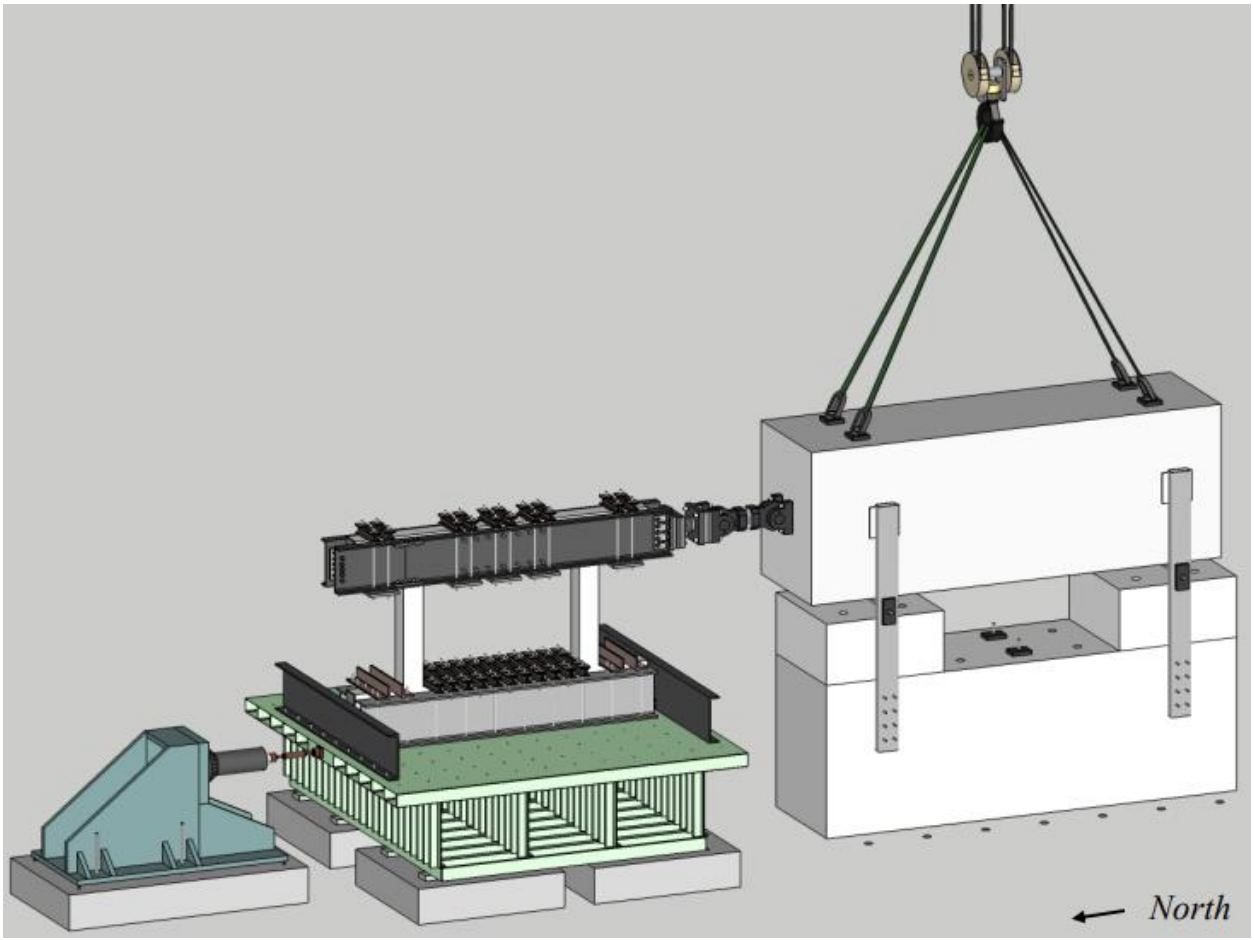

Figure 2-1: Isometric of Test Setup (Monical, 2022, Figure 2-1)

Figure 2-2: Photograph of Test Setup

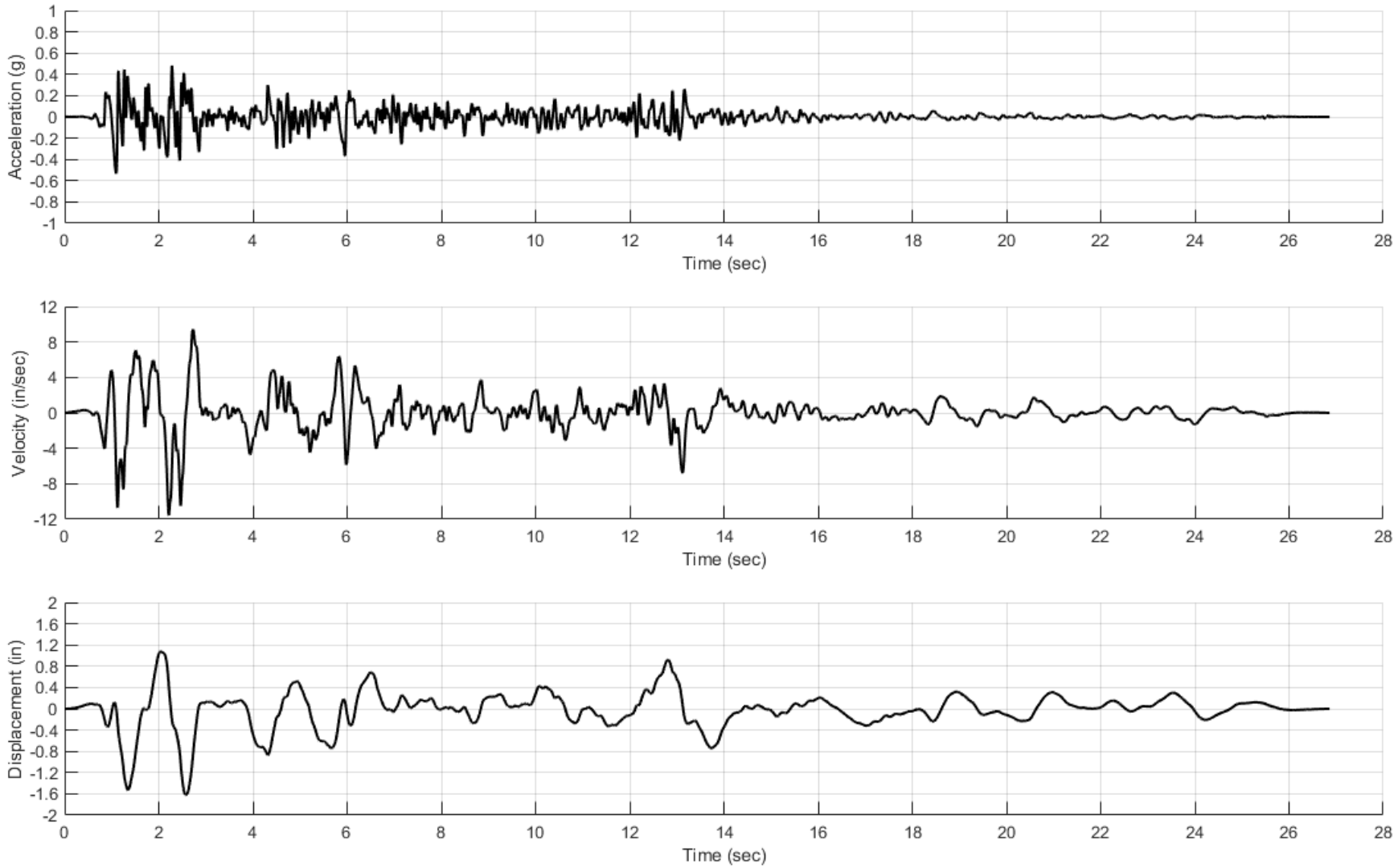

Figure 2-3: El Centro, 1940 NS, Target Ground Motion History (RSN 6, Time Compressed by 2) 100% Intensity[1]

[1] PEER Ground Motion Sign Convention (as displayed): (*Positive = North*) // Simulator Sign Convention: (*Positive = South*)

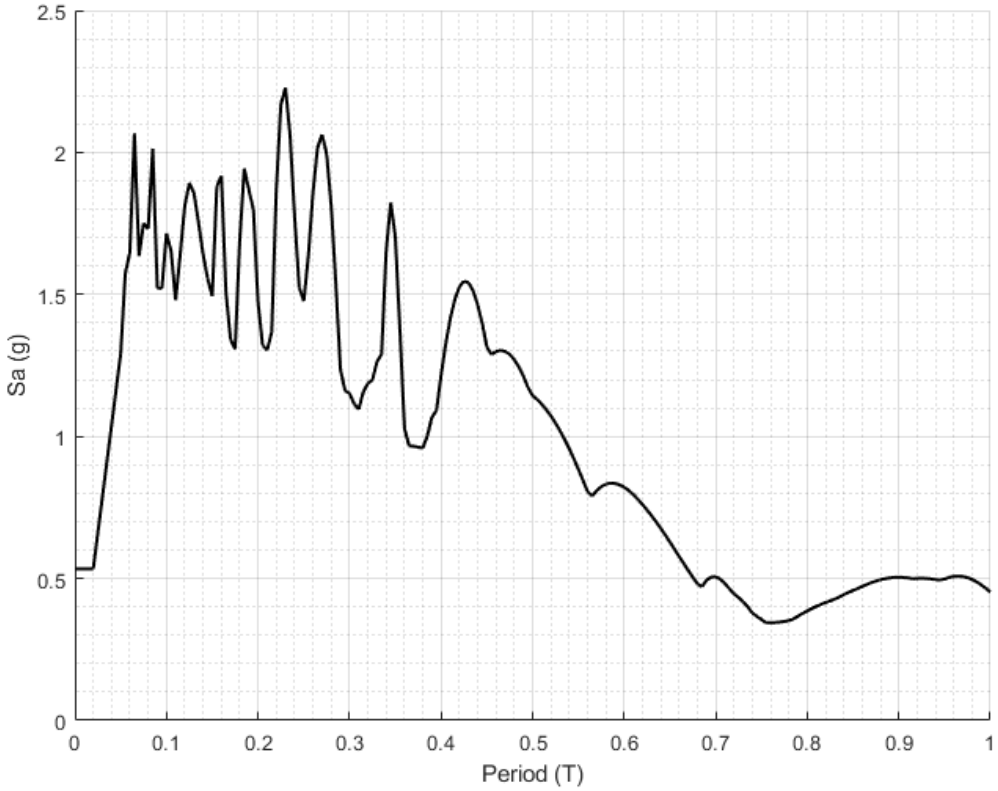

Figure 2-4: Target Acceleration Spectra at 100% Intensity, 2% Damping

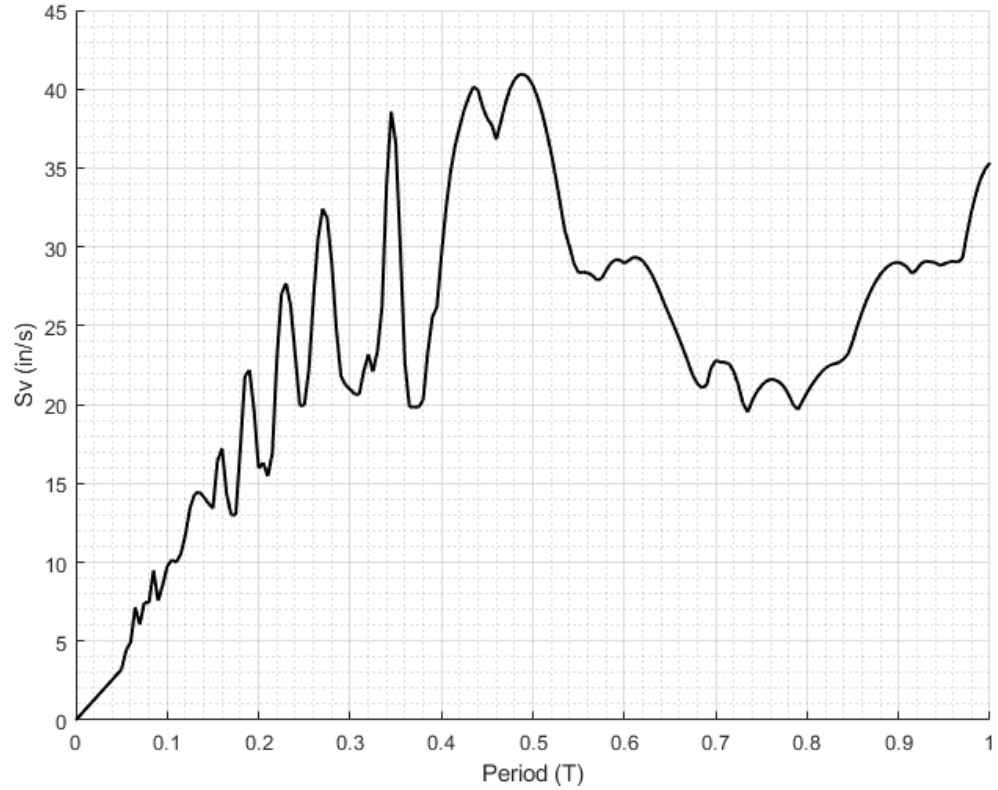

Figure 2-5: Target Velocity Spectra at 100% Intensity, 2% Damping

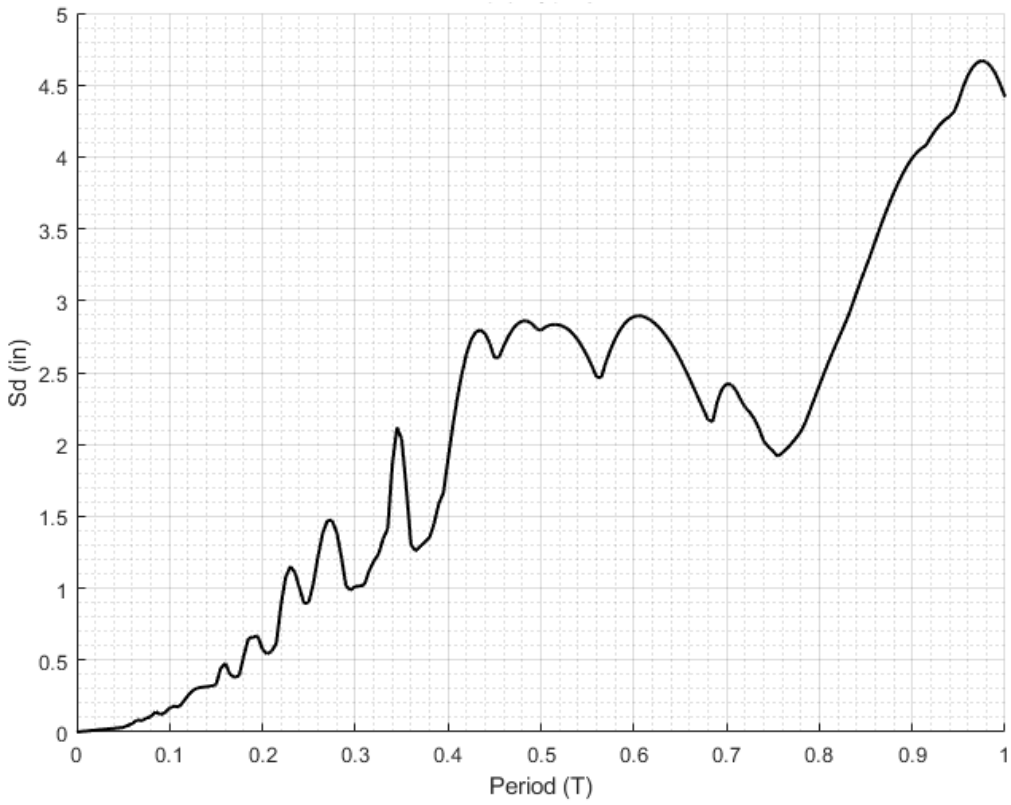

Figure 2-6: Target Displacement Spectra at 100% Intensity, 2% Damping

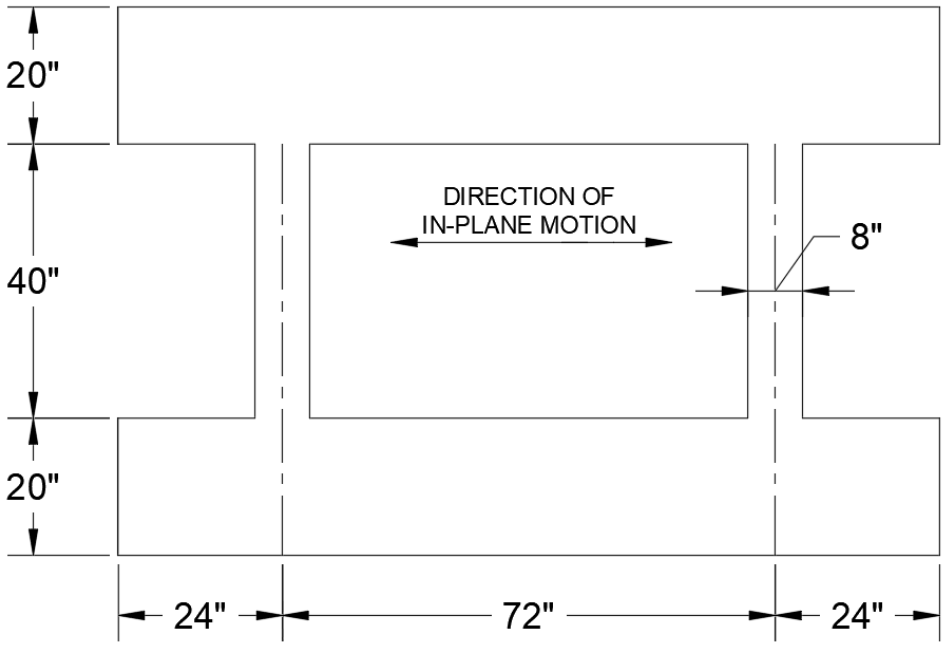

Figure 2-7: Elevation of Test Frame

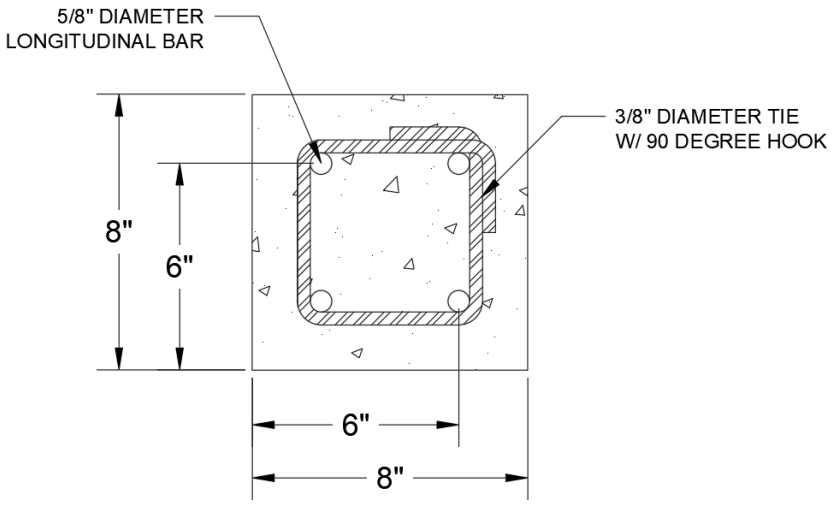

Figure 2-8: Column Cross-Section and Reinforcement

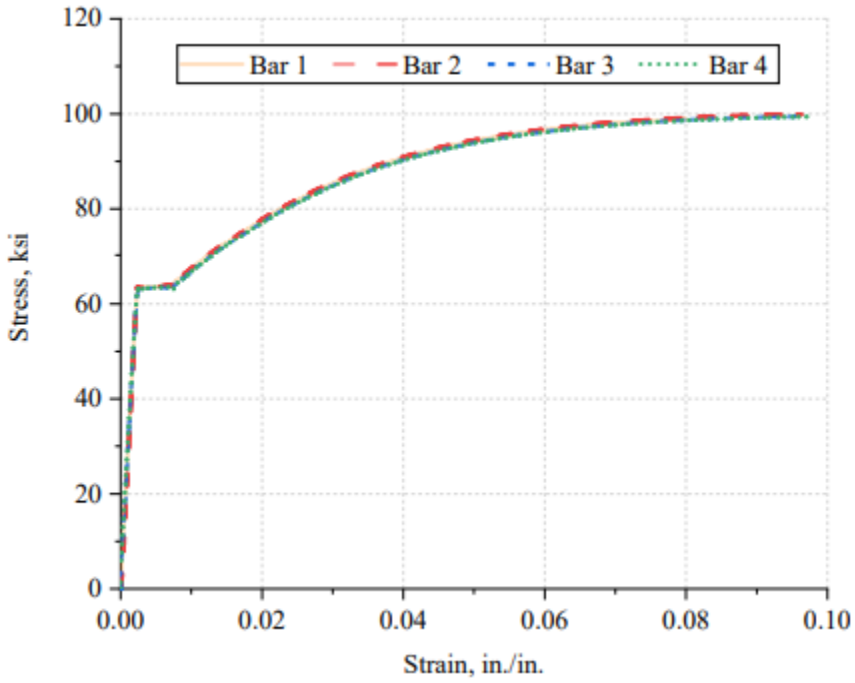

Figure 2-9: Measured Stress-Strain Curves for 5/8" Column Longitudinal Reinforcing Bars (Monical, 2022, Figure 2-4)

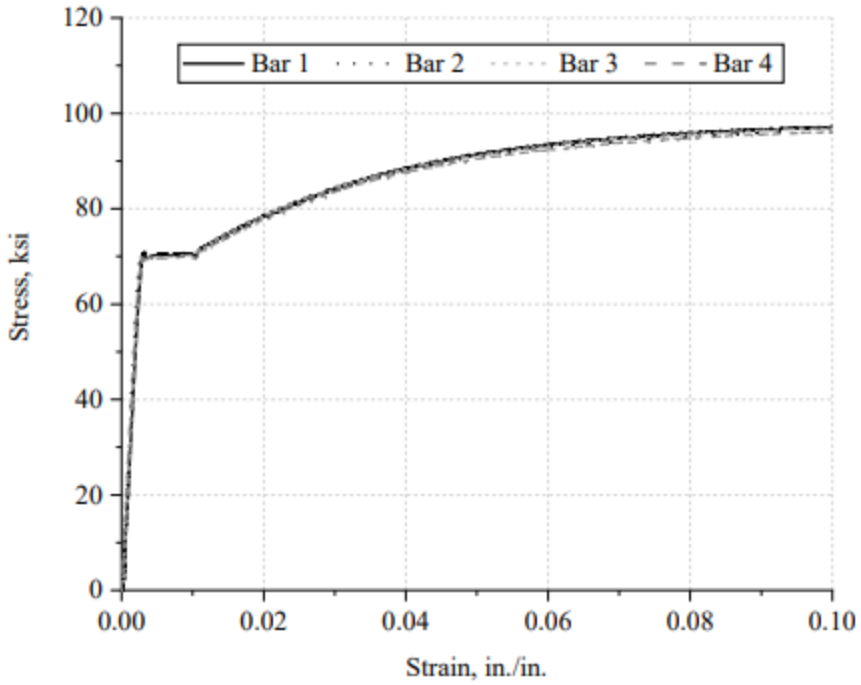

Figure 2-10: Measured Stress-Strain Curves for 3/8” Column Reinforcing Ties (Monical, 2022, Figure 2-6)

(a) North Column Isometric - Top

(c) South Column Isometric - Top

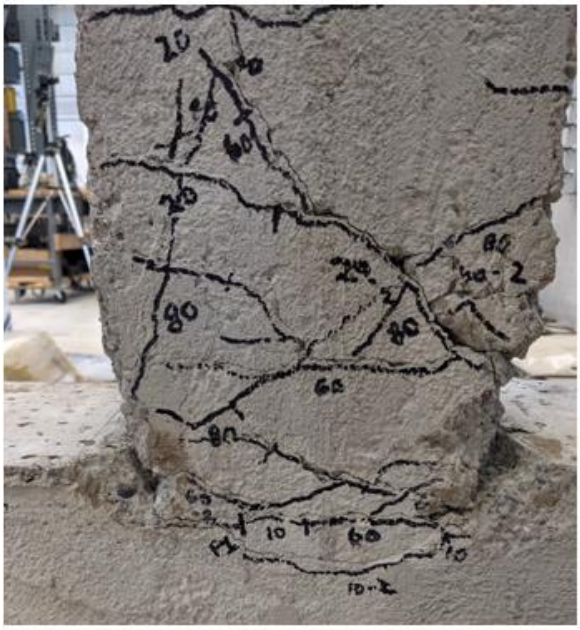

(b) North Column East Face – Base

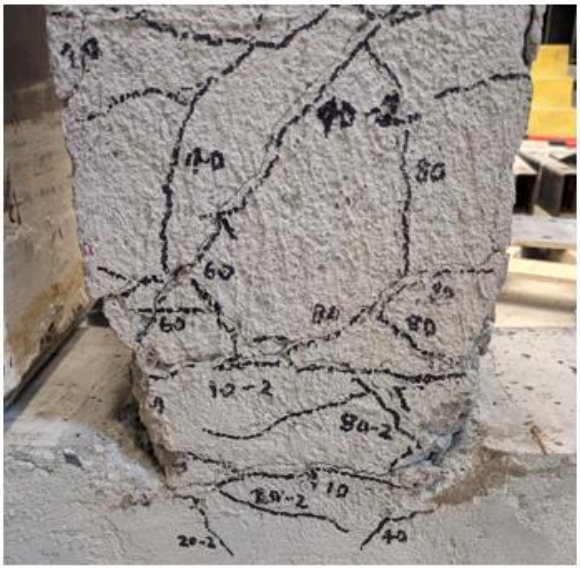

(c) South Column West Face – Base

Figure 2-11: Inherited Condition of Frame 1 Columns

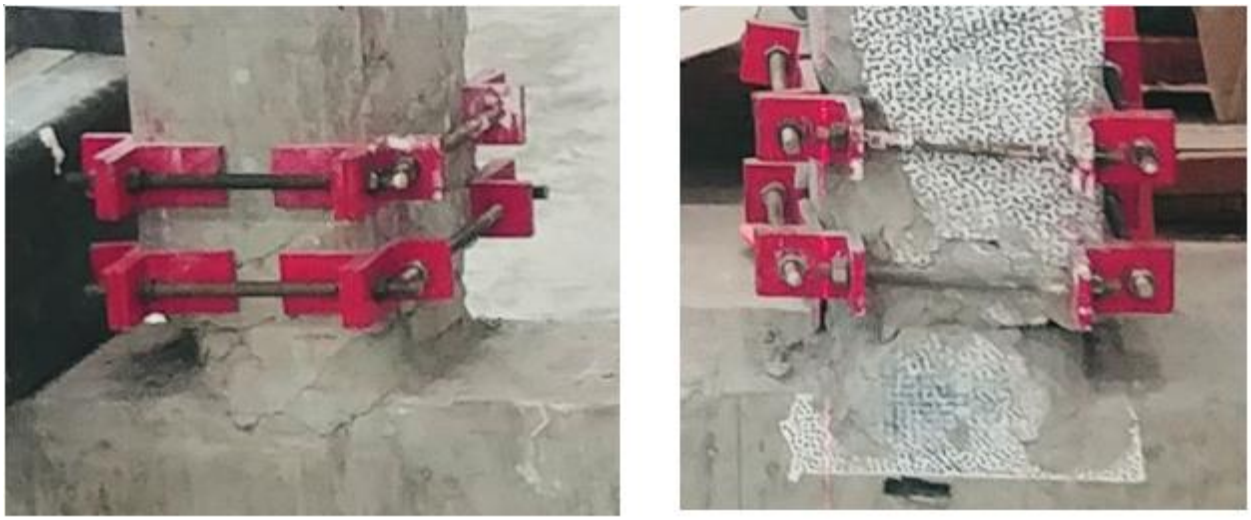

(a) North Column Base – West Face (b) South Column Base- West Face

Figure 2-12: Inherited Condition of Frame 2 Column Base[1]

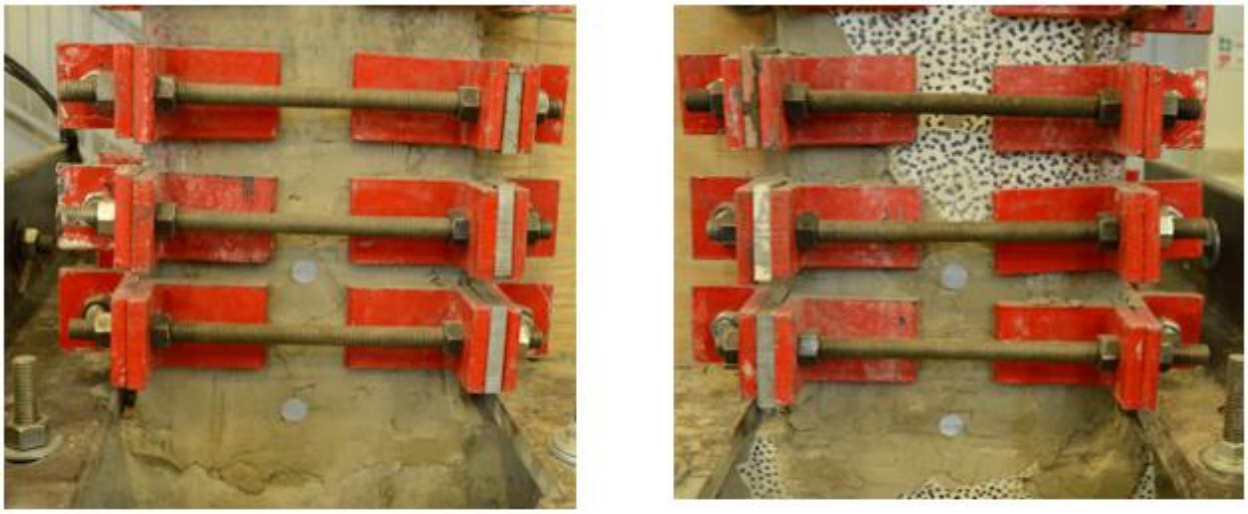

(a) North Column Base – West Face (b) South Column Base- West Face

Figure 2-13: Mortar Repaired Frame 2 Column Base[2]

[1] The bottom post-tensioned clamp had been prior to each photograph to better display spalling at the column bases.
[2] Image taken prior to series F2-C-4PB. Mortar repairs were performed prior to all non "-R" series

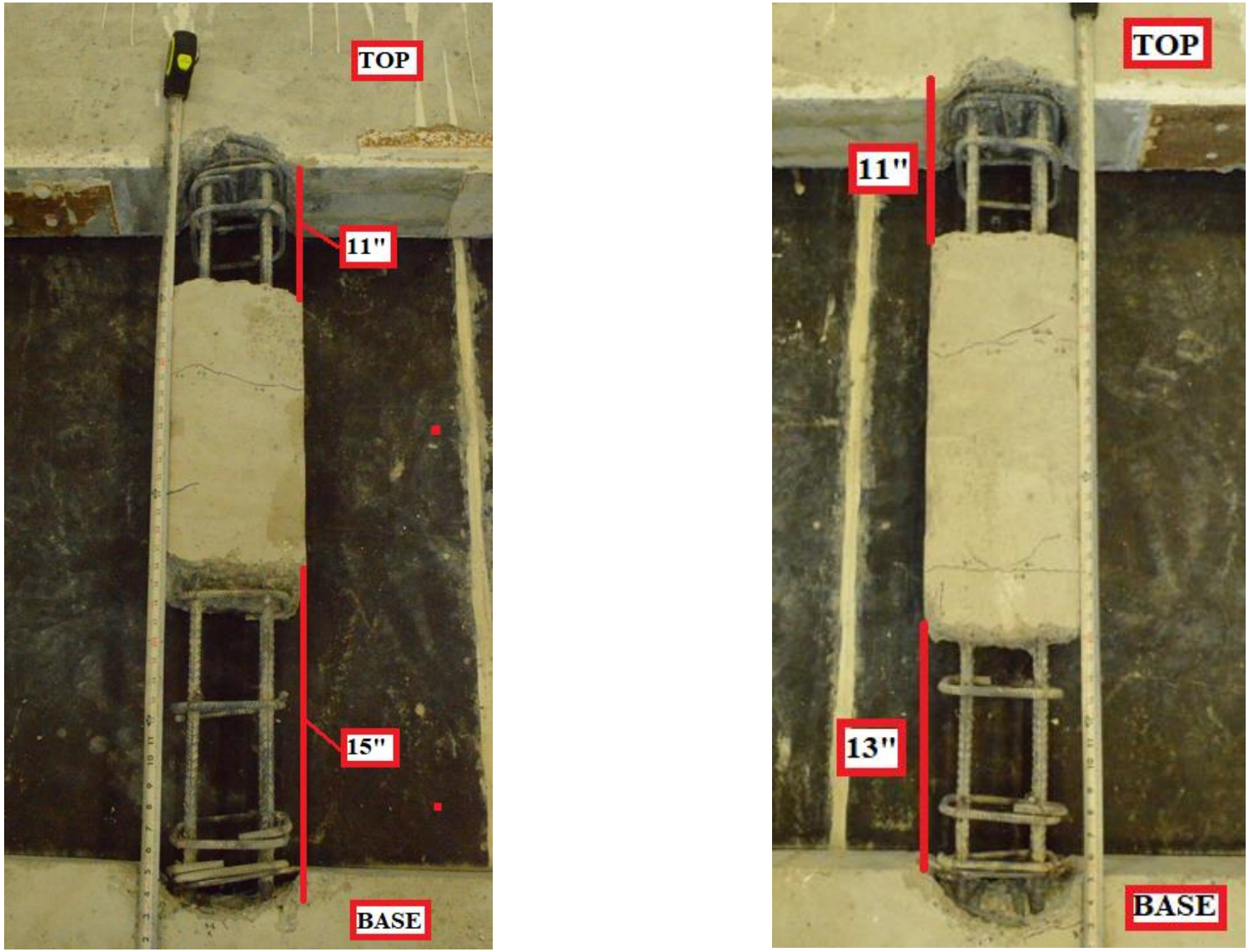

(a) North Column (b) South Column

Figure 2-14: Frame 2 Columns Post Concrete Removal

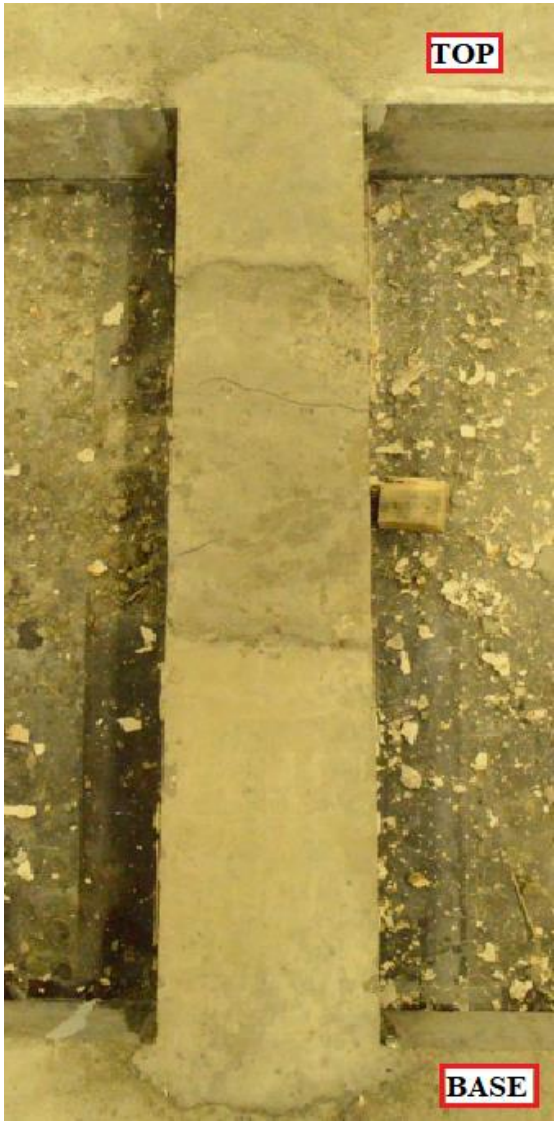

(a) North Column

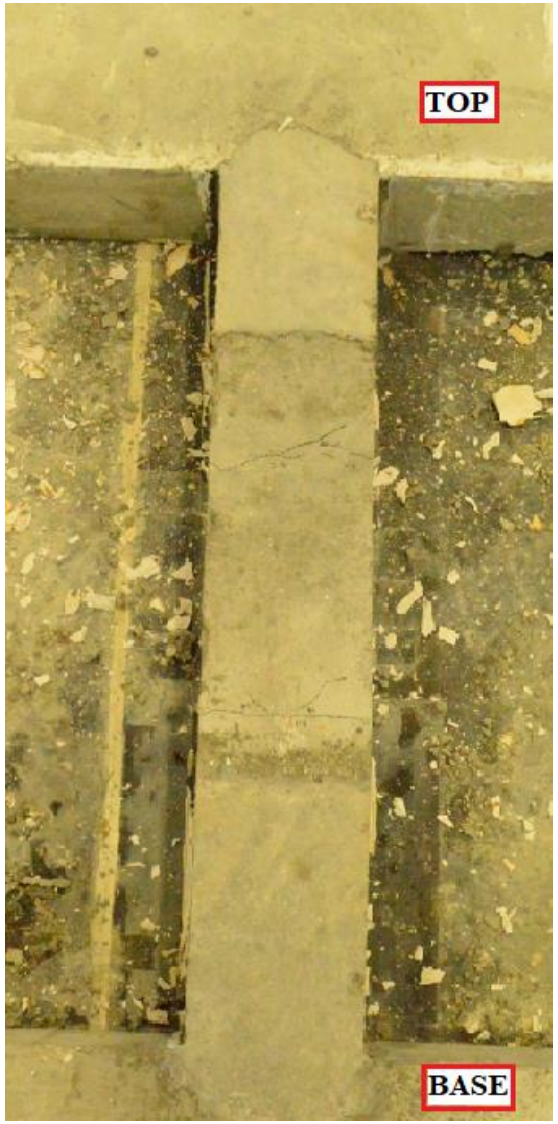

(b) South Column

Figure 2-15: Frame 2 Recast Columns

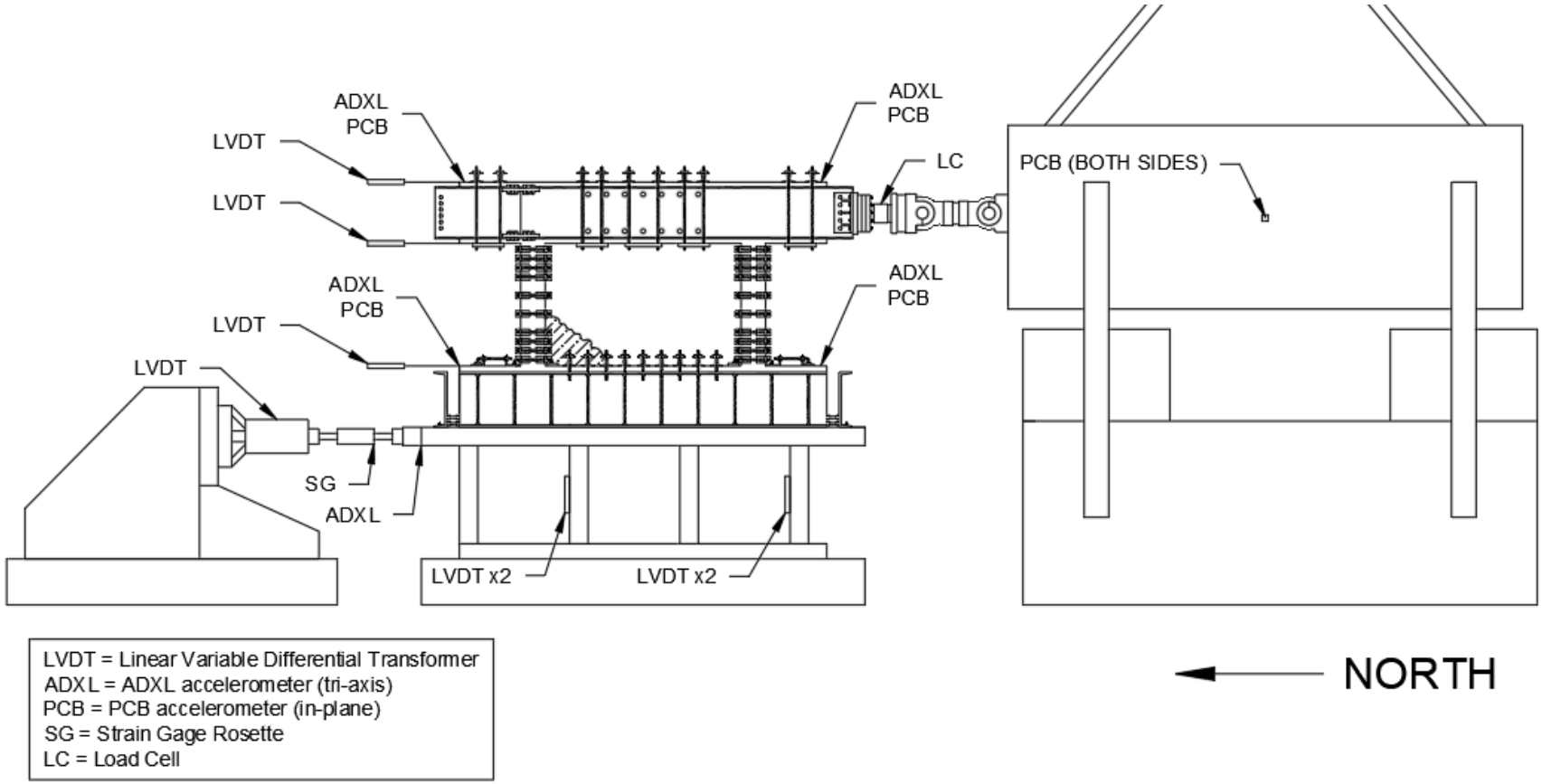

Figure 2-16: Elevation of Instrumentation Layout

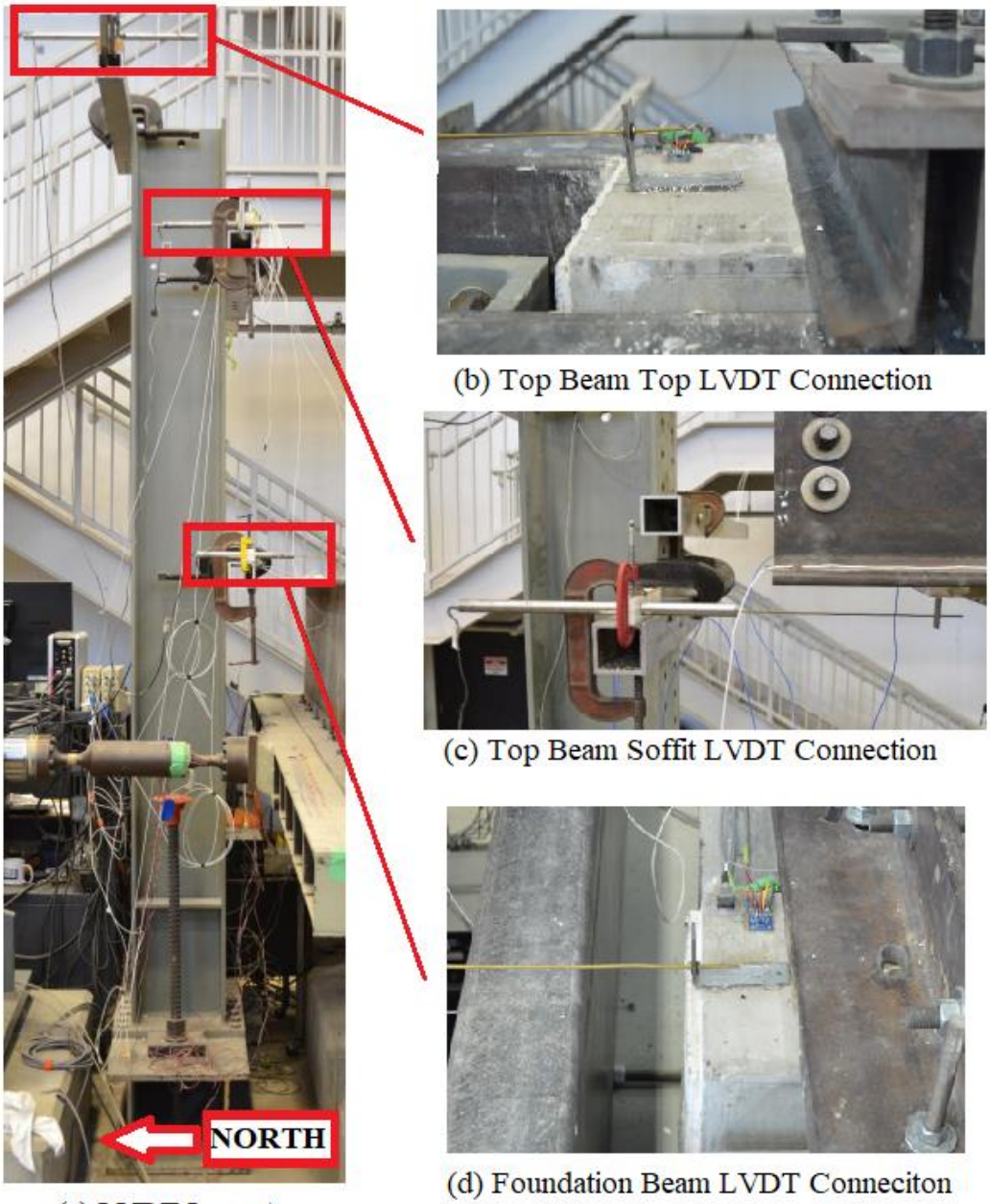

Figure 2-17: Frame In-Plane LVDTs Layout and Connections

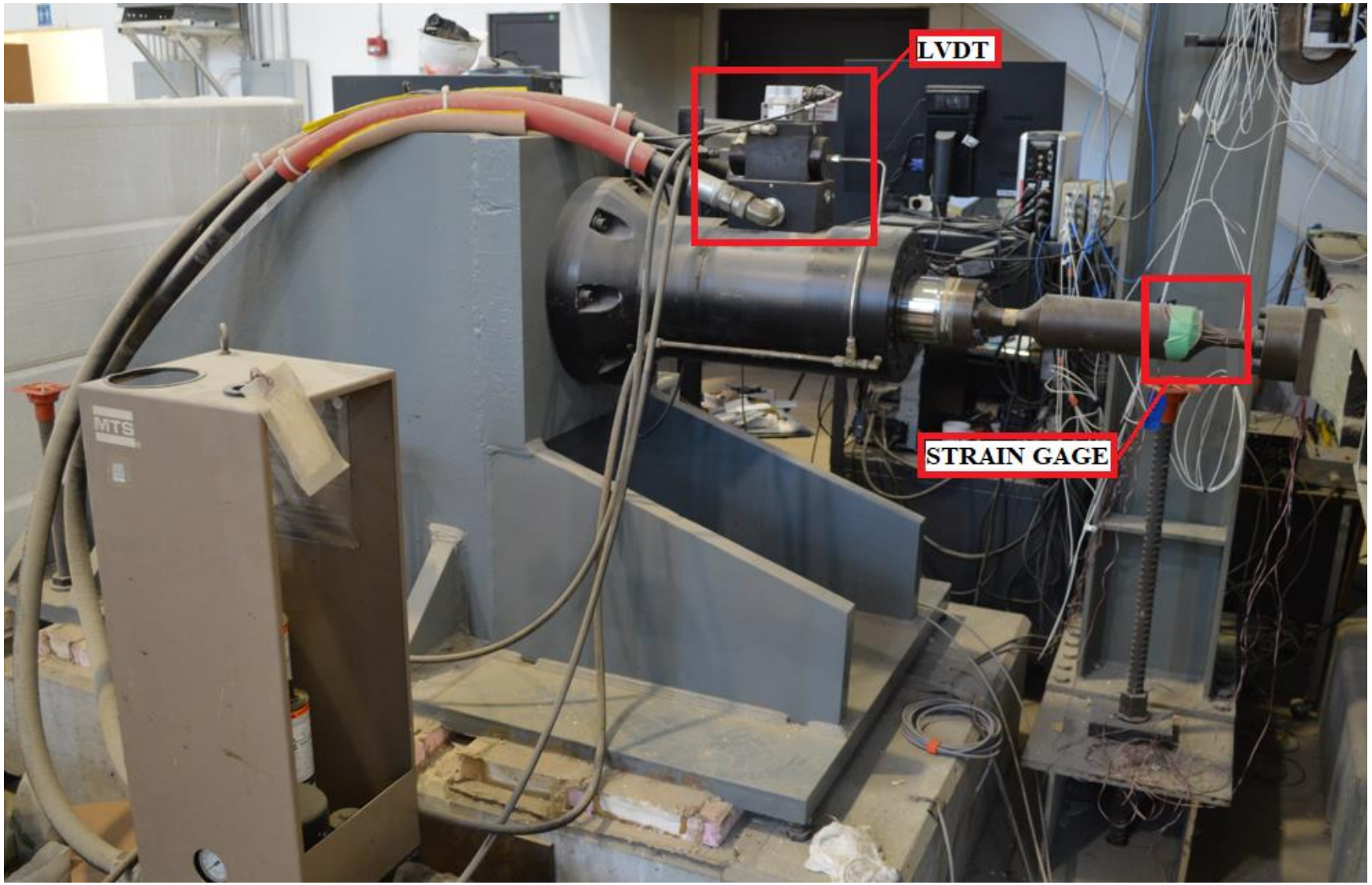

Figure 2-18: Servoram In-Plane LVDT and Strain Gage

(a) External mass preparing for lift

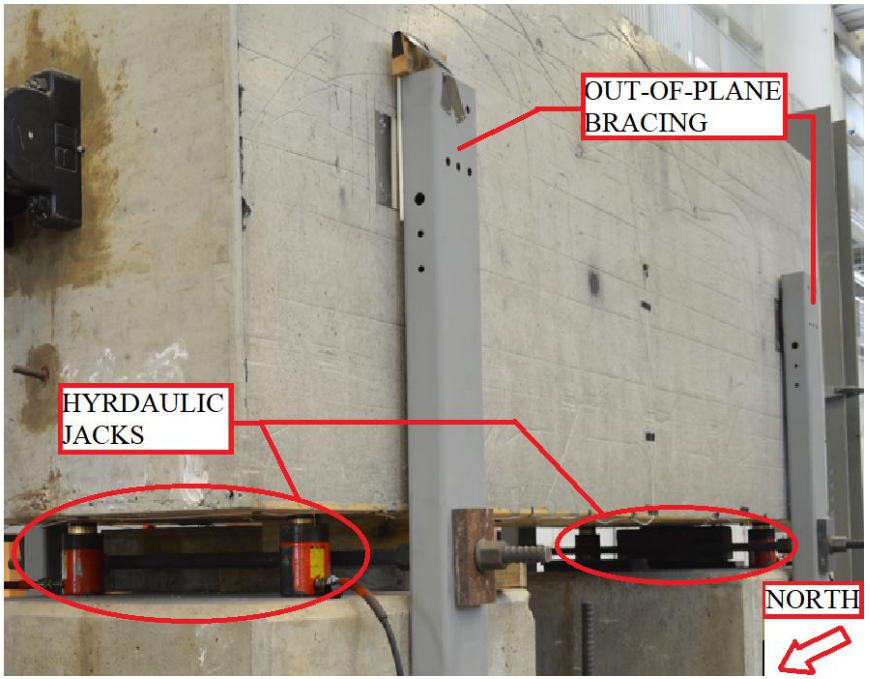

(b) Out-of-plane bracing and Hydraulic Jacks[1]

Figure 2-19: Reinforced Concrete Block Setup for External Suspended Mass

[1] Hydraulic Jacks were lowered once external mass was suspended from crane, and did not interact with the external mass during testing

Figure 2-20: Simulator Platform LVDTs (North Pair)

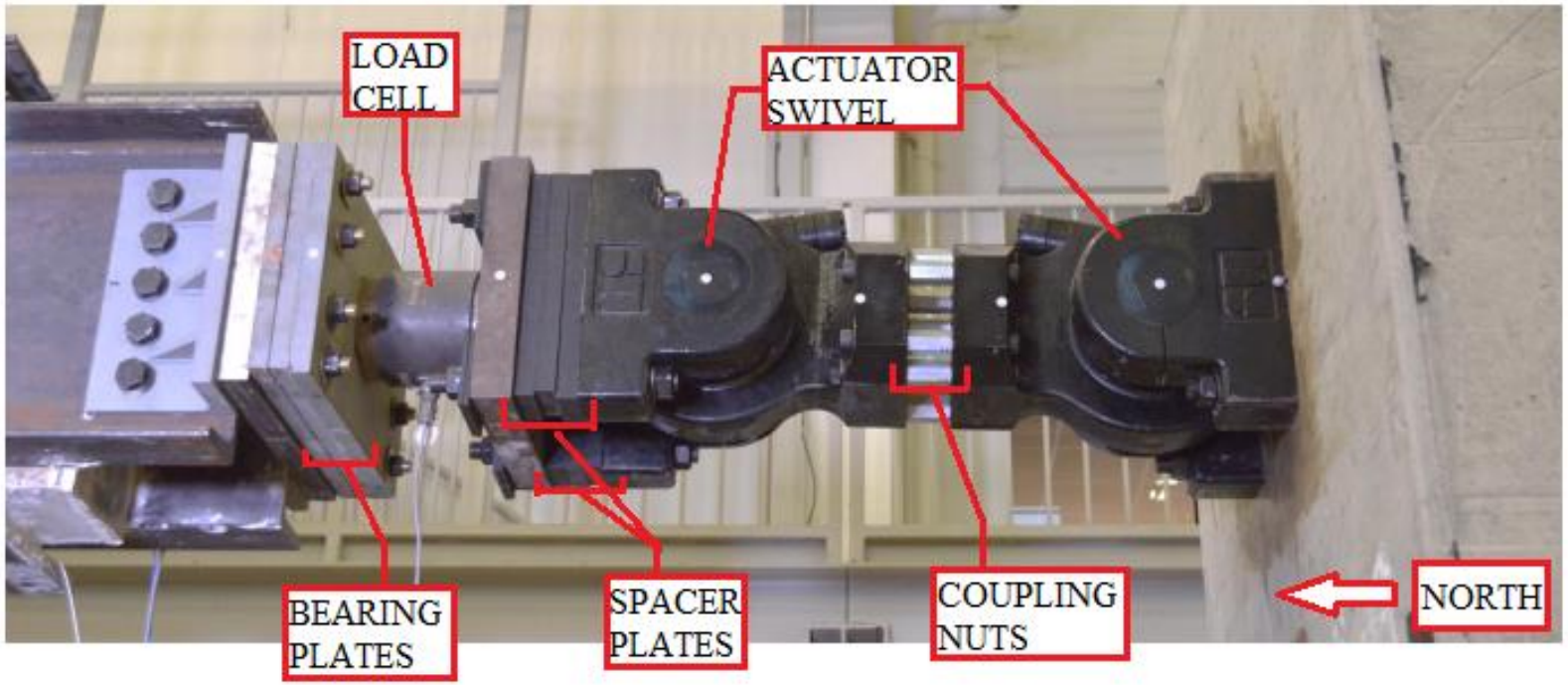

Figure 2-21: Dual-Swivel Link Connection from Frame to External Mass

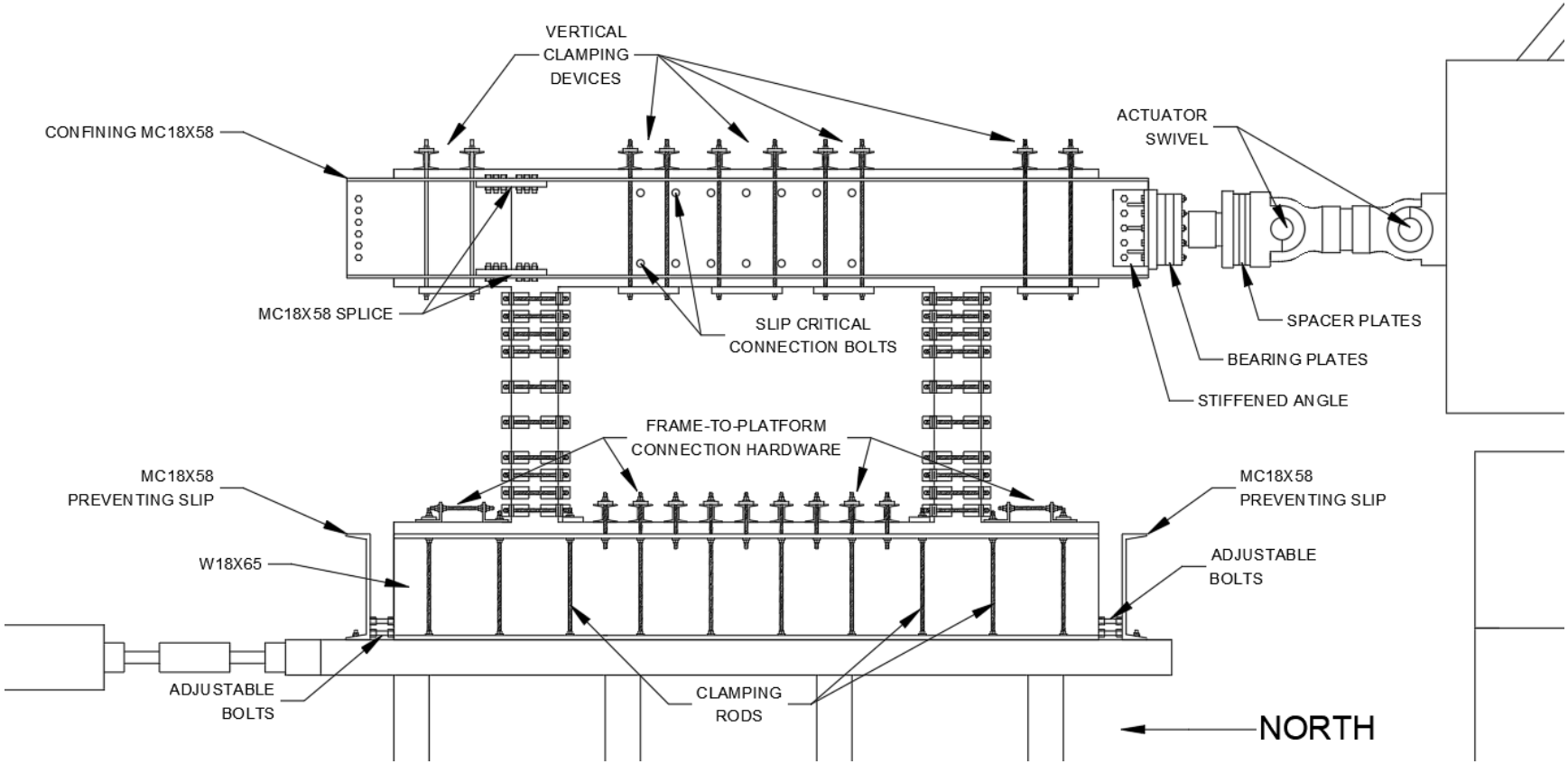

Figure 2-22: Elevation of Frame Connection Components

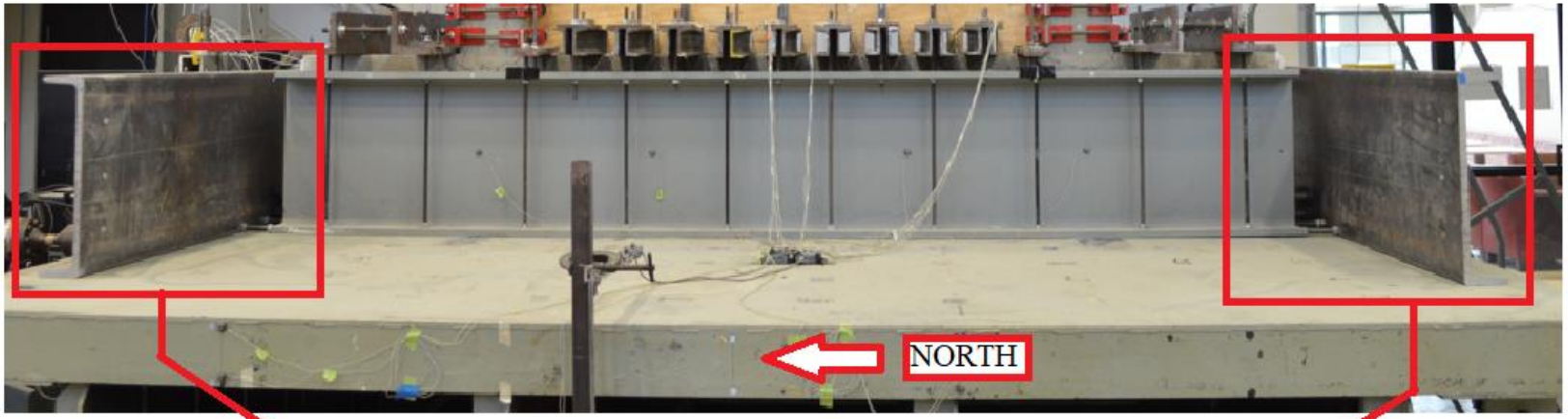

(a) MC18x58 Channels Perpendicular to in-plane motion

(b) North Adjustable Bolts

(b) South Adjustable Bolts

Figure 2-23: Channels and Adjustable Bolts Preventing Base Slip

Figure 2-24: APA Panel Rating Stamp

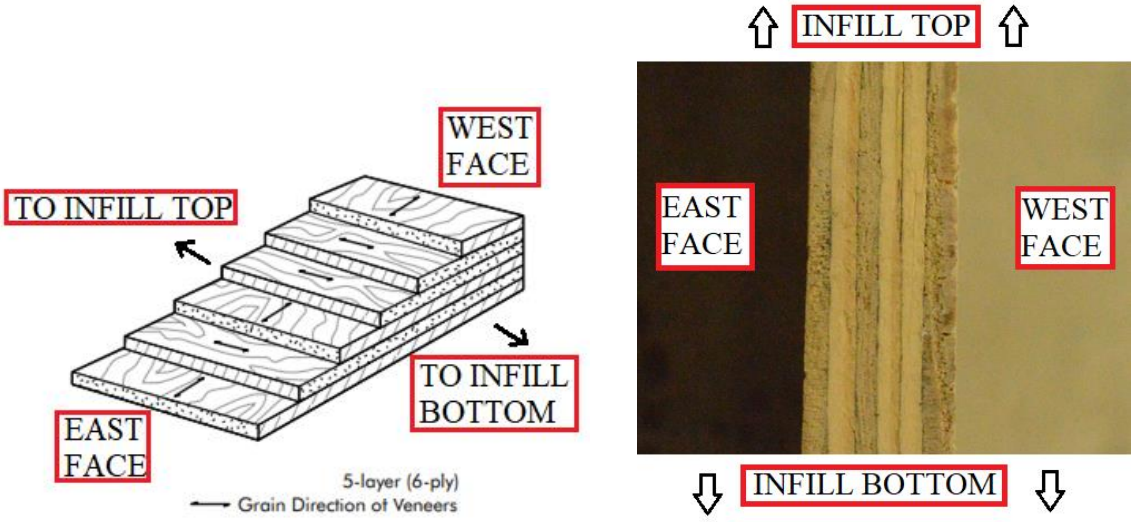

(a) APA D510 Grain Direction (b) Constructed infill edge Grain Direction

Figure 2-25: Veneer Grain Orientation for Typical 5-layer, 6-ply Sheathing Panel (Adapted from APA D510, 2020, Figure 3)

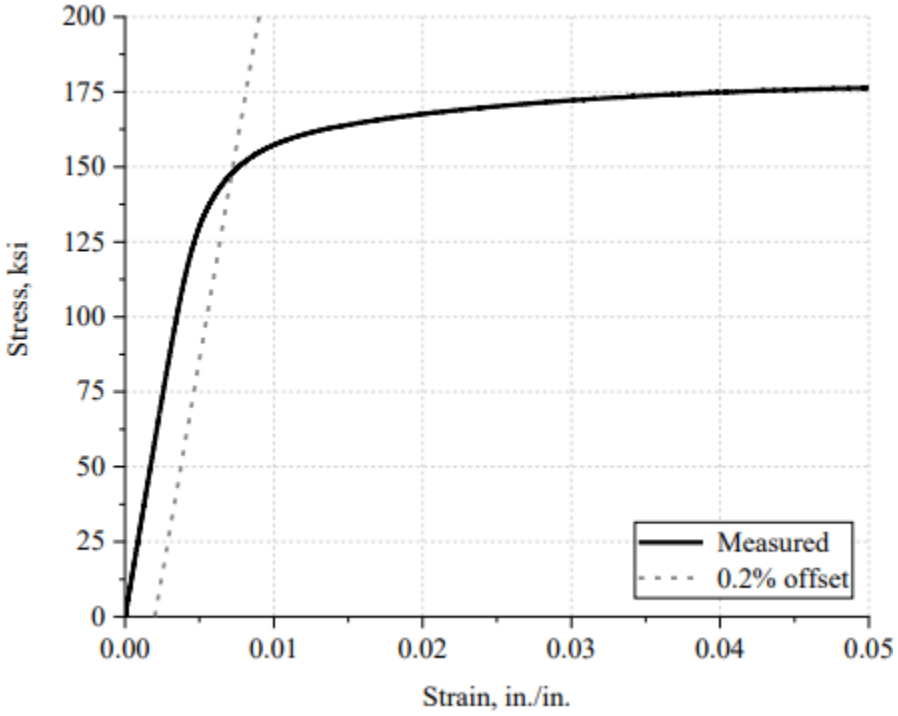

Figure 2-26: Measured Stress-Strain Curve for 1/2" High Strength Threaded Rod (Monical, 2022, Figure 2-8)

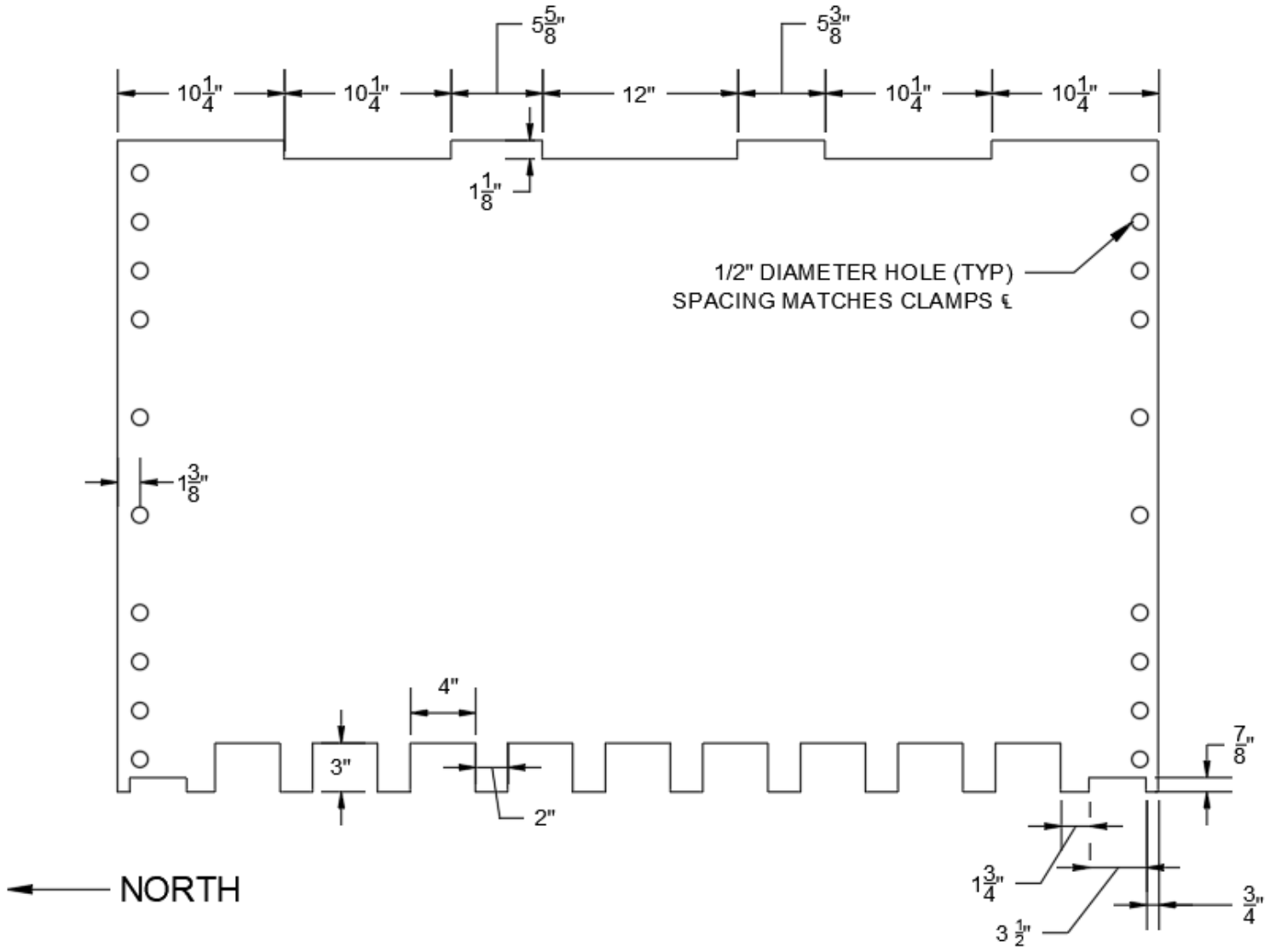

Figure 2-27: Wood Infill Elevation

Figure 2-28: Wood Infill Photograph[1]

[1]Displaying the western-most panel in the 4PB infill of used series F2-C-4PB. Damaged at some edges. Vertical pencil lines denote lamination screw gridlines

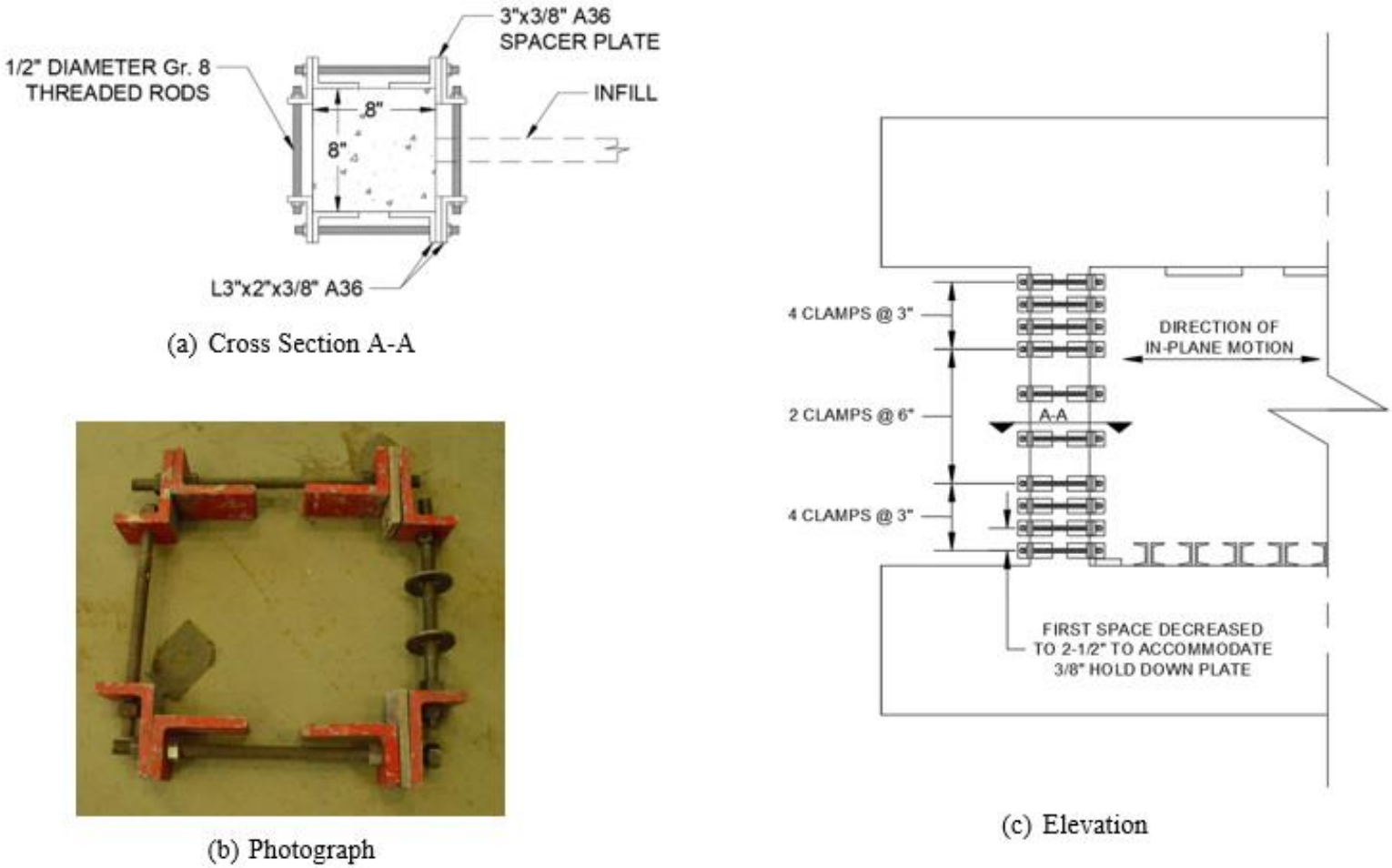

Figure 2-29: External Post-Tensioned Transverse Reinforcement Detail

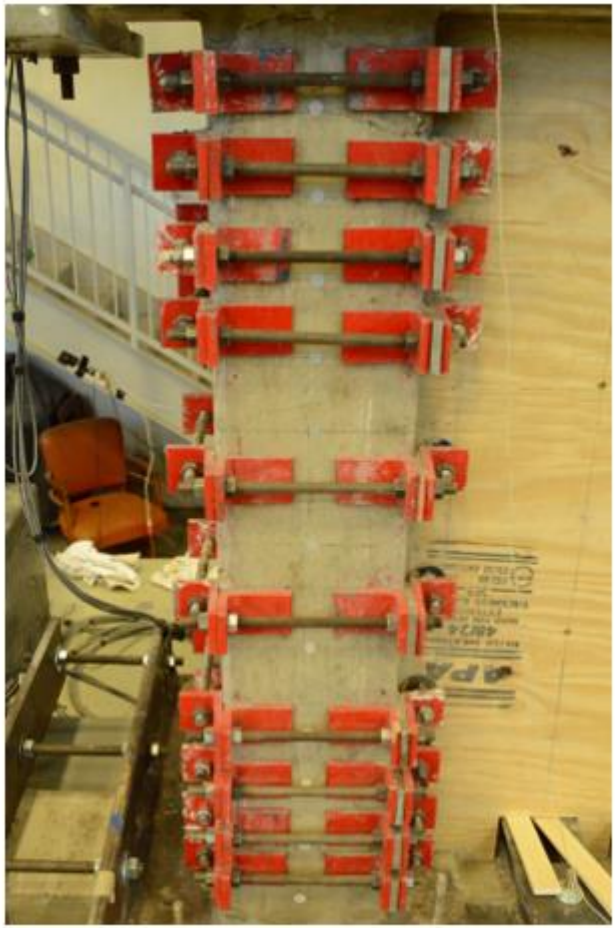

(a) Elevation

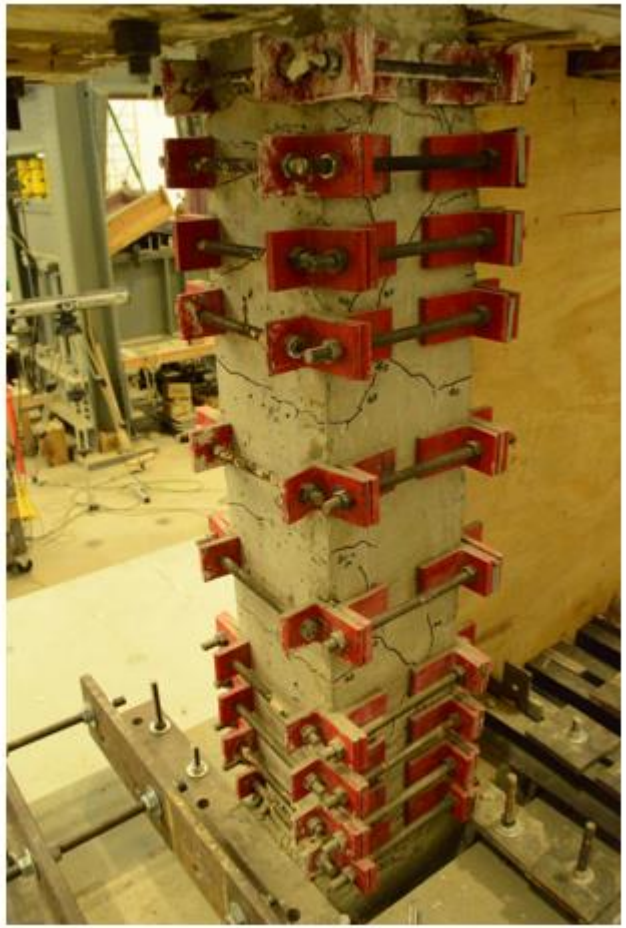

(d) Isometric

Figure 2-30: External Post-Tensioned Transverse Reinforcement – Photograph

Figure 2-31: Modulus of Elasticity (E_w) Beam Test Setup

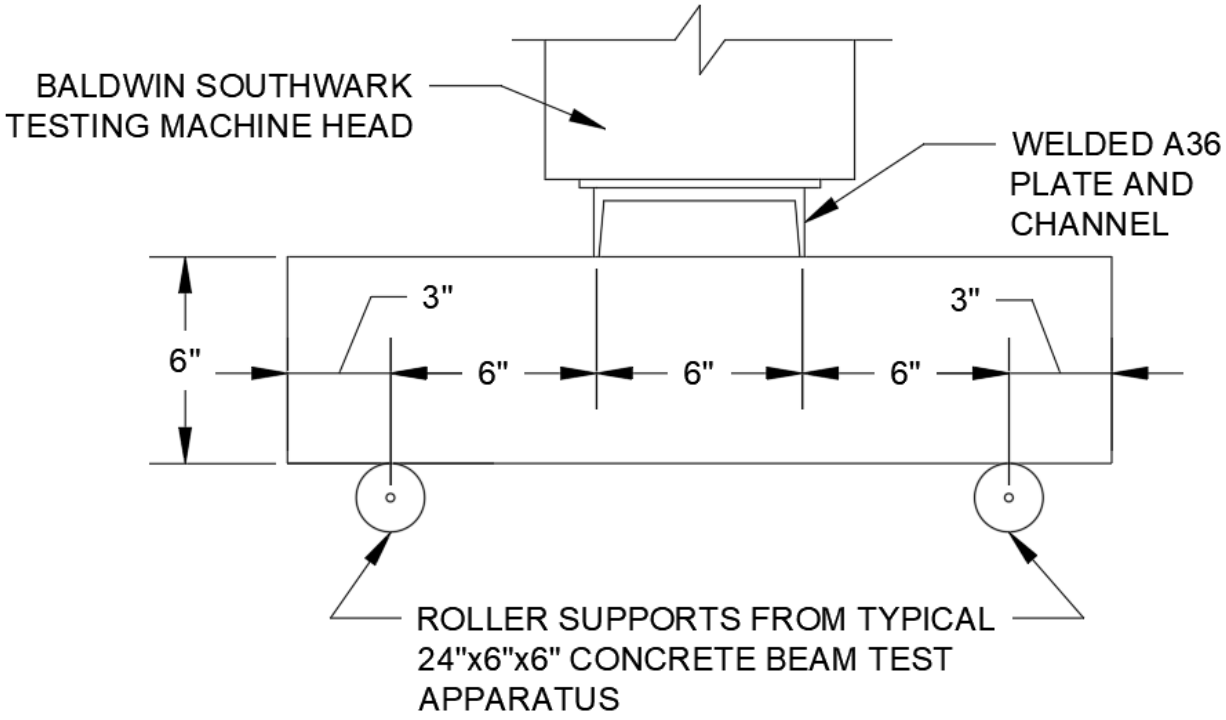

Figure 2-32: E_w Beam Test Elevation

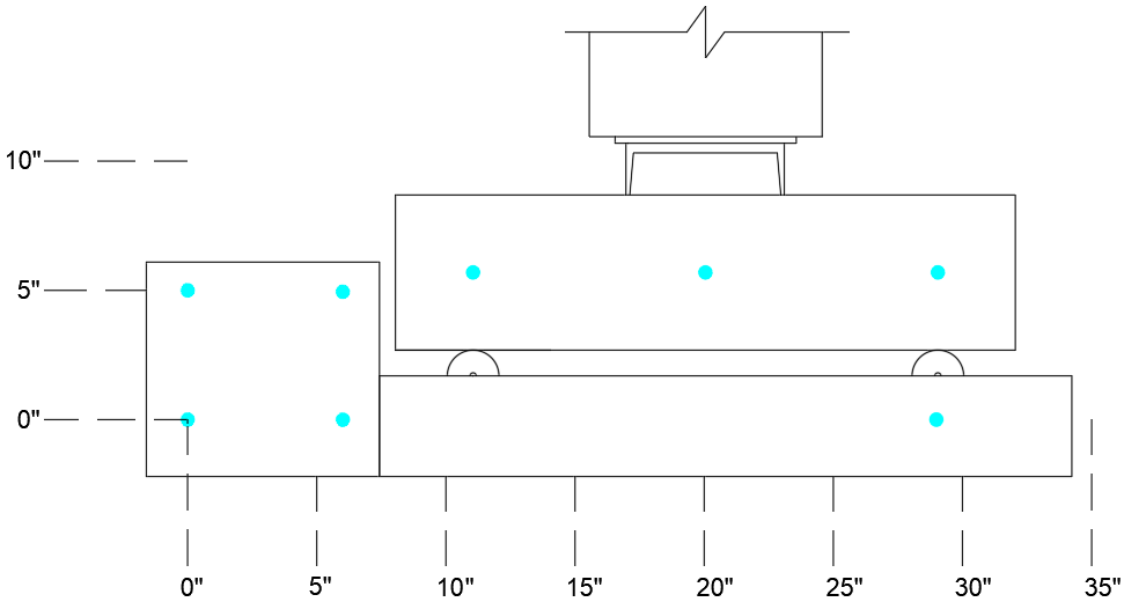

Figure 2-33: Optotrack Target Layout in E_w Beam Tests

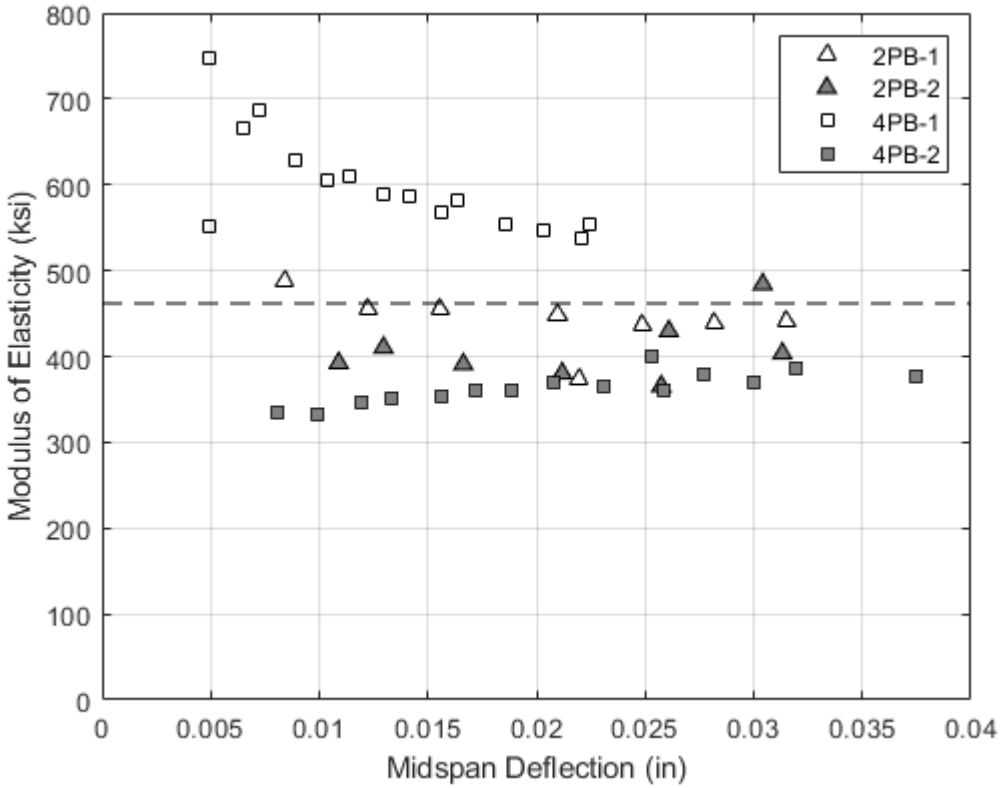

Figure 2-34: Modulus of Elasticity vs Midspan Deflection for E_w Beam Tests

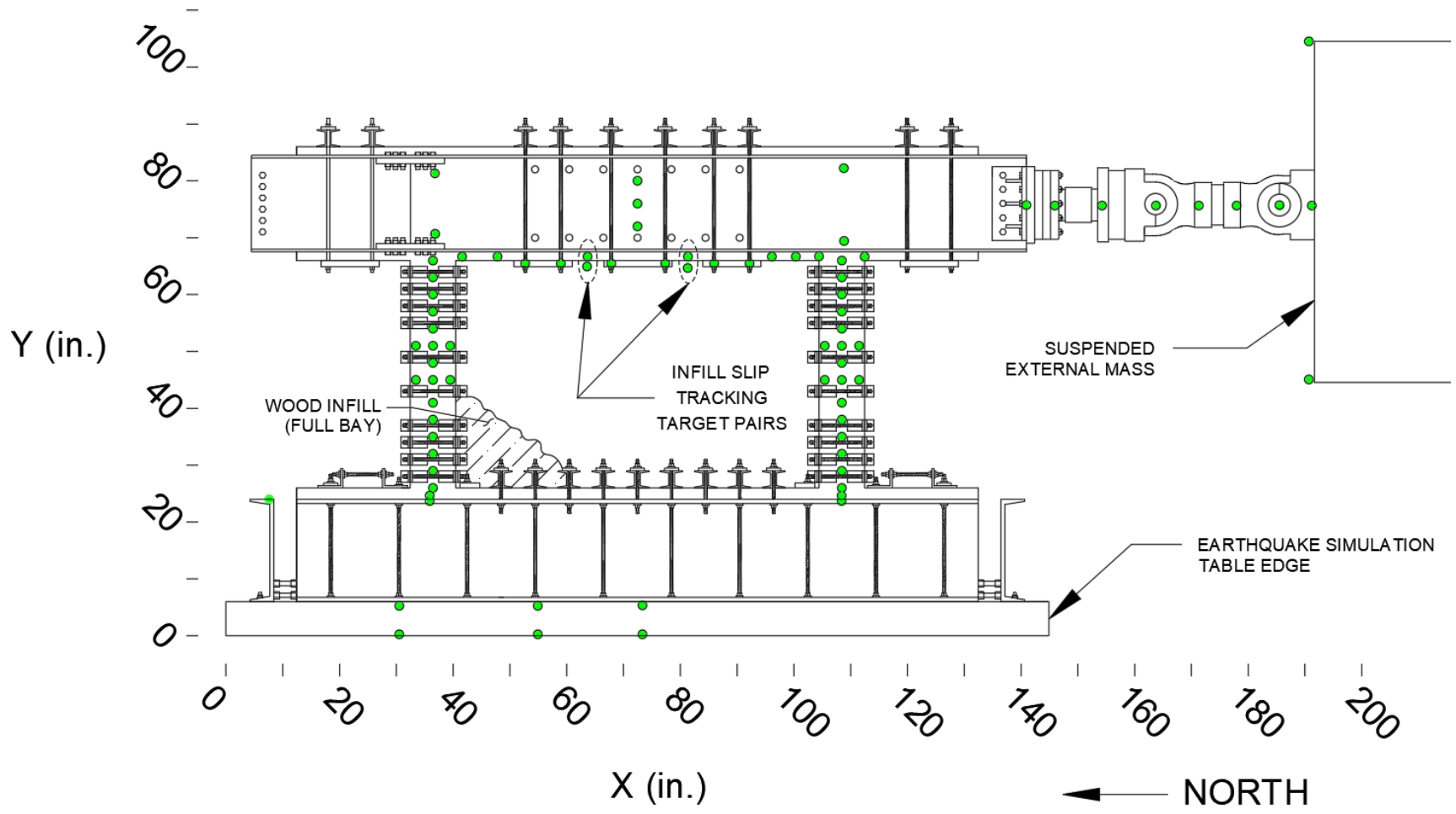

Figure 3-1: Optitrack Target Layout A[1][2]

[1] Deployed in series F1-C-2PB, F1-C-1PB
[2] Optitrack targets denoted by GREEN circles

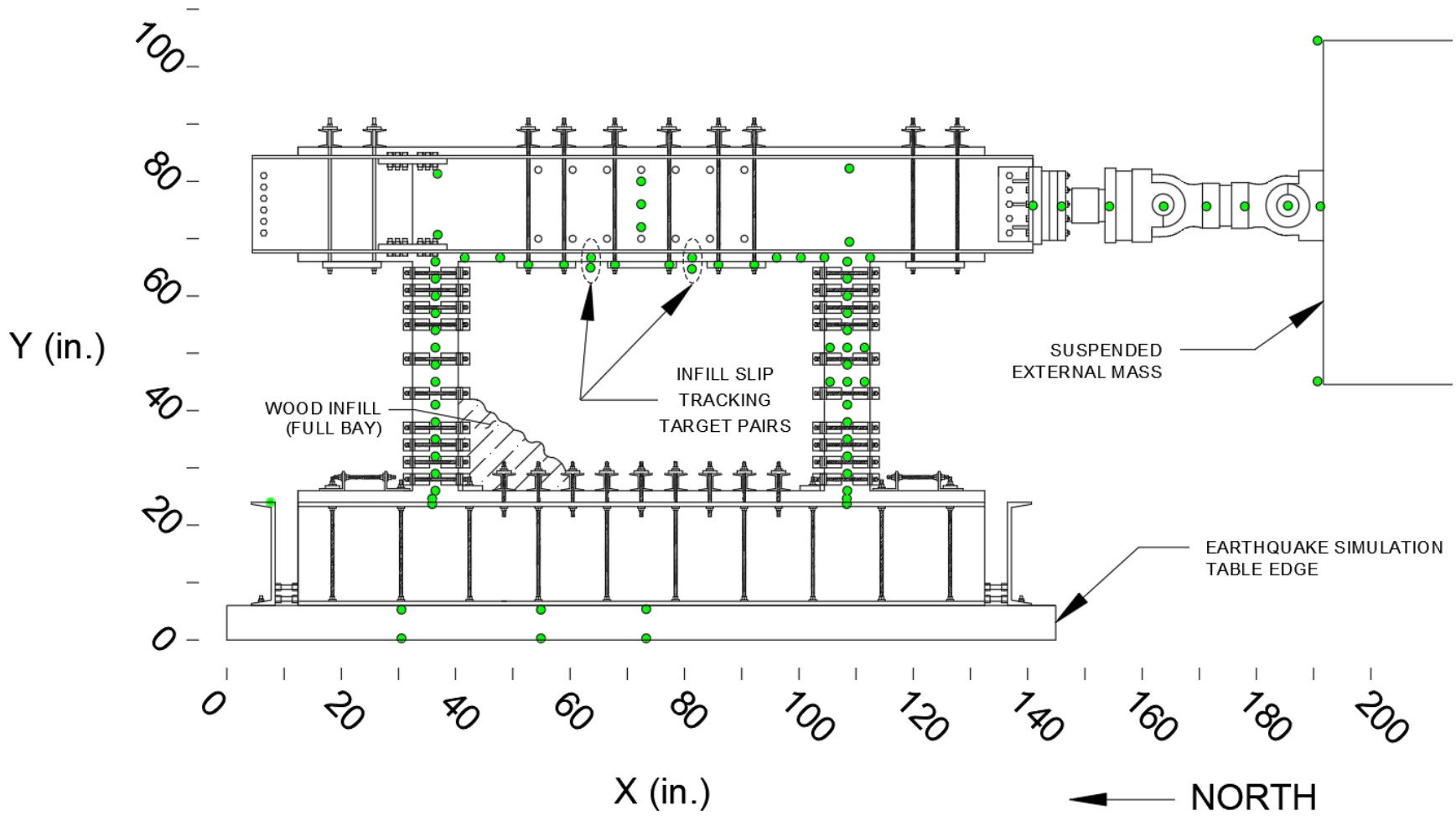

Figure 3-2: Optitrack Target Layout B[1]

[1] Deployed in series F2-C-4PB, F2-R-C-4PB, F2-R-C-2PB, F2-R-C-1PB, F2-R-C

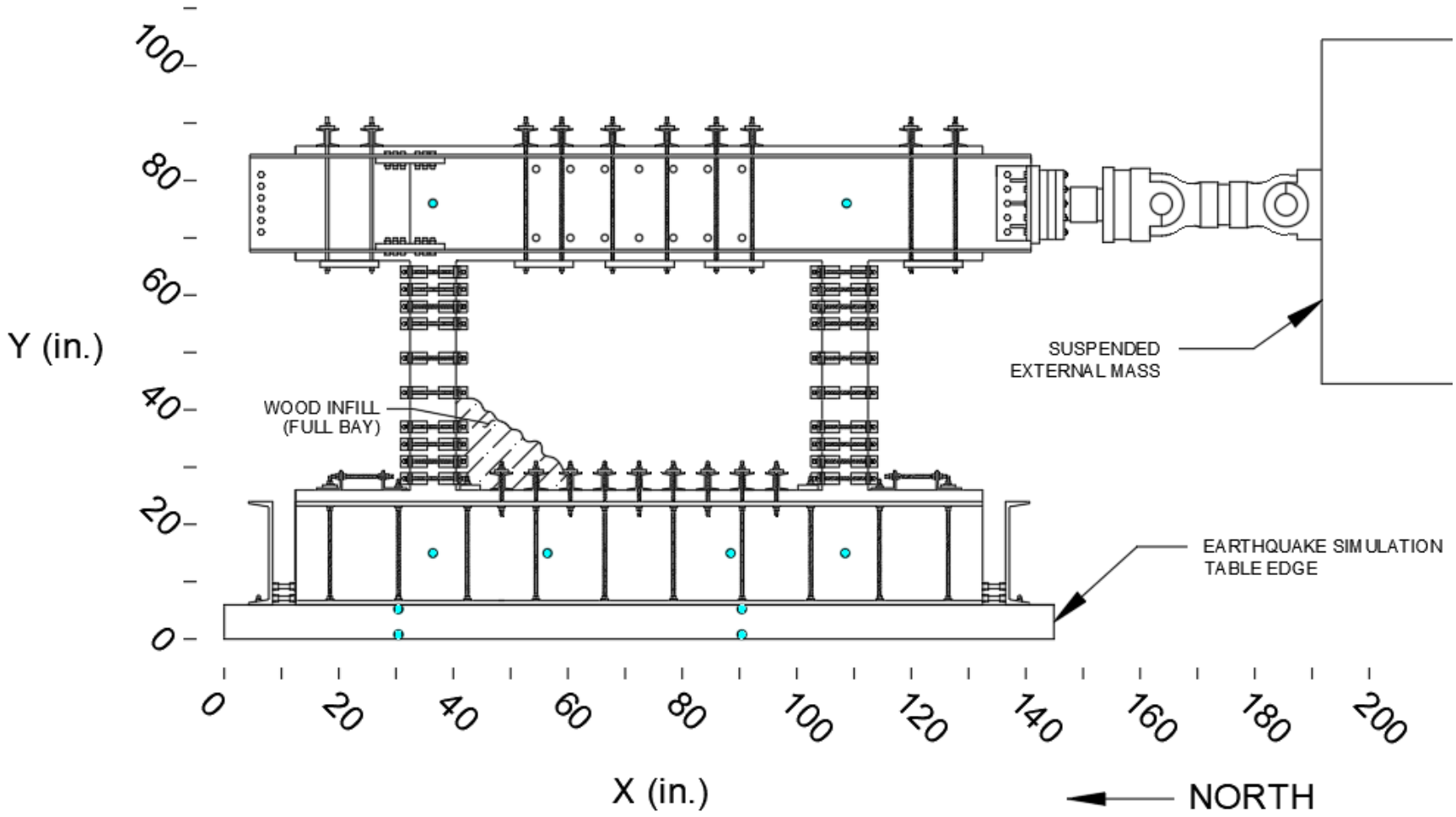

Figure 3-3: Optotrack Target Layout A[12]

[1] Deployed in series F2-C-4PB, F1-C-2PB, F2-R-C
[2] Optotrack targets denoted by CYAN circles

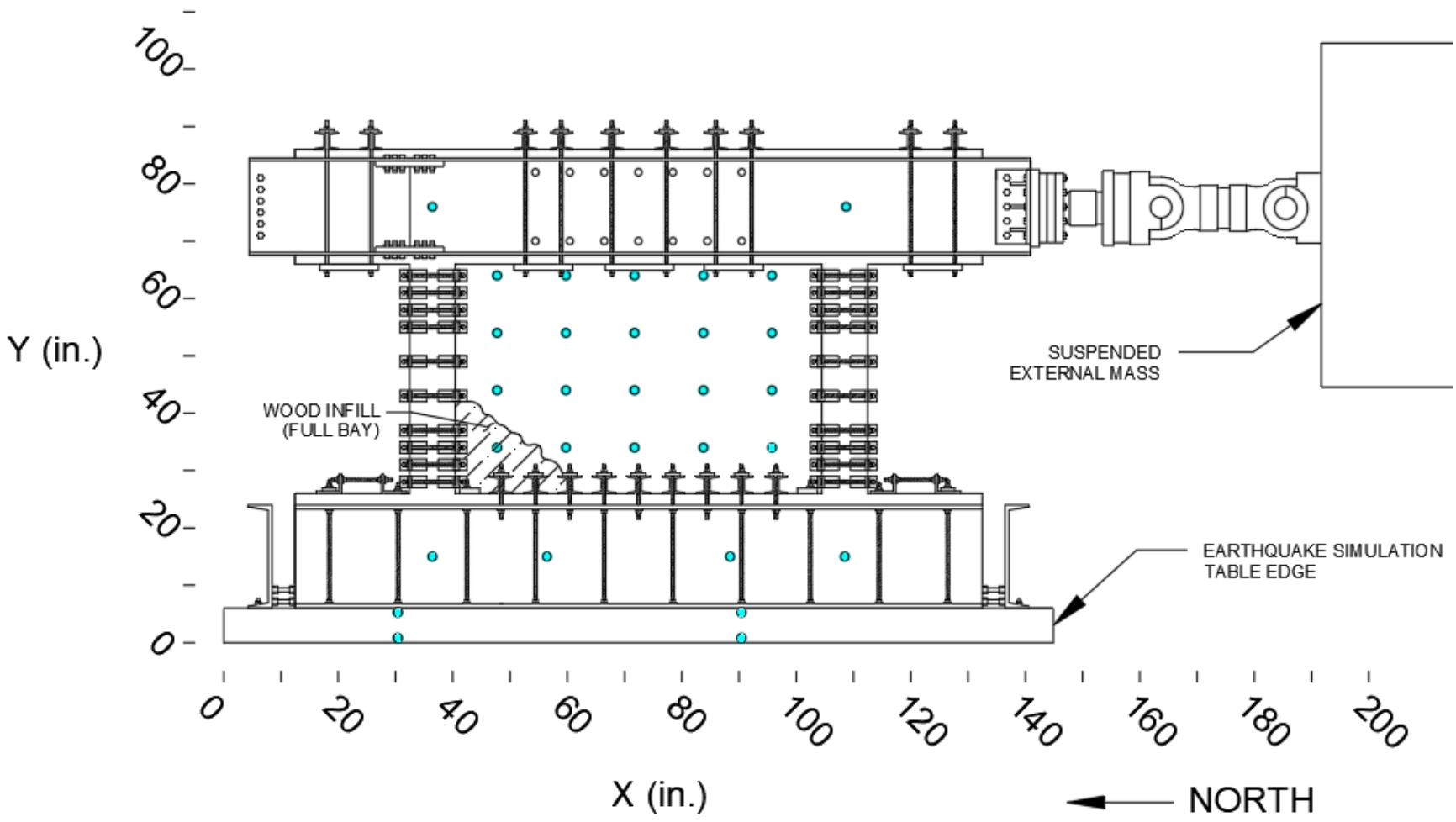

Figure 3-4: Optotrack Target Layout B[1]

[1] Deployed in series F1-C-1PB, F2-R-C-4PB, F2-R-C-2PB, F2-R-C-1PB

Figure 3-5: Frame Instrumented with Optitrack Target Layout B, Optotrack Layout B (Photograph)

Figure 3-6: Mortar Edge-Joint Between Infill and Frame prior to Series F2-C-4PB

Figure 3-7: Mortar Edge-Joint after Deterioration during Series F2-C-4PB

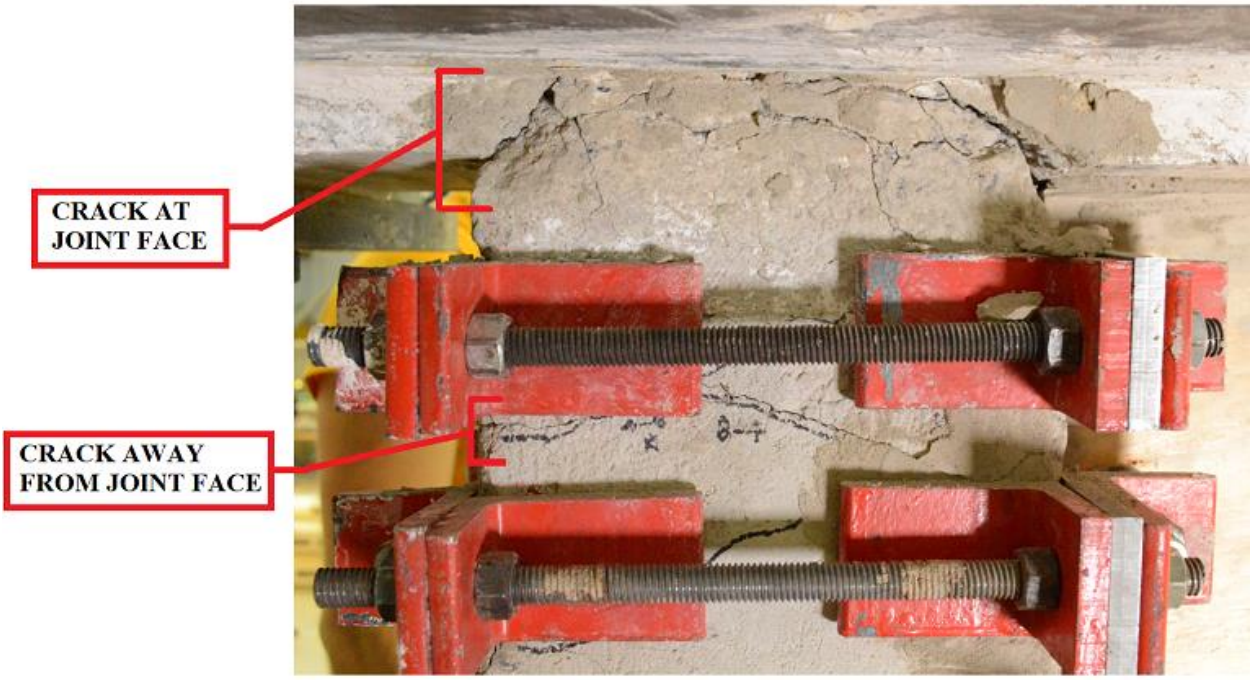

Figure 3-8: Crack Formation at Column Top after Run 105 of Frame 2, Series F2-C-4PB

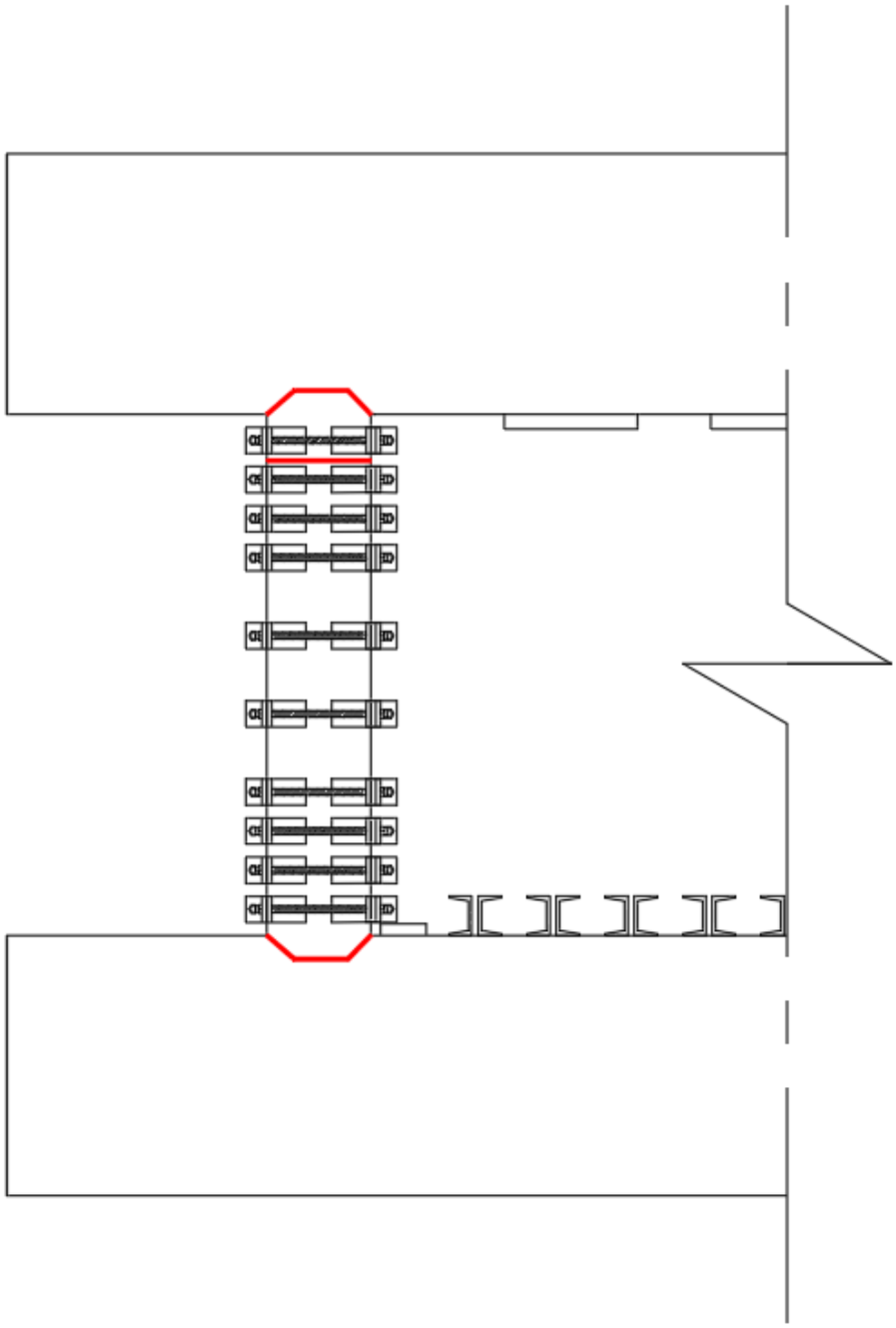

Figure 3-9: Primary Flexural Crack Location in Columns, Series F2-C-4PB[1]

[1] Cracks developed in matching locations on North and South columns of Frame 2

Figure 3-10: Single-ply Splitting at Infill Top, Western Face after Run 104 of Frame 2, Series F2-C-4PB

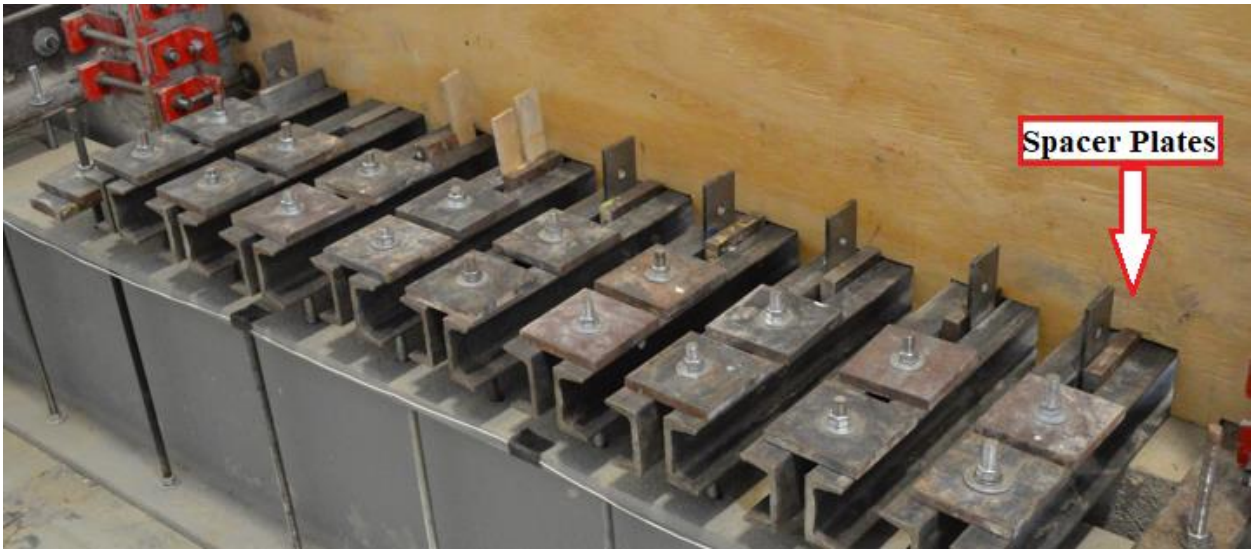

Figure 3-11: Channel Spacer Plates (Photograph)[1], Series F2-C-4PB

[1] Spacer plate widths sized to fill a given infill channel cutout. When exact width could not be achieved with steel plates, wood shims were vertically inserted.

(a) North Column with Clamps

(c) North Column without Clamps

(b) South Column with Clamps

(d) South Column without Clamps

Figure 3-12: Column West-face Base Concrete Spalling after Series F2-C-4PB

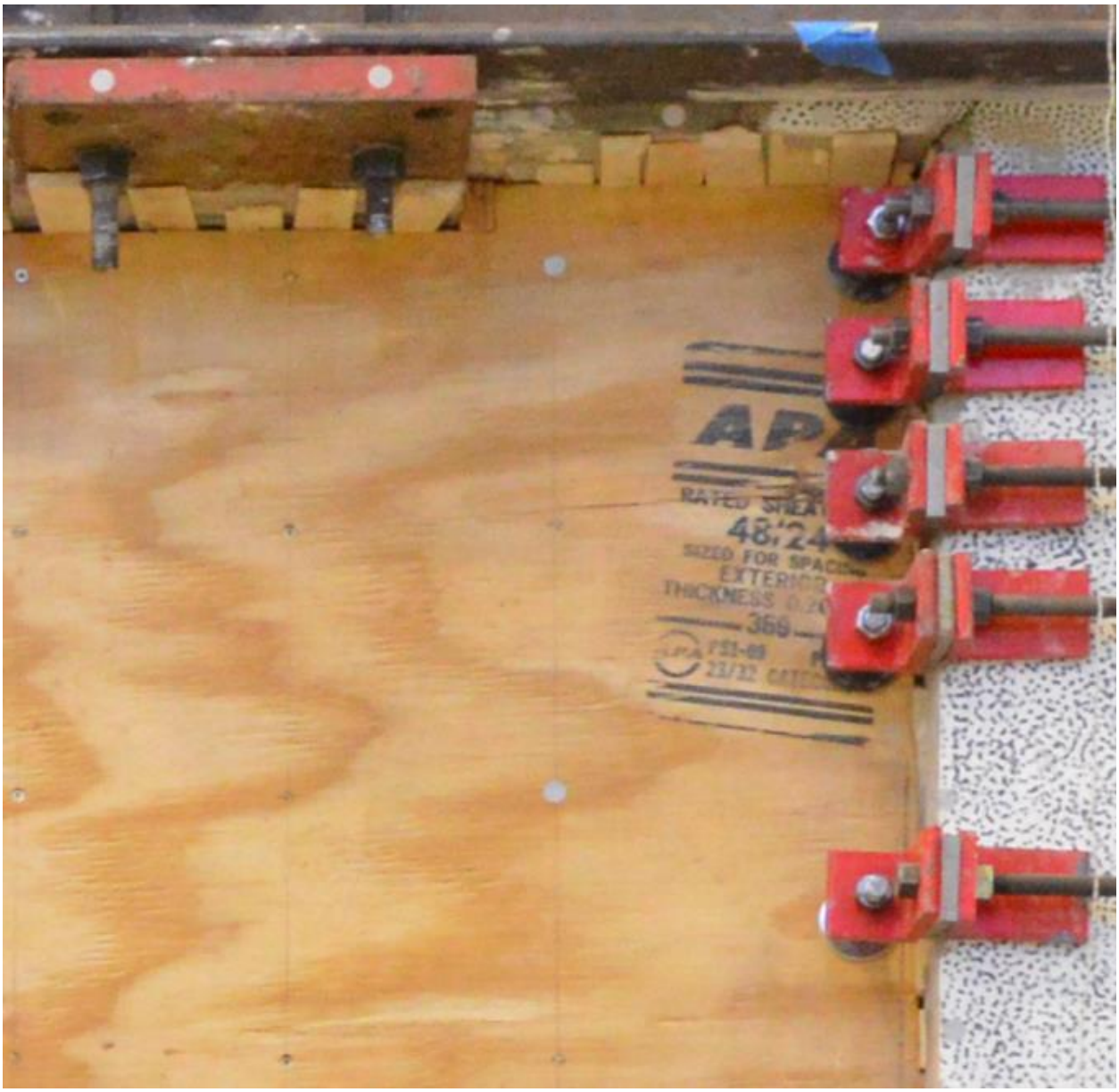

Figure 3-13: Shim Filled Edge Gap, Series F1-C-2PB

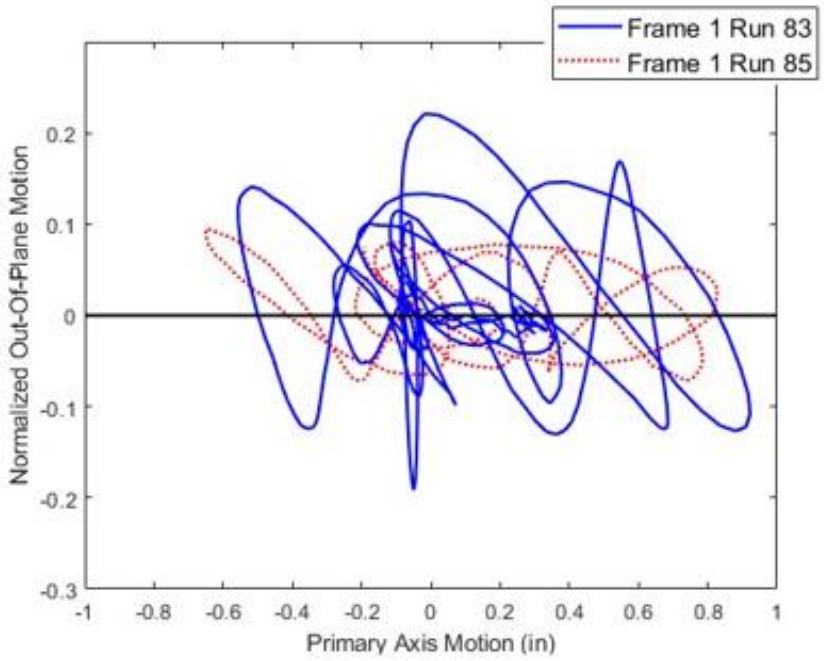

(a) North Column Centerline

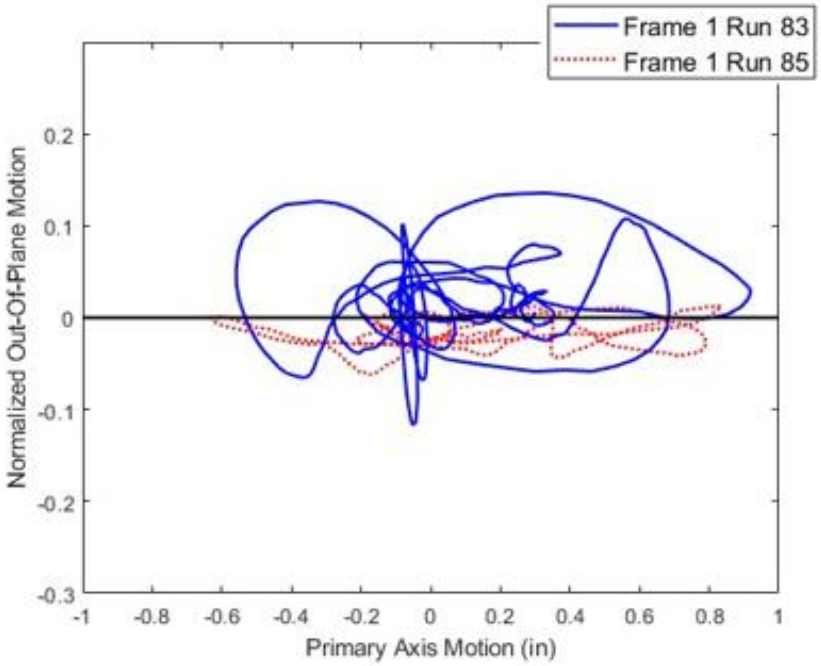

(b) South Column Centerline

Figure 3-14: Comparison of Top Beam Normalized Out-Of-Plane Motion vs In-Plane Motion, Frame 1 Run 83 and 85[1], Series F1-C-2PB

[1] Top beam out-of-plane motion is normalized by instantaneous in-plane displacement.

Figure 3-15: Deterioration of Shim Edge-Joint after Frame 1 Run 86,
Series F1-C-2PB

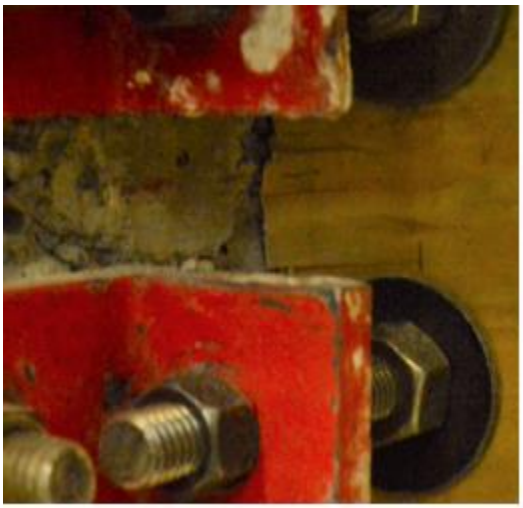

(b) East face, South Column Top

(b) East Face, South Column Bottom

Figure 3-16: Edge Crushing of Infill, Series F1-C-2PB

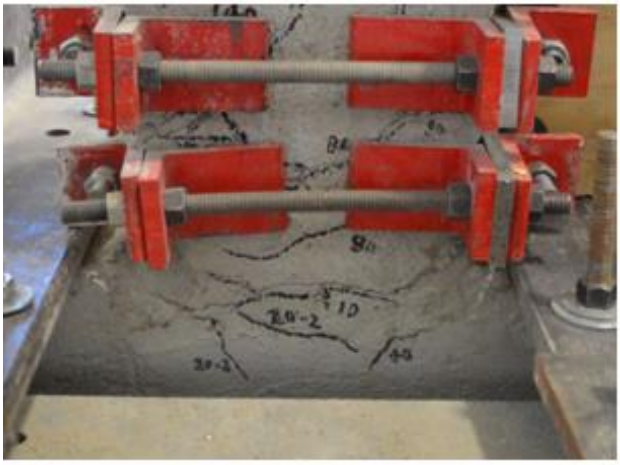

(a) South Column Base East Face
Repaired condition

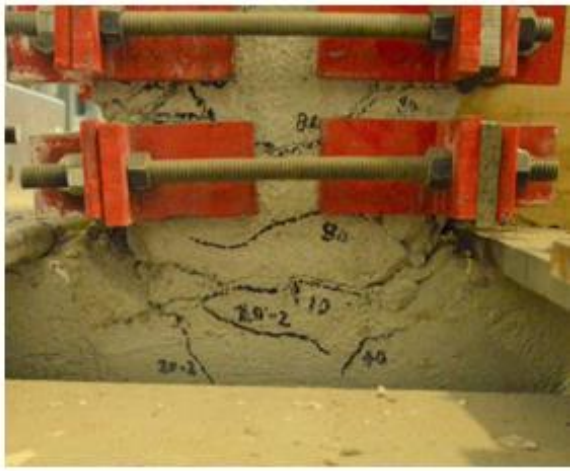

(b) South Column Base East Face
condition after Run 89

(c) South Column Base South Face
Repair Mortar Spalling after Run 89

Figure 3-17: Column Base Mortar Crumbling, Series F1-C-2PB

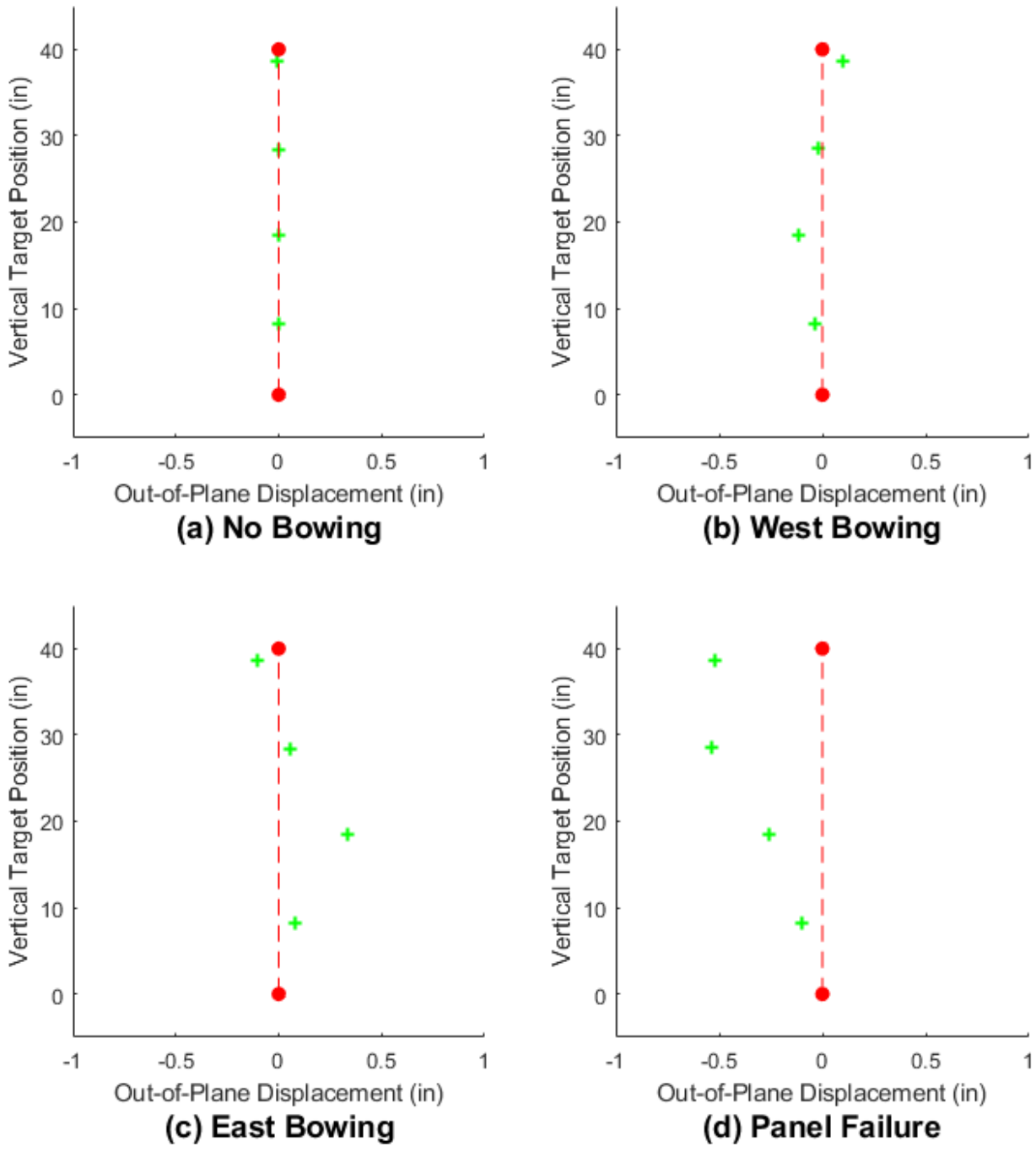

Figure 3-18: Bowing Amplitude along Northern Gridline of Optotrack Targets, Frame 1 Run 107, Series F1-C-1PB[1]

[1] Vertical target position is relative to the bay height, marked in red. The bottom of the bay occurs at Y = 0".

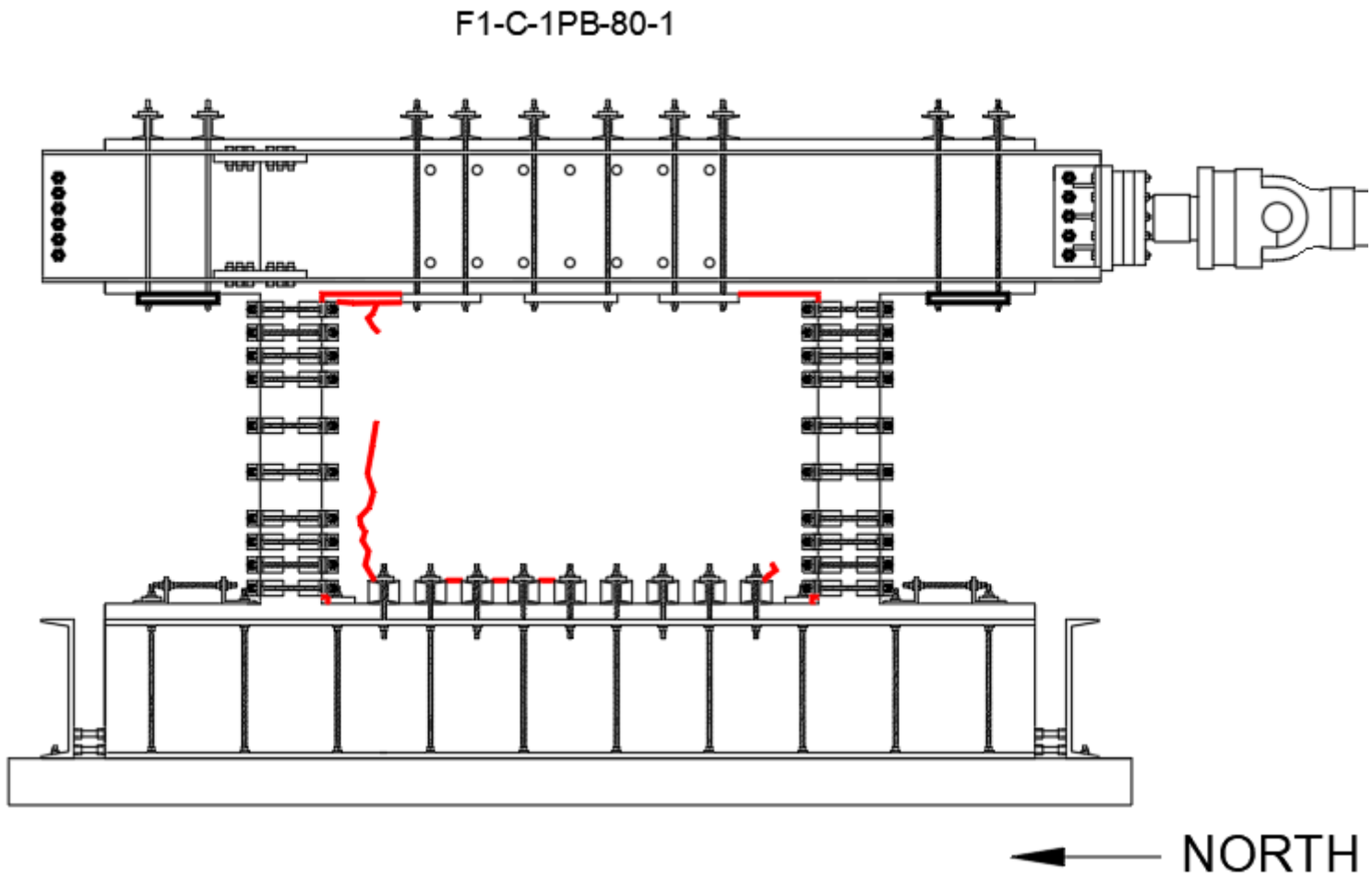

Figure 3-19: Crack Map on Infill after Frame 1 Run 107, Series F1-C-1PB

(a) North Edge Splitting, West Face

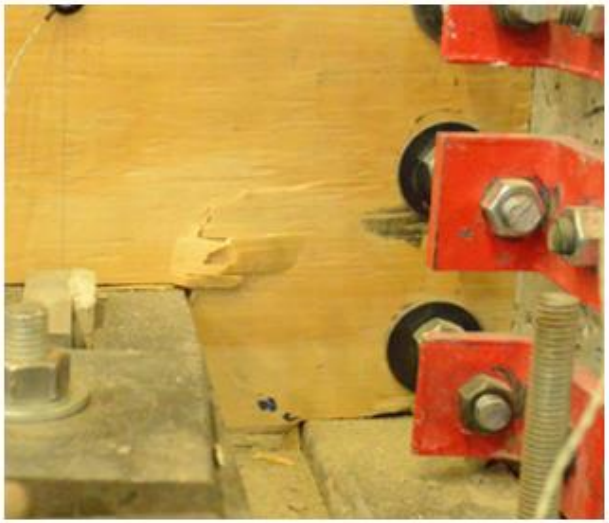

(b) South Edge Splitting, West Face Bottom

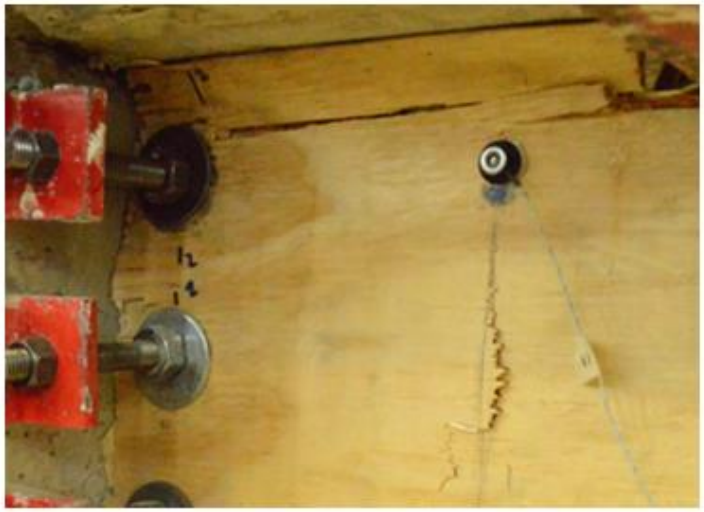

(c) North Edge Crushing, West Face Top

Figure 3-20: Infill Damage after Frame 1 Run 107, Series F1-C-1PB

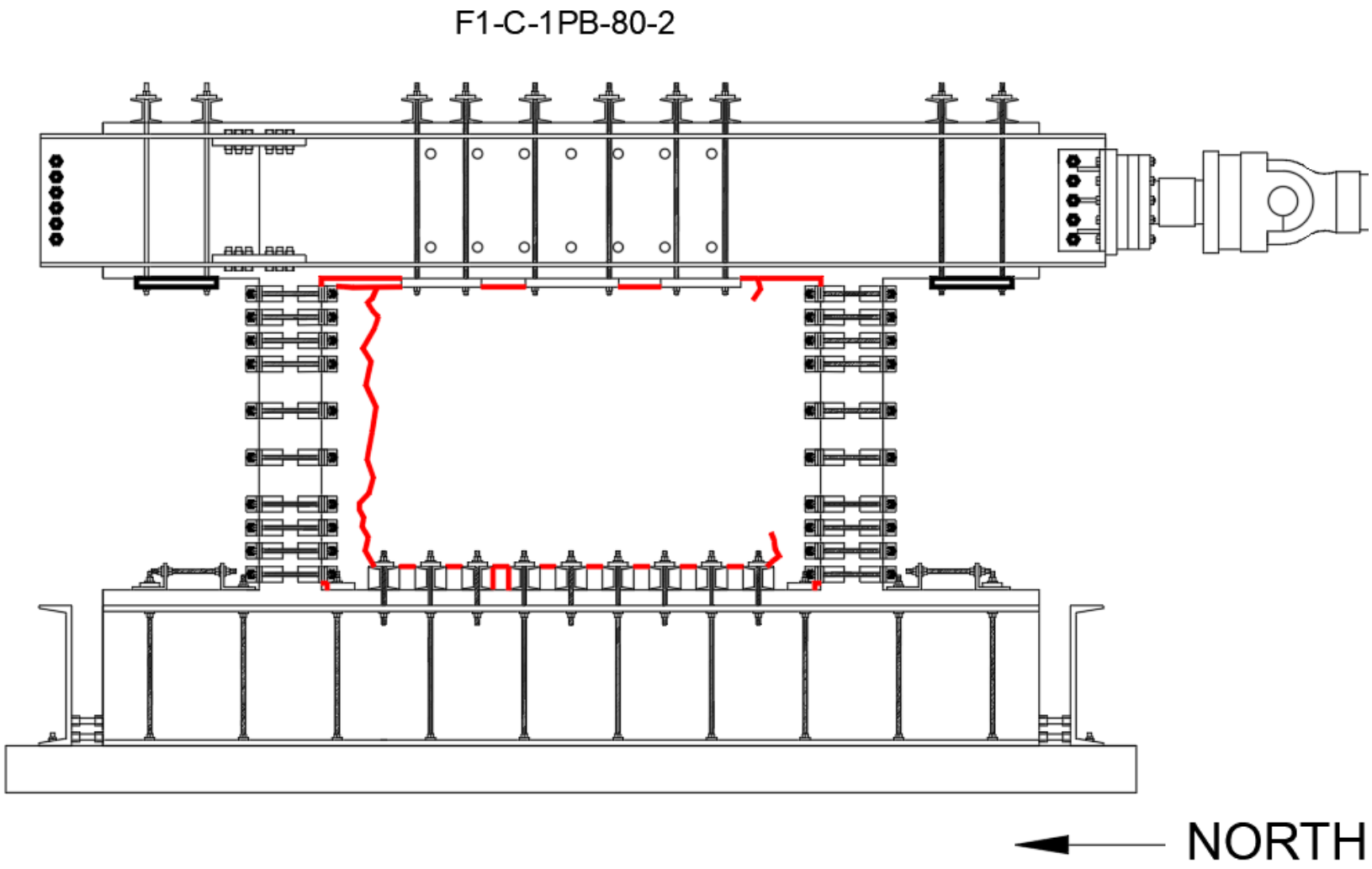

Figure 3-21: Crack Map on Infill after Frame 1 Run 108, Series F1-C-1PB

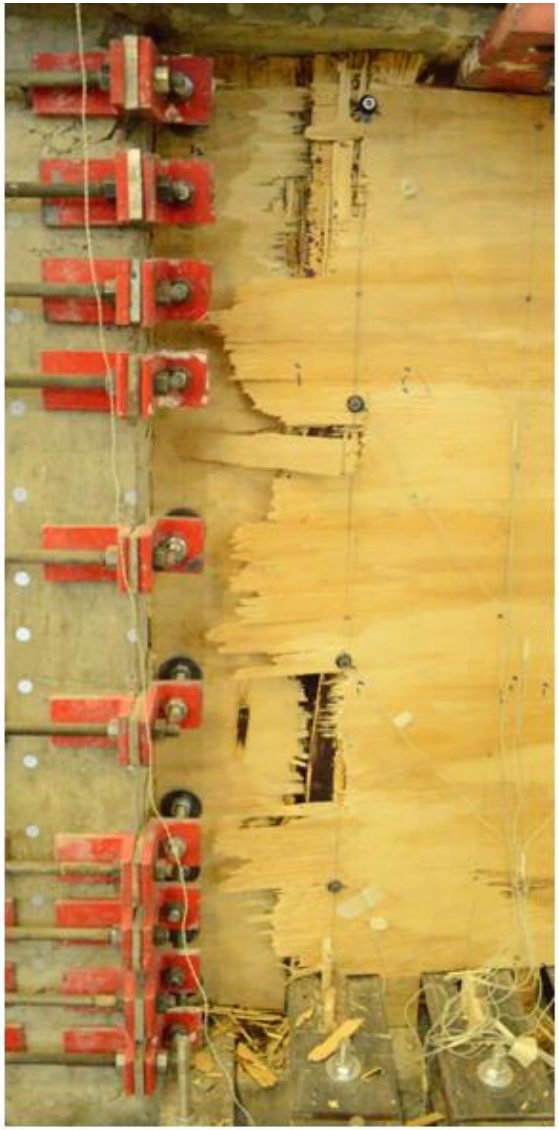

(a) Full-Thickness Failure, North Edge West Face

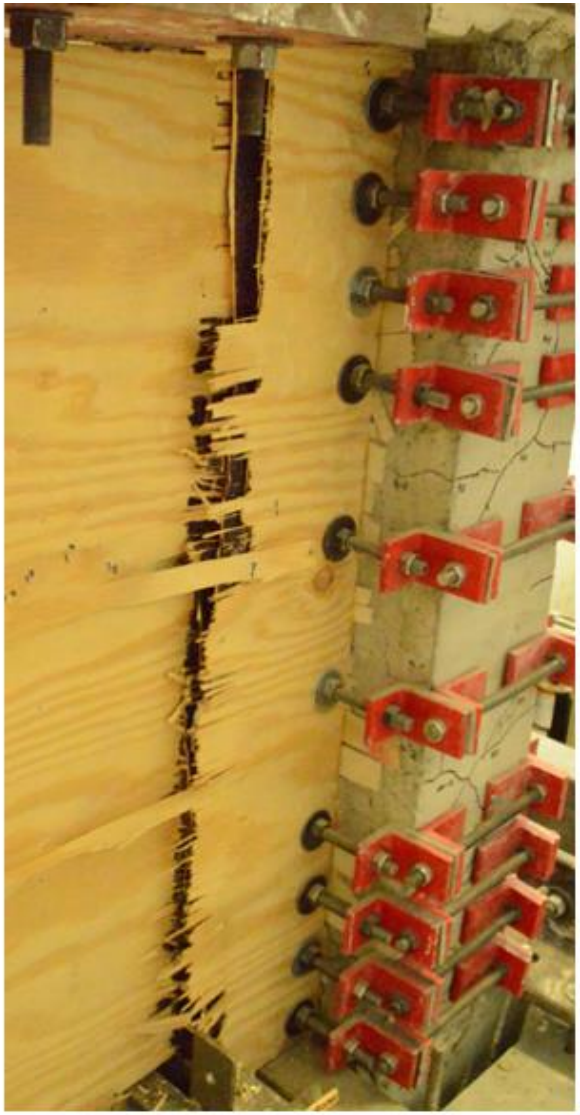

(b) Full-thickness Failure, North Edge East Face

Figure 3-22: Infill Failure after Frame 1 Run 108, Series F1-C-1PB

(a) North Column East Face, Repaired

(c) North Column East Face after Frame 1 Run 108

(b) South Column West Face, Repaired

(d) South Column West Face after Frame 1 Run 108

Figure 3-23: Column Base Damage after Series F1-C-1PB

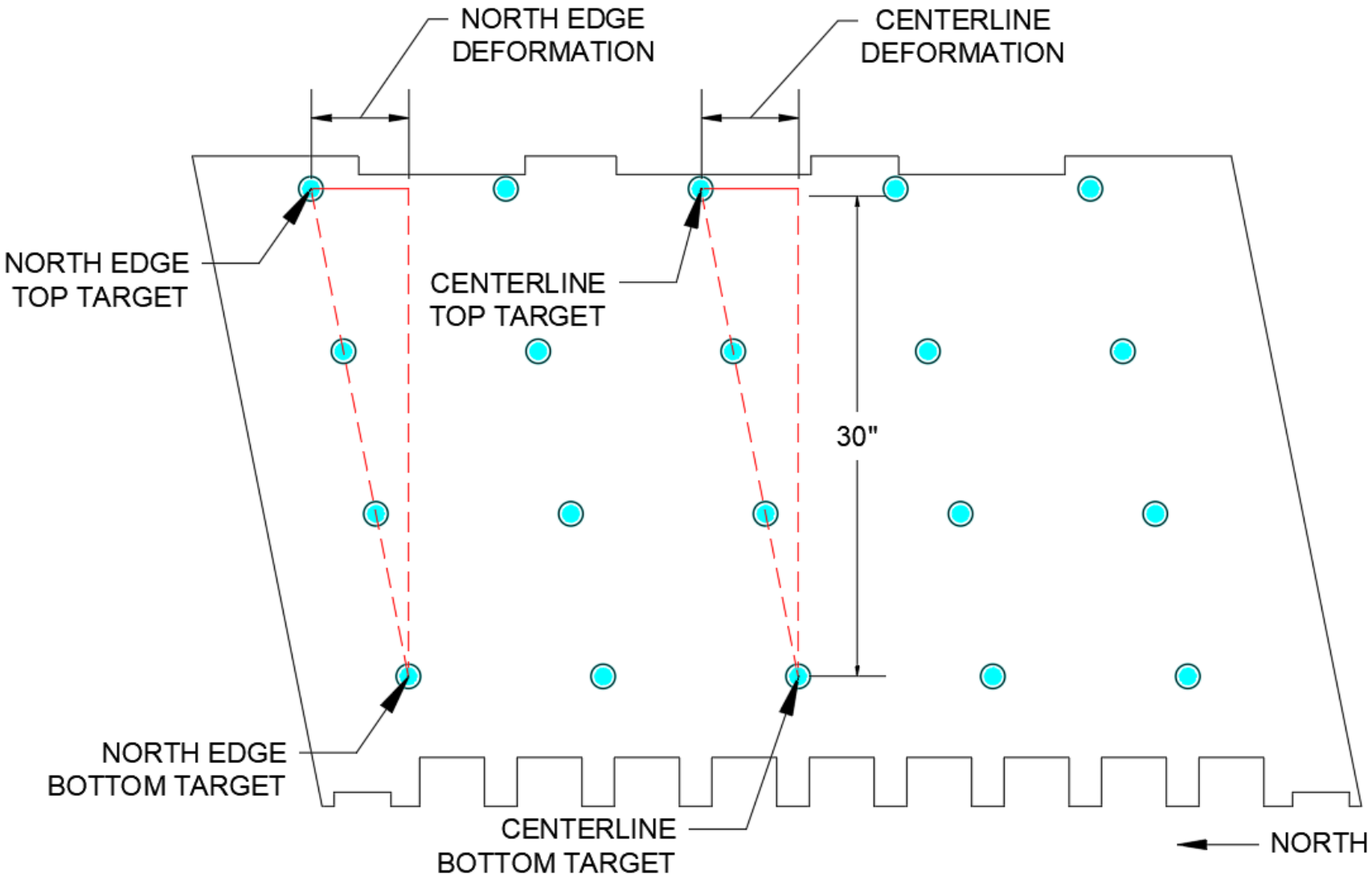

Figure 3-24: Illustration of Optotrack Infill Edge and Centerline Deformations

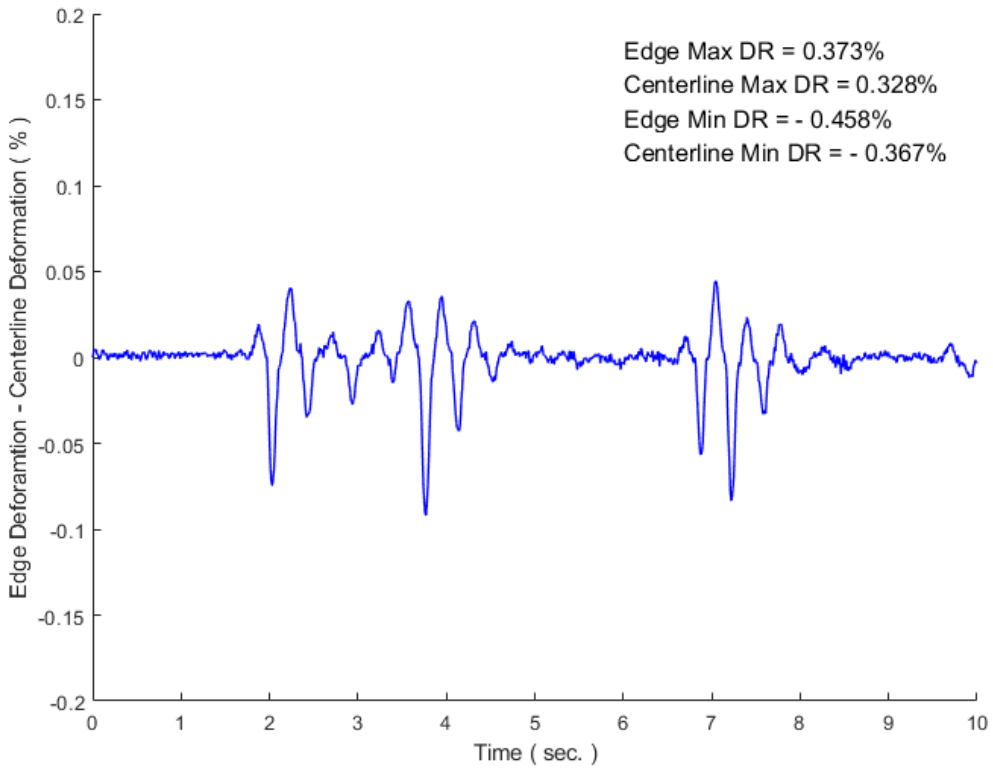

Figure 3-25: Difference of Edge and Centerline Infill Deformations, Frame 1 Run 103, Series F1-C-1PB

Figure 3-26: Partially Removed Infill, Frame 1 Runs 109-112, Series F1-C-1PB

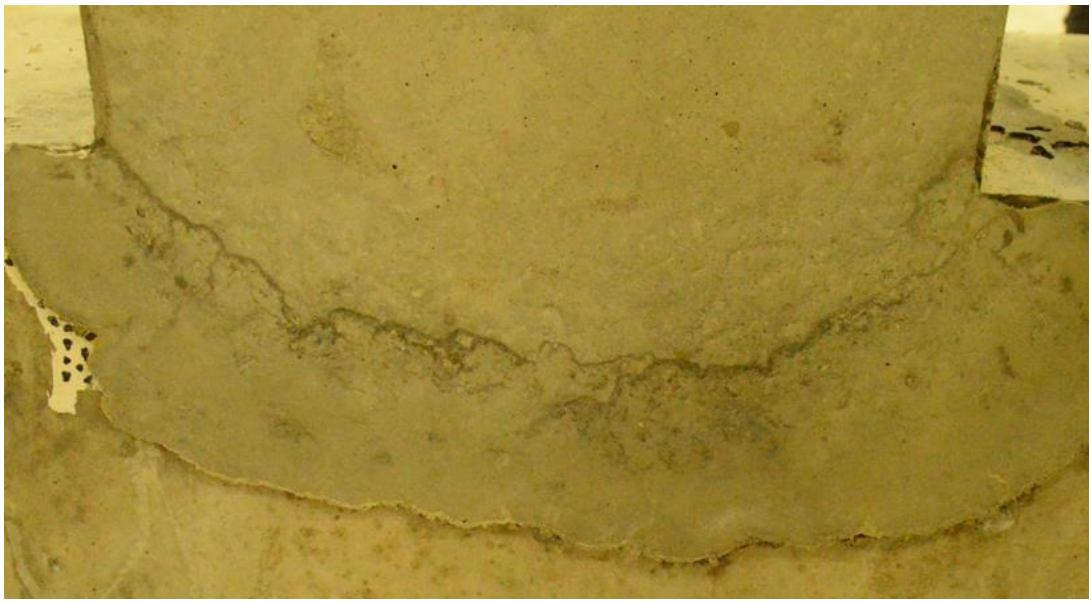

(a) Before Static 8.3-kip Loading

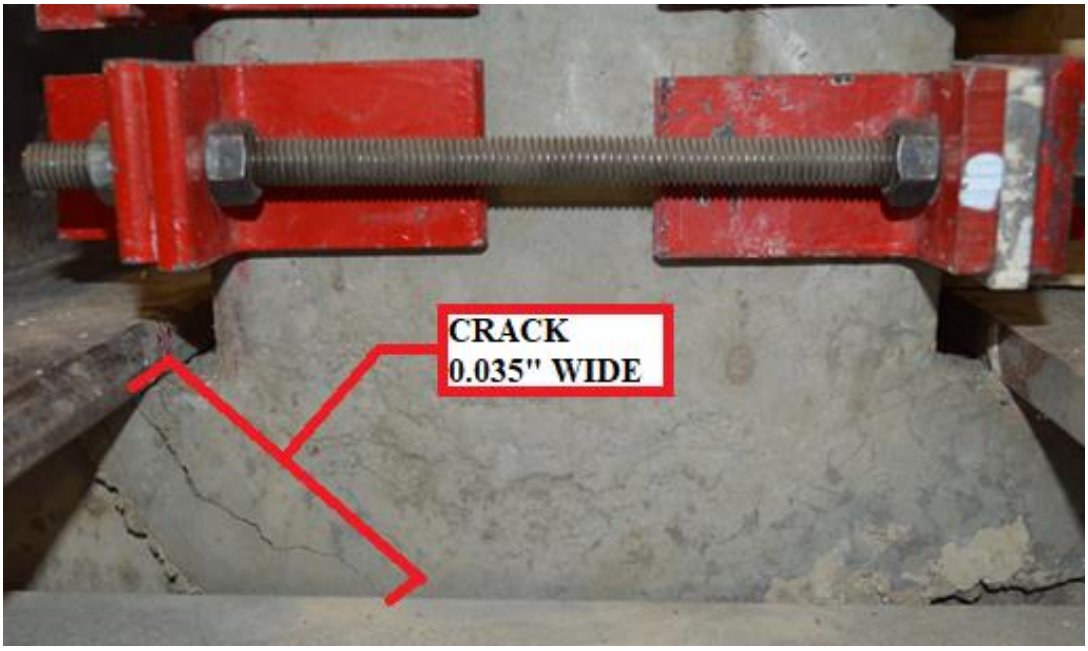

(b) After Static 8.3-kip Loading

Figure 3-27: Crack Formation after Hydraulic Pressure Loss, North Column Base, West Face

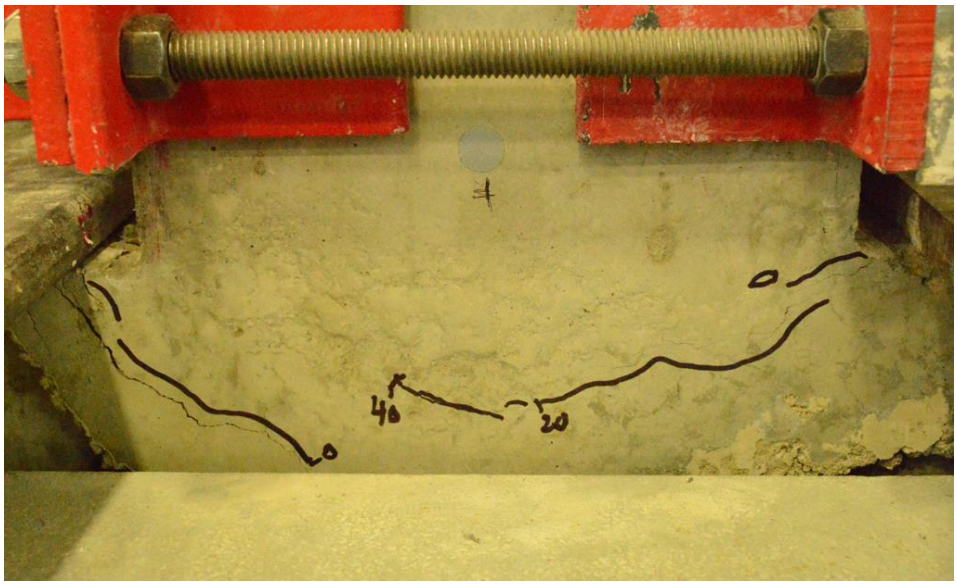

Figure 3-28: Crack formation at North Column Base after Series F2-R-C-4PB[1]

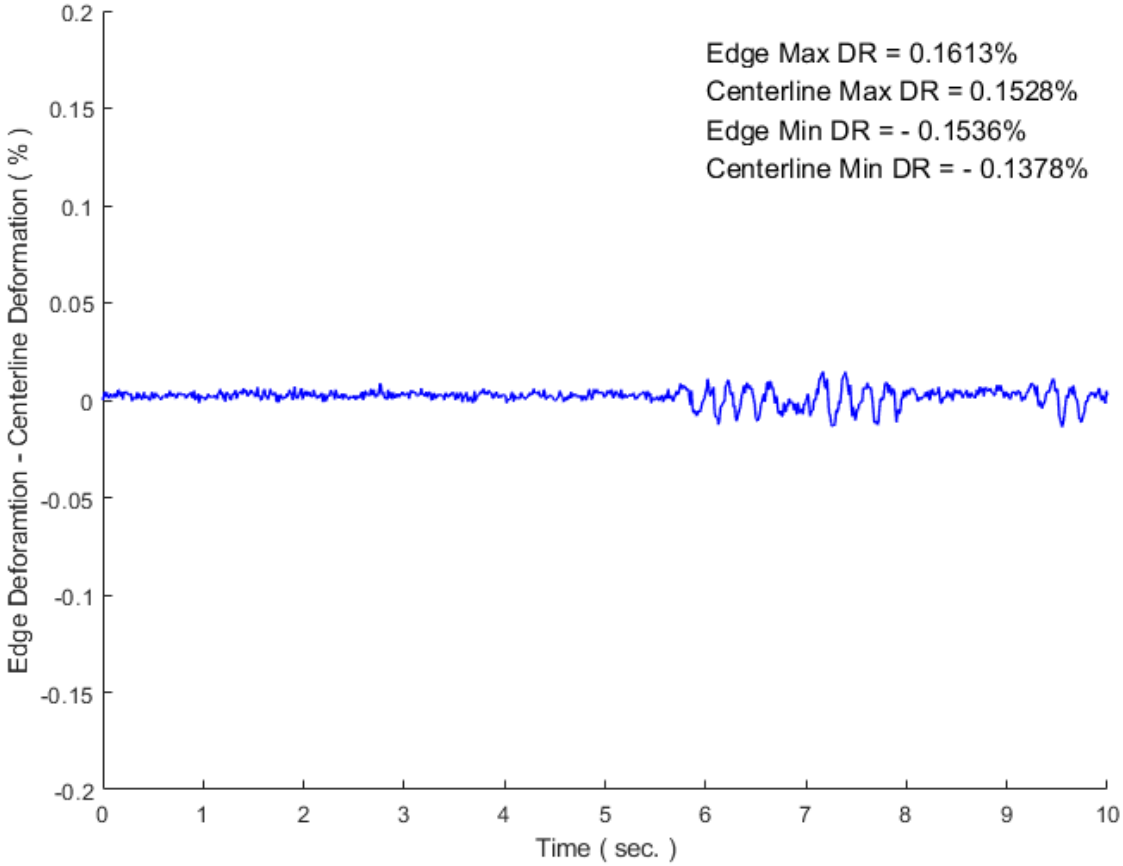

Figure 3-29: Difference of Edge and Centerline Infill Deformations,
Frame 2 Run 122, Series F2-R-C-4PB

[1] Cracks marked by "0" denotes the crack formed during 8.3-kip static loading

(a) North Column Base (b) South Column, 12" from base

Figure 3-30: Full Width Cold Joint Cracking after Frame 2 Run 129, Series F2-R-C-2PB

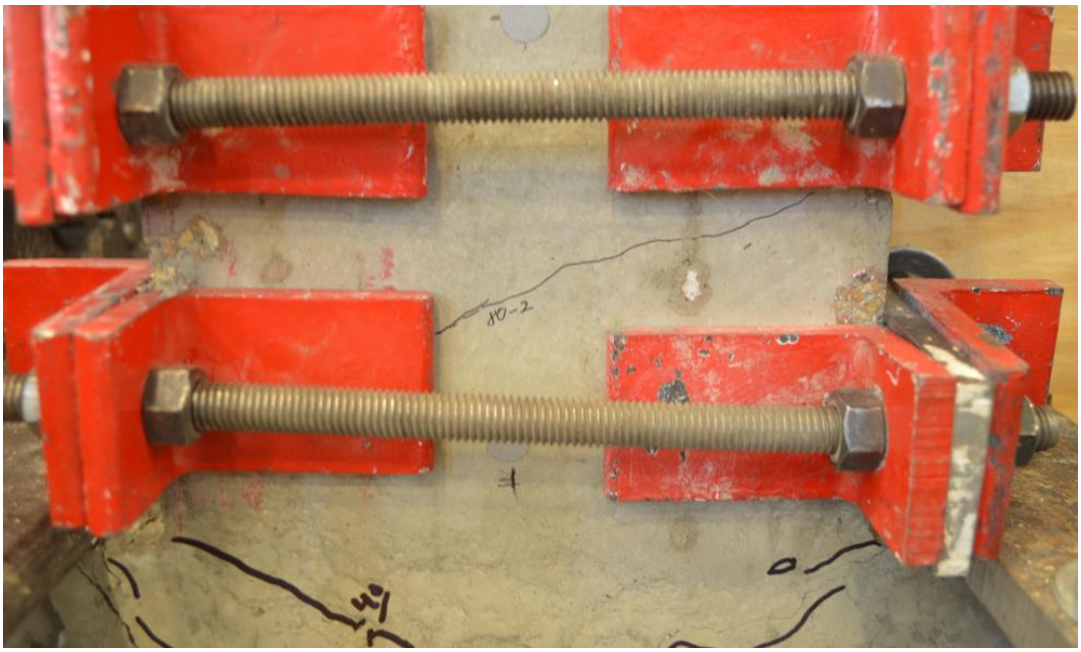

Figure 3-31: Hairline Diagonal Shear Crack at North Column Base after Frame 2 Run 133, Series F2-R-C-2PB

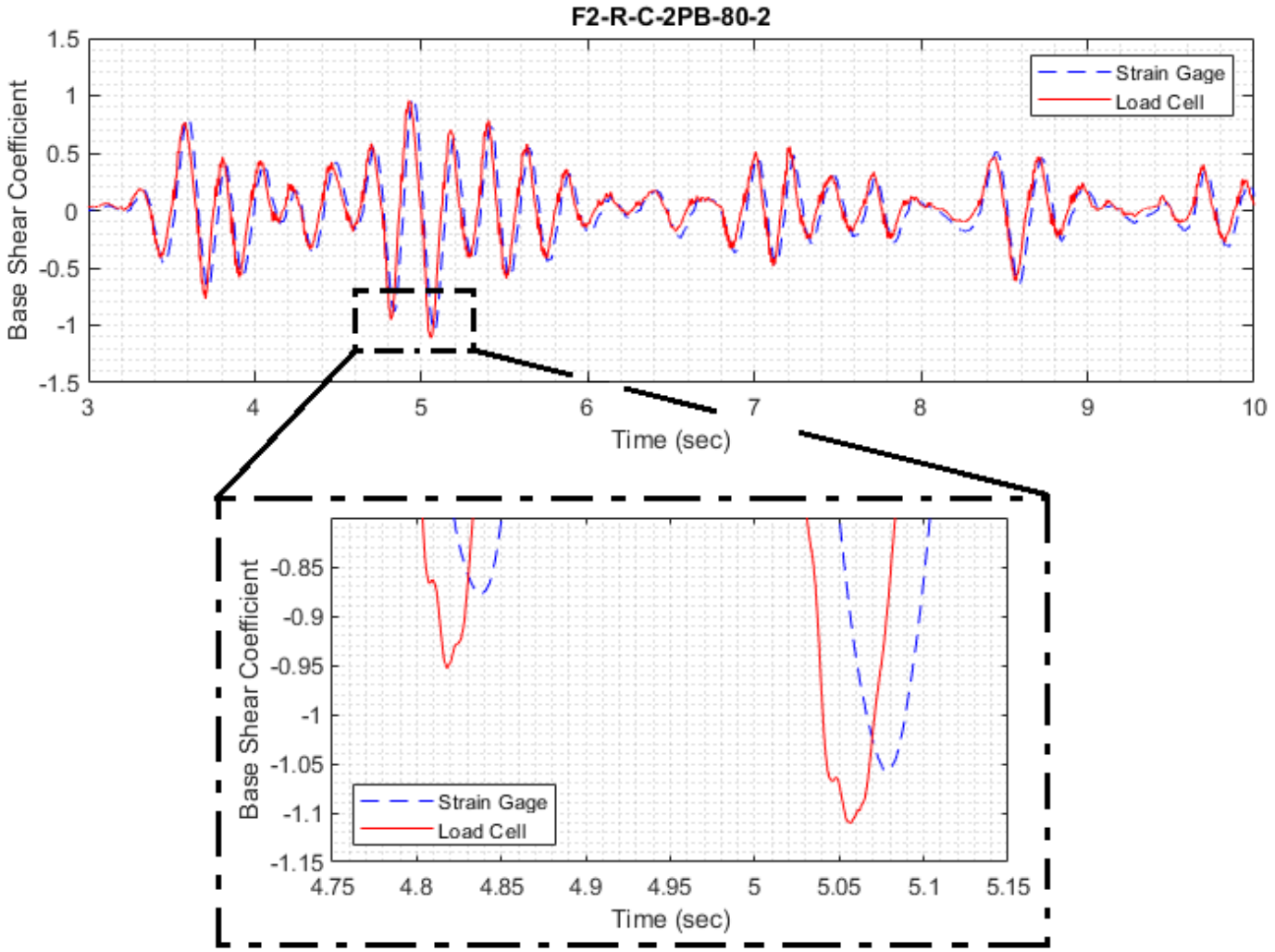

Figure 3-32: Load Cell vs Strain Gage Lateral Load Comparison, Frame 2 Run 133, Series F2-R-C-2PB[1]

[1] Strain Gage load derived from the average strain gage reading on the simulator platform flexure-link.

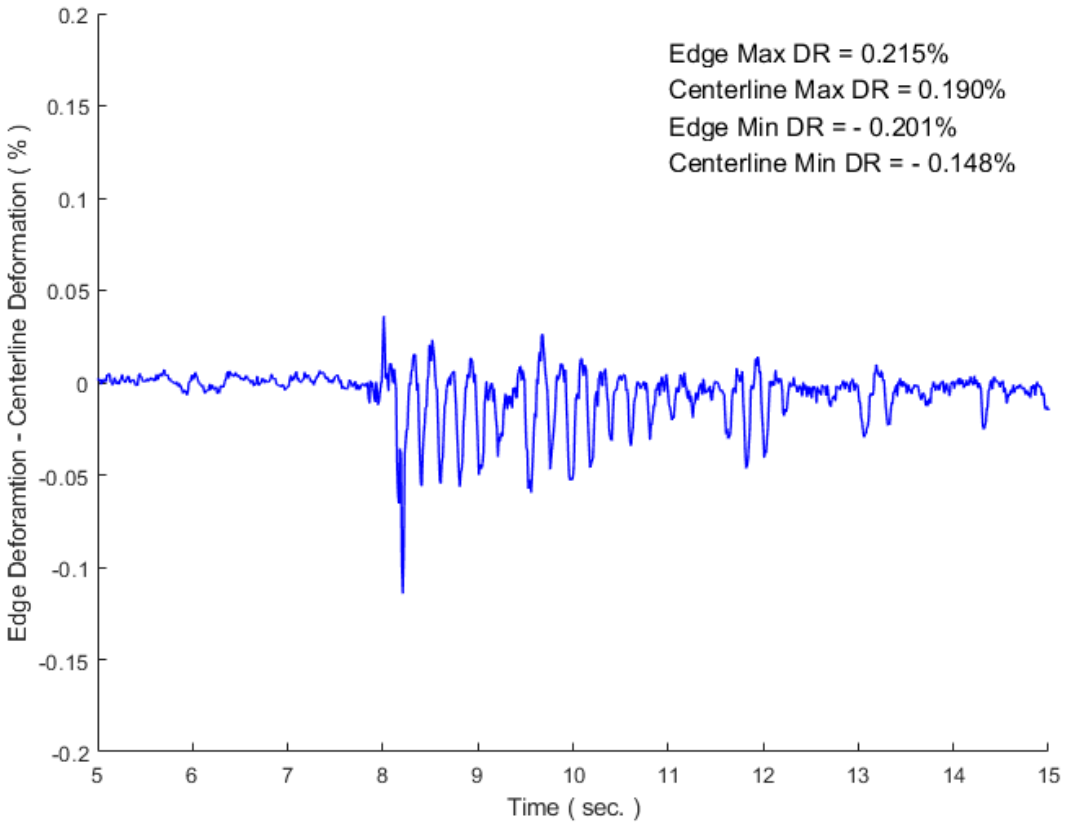

Figure 3-33: Difference of Edge and Centerline Infill Deformations, Frame 2 Run 128, Series F2-R-C-2PB

Figure 3-34: Single-ply Split Between North Vertical Clamping Devices Sustained during Frame 2 Run 132, Series F2-R-C-2PB

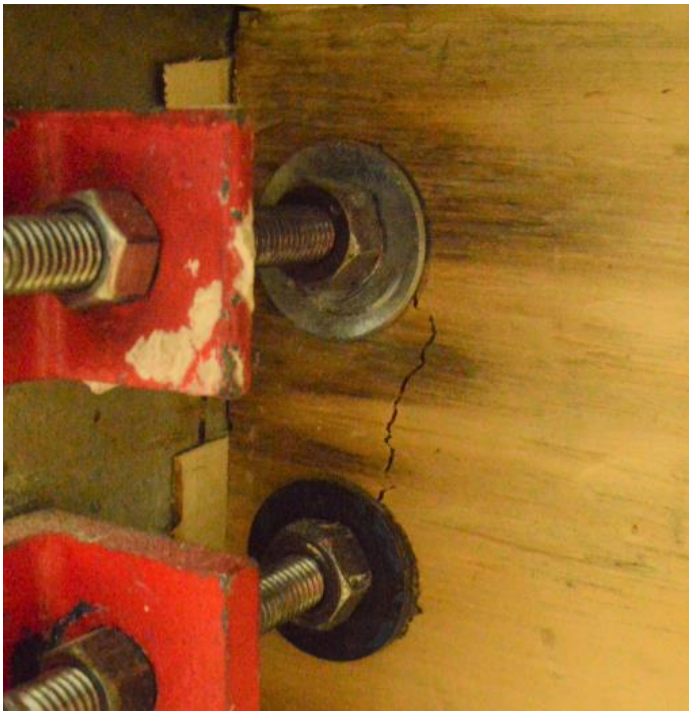

Figure 3-35: Edge Tear-out at Southern Column Top after Frame 2 Run 146, Series F2-R-C-1PB

(a) Before Series F2-R-C-1PB

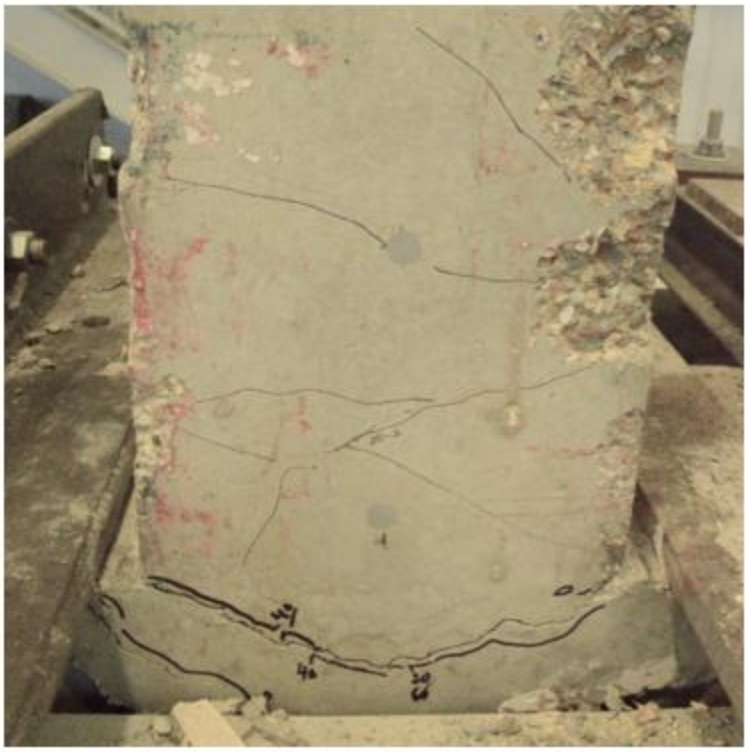

(b) After Series F2-R-C-1PB

Figure 3-36: Northern Column Base, West Face, Before and After Series F2-R-C-1PB

(a) Before Series F2-R-C-1PB

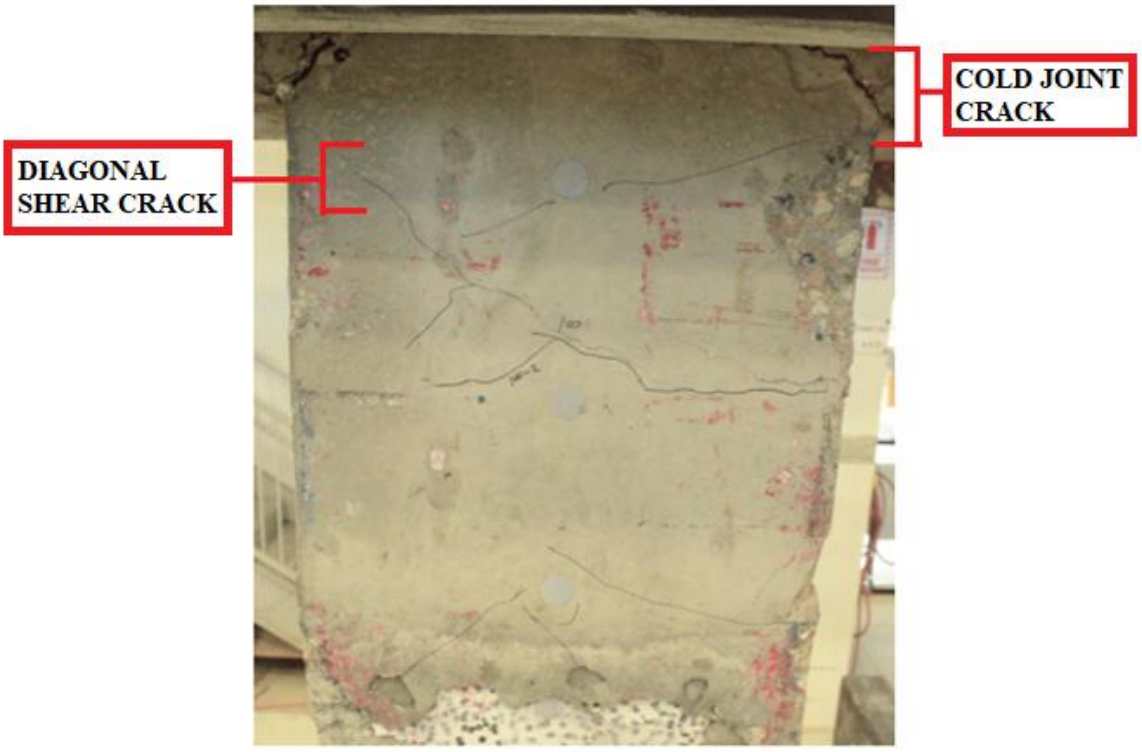

(b) After Series F2-R-C-1PB

Figure 3-37: Southern Column Top, West Face, Before and After Series F2-R-C-1PB

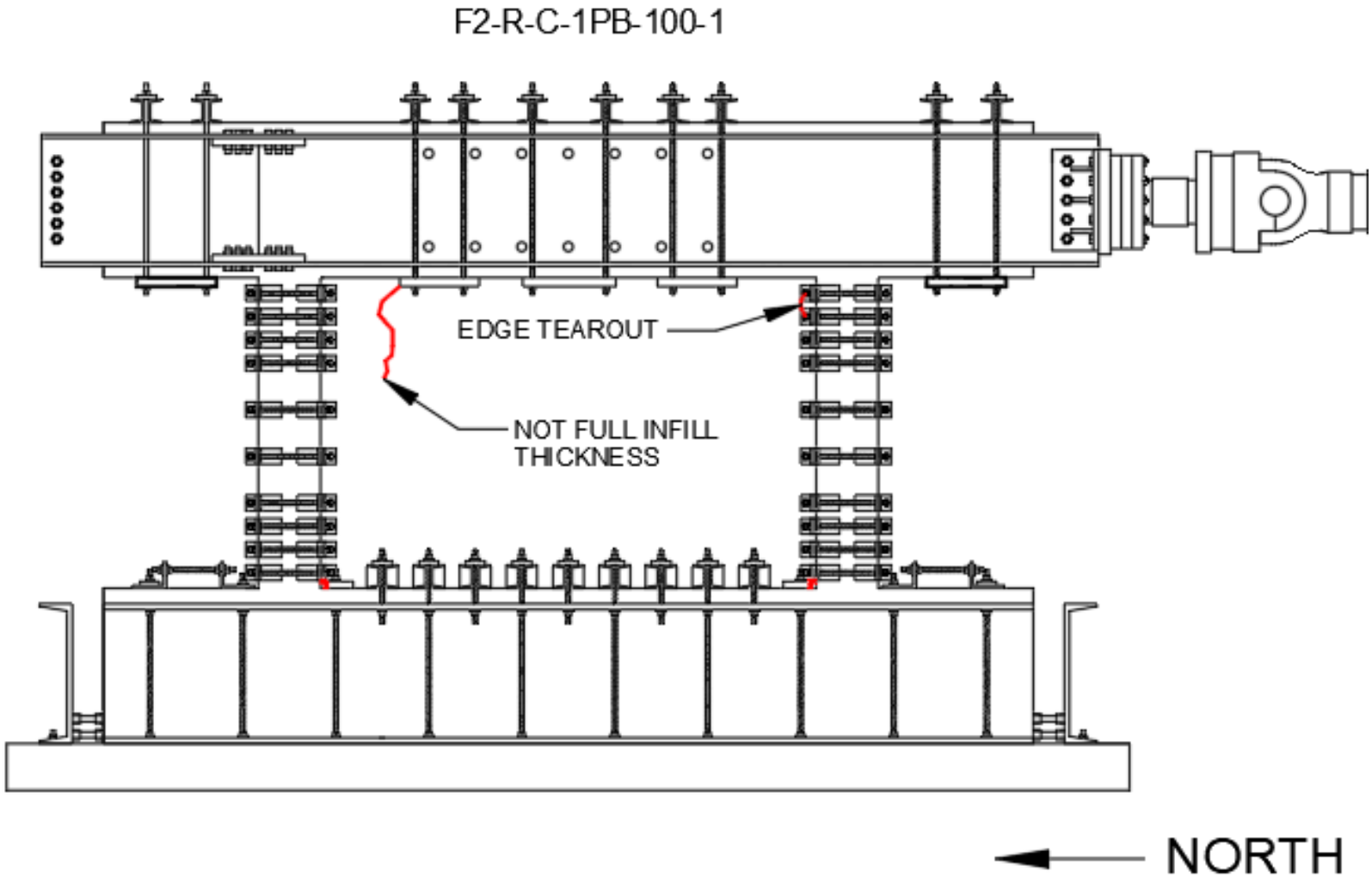

Figure 3-38: Crack Map after Frame 2 Run 148, Series F2-R-C-1PB

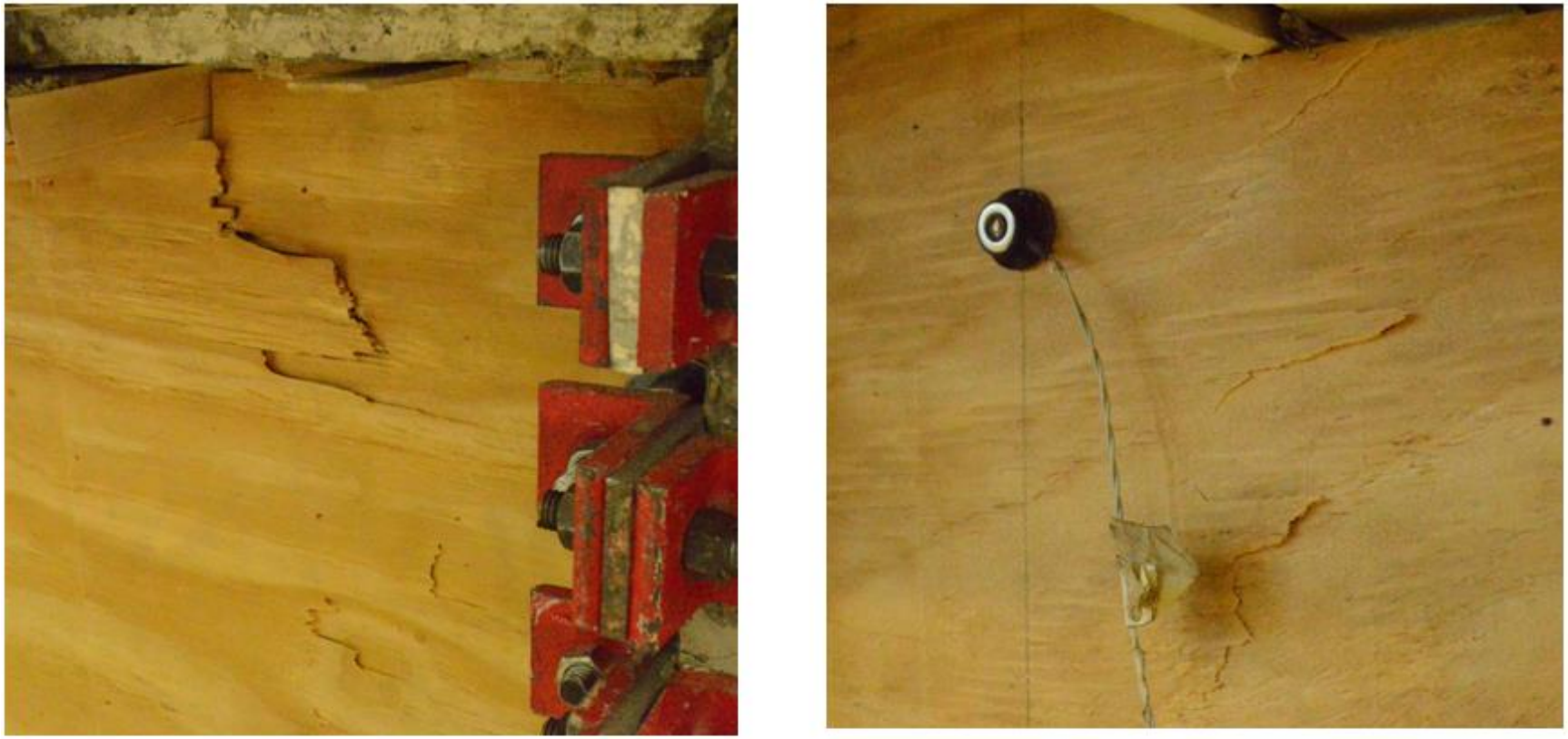

(a) East Face

(b) West Face

Figure 3-39: Infill Damage after Frame 2 Run 148, Series F2-R-C-1PB

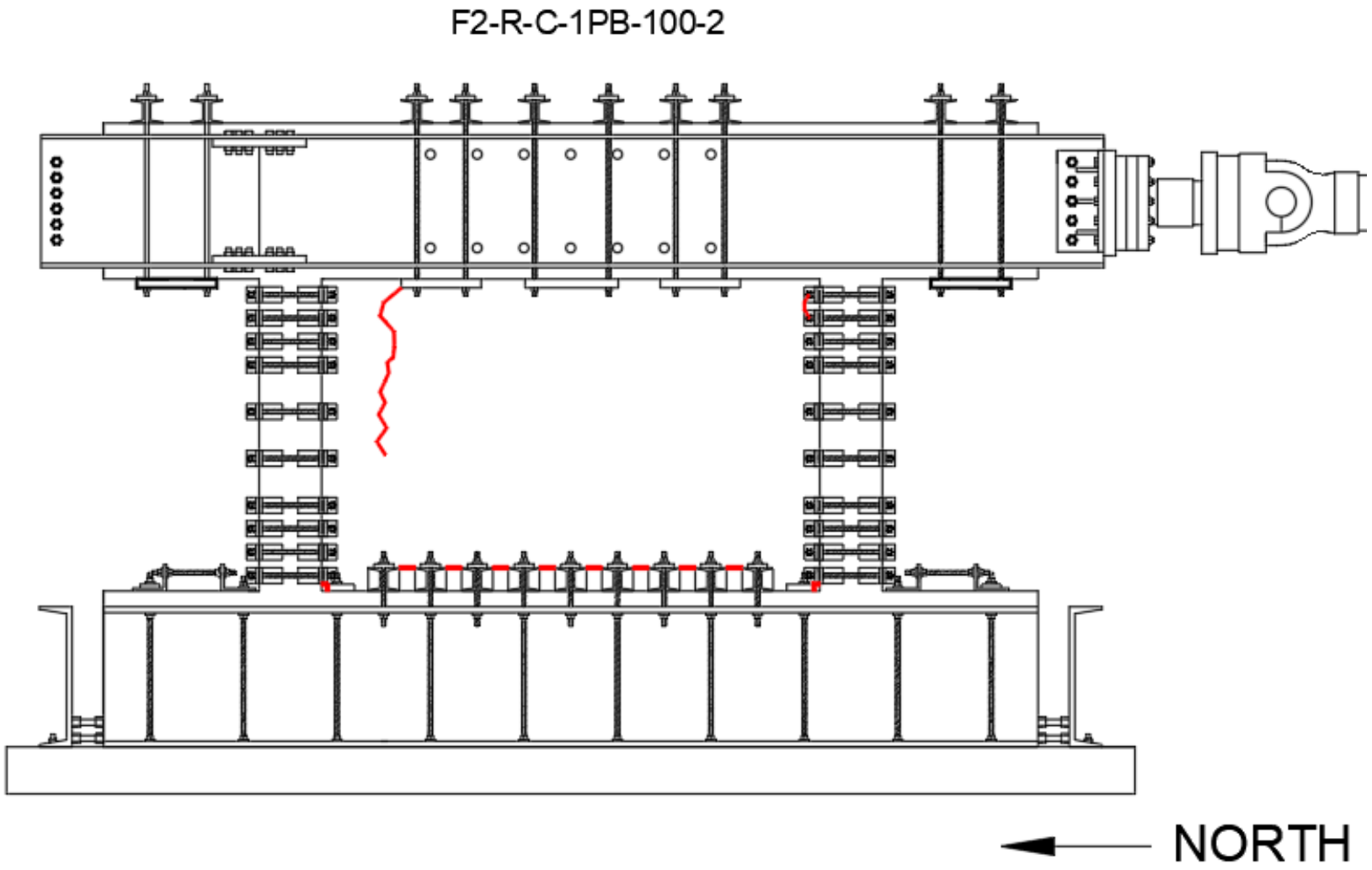

Figure 3-40: Crack Map after Frame 2 Run 149, Series F2-R-C-1PB

(a) East Face (b) West Face

Figure 3-41: Infill Failure after Frame 2 Run 149, Series F2-R-C-1PB

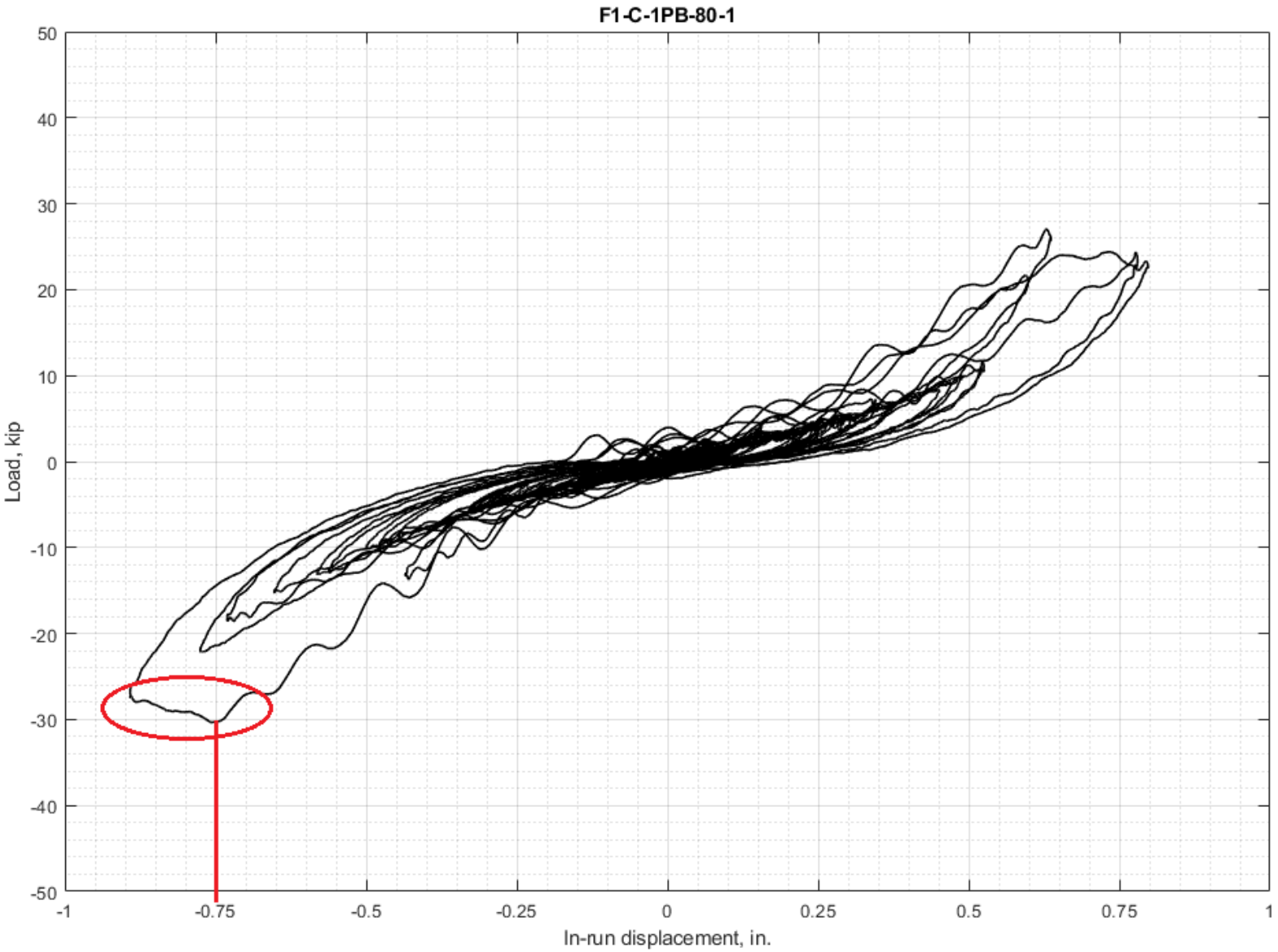

Figure 3-42: Force-Drift with Point of Infill Failure, Frame 1 Run 107

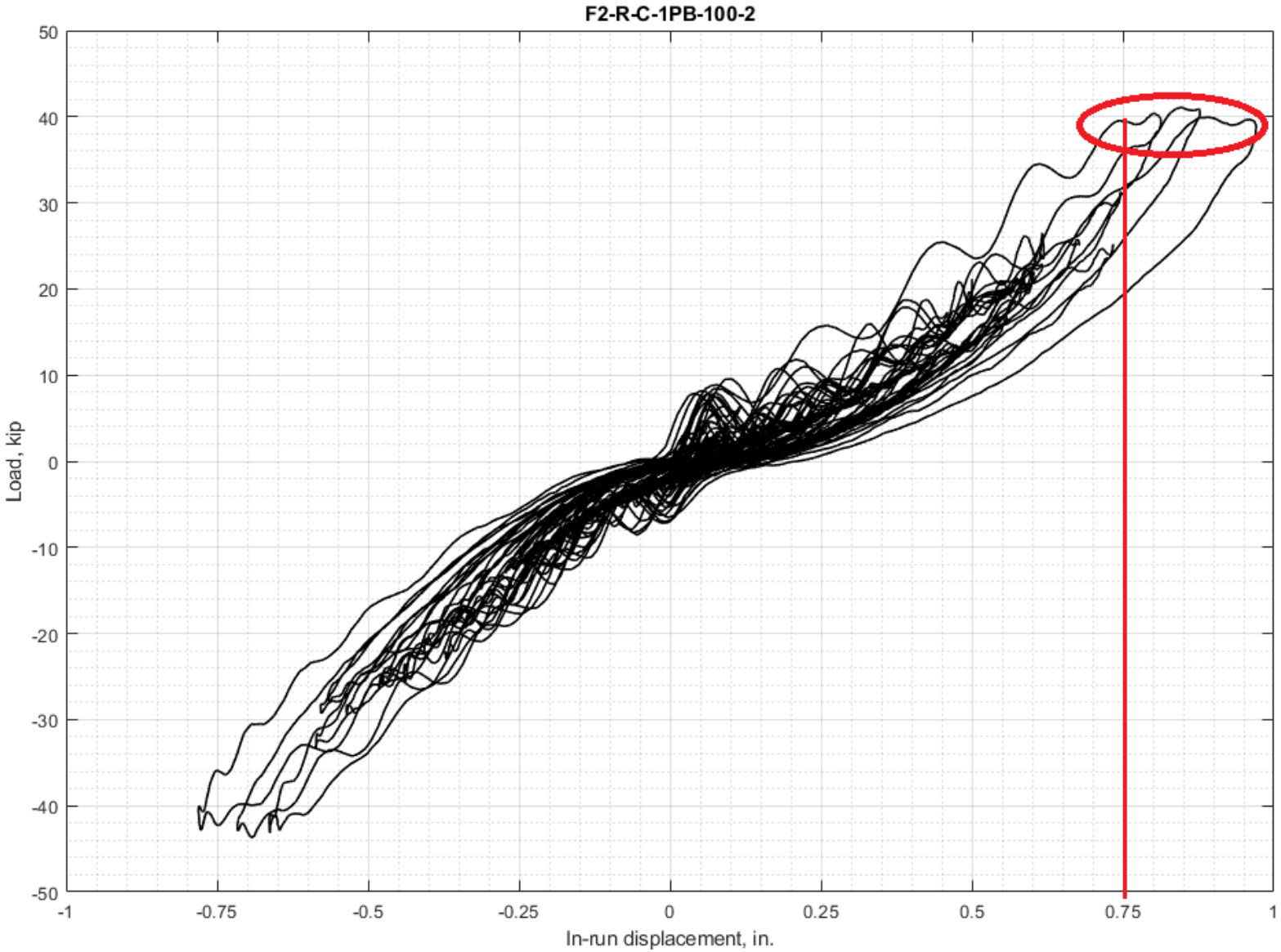

Figure 3-43: Force-Drift with Point of Infill Failure, Frame 2 Run 149

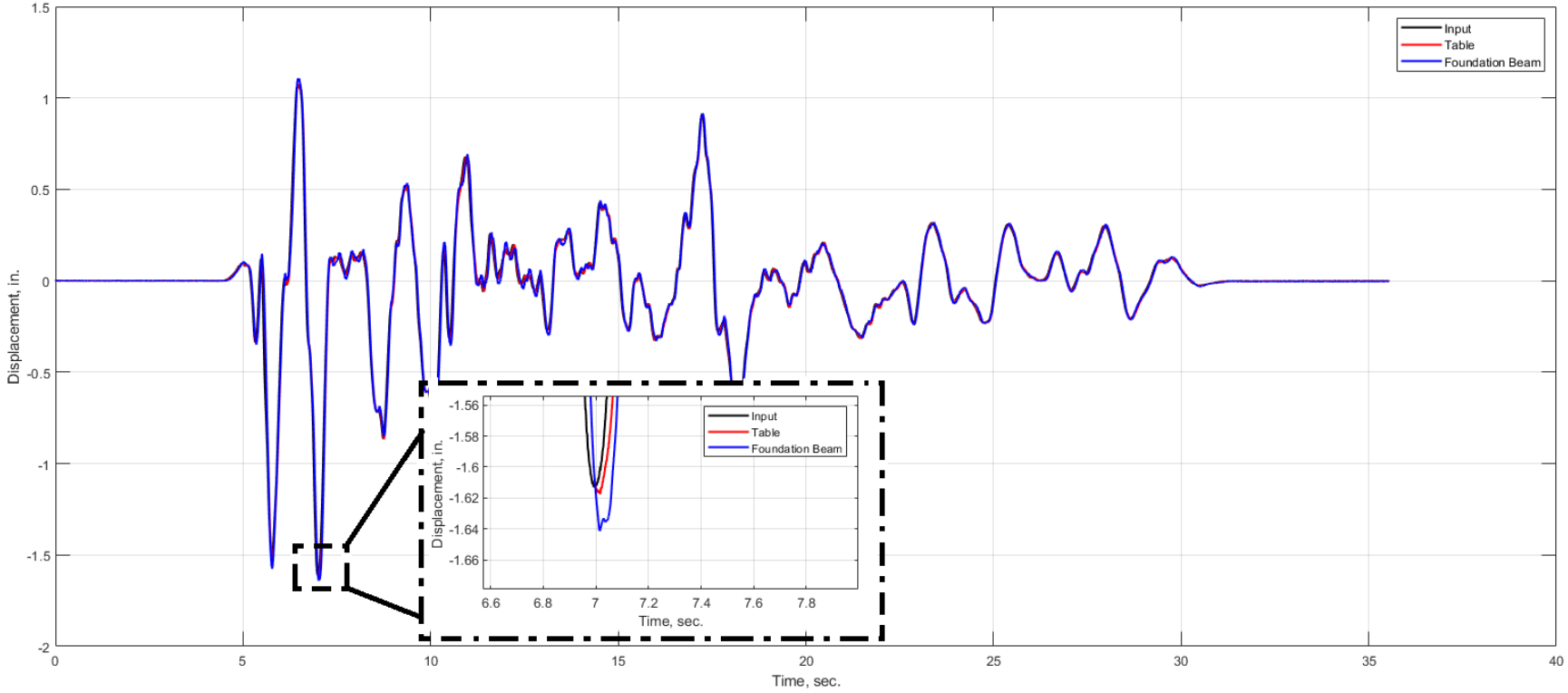

Figure 3-44: Servoram Displacement Input/Output Comparison

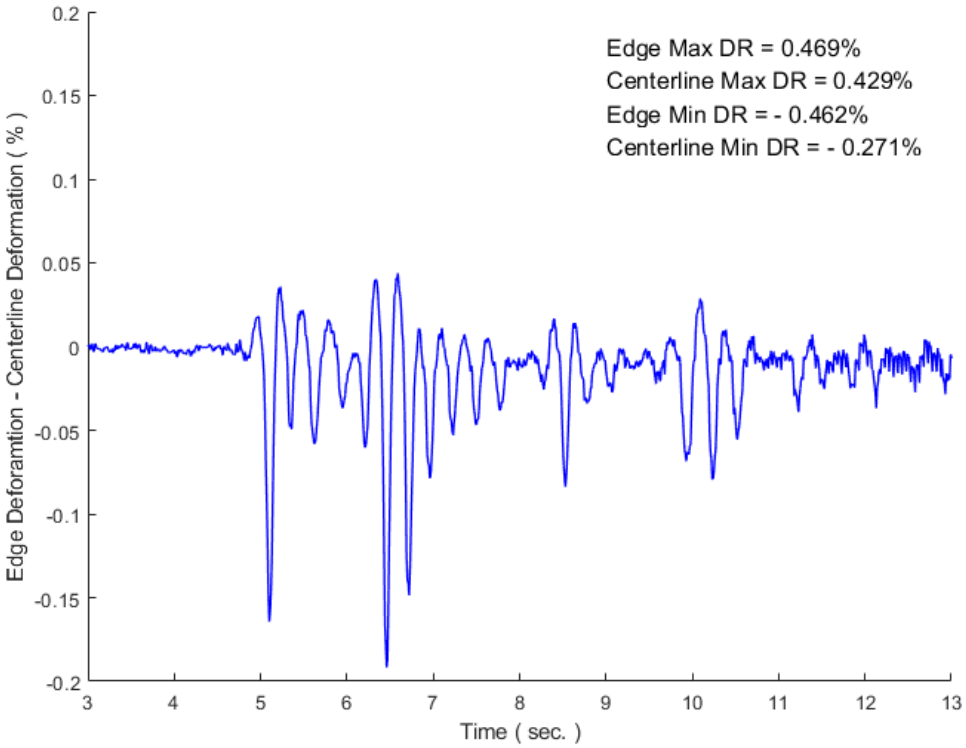

Figure 3-45: Difference of Edge and Centerline Infill Deformations, Frame 2 Run 142, Series F2-R-C-1PB

Figure 3-46: Test Setup, Series F2-R-C

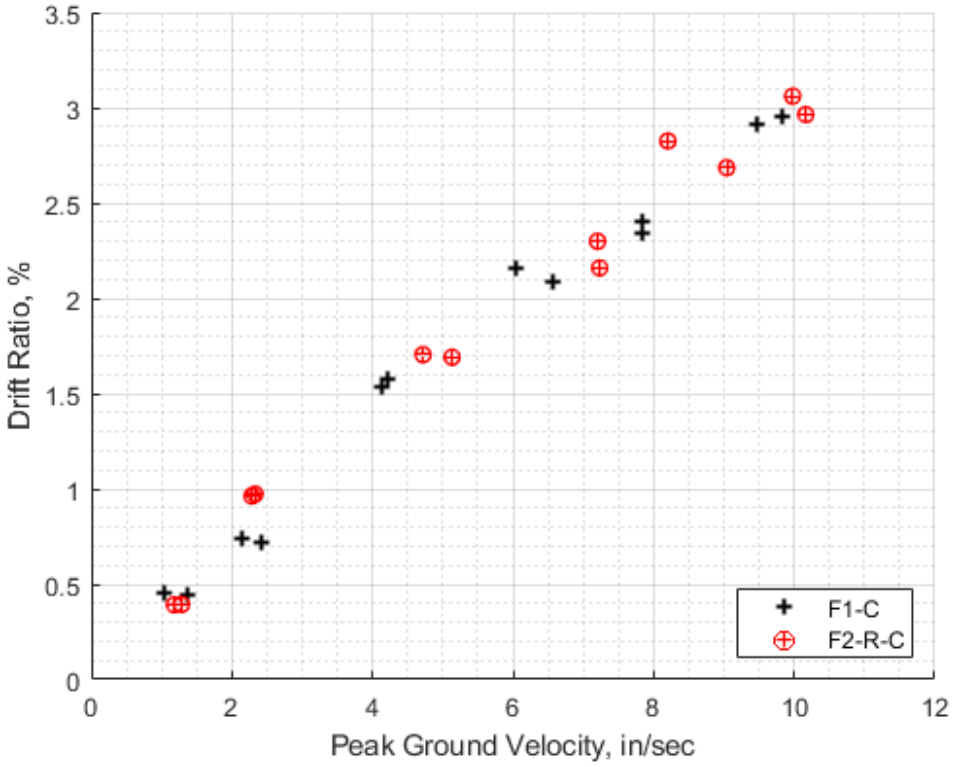

Figure 3-47: Comparison of Drift Ratio versus PGV for Series F1-C and F2-R-C

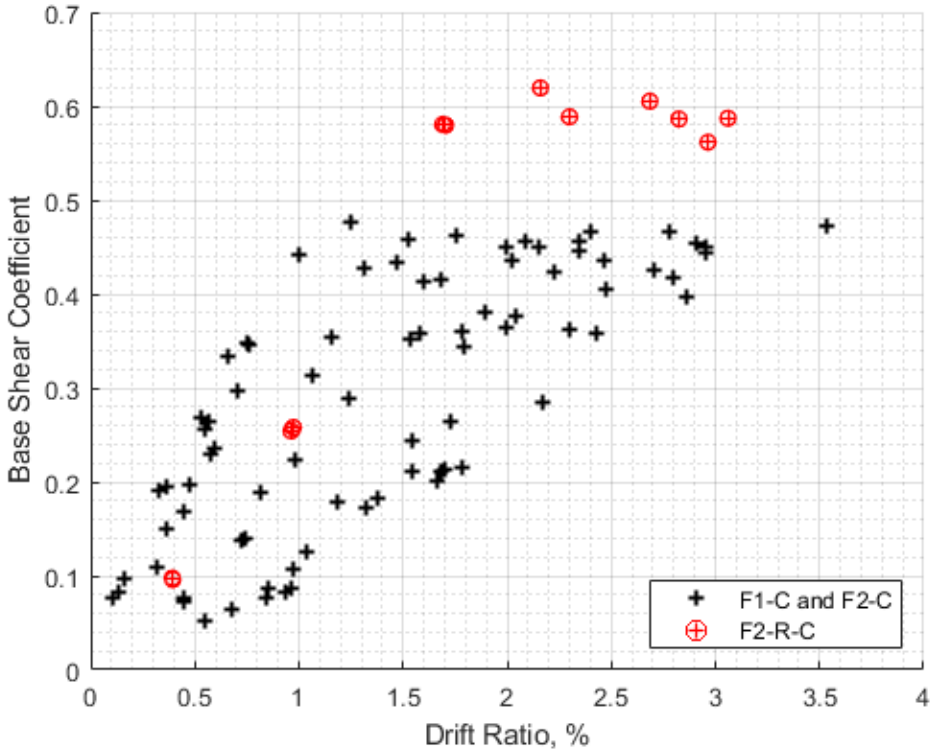

Figure 3-48: Base Shear Coefficient versus Drift Ratio for Series F1-C, F2-C, and F2-R-C

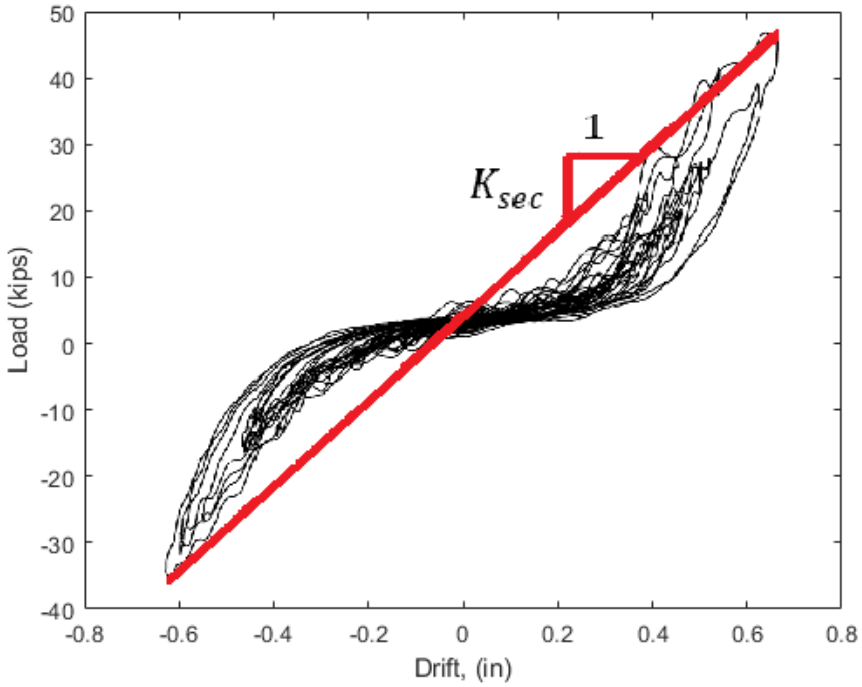

(a) Secant Stiffness from Load Cell Data

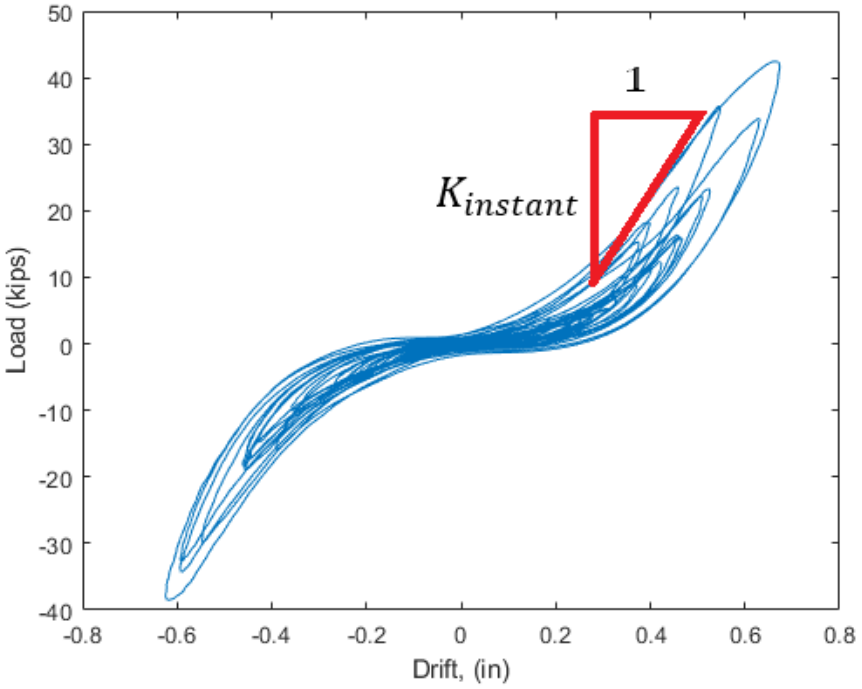

(b) Instantaneous Stiffness from ADXL Data

Figure 4-1: Illustration of Secant and Instantaneous Stiffness[1]

[1] See Section 4.2.3 or Figure 4-13 for derivation of instantaneous stiffness

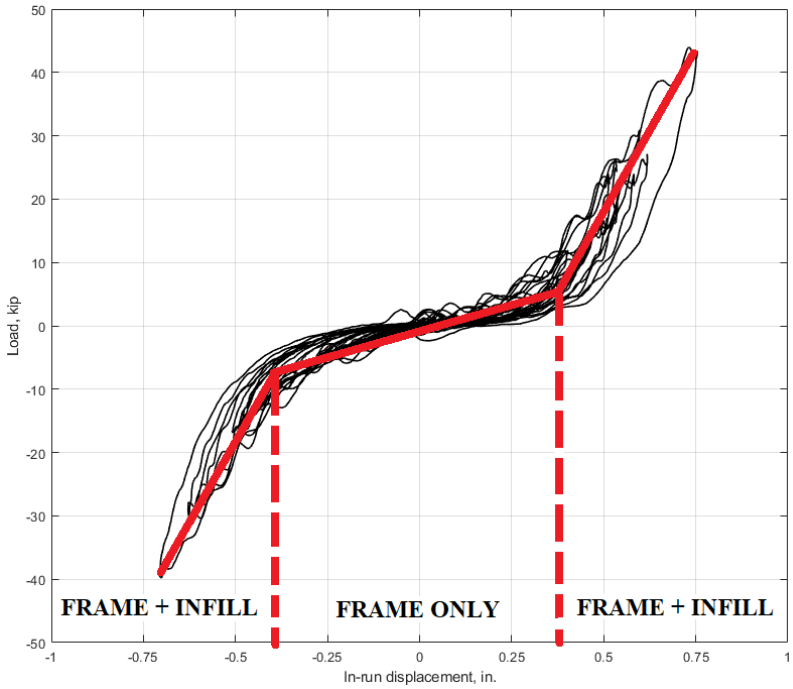

Figure 4-2: Bi-Linear Force vs Displacement Response of Damaged Frame Series

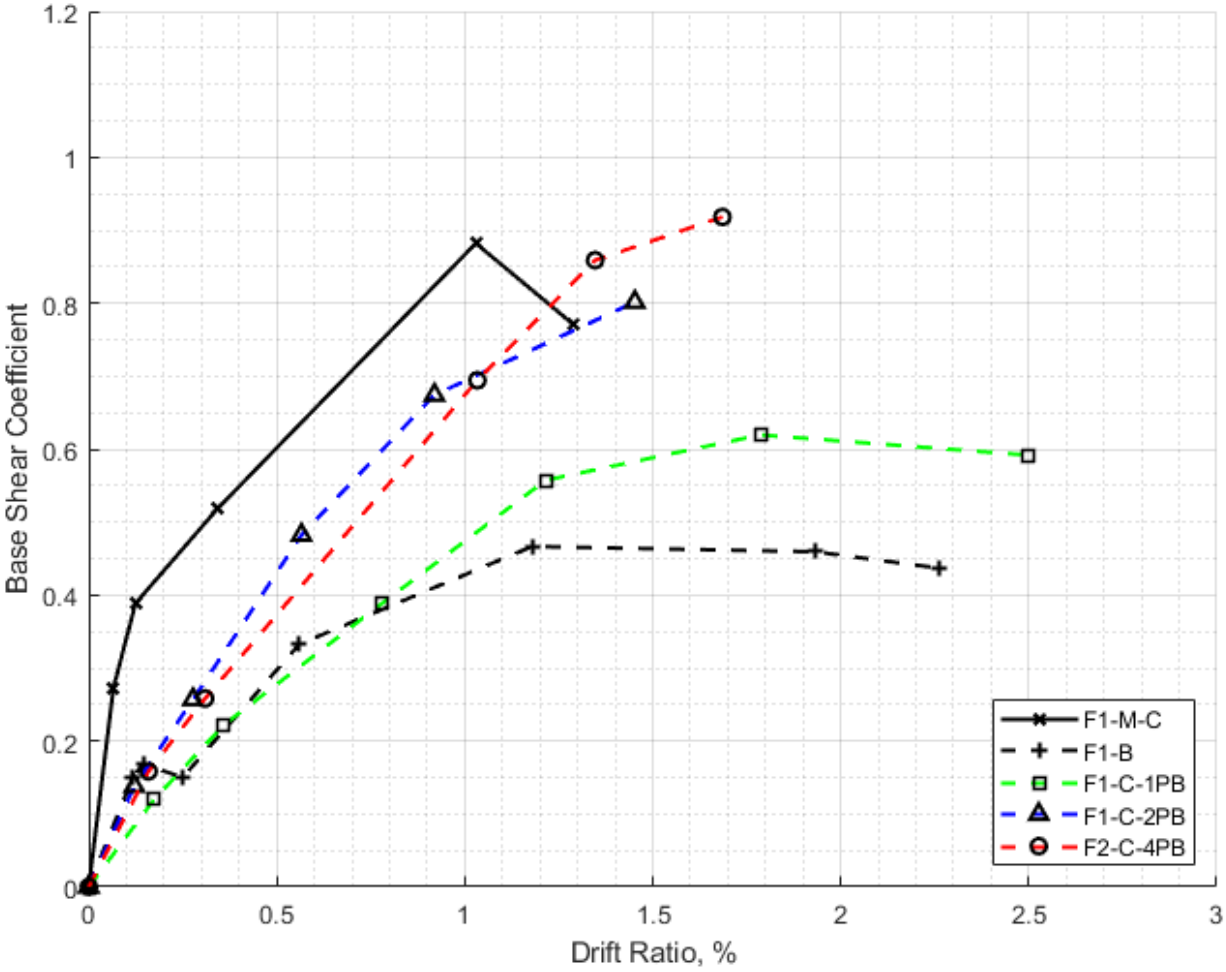

Figure 4-3: Load Envelope, Damaged Frame Series

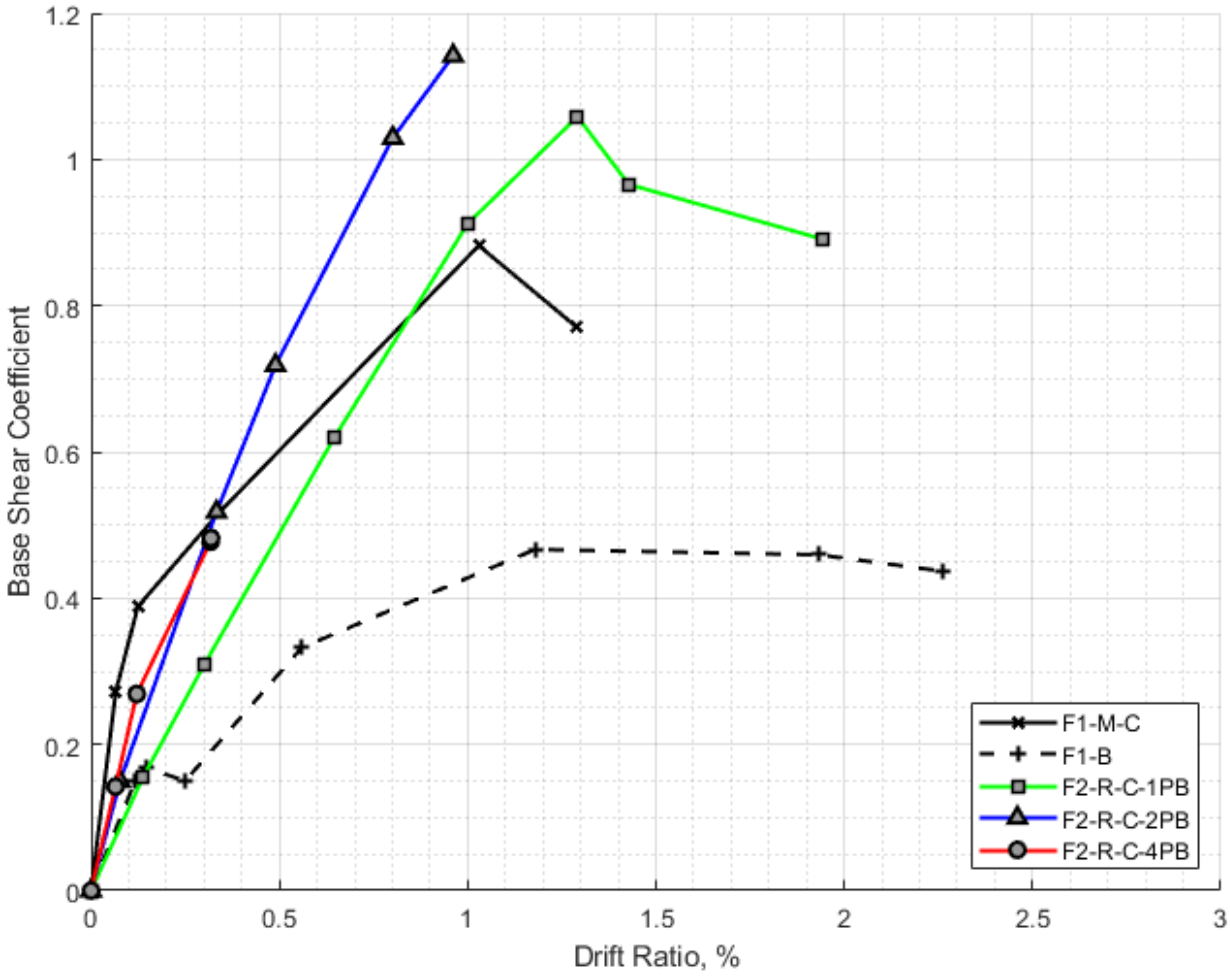

Figure 4-4: Load Envelope, Recast Frame Series

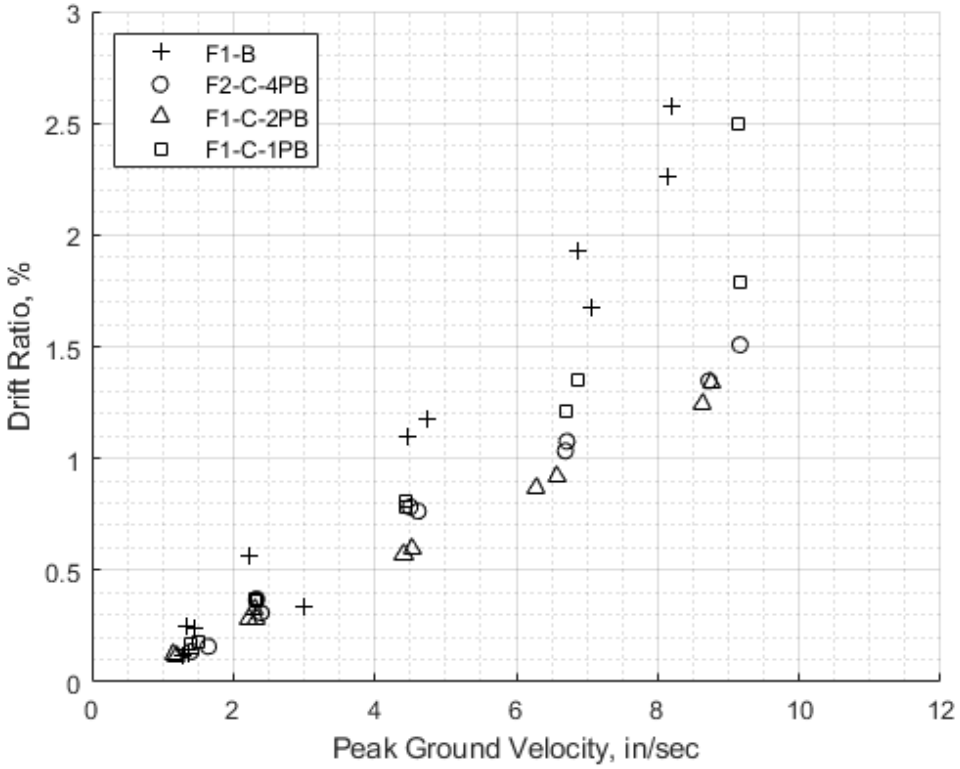

Figure 4-5: Drift Ratio vs PGV (Damaged Frame Series)

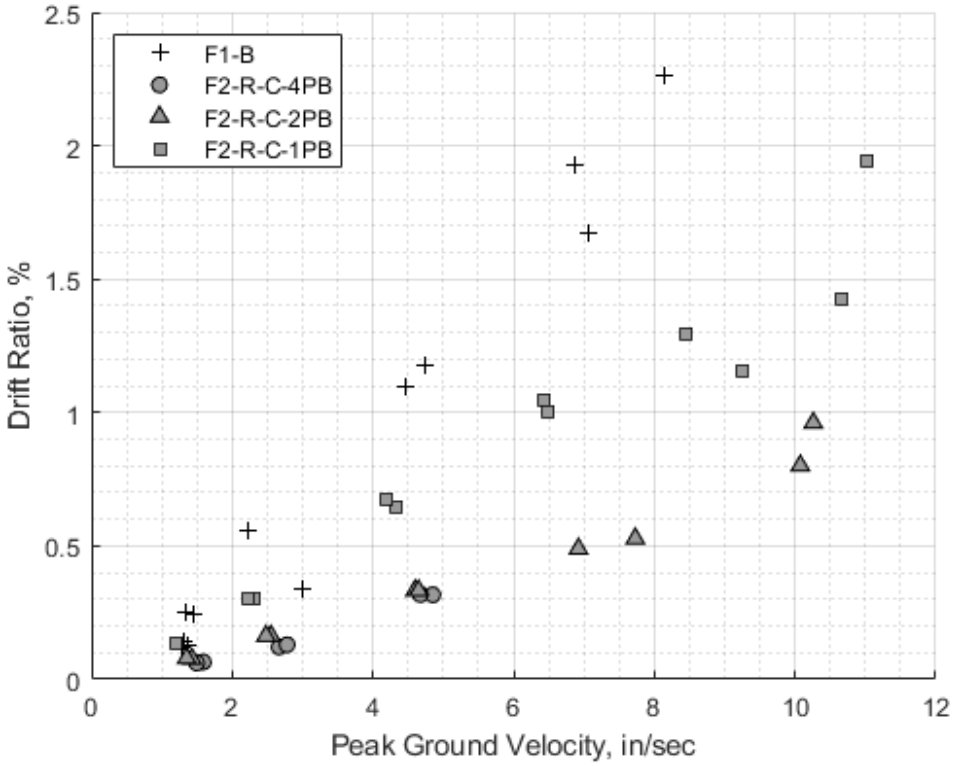

Figure 4-6: Drift Ratio vs PGV (Recast Frame Series)

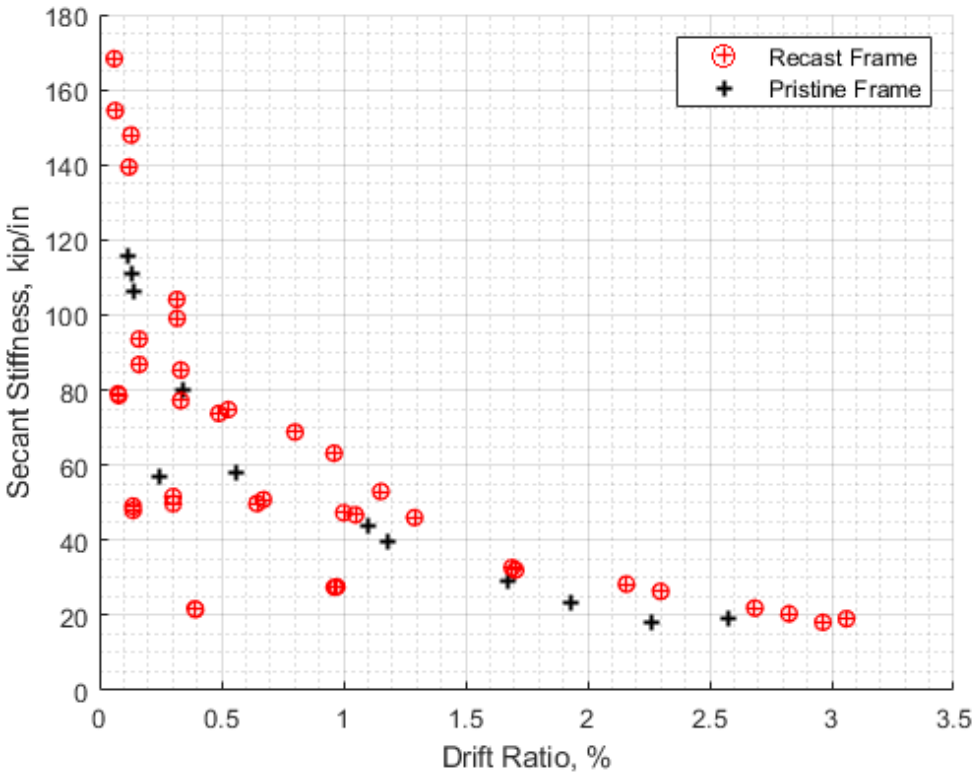

Figure 4-7: Secant Stiffness versus Drift Ratio for Series F1-B and Recast Frame Series

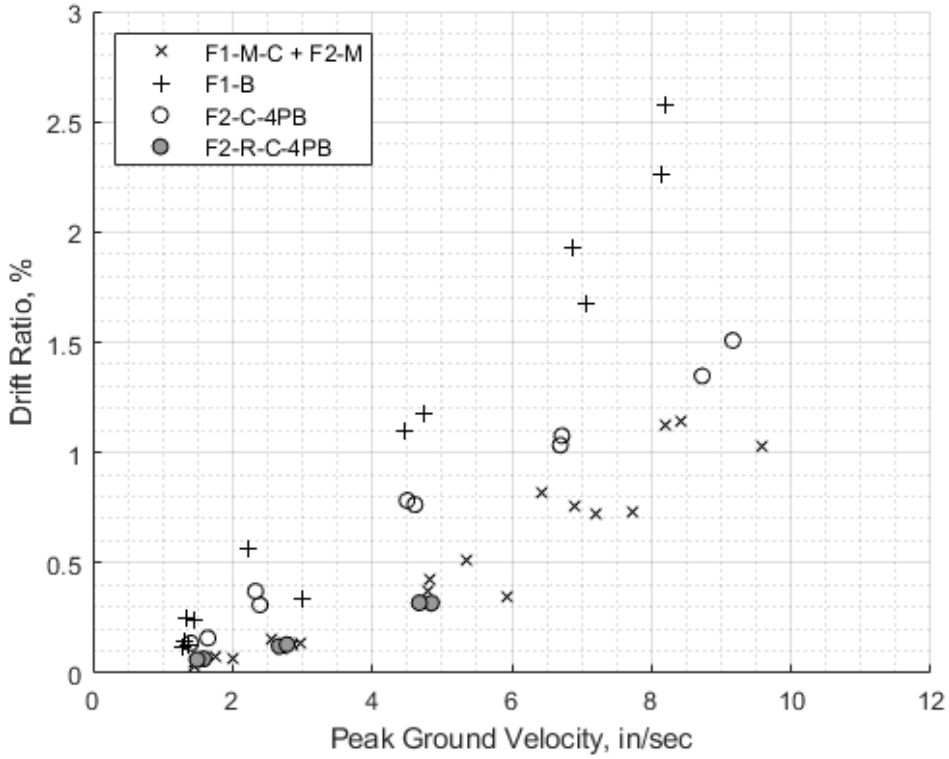

Figure 4-8: Drift Ratio vs PGV (4PB, Masonry Infill, Bare frame)

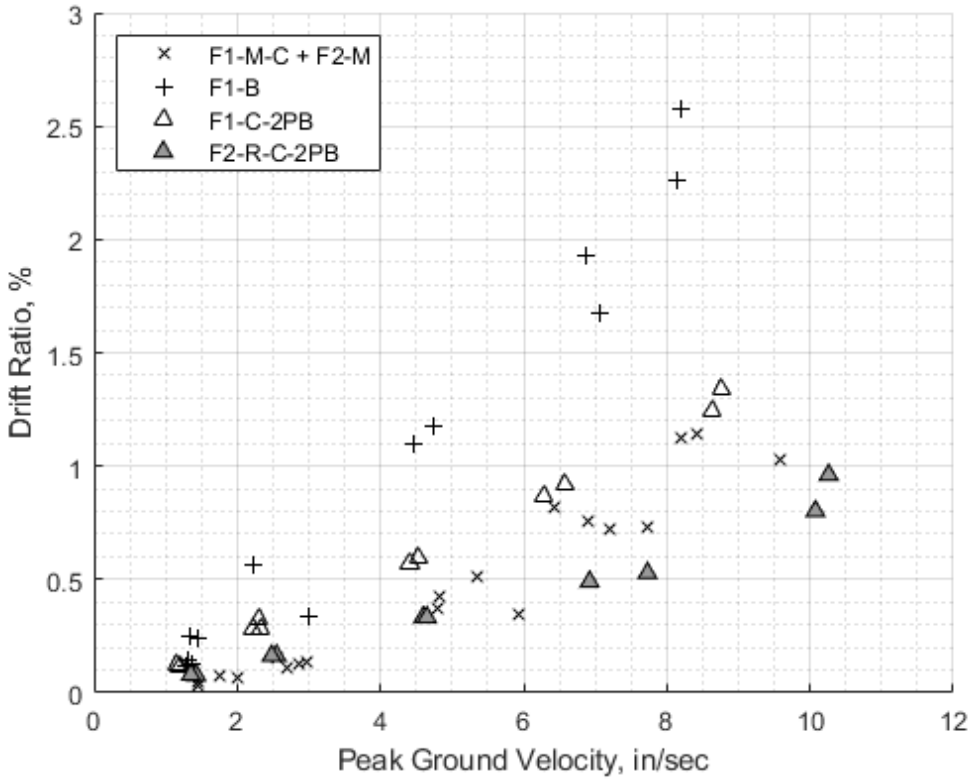

Figure 4-9: Drift Ratio vs PGV (2PB, Masonry Infill, Bare frame)

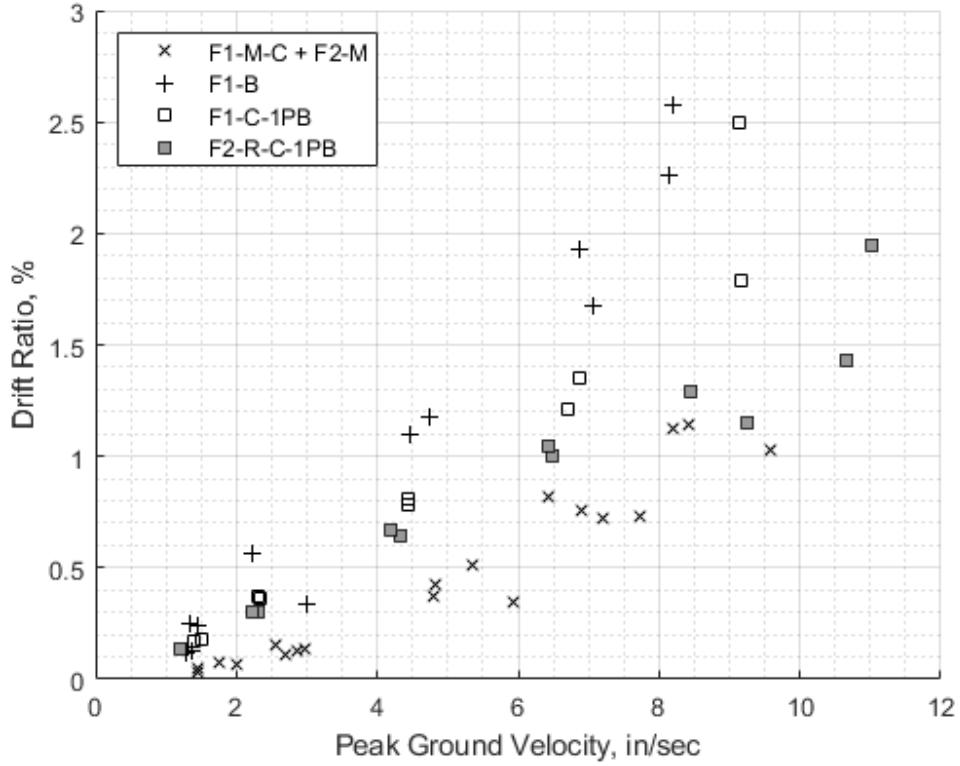

Figure 4-10: Drift Ratio vs PGV (1PB, Masonry Infill, Bare frame)

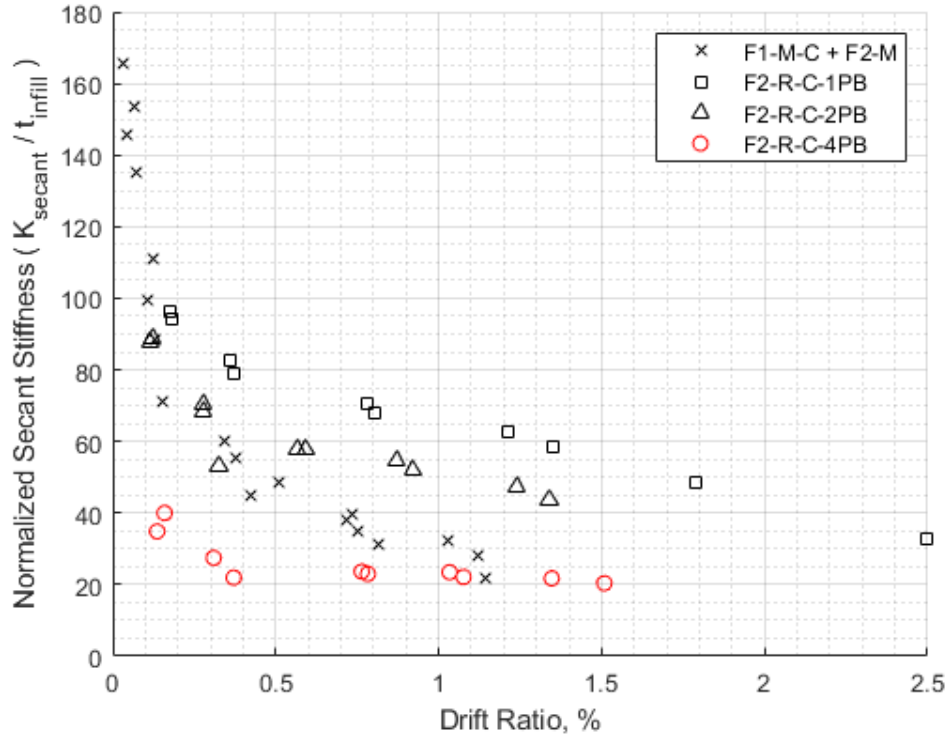

Figure 4-11: Thickness-Normalized Secant Stiffness vs Drift Ratio, Damaged Frames[1]

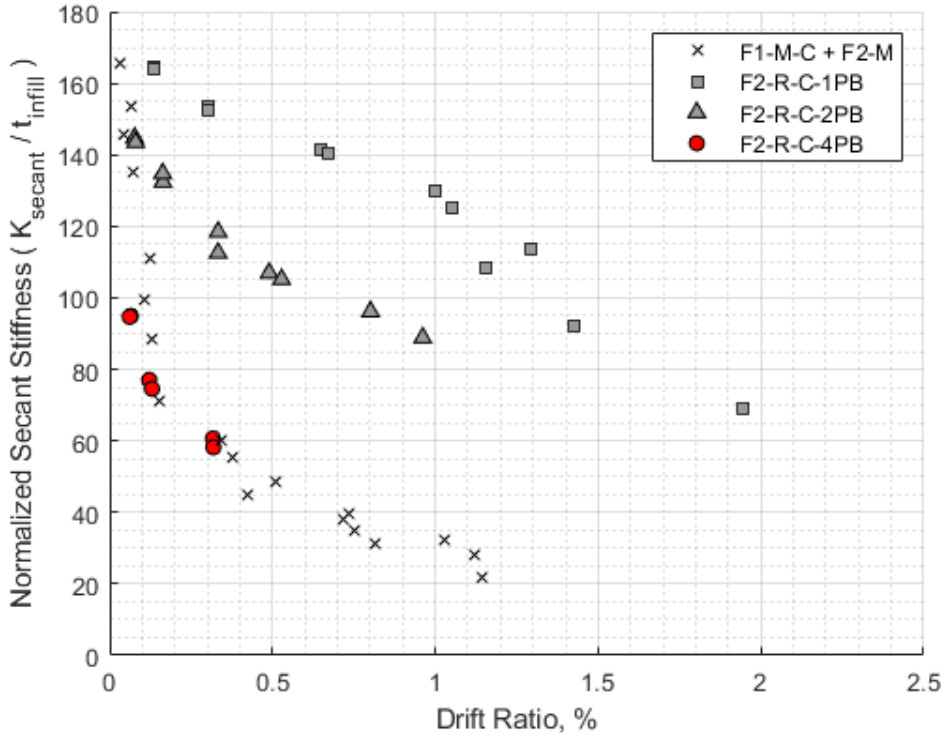

Figure 4-12 Thickness-Normalized Secant Stiffness vs Drift Ratio, Recast Frames

[1] Nominal Thickness: 1PB - 0.703", 2PB - 1.406", 4PB - 2.812", Masonry – 2.719"

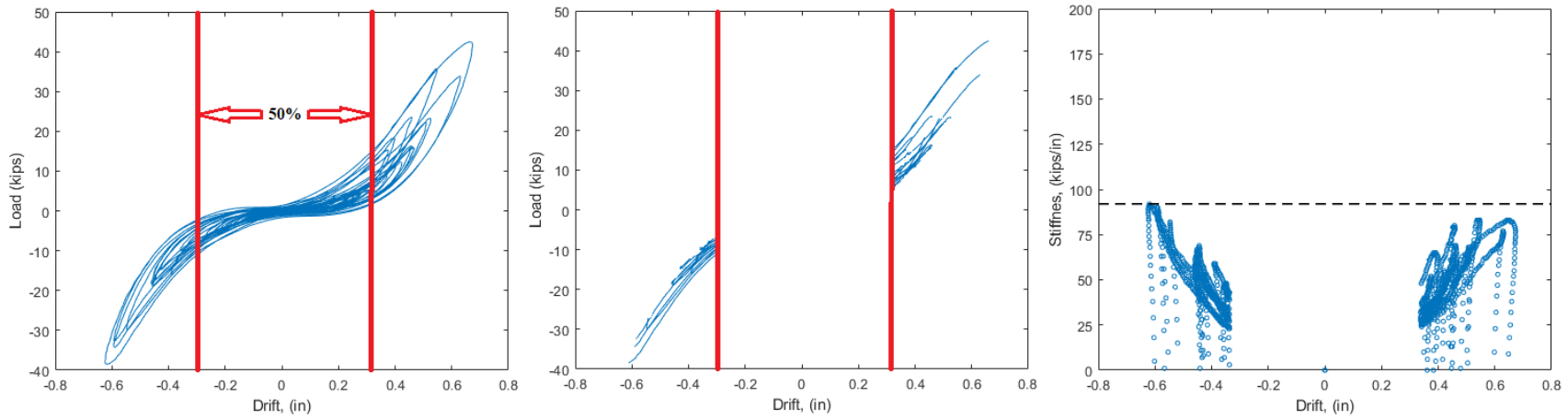

(a) Remove middle 50% of data (b) Remove unloading cycles (c) Derive peak instantaneous stiffness

Figure 4-13: Instantaneous Peak Stiffness Derivation[1]

[1] Plots constructed using ADXL and LVDT data from Frame 2 Run 106, Series F2-C-4PB

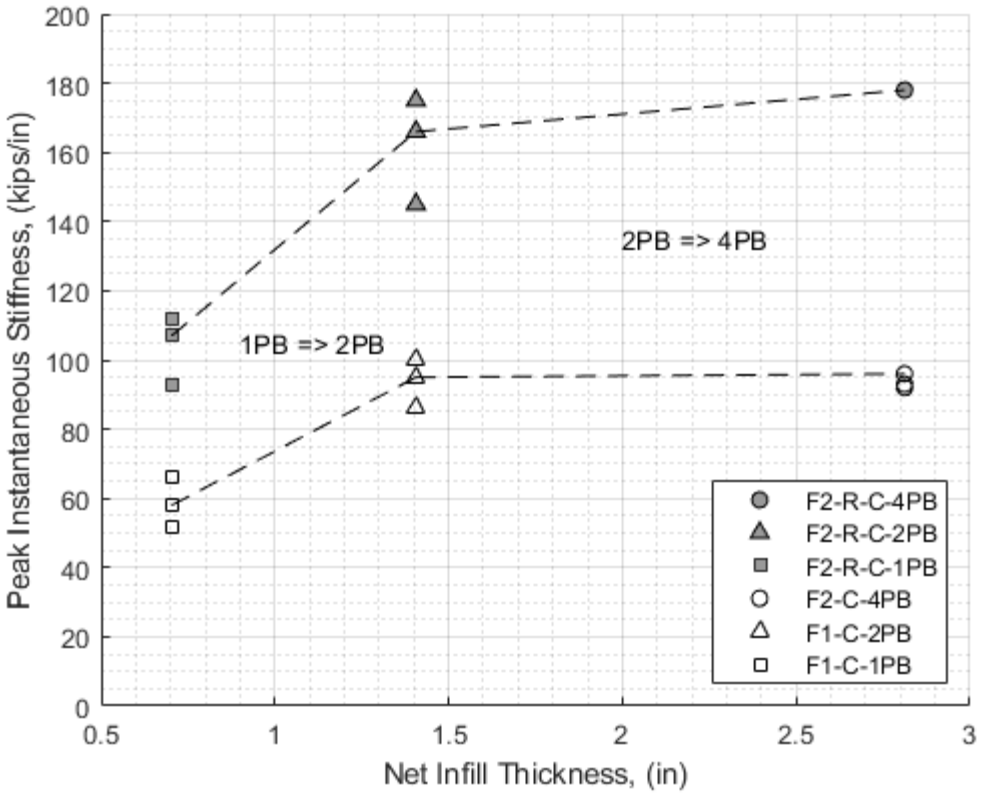

Figure 4-14: Peak Instantaneous Stiffness vs Nominal Infill Thickness, All series

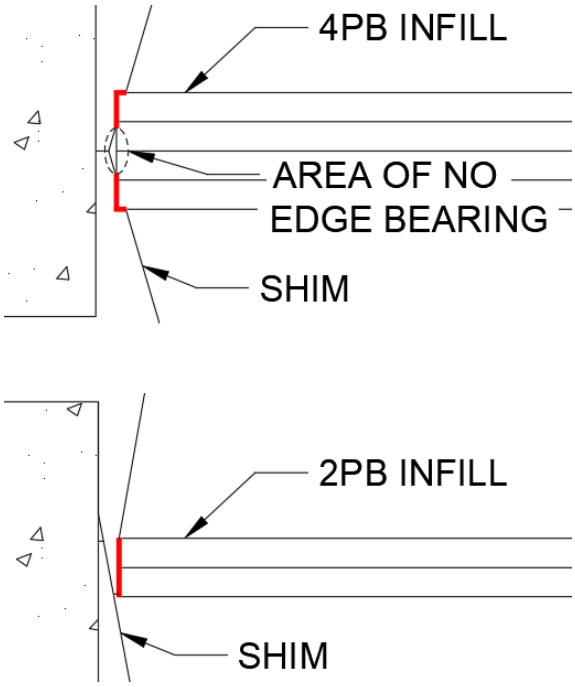

Figure 4-15: Idealized Shim Bearing Edge-Joint Contact Areas

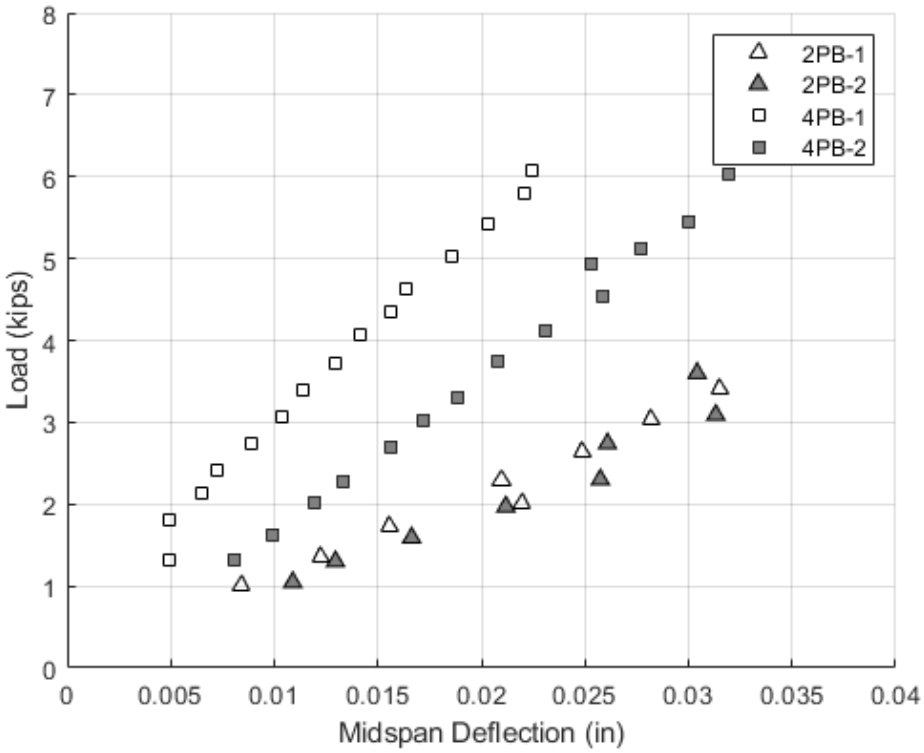

Figure 4-16: Beam Test Load vs Midspan Deflection

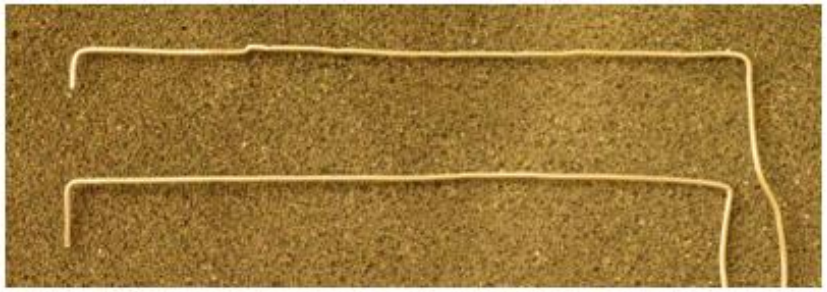

(a) Beam 4PB-1

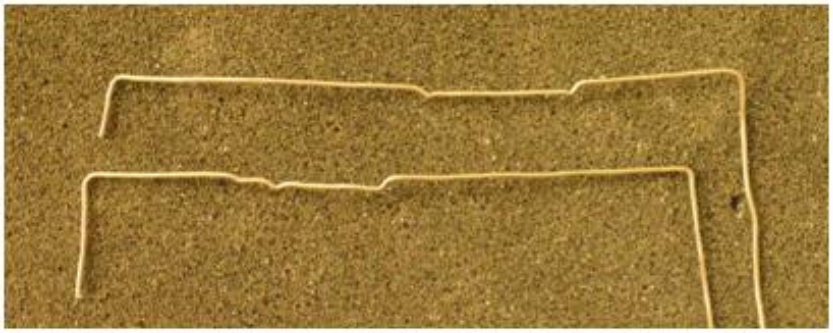

(b) Beam 4PB-2

Figure 4-17: Wire Edge-Profiles of 4PB Beams

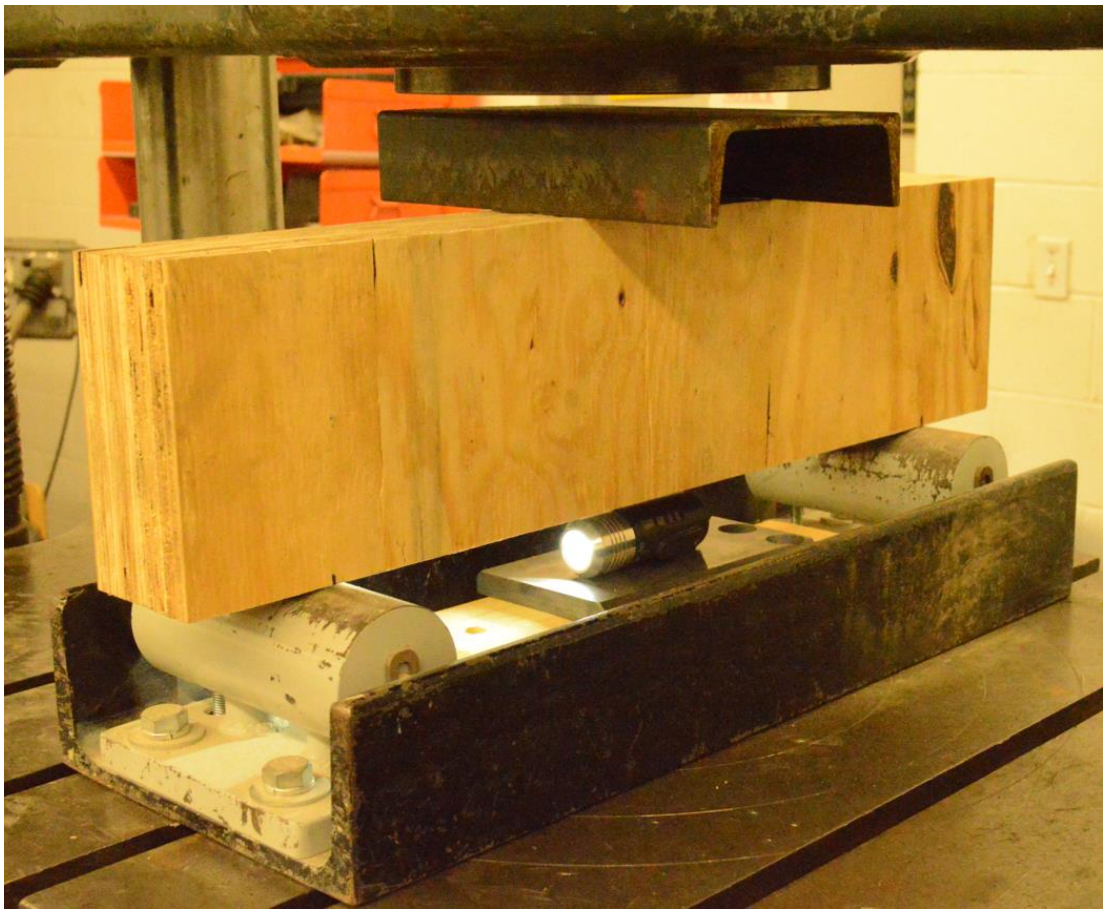

Figure 4-18: Backlighting Setup for 4-Point Bending Beams

(a) Unloaded (b) Loaded to ~2 kips

Figure 4-19: Backlit Beam 2PB-1

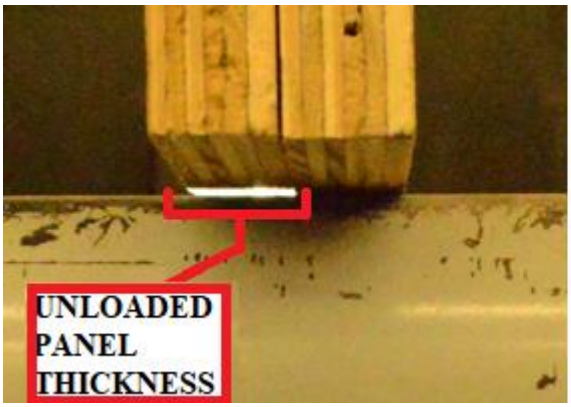

(a) Unloaded

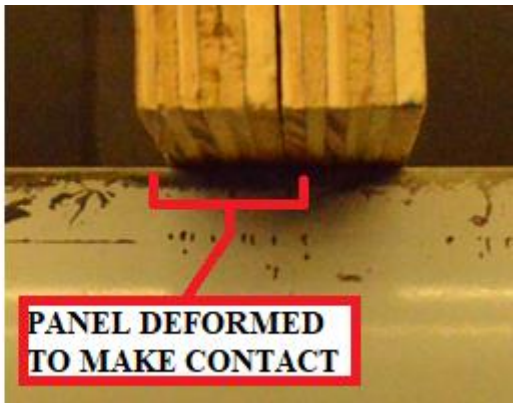

(b) Loaded to ~ 2 kips

Figure 4-20: Backlit Beam 2PB-2

(a) Unloaded

(b) Loaded to ~ 2 kips

Figure 4-21: Backlit Beam 4PB-1

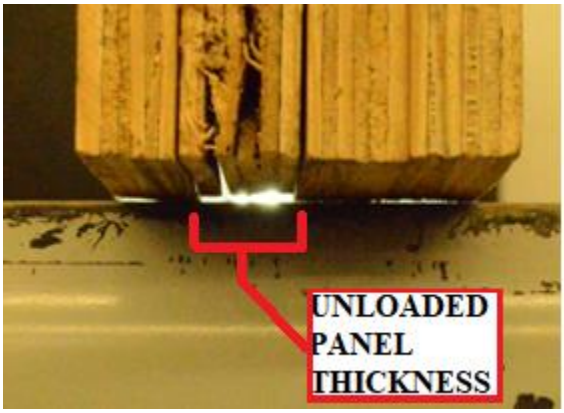

(a) Unloaded

(b) Loaded to ~ 2 kips

Figure 4-22: Backlit Beam 4PB-2

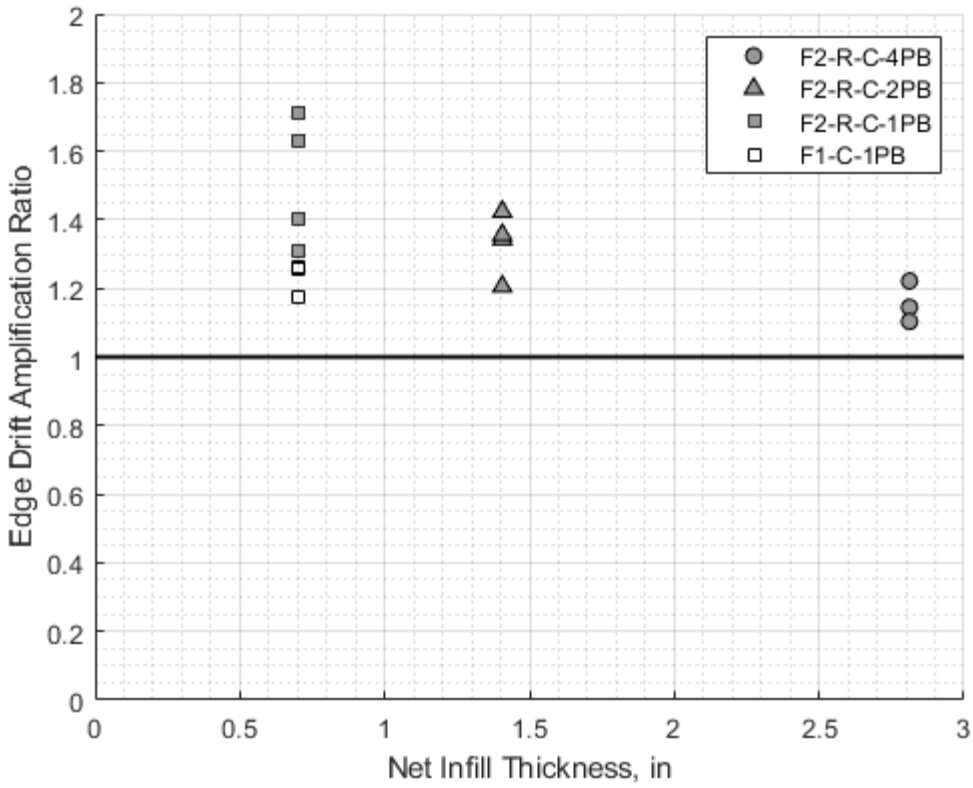

Figure 4-23: Ratio of Infill Edge to Centerline Drift Ratio during all Studied Optotrack Runs

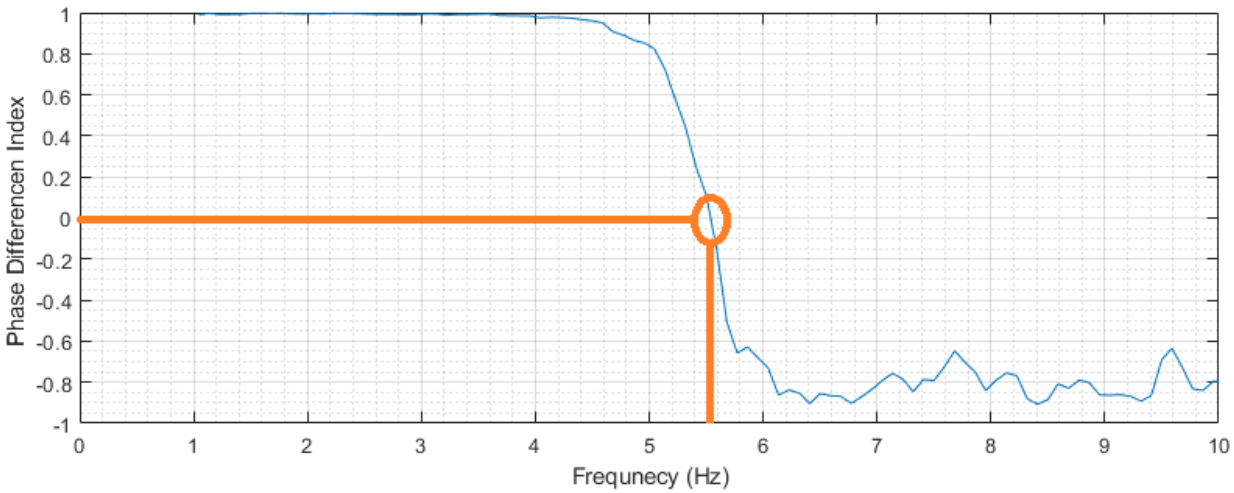

Figure 4-24: Phase Difference Index (PDI), Frame 2 Run 130, Series F2-R-C-2PB

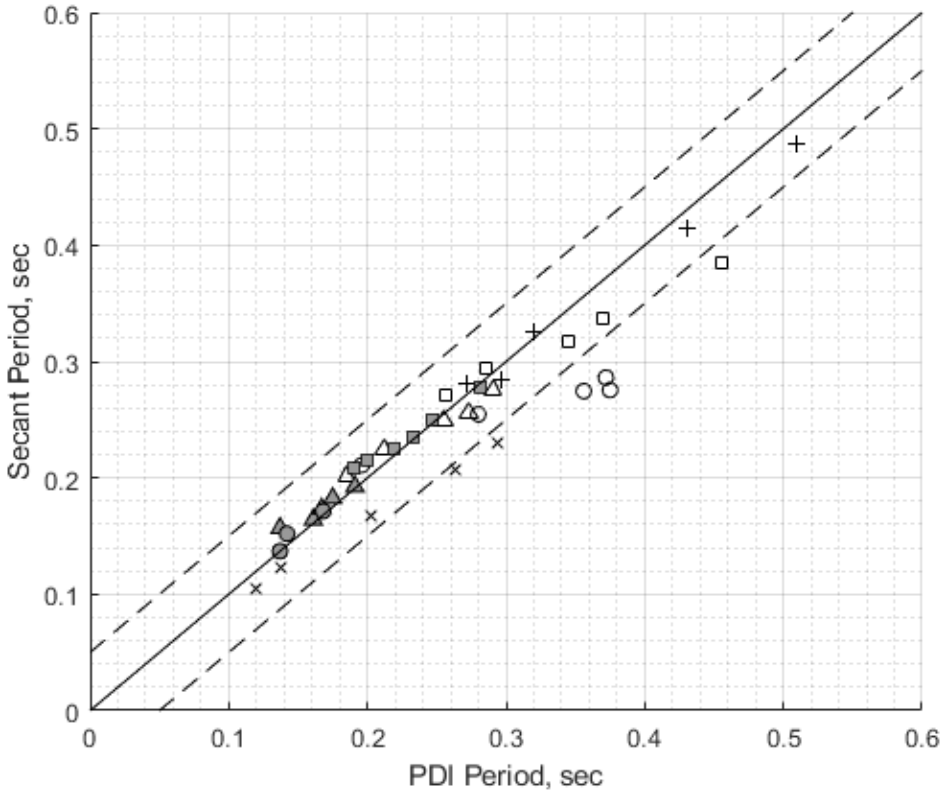

Figure 4-25: Comparison of Secant Period and PDI Period

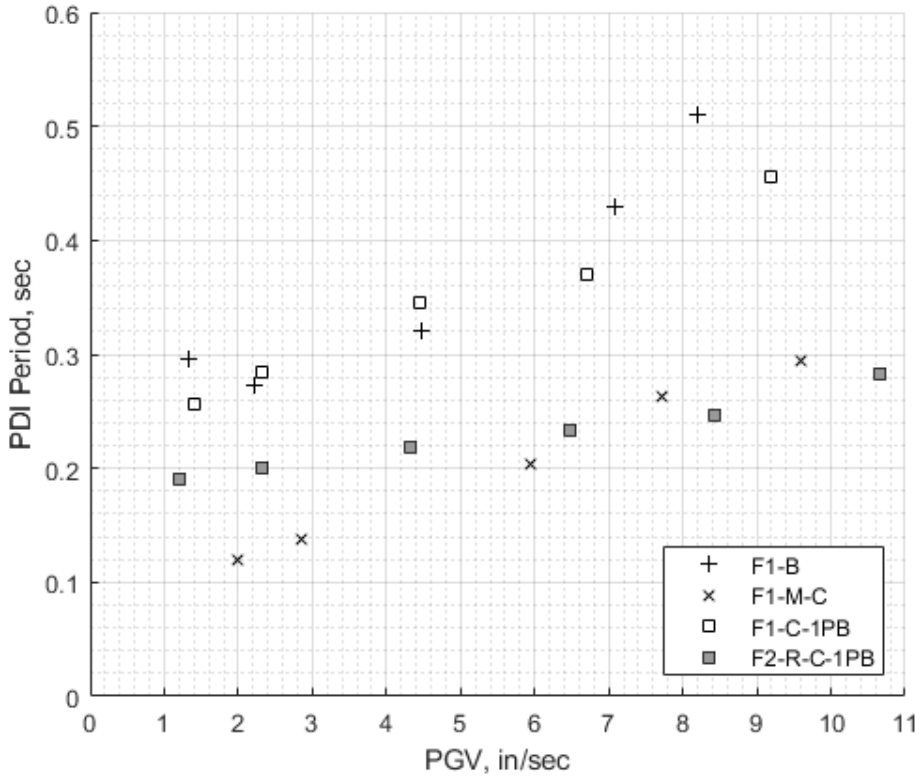

Figure 4-26: PDI Period versus PGV (1PB, Masonry Infill, Bare frame)

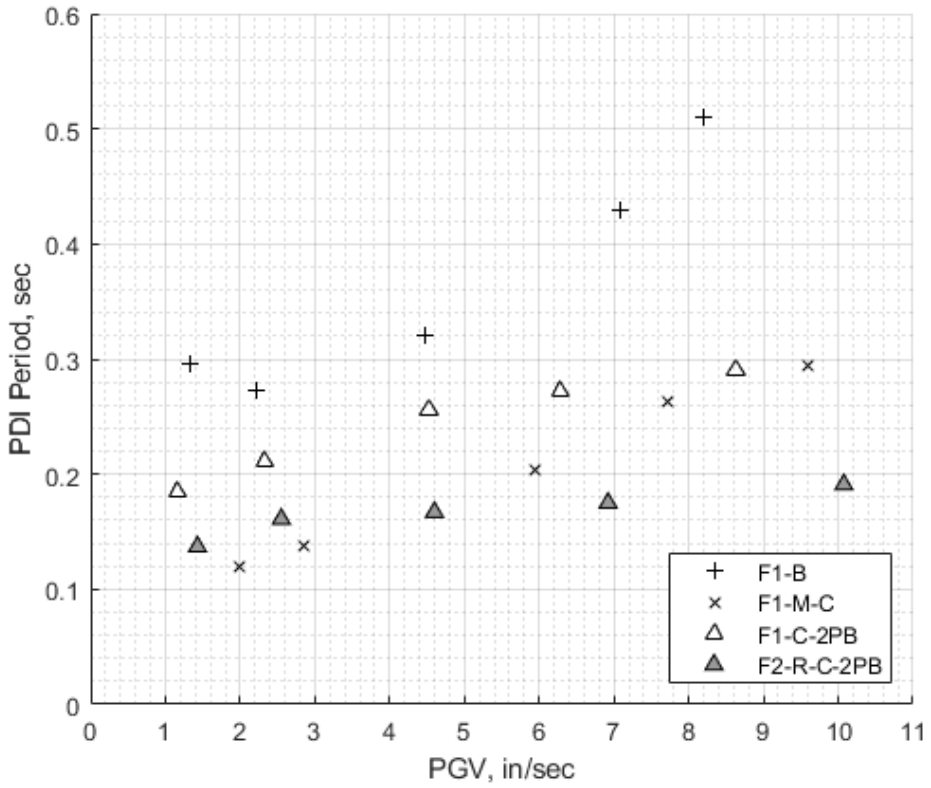

Figure 4-27: PDI Period versus PGV (2PB, Masonry Infill, Bare frame)

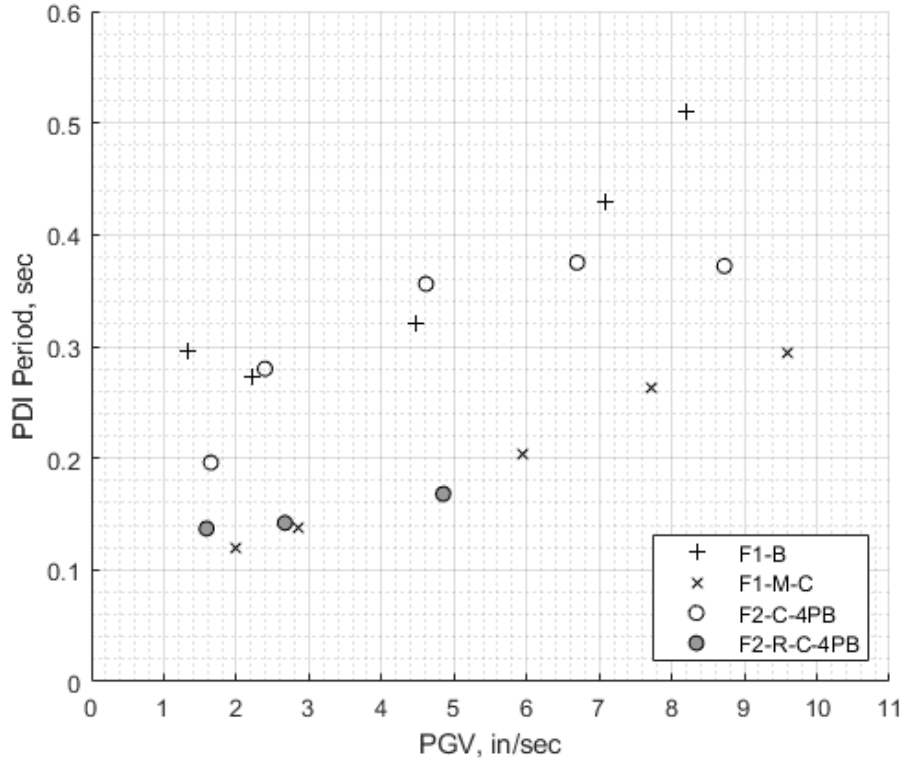

Figure 4-28: PDI Period versus Drift Ratio (4PB, Masonry Infill, Bare frame)

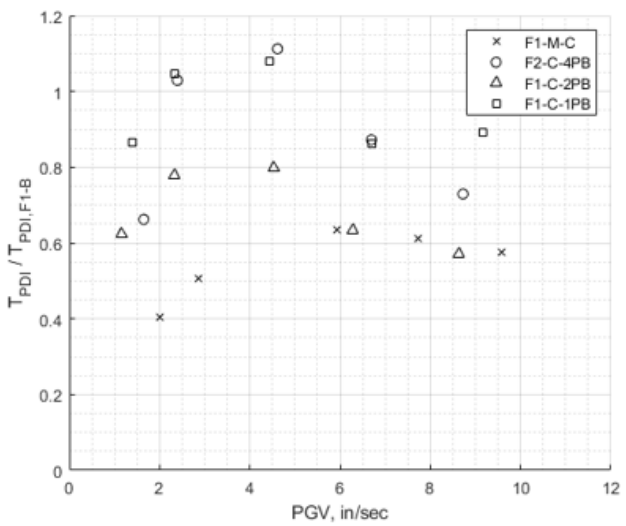

(a) Damaged Frame, PDI Period

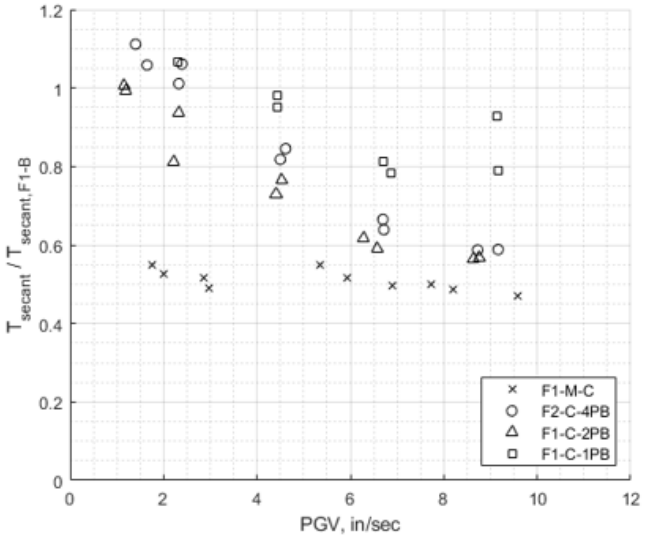

(c) Damaged Frame, Secant Period

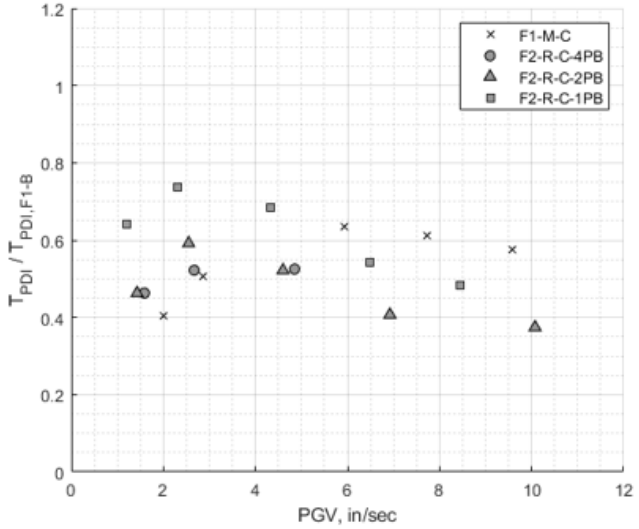

(b) Recast Frame, PDI Period

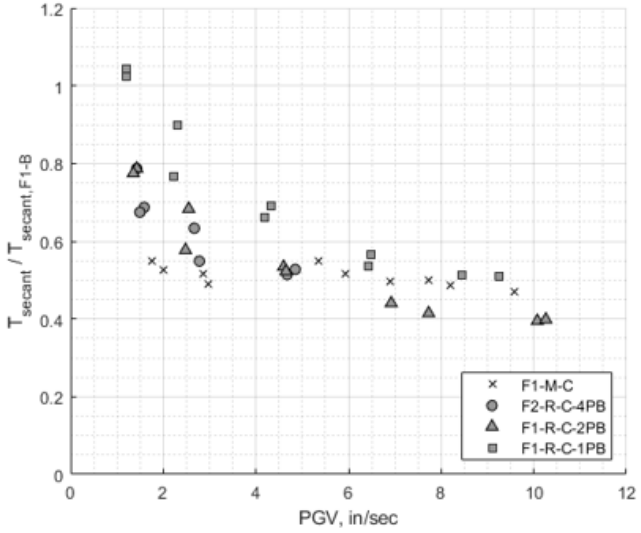

(d) Recast Frame, Secant Period

Figure 4-29: Periods of Infilled Frames Normalized by Series F1-B

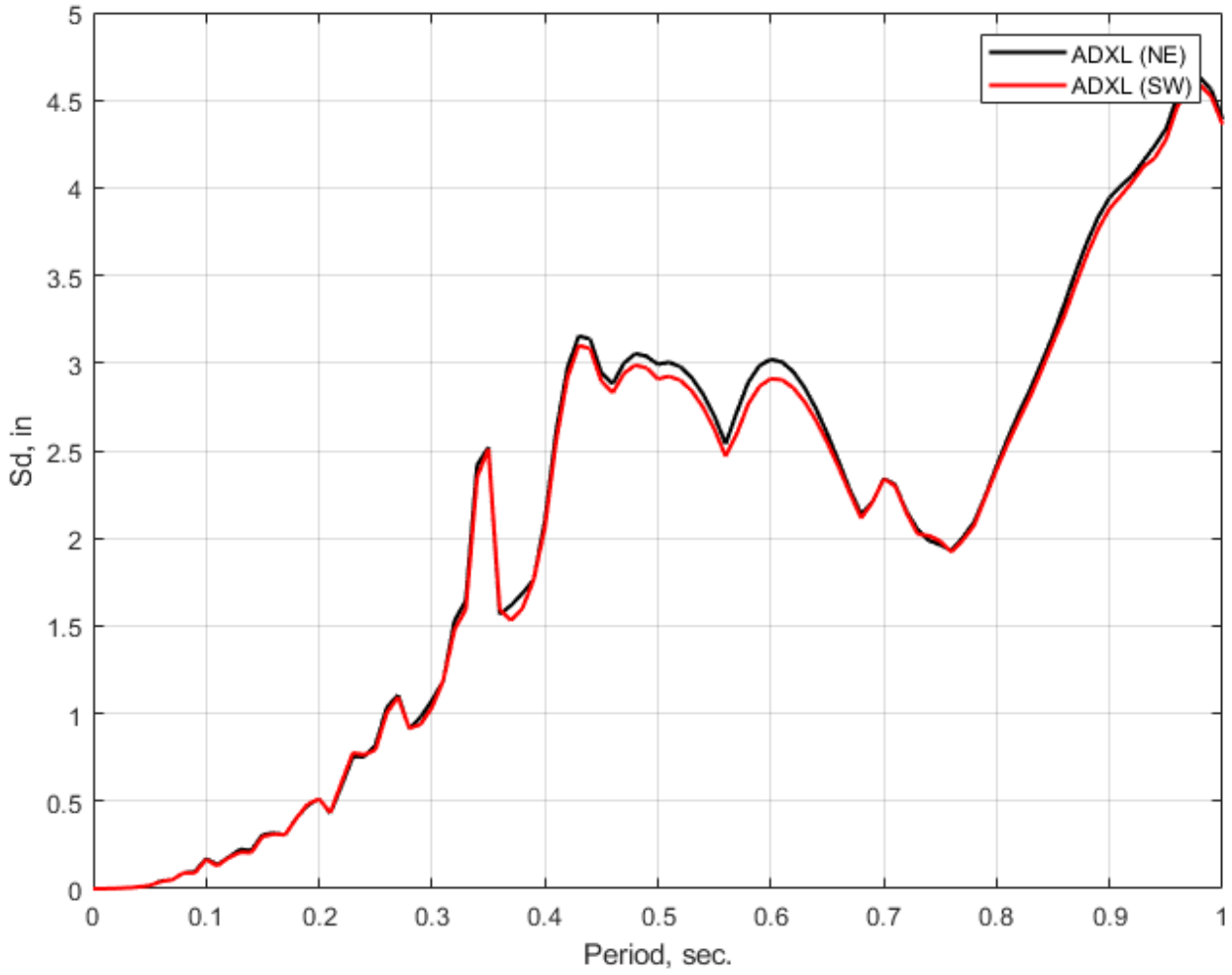

Figure 4-30: Displacement Spectra of Foundation Beam Measured Accelerations at 100% Intensity

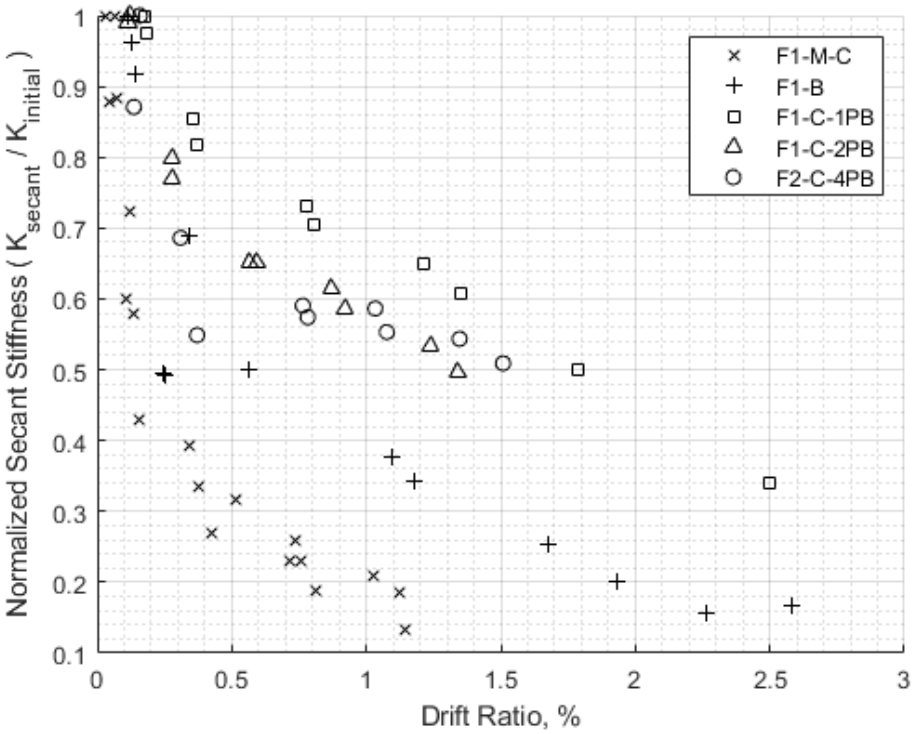

Figure 4-31: $K_{initial}$-Normalized Secant Stiffness vs Drift Ratio, Damaged Frames[1]

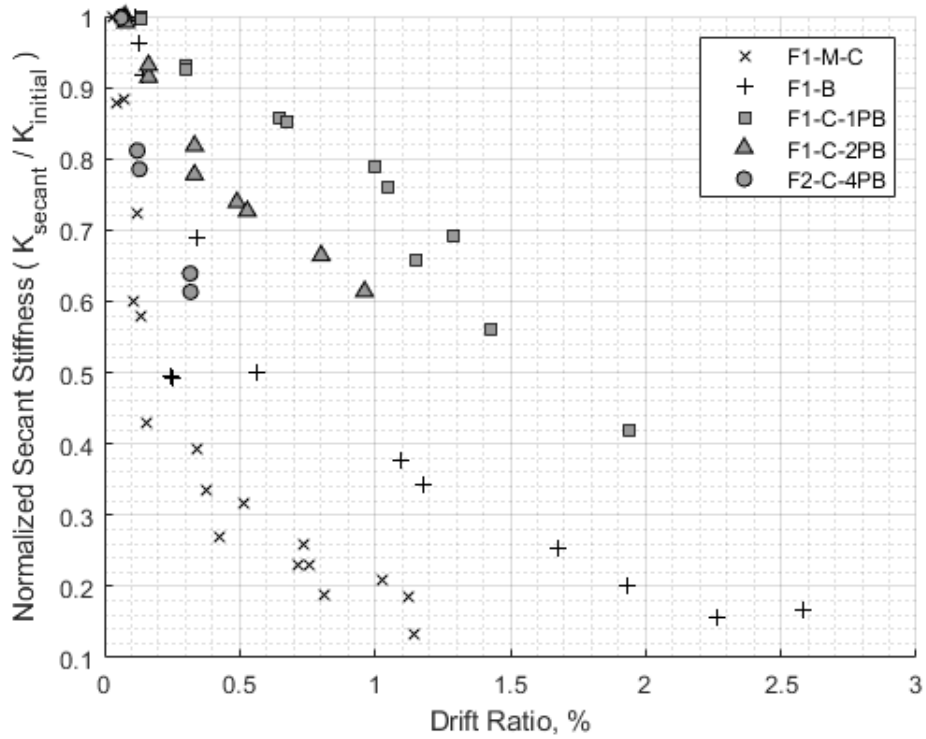

Figure 4-32: $K_{initial}$-Normalized Secant Stiffness vs Drift Ratio, Recast Frames

[1] Net Thickness: 1PB - 0.703", 2PB - 1.406", 4PB - 2.812", Masonry – 2.719"

APPENDIX A: MATERIALS AND CONSTRUCTION

This Appendix describes the materials and methods used to construct each specimen and test setup.

A.1: Concrete

Original-frame concrete was cast to a 28-day design strength of 3000 psi (Table A-1 and Table A-2). 3/8" diameter pea gravel was used as aggregate. The water to cement ratio at pour was approximately 0.56, accounting for additional water in the aggregate.

Recast-frame concrete was cast to a 28-day design strength of 6000 psi (Table A-3). MMConcrete Maximum-Strength Ready-Mix 60-pound bags were purchased and mixed using a 120-pound cement mixer (Figure A-1). Two bags were mixed at a time, forming lifts large enough to pour one half of a column repair and at least four 4"x8" standard cylinders. Though the exact ready-mix proportioning is proprietary information, a Mastercraft representative confirmed each bag contained approximately 12.0 pounds of cement paste and used 3/8" pea gravel aggregate. Table A-6 draws from the ready-mix safety data sheets to provide mix composition estimates. Each 60-lb bag of ready-mix called for a minimum 4 pints (4.17 lbf) of water, adding more to achieve the desired workability up to a maximum of 7 pints (7.30 lbf). The water to cement ratio at pour was approximately 0.42, or about 5 pints of total liquid added to the mixer per bag of ready-mix. To increase the strength of the cold joints, AKONA Concrete Bonding additive (Figure A-2) replaced the first 4 pints of water per bag of ready-mix.

A.2: Reinforcing Steel

Columns were reinforced with four 5/8" diameter deformed bars ($d = 6"$). Longitudinal bars were anchored 17.5" into the beam-column joints and an additional 14.5" into the foundation beams (Figure A-3). The measured yield stress of longitudinal reinforcement was approximately 63 ksi, according to uniaxial tension tests of four bars (Figure 2-9). Ties were 3/8" diameter deformed hoops with 90-degree hooks at each end, spaced at 6" along the clear height. The measured tensile yield stress of the ties was approximately 70 ksi (Figure 2-10).

Beams were reinforced with four 1” diameter deformed bars (longitudinal reinforcement ratio of 2.2%). Helical smooth steel wire 1/4” in diameter confined column longitudinal reinforcement in the beam-column joints (additional details in Figure A-4).

A.3: Wood Panel Infills

APA Rated Sheathing plywood panels were used in this study. Panels were purchased as 4’x8’, 6-ply Douglas-Fir / Southern Pine panels of the 23/32 performance category, bond category Exterior (Figure A-5). Panels were not Structural 1 rated. Each panel had a nominal thickness of 0.703” and had no sanded veneer layers for moisture control. Panels edges were cut with a circular table saw and cutouts made by orbital jigsaw. Panels were cut individually prior to infill lamination, as a result of tool limitations on cut depth. Each infill layer was cut entirely from a single 4’x8’ sheathing panel, with no interior splices. Abnormalities within panels such as large knots, cracks penetrating beyond the first ply, or discontinuity in edge plies disqualified sections of sheathing from being constructed into infills (Figure A-6), based on visual inspection by the writer.

Cutout infill panels were laminated with screws to achieve desired infill nominal widths. Of the three thicknesses of infill tested (4PB, 2PB, and 1PB), the 4PB and 2PB infills used screw-lamination to prevent buckling during tests. During any 4PB infill tests, four cutout plywood panels were screw-laminated with #9 x 3” GripRite construction screws (Figure A-7) in a 6”x6” grid. The first screw was driven into the upper south-west corner of the infill as the frame rested on the simulator platform, 2” below the upper concrete beam and 8” from the south column face (Figure A-8). Screws were driven horizontally from alternating east-west infill faces while an assistant applied confining pressure to the opposite side of the infill in the region of the screw. During 2PB tests, two cutout plywood panels were joined using #8 x 1.25” Spax construction screws (Figure A-9) using an identical grid pattern.

Each infill was constructed to leave approximately a 1/8” edge gap to the interior faces of the concrete frame. Because of inherited damage to the frames, especially at corners where extensive mortar repairs were required, edge gaps were not exact. At each column face, Nelson Beddar Wood 12” x 1.375” shims (Figure A-10) were hammered from alternating sides of the infill to fill the gap. Shim thickness tapered from 1/16” to 5/16”. The shims were super-glued the edge of the infill panels to hold them in place during large deformations. Once the bearing edge-joint was formed, 0.5” diameter holes were drilled through the infill parallel to the simulator

platform according to the pattern of Figure 2-27. Threaded rods used for the post-tensioned clamp system were slid through the holes (Figure A-11), forming a dowel-type connection between the infill and frame columns.

Along the bottom of the infill, nine pairs of steel channels and two 3”x0.75” steel plates prevented slip between the frame and simulator platform. The channel pairs were spaced 6” on center, in line with platform tie-ins into which 1/2” diameter threaded rods were tightened. Using an orbital jigsaw, 4” long by 3” tall cutout keys along the bottom edge of the wood infills were made to accommodate each pair of channels, and 3.5”x0.875” cutouts were made for the steel plates (Figure A-12). To ensure the frame would not slide beneath of these channels, spacer plates were hammered between the channels to fill out each cutout (Figure 3-11). Three of five of the vertical clamping devices described in Appendix A.6 passed within the infill bay. The largest, center grip consisted of a 12”x1” A36 steel plate, while the two side clamping assemblies consisted of A36 steel plates 10.25”x1”. An orbital jigsaw was again used to cut matching holes in each infill, with shims filling the edge gaps (Figure A-13).

The moisture content of the plywood at the time of testing for the infills and beams was not recorded. The moisture content of the panels was assumed to be the plywood equilibrium moisture content during all tests, as plywood panels were stored indoors adjacent to the earthquake simulator at all times. No panel was exposed to weather or moisture between purchase and testing.

A.4: External Mass

A reinforced concrete block 14’x5’x4’ formed the external suspended mass, as constructed by Pollalis (2021) (Figure A-14). When not suspended, the block rested on four hydraulic jacks on top of a base concrete block of matching dimensions, post-tensioned to the Bowen Lab strong-floor in four locations. The block was lifted by four screw-pin shackles which connected lifting inserts to two lifting straps. The crane hook was approximately 35 feet above the external suspended mass center. Out-of-plane bracing for the suspended mass was provided by four HSS8x4x1/4 sections clamped to the concrete base block by eight 5/8” diameter threaded rods imbedded 12” into the base block. Attached to the top of the HHS sections were Teflon pads to reduce friction between the external mass and bracing during ground motions when contact occurred during dynamic testing, as visible in Figure 2-19. Adjustable nuts on 1-1/4” diameter

deformed bars passing underneath the suspended mass and through the HHS sections were used to tighten or loosen the alignment of the out-of-plane bracing about the suspended concrete block.

The weight of the external suspended mass was 44.5 kips (Table 2-2) as determined by Monical (2022) using a MSI Porta-Weight Plus crane scale (Model No. 4300) with a 70-kip capacity and ±20 lbf resolution.

A.5: Connection of Frame to Simulator Platform

A labeled isometric view of the test setup is provided in Figure A-15.

A gypsum layer was applied between the foundation beam bottom face and simulator platform upon placement of the frame to the tested. Frames were flanked parallel to the direction of ground motions by two W18x65 steel beams. Every 12” inches, 1/2” diameter threaded rods were fitted through holes in both flanges of the W-sections and tightened into the simulator platform to provide an approximately 220 kip clamping force between frame and platform. Every alternate six inches, 1/2” diameter threaded rods passed through holes in the W18x65 top flanges, adding redundancy to the connection. Threaded rods were clamped to the frame foundation beam via slip-critical connection formed by tightening 3/4” nuts onto A36 plates holding down nine pairs of steel channels passing through the frame bay and steel plates flanking the columns. Perpendicular to the direction of ground motion, two MC18x58 steel channels were attached to the platform via threaded rods and snug tight bolts passing through the bottom flange every 6”. Six adjustable bolts were wrench tightened to bear between the MC18x58 channels and the edge face of the frame foundation beam to prevent slip. In addition, two adjustable bolts each bore between at north and south edges of the in-plane W18x65 sections and the out-of-plane channels.

A.6: Connection of Frame to External Suspended Mass

The frame top beam was flanked by two 11.5-foot MC18x58 steel channels, each with a longitudinal splice 30” from the in-plane north end of the specimen. The splice consisted of four one-foot-long steel plates, 2-7/8”x1” in cross section (Figure A-16) splicing the MC18x58 top and bottom flanges. Six 3”x3/4” diameter ASTM A325 bolts were tensioned to approximately 30 kips each on each of the sets of two steel plates, three bolts per splice side. The spliced channels formed a slip-critical connection with the frame top beam via fourteen 1” diameter high-strength threaded

rods passing through holes drilled in the steel channels and cast into the concrete beams near midspan (Figure A-17). The total clamping force was approximately 300 kips. A layer of gypsum was poured between the east concrete face and steel channel prior to tightening to ensure a smooth connection. At the north face of the frame top beam, six 7/8” diameter bolts bore on a pair of angles attached to the MC18x58 channels (Figure A-18). At the south face of the frame top beam, a nut on a 2” diameter threaded rod bore on steel plates attached to the MC18x58 channels and the load-cell and dual-swivel link system connecting the frame to the external suspended mass (Figure 2-21). Five vertical clamping devices confined the frame top beam to restrain splitting cracks forming between holes in the beam through which threaded rods passed. Each vertical clamping device consisted of a 1” steel plate and four threaded rods passing through the flanges of the MC18 channels flanking the top beam (Figure A-17). The combined confining force from vertical clamping devices was approximately 50 kips.

A 100-kip capacity load cell was connected to the south end of the frame top beam MC18 channels via two 2” diameter threaded rods tightened into holds in the center of the load cell and to a tensioner tightened to 100 kips on each end of a standard nut style mechanical connector (Figure A-19). The load cell assembly was mounted to the MC18 channel pair south end via eight 7”x3/4” diameter bolts, tightened to approximately 20 kips each (Figure A-20). The load cell assembly was connected to the end of the dual-swivel link designed by Monical (2022) consisting of two 995 HT Shore Western hydraulic actuator base swivels tightened together.

The southern swivel was connected to the external mass block by four 1” diameter threaded rods, driven 28” into the reinforced concrete block (Figure A-21) and tightened to 50 kips each. Rods were embedded with high strength, Hilti HIT-RE 500 V3 epoxy cartridges. Holes were drilled with a 36” long, 1-1/8” diameter Hilti TE-YX Imperial Hammer drill bit and were cleaned with a 1-1/8” diameter wire brush and pressurized air. The connection of the southern swivel to the external mass block was performed by Monical (2022) prior to the start of this study.

The final connection between external mass and frame was at the load-cell assembly at the northern end of the dual-swivel link. The steps to complete this connection without excessive lateral loading of the frame are illustrated in Figure A-22. The swivel link was first lifted to horizontal by overhead crane with the external mass resting on hydraulic jacks. A walkie-stacker then supported the dual-swivel link, and the crane head was moved to suspend the reinforced concrete block. Sets of three 1” thick steel plates were placed between the load cell assembly and

northern swivel, with four 1” diameter threaded rods passing through holes in the swivel and spacer plates. Nuts on the threaded rods were tightened with a 5-foot cheater bar. The total clamping force was approximately 180 kips. The DAQ recorded load cell readings at 100Hz during frame-mass connections; no lateral load above 1.5 kips on an infilled frame was permitted. The free hanging external mass was pulled towards the frame top beam as the bolts were tightened, and its hanging position could be adjusted with the crane to minimize the lateral force on the frame.

A.7: Four-Point Bending Beam Tests

The bending Modulus of Elasticity of the sheathing panels was determined via 4-point bending tests. Four beams of varying width were constructed, 24” long by 6” deep. Test were completed using the Baldwin Southwark Tate-Emery Testing Machine with the Instron Extend Upgrade at Bowen Lab (Figure A-23). The midspan deflection of each beam was measured at intervals of approximately 330 lbf between 1.0 to 6.0 kips. The load was recorded manually off the reading by the Tate-Emery Testing Machine load cell to the nearest 10 lbf. A head built from a 6” steel channel welded to a 0.25” A36 steel plate was constructed to apply point loads at 1/3 the distance between the roller supports (Figure 2-32 and Figure A-24). The total weight of the head was 9.0 lbs. The interval of loading for each test varied as the displacement was controlled manually via a knob and not directly programmed.

Beam widths (2.81” or 1.41”) were selected to match the infill thicknesses constructed in the dynamic tests of infilled frames. Each beam was laminated with 4 screws 6” on center. Screws were driven from alternating faces while clamps compressed the panels together.

Optotrack digital imaging was used to measure the midspan deflection of the beams within ±0.005”. Targets were placed 3” from the bottom of the beams over each exterior roller support and at the midspan (Figure 2-33). The midspan deflection was defined as the vertical distance between the line connecting the support targets to the height of the midspan target (Figure A-25). Data was collected in millimeters at 100Hz for the duration of the loading and unloading process, and was later converted to inches.

The following assumptions were made in the estimation of the Modulus of Elasticity of the wood once the loads and deflections had been measured for each beam:

- The cross section of each beam was uniform and had no gross abnormalities.
- The beams did not rotate out of plane or buckle during testing.

- Panel failure was not approached during loading.

Modulus of Elasticity was calculated from load and displacement according to the Equation A.1, derived from the mechanics of simply supported beams under two uniformly spaced point loads, rearranged into Equation A.2.

$$\Delta_{midspan} = \frac{Pa}{24EI}(3l^2 - 4a^2) \quad \text{(Equation A-1)}$$

$$E = \frac{Pa(3l^2 - 4a^2)}{24\,\Delta_{midspan} I} \quad \text{(Equation A-2)}$$

where:

P = Force of a single point load in pounds

L = Total span between the supports

a = Distance P is applied from the closest support, or L/3 in this test

E = Modulus of Elasticity of the material

I = Cross sectional moment of inertia

Table A-1: Original Frame Concrete, Compressive Strength of Standard 6”x12” Concrete Test Cylinders through 28 Days After Cast (Monical, 2022, Table B-2).

Age, days	Compressive strength of test cylinders, psi		
	Each	Mean	Std. dev.
3	1600	1700	100
	1800		
	1650		
7	2000	2000	30
	2000		
	1950		
14	2400	2400	30
	2450		
	2450		
21	2800	2700	80
	2750		
	2650		
28	3200	3100	80
	3150		
	3050		

Table A-2: Original Frame Concrete, Measured Properties of Concrete on First Day of Tests of F1 and F2 (Monical, 2022, Table B-3)

Specimen	Age, days	f'_c, psi		E_c, ksi		f_r, psi		f_t, psi	
		Each	Mean	Each	Mean	Each	Mean	Each	Mean
F1	129	3800	3800	3200	3200	500	500	450	400
		3750		3250		-		400	
		3850		3250		-		400	
F2	339	3550	3500	2950	3100	600	600	350	300
		3500		3100		600		300	
		3500		3150		-		300	

Table A-3: Recast Frame Concrete, Compressive Strength of Standard 4”x8” Concrete Test Cylinders through 25 Days after Cast

Age, days[1]	Compressive strength of test cylinders, psi		
	Each	Mean	Std. Dev.
3	4900	4770	190
	4550		
	4850		
7	4800	5300	430
	5600		
	5500		
25	5500	5400	290
	5050		
	5600		

Table A-4: Recast Frame Concrete, Split Tensile Strength of Standard 4”x8” Concrete Test Cylinders through 25 Days After Cast

Age, days[2]	Split tensile strength of test cylinders, psi		
	Each	Mean	Std. Dev.
3	480	495	20
	510		
7	530	555	35
	580		
25	620	565	80
	510		

[1] Final cylinder tests were performed at 25-day concrete age to record concrete properties on the first day of testing for series F2-R-C-4PB.
[2] See Footnote 1.

Table A-5: Original Frame Concrete, Mix Proportions (Monical, 2022, Table B-4)

Material	Batched quantity, lbf	Actual water, gal	Description	Source
Buzzi cement	1180	x	ASTM C150, Type I cement	Buzzi
fly ash	440	x	ASTM C618, Class F fly ash	Headwaters
Pea gravel	6600	2	INDOT, 3/8-in. pea gravel	US Aggregates
#23 sand	6640	31	INDOT, natural sand	US Aggregates
Water	636	76.2	N/A	Irving Materials, Inc.
MasterGlenium 7511	29	x	Water-reducing admixture	Irving Materials, Inc.

Table A-6: Ready-Mix Concrete Approximate Contents

Maximum Strength Concrete Mix (60 lbf), Rapid Set 6500 PSI Formula (Fiber reinforced).

Mastercraft by Midwest Manufacturing

Model No. 1891020, SKU: 1891020

Material	CAS No.	Percent by Weight
Portland Cement[1]	65997-15-1	20
Sand, Silica, Quartz	14808-60-7	40 to 70
Calcium Sulfoaluminate	65997-16-2	10 to 30
Calcium Aluminate	12042-68-1	5 to 10
Calcium Sulfate	10101-41-4	1 to 5
Limestone Dust	01317-65-3	1 to 5

[1] Percent of Portland Cement by weight derived from conversation with Midwest Manufacturing Concrete Block Employee. Other ready-mix material percentiles by weight are proprietary.

Table A-7: Recast Frame Concrete, Mix Proportions per Batch

Materials	Batched quantity, lbf	Actual liquid, gallons	Description	Source
Batch 1[1]				
Ready-Mix concrete (2 bags)	120	x	Max Strength Concrete Ready Mix	Menards
Water	3.5	0.42	N/A	Bowen Lab
Bonding Admixture	8.36	2.00	Akona Concrete Bonding Additive	Menards
Batch 2				
Ready-Mix concrete (2 bags)	120	x	Max Strength Concrete Ready Mix	Menards
Water	2.3	0.27	N/A	Bowen Lab
Bonding Admixture	8.36	2.00	Akona Concrete Bonding Additive	Menards
Batch 3				
Ready-Mix concrete (2 bags)	120	x	Max Strength Concrete Ready Mix	Menards
Water	1.9	0.23	N/A	Bowen Lab
Bonding Admixture	8.36	2.00	Akona Concrete Bonding Additive	Menards
Batch 4[2]				
Ready-Mix concrete (2 bags)	120	x	Max Strength Concrete Ready Mix	Menards
Water	2.6	0.31	N/A	Bowen Lab
Bonding Admixture	8.36	2.00	Akona Concrete Bonding Additive	Menards

[1] Highest quantity of extra water added as hand-mixer was not wetted prior to mixing
[2] Hand-mixer cleaned prior to final batch 4

Table A-8: Beam Test (Infill modulus of elasticity) Load and Deflection Data

Specimen	Load (lbf)	Midspan Deflection (in)	E_w (ksi)
Beam 2PB-1	1000	0.0084	490
	1360	0.0122	460
	1730	0.0155	460
	2000	0.0219	370
	2300	0.021	450
	2650	0.0249	440
	3030	0.0282	440
	3400	0.0315	440
		average E_w	440

Specimen	Load (lbf)	Midspan Deflection (in)	E_w (ksi)
Beam 2PB-2	1050	0.0109	390
	1300	0.013	410
	1590	0.0166	390
	1970	0.0212	380
	2300	0.0257	370
	2740	0.0261	430
	3090	0.0313	400
	3600	0.0304	480
		average E_w	410

Specimen	Load (lbf)	Midspan Deflection (in)	E (ksi)
Beam 4PB-1	1320	0.0049	550
	1810	0.005	750
	2130	0.0065	670
	2420	0.0072	690
	2750	0.0089	630
	3070	0.0104	600
	3400	0.0114	610
	3730	0.0129	590
	4060	0.0142	590
	4340	0.0156	570
	4640	0.0163	580
	5020	0.0185	550
	5430	0.0203	550
	5800	0.022	540
	6070	0.0224	550
		average E_w	600

Specimen	Load (lbf)	Midspan Deflection (in)	E_w (ksi)
Beam 4PB-2	1320	0.0081	330
	1610	0.0099	330
	2020	0.0119	350
	2280	0.0133	350
	2700	0.0156	350
	3030	0.0172	360
	3310	0.0188	360
	3750	0.0208	370
	4120	0.0231	360
	4540	0.0258	360
	4940	0.0253	400
	5130	0.0277	380
	5440	0.03	370
	6030	0.032	390
	6910	0.0375	380
		average E_w	365

Figure A-1: Bowen Lab Concrete Mixer with 120lb, 3.5 Cubic Foot Capacity

Figure A-2: AKONA Concrete Bonding Additive

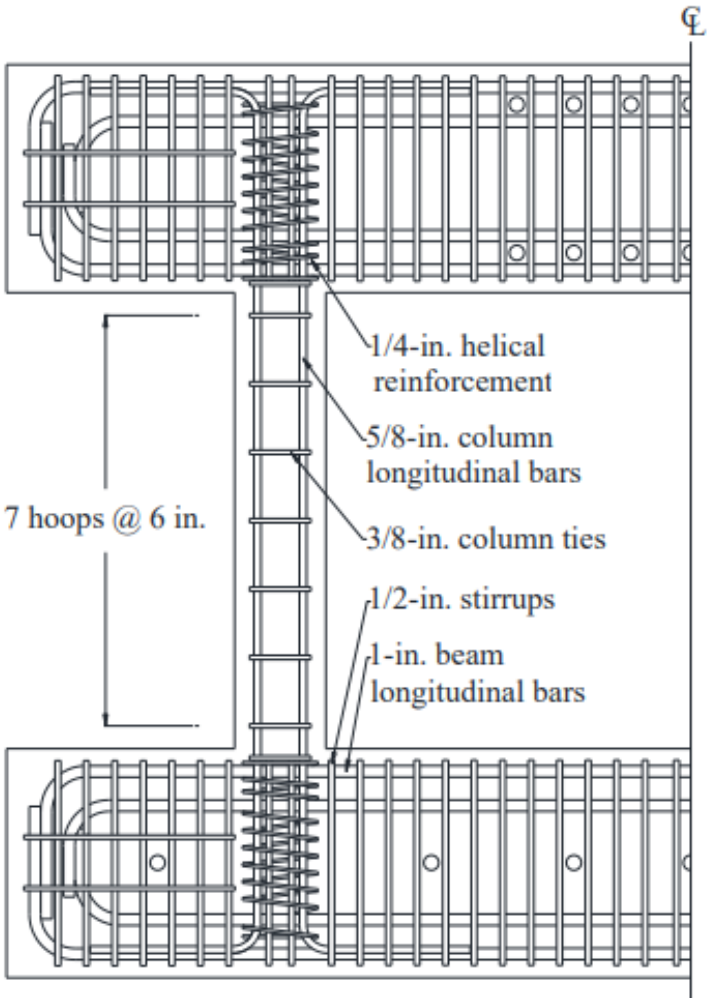

Figure A-3: Reinforcement Layout (Monical, 2022, Figure B-6)

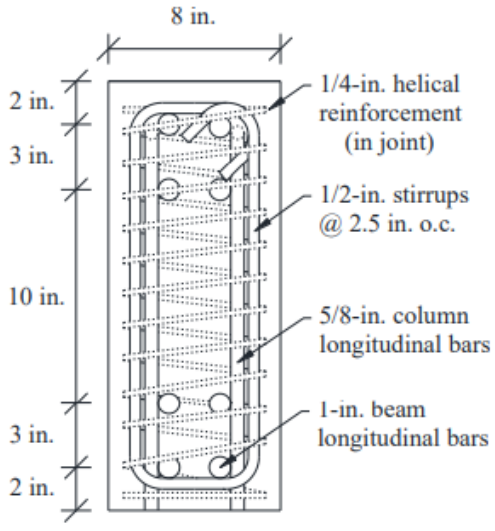

Figure A-4: Beam Cross Section and Typical Reinforcement (Monical, 2022, Figure B-7)

Figure A-5: APA Rating Stamp

(a) Missing plies at panel edge

(b) Multi-ply face splitting

(c) Veneer holes / burnouts

Figure A-6: Disqualifying Plywood Abnormalities

Figure A-7: #9 x 3" GripRite Construction Screws

Figure A-8: Screw Grid Orientation

Figure A-9: #8 x 1-1/4” Spax Multi-purpose Construction Screws

Figure A-10: Wood Shims for Edge-Joints

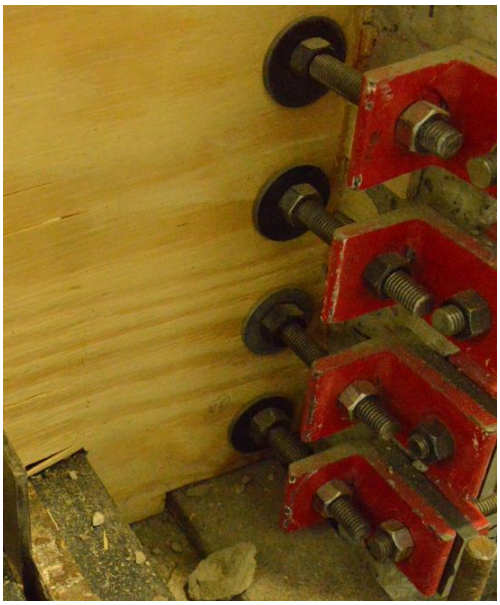

(a) In frame

(a) Post-failure infill

Figure A-11: Post-Tensioned Clamp Threaded Rods Passing through Wood Infill (Test Series F1-C-1PB)

Figure A-12: Typical Infill Corner Cutout

Figure A-13: Wood Shims Filling Frame to Infill Edge Gap

Figure A-14: Reinforced Concrete Block (External Suspended Mass) as a Foundation Block Constructed by Pollalis (2021)

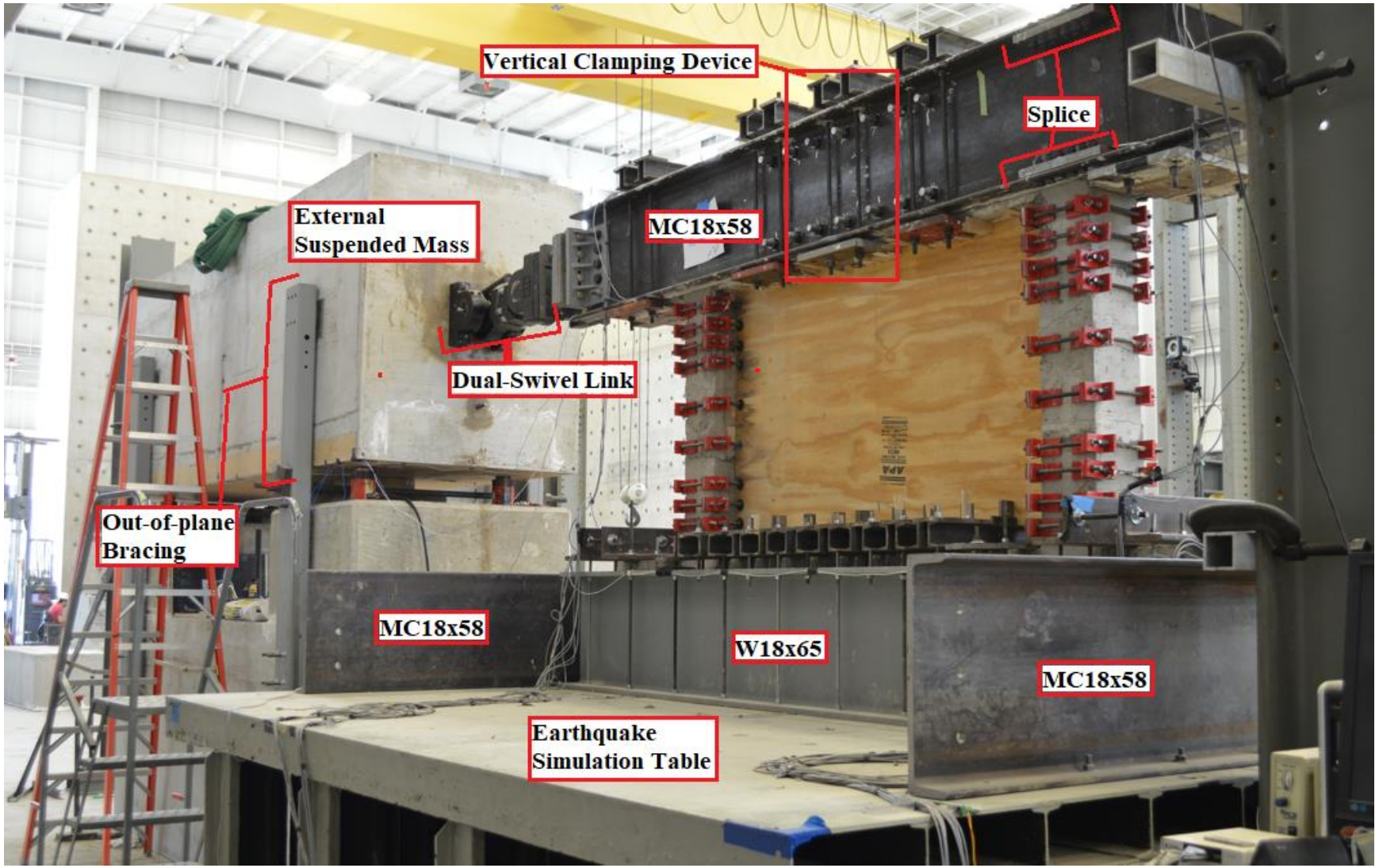

Figure A-15: Test Setup - Isometric

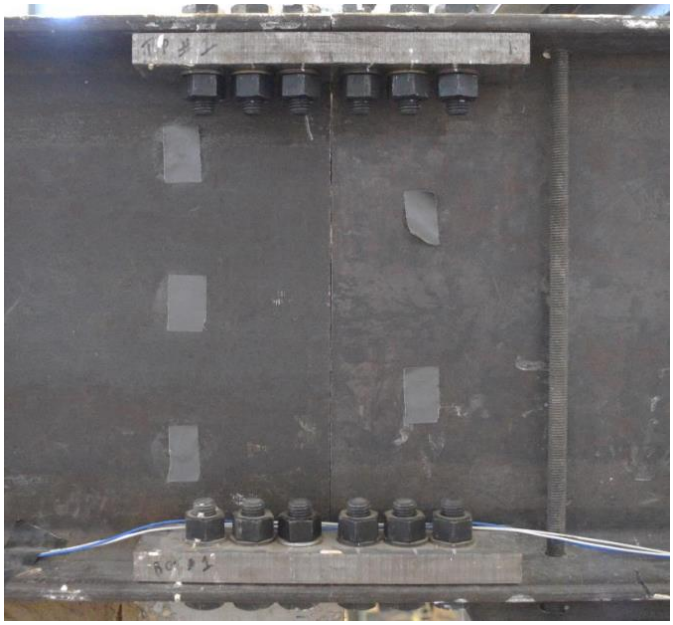

Figure A-16: Top Beam Channel Splice Detail (East Face)

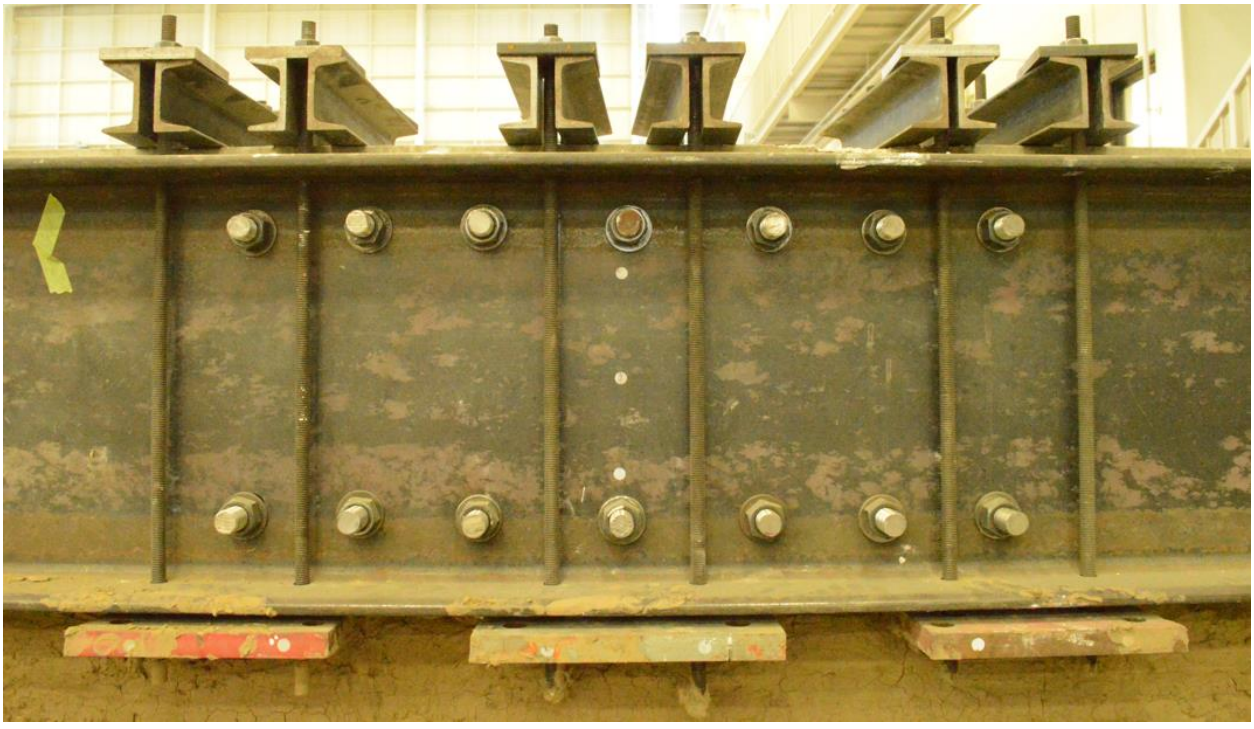

Figure A-17: Slip-critical Top Beam Connection and Vertical Clamping Devices (West Face)

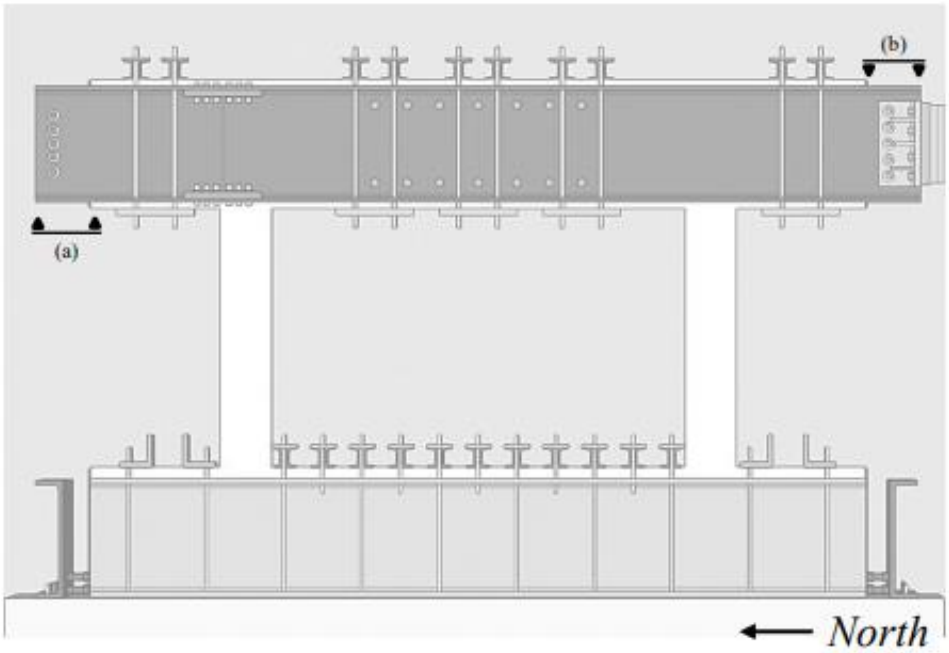

Figure A-18: Adjustable Bolts Preventing Slip between Confining Channels and Top Beam (Monical, 2022, Figure 2-16)

Figure A-19: Standard Nut Style Mechanical Tensioner Manufactured by Superbolt, Inc. (Monical, 2022, Figure B-22)

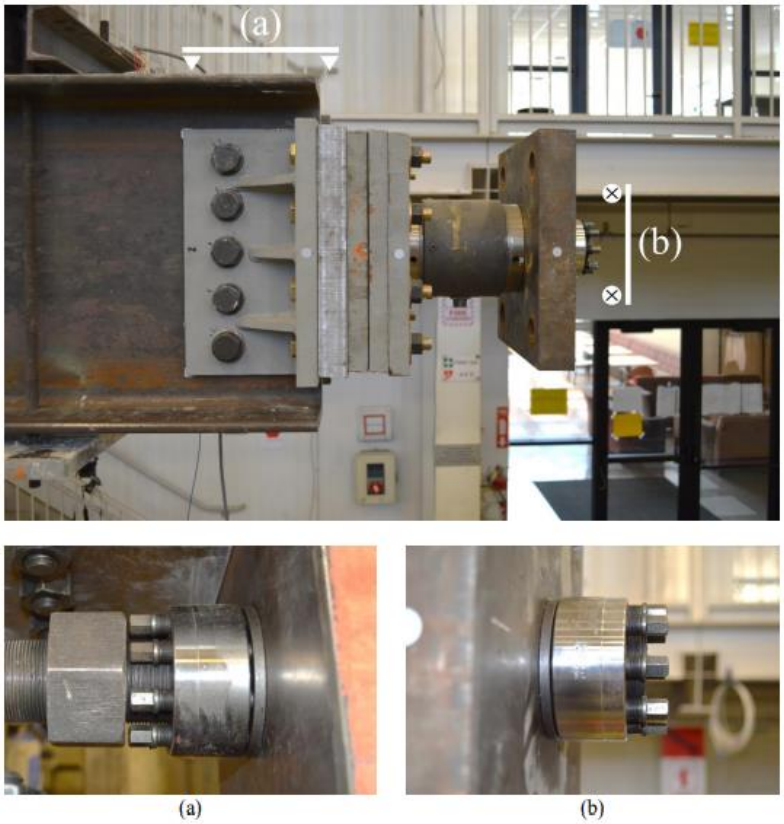

Figure A-20: Load Cell Assembly (Monical, 2022, Figure B-21)

Figure A-21: Four 1-in. High-Strength Threaded Rods Embedded into North Face of External Suspended Mass (Monical, 2022, Figure B-24)

(1) Crane lifts link, external mass resting

(2) Walkie-Stacker supports link.
Crane straps are ready to be removed

(3) Walkie-Stacker supports link, Crane lifts external mass.
Spacer plates can now be inserted, and connection tightened

Figure A-22: Process to Connect External Mass to Frame without Applying Lateral Load

Figure A-23: Baldwin Southwark Tate-Emery Testing Machine with the Instron Extend Upgrade

Figure A-24: E_w Beam Test Load Spacing

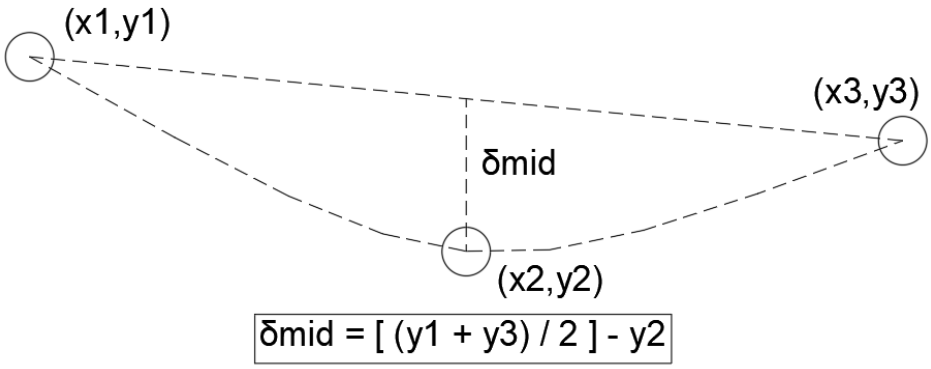

Figure A-25: E_w Beam Test Midspan Deflection Calculation

APPENDIX B: PROCEDURES AND INSTRUMENTATION

B.1: Frame Preparation Prior to Series

Prior to Series F2-C-4PB, F1-C-2PB, and F1-C-1PB, column concrete spalling was repaired with type-N Mortar (Figure B-1), primarily at the column base. Loose concrete was removed from the frame columns near the joints and exposed surfaces were cleaned with compressed air. The 28-day compressive strength of the mortar was approximately 1700 psi (Monical, 2022, Table B-8). The mortar was not held in place by formwork, rather the low workability of the mortar mix allowed the mortar to free stand as it cured. The shape of the 8" square column cross-section was recreated with mortar to ensure clean transfer of exterior confinement forces from the post-tensioned clamps at the corners of the column. Severe flexural cracking had occurred at all column-joint faces in both test frames. Mortar was applied to fill cracks but did not reach into the column core. Example mortar repairs are displayed in Figure 3-6, completed after frames were secured to the simulator platform such that repairs would not be damaged during frame transportation.

All test series followed the remaining listed procedure. Construction and attachment of the infills was performed after the frame was secured to the simulation platform as explained in Appendix A. Infill bearing edge-joints were partially formed to contain the infills prior to screw-lamination of panels. 0.5" holes were driven horizontally through the infills, 1.375" inches from the nearest column face, and the external clamp threaded rods slid through. The clamps were hand tightened first, then tightened with a torque wrench to apply approximately a bar stress of 40 ksi. Using two nuts on the threaded rods passing through the infill thickness, the infill alignments were adjusted until the panels were centered in the frame bay (Figure B-2). Once the infill was centered, steel channel pairs and plates forming the frame to platform connection along the foundation beam were slid into keys at the bottom of the infills and braced with spacer plates. The frame was now infilled and ready to be instrumented.

B.2: Instrumentation and Calibration

Displacements of the frame were measured using Linear Variable Differential Transformers (LVDTs). Figure 2-16 displays the complete sensor layout. Data were taken at 1000Hz. LVDTs recorded horizontal, in-plane displacement of the simulator platform at the hydraulic ram head's connection (2" stroke), the upper north edge of the frame foundation beam (3" stroke), the lower north edge of the frame top beam (5" stroke), and the upper north edge of the frame top beam (6" stroke). Four LVDTs also recorded the vertical deflection of the simulator platform (2" stroke) (Figure 2-20), alternating upwards and downwards as positive in two sets of two at the north and south ends of the simulator platform. Calibration of the LVDTs showed the maximum error of displacement was smaller than 0.01" for LVDTs with strokes 2" or less and smaller than 0.02" for LVDTs with strokes larger 2".

B.3: Accelerometers

Accelerations were measured using ADXL335 tri-axial MEMS accelerometers, powered using a constant DC supply of 3.3 Volts. The axes of acceleration recorded were: In-plane (south-north), out of plane (east-west), and vertical (up-down). The ADXLs had an acceleration range of ±3g and a frequency range of 0 to 1600 Hz about the horizontal axes and 0.5-550 Hz about the vertical axis. The ADXL accelerometers were the primary source of acceleration data in analysis. Accelerations were also measured using PCB Piezotronics Model 333B52 uni-directional piezoelectric accelerometers that were powered using PCB 482A22 4-525 channel signal conditioners. These piezoelectric accelerometers had an acceleration range of ±5g and a frequency range of 0.5 to 3000 Hz. 6 PCB accelerometers were used on each test: 4 on the frame and 2 on the external mass, all measuring horizontal in-plane accelerations. Accelerometers were glued to smoothed surfaces on the frame and external mass, according to the orientation in Figure B-3.

ADXL accelerometers were calibrated against the effect of gravity. A given ADXL was twice held in three positions (neutral, reading against gravity, reading with gravity) in correlation to the desired direction of calibration for a minimum of five seconds each with the DAQ collecting data at 1000 Hz. The calibration constant, in Volts/g, was deemed as the half the difference between the average reading of 1000 data points from the ADXL reading with and against gravity. All ADXL calibration constants were within ±0.04 Volts/g from the designed constant of 0.33

Volts/g. Each time a new frame was secured to the platform, a new set of ADXL accelerometers were soldered, calibrated, and glued to the frame. ADXLs were not replaced with each new infill. Data for ADXL accelerometers were filtered, trimmed, corrected, and integrated using a procedure developed by Monical (2022, Appendix B) as summarized below.

First, all raw ADXL acceleration histories were filtered using a fourth-order Butterworth bandpass filter with a high-pass frequency of 0.25 Hz and low-pass frequency of 15 Hz. The high- and low-pass frequencies were selected based on matching target and measured acceleration histories and displacement spectra (see Monical, 2022, Table 2-1 and Figures 2-42 through 2-49). Second, filtered base ADXL acceleration data were trimmed within 5.0 seconds of the beginning and end of each test run. The trimmed and filtered ADXL data were integrated using the trapezoidal rule to produce ADXL velocity histories. Velocity histories were corrected via second-order polynomial function such that the trimmed ground motion start and end values were approximately zero. The previous two steps were repeated to develop ADXL displacement histories. ADXL displacement histories were less precise than the raw LVDT data as a result of the aforementioned repeated integrations and corrections, thus LVDT displacement histories were the primary form of displacement data used in analysis.

B.4: Lateral Load Measurement

A Lebow Model 3156-100K load cell measured lateral forces between the external suspended mass and frame top beam (Figure B-4). The load cell rated capacity was 100 kips, calibrated in 10-kip increments by J. Monical and P. Shah, with a maximum error no larger than 1 kip (Table B-1). Alternate loadings could be estimated from a pair 45° rectangular strain gauge rosettes attached the flexural link connecting the servoram head to the simulator platform (Figure B-5). The maximum discrepancy between lateral load from the average strain gage reading and load cell during the most demanding run of this experimental program was 2.5 kips during the region highlighted in Figure 3-32. The primary source load data used in this program was the load cell, which provided exact lateral forces acting on the frame top beam.

B.5: Earthquake Simulator

Bowen Laboratory's earthquake simulator reproduced uniaxial ground motions via a dynamic hydraulic actuator with 75 kip rated capacity mounted to a steel anchor block. To prevent damage to the servoram, a flexure link was connected between the platform and ram with a 70-kip yield limit. The simulator platform is limited in performance by peak ground accelerations of $2g$, peak ground velocities of $12\ in/sec$, or peak NS displacements of $2\ in$. El Centro, NS ground motion records were compressed in time by a factor of 2.0, then linearly scaled in amplitude by 1.9 to fit within these simulator performance limits. Ground motion inputs were displacement controlled by an MTS FlexTest 60 digital controller. Complete details of the earthquake simulator are provided in Sozen (1969) and Gulkan (1971).

B.6: Optical Tracking Systems

Optitrack from NaturalPoint Inc. measured tri-axis displacements at target locations described in Figure 3-1 and 3-2. Data was collected at 100Hz using Motive software connected by ethernet to four Prime 41 cameras and stored in CSV files. Optitrack cameras were wand calibrated prior to each day of testing, with a mean error not larger than ± 0.015 inches.

A Northern Digital Optotrack Pro 600 optical tracking system measured tri-axis displacements of infrared targets arranged according either Figure 3-3 or 3-4. Data was sampled continuously at 100 Hz and stored in TAK files. The laser system tracked targets to ± 0.005 inch.

Because of the volatile dynamic nature of simulations, some optical targets became briefly undetected by the tracking systems during runs. Missing data was linearly interpolated between last known point of detection and first target reappearance when this phenomenon occurred. Custom MATLAB scripts transformed both types of optical target displacement data into matching North-South axes (x-axis corresponding to in-plane motion) based on reference plane targets on the west face of the simulator platform (MathWorks, 2018).

B.7: Data Acquisition System (DAQ)

Data were collected using a National Instruments SCXI-1000 chassis and National Instruments SCB-68 connector block. National Instruments LabVIEW software formatted the DAQ. Data was collected at 1000Hz during each test using this DAQ for accelerations (ADXL and PCB), displacements (LVDT), forces (Load Cell), and strains (Strain Gages). Table B-2 through Table B-7 describe the sensor layout and DAQ organization during each series. Data was stored in TDMS files organized by date of testing with Notepad++.

Table B-1: Load Cell Calibration Data

Vex	Sensitivity[1]	Accuracy	Max Error
10	0.0239	1.10%	1.062 kips

Load, kip	Output, mV	Output, mV/Vex	ΔOutput, mV/Vex	Calculated Displacement, ΔOutput / Sensitivity	Error, in
0.0	-0.405	-0.01	-0.01	-0.00008	0.000
10.0	2.080	0.03	0.03	0.00042	-10.000
20.3	4.460	0.06	0.06	0.00091	-20.299
29.9	6.800	0.08	0.08	0.00138	-29.899
39.4	9.100	0.11	0.11	0.00185	-39.398
49.5	11.700	0.15	0.15	0.00238	-49.498
59.6	14.100	0.18	0.18	0.00286	-59.597
70.3	16.300	0.20	0.20	0.00331	-70.297
79.8	18.700	0.23	0.23	0.00380	-79.796
89.5	21.100	0.26	0.26	0.00429	-89.496
94.0	22.200	0.28	0.28	0.00451	-93.995
80.3	18.80	0.23	0.23	0.00382	-80.296
61.3	14.20	0.18	0.18	0.00288	-61.297
40.5	9.34	0.12	0.12	0.00190	-40.498
20.1	4.50	0.06	0.06	0.00091	-20.099
0.0	-0.41	-0.01	-0.01	-0.00008	0.000

[1] Sensitivity = Slope of Linear Regression of Load (kips) versus Output (MV/Vex)

Table B-2: Sensor Locations, All Series

Sensor Number	Sensor Type	Location and Description
0	Accelerometer	Top northeast corner of foundation beam measuring in-plane base accelerations
1	Accelerometer	Top southwest corner of foundation beam measuring in-plane base accelerations
2	Accelerometer	Top northeast corner of top beam measuring in-plane roof accelerations
3	Accelerometer	Top southwest corner of top beam measuring in-plane roof accelerations
4	Accelerometer	Middle of east face of RC block measuring in-plane accelerations
5	Accelerometer	Middle of west face of RC block measuring in-plane accelerations
6	LVDT	Below northeast side of simulator platform measuring displacement of platform
7	LVDT	Below northwest side of simulator platform measuring displacement of platform
8	LVDT	Below southwest side of simulator platform measuring displacement of platform
9	LVDT	Below southeast side of simulator platform measuring displacement of platform
10	LVDT	Top of foundation beam measuring in-plane base displacement
11	LVDT	Soffit of top beam measuring in-plane roof displacement
12	LVDT	Top of top beam measuring in-plane roof displacement
13	Strain Gage*	Middle of east face of flexure link oriented 45 counterclockwise from horizontal
14	Strain Gage**	Middle of east face of flexure link oriented horizontal
15	Strain Gage*	Middle of east face of flexure link oriented 45 clockwise from horizontal
16	Strain Gage*	Middle of west face of flexure link oriented 45 counterclockwise from horizontal
17	Strain Gage**	Middle of west face of flexure link oriented horizontal
18	Strain Gage*	Middle of west face of flexure link oriented 45 clockwise from horizontal
19	LVDT	Inside servoram measuring in-plane displacement of simulator platform (feedback signal)
20	LVDT	Inside servoram measuring in-plane displacement of simulator platform (command signal)
21	Load Cell	Sandwiched between top beam and dual-swivel link measuring lateral load

*Strain gage factor $S_g = 2.090$ and transverse sensitivity $K_t = 0.8\%$

** Strain gage factor $S_g = 2.135$ and transverse sensitivity $K_t = 0.4\%$

Table B-2: Sensor Locations, All Series (continued)

Sensor Number	Sensor Type	Location and Description
22	Accelerometer	Top of southwest corner of foundation beam measuring vertical base accelerations
23	Accelerometer	Top of southwest corner of foundation beam measuring out-of-plane base accelerations
24	Accelerometer	Top of southwest corner of foundation beam measuring in-plane base accelerations
25	Accelerometer	Top of southwest corner of top beam measuring vertical roof accelerations
26	Accelerometer	Top of southwest corner of top beam measuring out-of-plane roof accelerations
27	Accelerometer	Top of southwest corner of top beam measuring in-plane roof accelerations
28	Accelerometer	Top of northeast corner of top beam measuring vertical roof accelerations
29	Accelerometer	Top of northeast corner of top beam measuring out-of-plane roof accelerations
30	Accelerometer	Top of northeast corner of top beam measuring in-plane roof accelerations
31	Accelerometer	Top of northeast corner of foundation beam measuring vertical base accelerations
32	Accelerometer	Top of northeast corner of foundation beam measuring out-of-plane base accelerations
33	Accelerometer	Top of northeast corner of foundation beam measuring in-plane base accelerations
34	Accelerometer	Northeast corner of simulator platform measuring in-plane platform accelerations

Table B-3: Sensor Summary, Series F2-C-4PB

Sensor Number	Sensor Type	Model	Serial Number	Direction	Sensitivity		Excitation volts
					Calibration Constant	Units	
0	Accelerometer	PCB 333B52	34413	South	1.048	V/g	-
1	Accelerometer	PCB 333B52	34454	South	1.077	V/g	-
2	Accelerometer	PCB 333B52	34411	South	1.045	V/g	-
3	Accelerometer	PCB 333B52	34415	South	1.051	V/g	-
4	Accelerometer	PCB 333B52	34412	South	1.061	V/g	-
5	Accelerometer	PCB 333B52	34414	North	0.96	V/g	-
6	LVDT	Schaevitz DC-E250	13292	-	39.554	V/in	±15V
7	LVDT	Schaevitz DC-E250	13301	-	40.929	V/in	±15V
8	LVDT	Schaevitz DC-E250	13609	-	41.91	V/in	±15V
9	LVDT	Schaevitz DC-E250	12971	-	40.167	V/in	±15V
10	LVDT	Schaevitz DC-E2000	2479	-	5.02	V/in	±15V
11	LVDT	Schaevitz DC-E3000	1684	-	3.345	V/in	±15V
12	LVDT	Schaevitz DC-E5000	1275	-	1.908	V/in	±15V
13	Strain Gage	CEA-06-250UR-350	1	North 45° CW	1	in./in.	2.5V
14	Strain Gage	CEA-06-250UR-350	2	North	1	in./in.	2.5V
15	Strain Gage	CEA-06-250UR-350	3	North 45° CCW	1	in./in.	2.5V
16	Strain Gage	CEA-06-250UR-350	1	North 45° CW	1	in./in.	2.5V
17	Strain Gage	CEA-06-250UR-350	2	North	1	in./in.	2.5V
18	Strain Gage	CEA-06-250UR-350	3	North 45° CCW	1	in./in.	2.5V
19	LVDT	-	-	-	1.812	V/in	-
20	LVDT	-	-	-	1.81	V/in	-
21	Load Cell*	Lebow 3156 - 100K	2468	-	-0.00023941	V/kip	10V

Table B-3: Sensor Summary, Series F2-C-4PB (continued)

Sensor Number	Sensor Type	Model	Serial Number	Direction	Sensitivity		Excitation volts
					Calibration Constant	Units	
22	Accelerometer	ADXL335	232	Up	0.3217	V/g	3.3V
23	Accelerometer	ADXL335	233	East	0.3276	V/g	3.3V
24	Accelerometer	ADXL335	234	South	0.3259	V/g	3.3V
25	Accelerometer	ADXL335	240	Up	0.3283	V/g	3.3V
26	Accelerometer	ADXL335	241	East	0.3120	V/g	3.3V
27	Accelerometer	ADXL335	242	South	0.3197	V/g	3.3V
28	Accelerometer	ADXL335	309	Up	0.3242	V/g	3.3V
29	Accelerometer	ADXL335	310	East	0.3307	V/g	3.3V
30	Accelerometer	ADXL335	311	South	0.3263	V/g	3.3V
31	Accelerometer	ADXL335	221	Up	0.3215	V/g	3.3V
32	Accelerometer	ADXL335	222	East	0.3268	V/g	3.3V
33	Accelerometer	ADXL335	223	South	0.3255	V/g	3.3V
34	Accelerometer	ADXL335	-	East	0.3300	V/g	3.3V

Table B-4: Sensor Summary, Series F1-C-2PB and F1-C-1PB

Sensor Number	Sensor Type	Model	Serial Number	Direction	Sensitivity		Excitation volts
					Calibration Constant	Units	
0	Accelerometer	PCB 333B52	34413	South	1.048	V/g	-
1	Accelerometer	PCB 333B52	34454	South	1.077	V/g	-
2	Accelerometer	PCB 333B52	34411	South	1.045	V/g	-
3	Accelerometer	PCB 333B52	34415	South	1.051	V/g	-
4	Accelerometer	PCB 333B52	34412	South	1.061	V/g	-
5	Accelerometer	PCB 333B52	34414	North	0.96	V/g	-
6	LVDT	Schaevitz DC-E250	13292	-	39.554	V/in	±15V
7	LVDT	Schaevitz DC-E250	13301	-	40.929	V/in	±15V
8	LVDT	Schaevitz DC-E250	13609	-	41.91	V/in	±15V
9	LVDT	Schaevitz DC-E250	12971	-	40.167	V/in	±15V
10	LVDT	Schaevitz DC-E2000	2479	-	5.02	V/in	±15V
11	LVDT	Schaevitz DC-E3000	1684	-	3.345	V/in	±15V
12	LVDT	Schaevitz DC-E5000	1275	-	1.908	V/in	±15V
13	Strain Gage	CEA-06-250UR-350	1	North 45° CW	1	in./in.	2.5V
14	Strain Gage	CEA-06-250UR-350	2	North	1	in./in.	2.5V
15	Strain Gage	CEA-06-250UR-350	3	North 45° CCW	1	in./in.	2.5V
16	Strain Gage	CEA-06-250UR-350	1	North 45° CW	1	in./in.	2.5V
17	Strain Gage	CEA-06-250UR-350	2	North	1	in./in.	2.5V
18	Strain Gage	CEA-06-250UR-350	3	North 45° CCW	1	in./in.	2.5V
19	LVDT	-	-	-	1.812	V/in	-
20	LVDT	-	-	-	1.81	V/in	-
21	Load Cell*	Lebow 3156 - 100K	2468	-	-0.00023941	V/kip	10V

Table B-4: Sensor Summary, Series F1-C-2PB and F1-C-1PB

Sensor Number	Sensor Type	Model	Serial Number	Direction	Sensitivity		Excitation volts
					Calibration Constant	Units	
22	Accelerometer	ADXL335	232	Up	0.3170	V/g	3.3V
23	Accelerometer	ADXL335	233	East	0.3290	V/g	3.3V
24	Accelerometer	ADXL335	234	South	0.3250	V/g	3.3V
25	Accelerometer	ADXL335	240	Up	0.3260	V/g	3.3V
26	Accelerometer	ADXL335	241	East	0.3250	V/g	3.3V
27	Accelerometer	ADXL335	242	South	0.3210	V/g	3.3V
28	Accelerometer	ADXL335	309	Up	0.3180	V/g	3.3V
29	Accelerometer	ADXL335	310	East	0.3260	V/g	3.3V
30	Accelerometer	ADXL335	311	South	0.3310	V/g	3.3V
31	Accelerometer	ADXL335	221	Up	0.3190	V/g	3.3V
32	Accelerometer	ADXL335	222	East	0.3270	V/g	3.3V
33	Accelerometer	ADXL335	223	South	0.3290	V/g	3.3V
34	Accelerometer	ADXL335	-	East	0.3300	V/g	3.3V

Table B-5: Sensor Summary, Series F2-R-C-4PB, F2-R-C-2PB, F2-R-C-1PB, and F2-R-C

Sensor Number	Sensor Type	Model	SN	Direction	Sensitivity		Excitation volts
					Calibration Constant	Units	
0	Accelerometer	PCB 333B52	34413	South	1.048	V/g	-
1	Accelerometer	PCB 333B52	34454	South	1.077	V/g	-
2	Accelerometer	PCB 333B52	34411	South	1.045	V/g	-
3	Accelerometer	PCB 333B52	34415	South	1.051	V/g	-
4	Accelerometer	PCB 333B52	34412	South	1.061	V/g	-
5	Accelerometer	PCB 333B52	34414	North	0.96	V/g	-
6	LVDT	Schaevitz DC-E250	13292	-	39.554	V/in	±15V
7	LVDT	Schaevitz DC-E250	13301	-	40.929	V/in	±15V
8	LVDT	Schaevitz DC-E250	13609	-	41.91	V/in	±15V
9	LVDT	Schaevitz DC-E250	12971	-	40.167	V/in	±15V
10	LVDT	Schaevitz DC-E2000	2479	-	5.02	V/in	±15V
11	LVDT	Schaevitz DC-E3000	1684	-	3.345	V/in	±15V
12	LVDT	Schaevitz DC-E5000	1275	-	1.908	V/in	±15V
13	Strain Gage	CEA-06-250UR-350	1	North 45° CW	1	in./in.	2.5V
14	Strain Gage	CEA-06-250UR-350	2	North	1	in./in.	2.5V
15	Strain Gage	CEA-06-250UR-350	3	North 45° CCW	1	in./in.	2.5V
16	Strain Gage	CEA-06-250UR-350	1	North 45° CW	1	in./in.	2.5V
17	Strain Gage	CEA-06-250UR-350	2	North	1	in./in.	2.5V
18	Strain Gage	CEA-06-250UR-350	3	North 45° CCW	1	in./in.	2.5V
19	LVDT	-	-	-	1.812	V/in	-
20	LVDT	-	-	-	1.81	V/in	-
21	Load Cell*	Lebow 3156 - 100K	2468	-	-0.00023941	V/kip	10V

Table B-5: Sensor Summary, Series F2-R-C-4PB, F2-R-C-2PB, F2-R-C-1PB, and F2-R-C (continued)

Sensor Number	Sensor Type	Model	SN	Direction	Sensitivity		Excitation volts
					Calibration Constant	Units	
22	Accelerometer	ADXL335	232	Up	0.3207	V/g	3.3V
23	Accelerometer	ADXL335	233	East	0.3256	V/g	3.3V
24	Accelerometer	ADXL335	234	South	0.3225	V/g	3.3V
25	Accelerometer	ADXL335	240	Up	0.3263	V/g	3.3V
26	Accelerometer	ADXL335	241	East	0.3208	V/g	3.3V
27	Accelerometer	ADXL335	242	South	0.3185	V/g	3.3V
28	Accelerometer	ADXL335	309	Up	0.3228	V/g	3.3V
29	Accelerometer	ADXL335	310	East	0.3313	V/g	3.3V
30	Accelerometer	ADXL335	311	South	0.3283	V/g	3.3V
31	Accelerometer	ADXL335	221	Up	0.3249	V/g	3.3V
32	Accelerometer	ADXL335	222	East	0.3254	V/g	3.3V
33	Accelerometer	ADXL335	223	South	0.3265	V/g	3.3V
34	Accelerometer	ADXL335	-	East	0.3300	V/g	3.3V

Table B-6: Data Acquisition System Summary, Series F2-C-4PB, F1-C-2PB, F1-C-2PB

Sensor Number	Sensor Type	Chassis		Module		Card	
		Type	Number	Type	Number	Type	Channel Number
0	Accelerometer	SCB68	-	-	-	-	0
1	Accelerometer	SCB68	-	-	-	-	1
2	Accelerometer	SCB68	-	-	-	-	2
3	Accelerometer	SCB68	-	-	-	-	3
4	Accelerometer	SCB68	-	-	-	-	4
5	Accelerometer	SCB68	-	-	-	-	7
6	LVDT	SCXI1000	1	SCXI-1520	1	SCXI 1314	0
7	LVDT	SCXI1000	1	SCXI-1520	1	SCXI 1314	1
8	LVDT	SCXI1000	1	SCXI-1520	1	SCXI 1314	2
9	LVDT	SCXI1000	1	SCXI-1520	1	SCXI 1314	3
10	LVDT	SCXI1000	1	SCXI-1520	1	SCXI 1314	4
11	LVDT	SCXI1000	1	SCXI-1520	1	SCXI 1314	5
12	LVDT	SCXI1000	1	SCXI-1520	1	SCXI 1314	6
13	Strain Gage	SCXI1000	1	SCXI-1521	2	SCXI 1317	0
14	Strain Gage	SCXI1000	1	SCXI-1521	2	SCXI 1317	1
15	Strain Gage	SCXI1000	1	SCXI-1521	2	SCXI 1317	2
16	Strain Gage	SCXI1000	1	SCXI-1521	2	SCXI 1317	3
17	Strain Gage	SCXI1000	1	SCXI-1521	2	SCXI 1317	4
18	Strain Gage	SCXI1000	1	SCXI-1521	2	SCXI 1317	5
19	LVDT	SCXI1000	1	SCXI-1121	4	SCXI-1321	0
20	LVDT	SCXI1000	1	SCXI-1121	4	SCXI-1321	1
21	Load Cell	SCXI1000	1	SCXI-1121	4	SCXI-1321	3

Table B-6: Data Acquisition System Summary, Series F2-C-4PB, F1-C-2PB, F1-C-2PB (continued)

Sensor Number	Sensor Type	Chassis		Module		Card	
		Type	Number	Type	Number	Type	Channel Number
22	Accelerometer	SCXI1000	2	SCXI-1121	1	SCXI-1321	0
23	Accelerometer	SCXI1000	2	SCXI-1121	1	SCXI-1321	1
24	Accelerometer	SCXI1000	2	SCXI-1121	1	SCXI-1321	2
25	Accelerometer	SCXI1000	2	SCXI-1121	2	SCXI-1321	0
26	Accelerometer	SCXI1000	2	SCXI-1121	2	SCXI-1321	1
27	Accelerometer	SCXI1000	2	SCXI-1121	2	SCXI-1321	2
28	Accelerometer	SCXI1000	2	SCXI-1121	4	SCXI-1321	1
29	Accelerometer	SCXI1000	2	SCXI-1121	4	SCXI-1321	2
30	Accelerometer	SCXI1000	2	SCXI-1121	4	SCXI-1321	3
31	Accelerometer	SCXI1000	3	SCXI-1121	1	SCXI-1321	0
32	Accelerometer	SCXI1000	3	SCXI-1121	1	SCXI-1321	1
33	Accelerometer	SCXI1000	3	SCXI-1121	1	SCXI-1321	2
34	Accelerometer	SCXI1000	3	SCXI-1121	1	SCXI-1321	3

Table B-7: Data Acquisition System Summary, Series F2-R-C-4PB, F2-R-C-2PB, F2-R-C-1PB, and F2-R-C

Sensor Number	Sensor Type	Chassis		Module		Card	
		Type	Number	Type	Number	Type	Channel Number
0	Accelerometer	SCB68	-	-	-	-	0
1	Accelerometer	SCB68	-	-	-	-	1
2	Accelerometer	SCB68	-	-	-	-	2
3	Accelerometer	SCB68	-	-	-	-	3
4	Accelerometer	SCB68	-	-	-	-	4
5	Accelerometer	SCB68	-	-	-	-	7
6	LVDT	SCXI1000	1	SCXI-1520	1	SCXI 1314	0
7	LVDT	SCXI1000	1	SCXI-1520	1	SCXI 1314	1
8	LVDT	SCXI1000	1	SCXI-1520	1	SCXI 1314	2
9	LVDT	SCXI1000	1	SCXI-1520	1	SCXI 1314	3
10	LVDT	SCXI1000	1	SCXI-1520	1	SCXI 1314	4
11	LVDT	SCXI1000	1	SCXI-1520	1	SCXI 1314	5
12	LVDT	SCXI1000	1	SCXI-1520	1	SCXI 1314	6
13	Strain Gage	SCXI1000	1	SCXI-1521	2	SCXI 1317	0
14	Strain Gage	SCXI1000	1	SCXI-1521	2	SCXI 1317	1
15	Strain Gage	SCXI1000	1	SCXI-1521	2	SCXI 1317	2
16	Strain Gage	SCXI1000	1	SCXI-1521	2	SCXI 1317	3
17	Strain Gage	SCXI1000	1	SCXI-1521	2	SCXI 1317	4
18	Strain Gage	SCXI1000	1	SCXI-1521	2	SCXI 1317	5
19	LVDT	SCXI1000	1	SCXI-1121	4	SCXI-1321	0
20	LVDT	SCXI1000	1	SCXI-1121	4	SCXI-1321	1
21	Load Cell	SCXI1000	1	SCXI-1121	4	SCXI-1321	3

Table B-7: Data Acquisition System Summary, Series F2-R-C-4PB, F2-R-C-2PB, F2-R-C-1PB, and F2-R-C (continued)

Sensor Number	Sensor Type	Chassis		Module		Card	
		Type	Number	Type	Number	Type	Channel Number
22	Accelerometer	SCXI1000	2	SCXI-1121	1	SCXI-1321	0
23	Accelerometer	SCXI1000	2	SCXI-1121	1	SCXI-1321	1
24	Accelerometer	SCXI1000	2	SCXI-1121	1	SCXI-1321	2
25	Accelerometer	SCXI1000	2	SCXI-1121	2	SCXI-1321	0
26	Accelerometer	SCXI1000	2	SCXI-1121	2	SCXI-1321	1
27	Accelerometer	SCXI1000	2	SCXI-1121	2	SCXI-1321	2
28	Accelerometer	SCXI1000	2	SCXI-1121	4	SCXI-1321	1
29	Accelerometer	SCXI1000	2	SCXI-1121	4	SCXI-1321	2
30	Accelerometer	SCXI1000	2	SCXI-1121	4	SCXI-1321	3
31	Accelerometer	SCXI1000	3	SCXI-1121	1	SCXI-1321	0
32	Accelerometer	SCXI1000	3	SCXI-1121	1	SCXI-1321	2*
33	Accelerometer	SCXI1000	3	SCXI-1121	1	SCXI-1321	1*
34	Accelerometer	SCXI1000	3	SCXI-1121	1	SCXI-1321	3

*The channels for Sensors 32 and 33 were flipped during Frame 2 Runs 118, 119, and 120

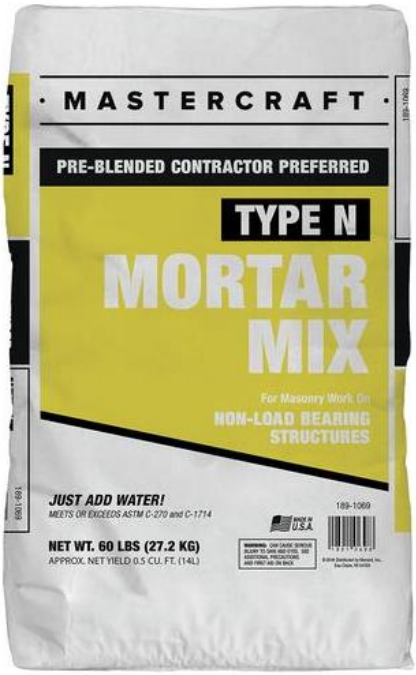

Figure B-1: Type-N Mortar Mix, 60-lb Bag

(a) Centerlines On Interior Column Face

(b) Nuts used to adjust local infill position

Figure B-2: Centering Infills within the Frame

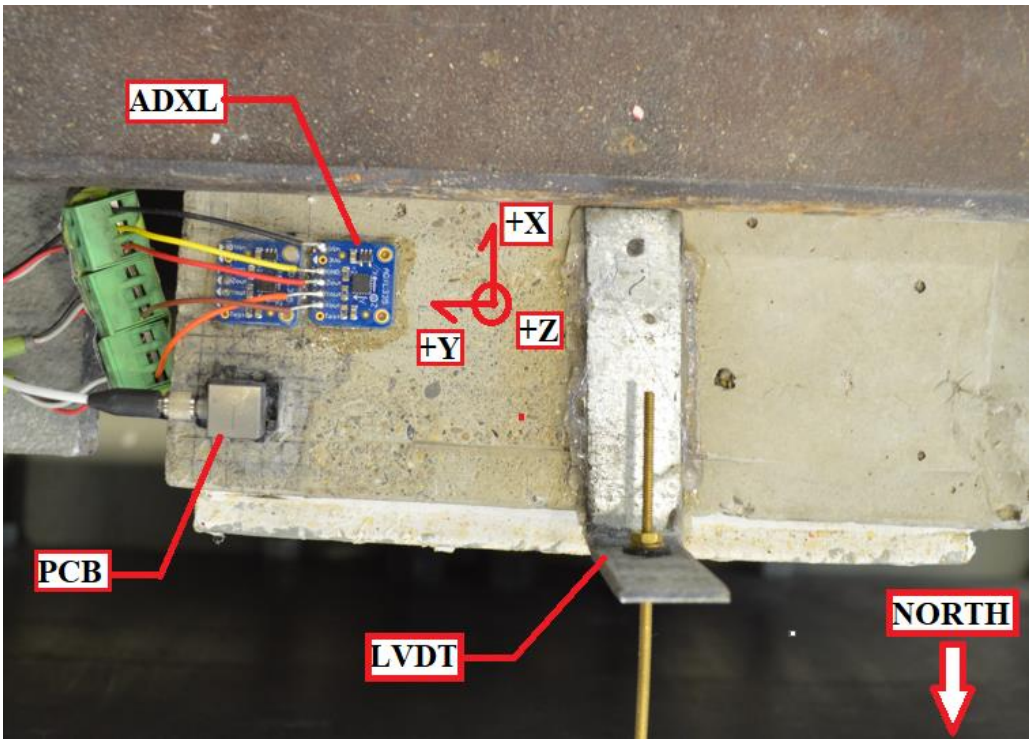

Figure B-3: Accelerometer Orientation (Foundation Beam Top)

Figure B-4: Lebow 3156-100K Load Cell

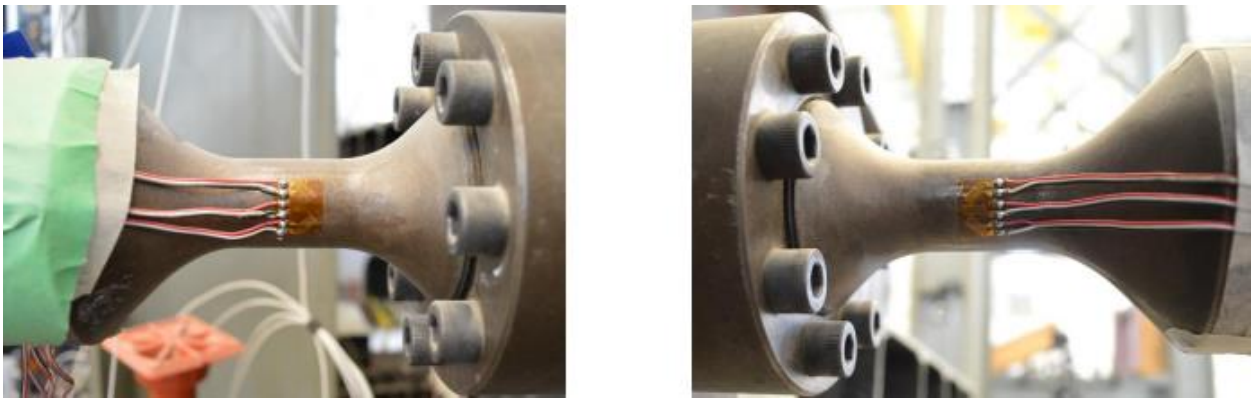

(a) West Face (b) East Face

Figure B-5: Strain Gages on Servoram Flexural Link

APPENDIX C: FRAME 2 RECAST DETAIL

After termination of Series F1-C-1PB the original column concrete near each of the four beam-column joints of Frame 2 was removed. Using a jackhammer, concrete was removed a minimum of 2" beyond the farthest inclined crack from each beam-column joint. This distance was chosen to ensure that undetected microcracking in the concrete was also removed. Each column was 40 inches in clear height, and the amount of concrete removed near each beam-column joint is shown in Figure 2-14. The faces on which cold joints would develop were made to be horizontal across the column section and were cleaned with water and compressed air.

Concrete was first removed from the west-facing side of the frame standing vertically (Figure C-1); the west side being the smoothest face that contacted the formwork when the frames were originally cast. The frame was next lifted using the inserts cast into the top beam and laid flat on formwork on the west face (Figure C-2). The 4PB infill used in Series F2-C-4PB remained in place during frame transportation and tipping. The remaining column concrete at near each joint was removed via jackhammer once the frame had been laid flat and the 4PB infill was extracted.

Exposed rebar ties were realigned to match as-built dimensions from the original cast ($s = 6"$). Exposed rebar was scrubbed with a rough-bristled brush and washed with water to remove concrete dust. Formwork was constructed around exposed rebar from 0.75" HDO Xact2Form plywood panels and 2" x 4" S-P-F studs (Figure C-3). All formwork edges exposed to new concrete were caulked and formwork faces were oiled prior to casting. Exposed faces of original cast concrete were watered prior to casting. Concrete was hand-mixed to cast the repairs. Pours were vibrated with an electrical vibrator to remove air and ensure clean contact at the cold joints; pours are visible in-situ in Figure C-4. The mixer was scraped of residual concrete prior to each lift, but excess moisture was not removed. Table C-1 provides the weight of water added to each mix once the desired workability was achieved, and the number of 4"x8" cylinders produced from each mix. Cylinders from each mix achieved $f_c' \geq 5000\ psi$ in compression tests prior to the first run of Series F2-R-C-4PB.

The new concrete cured under burlap that was wetted daily. Formwork was stripped after 7 days, and the frame tilted up via overhead crane connected to lifting inserts in the top beam. No shrinkage cracks or honeycombing of recast concrete was visible. At the column bases, new

concrete had crept partially beneath the bottom beam, adding a 1/16” lip over the cold joint (Figure C-5). The lip was not removed prior to testing to avoid unnecessary damage to the cold joint.

Table C-1: Recast Concrete Mix Proportions

Column Location	Akona Additive, lbf	Water, lbf	Cylinders Cast	Notes:
North Top	4.2	3.5	1	Dry mixer used
North Bottom	4.2	2.4	3	
South Top	4.2	1.9	5	
South Bottom	4.2	2.6	5	Mixer cleaned prior to use

(a) North Column Top

(c) South Column Top

(b) North Column Base

(d) South Column Base

Figure C-1: West Face after Vertical Concrete Removal

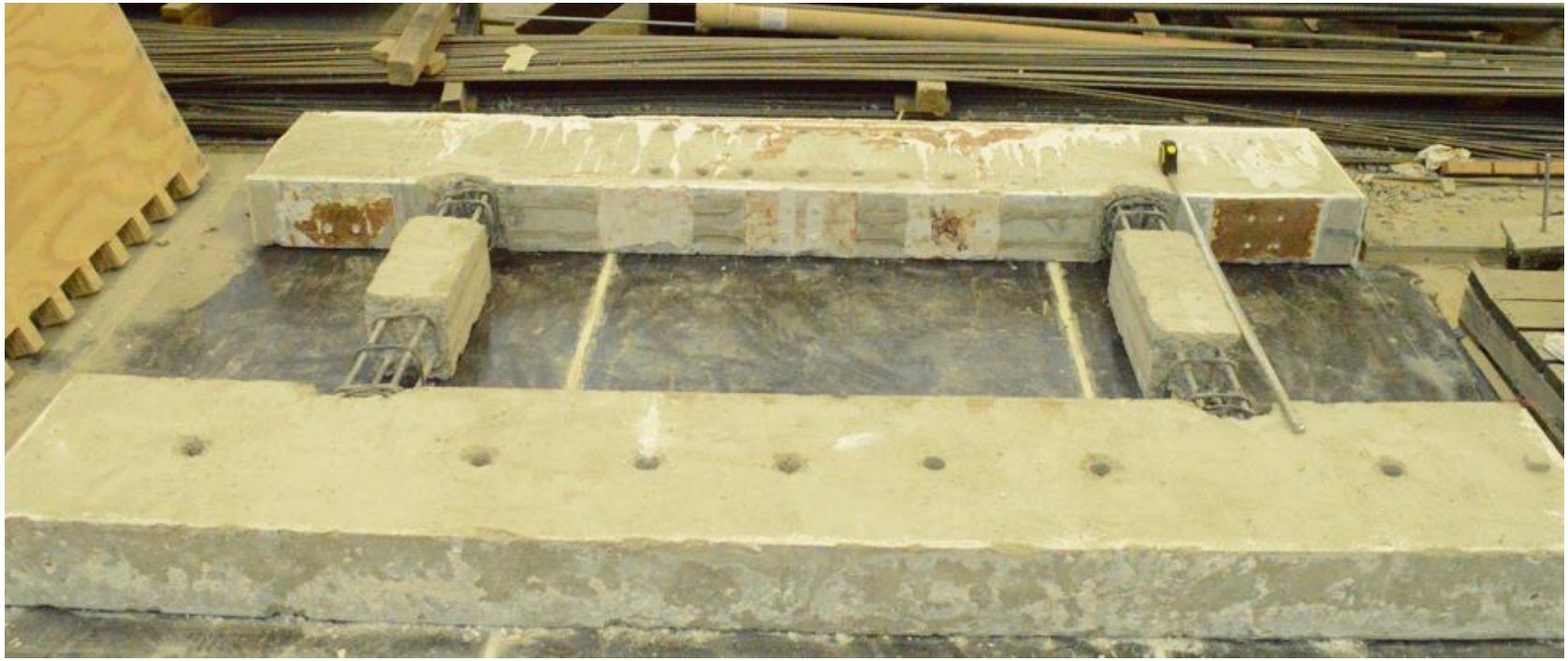

Figure C-2: Recast Frame 2 on Formwork with Column Concrete Removed

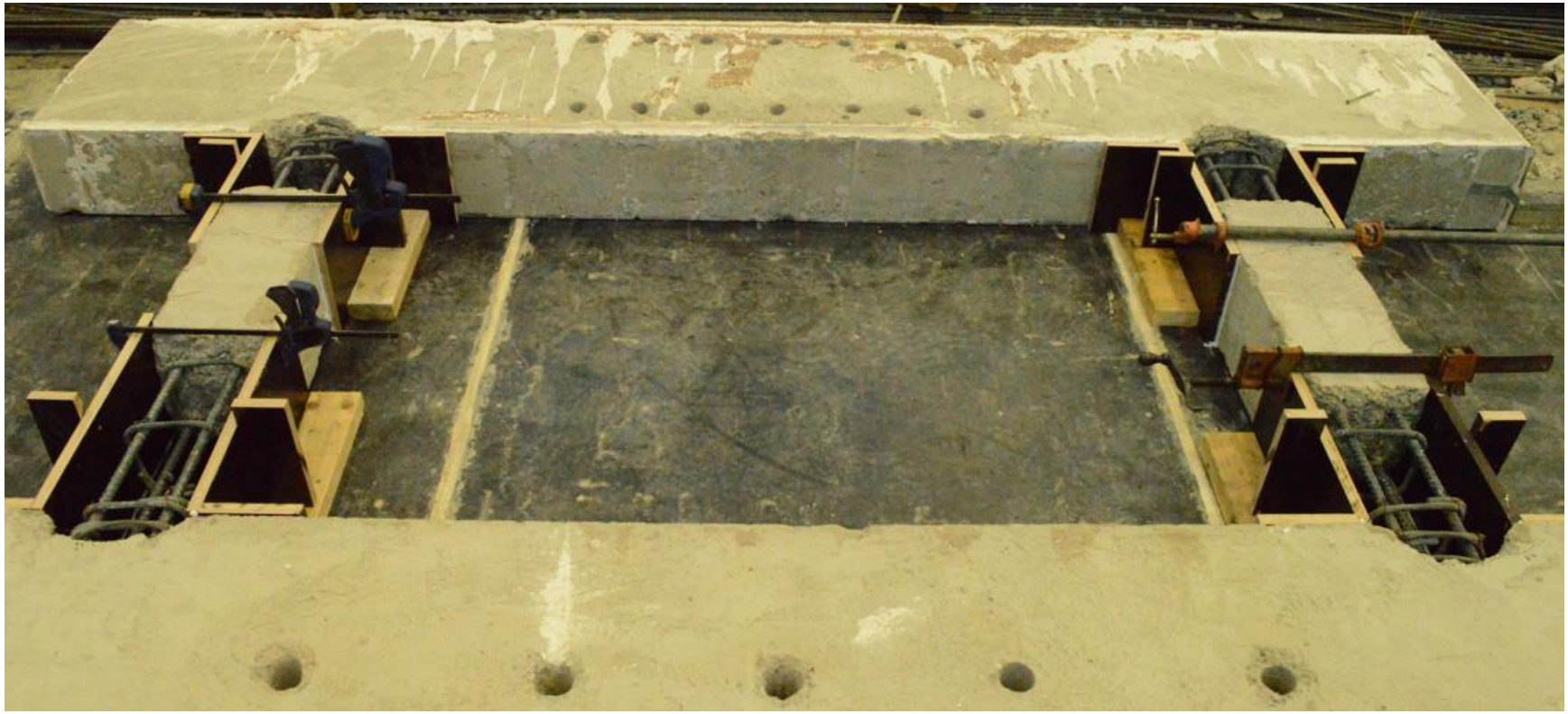

Figure C-3: Formwork for Frame 2 Repairs

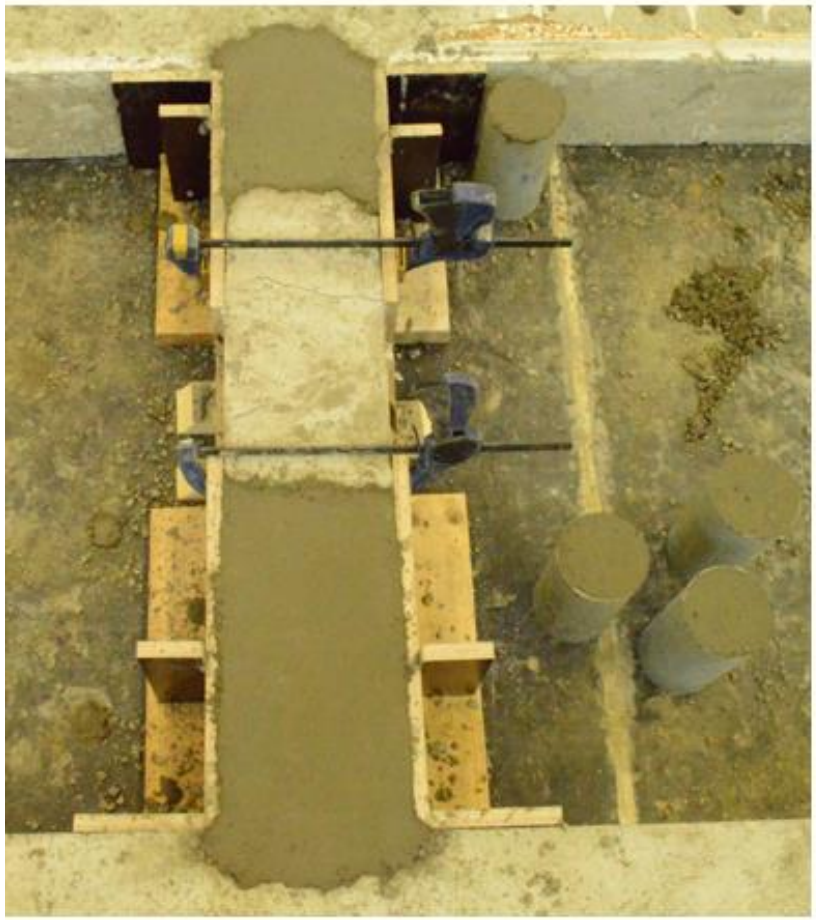

(a) North Column and Cylinders

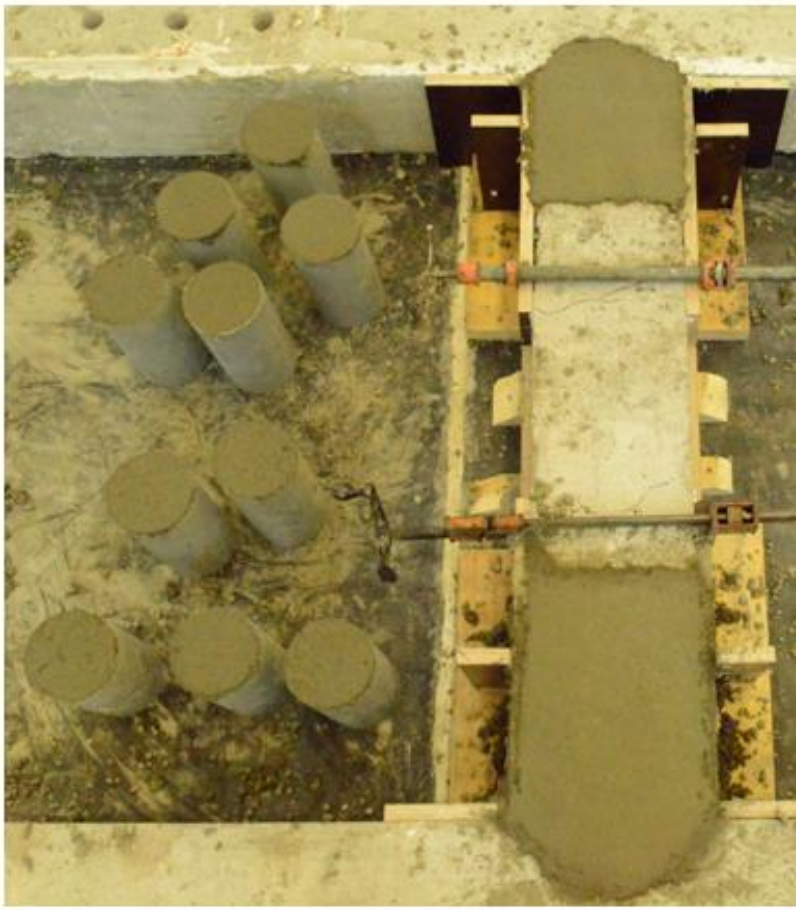

(b) South Column and Cylinders

Figure C-4: Recast Columns on Casting Day

(a) North Column Top

(b) North Column Bottom

Figure C-5: Recast Column West Face Close-ups

(c) South Column Top

(b) South Column Bottom

Figure C-5: Recast Column West Face Close-ups (continued)

APPENDIX D: COMPLETE STRUCTURAL RESPONSE HISTORY

The structural response for each ground motion is first presented. Each figure represents one ground motion from a given test series displaying five subplots plotted against time. First, the base acceleration (g) is plotted based on readings from the northeast foundation beam ADXL accelerometer. Second, base velocity (in / sec) from the trimmed and corrected integration of the northeast foundation beam ADXL acceleration history. Third, the base displacement (in) history from the foundation beam LVDT displacement. Fourth, story drift (in) is plotted, derived as the average specimen top beam LVDT displacement minus the foundation beam LVDT displacement. Finally, lateral load (kip) as read from the load cell. Plots were produced using the MATLAB function *subtightplot* (Nievinski, 2022).

The second set of figures plots lateral load (kip) versus story drift (in), using the aforementioned definitions. Both sets of figures are presented in time sequential order from the first to last ground motion performed, according to Table 3-9 through Table 3-15.

.

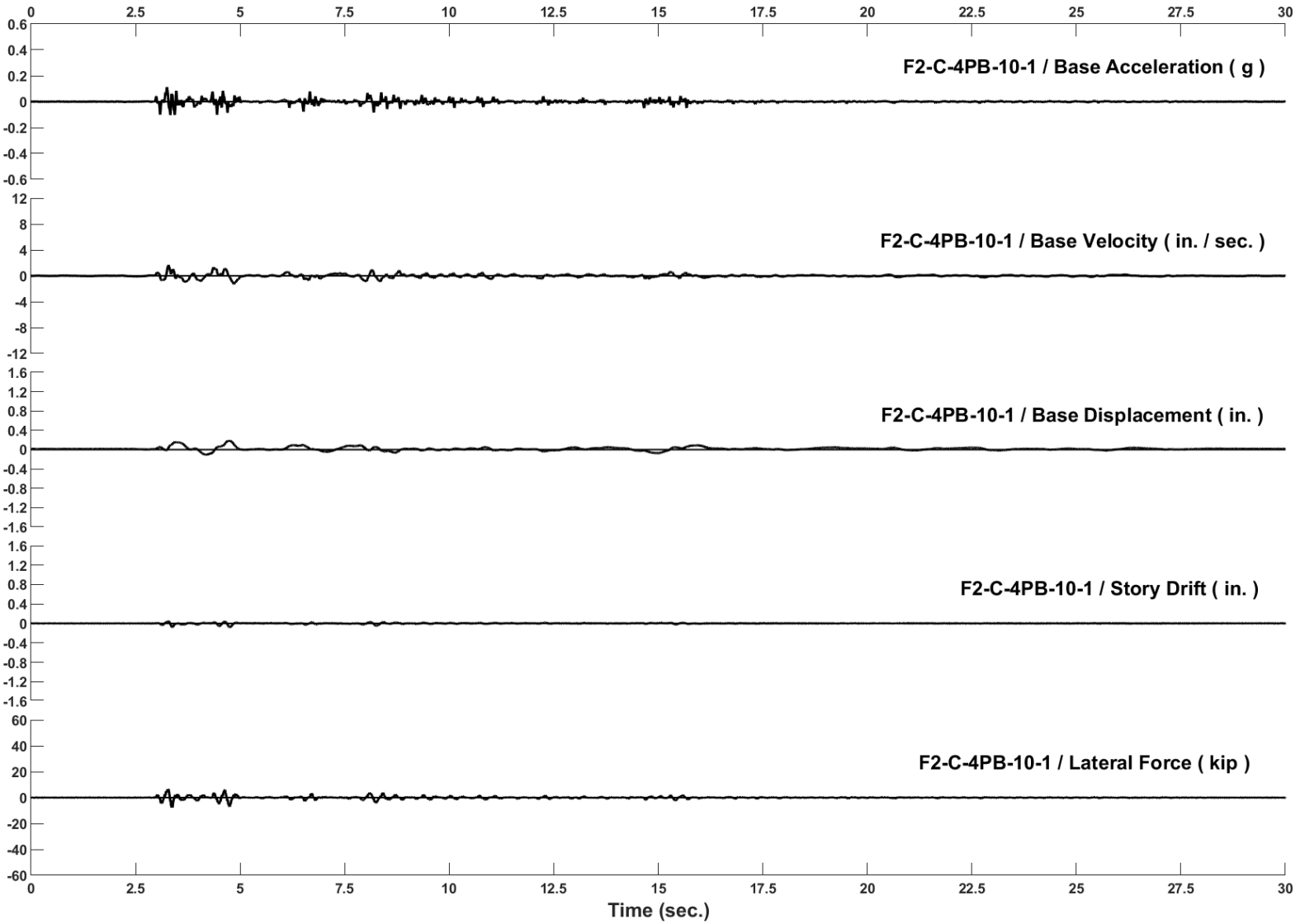

Figure D-1: Run 98, Frame 2, Structural Response and Base Motion History

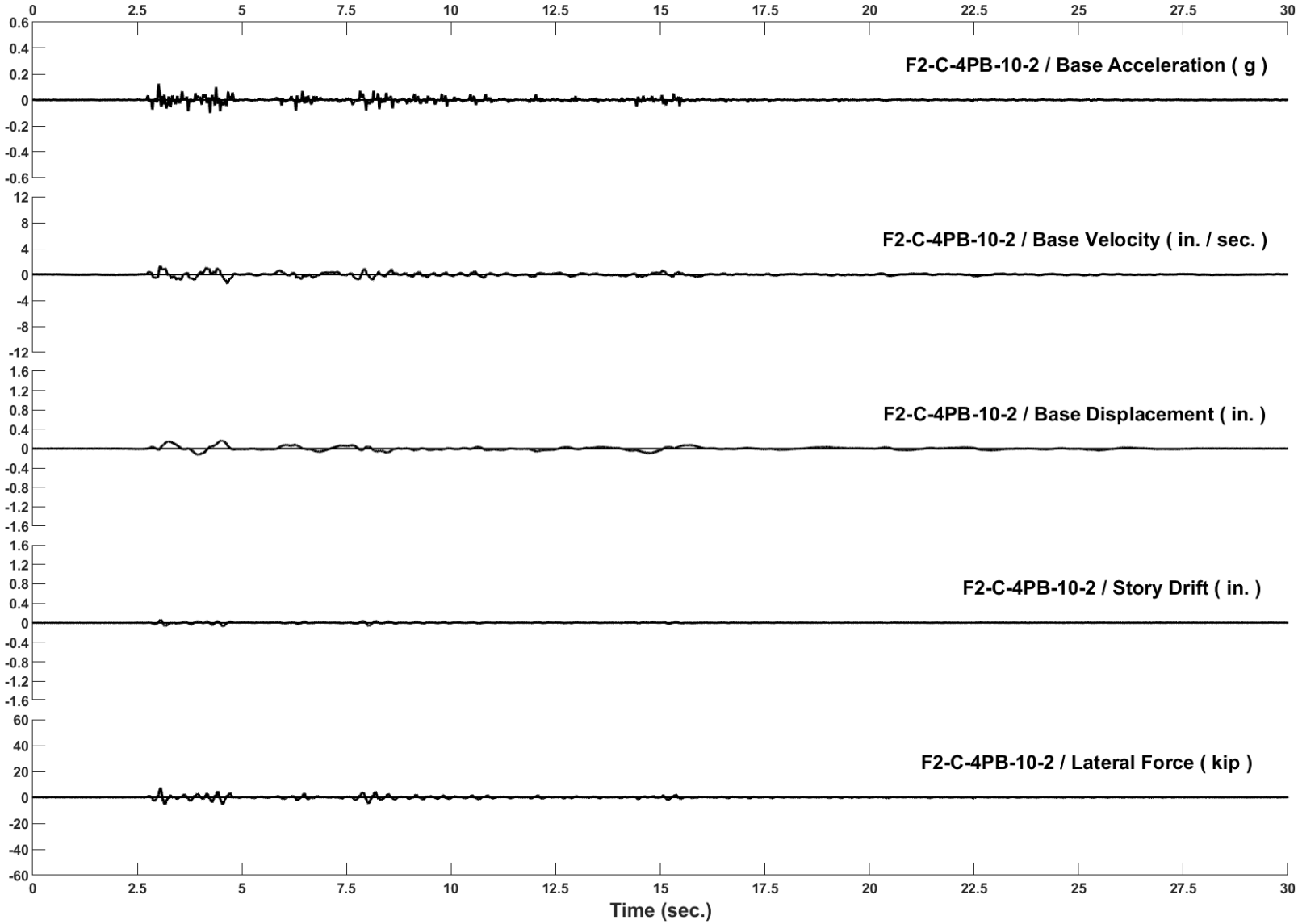

Figure D-2: Run 99, Frame 2, Structural Response and Base Motion History

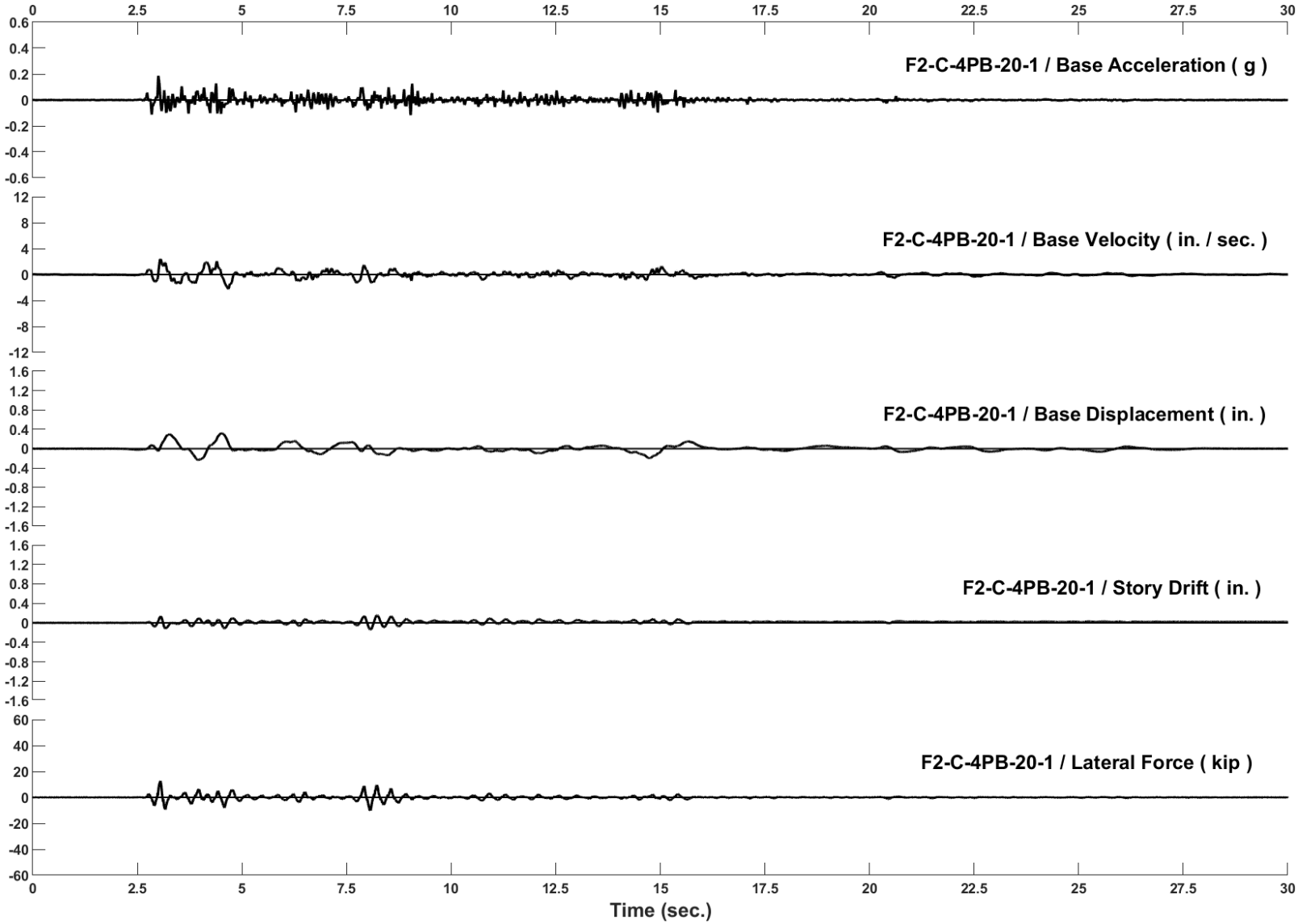

Figure D-3: Run 100, Frame 2, Structural Response and Base Motion History

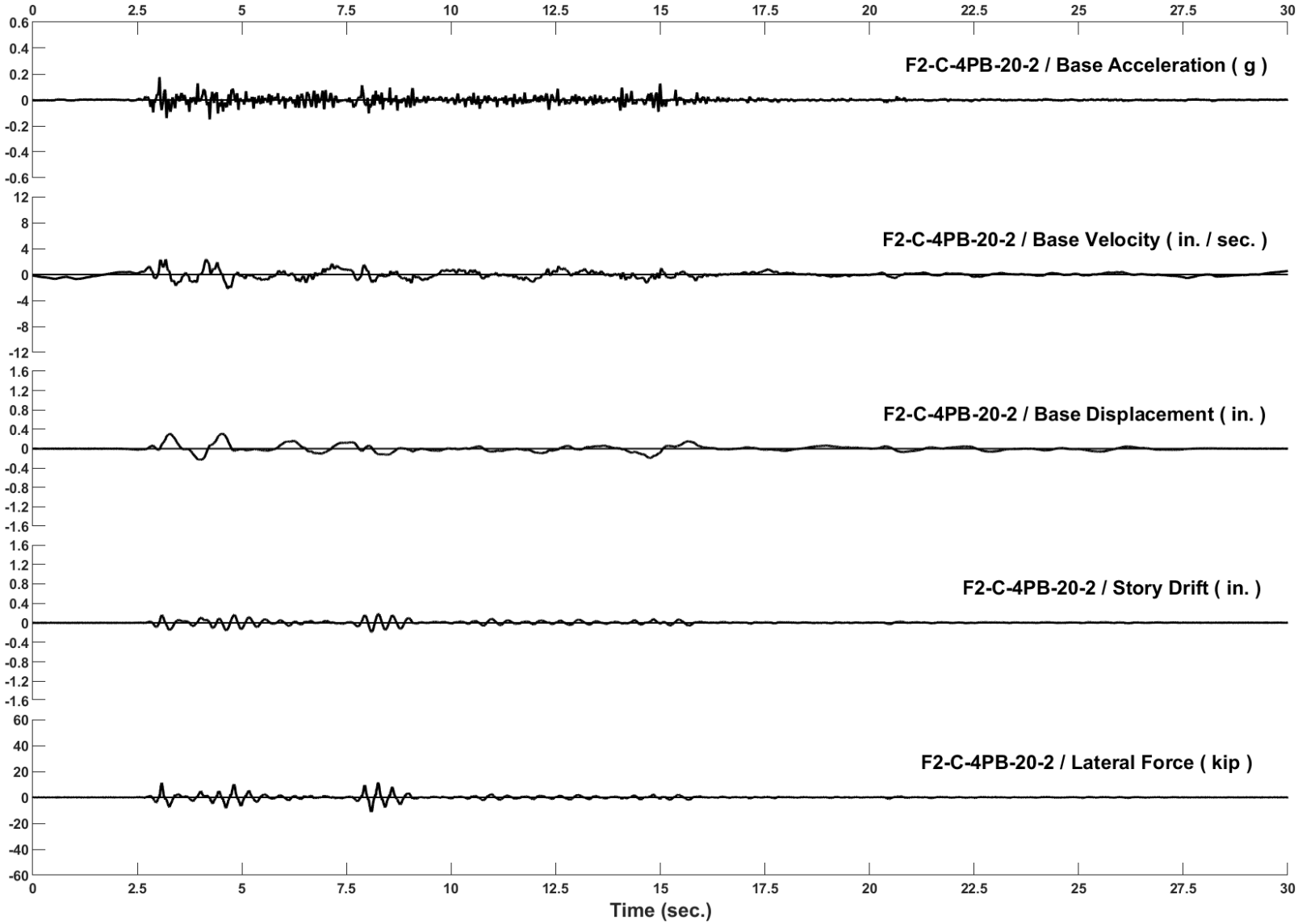

Figure D-4: Run 101, Frame 2, Structural Response and Base Motion History

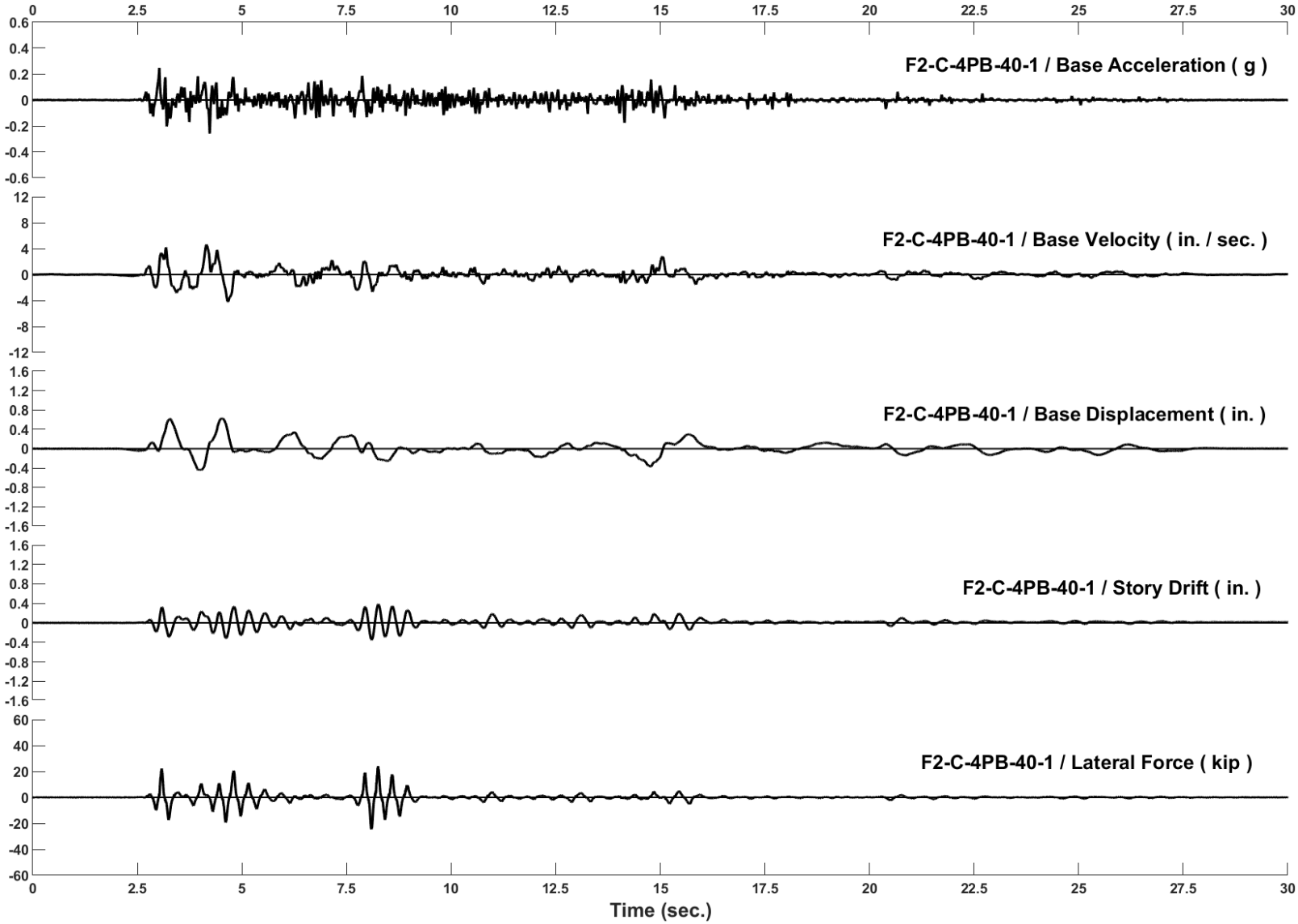

Figure D-5: Run 102, Frame 2, Structural Response and Base Motion History

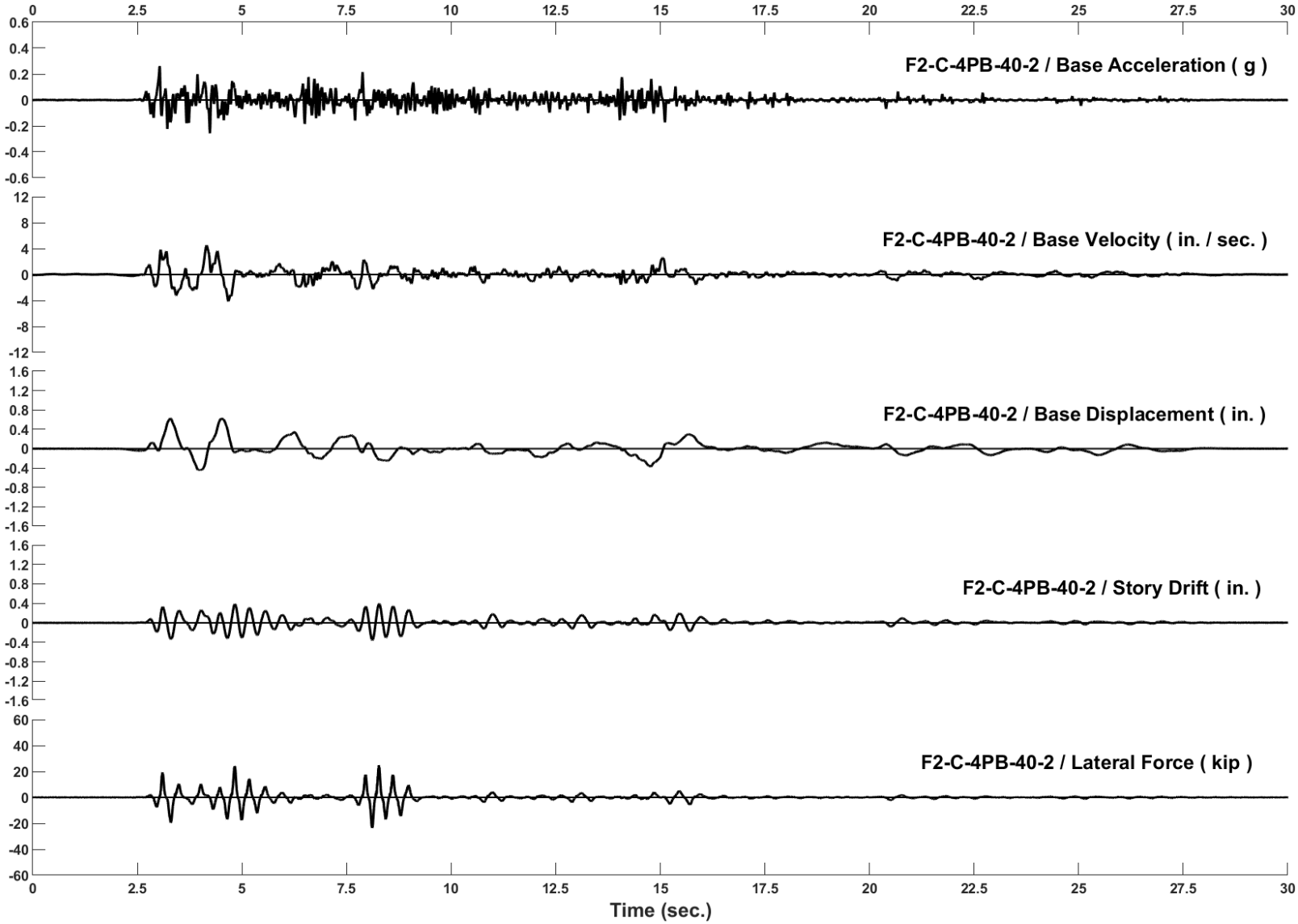

Figure D-6: Run 103, Frame 2, Structural Response and Base Motion History

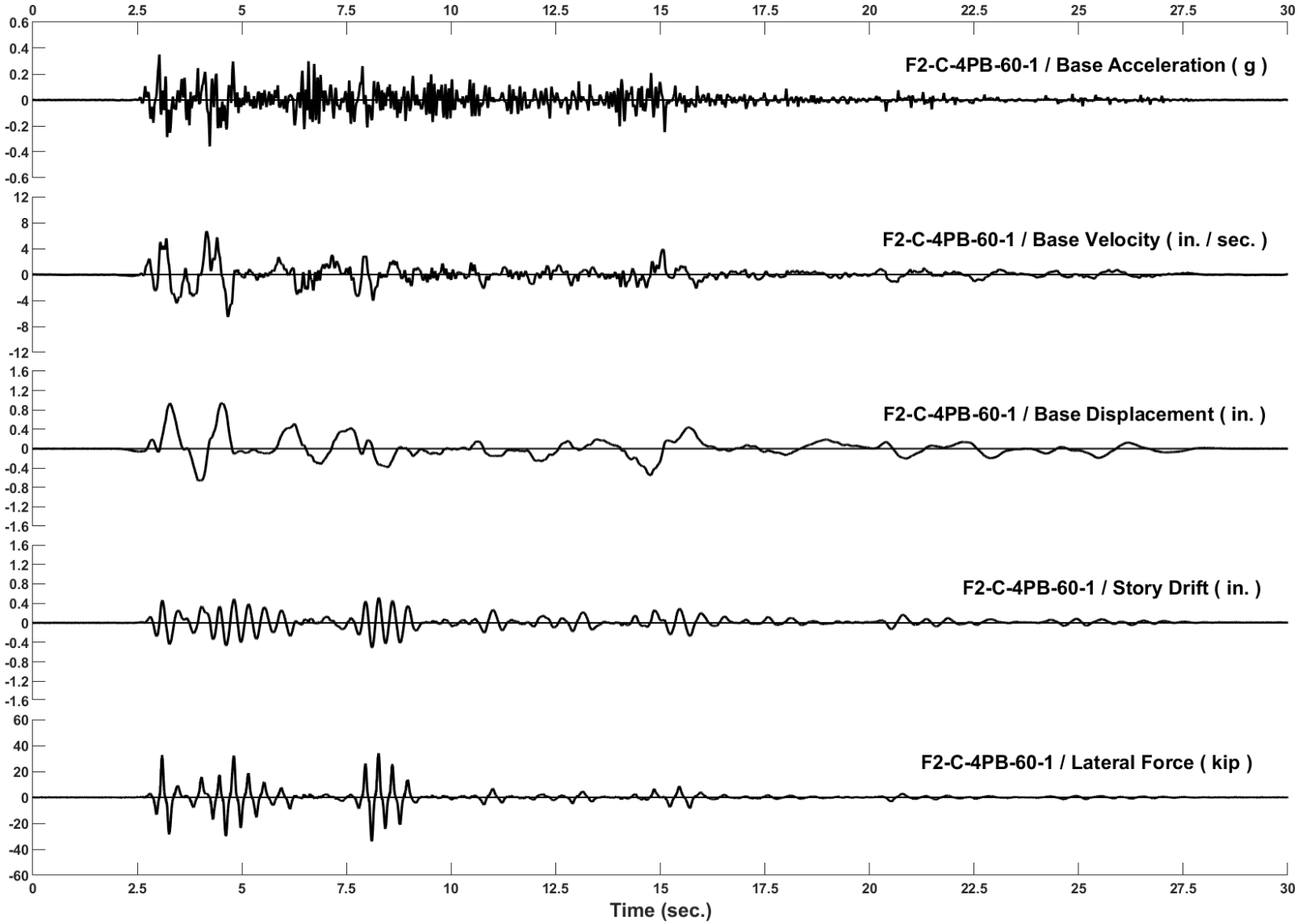

Figure D-7: Run 104, Frame 2, Structural Response and Base Motion History

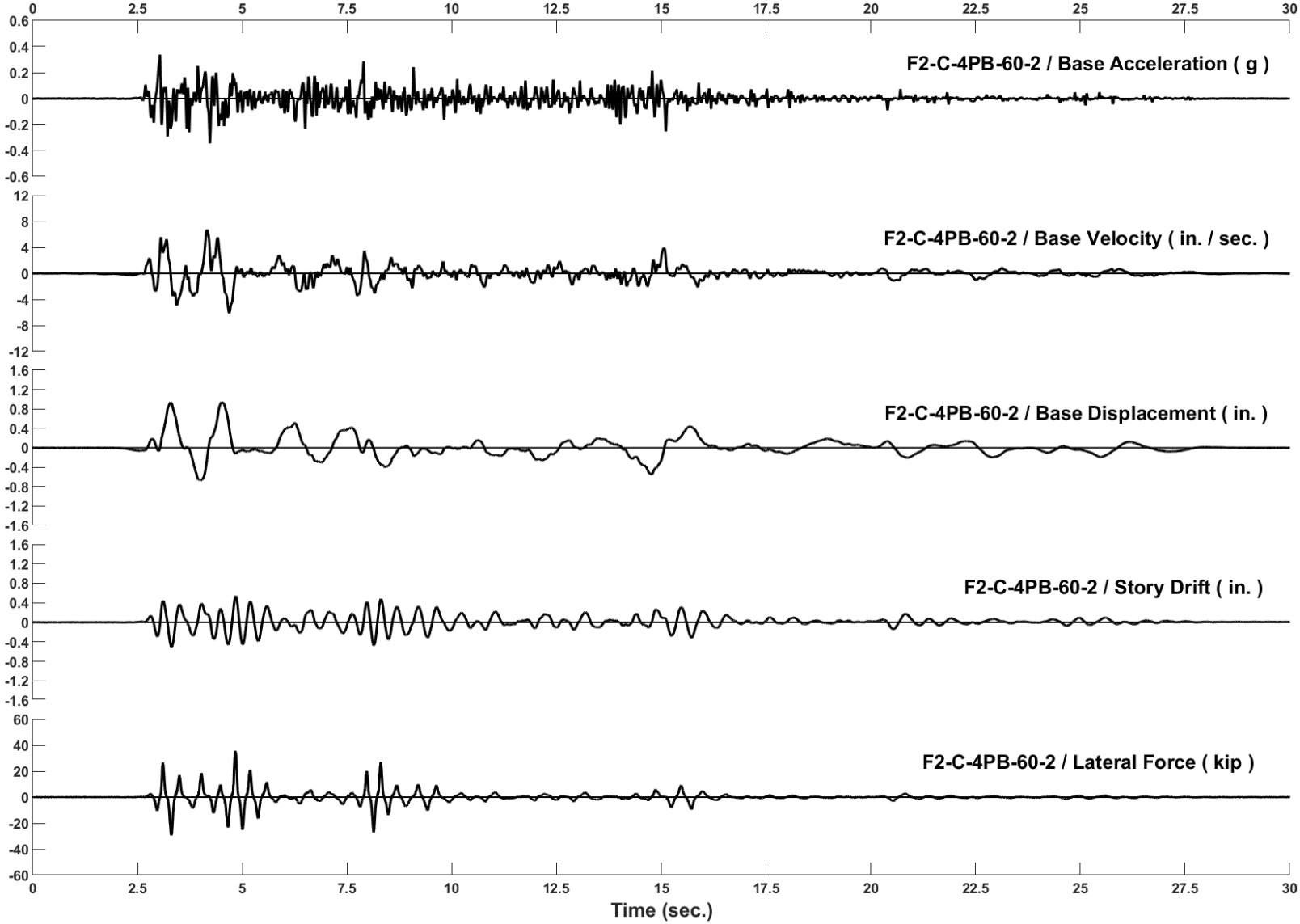

Figure D-8: Run 105, Frame 2, Structural Response and Base Motion History

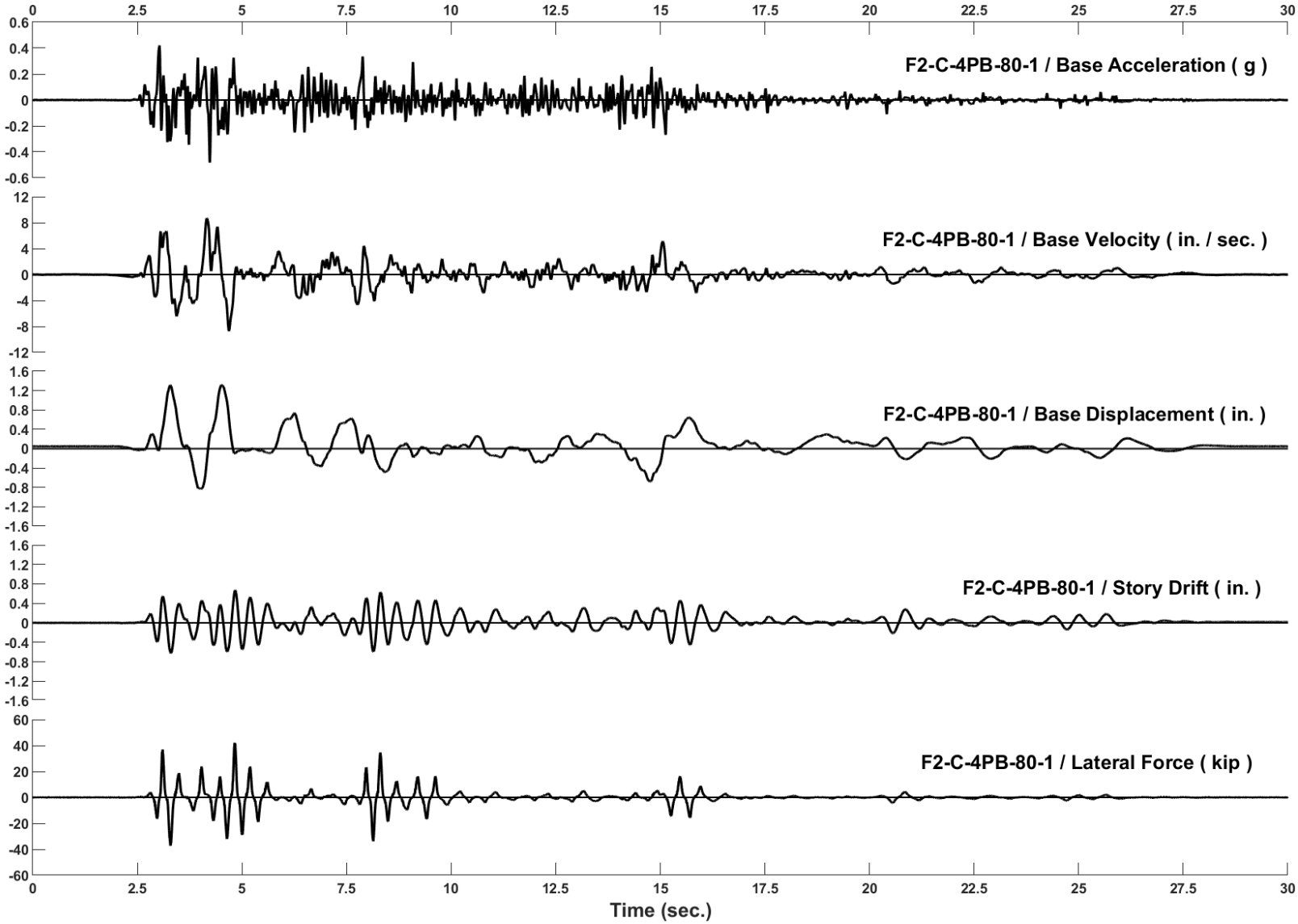

Figure D-9: Run 106, Frame 2, Structural Response and Base Motion History

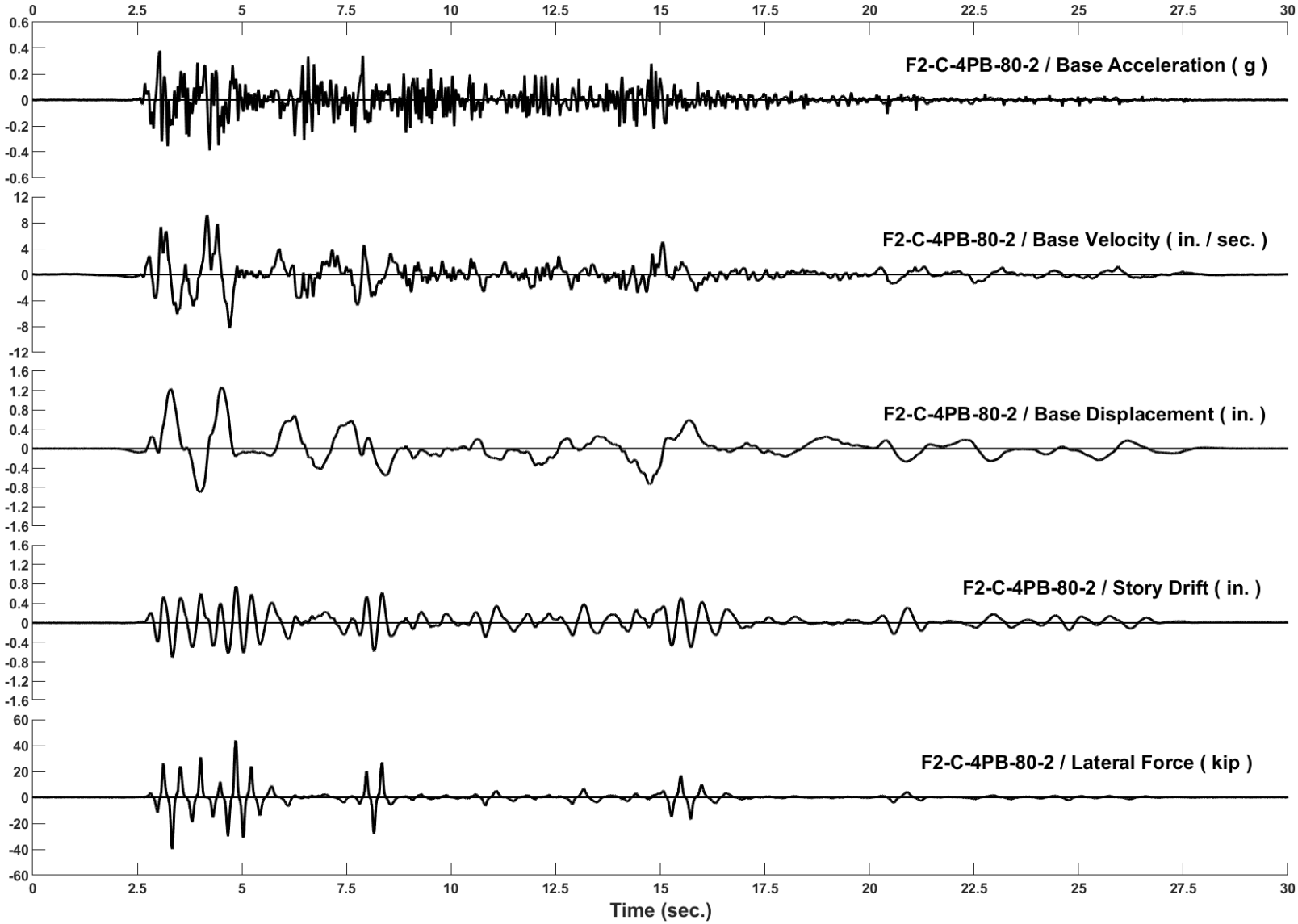

Figure D-10: Run 107, Frame 2, Structural Response and Base Motion History

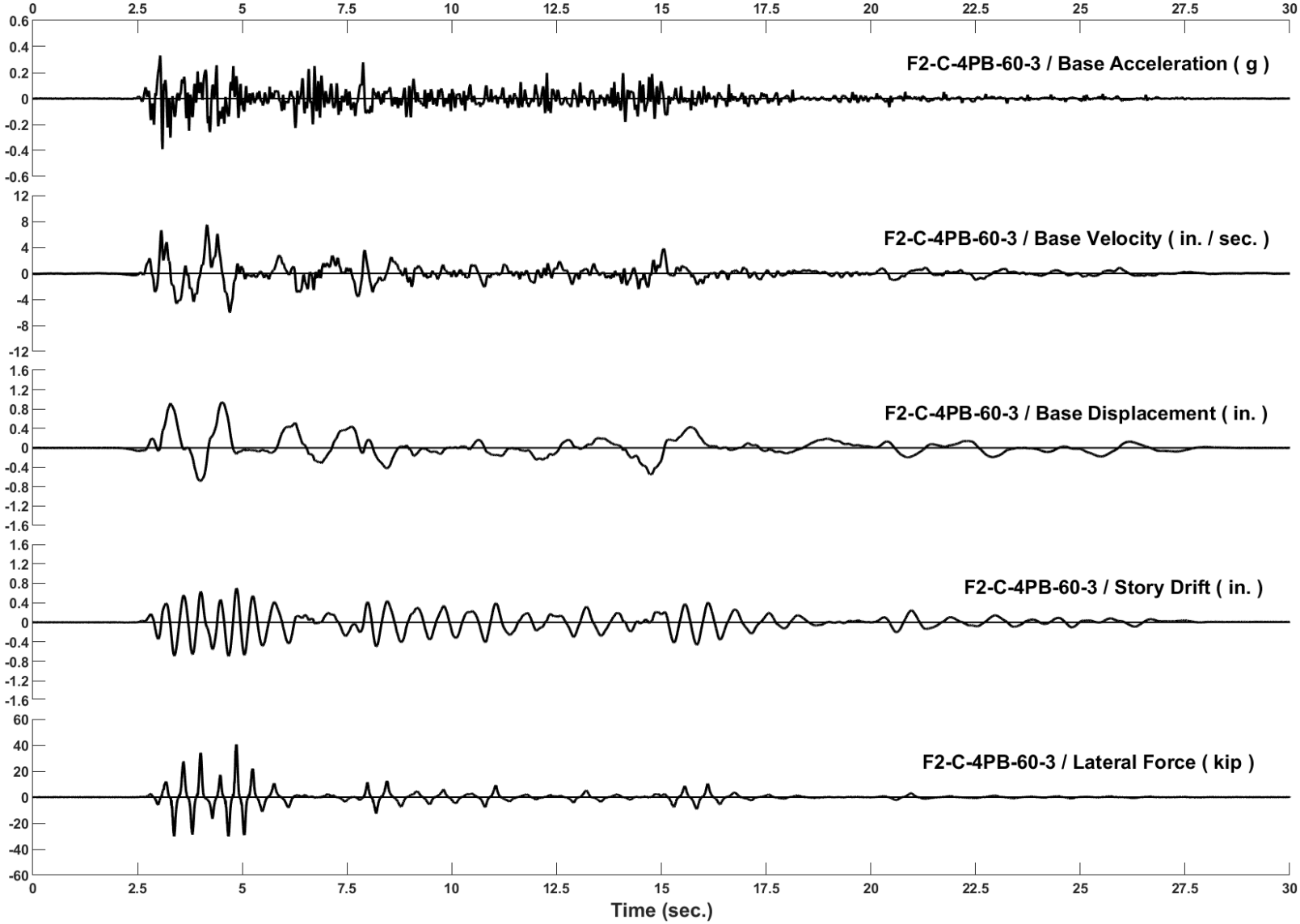

Figure D-11: Run 108, Frame 2, Structural Response and Base Motion History

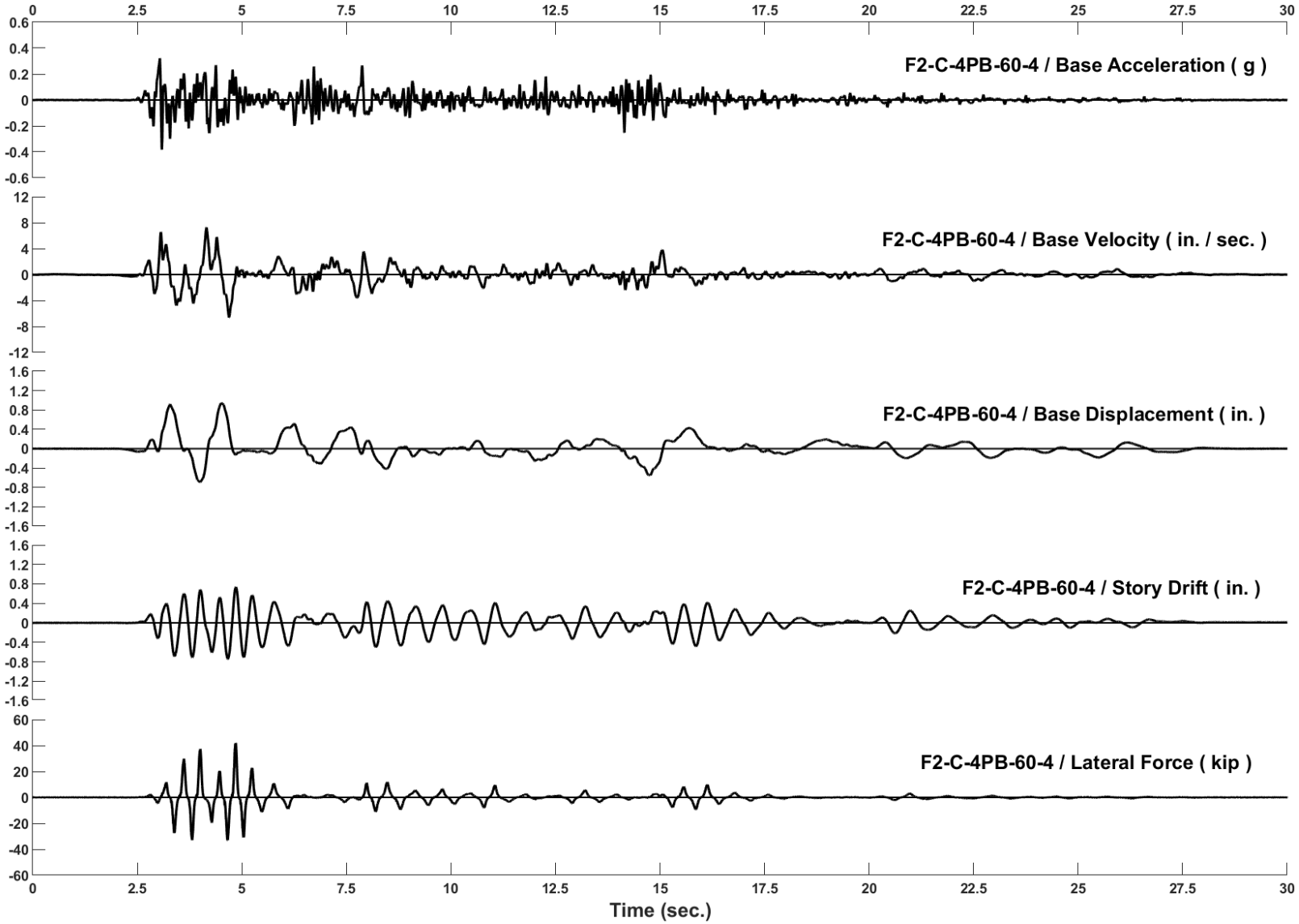

Figure D-12: Run 109, Frame 2, Structural Response and Base Motion History

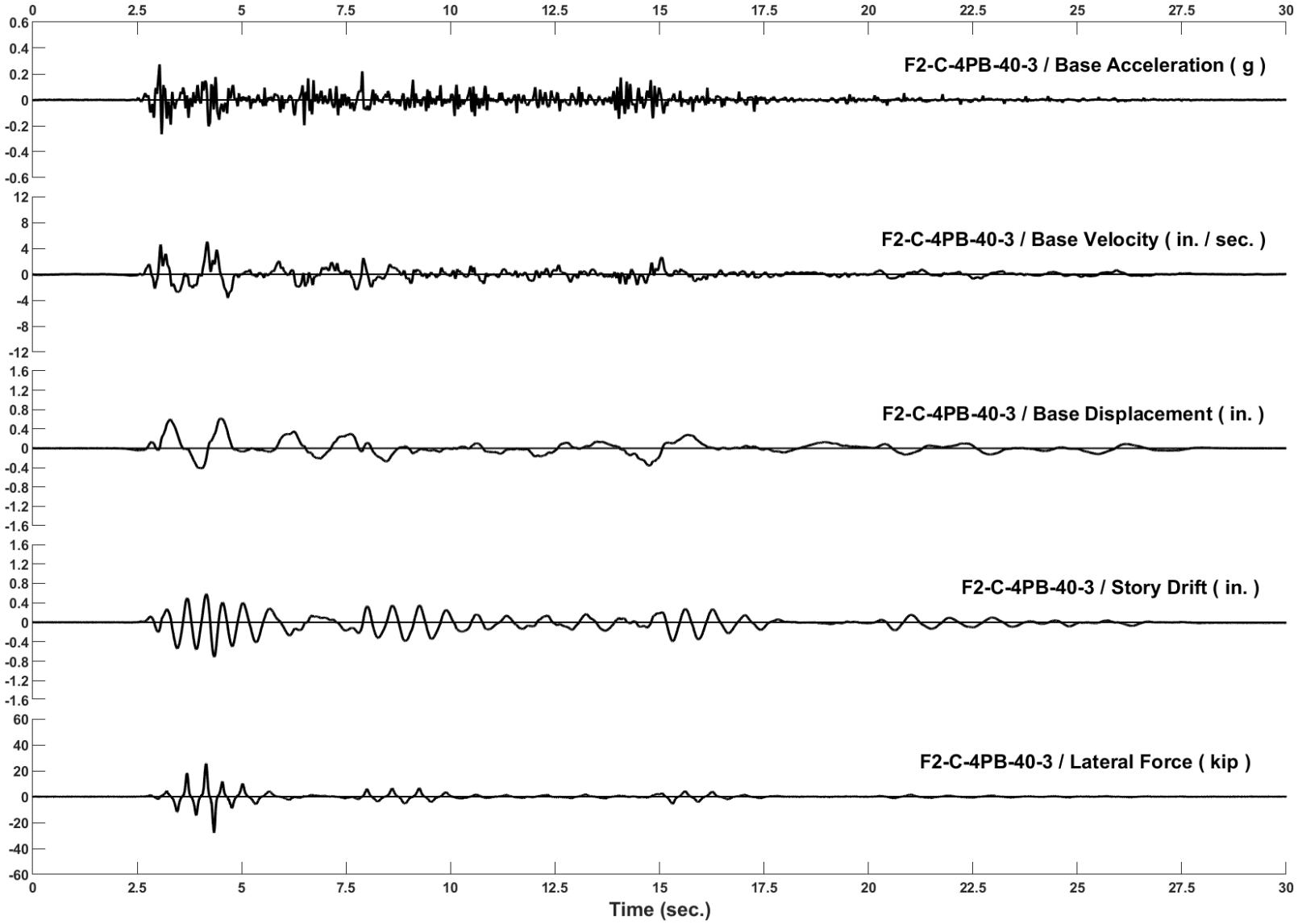

Figure D-13: Run 110, Frame 2, Structural Response and Base Motion History

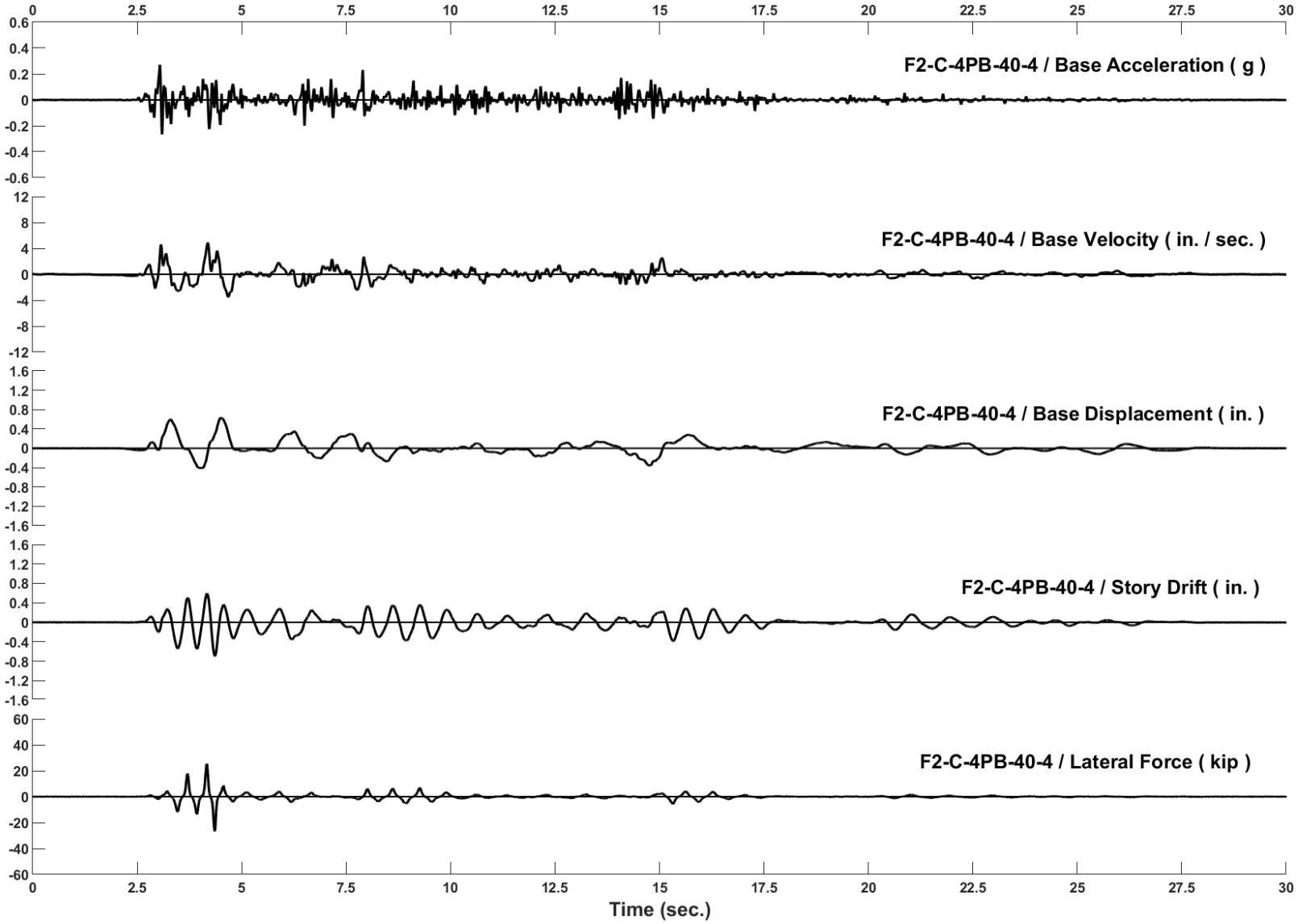

Figure D-14: Run 111, Frame 2, Structural Response and Base Motion History

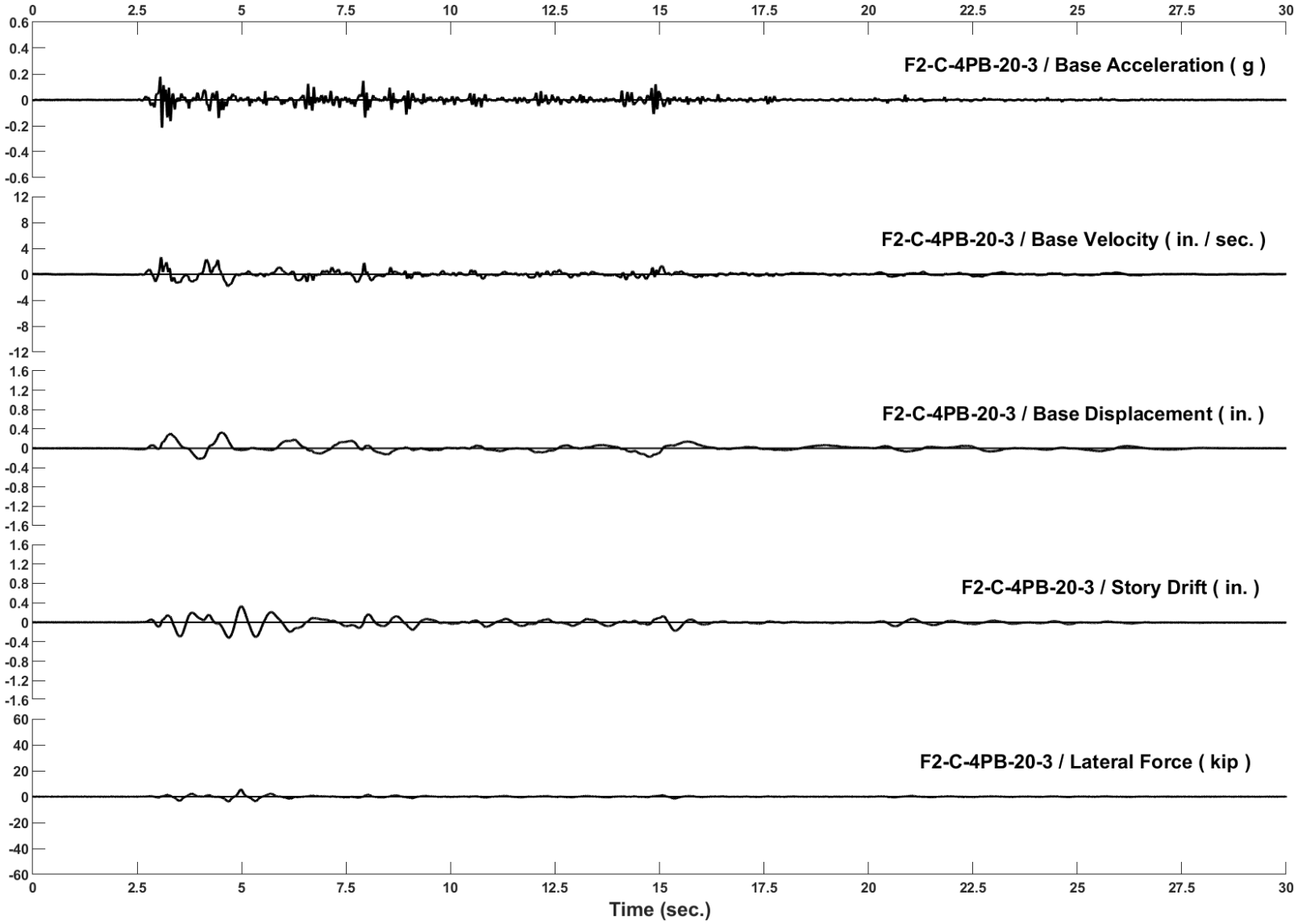

Figure D-15: Run 112, Frame 2, Structural Response and Base Motion History

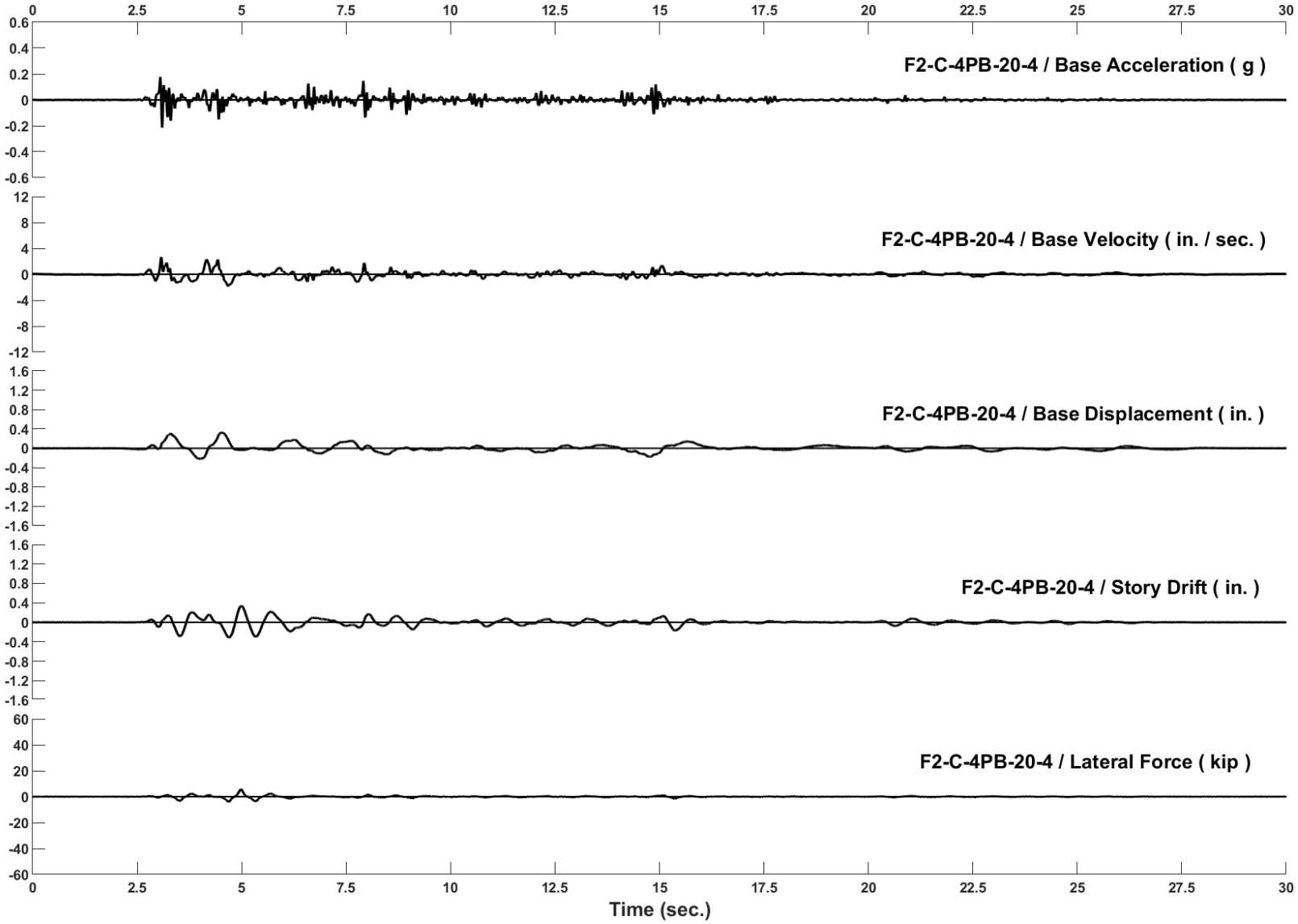

Figure D-16: Run 113, Frame 2, Structural Response and Base Motion History

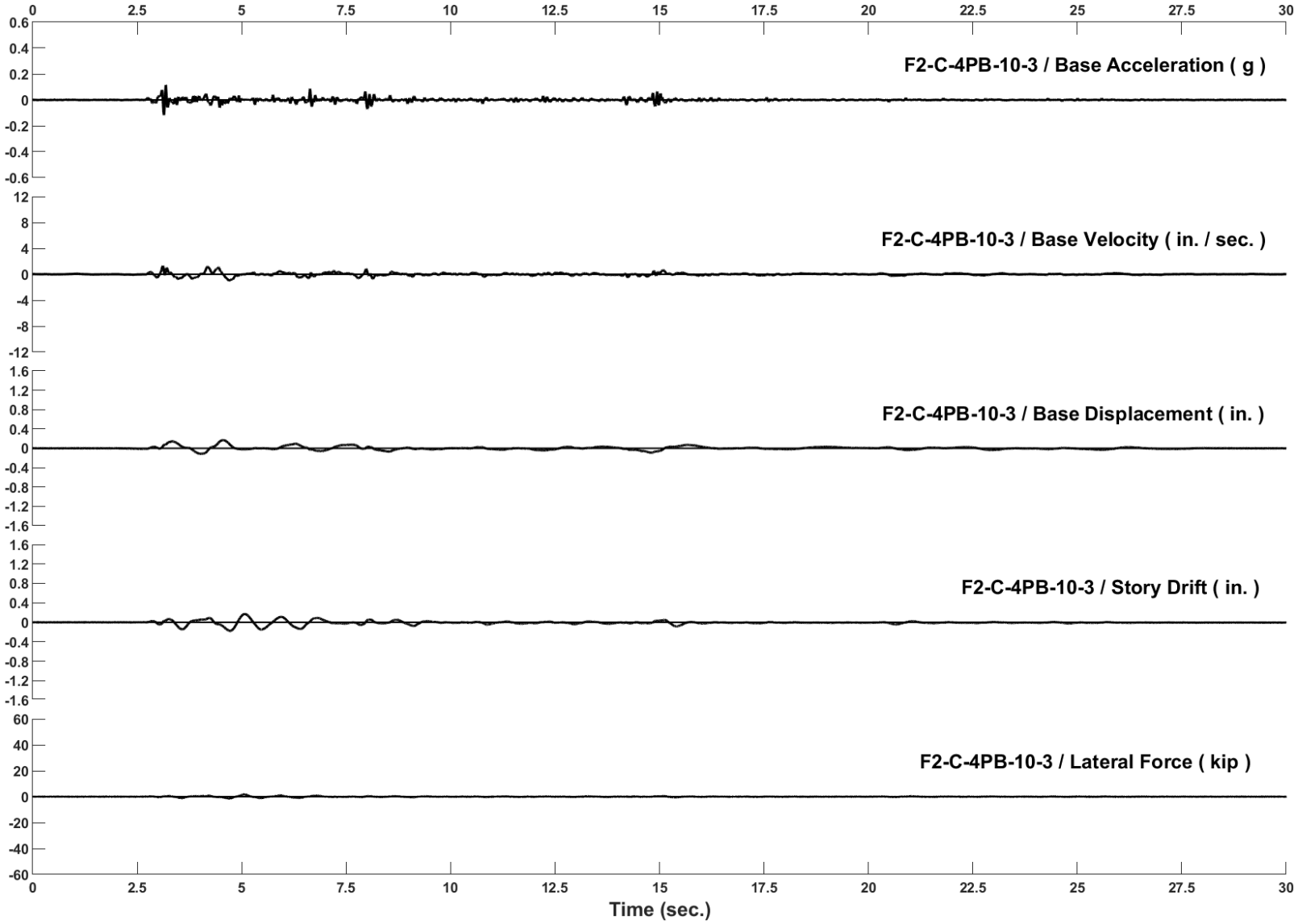

Figure D-17: Run 114, Frame 2, Structural Response and Base Motion History

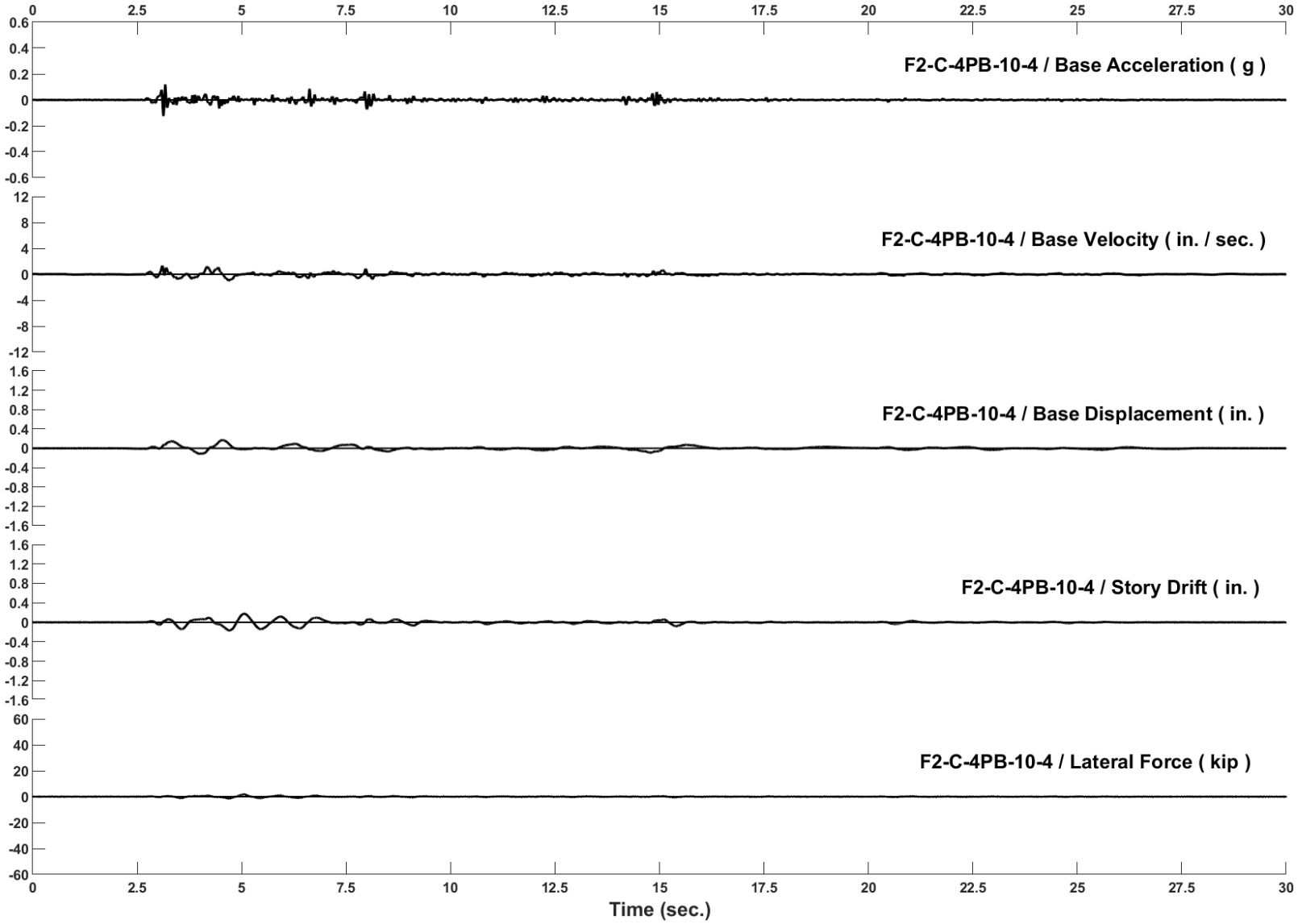

Figure D-18: Run 115, Frame 2, Structural Response and Base Motion History

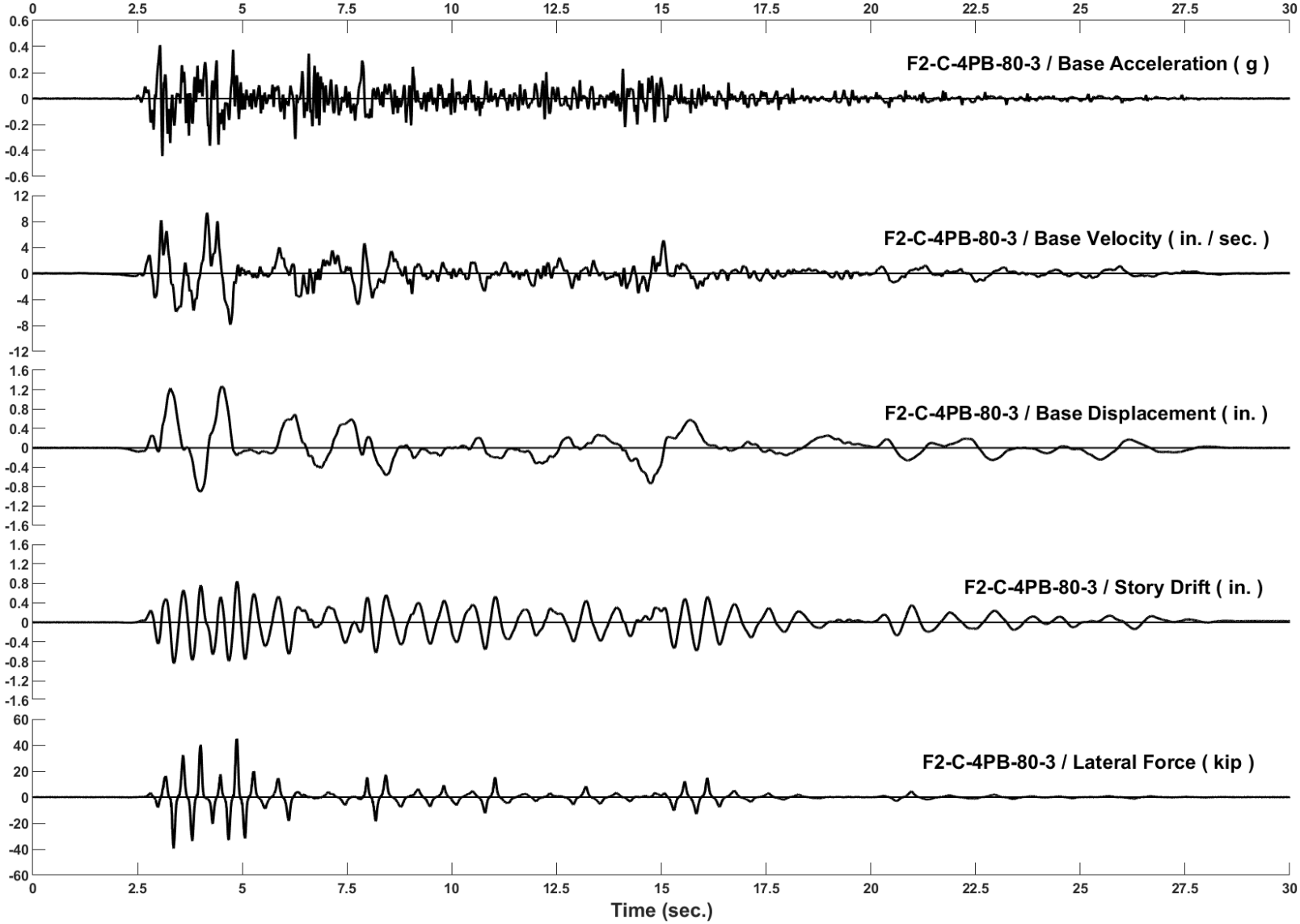

Figure D-19: Run 116, Frame 2, Structural Response and Base Motion History

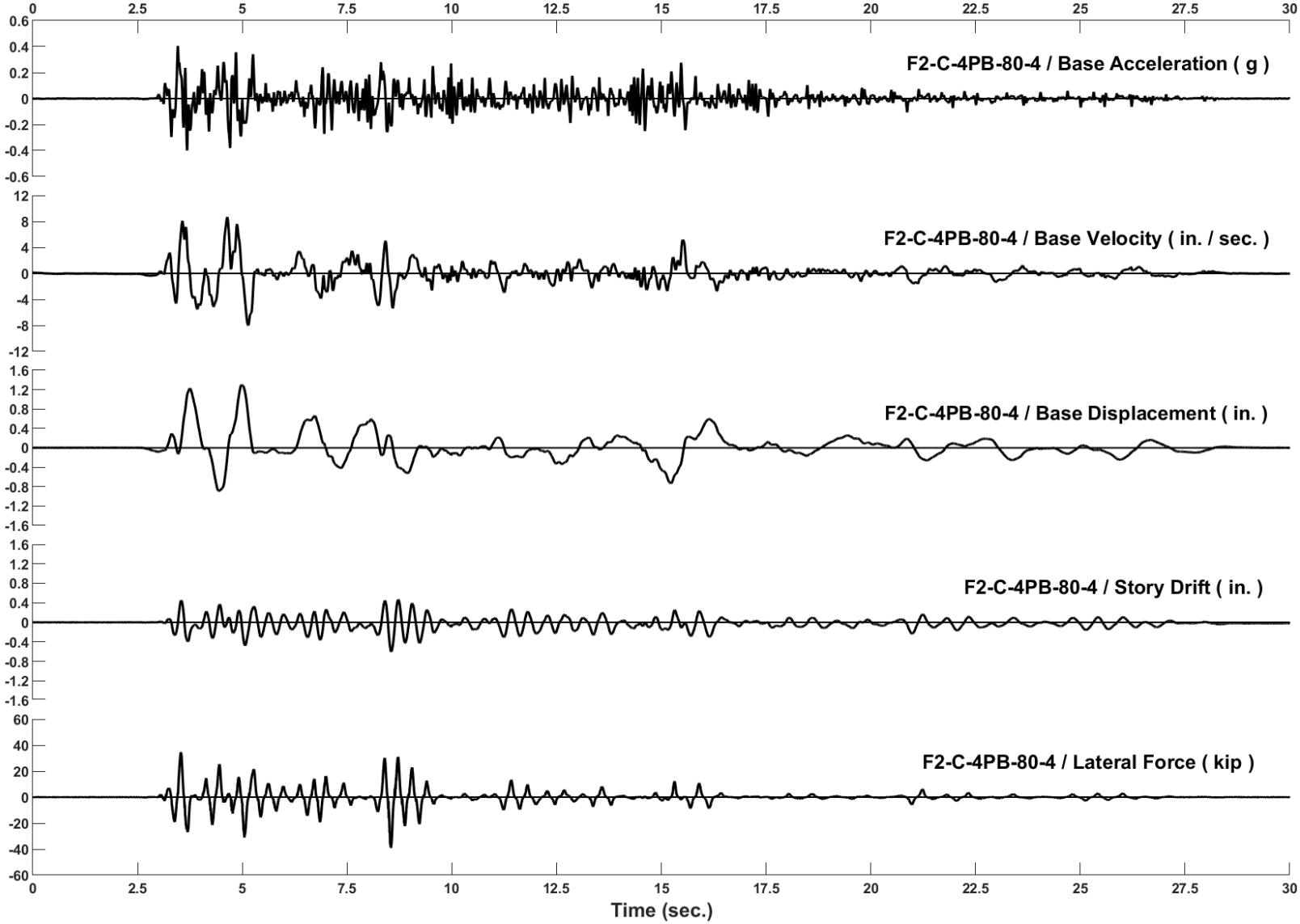

Figure D-20: Run 117, Frame 2, Structural Response and Base Motion History

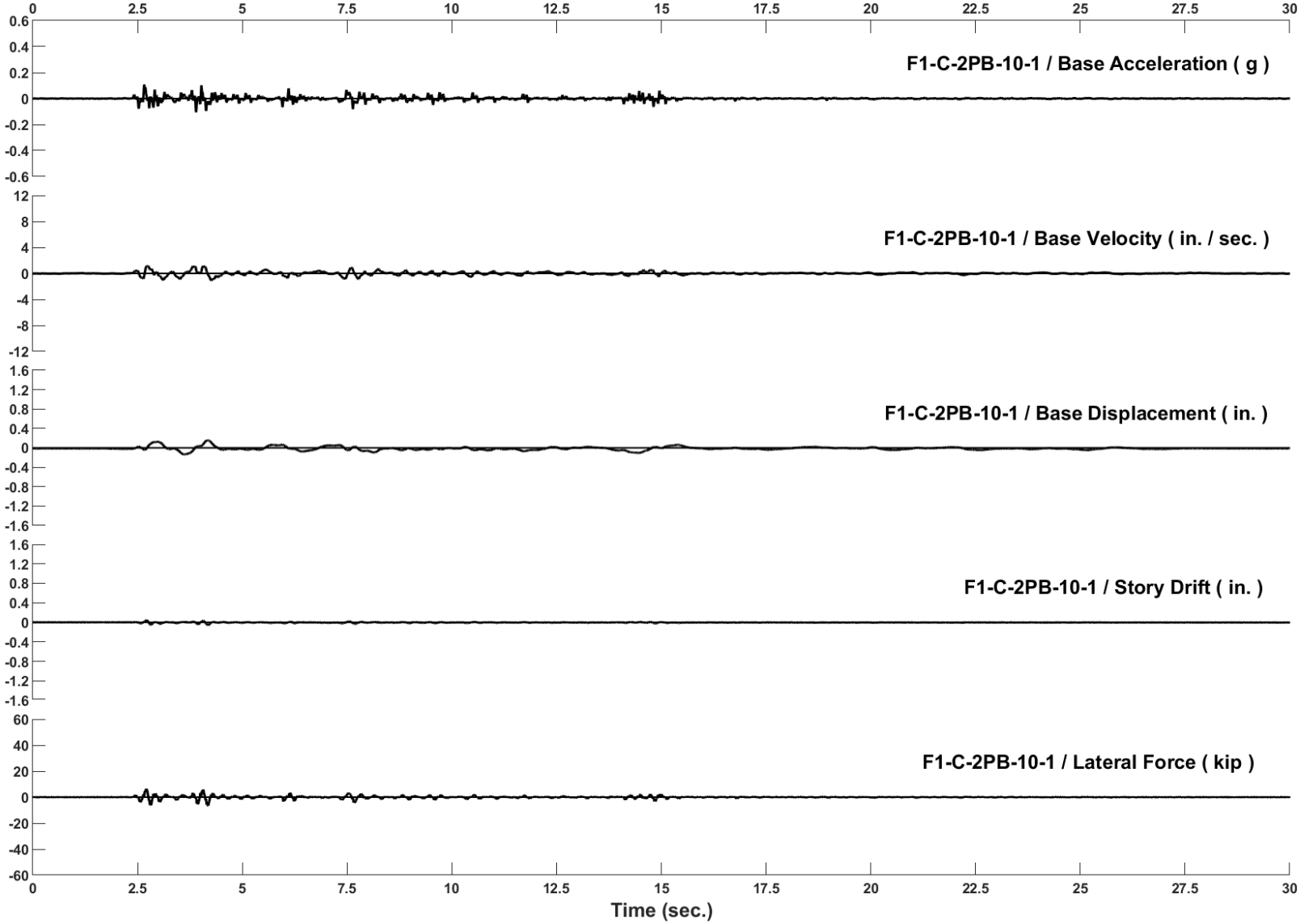

Figure D-21: Run 79, Frame 1, Structural Response and Base Motion History

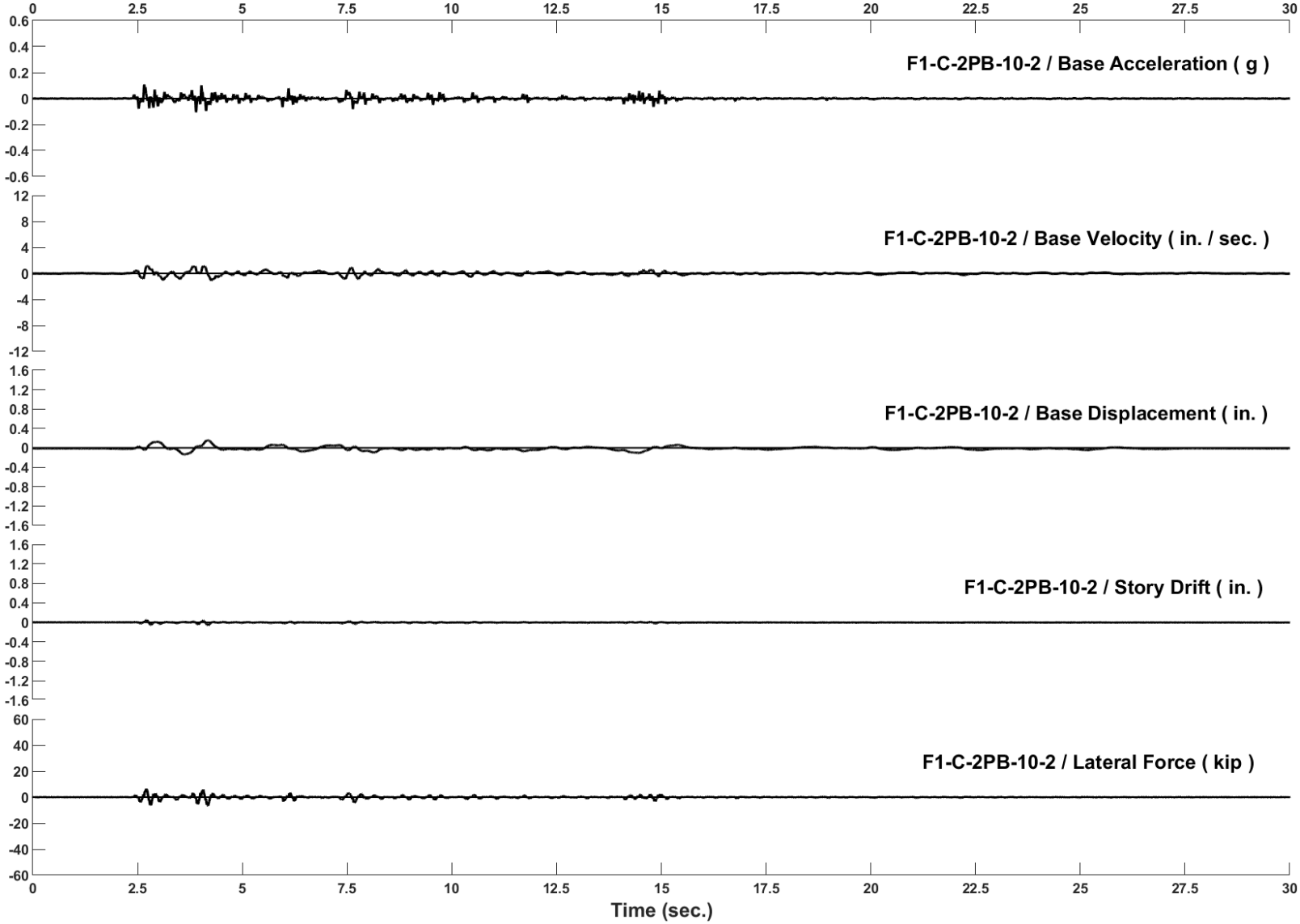

Figure D-22: Run 80, Frame 1, Structural Response and Base Motion History

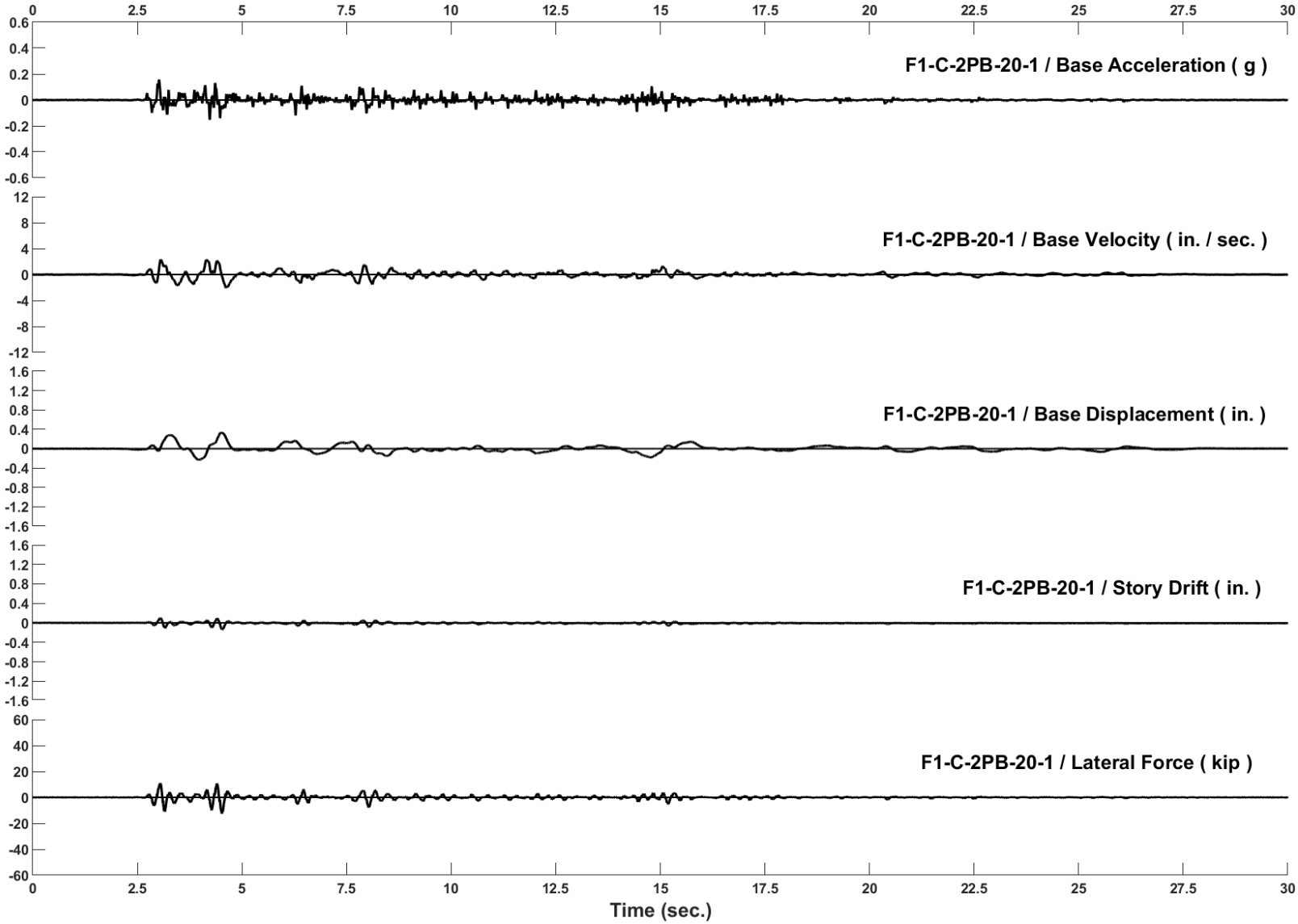

Figure D-23: Run 81, Frame 1, Structural Response and Base Motion History

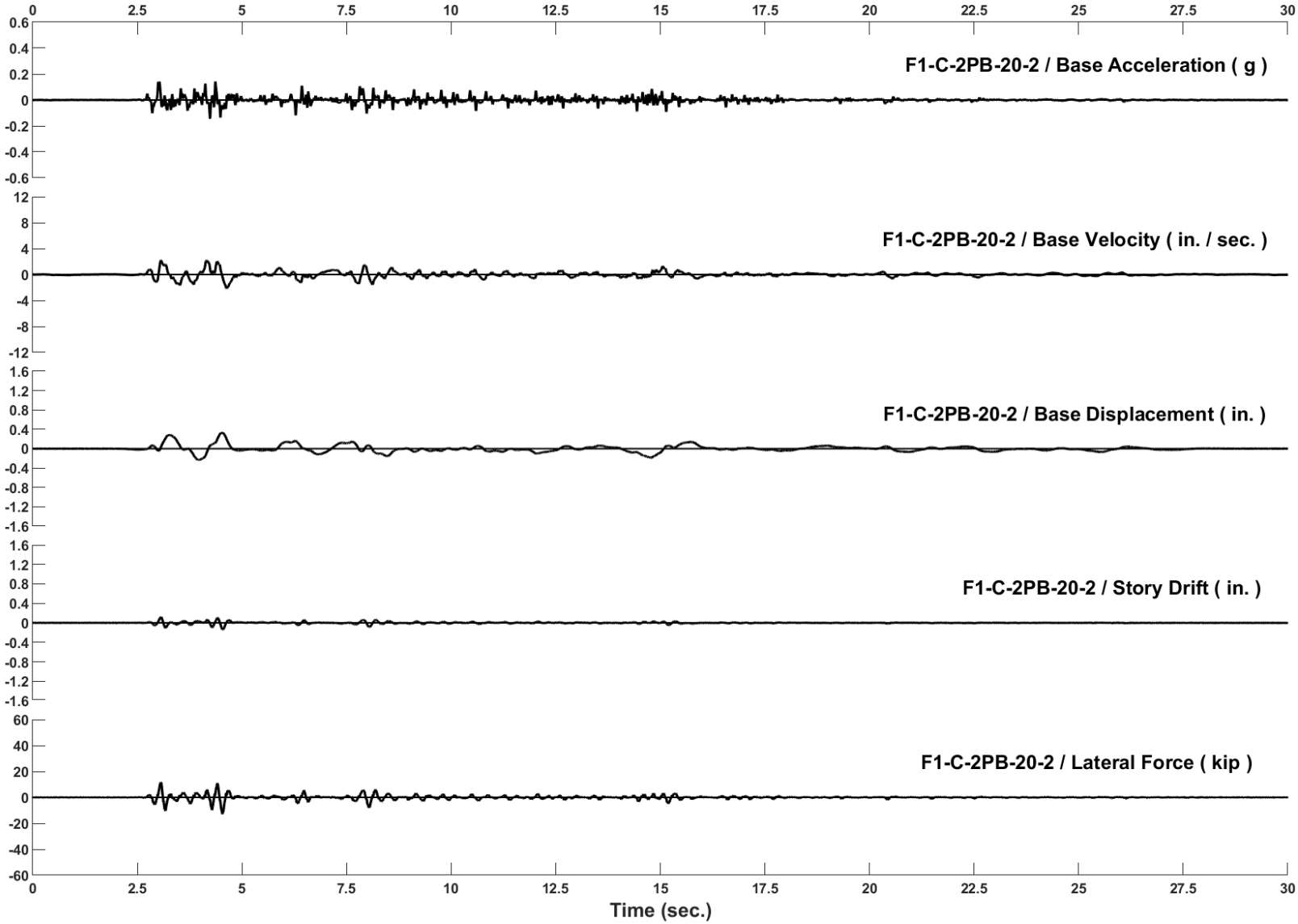

Figure D-24: Run 82, Frame 1, Structural Response and Base Motion History

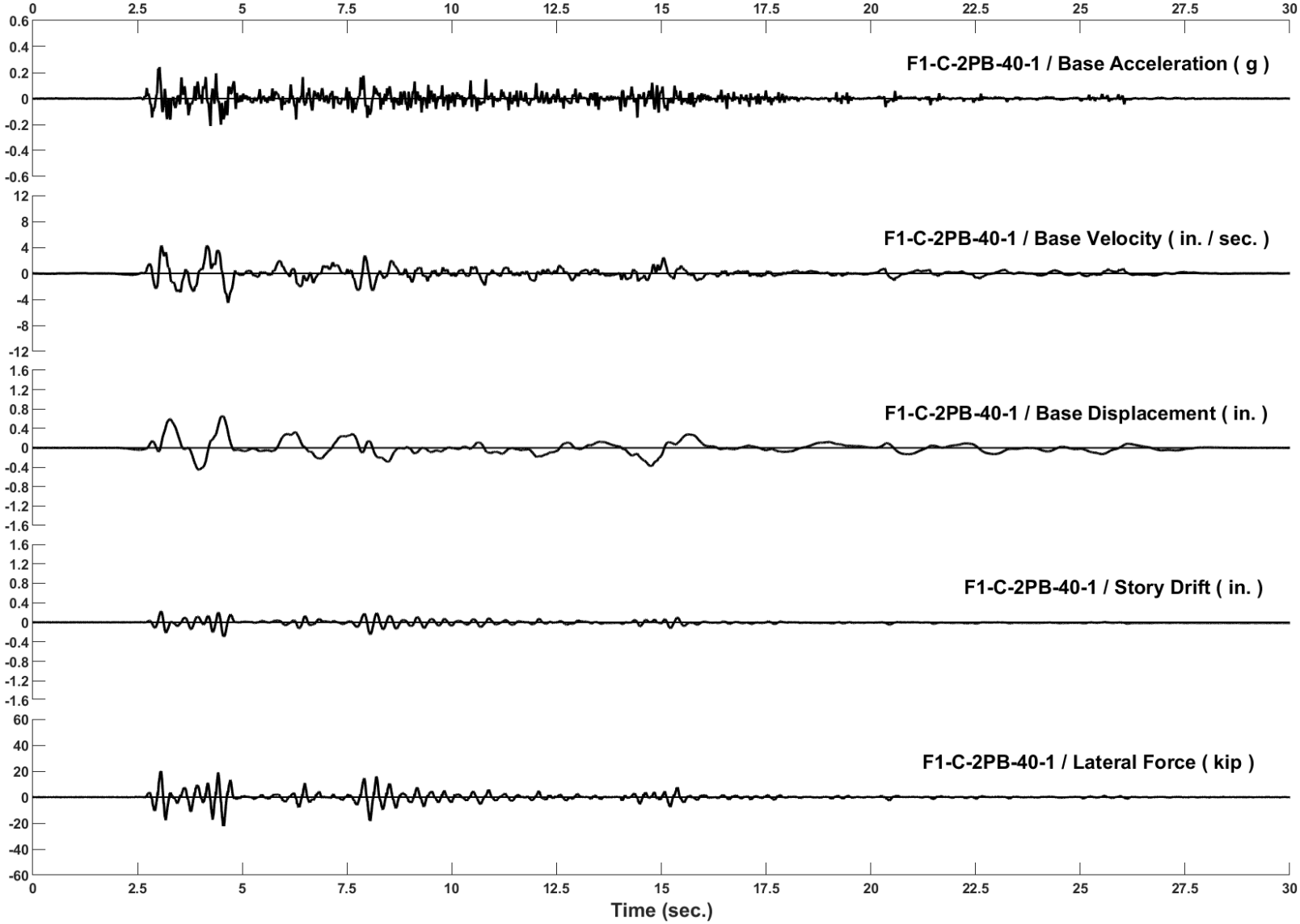

Figure D-25: Run 83, Frame 1, Structural Response and Base Motion History

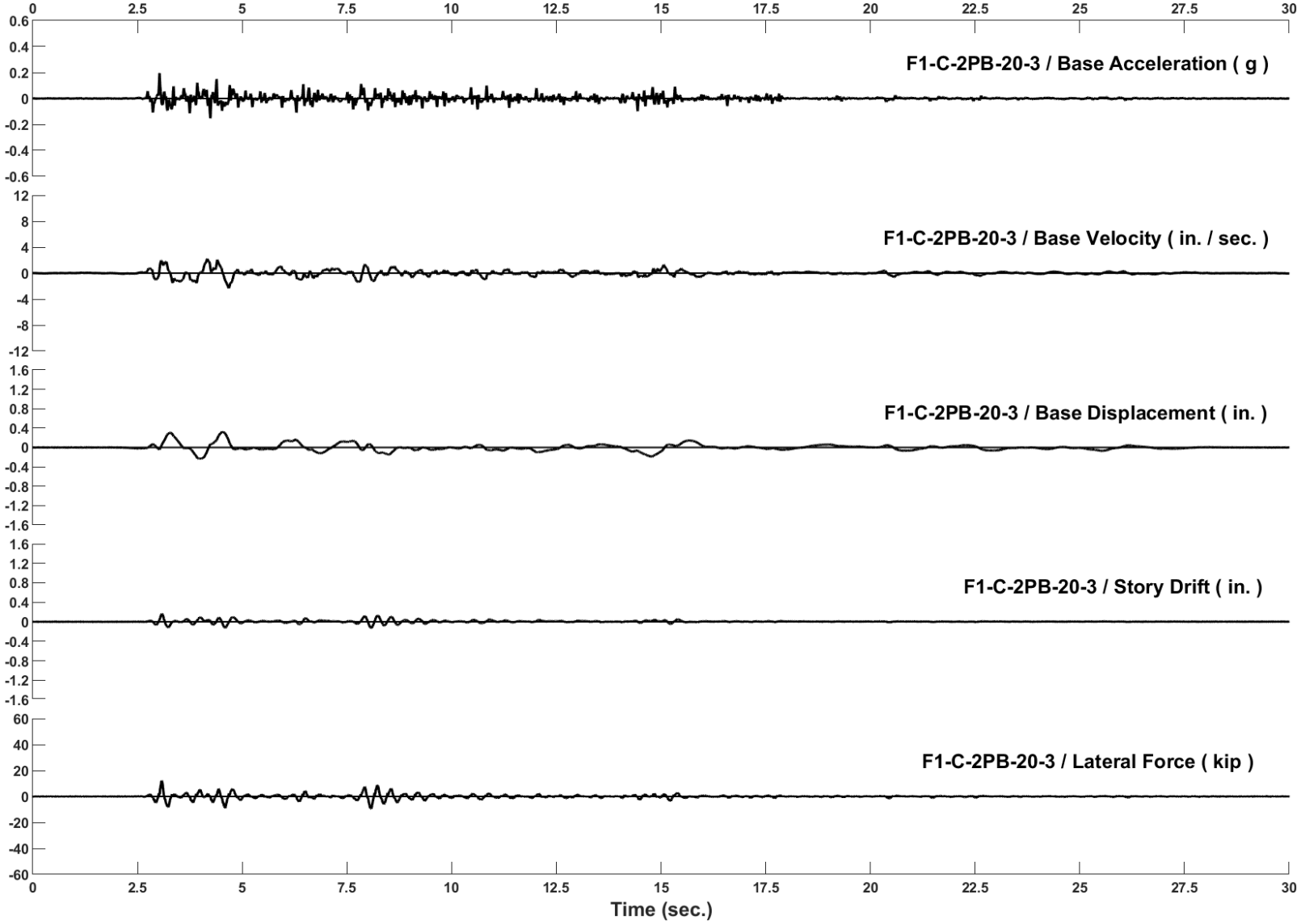

Figure D-26: Run 84, Frame 1, Structural Response and Base Motion History

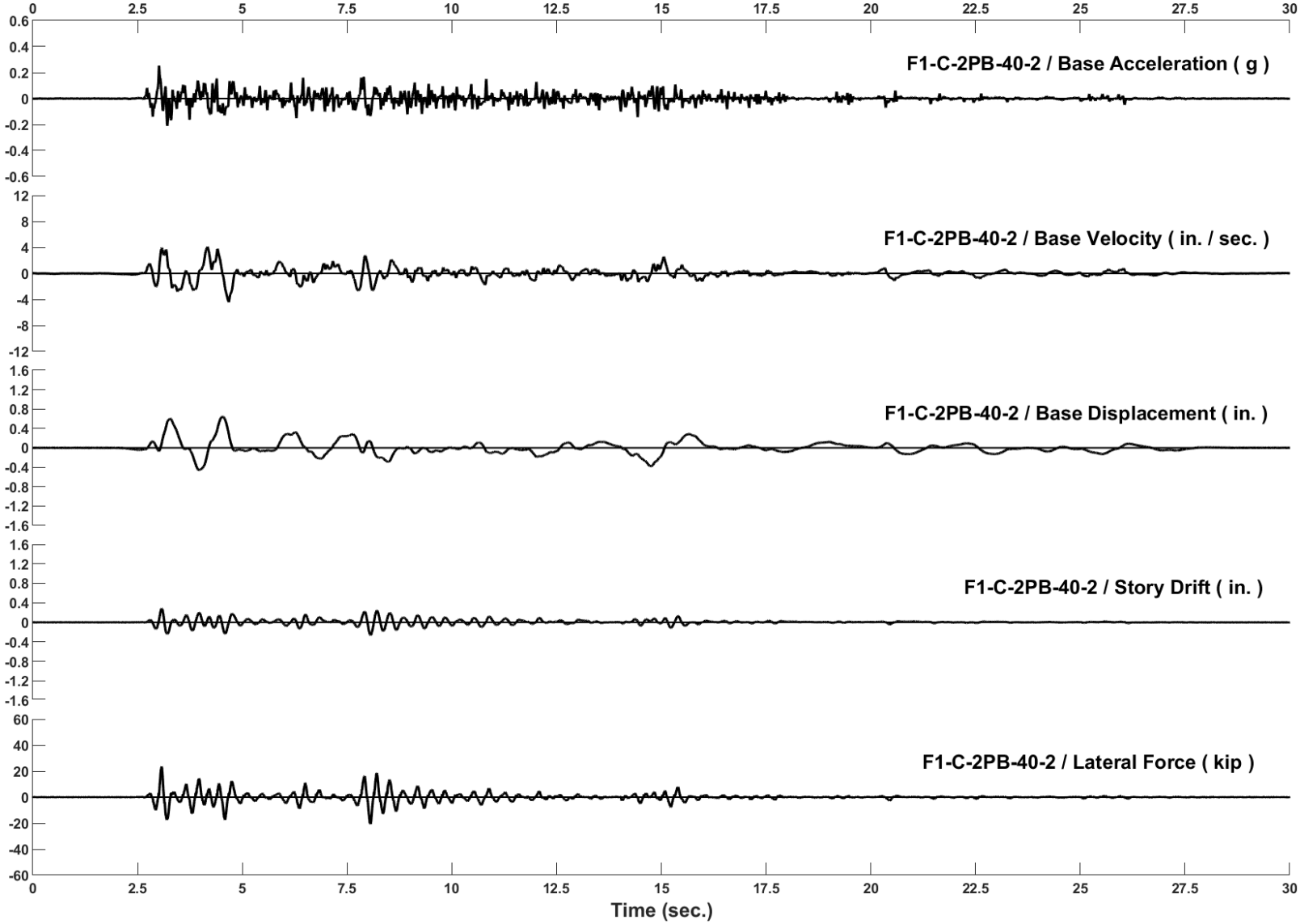

Figure D-27: Run 85 Frame 1, Structural Response and Base Motion History

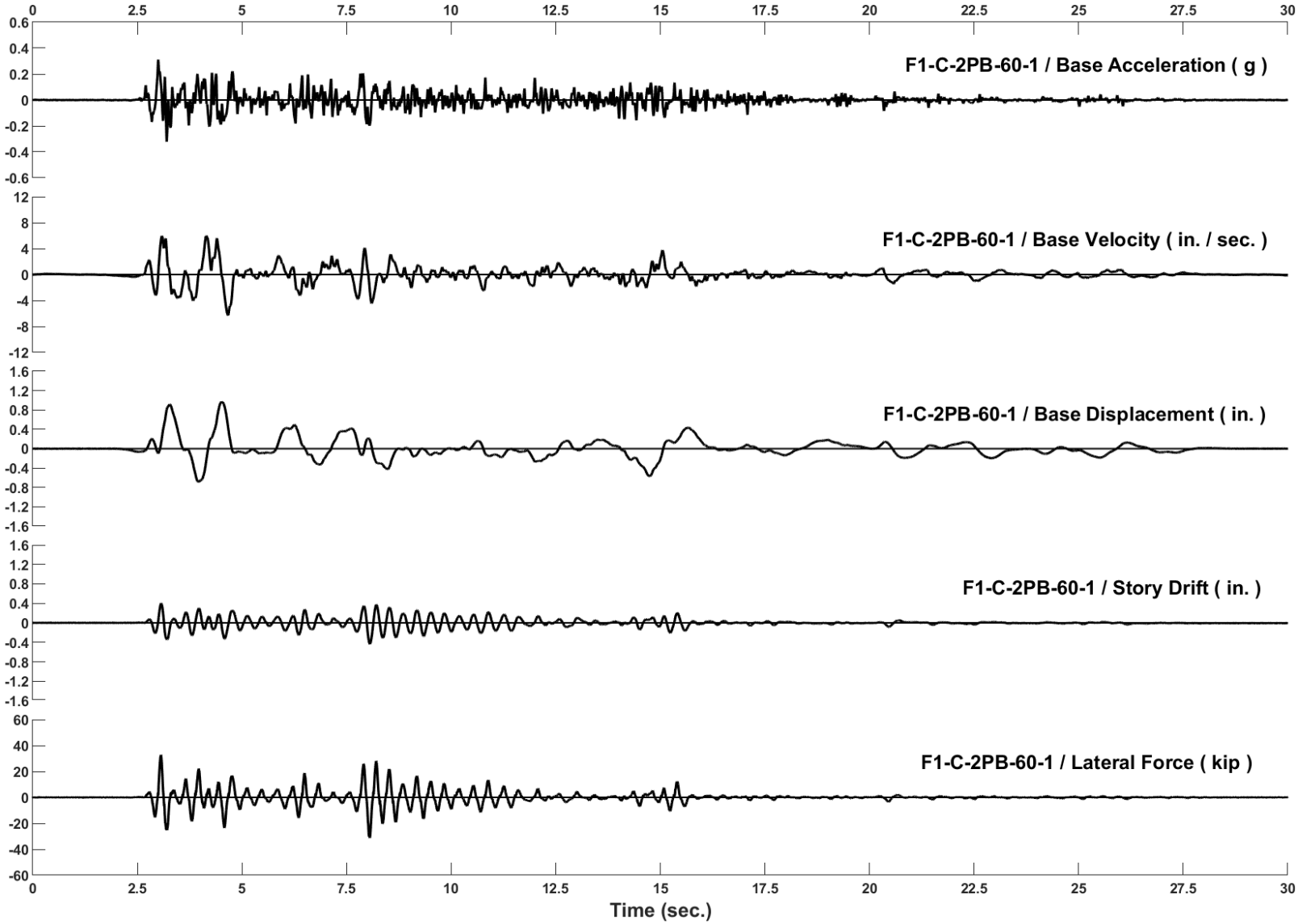

Figure D-28: Run 86, Frame 1, Structural Response and Base Motion History

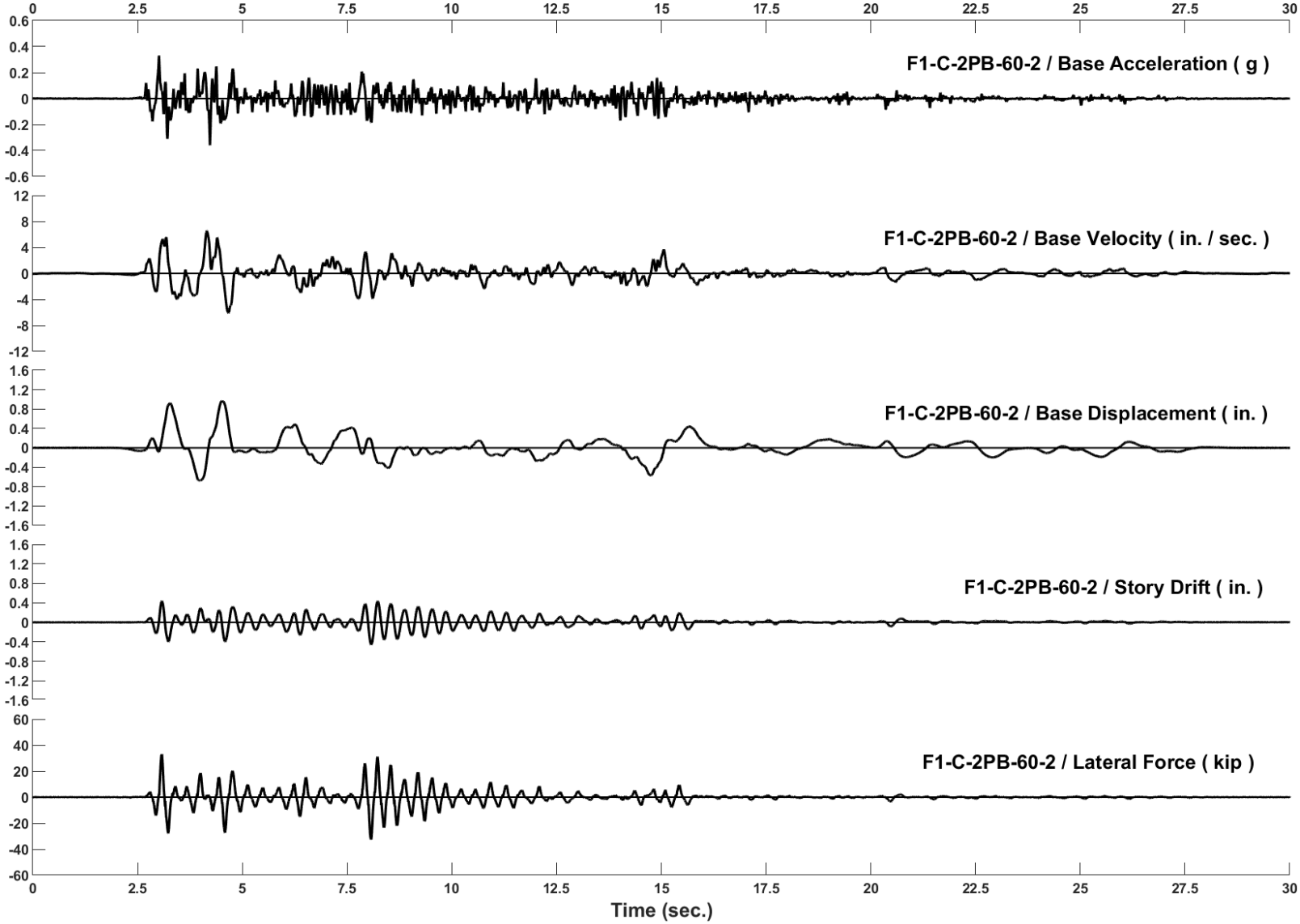

Figure D-29: Run 87, Frame 1, Structural Response and Base Motion History

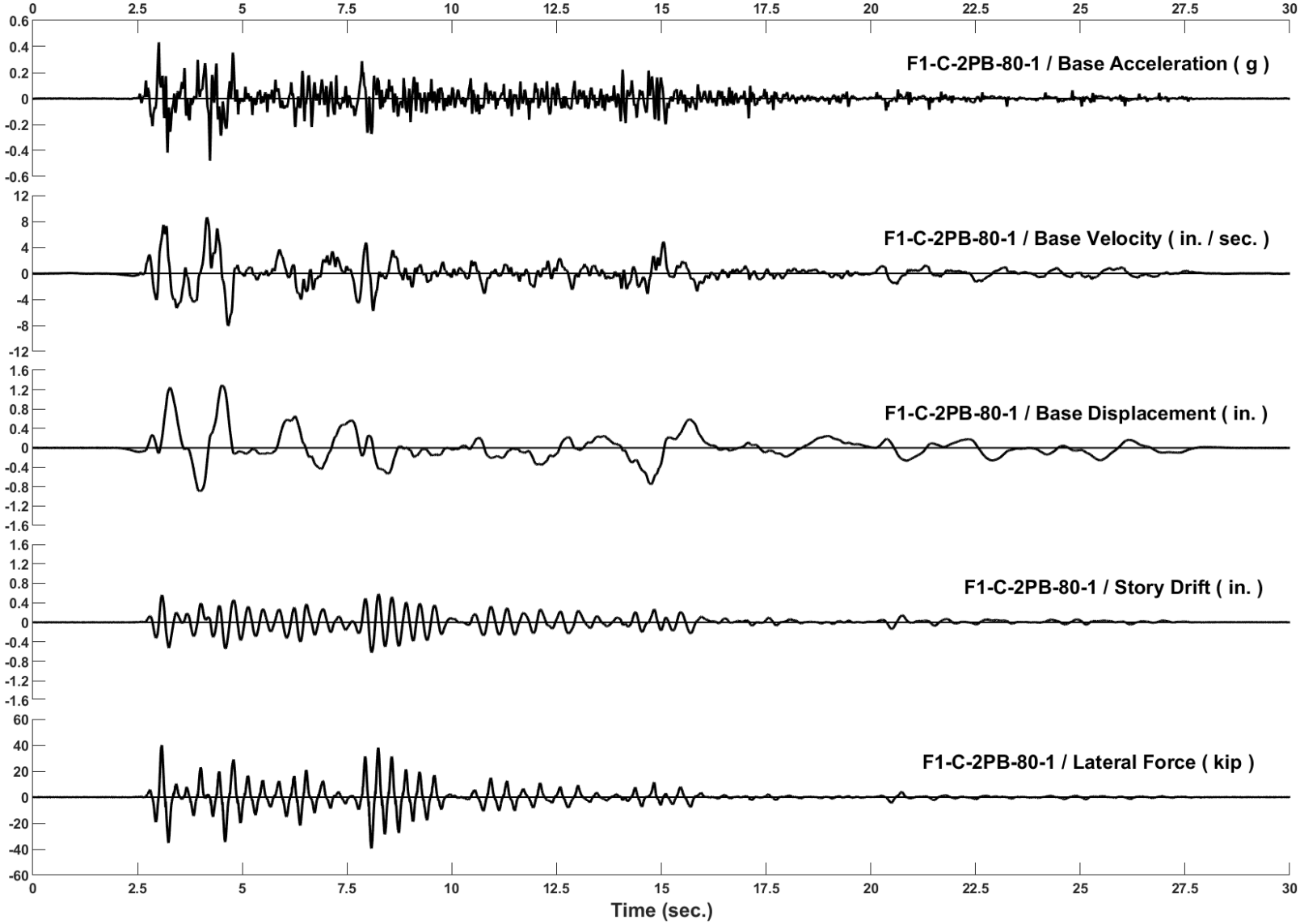

Figure D-30: Run 88, Frame 1, Structural Response and Base Motion History

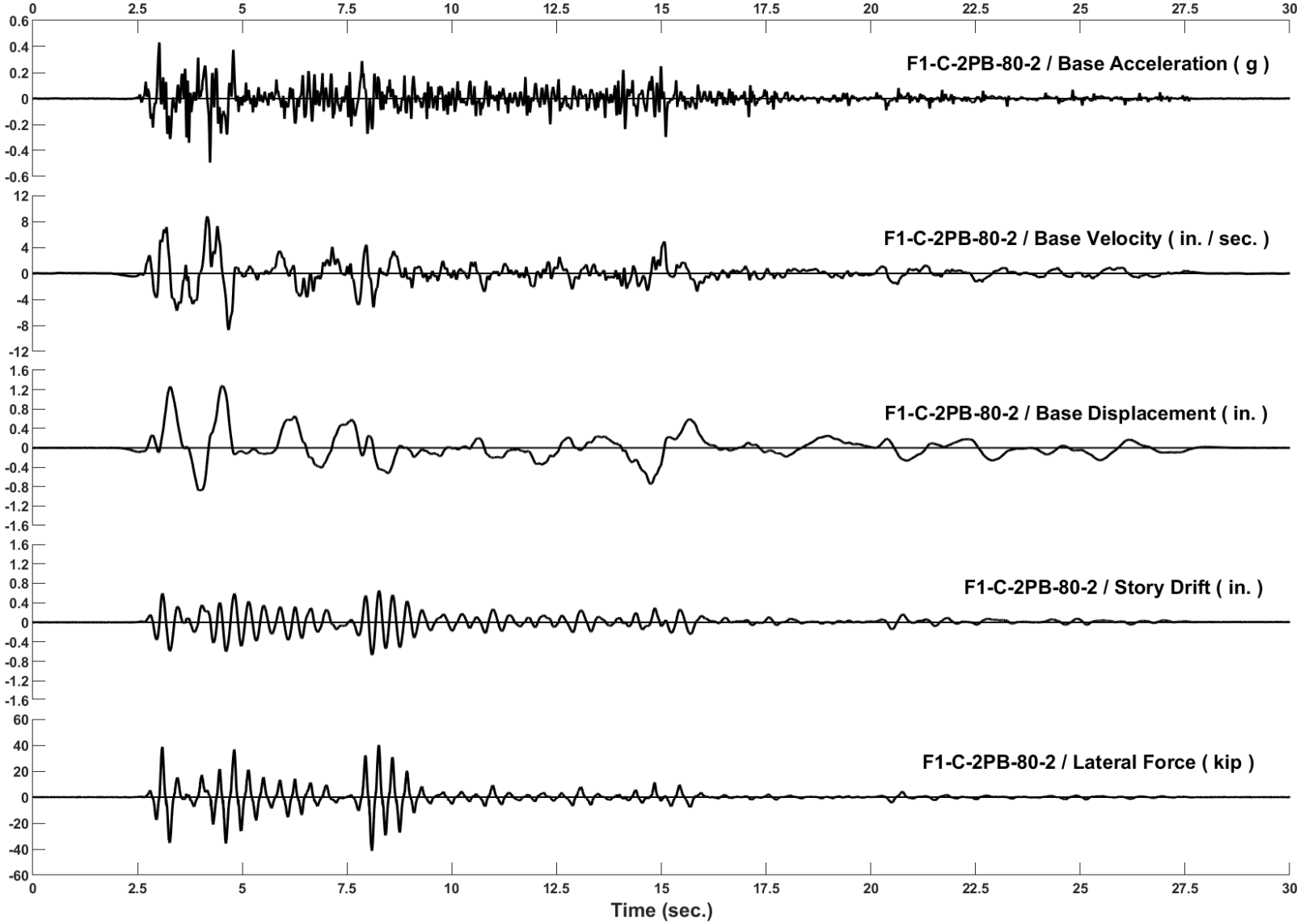

Figure D-31: Run 89, Frame 1, Structural Response and Base Motion History

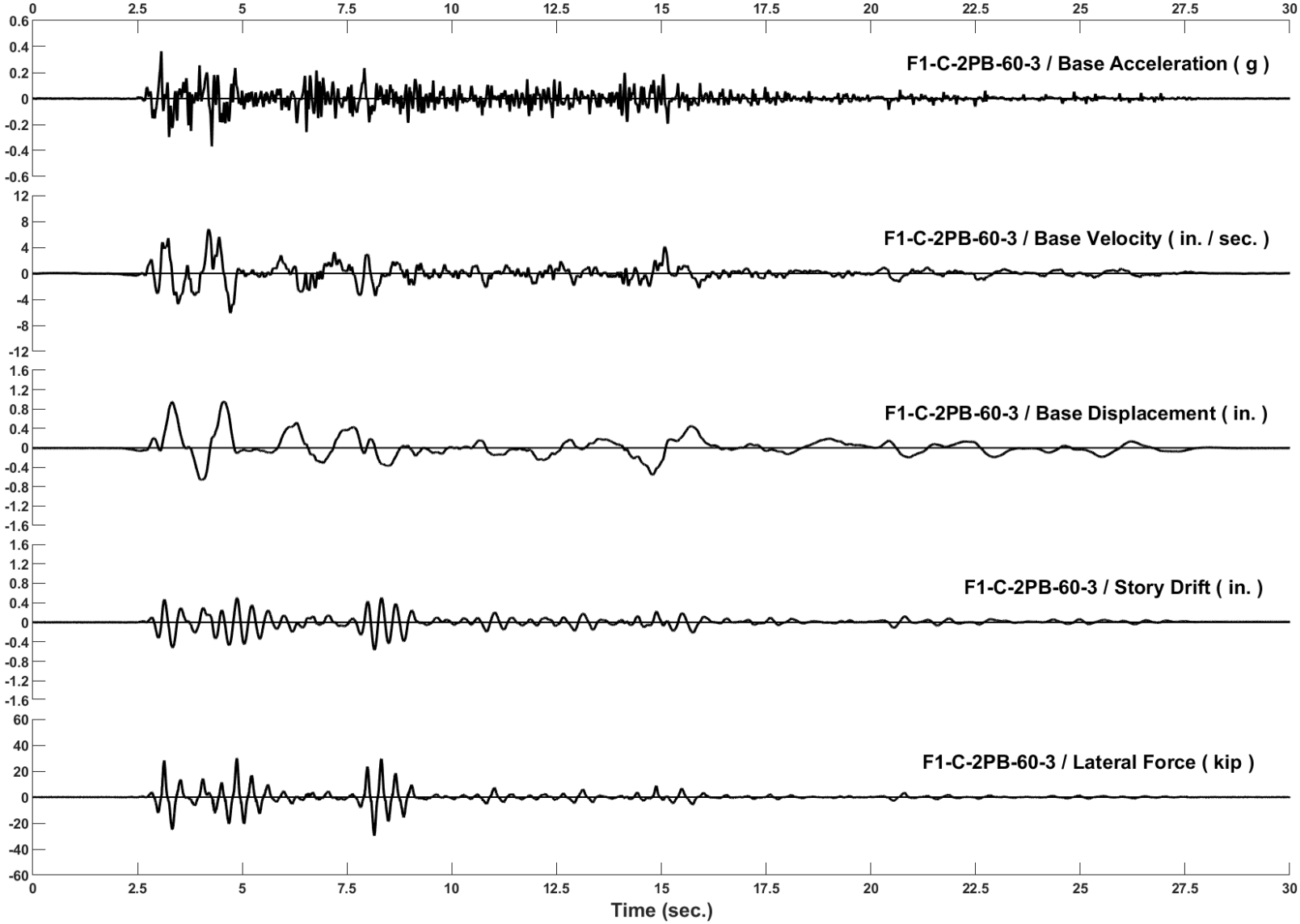

Figure D-32: Run 90, Frame 1, Structural Response and Base Motion History

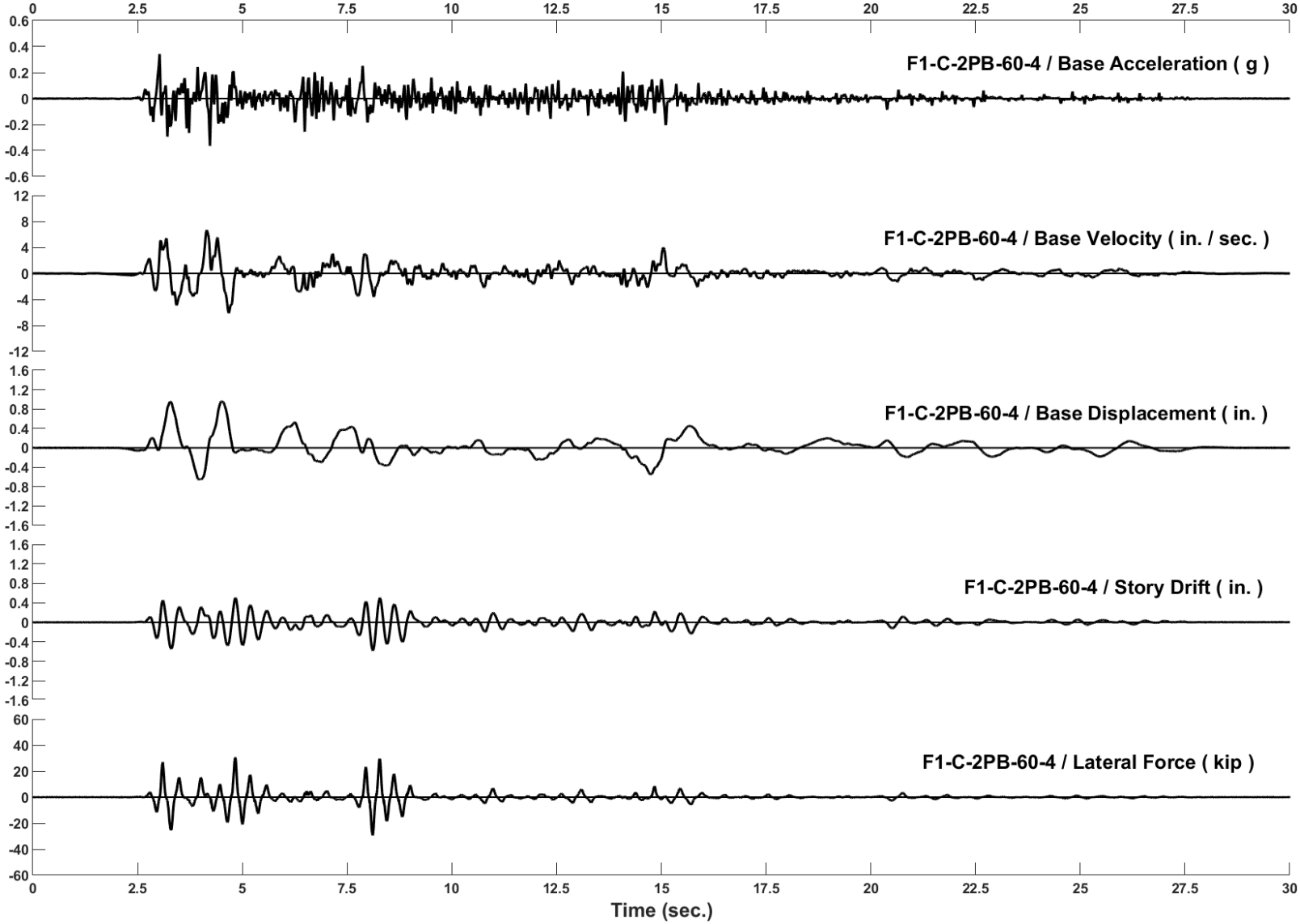

Figure D-33: Run 91, Frame 1, Structural Response and Base Motion History

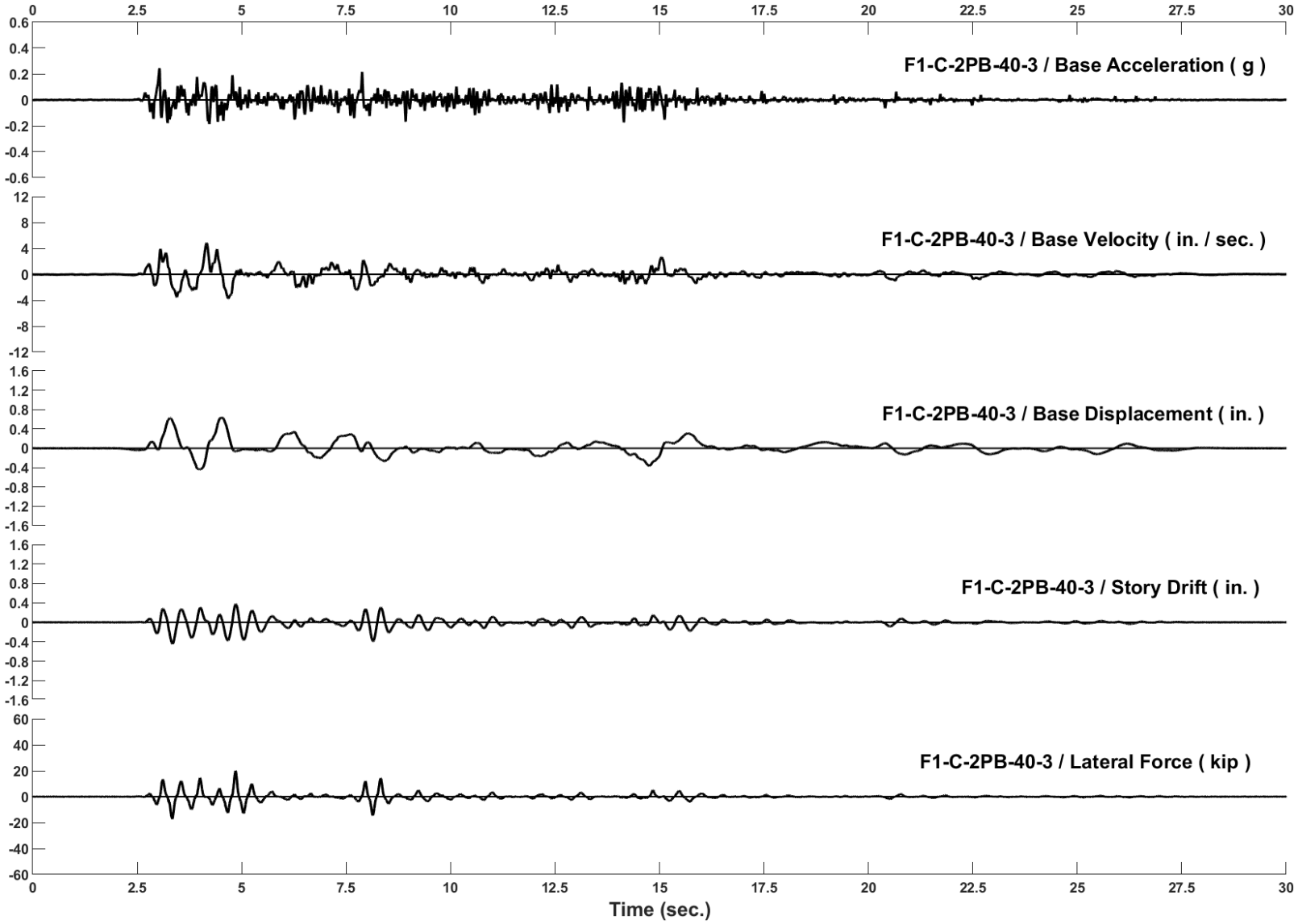

Figure D-34: Run 92, Frame 1, Structural Response and Base Motion History

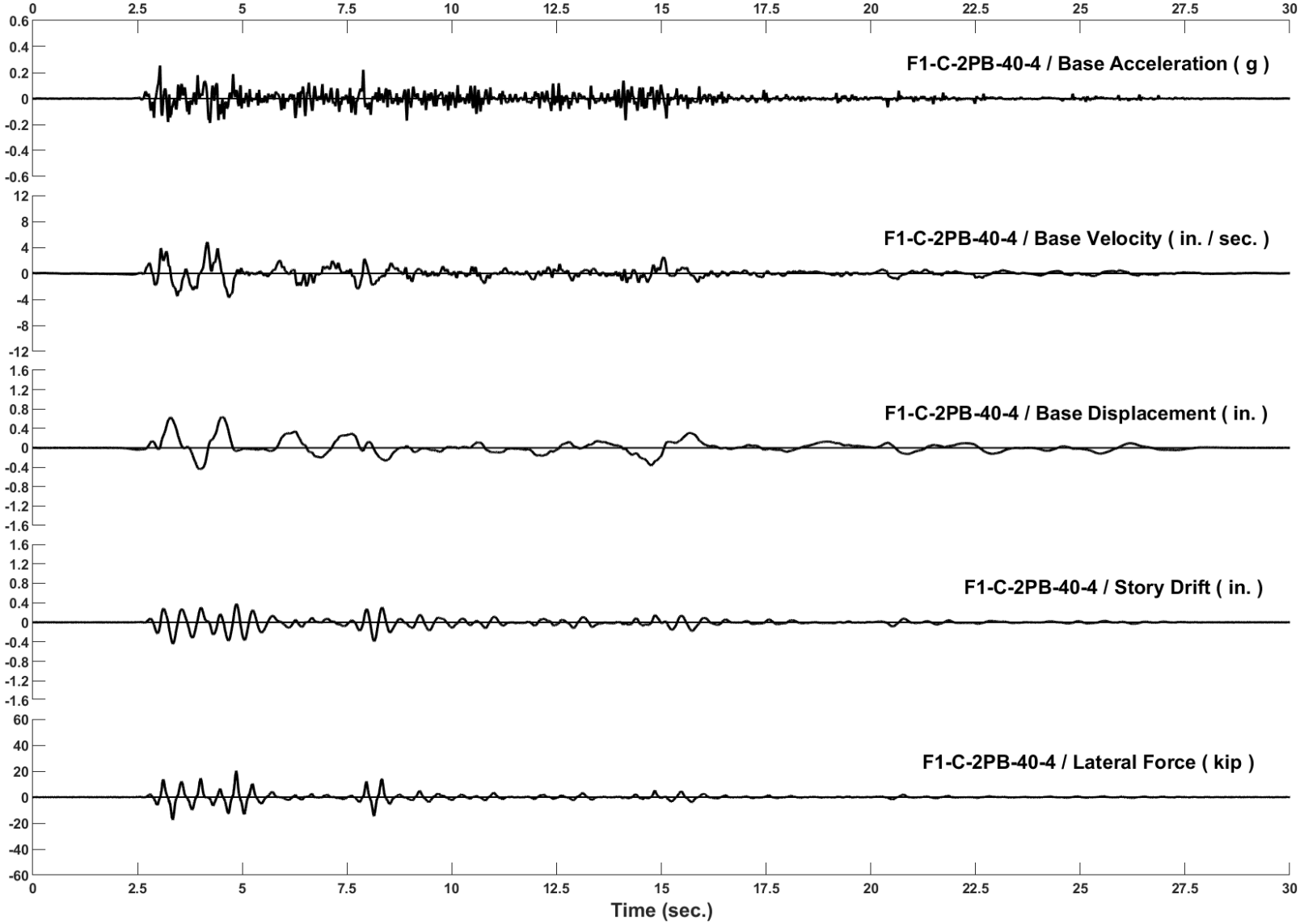

Figure D-35: Run 93, Frame 1, Structural Response and Base Motion History

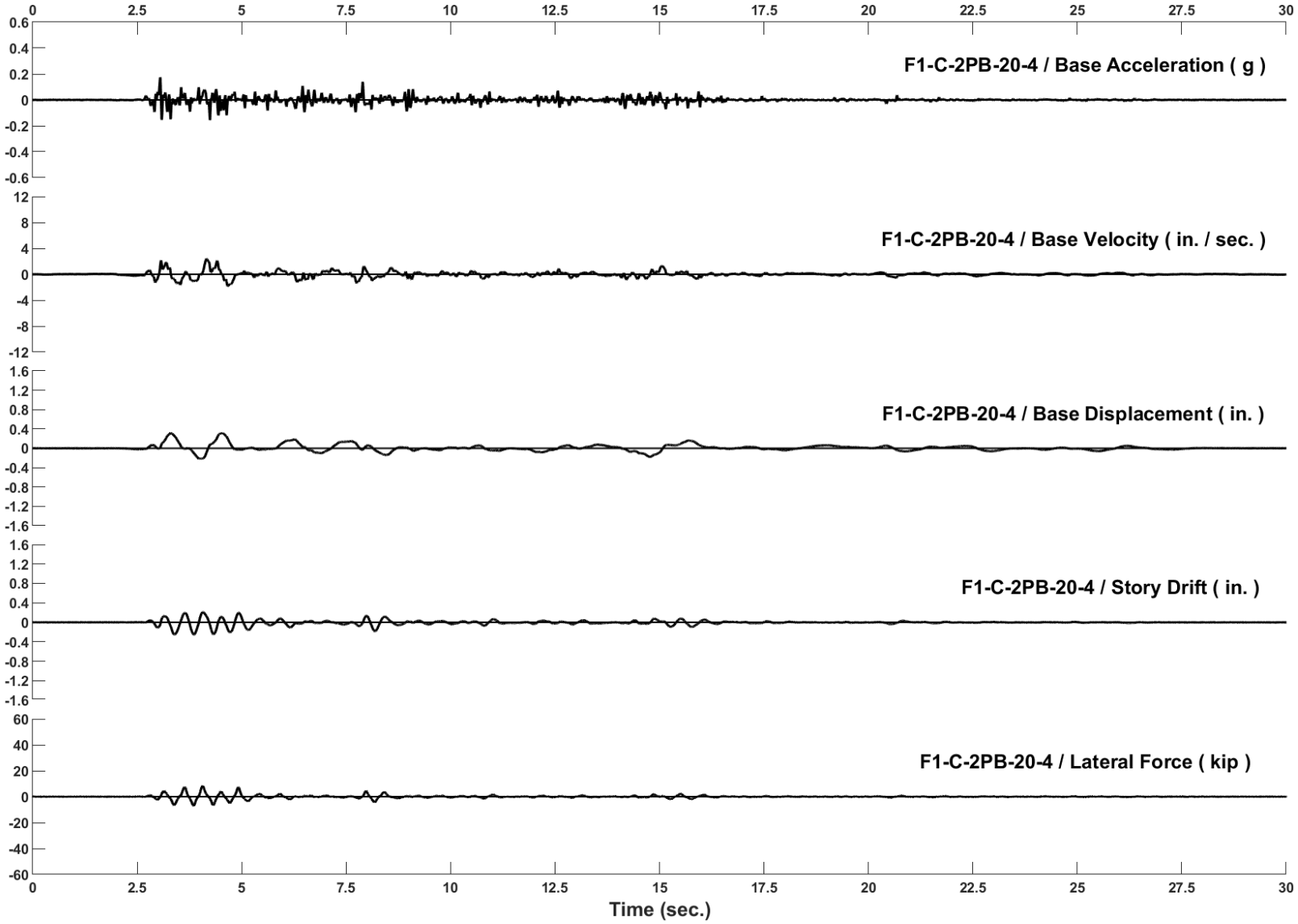

Figure D-36: Run 94, Frame 1, Structural Response and Base Motion History

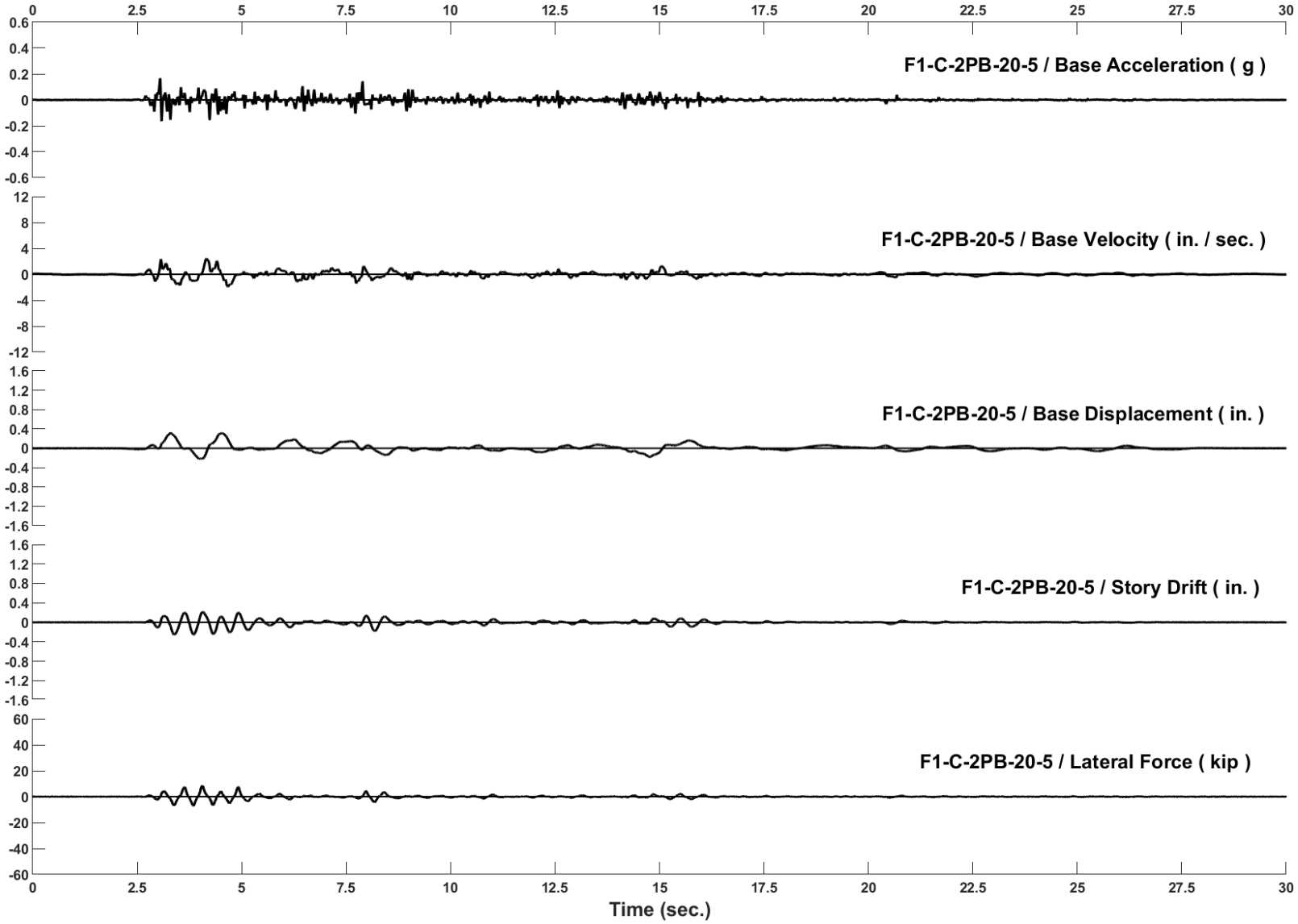

Figure D-37: Run 95, Frame 1, Structural Response and Base Motion History

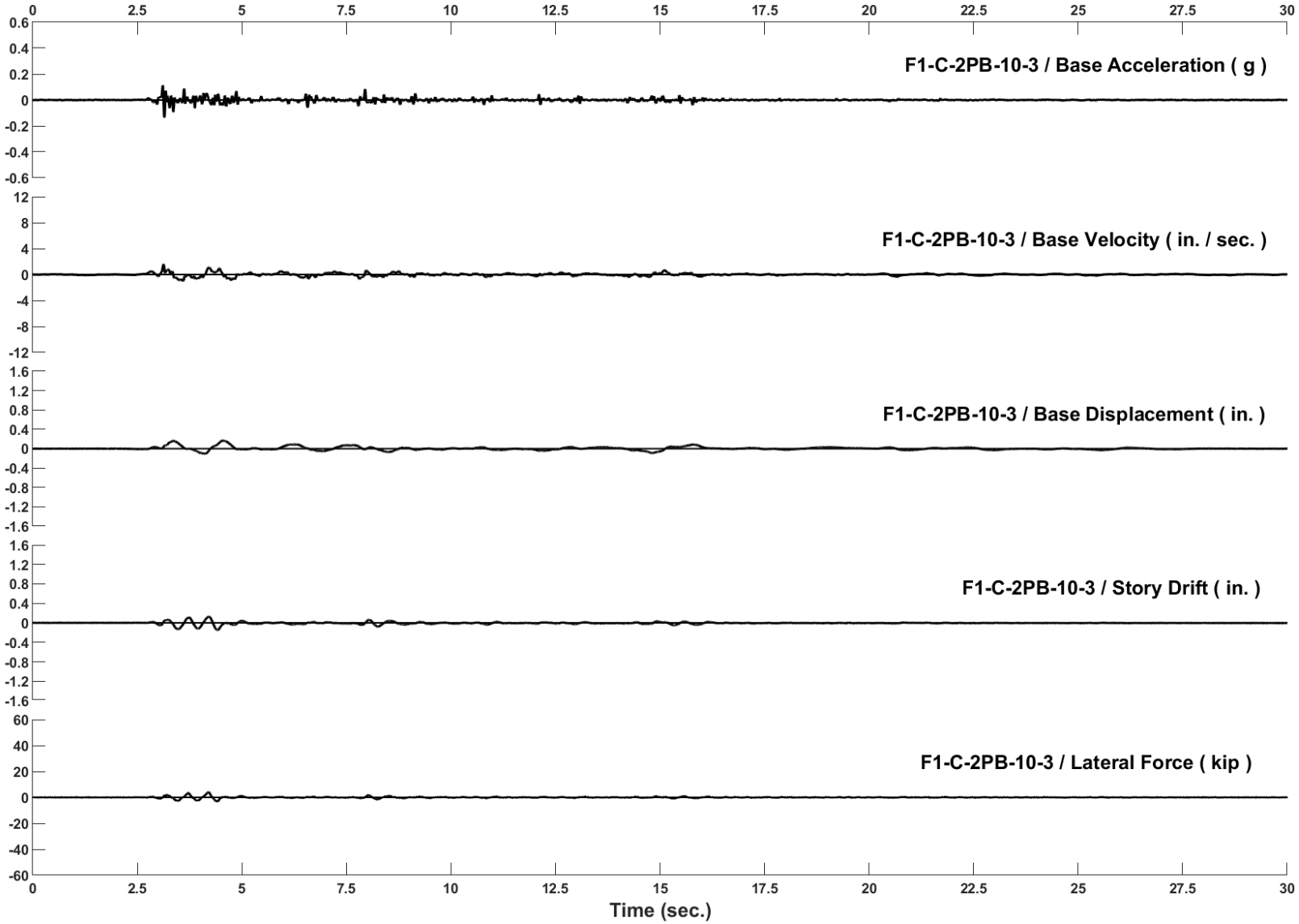

Figure D-38: Run 96, Frame 1, Structural Response and Base Motion History

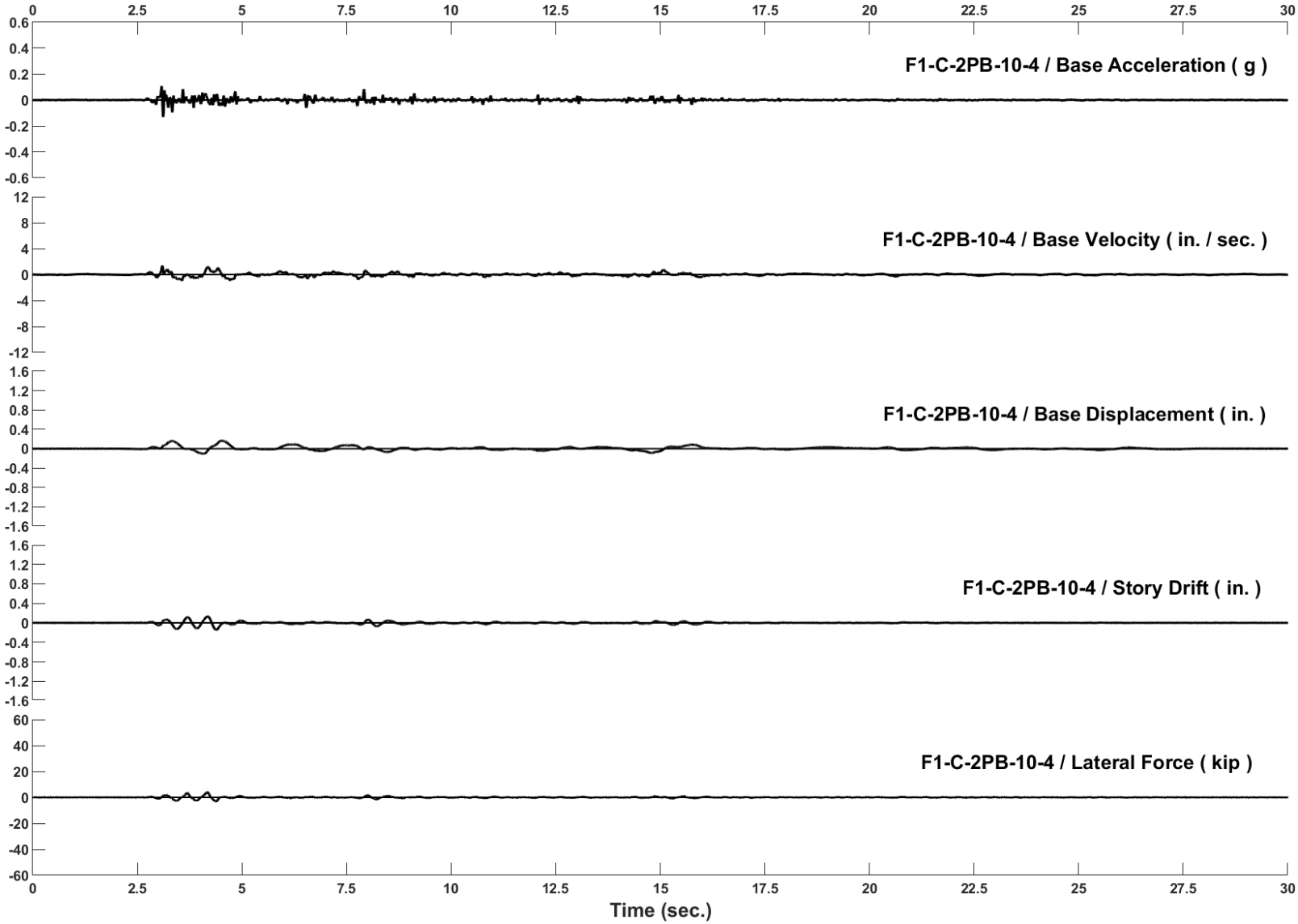

Figure D-39: Run 97, Frame 1, Structural Response and Base Motion History

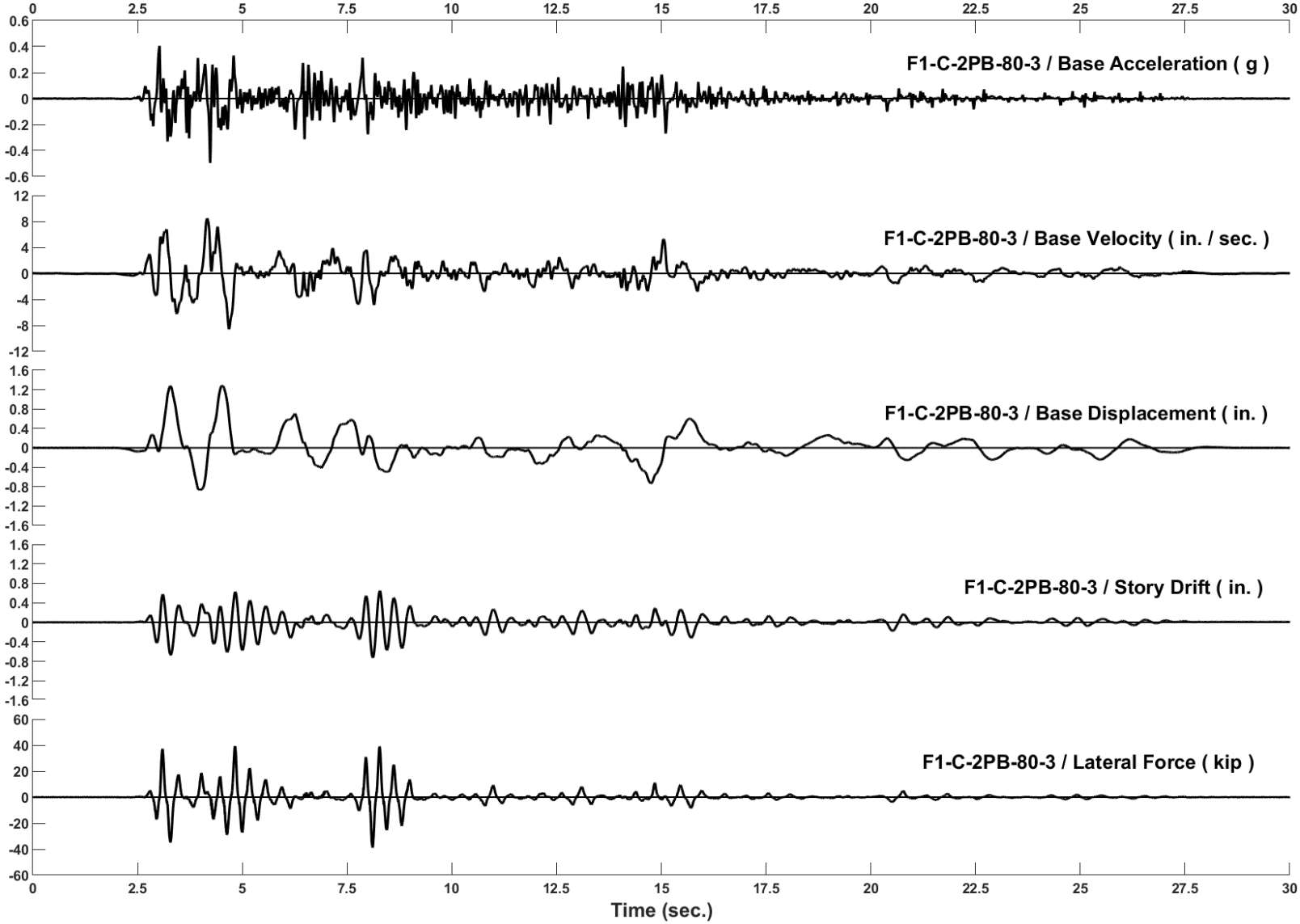

Figure D-40: Run 98, Frame 1, Structural Response and Base Motion History

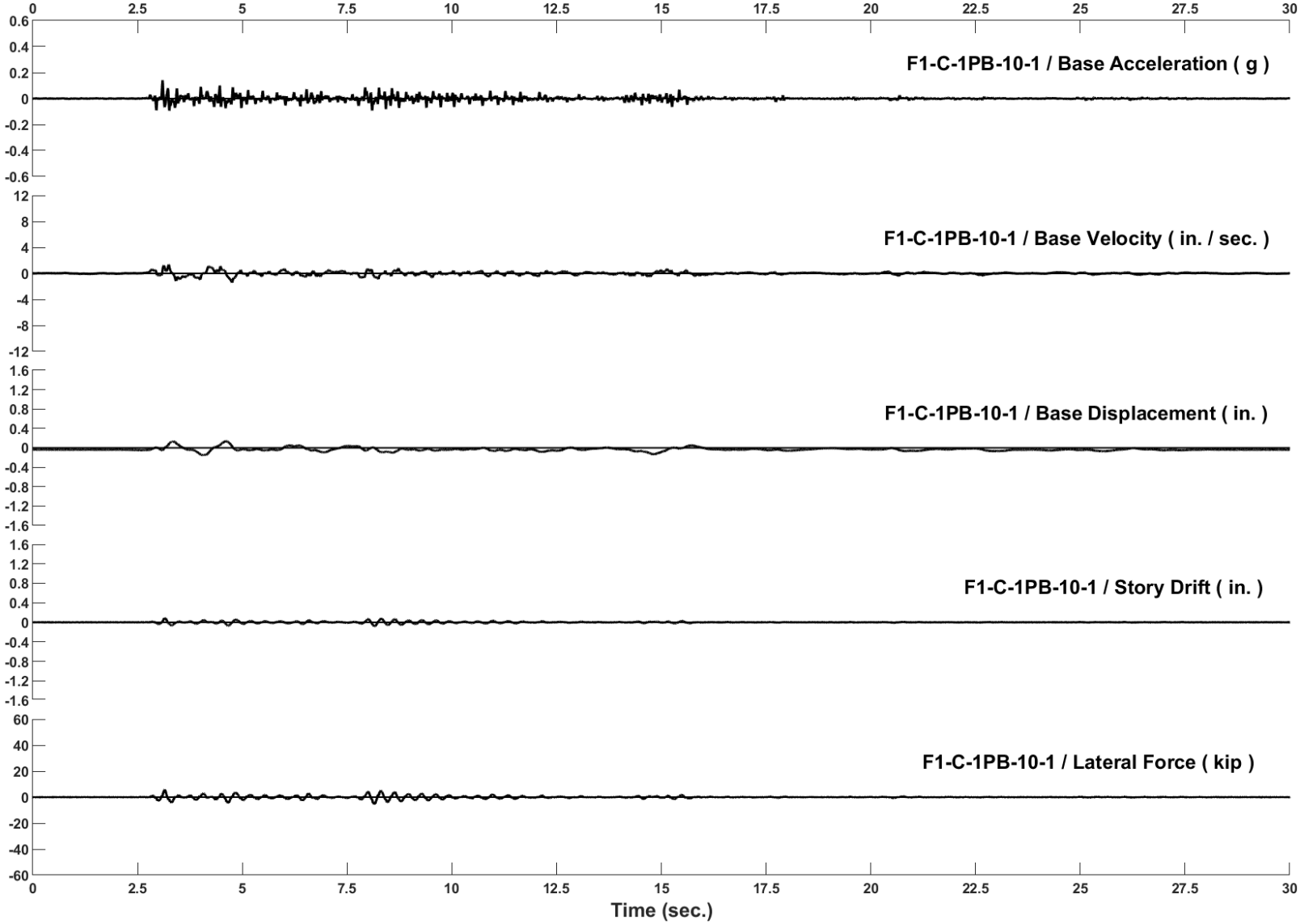

Figure D-41: Run 99, Frame 1, Structural Response and Base Motion History

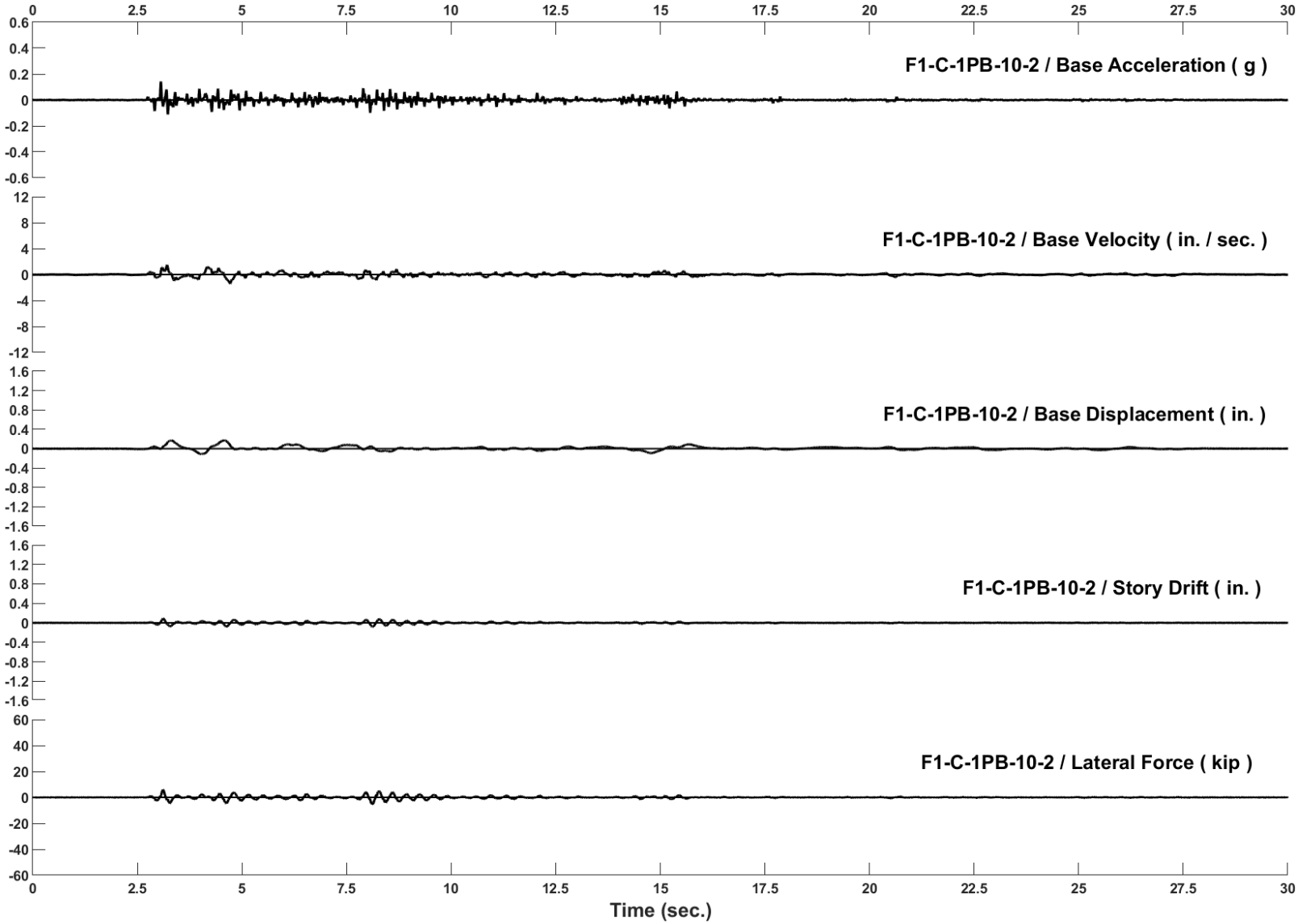

Figure D-42: Run 100, Frame 1, Structural Response and Base Motion History

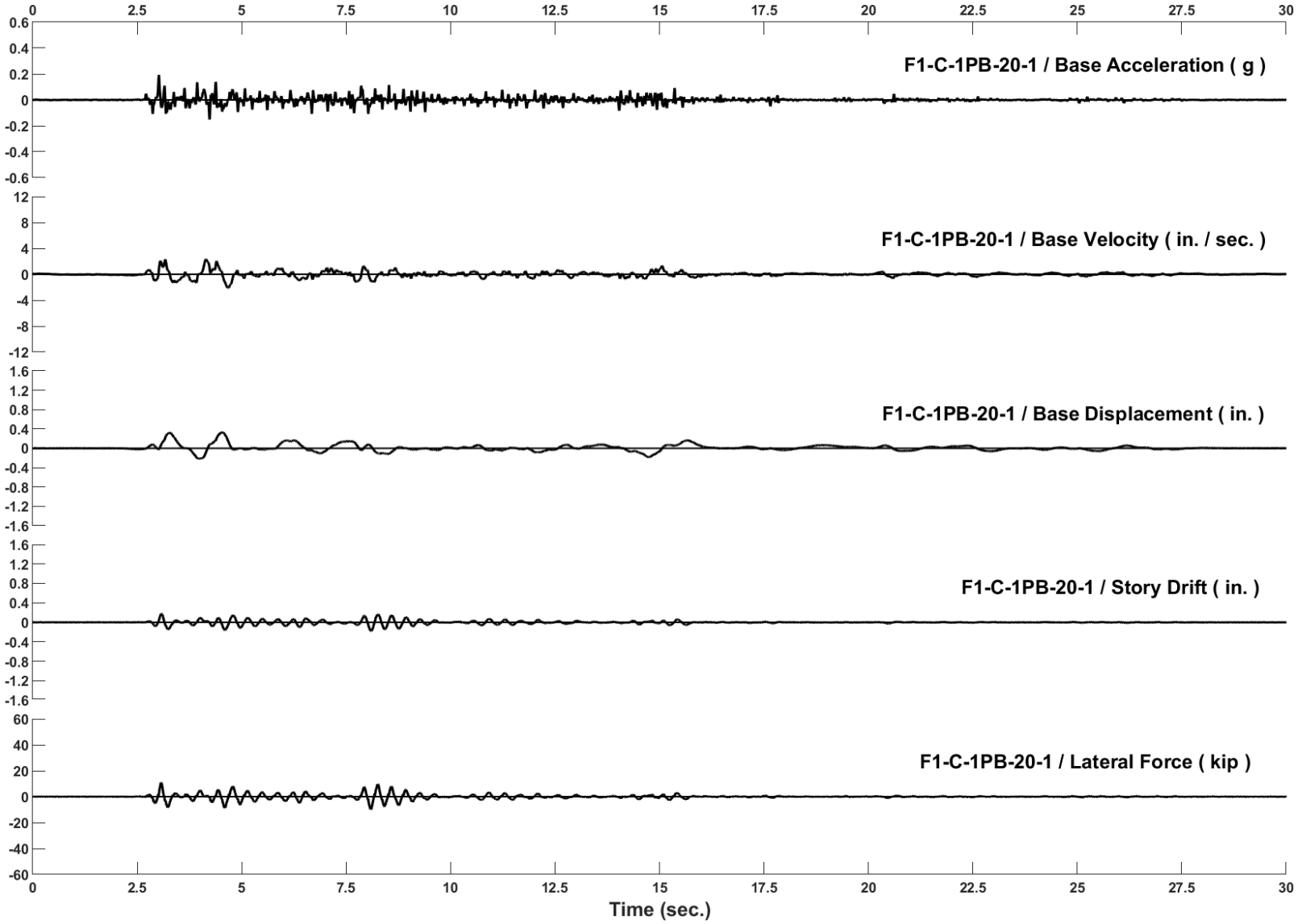

Figure D-43: Run 101, Frame 1, Structural Response and Base Motion History

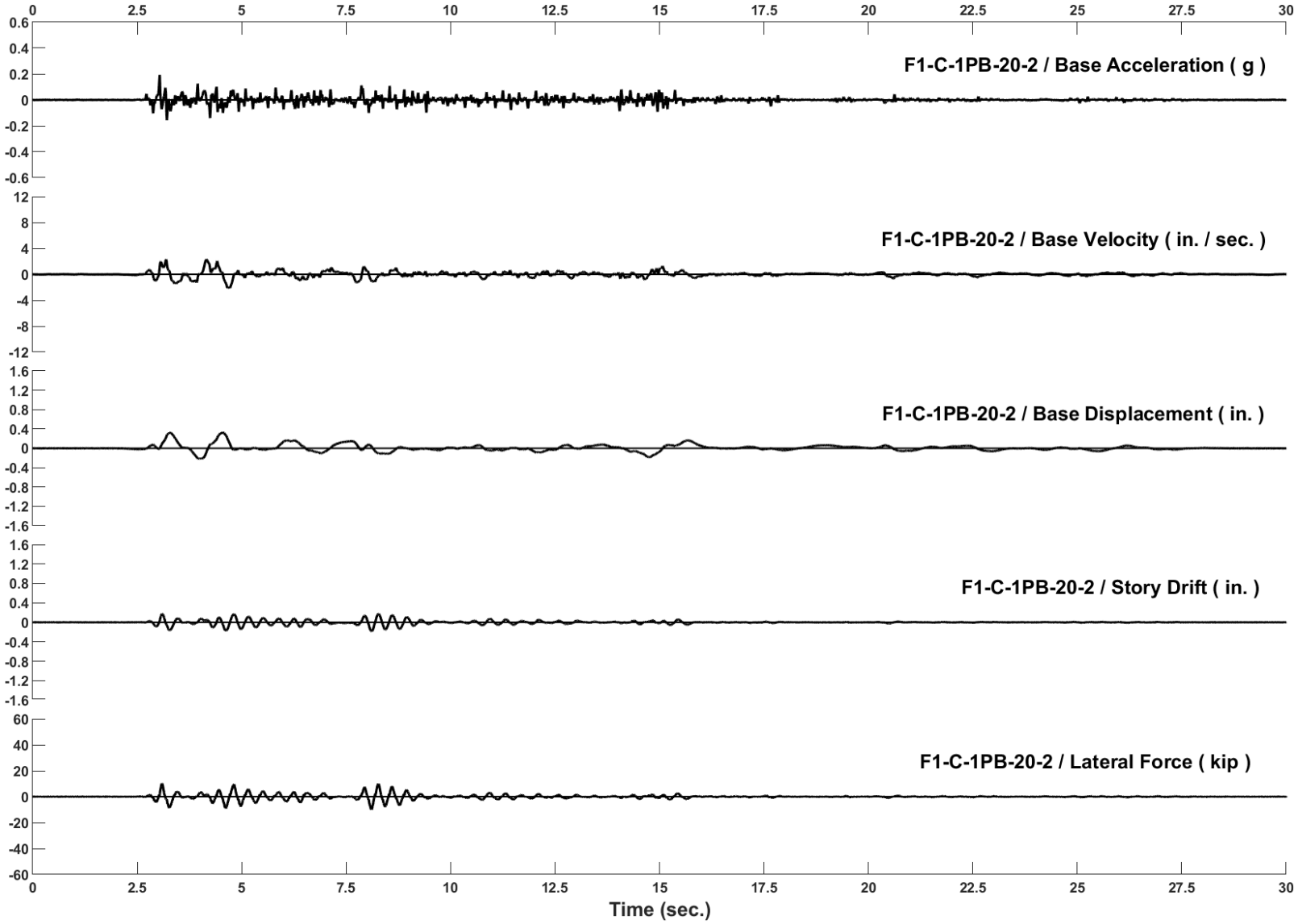

Figure D-44: Run 102, Frame 1, Structural Response and Base Motion History

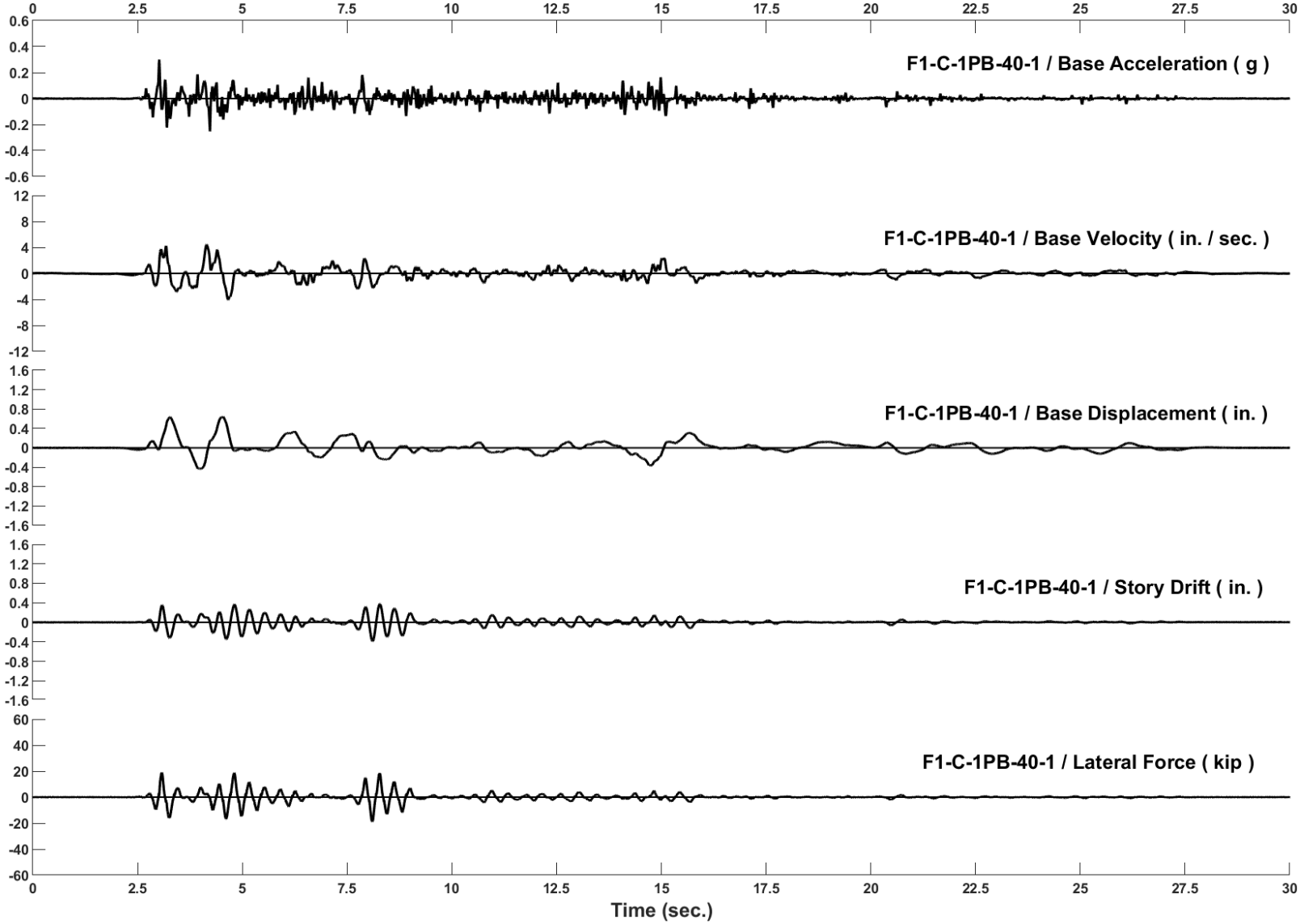

Figure D-45: Run 103, Frame 1, Structural Response and Base Motion History

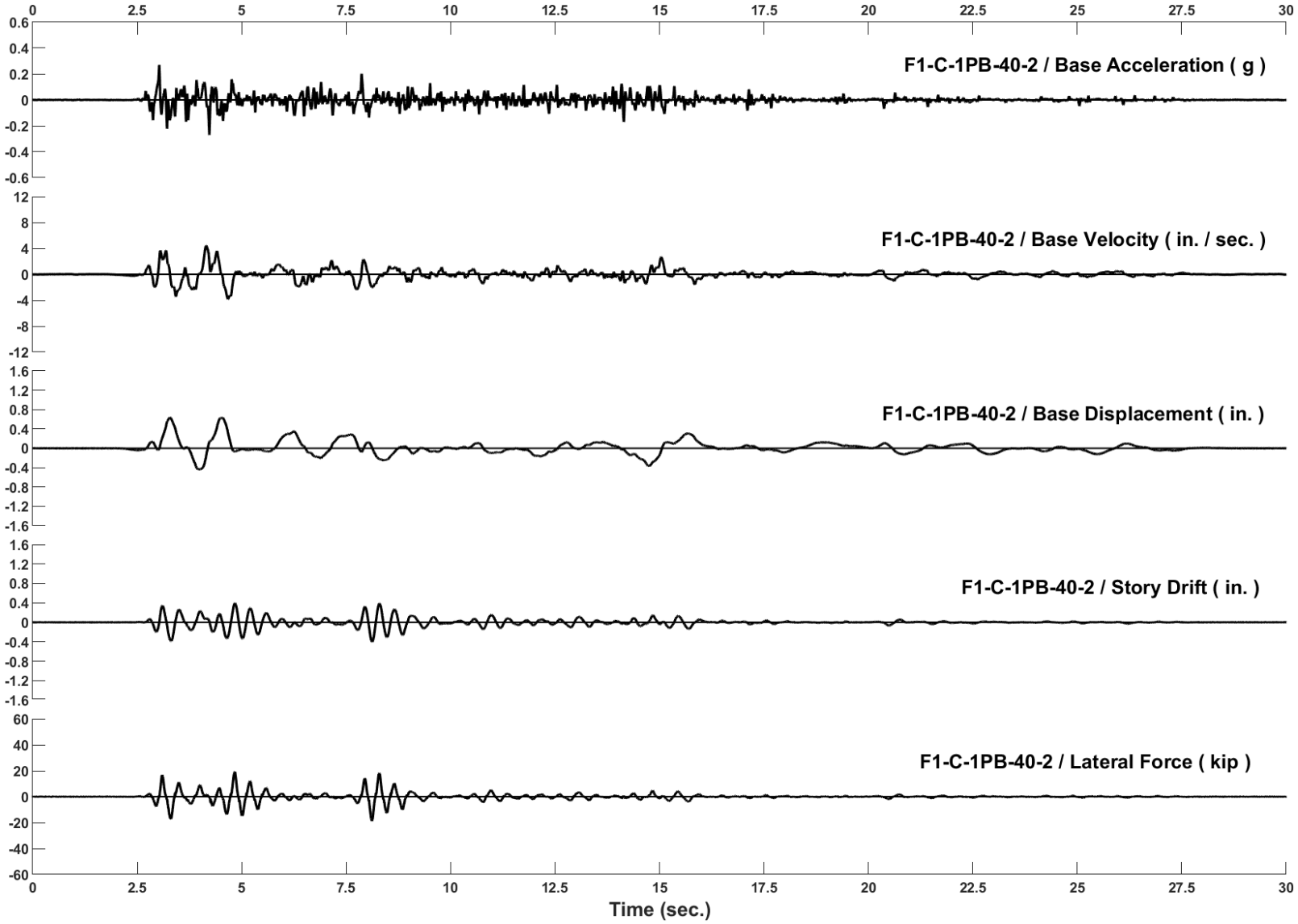

Figure D-46: Run 104, Frame 1, Structural Response and Base Motion History

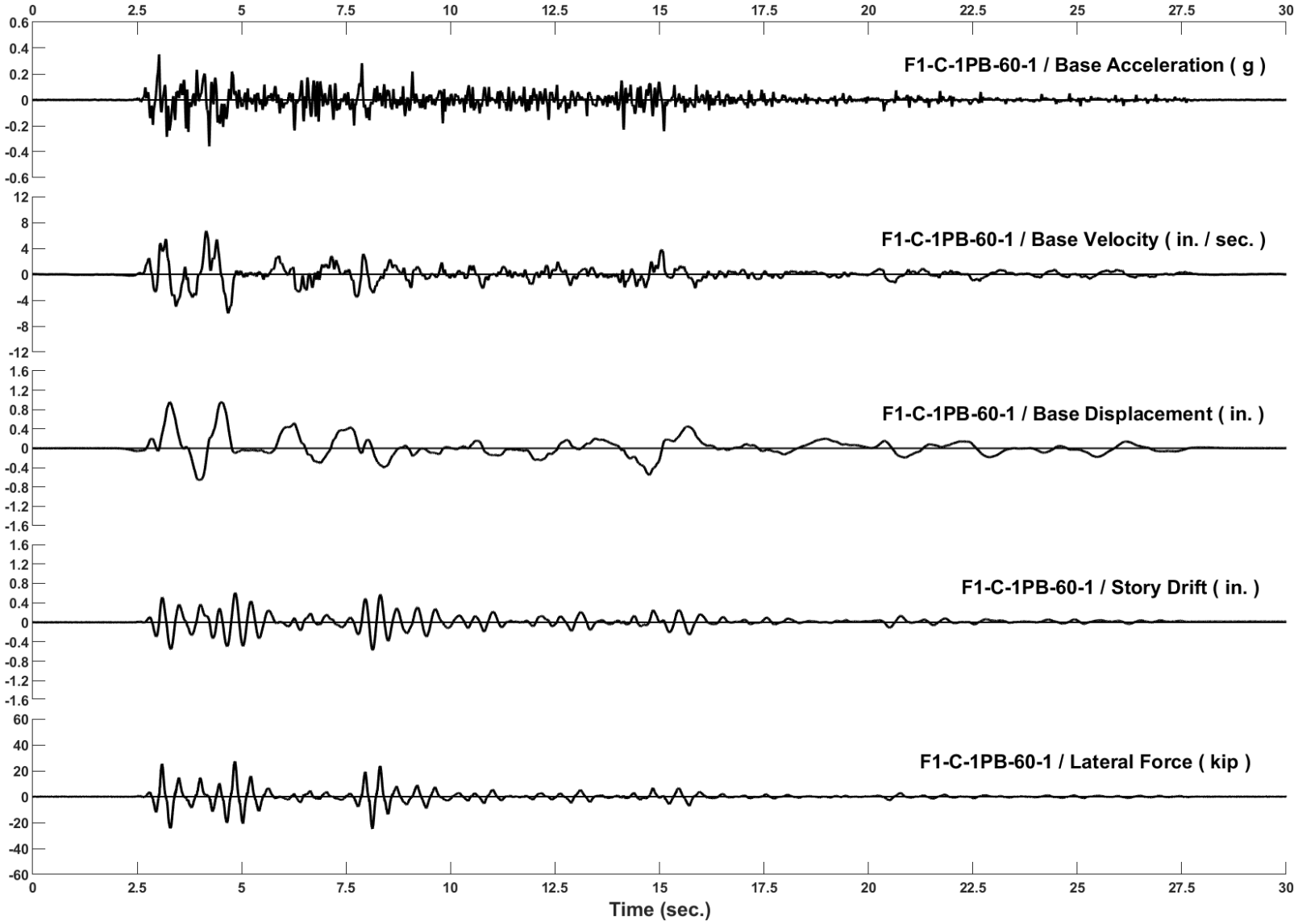

Figure D-47: Run 105, Frame 1, Structural Response and Base Motion History

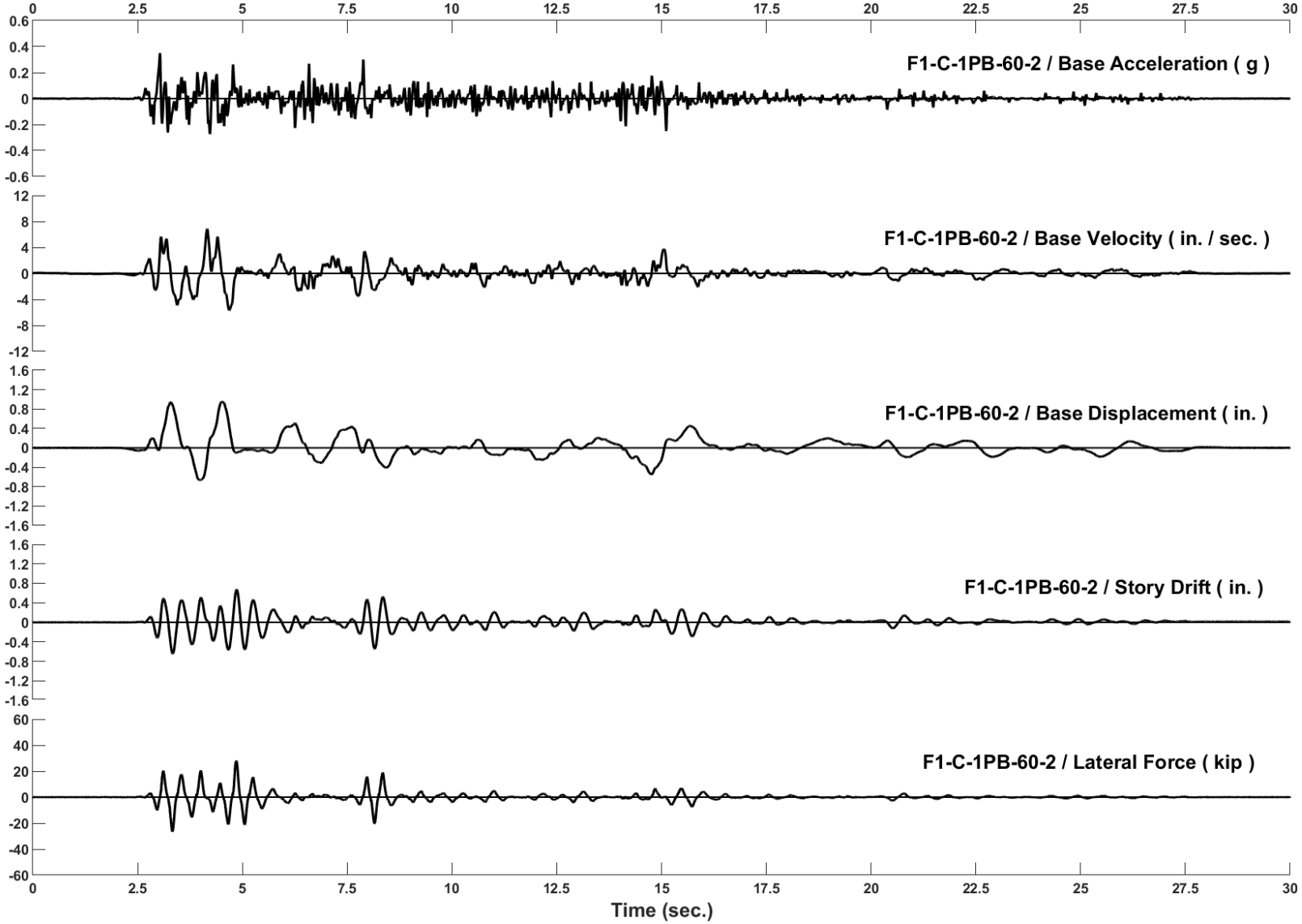

Figure D-48: Run 106, Frame 1, Structural Response and Base Motion History

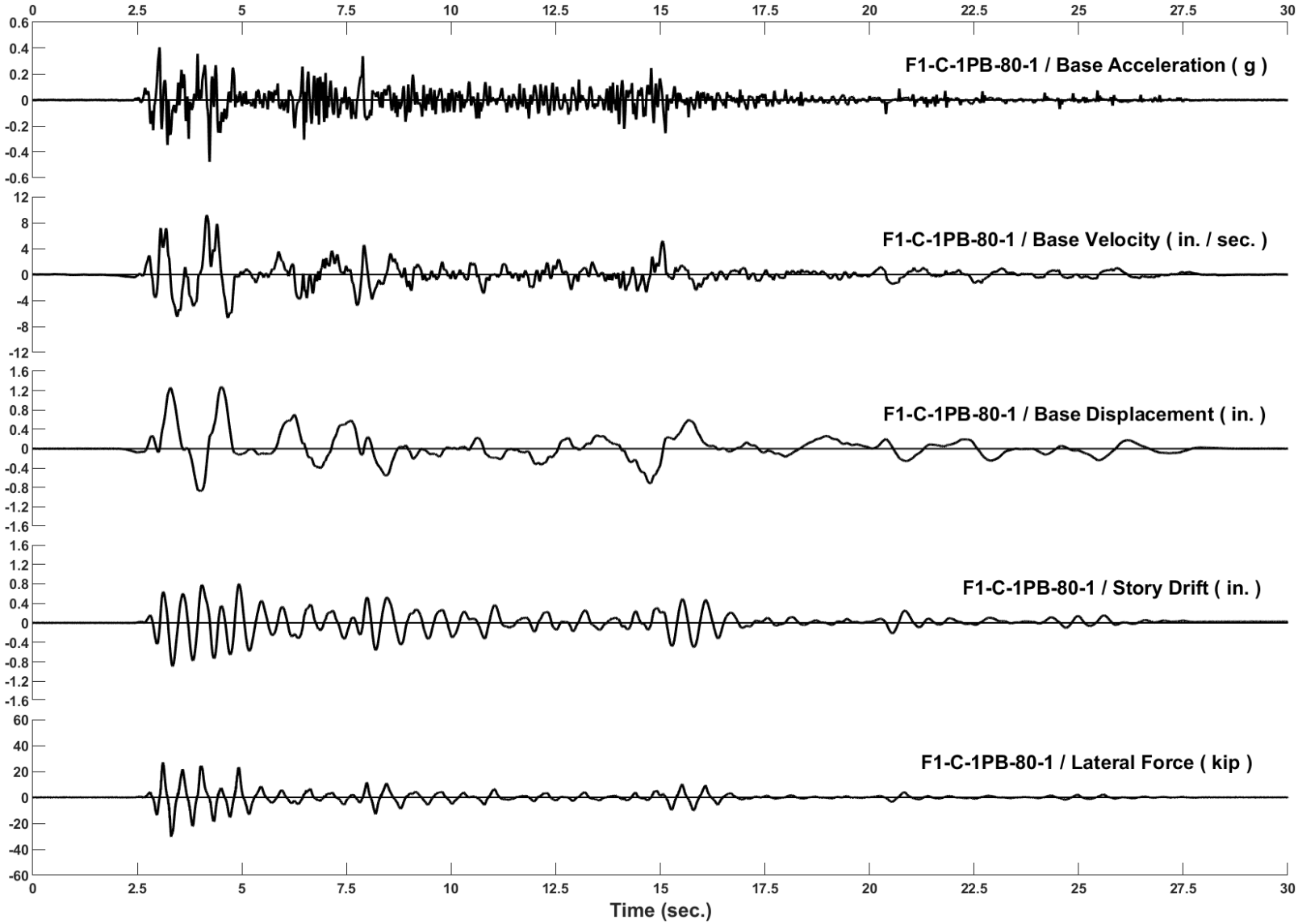

Figure D-49: Run 107, Frame 1, Structural Response and Base Motion History

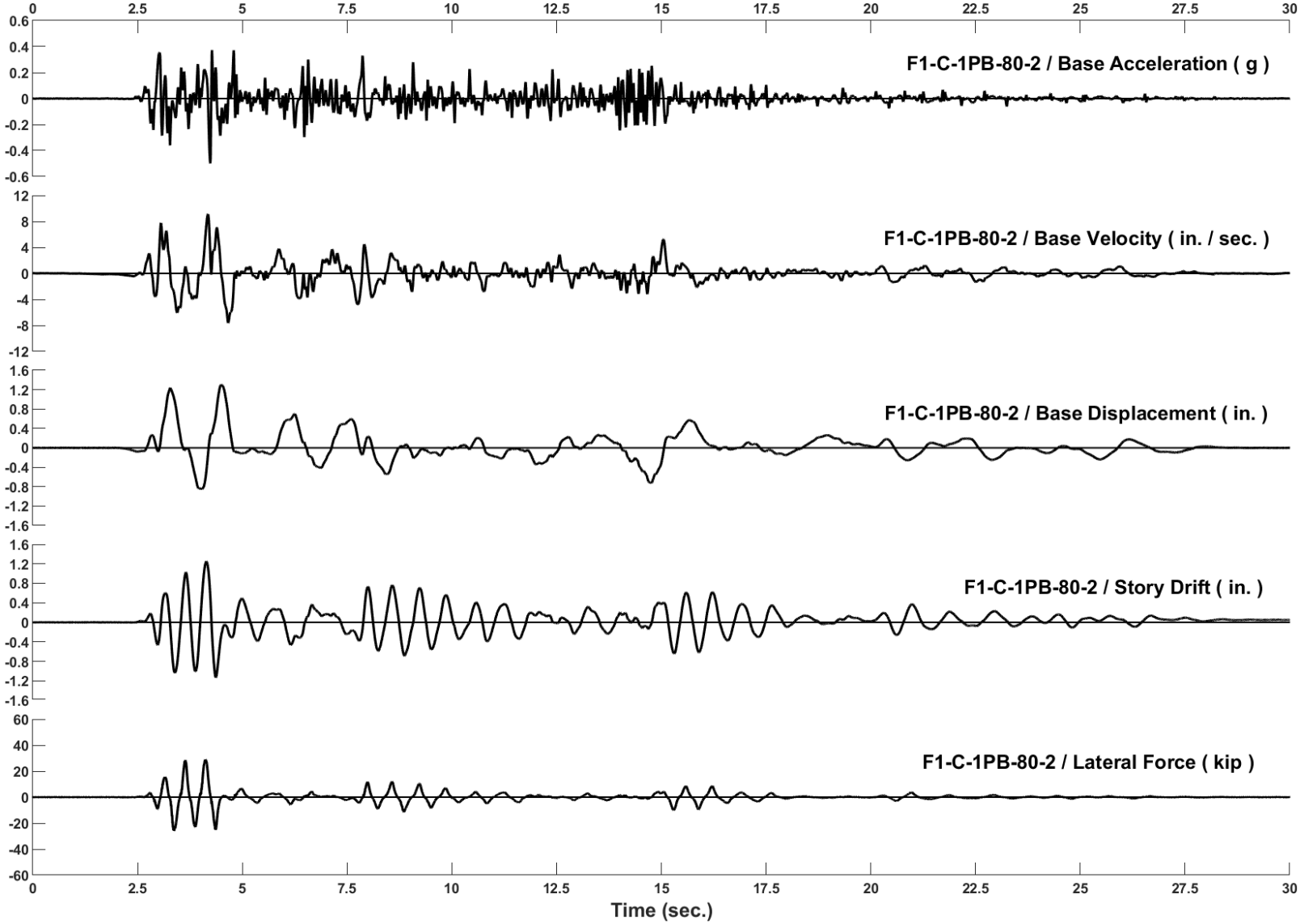

Figure D-50: Run 108, Frame 1, Structural Response and Base Motion History

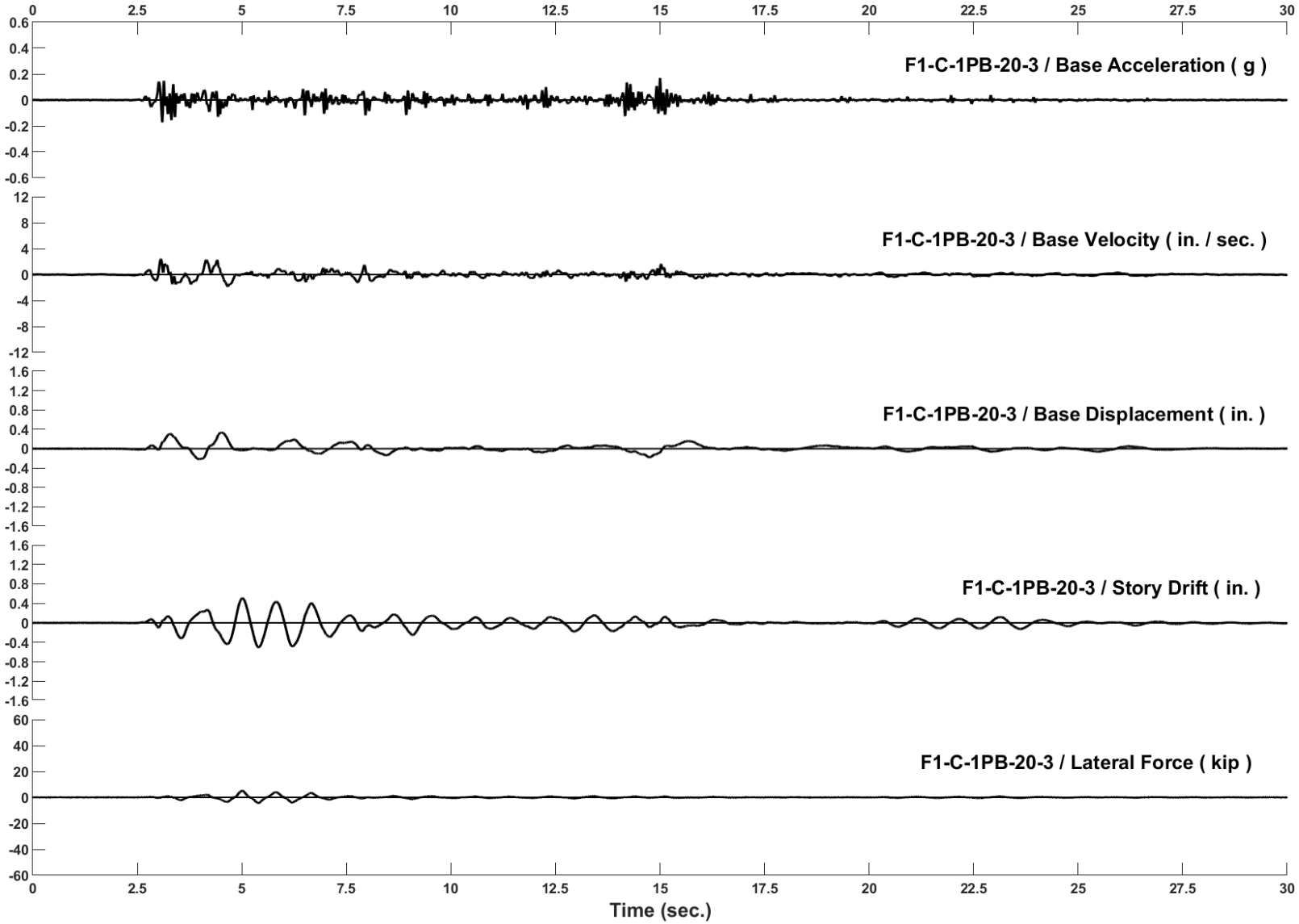

Figure D-51: Run 109, Frame 1, Structural Response and Base Motion History (infill removed)

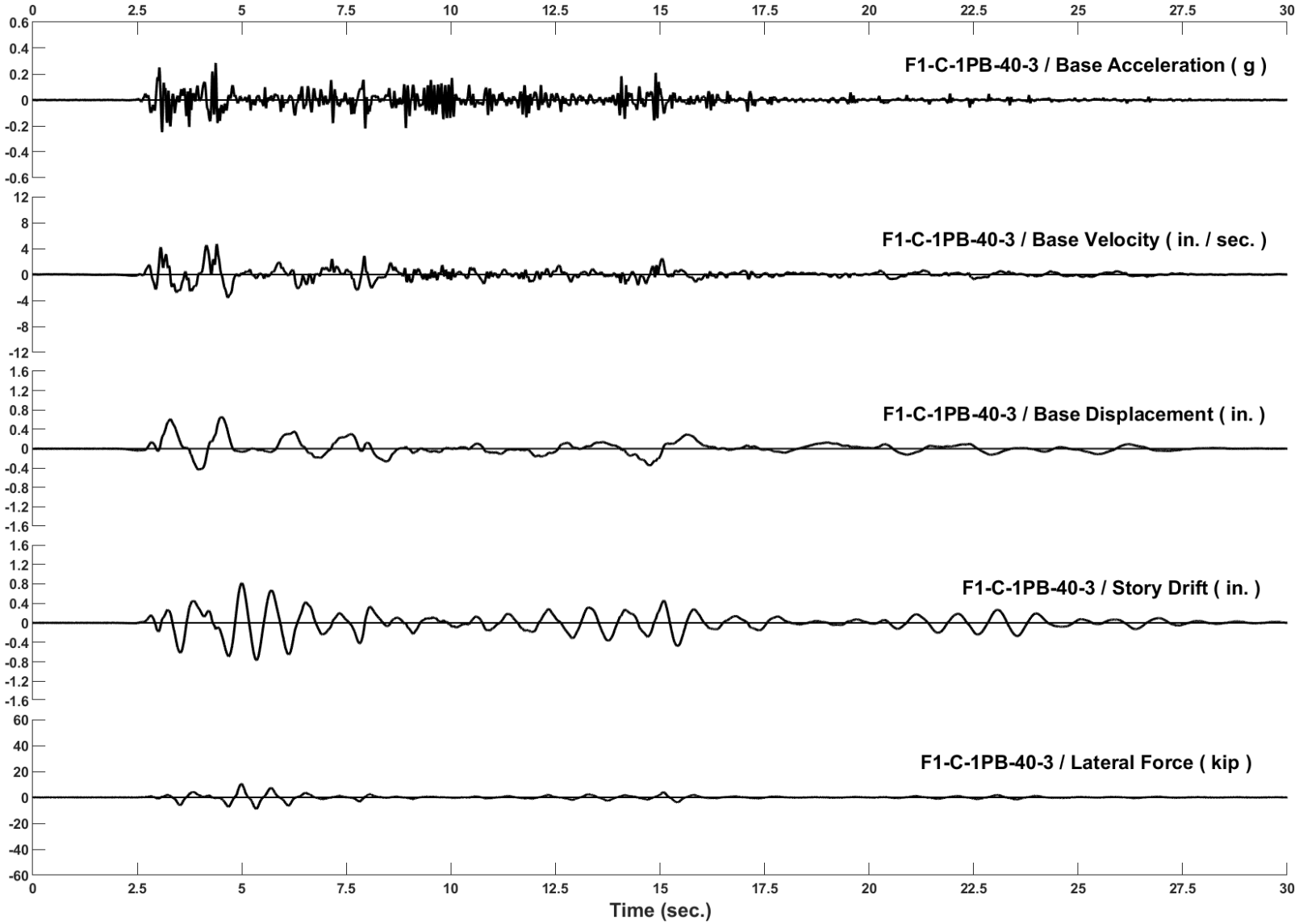

Figure D-52: Run 110, Frame 1, Structural Response and Base Motion History (infill removed)

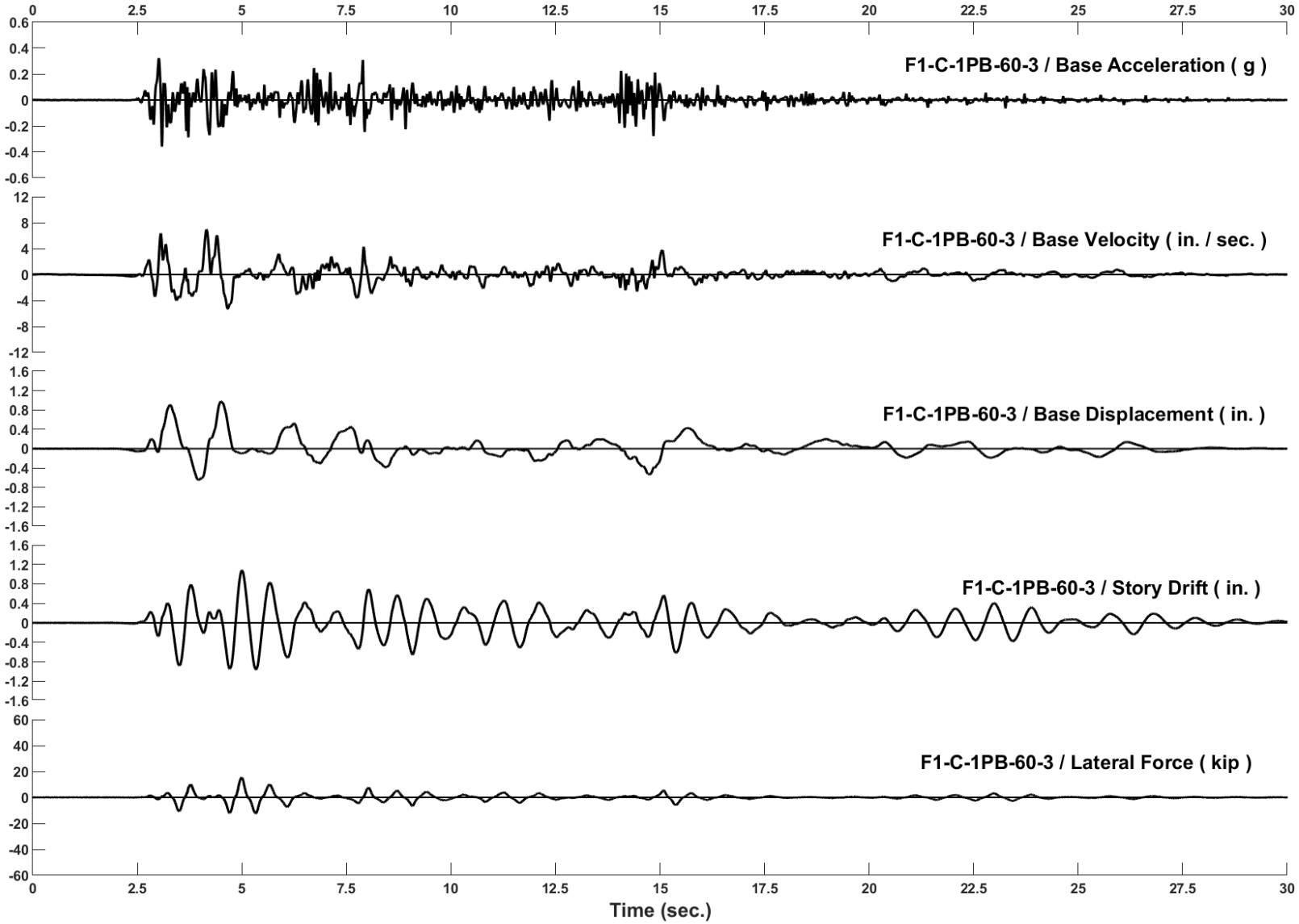

Figure D-53: Run 111, Frame 1, Structural Response and Base Motion History (infill removed)

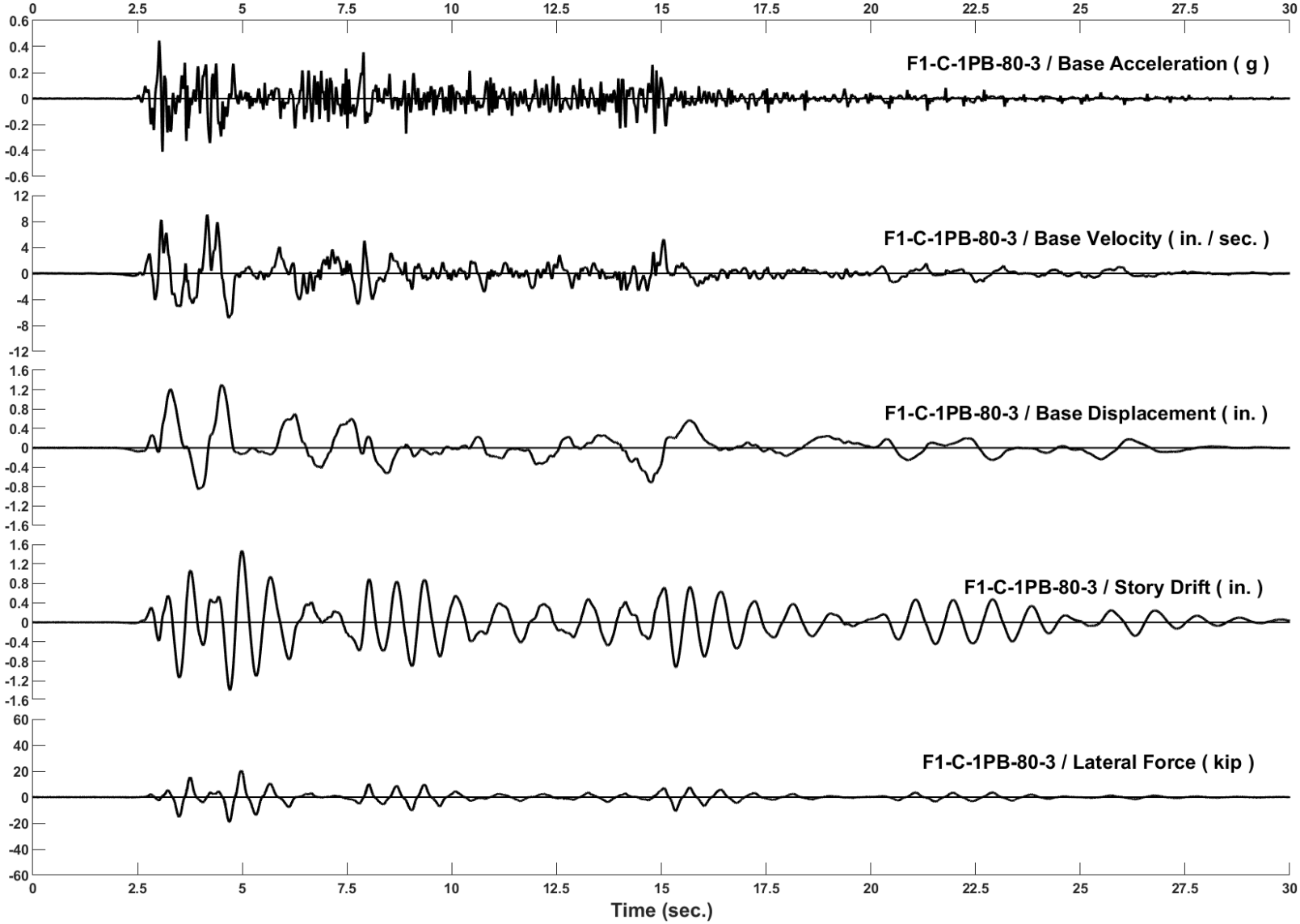

Figure D-54: Run 112, Frame 1, Structural Response and Base Motion History (infill removed)

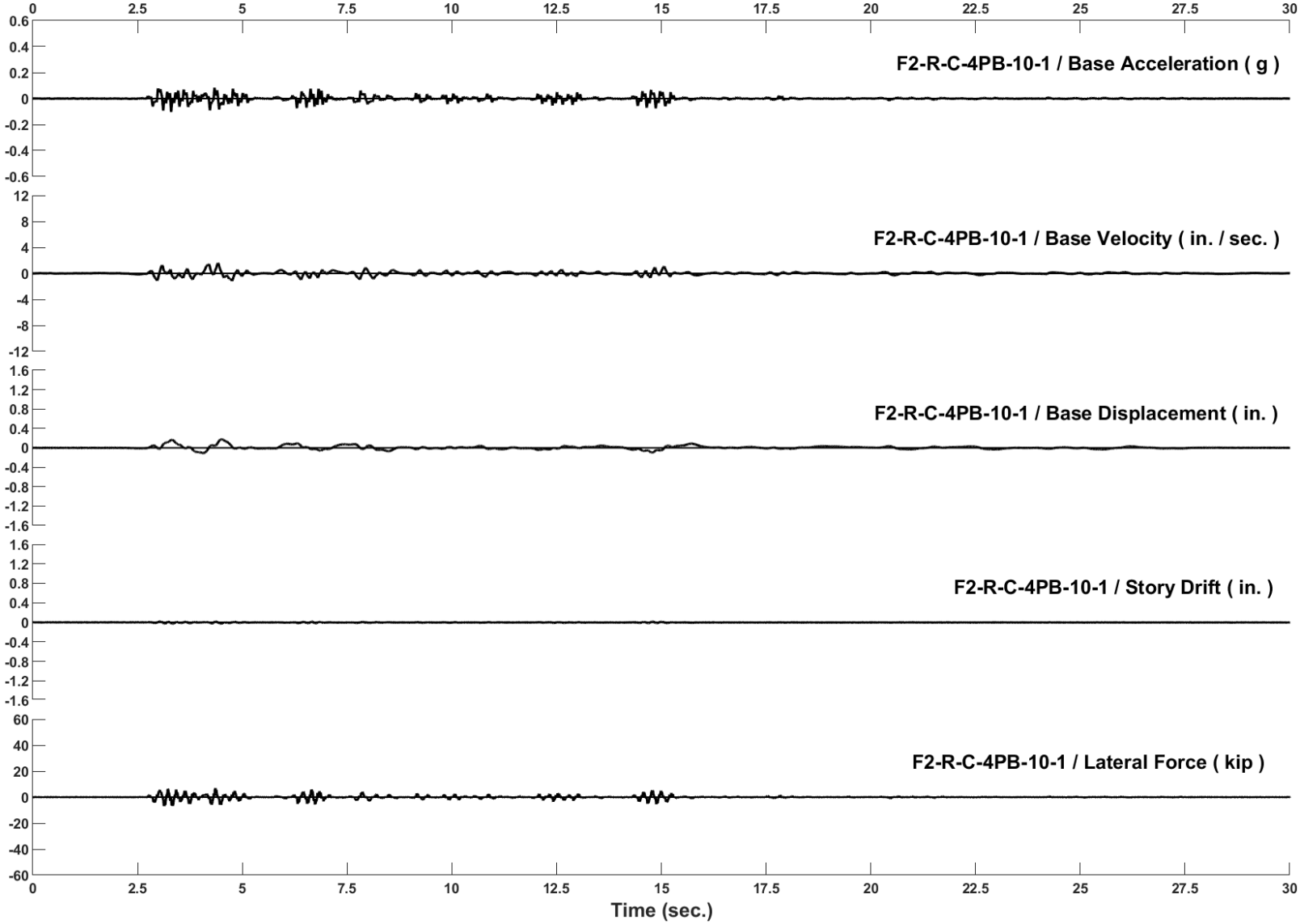

Figure D-55: Run 118, Frame 2, Structural Response and Base Motion History

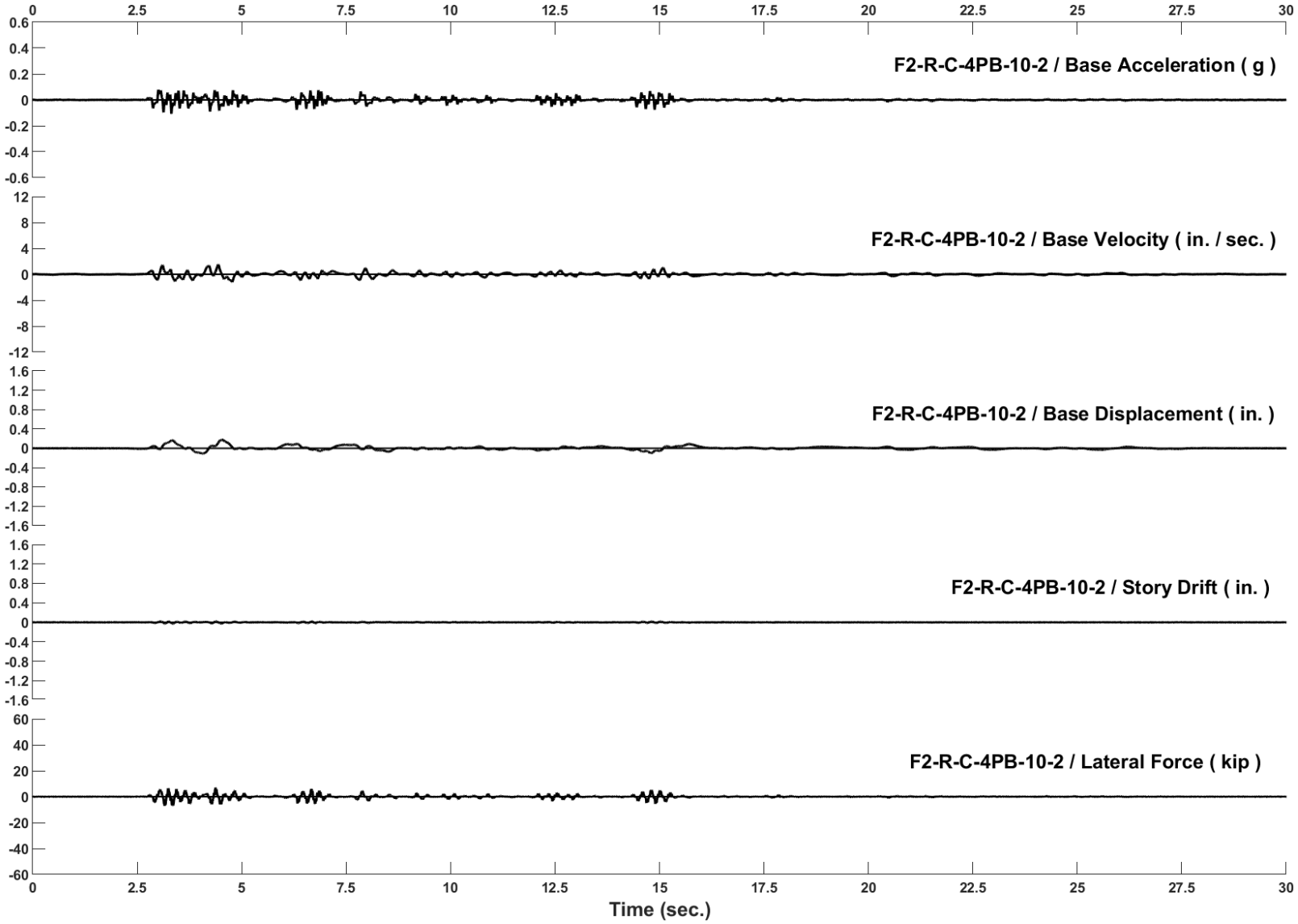

Figure D-56: Run 119, Frame 2, Structural Response and Base Motion History

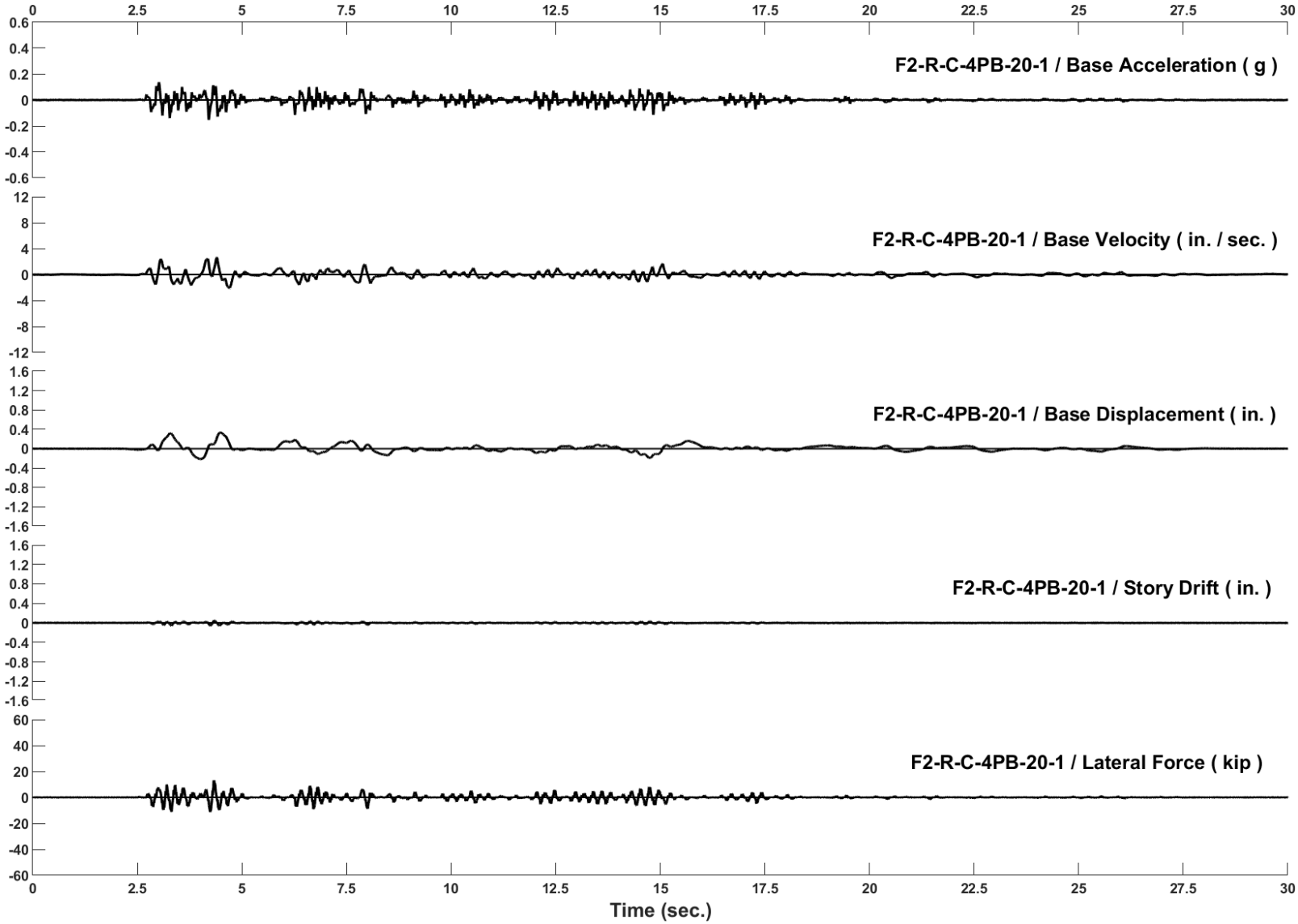

Figure D-57: Run 120, Frame 2, Structural Response and Base Motion History

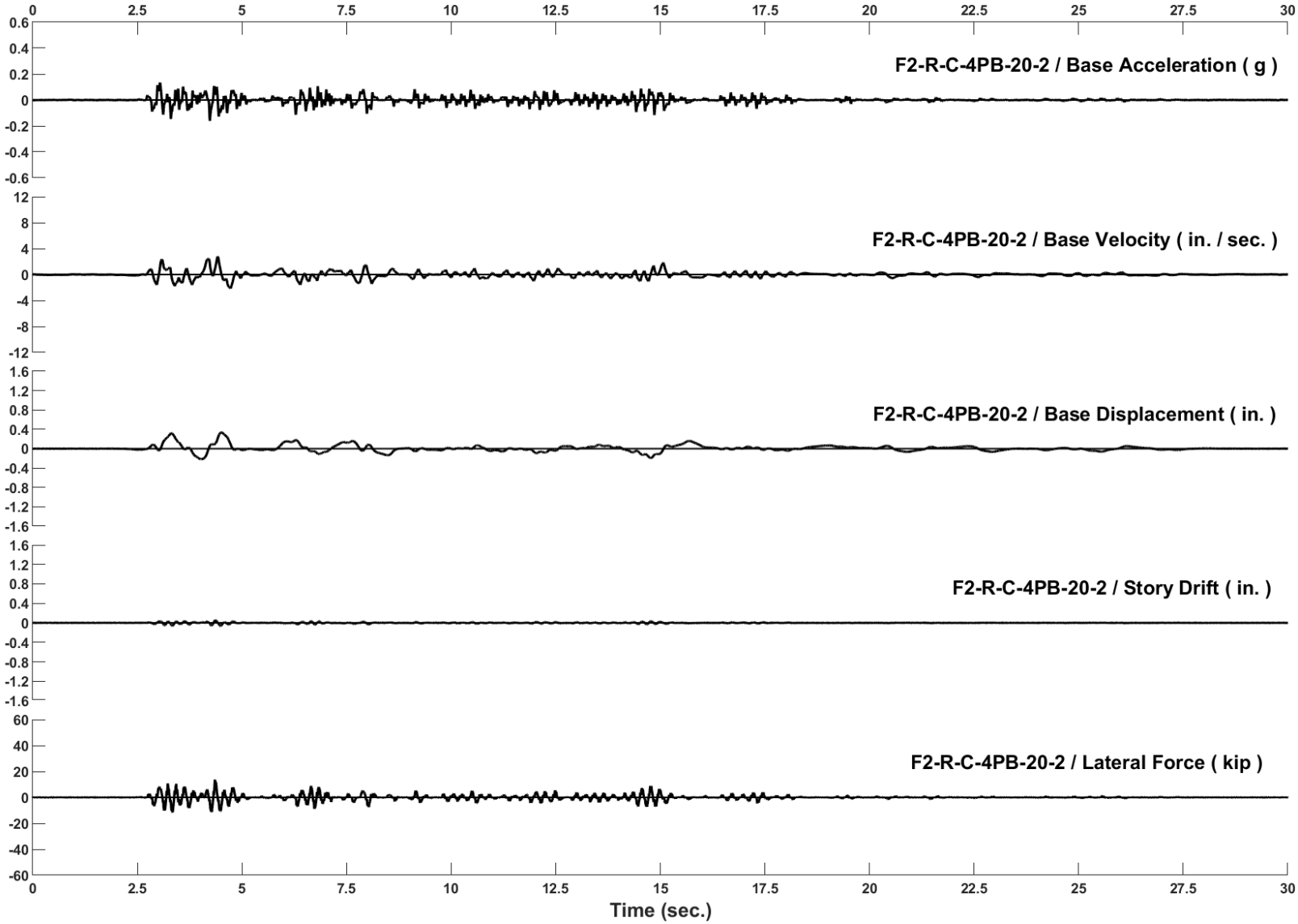

Figure D-58: Run 121, Frame 2, Structural Response and Base Motion History

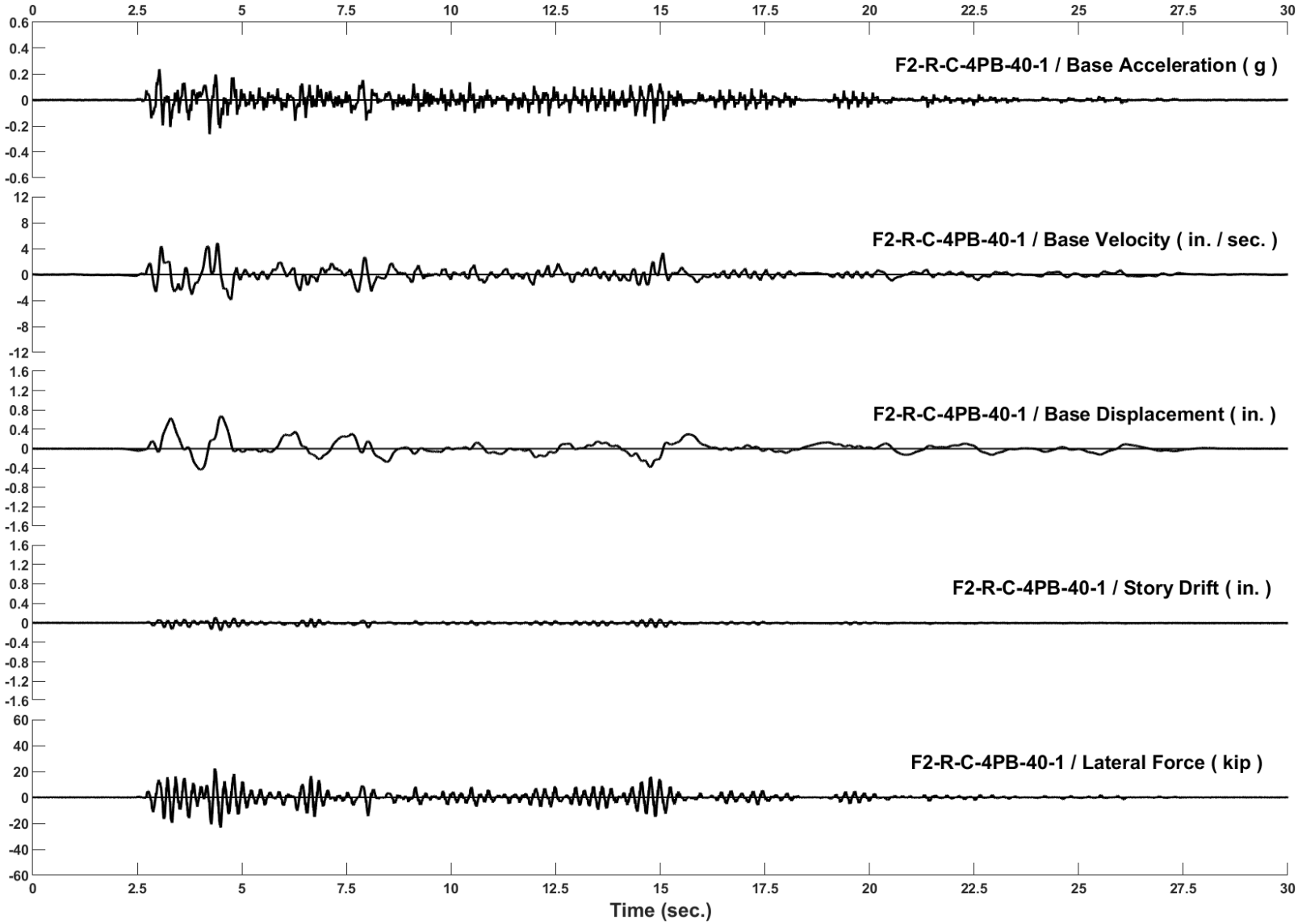

Figure D-59: Run 122, Frame 2, Structural Response and Base Motion History

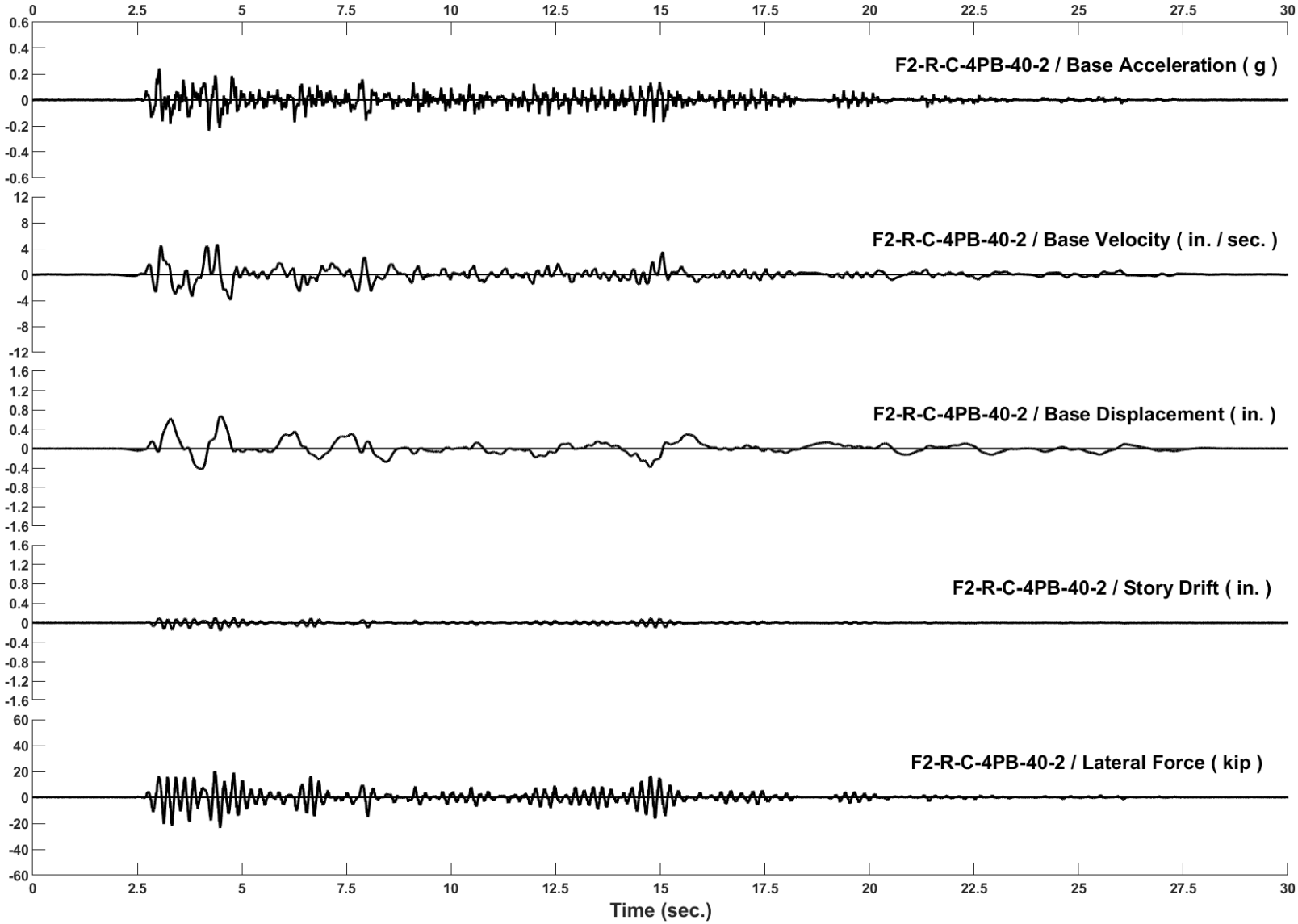

Figure D-60: Run 123, Frame 2, Structural Response and Base Motion History

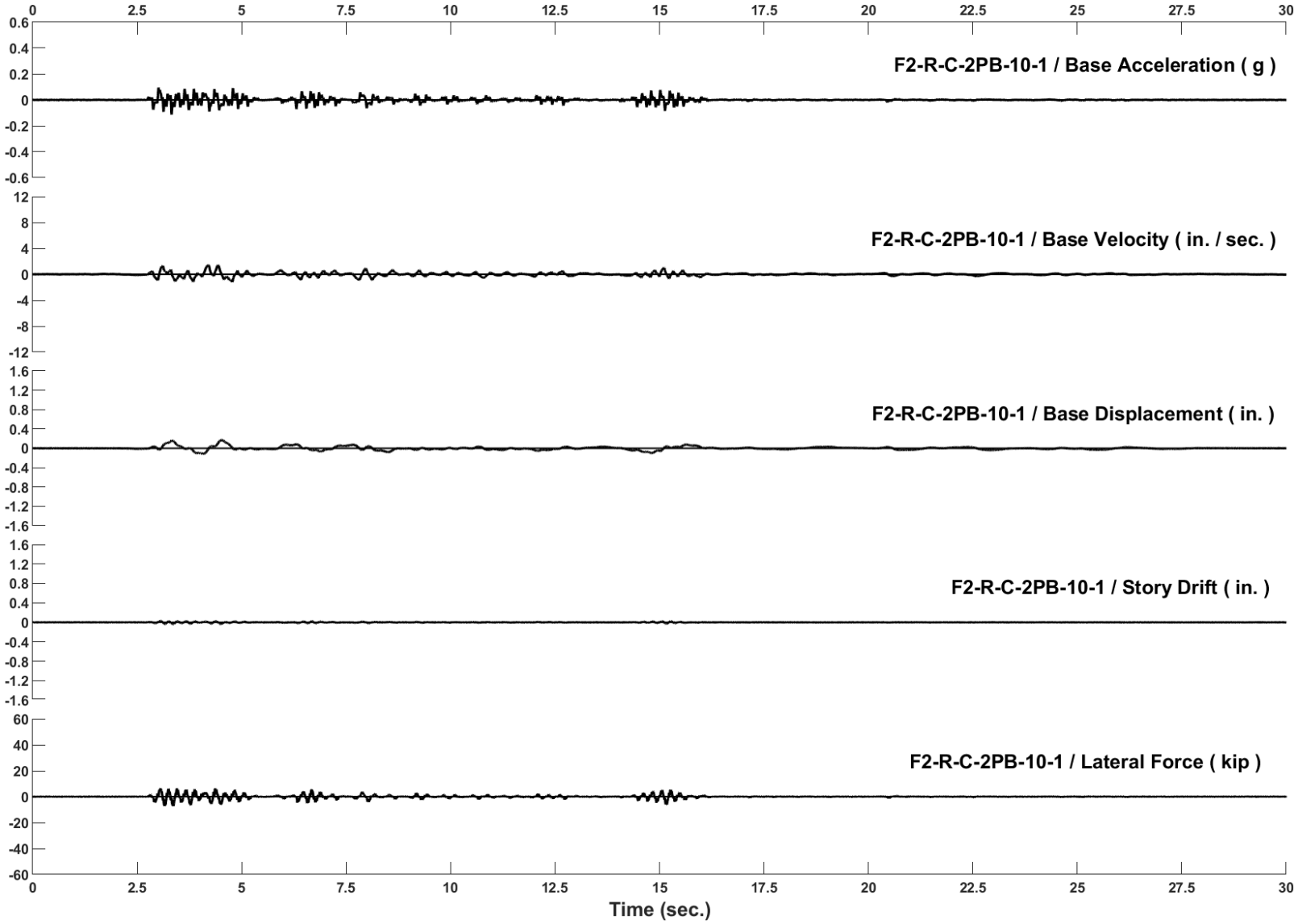

Figure D-61: Run 124, Frame 2, Structural Response and Base Motion History

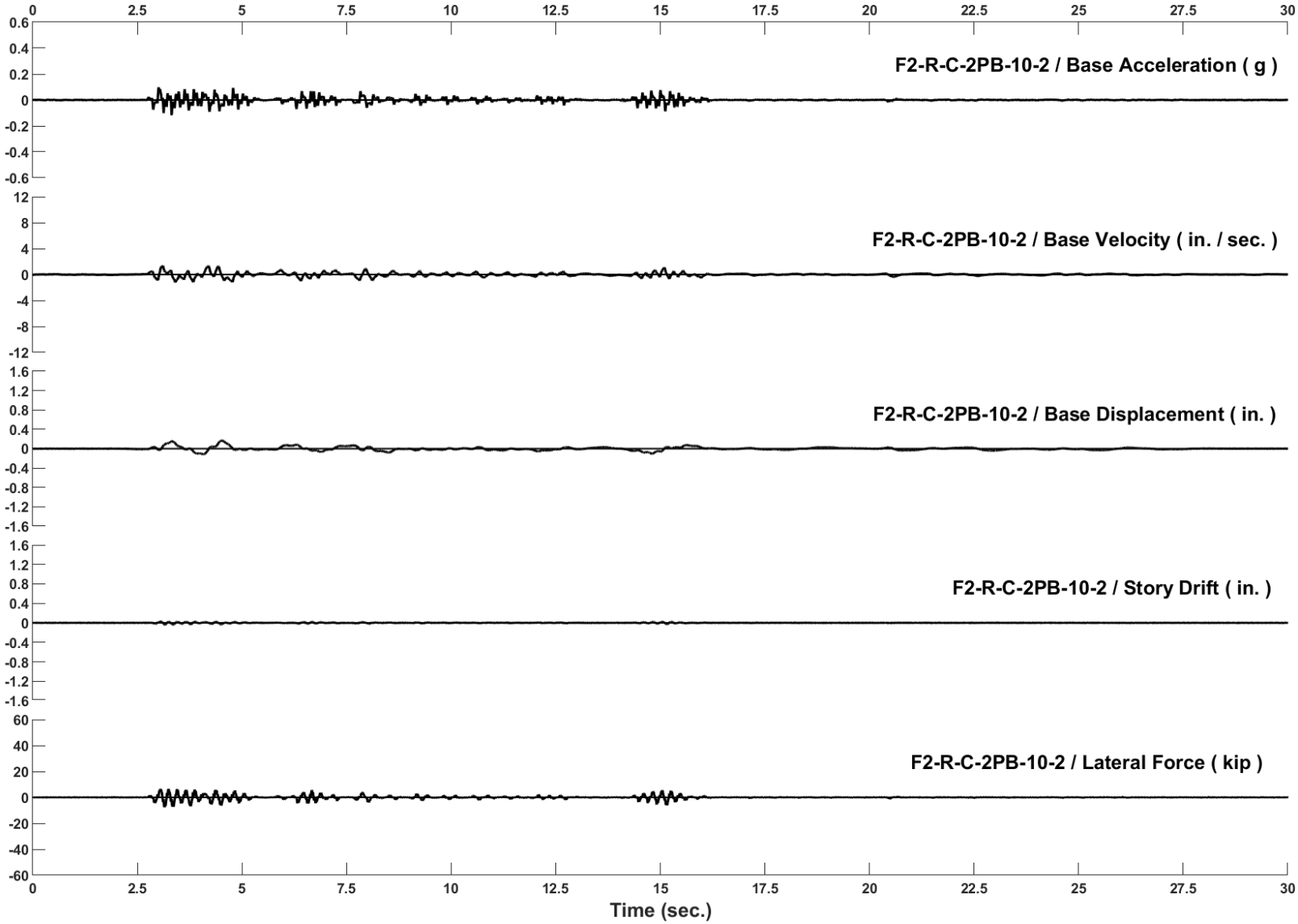

Figure D-62: Run 125, Frame 2, Structural Response and Base Motion History

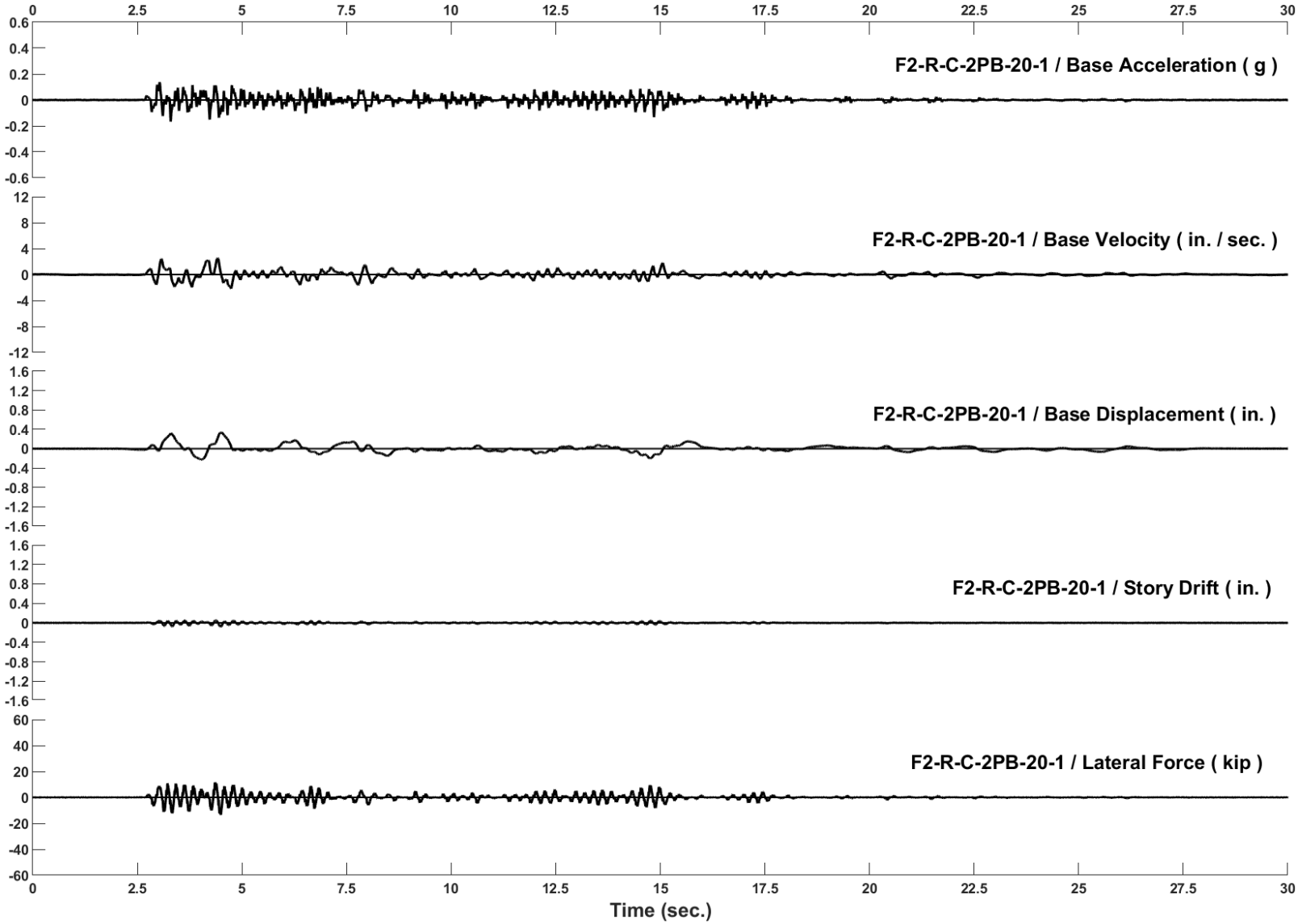

Figure D-63: Run 126, Frame 2, Structural Response and Base Motion History

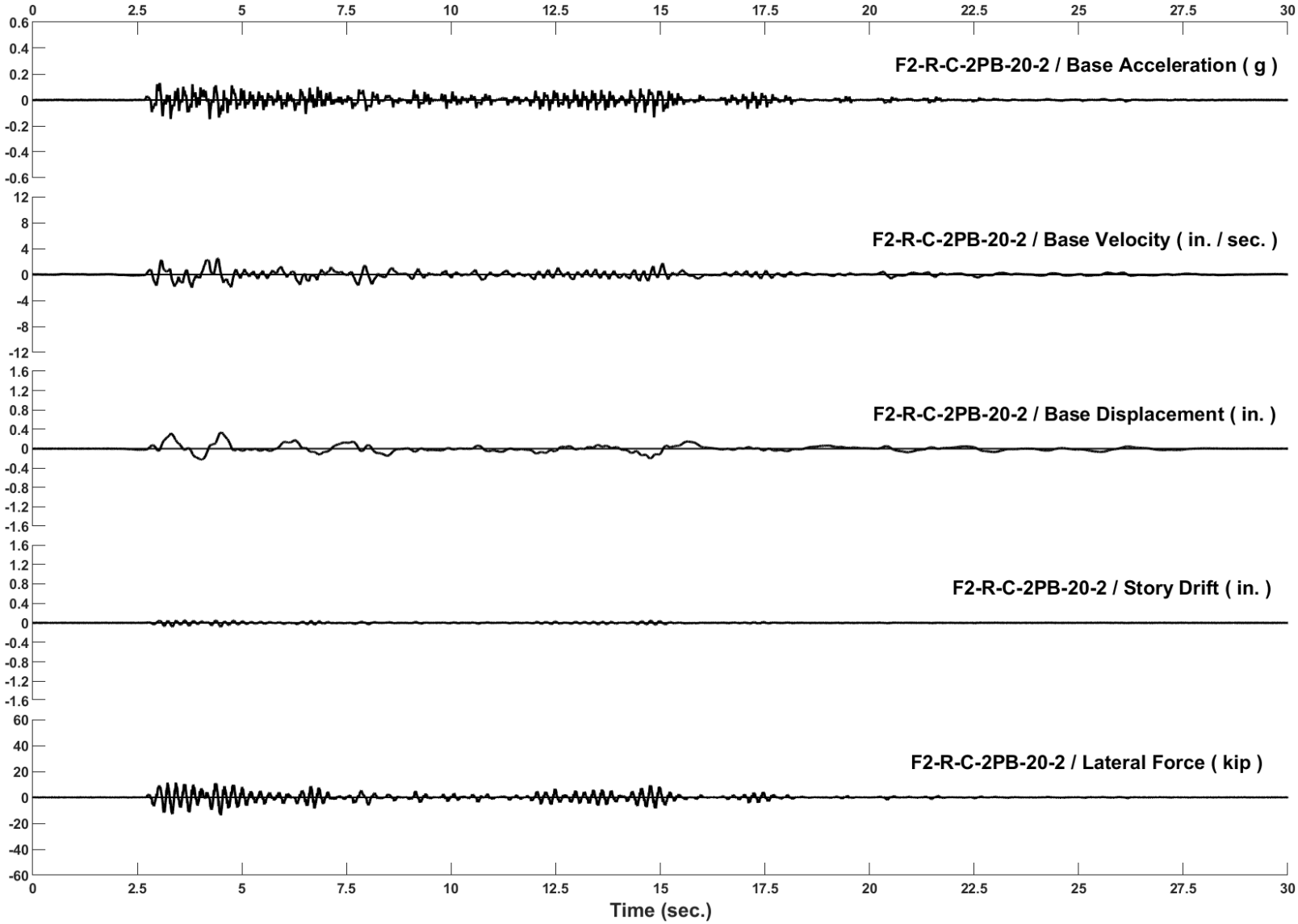

Figure D-64: Run 127, Frame 2, Structural Response and Base Motion History

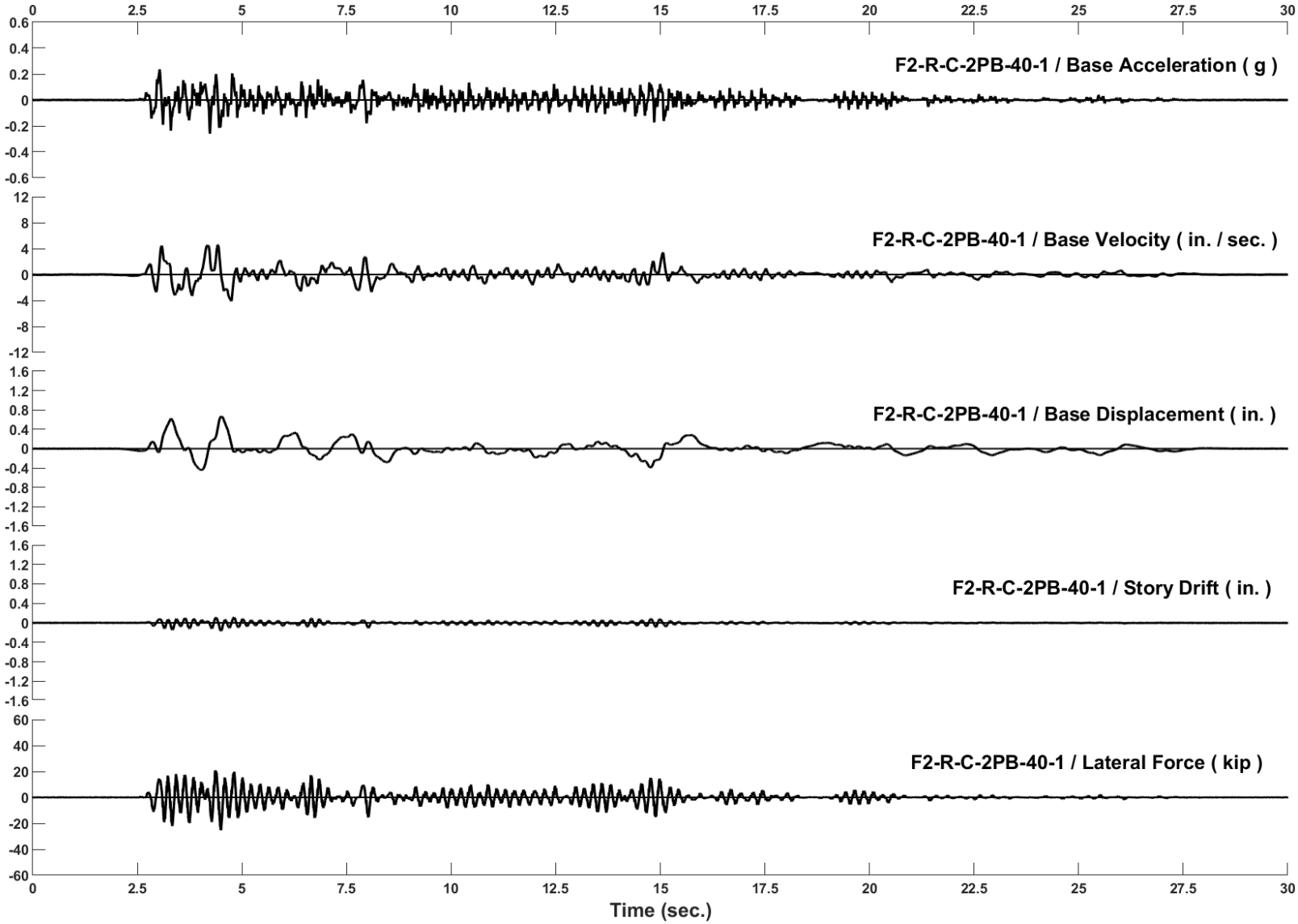

Figure D-65: Run 128, Frame 2, Structural Response and Base Motion History

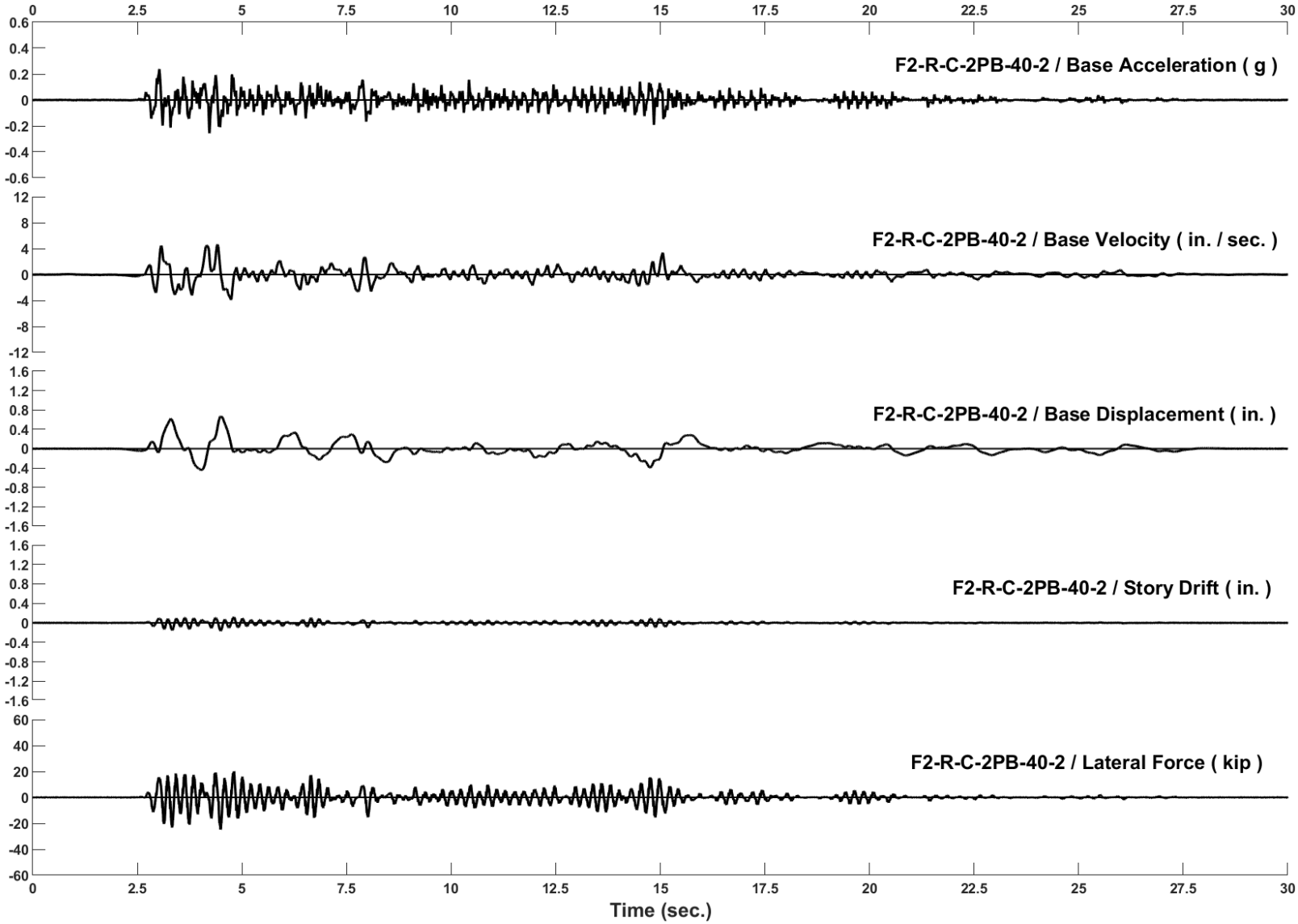

Figure D-66: Run 129, Frame 2, Structural Response and Base Motion History

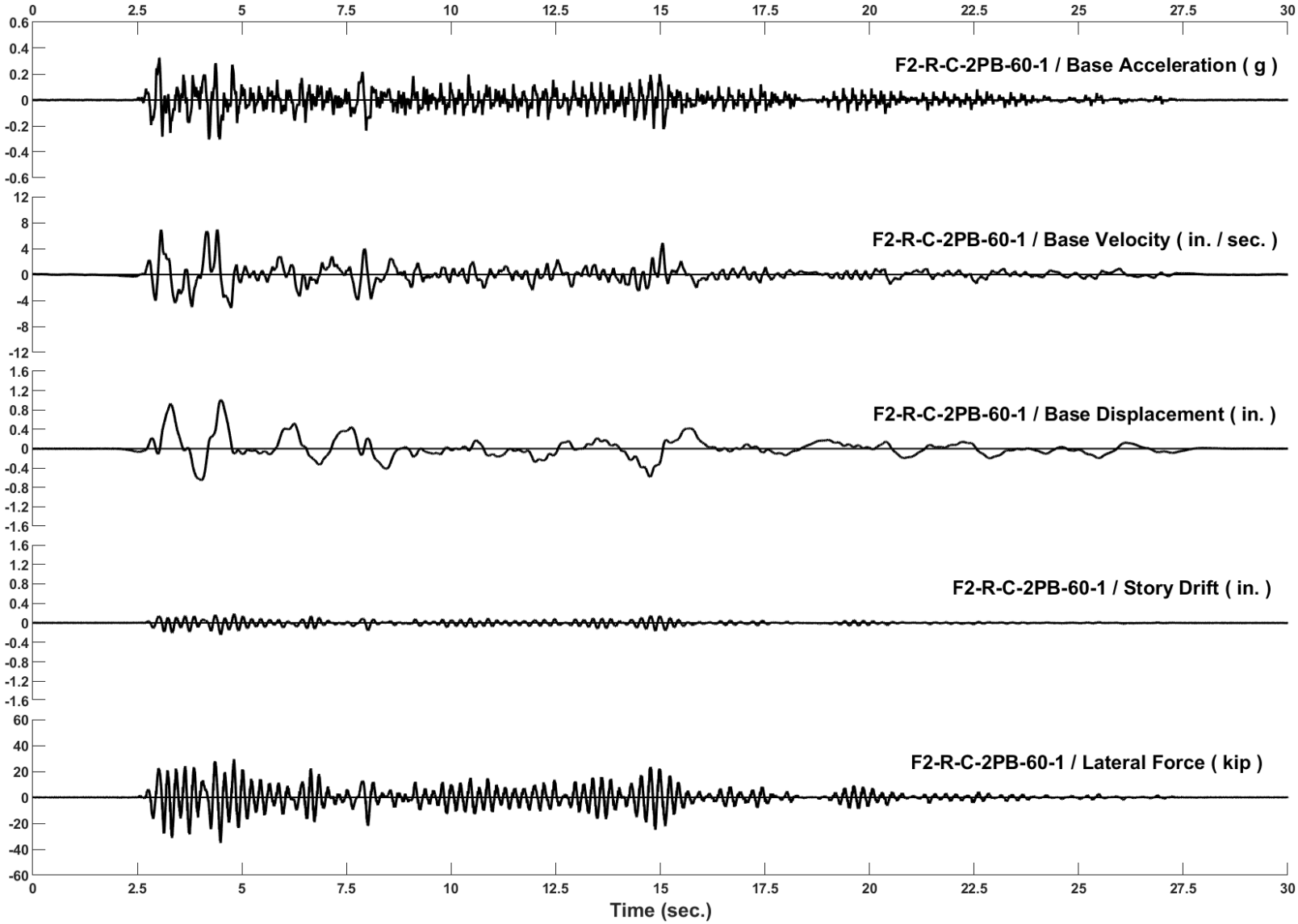

Figure D-67: Run 130, Frame 2, Structural Response and Base Motion History

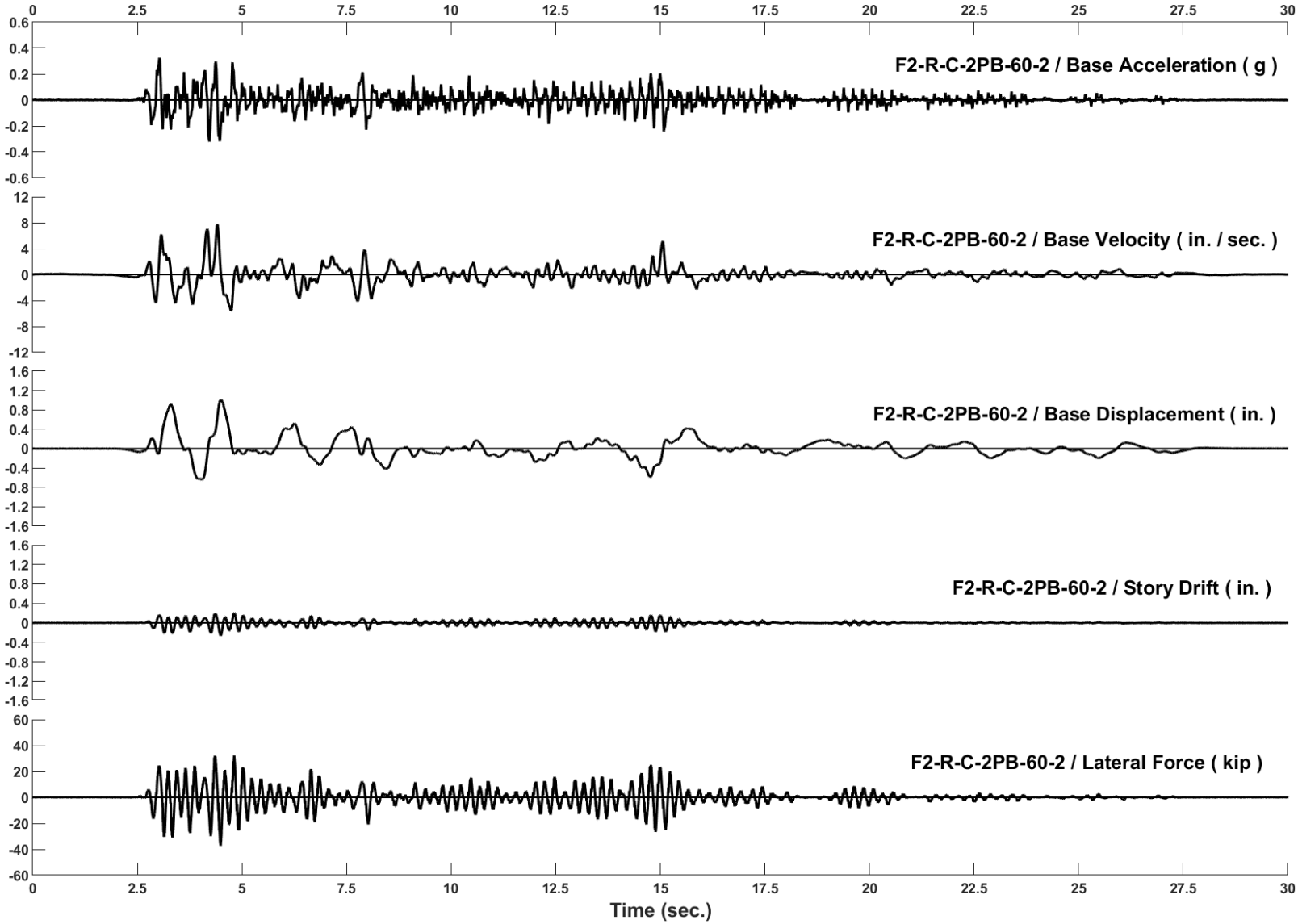

Figure D-68: Run 131, Frame 2, Structural Response and Base Motion History

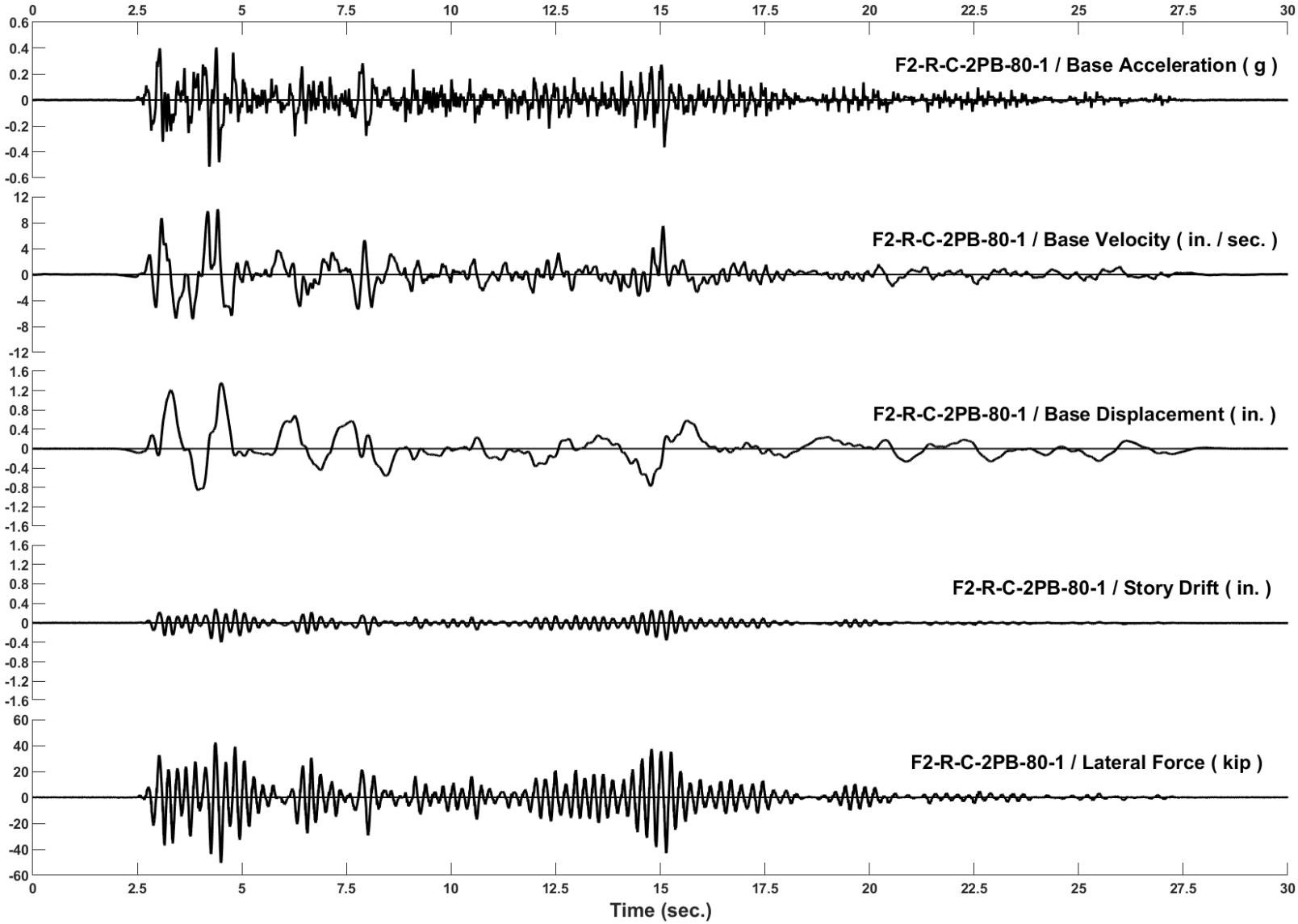

Figure D-69: Run 132, Frame 2, Structural Response and Base Motion History

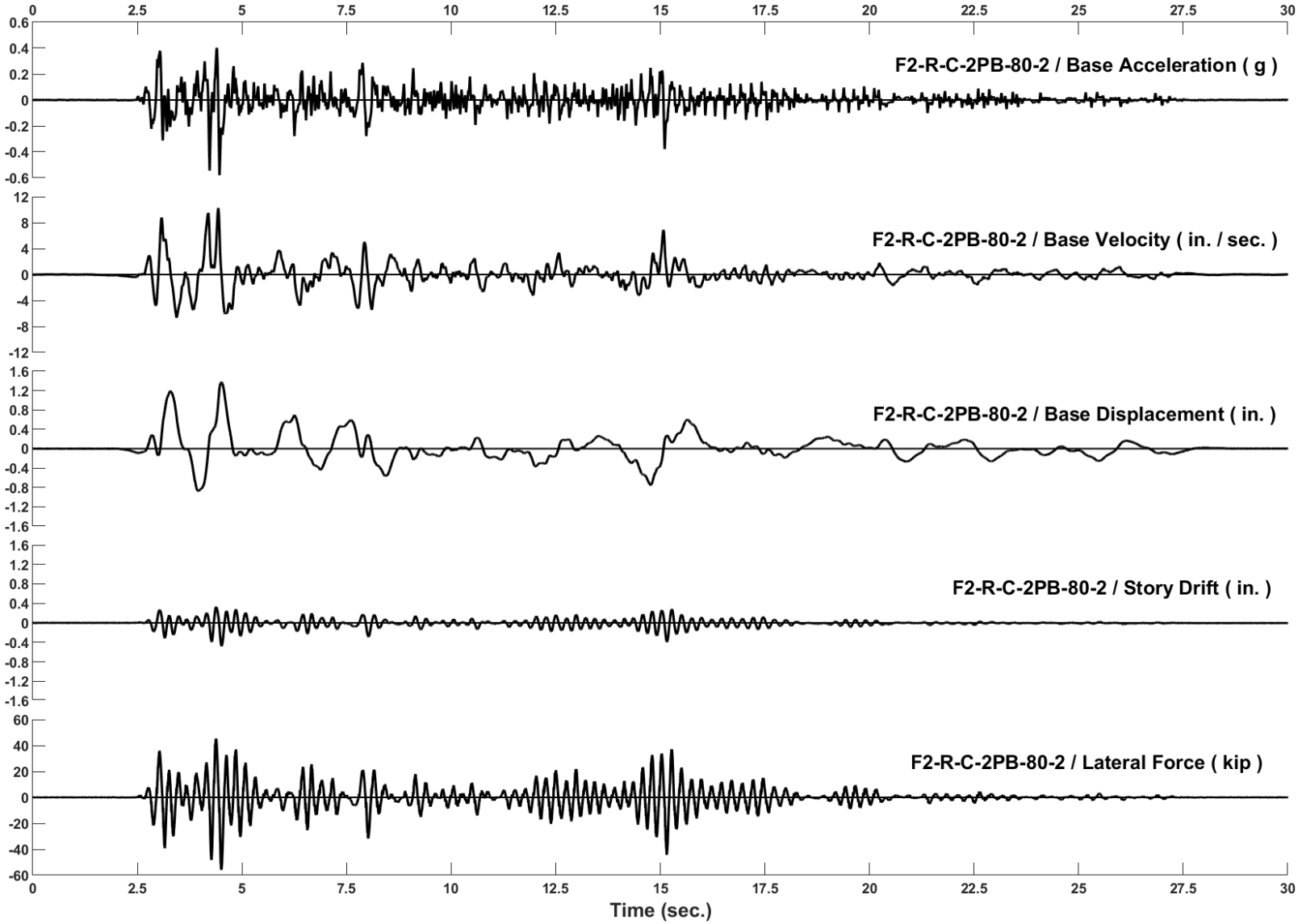

Figure D-70: Run 133, Frame 2, Structural Response and Base Motion History

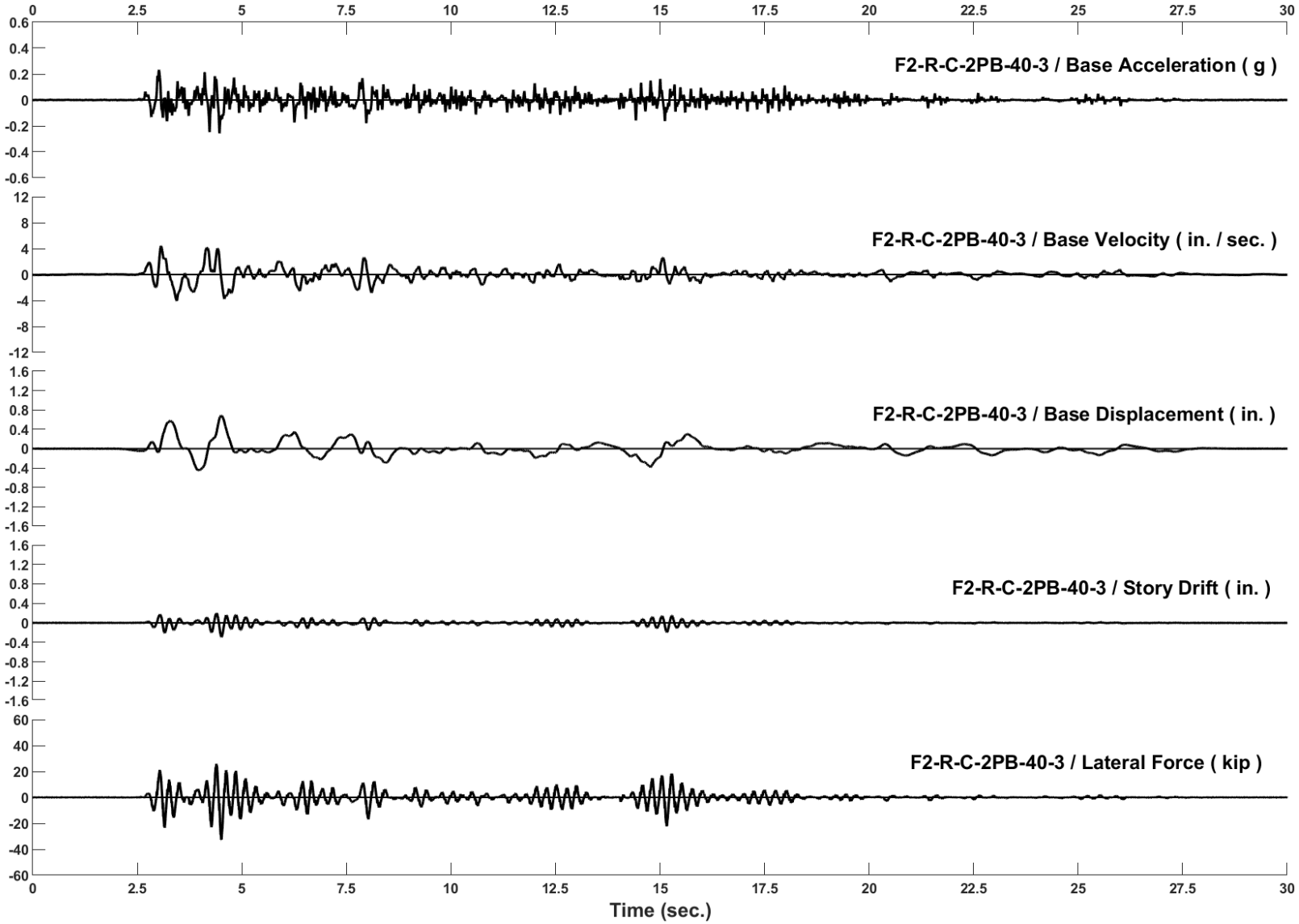

Figure D-71: Run 134, Frame 2, Structural Response and Base Motion History

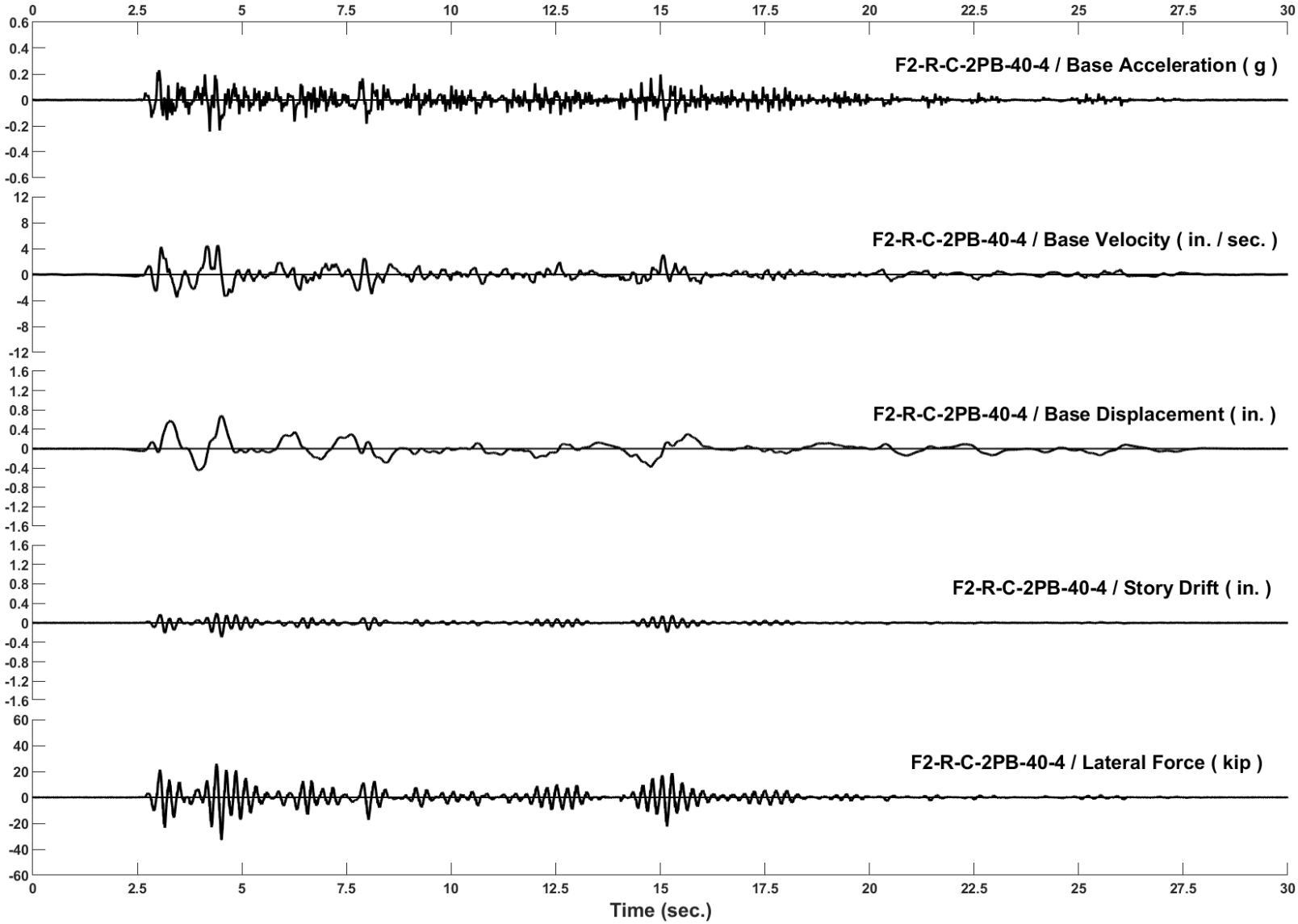

Figure D-72: Run 135, Frame 2, Structural Response and Base Motion History

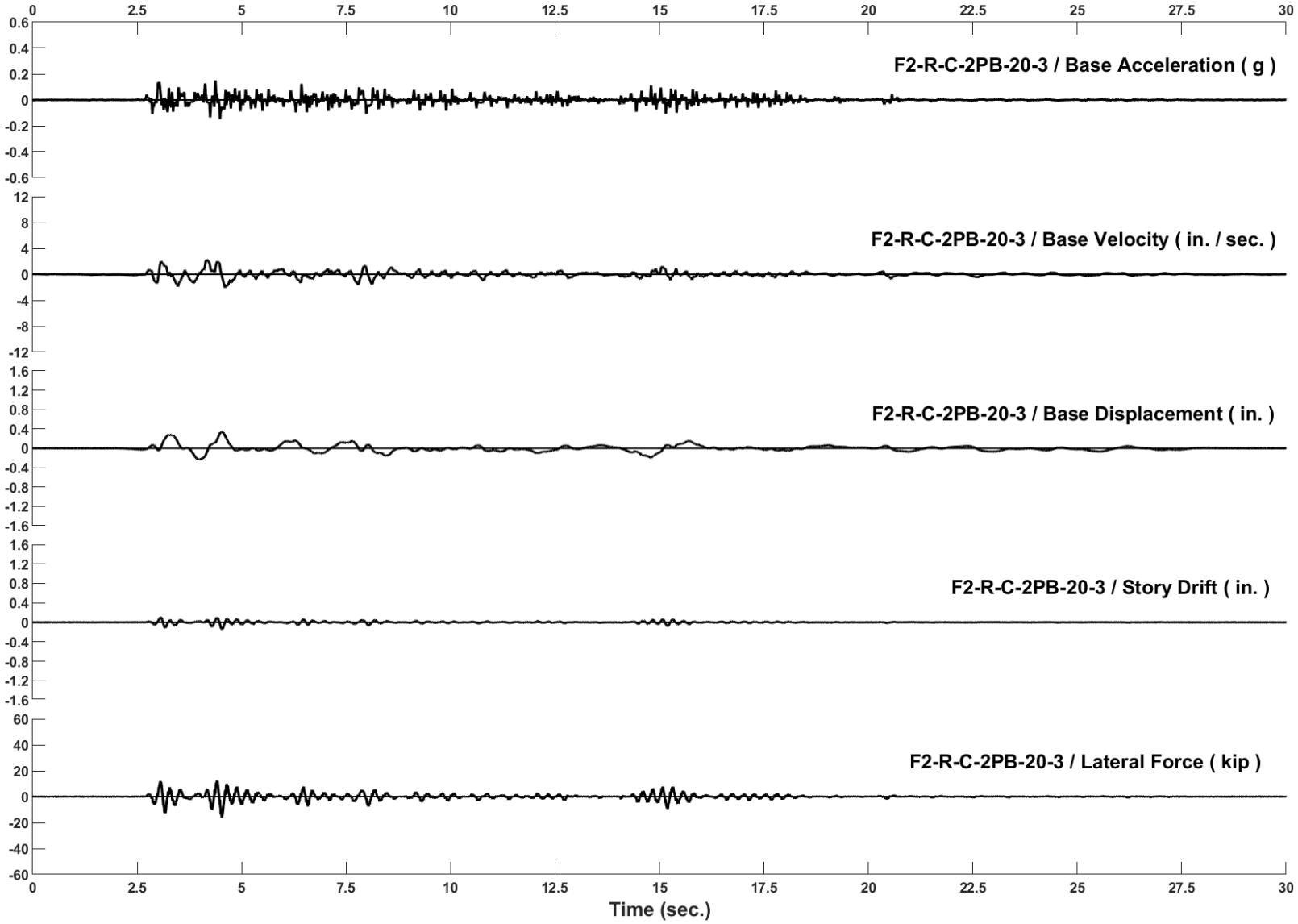

Figure D-73: Run 136, Frame 2, Structural Response and Base Motion History

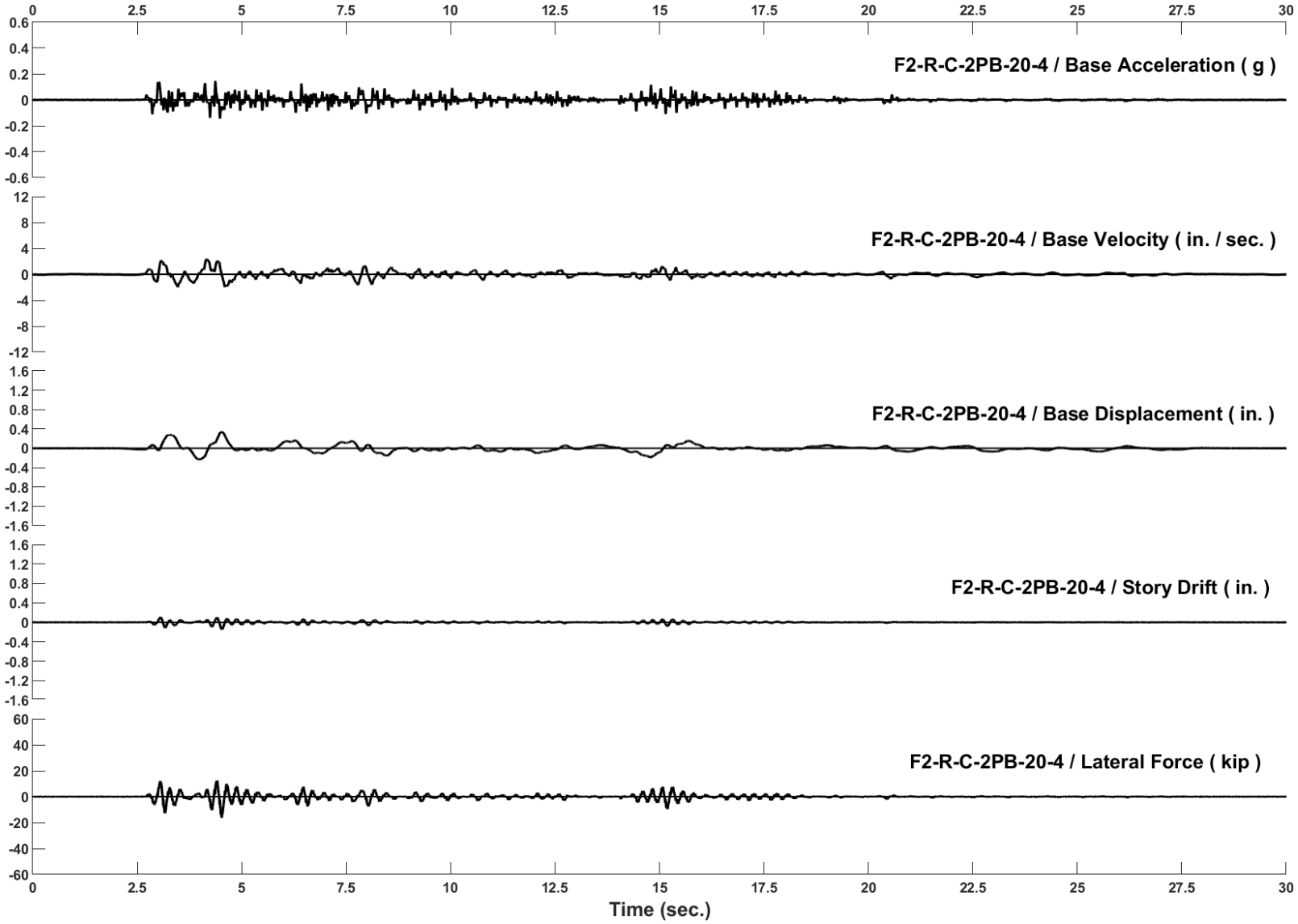

Figure D-74: Run 137, Frame 2, Structural Response and Base Motion History

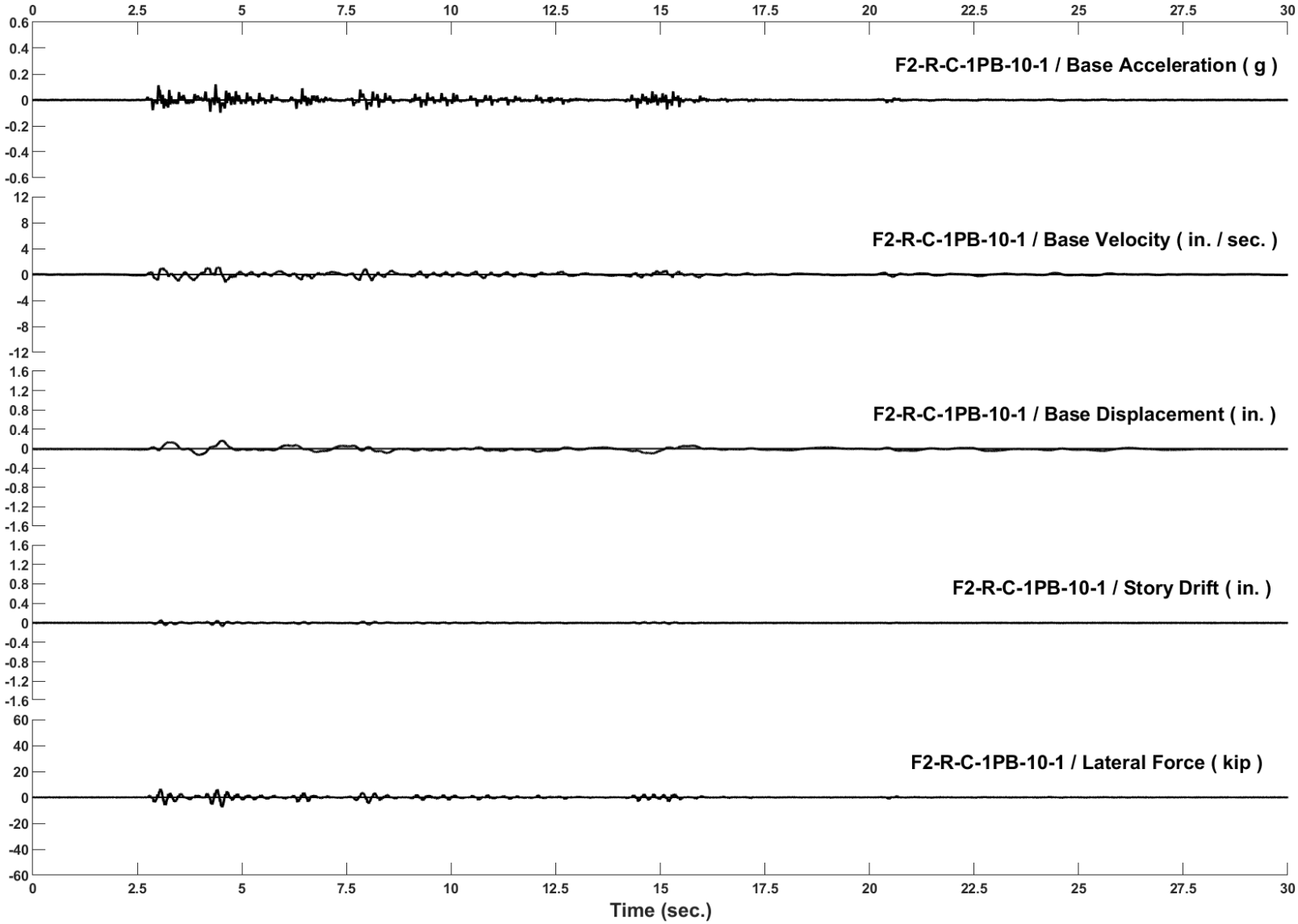

Figure D-75: Run 138, Frame 2, Structural Response and Base Motion History

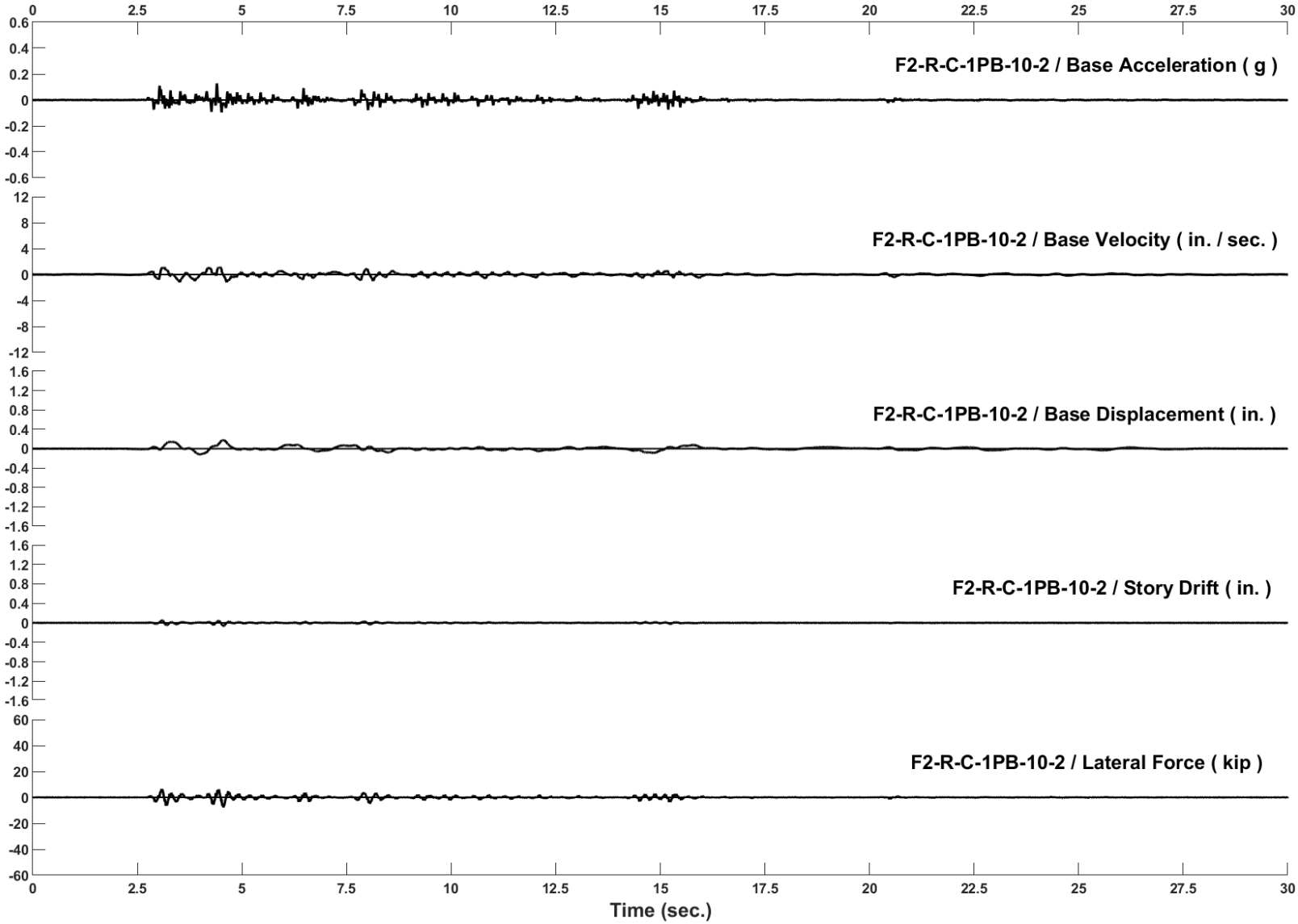

Figure D-76: Run 139, Frame 2, Structural Response and Base Motion History

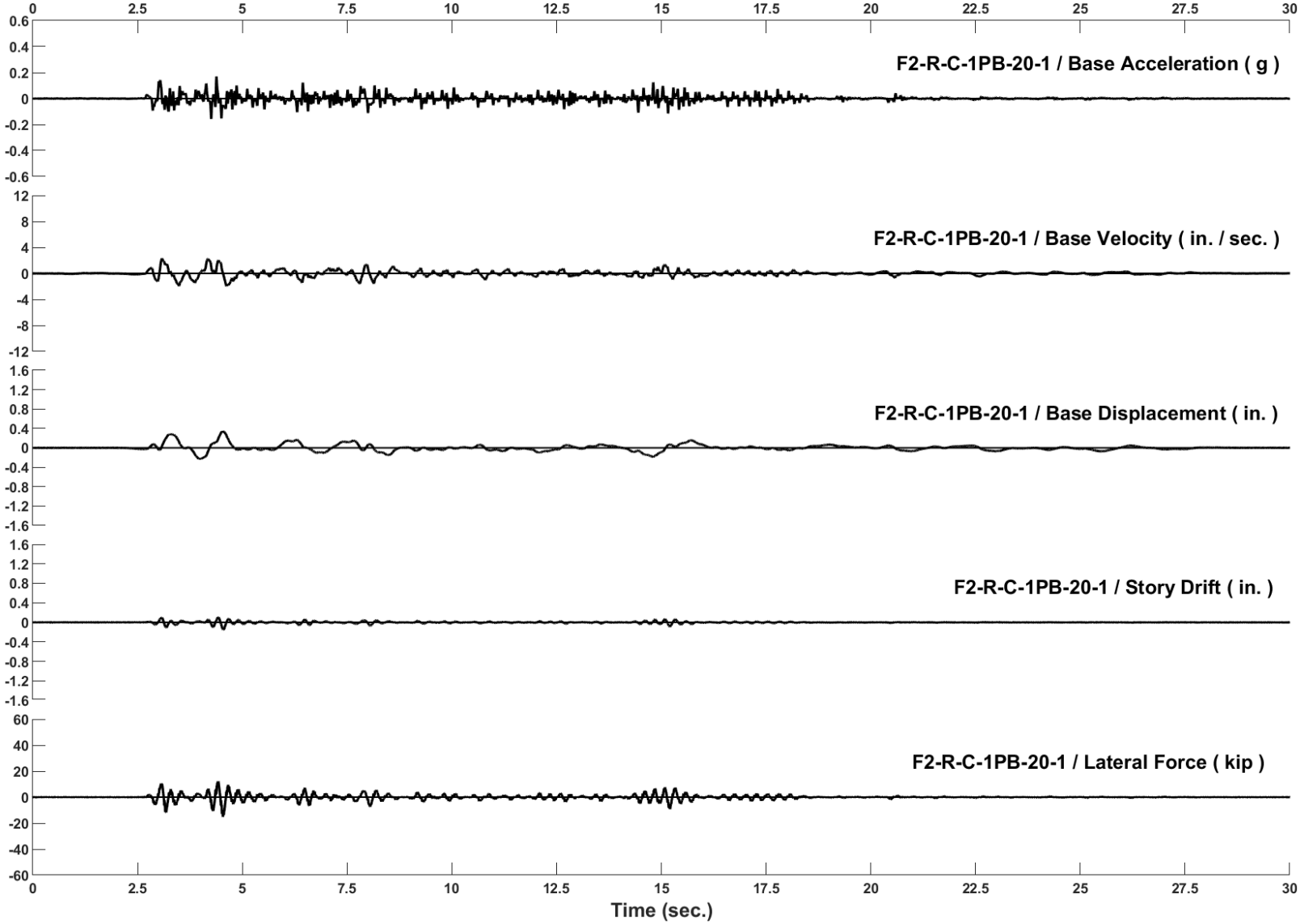

Figure D-77: Run 140, Frame 2, Structural Response and Base Motion History

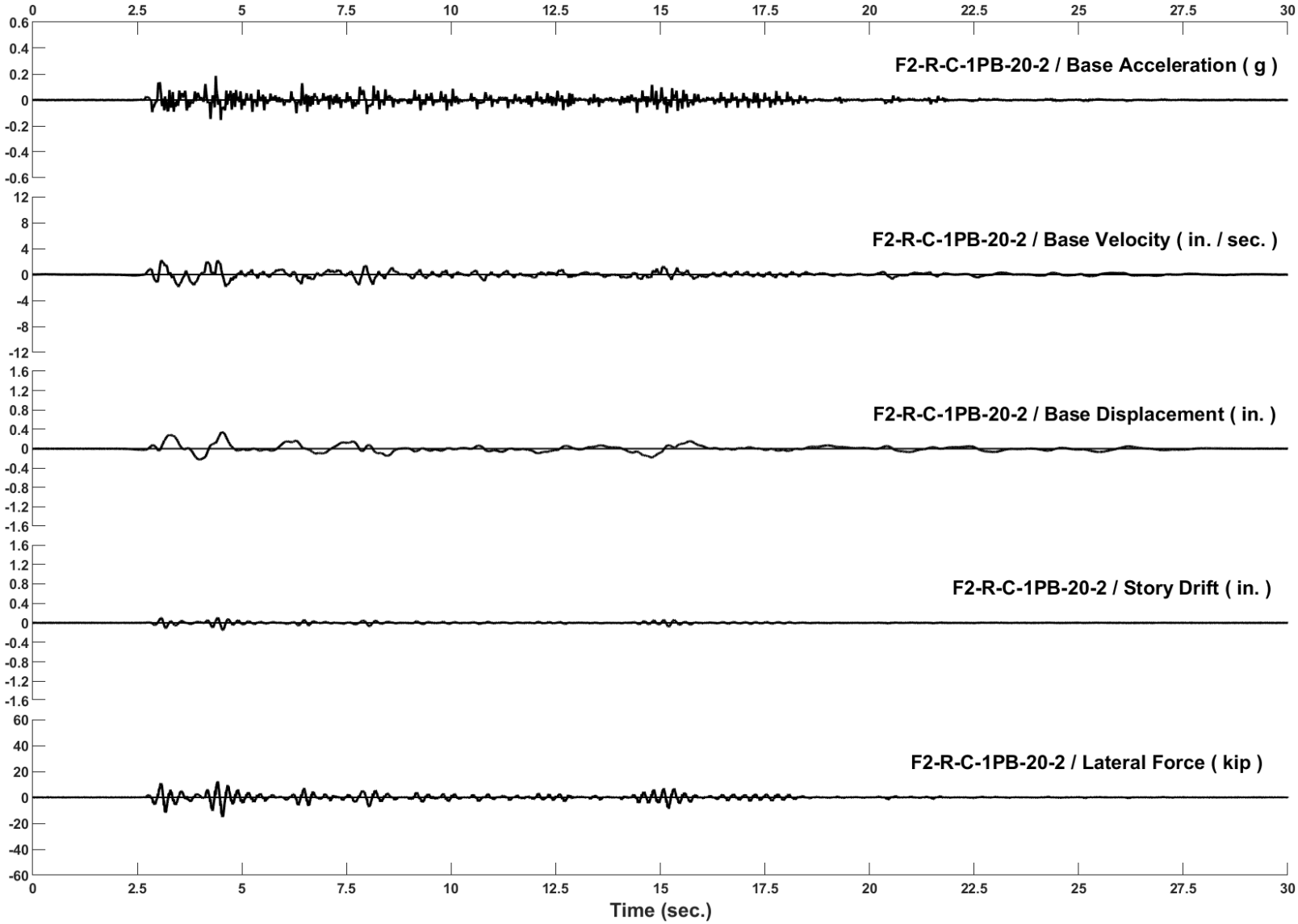

Figure D-78: Run 141, Frame 2, Structural Response and Base Motion History

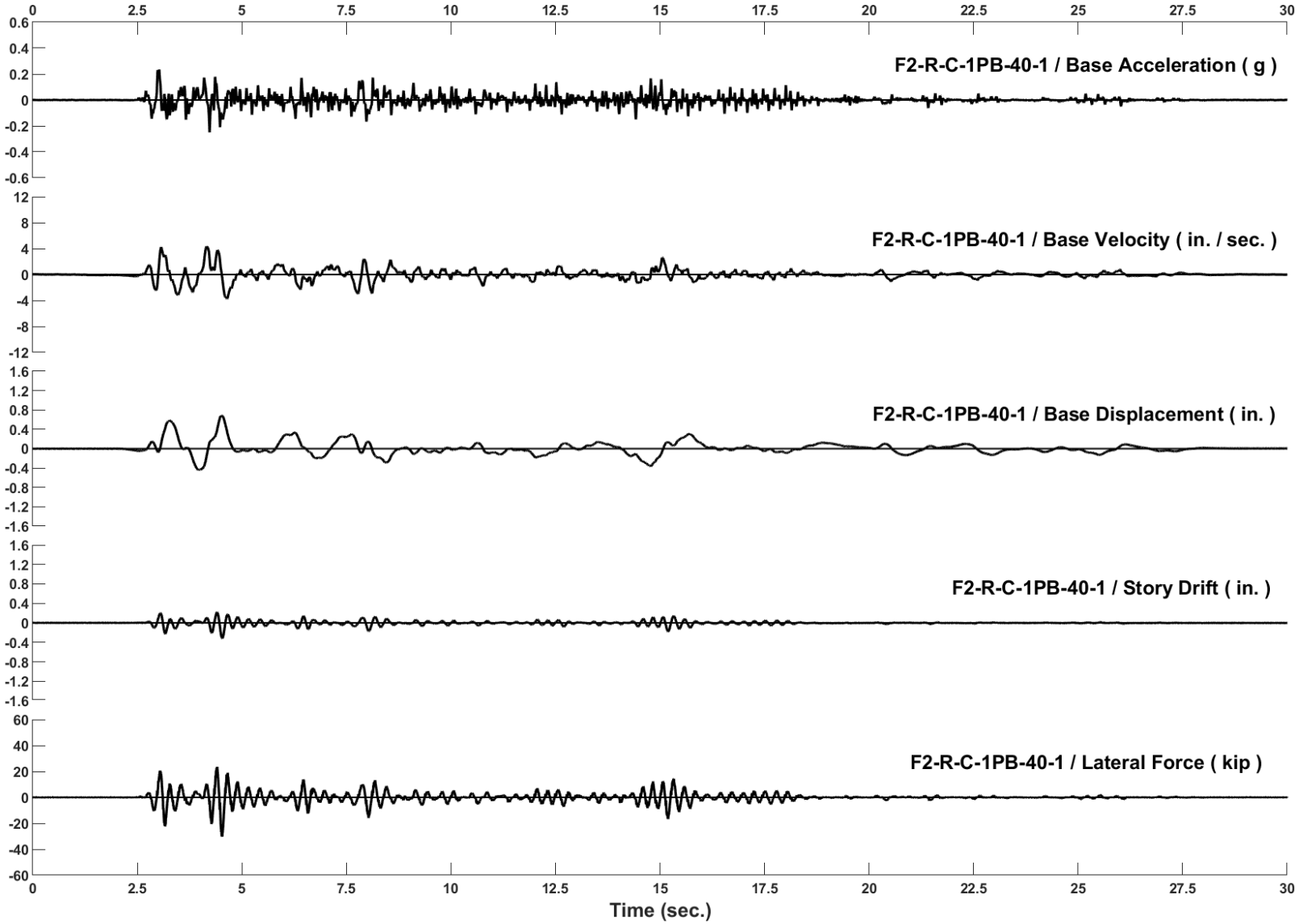

Figure D-79: Run 142, Frame 2, Structural Response and Base Motion History

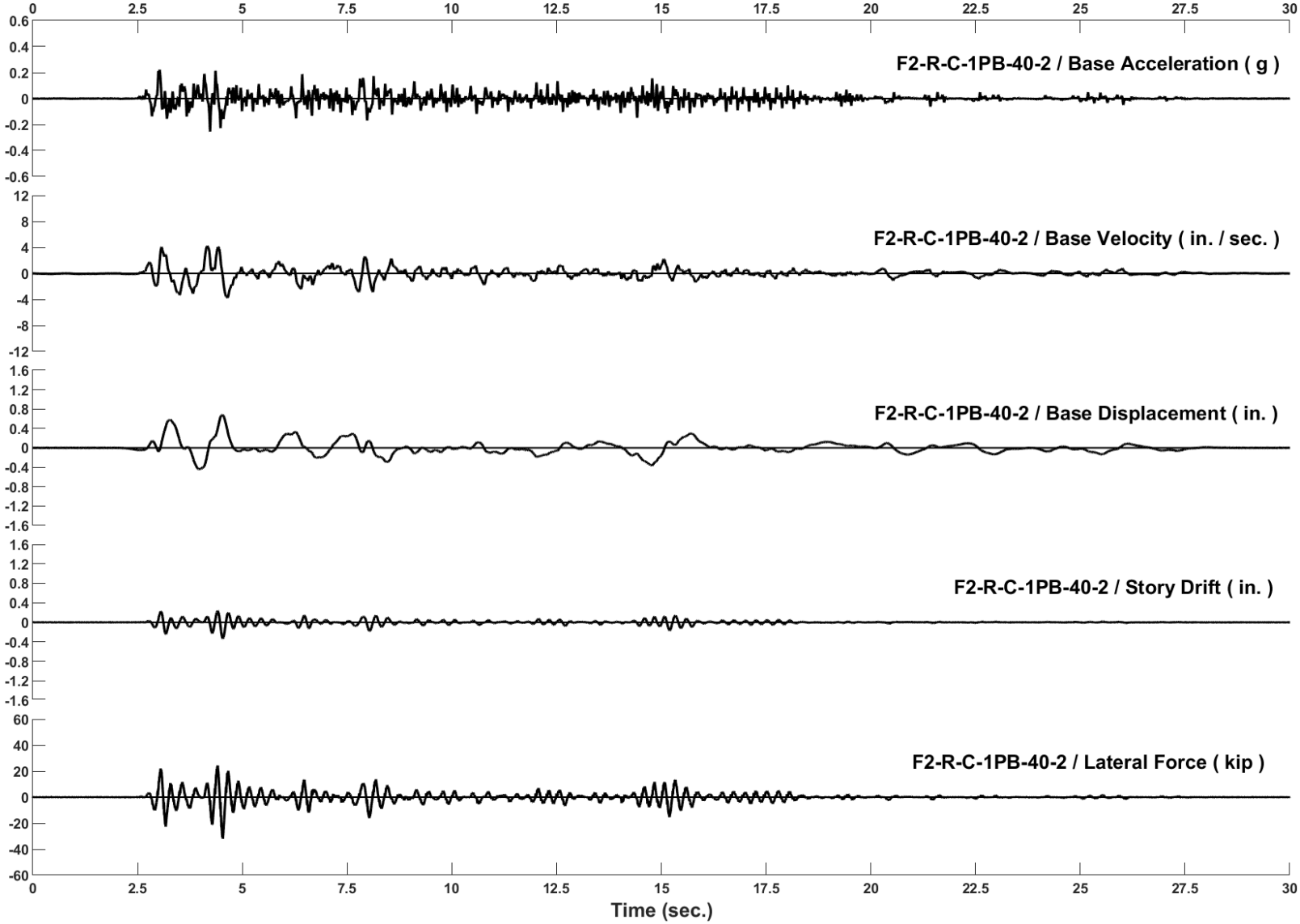

Figure D-80: Run 143, Frame 2, Structural Response and Base Motion History

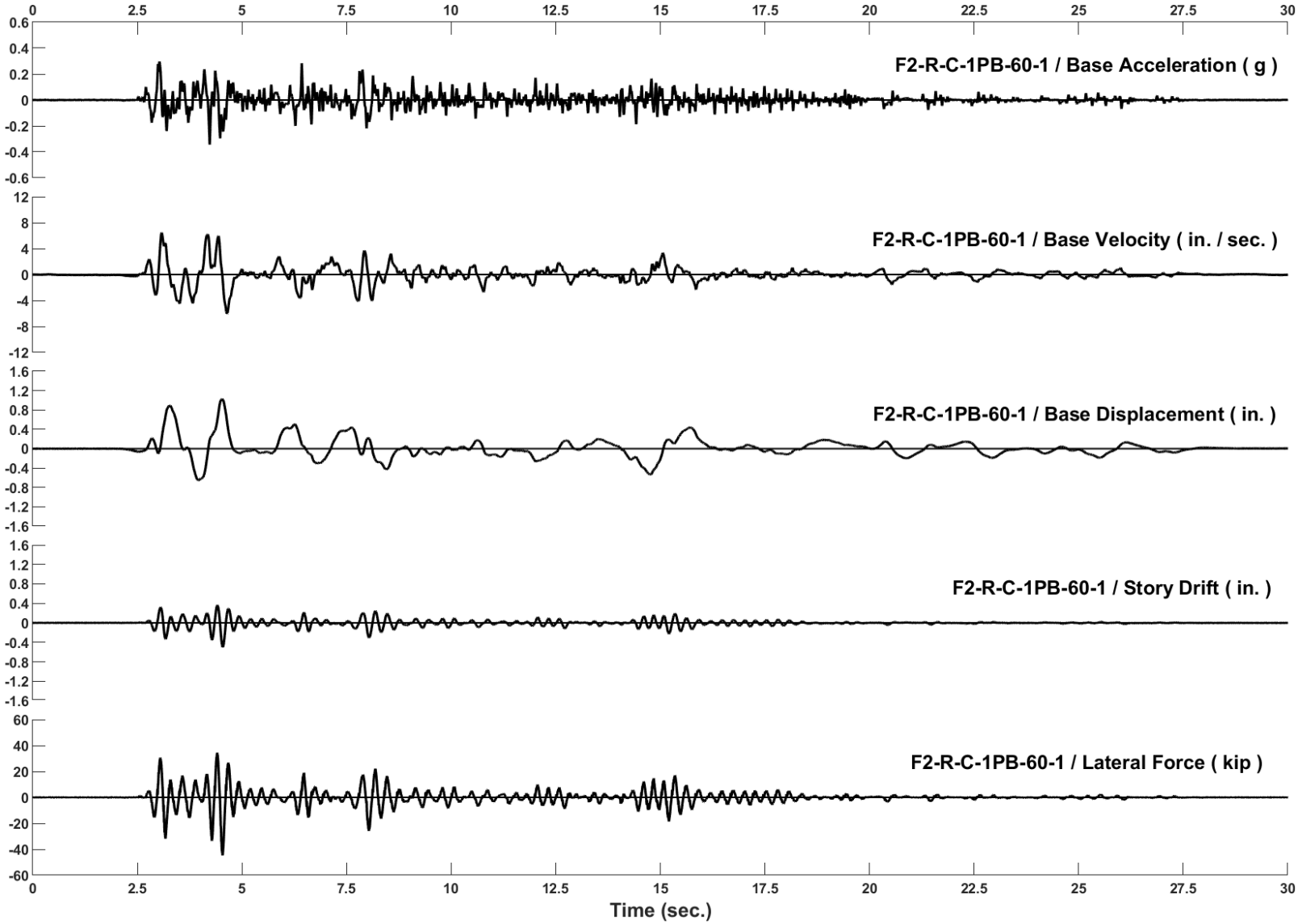

Figure D-81: Run 144, Frame 2, Structural Response and Base Motion History

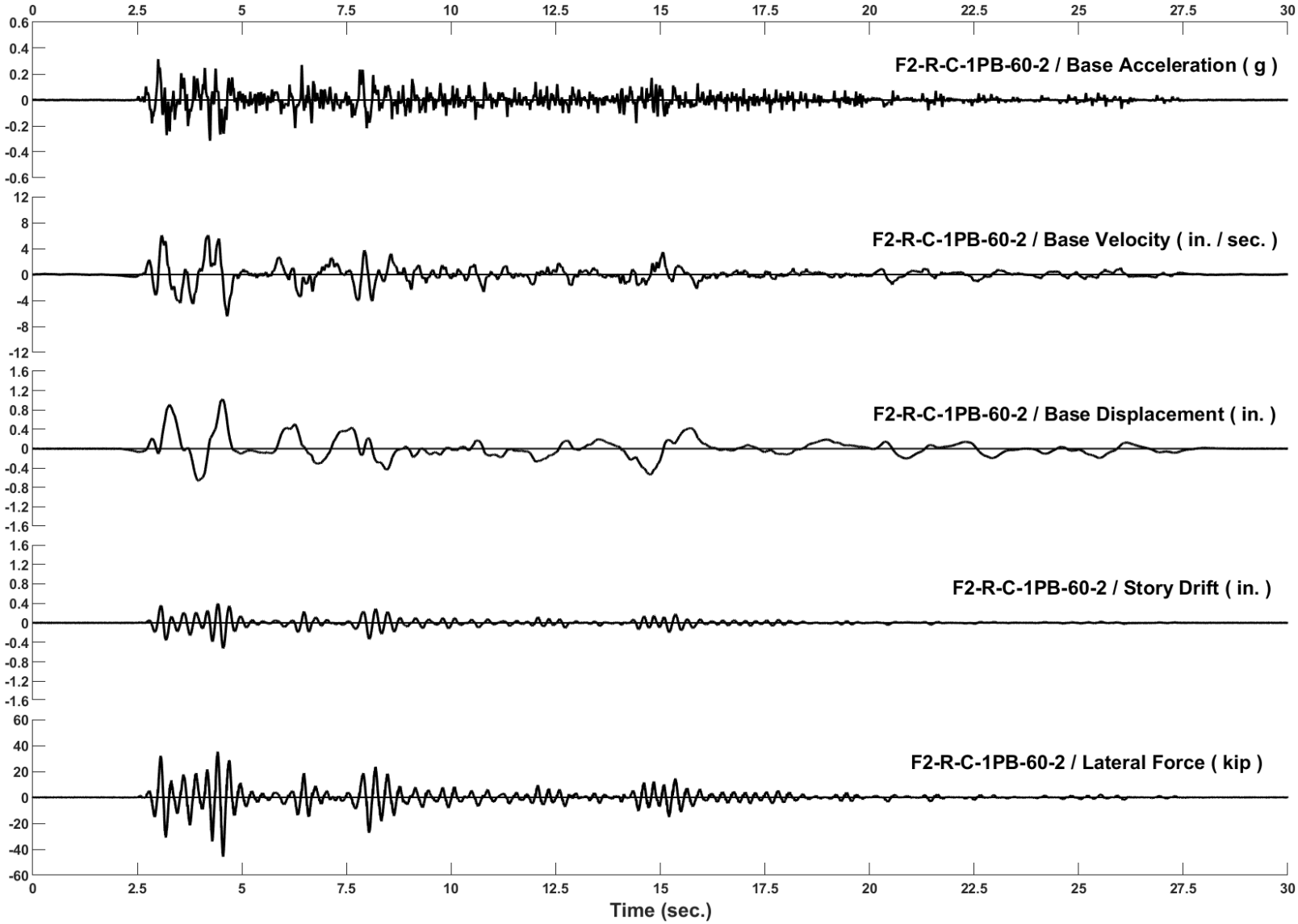

Figure D-82: Run 145, Frame 2, Structural Response and Base Motion History

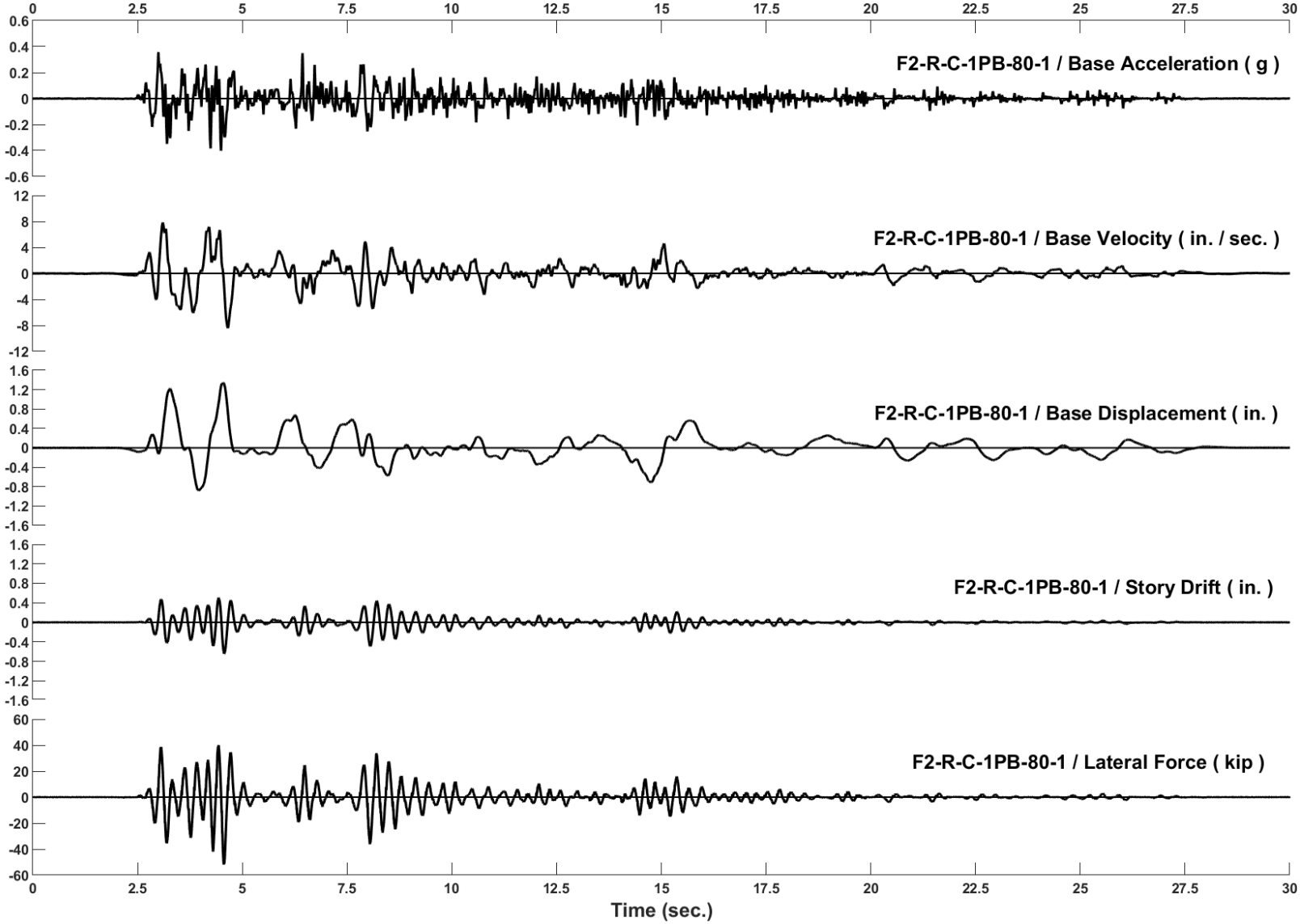

Figure D-83: Run 146, Frame 2, Structural Response and Base Motion History

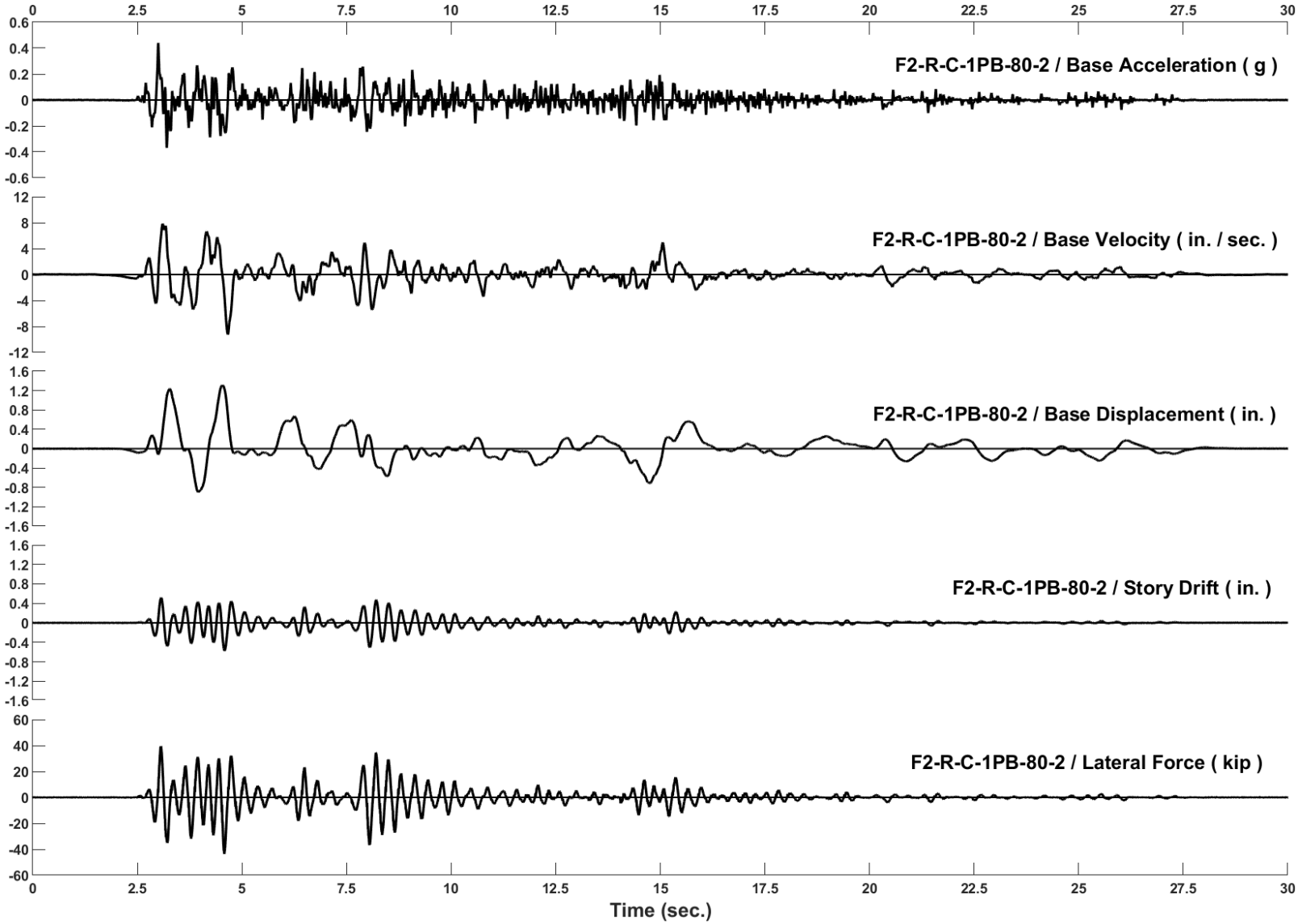

Figure D-84: Run 147, Frame 2, Structural Response and Base Motion History

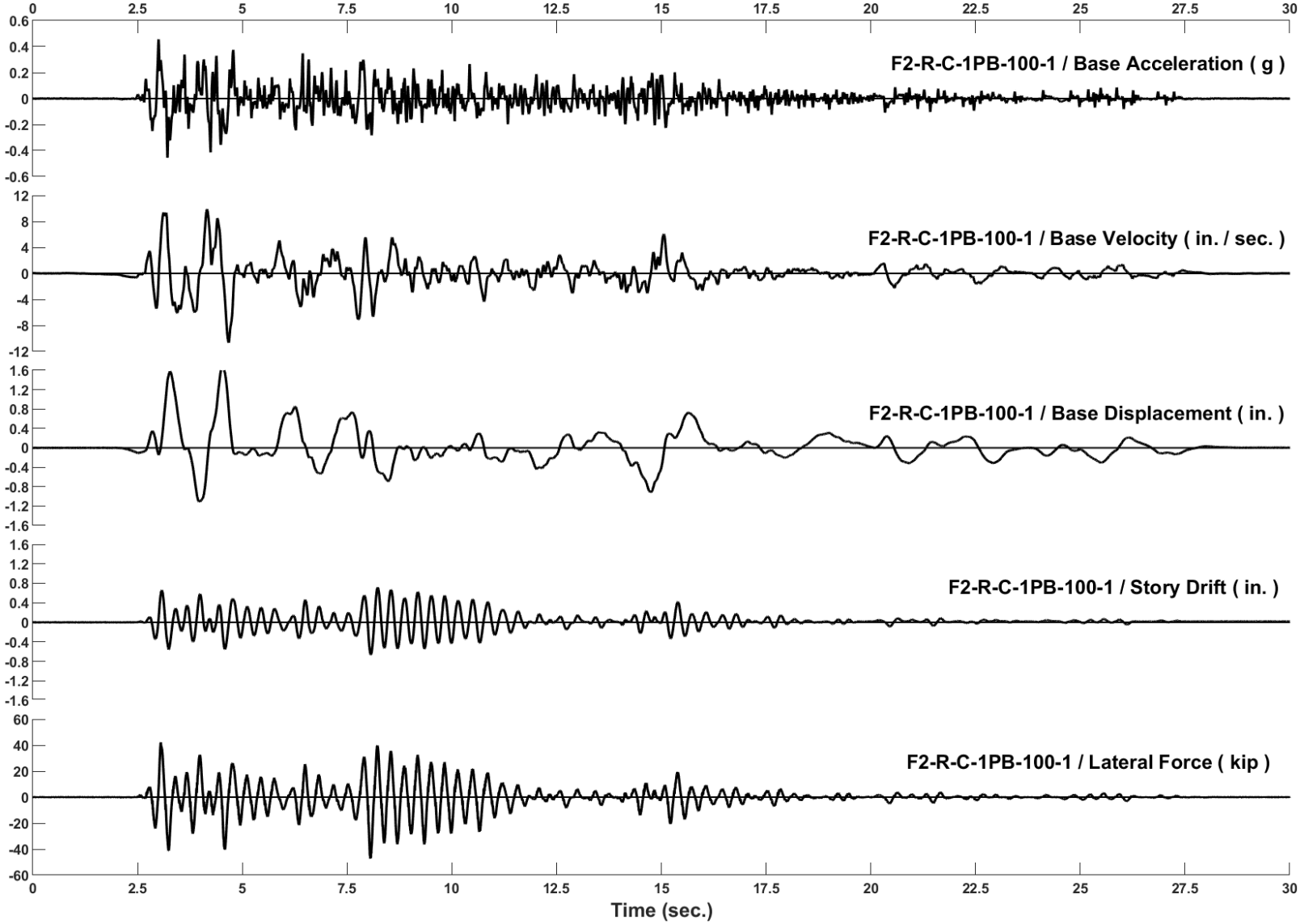

Figure D-85: Run 148, Frame 2, Structural Response and Base Motion History

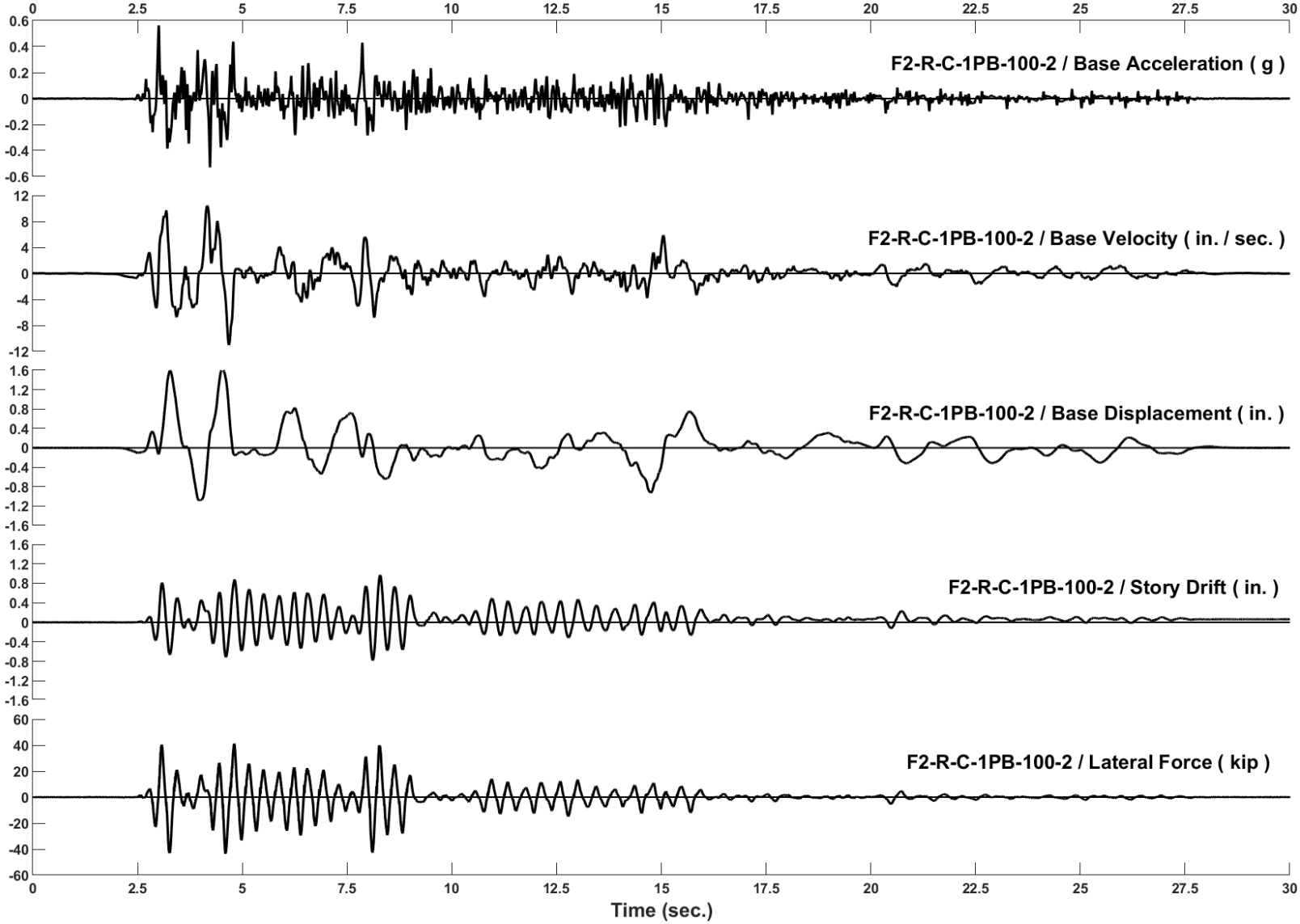

Figure D-86: Run 149, Frame 2, Structural Response and Base Motion History

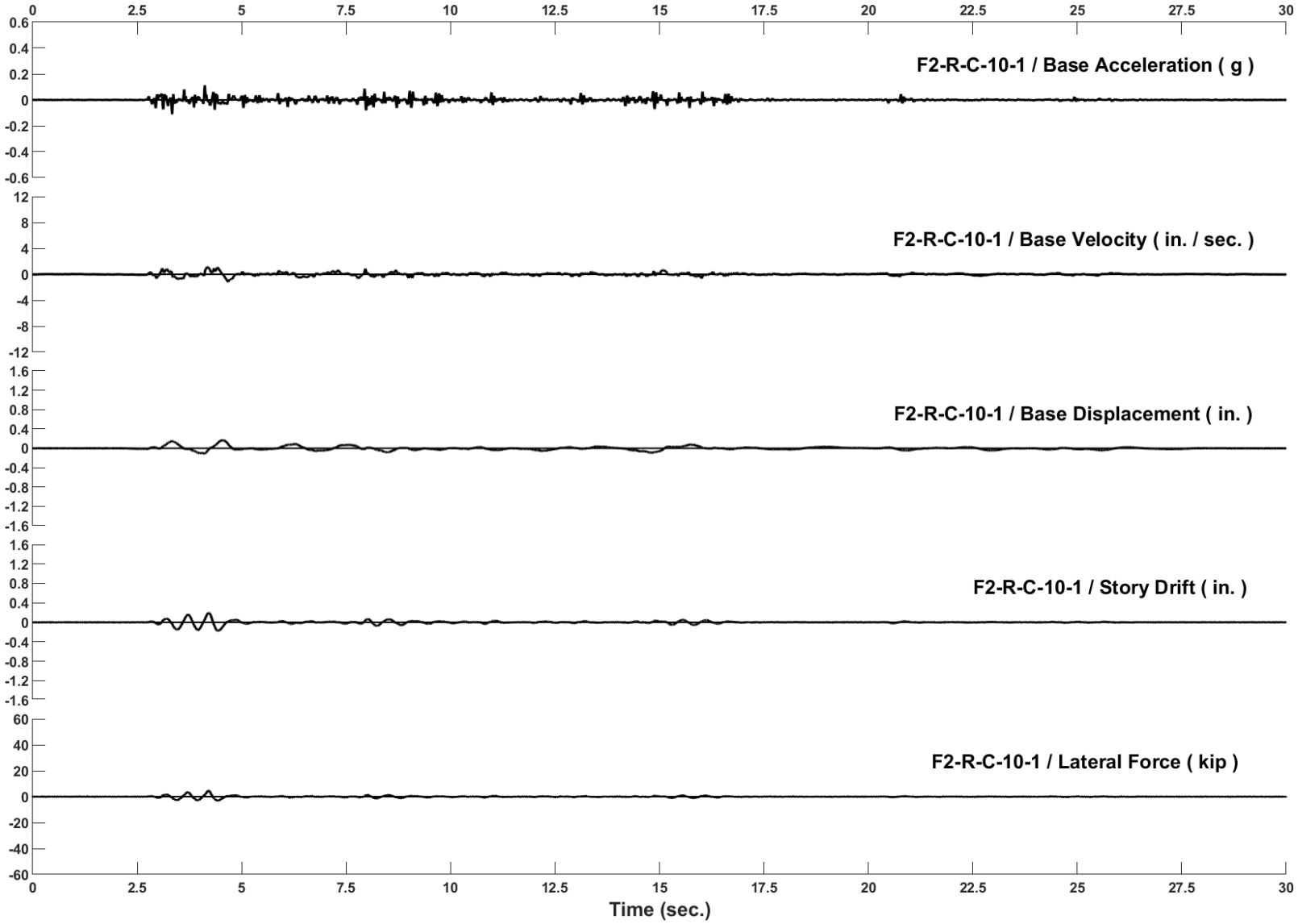

Figure D-87: Run 150, Frame 2, Structural Response and Base Motion History

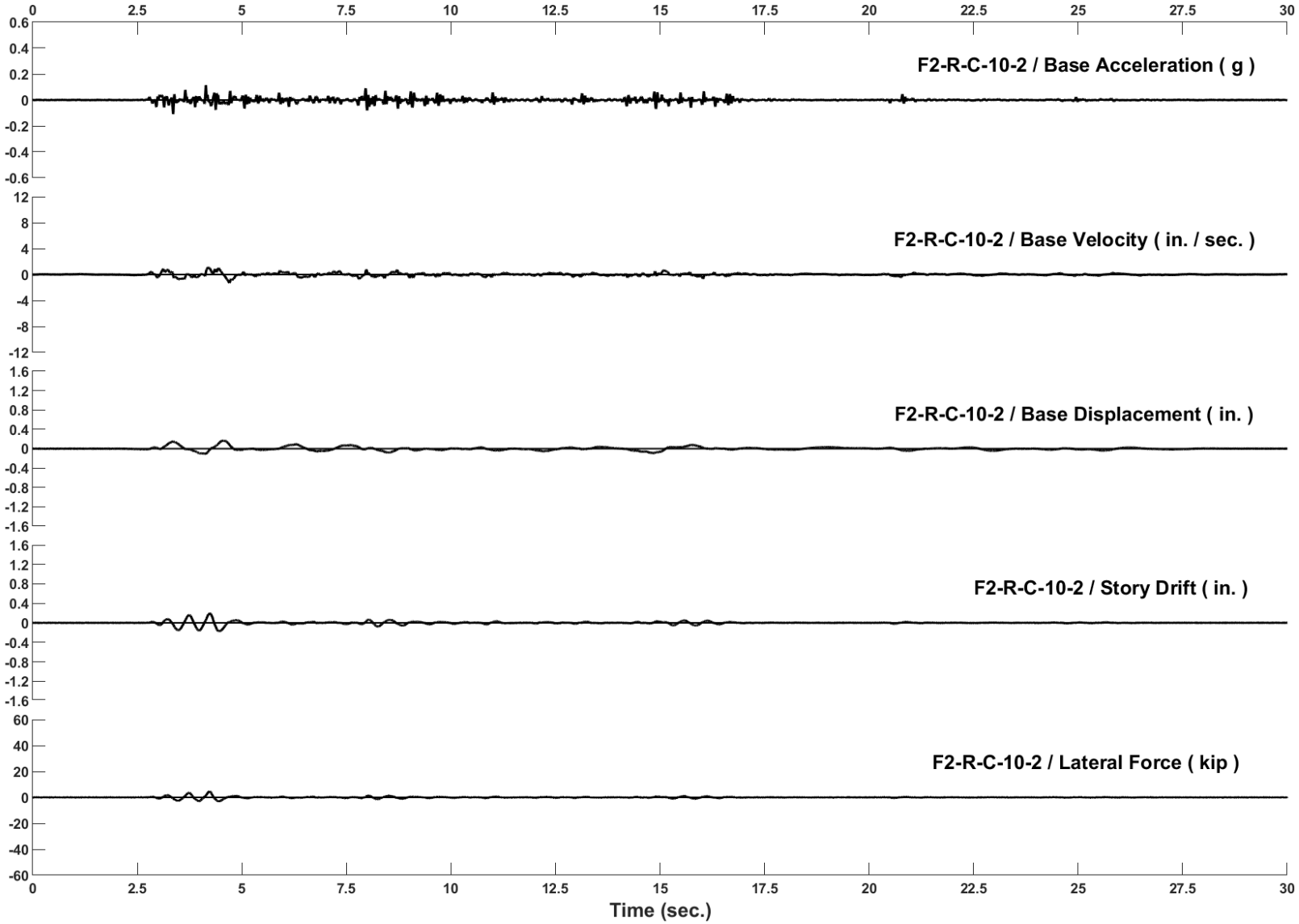

Figure D-88: Run 151, Frame 2, Structural Response and Base Motion History

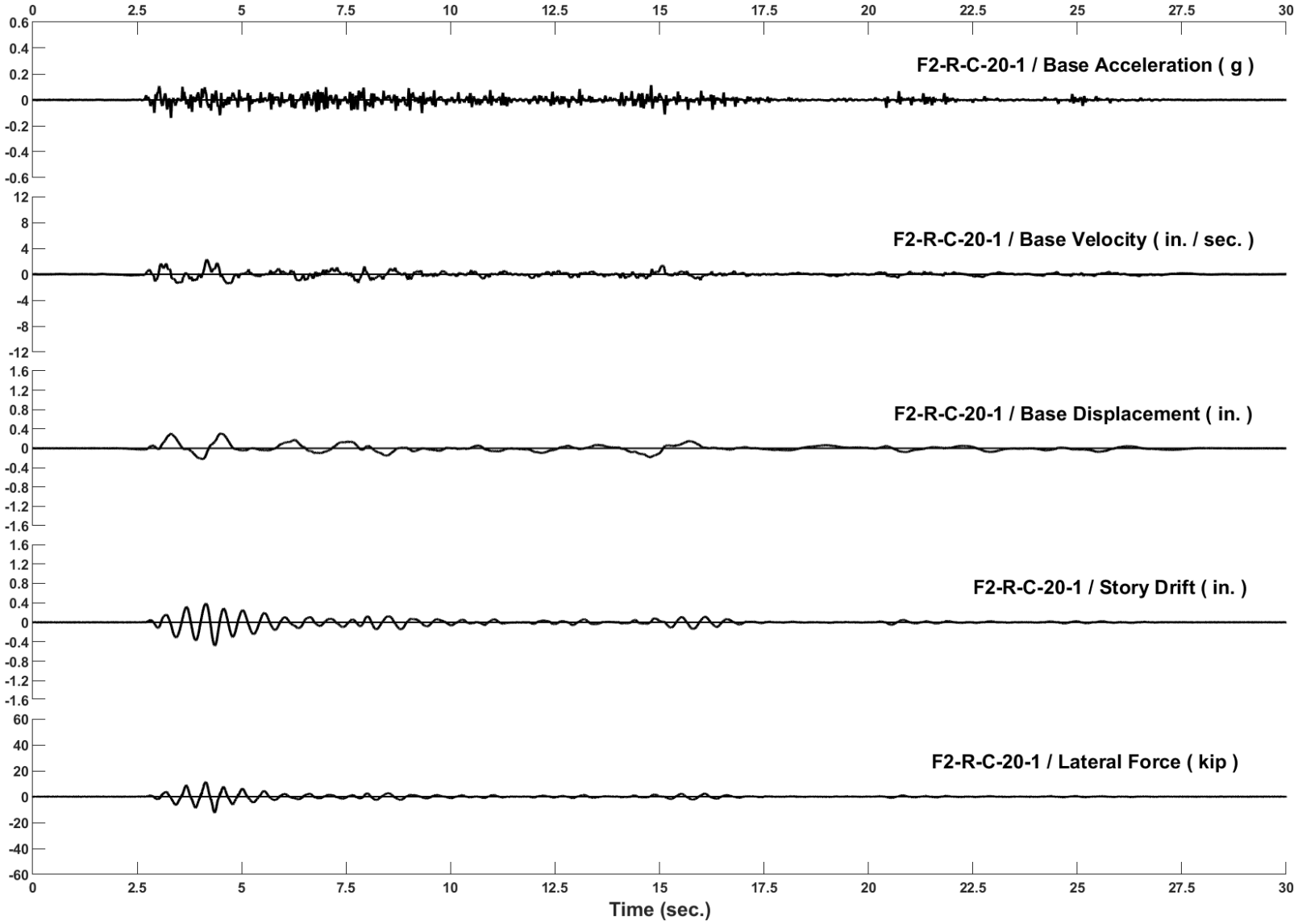

Figure D-89: Run 152, Frame 2, Structural Response and Base Motion History

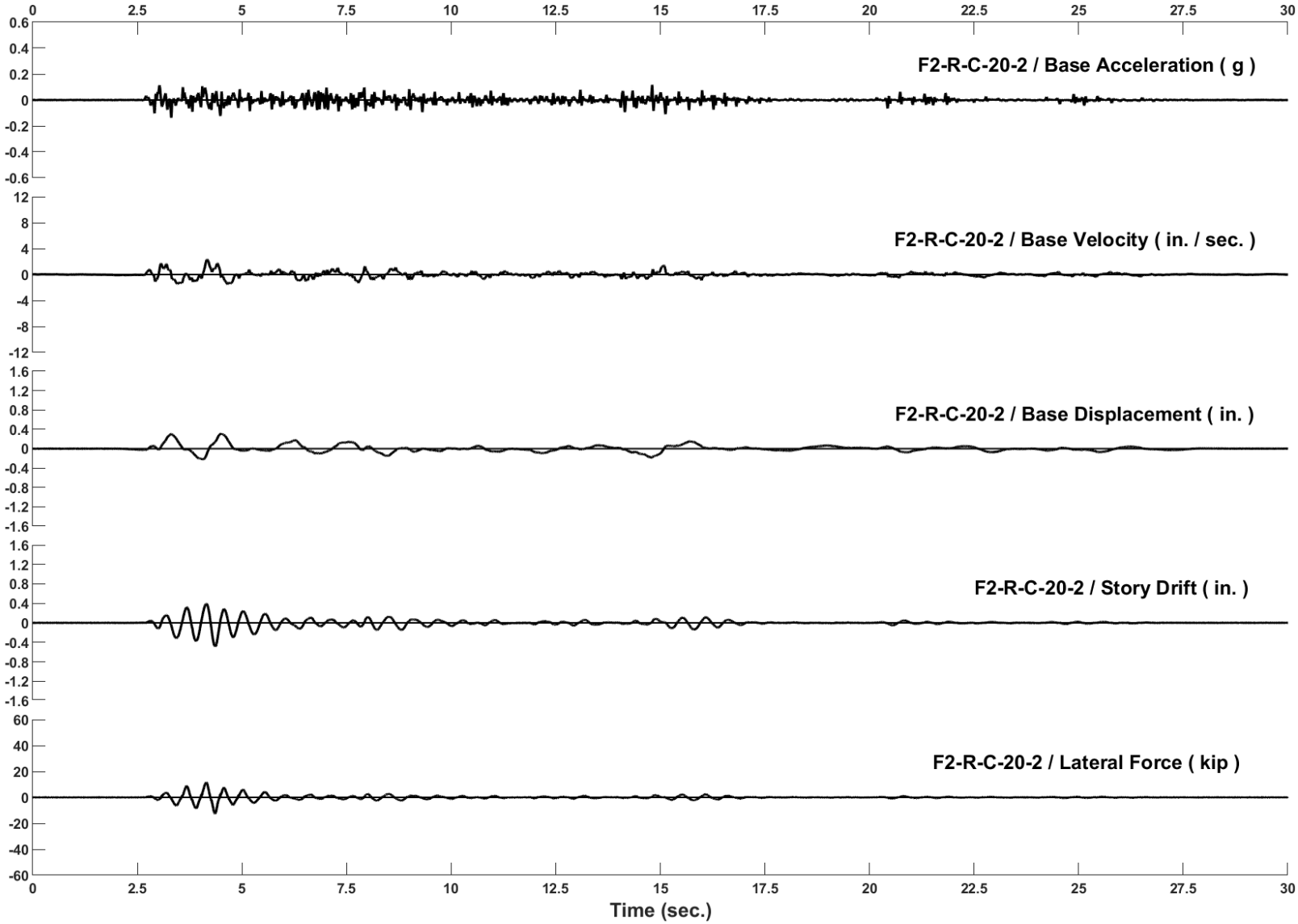

Figure D-90: Run 153, Frame 2, Structural Response and Base Motion History

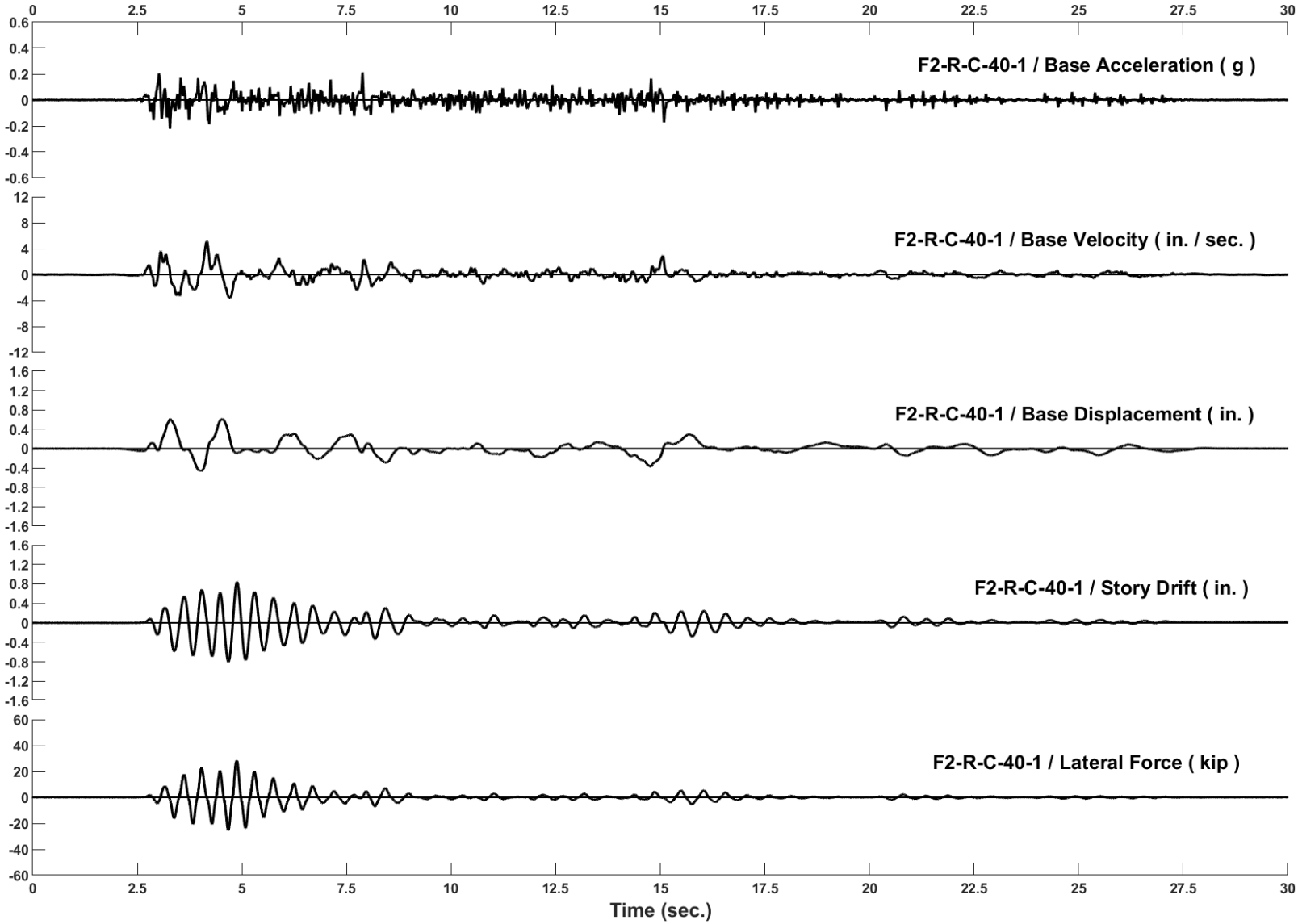

Figure D-91: Run 154, Frame 2, Structural Response and Base Motion History

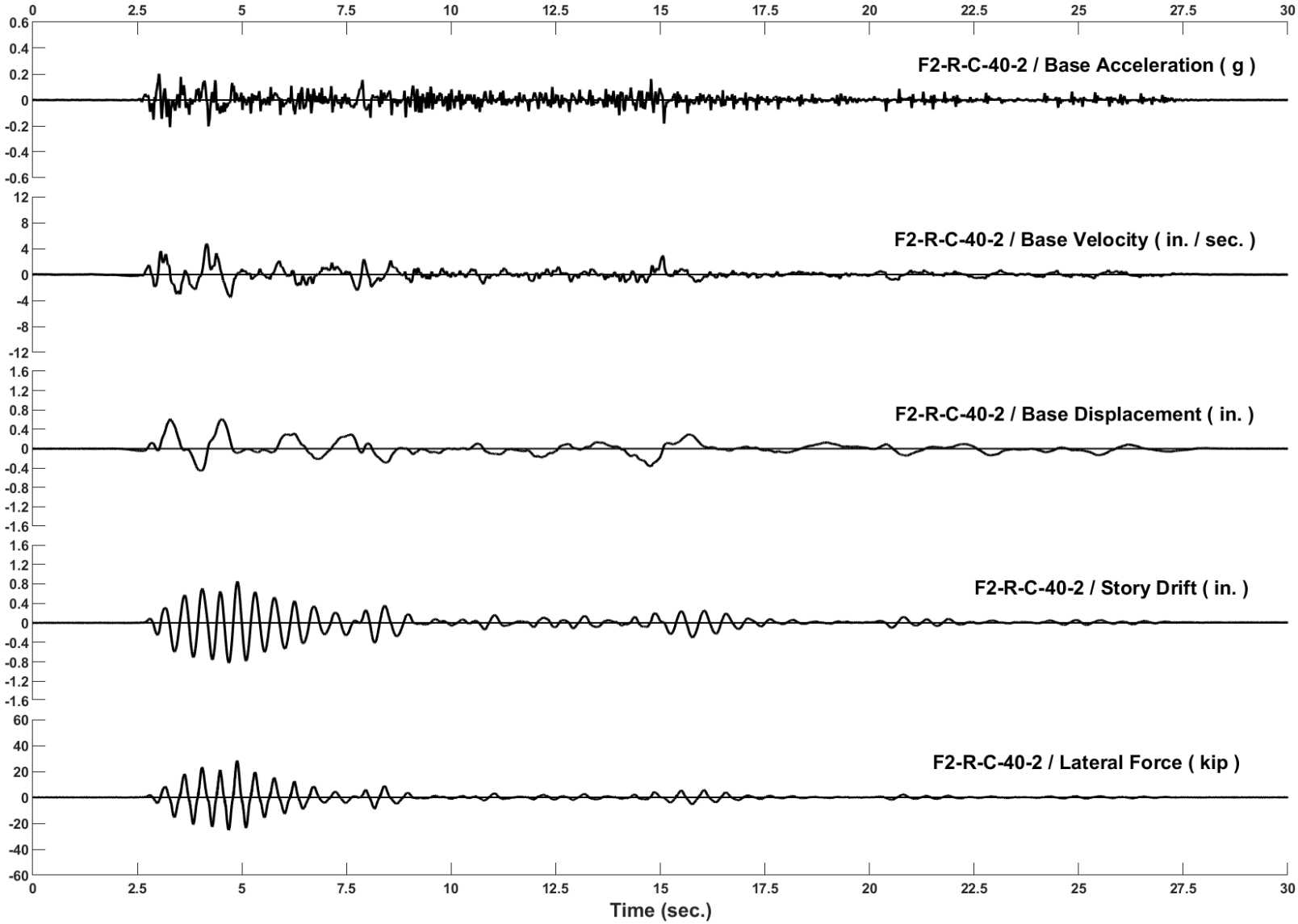

Figure D-92: Run 155, Frame 2, Structural Response and Base Motion History

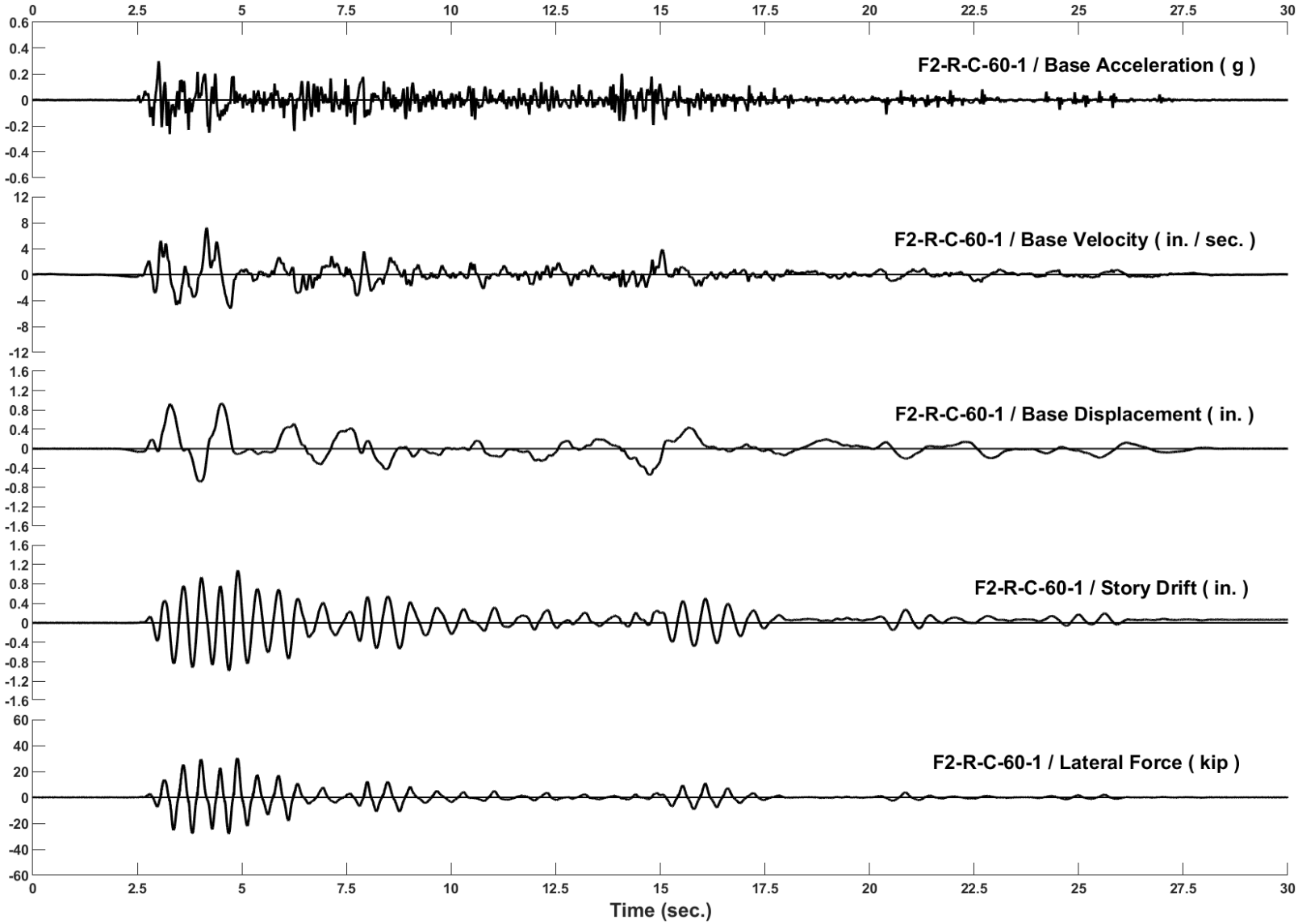

Figure D-93: Run 156, Frame 2, Structural Response and Base Motion History

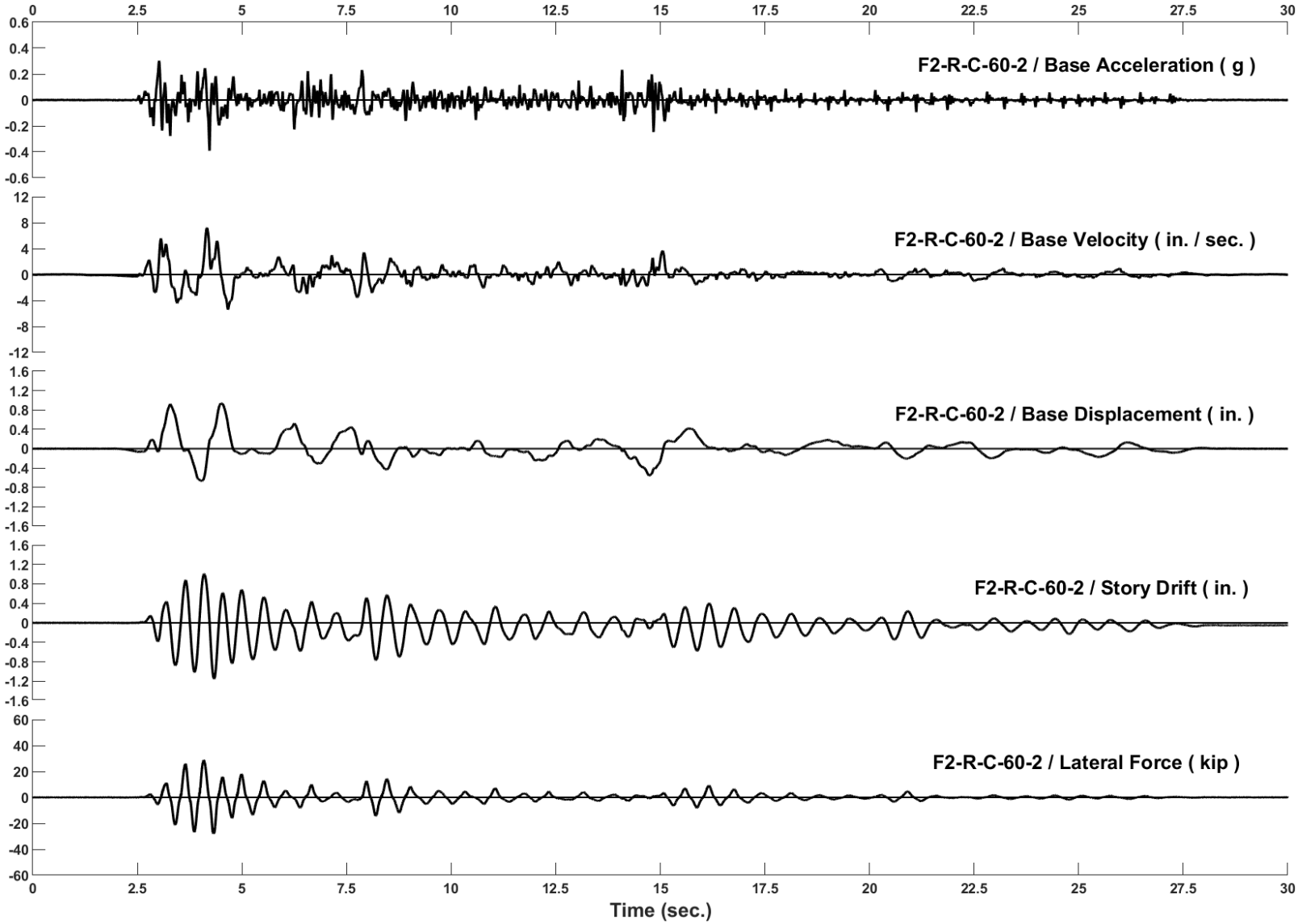

Figure D-94: Run 157, Frame 2, Structural Response and Base Motion History

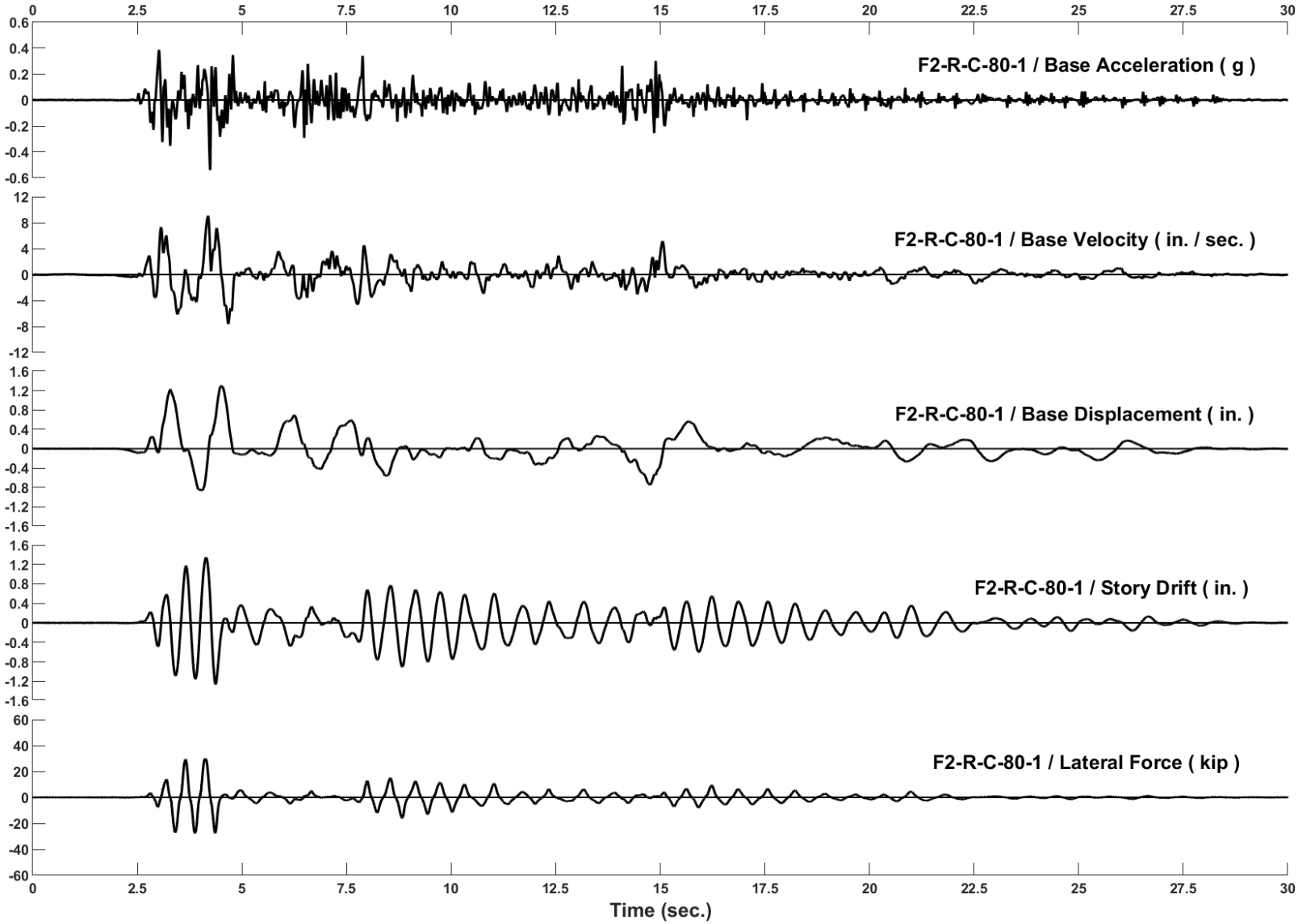

Figure D-95: Run 158, Frame 2, Structural Response and Base Motion History

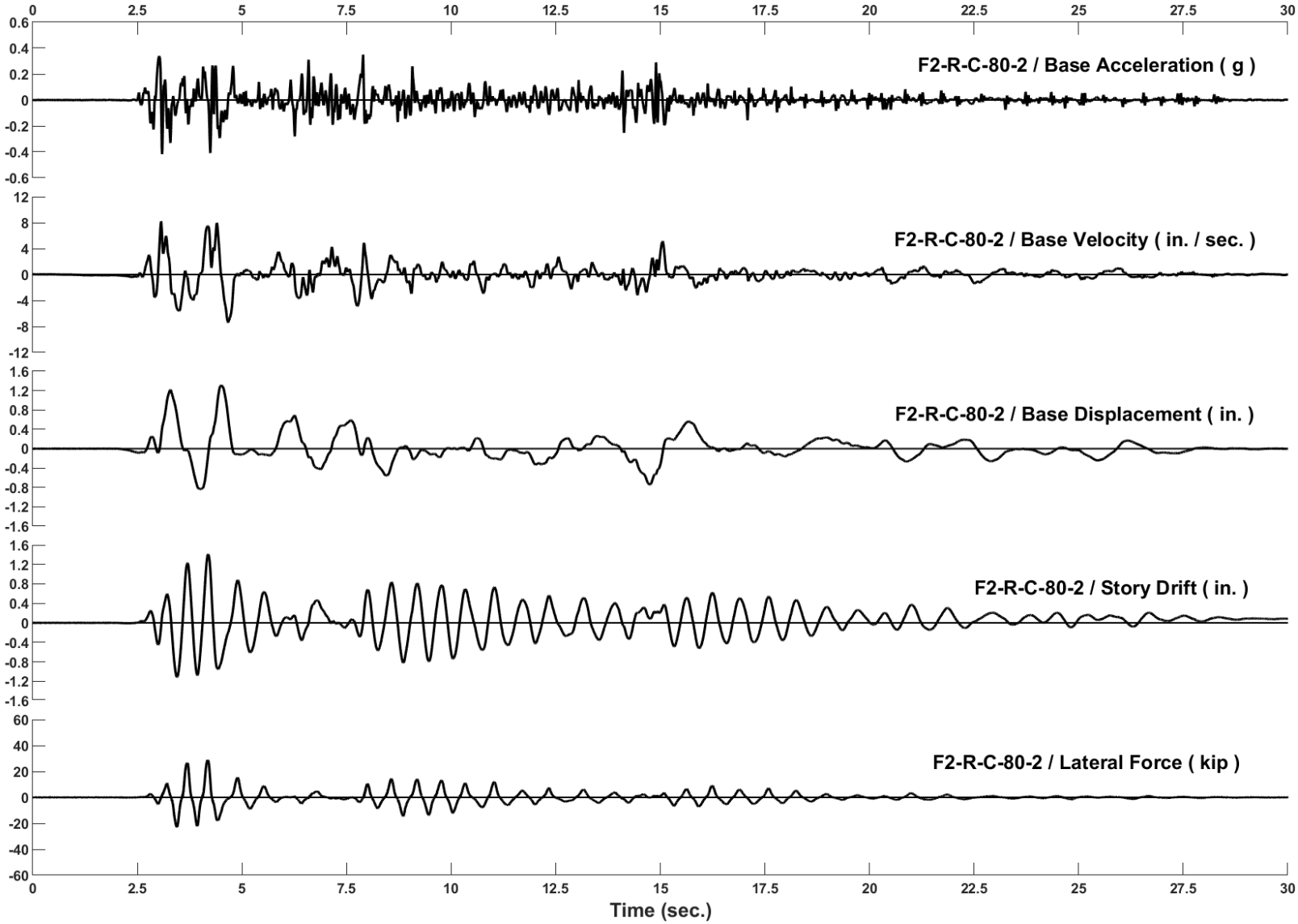

Figure D-96: Run 159, Frame 2, Structural Response and Base Motion History

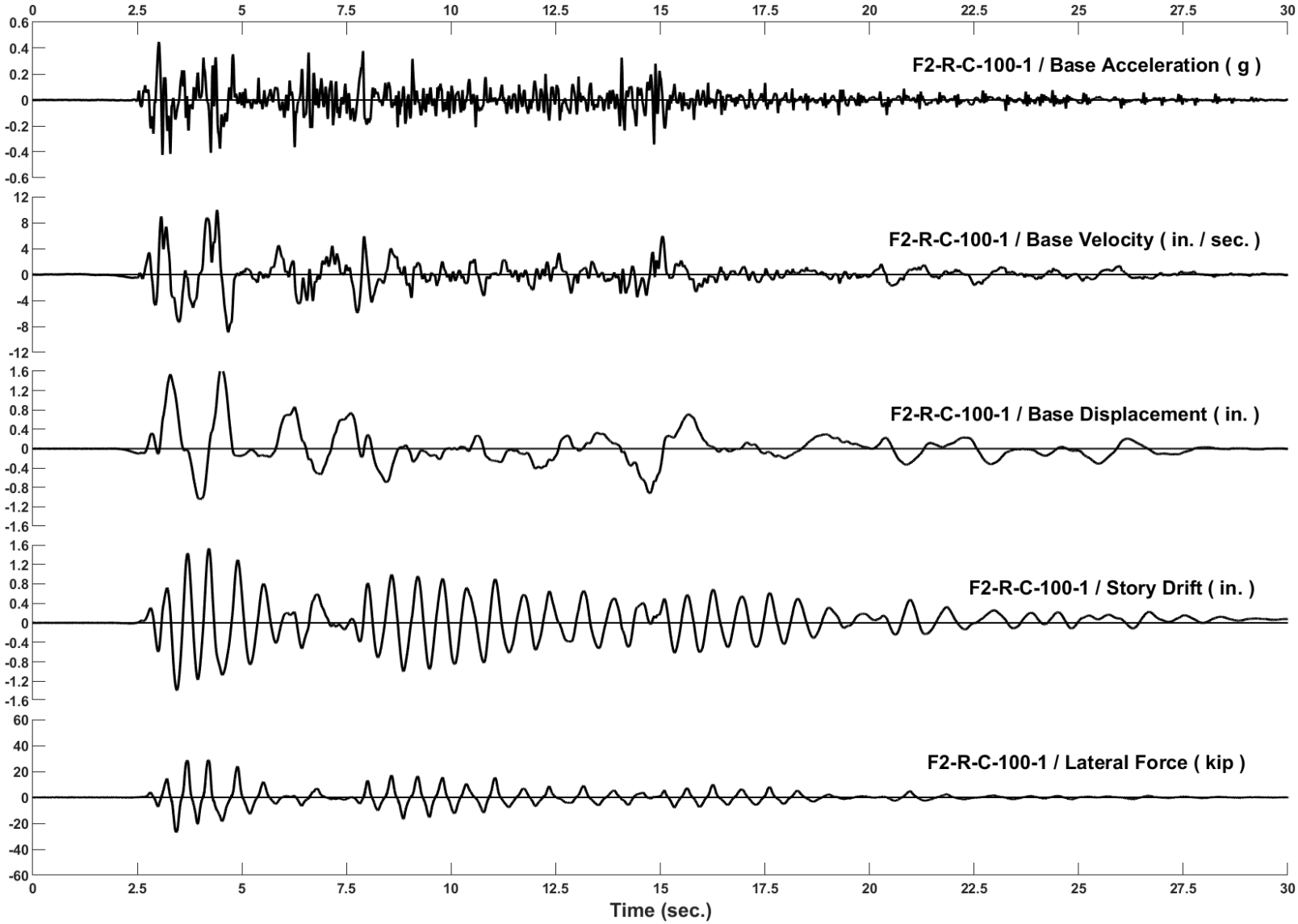

Figure D-97: Run 160, Frame 2, Structural Response and Base Motion History

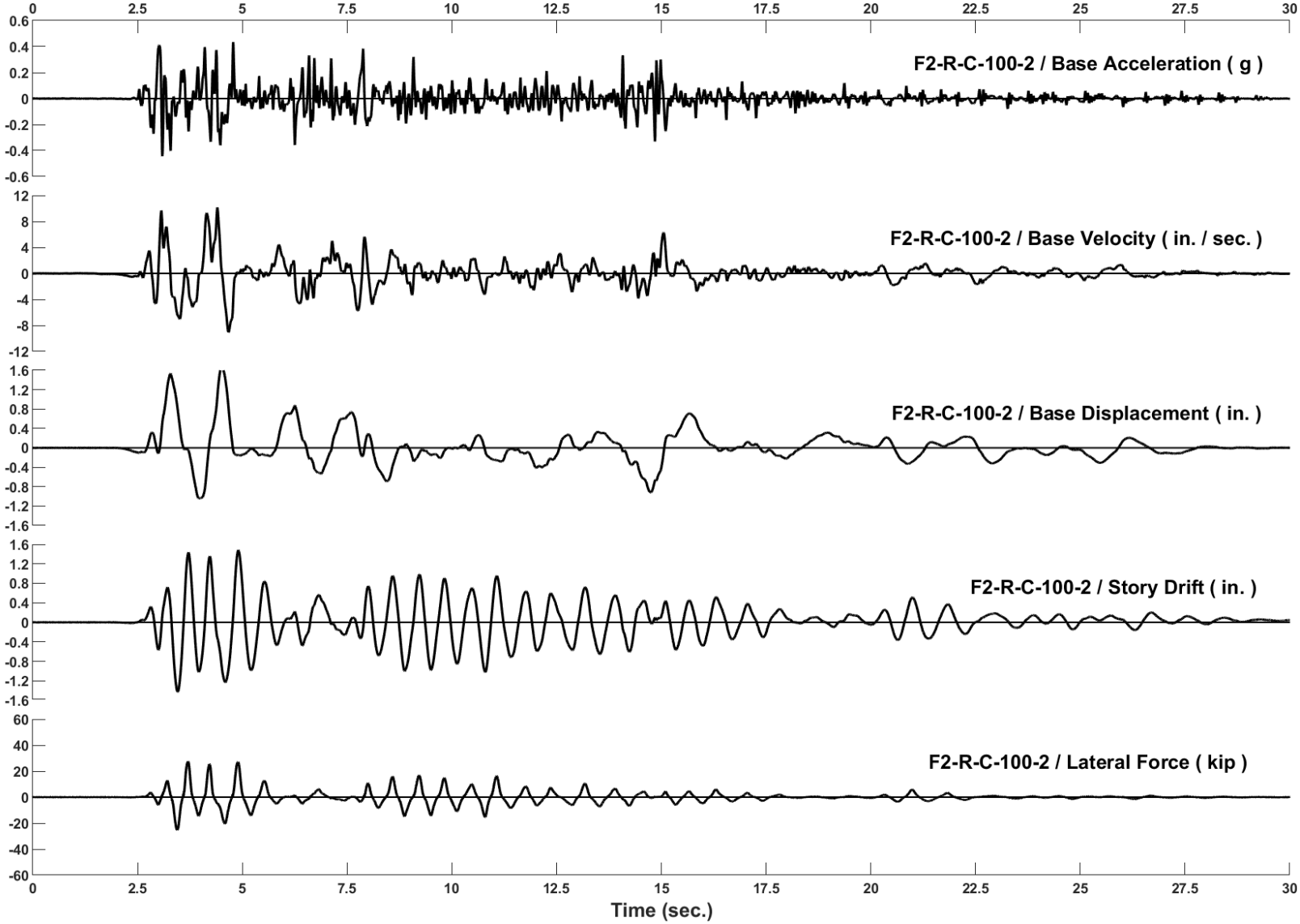

Figure D-98: Run 161, Frame 2, Structural Response and Base Motion History

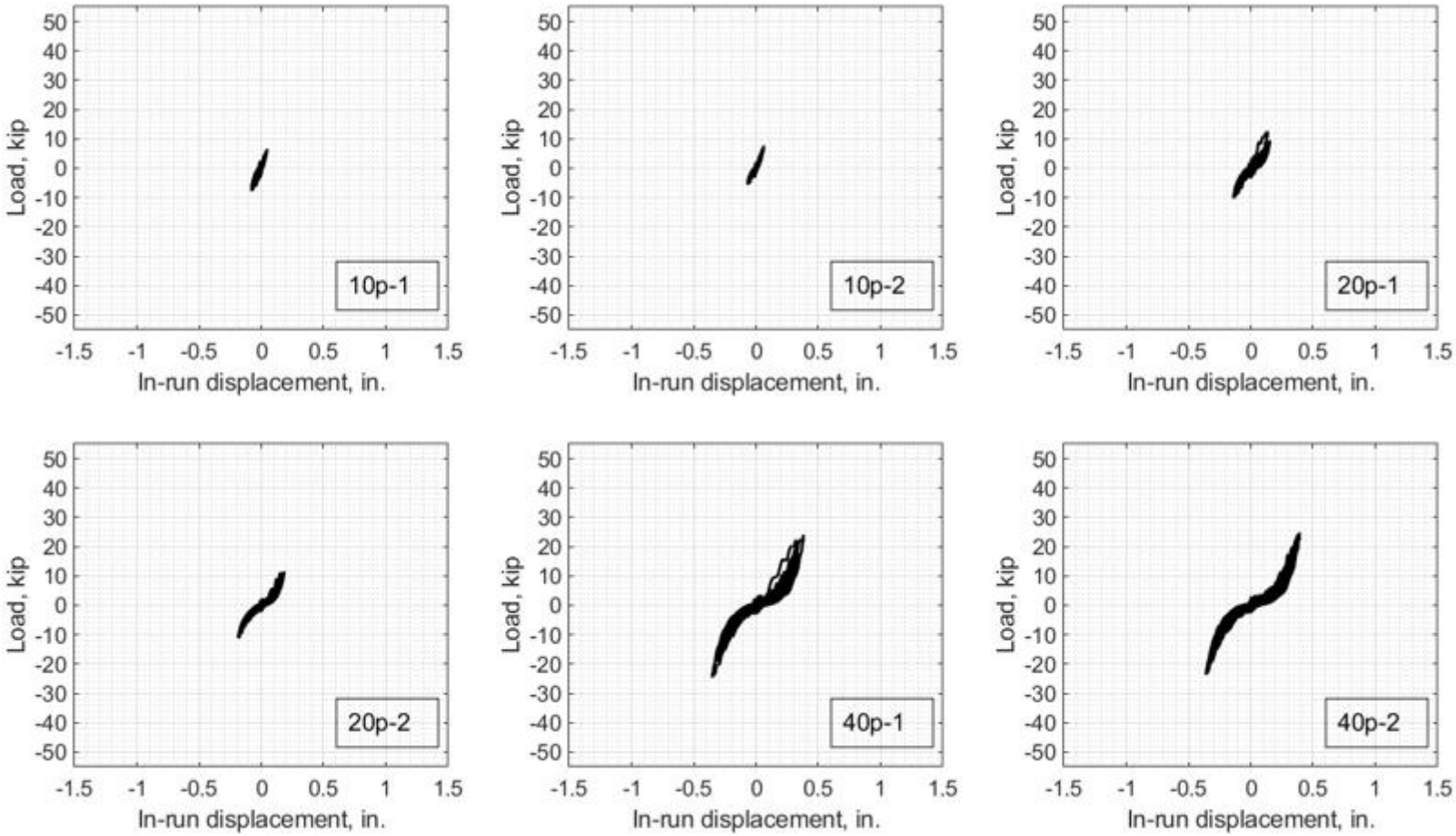

Figure D-99: Force-Drift response in Series F2-C-4PB

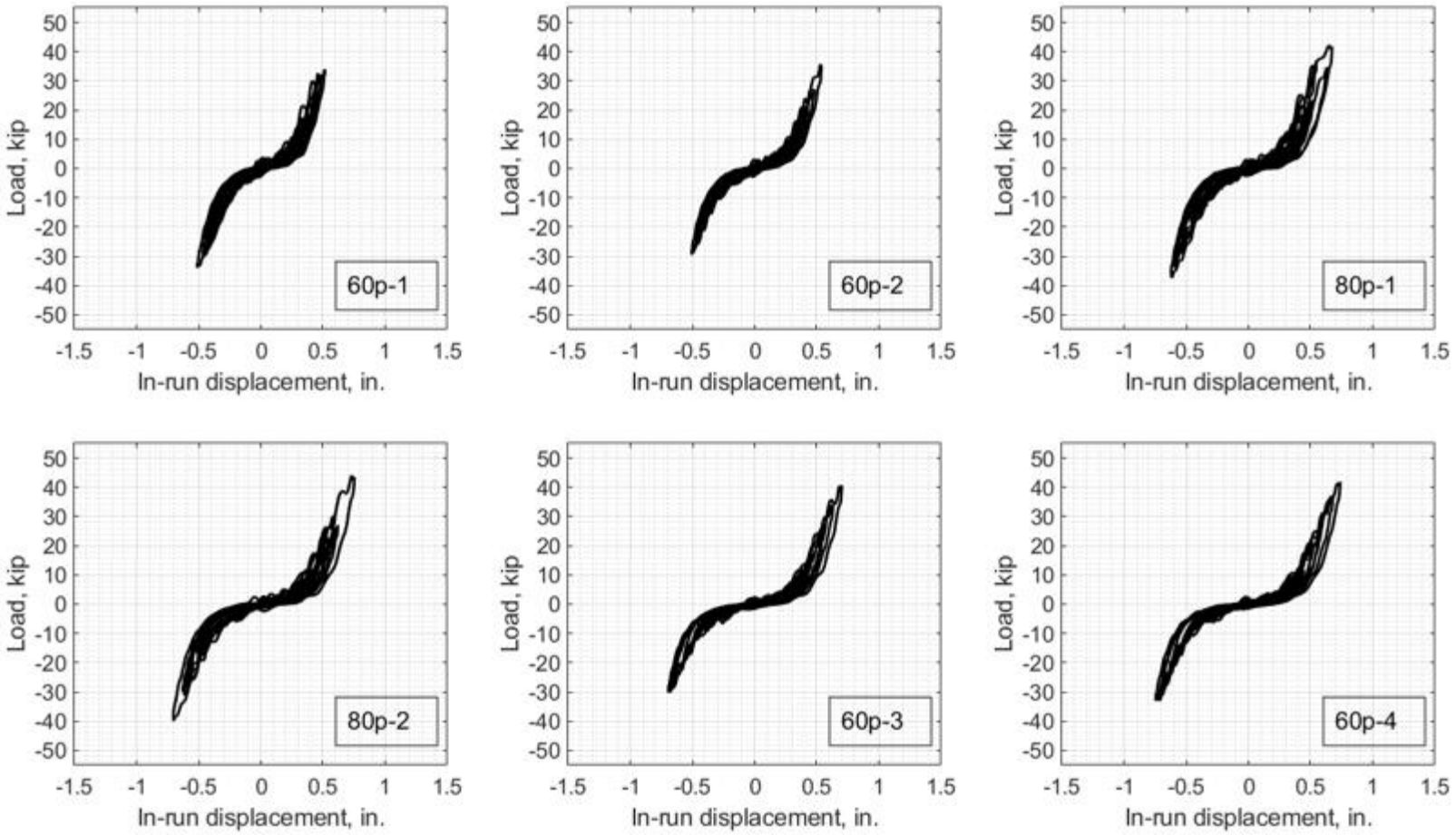

Figure D-99: Force-Drift response in Series F2-C-4PB (continued)

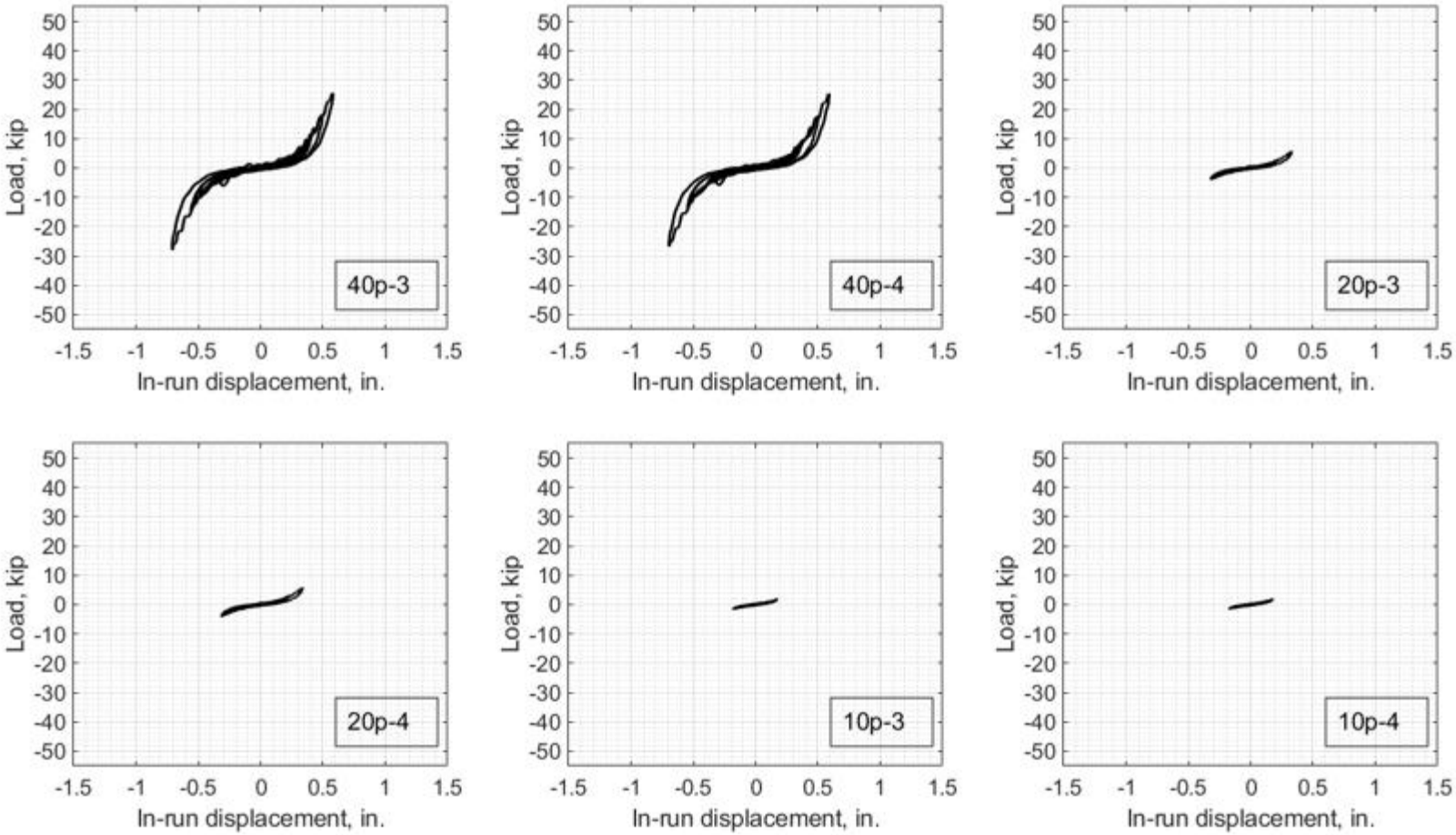

Figure D-99: Force-Drift response in Series F2-C-4PB (continued)

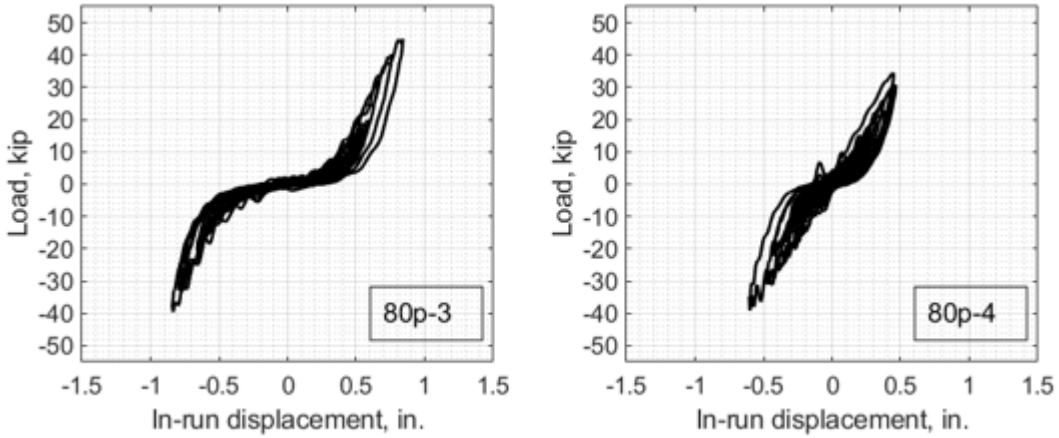

Figure D-99: Force-Drift response in Series F2-C-4PB (continued)

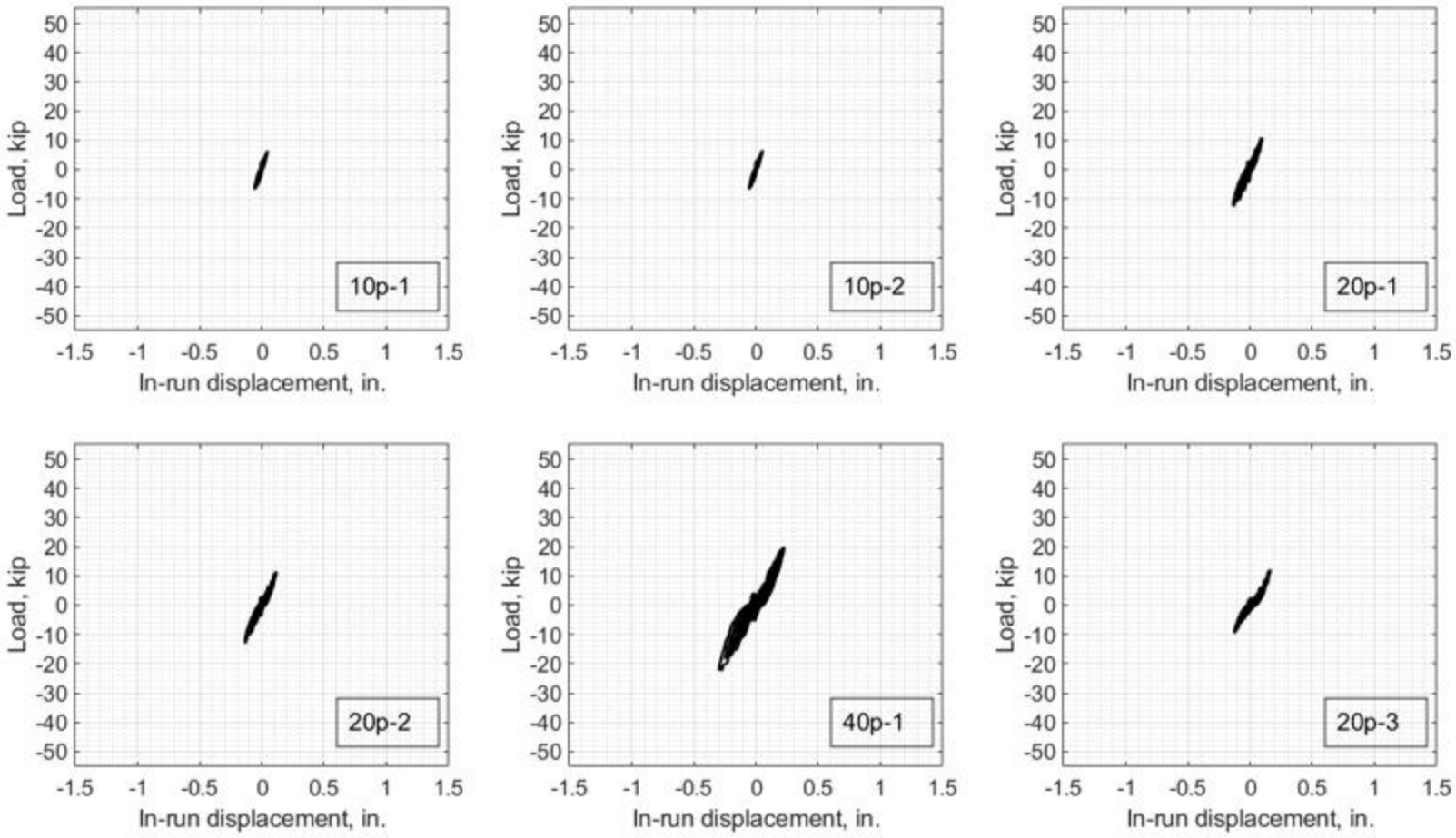

Figure D-100: Force-Drift response in Series F1-C-2PB

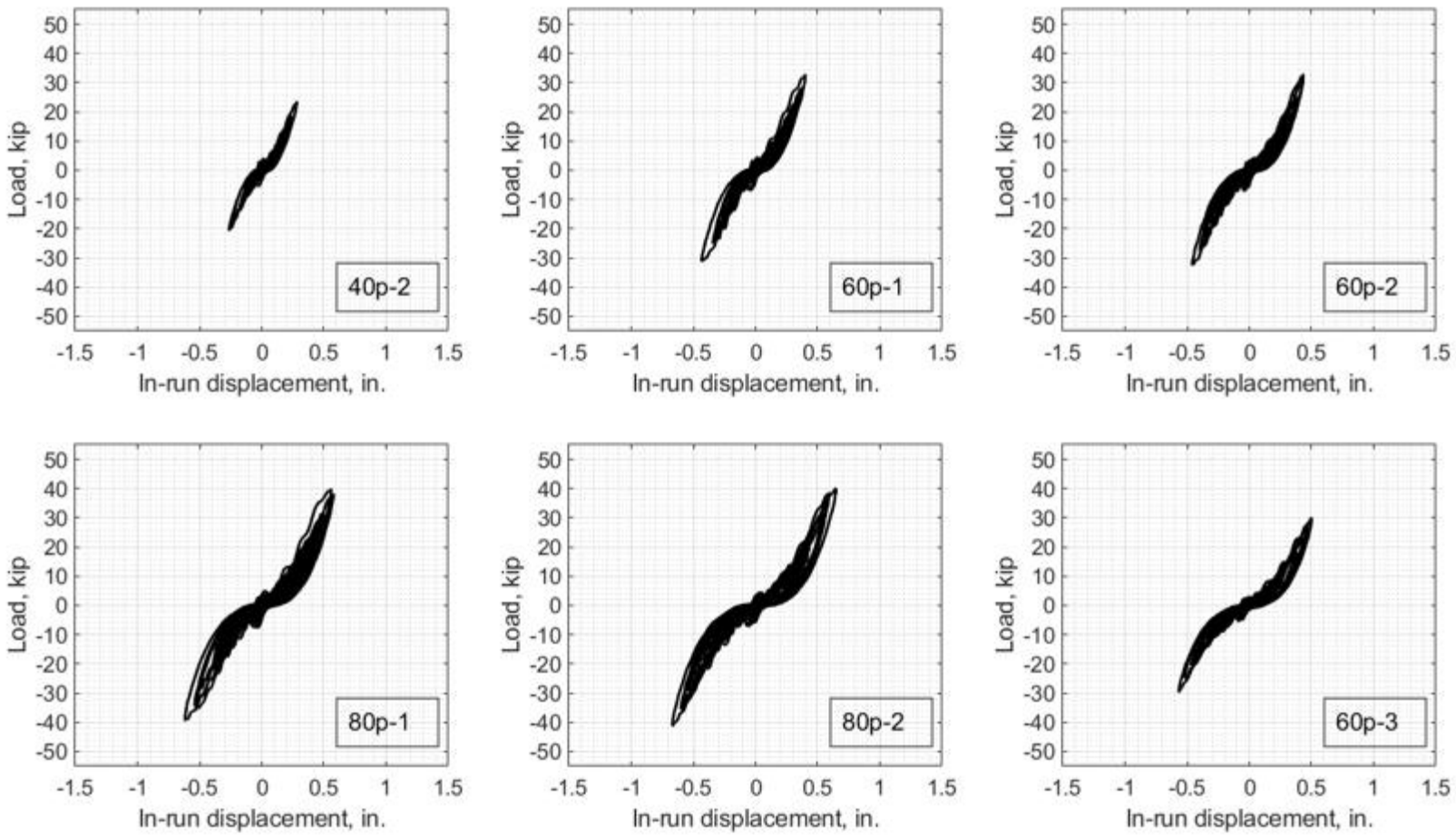

Figure D-100: Force-Drift response in Series F1-C-2PB (continued)

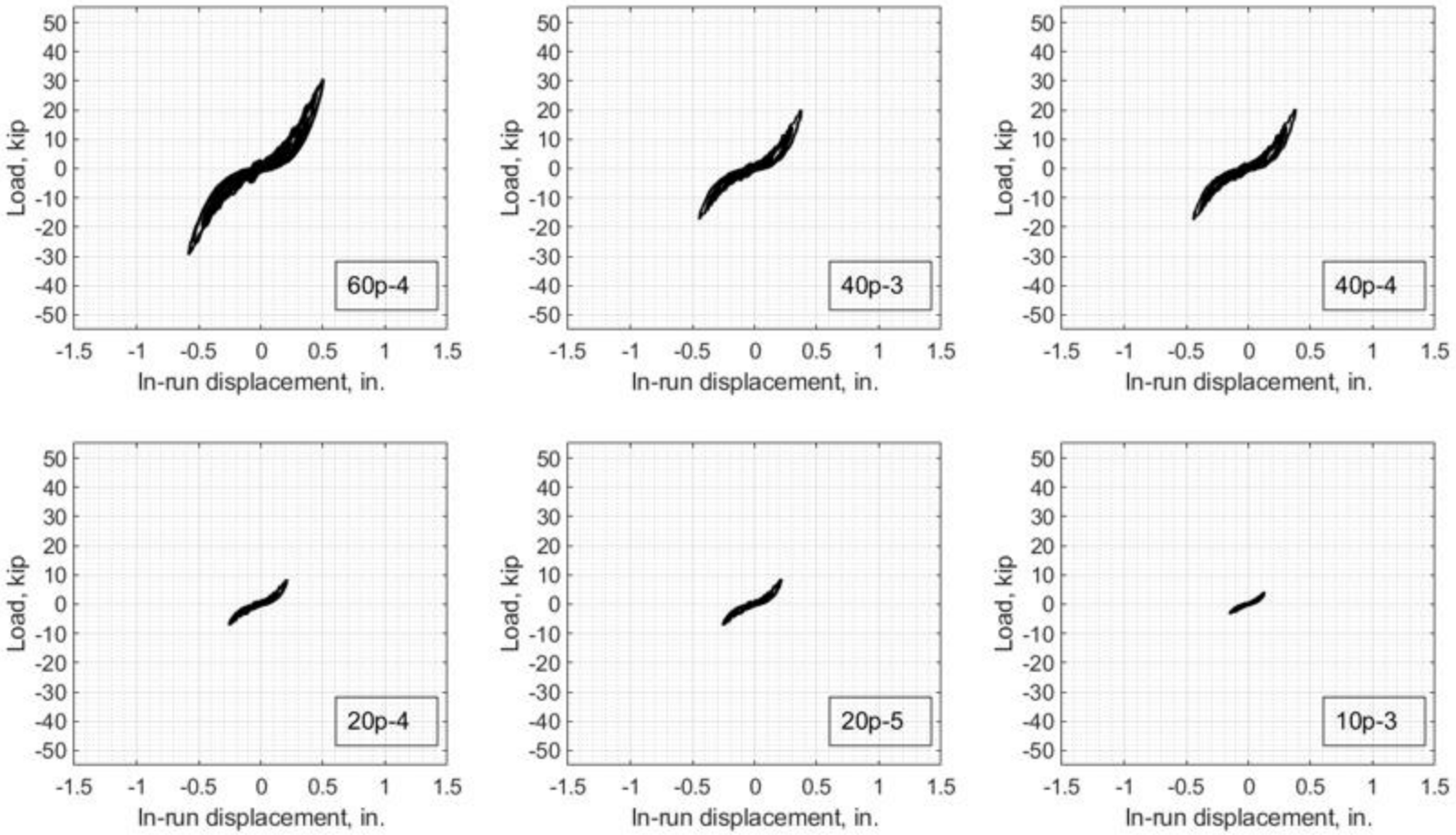

Figure D-100: Force-Drift response in Series F1-C-2PB (continued)

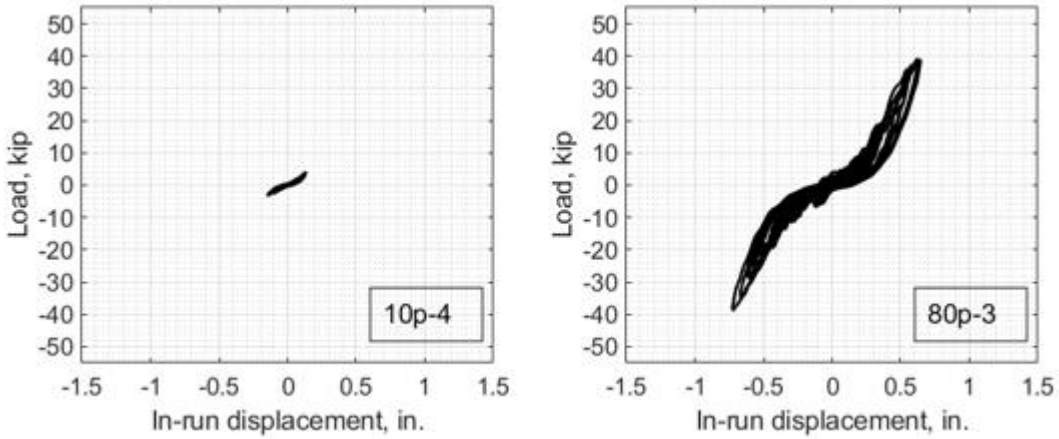

Figure D-100: Force-Drift response in Series F1-C-2PB (continued)

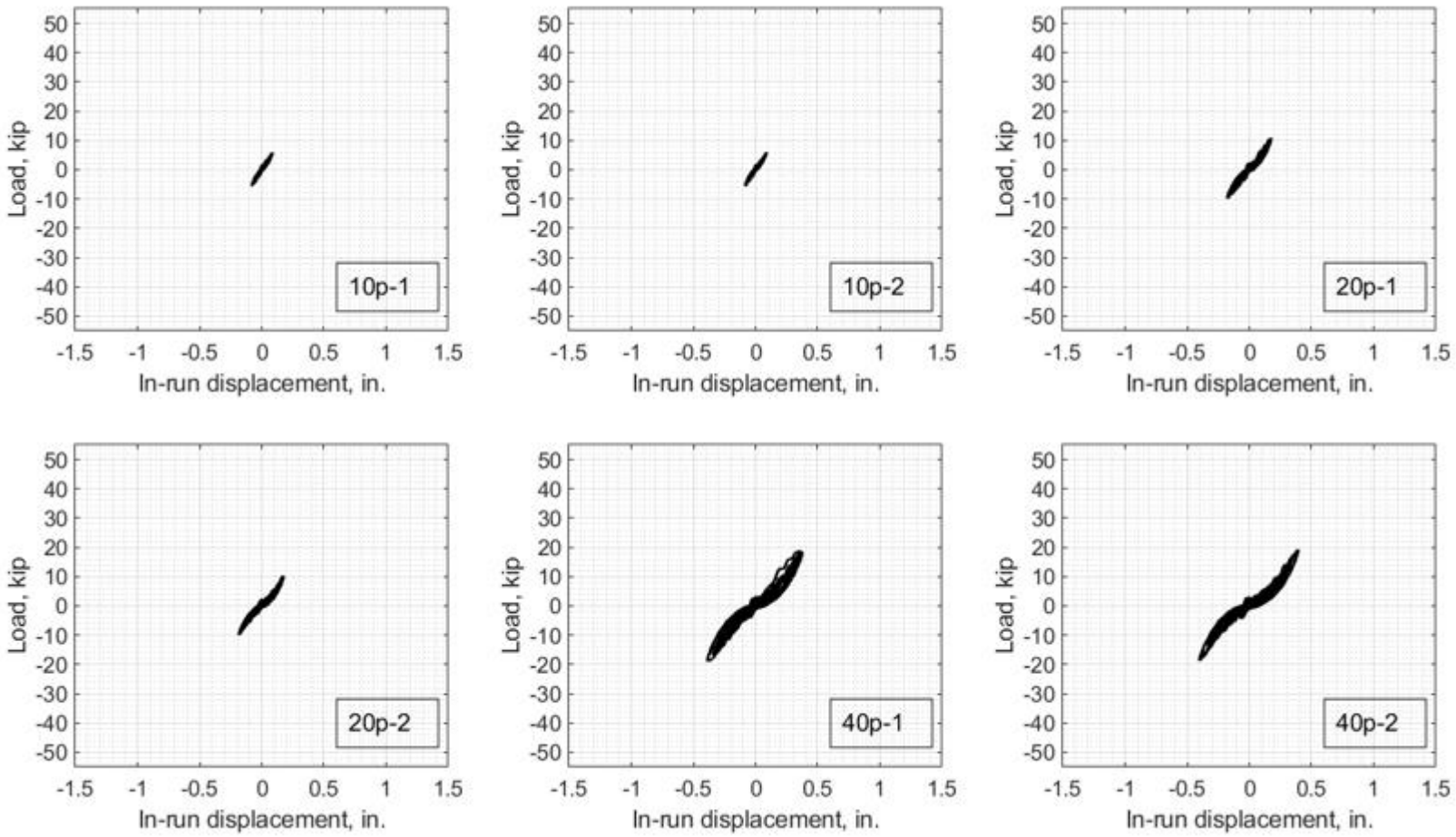

Figure D-101: Force-Drift response in Series F1-C-1PB

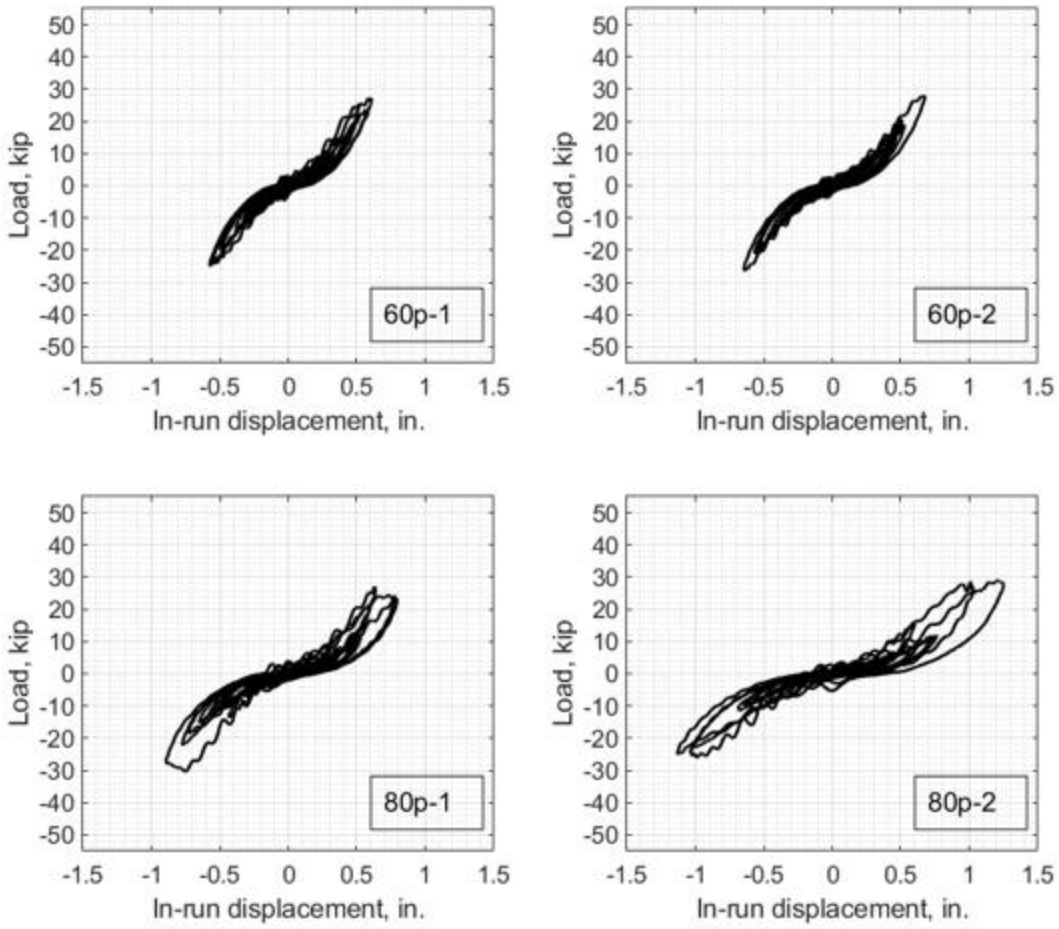

Figure D-101: Force-Drift response in Series F1-C-1PB (continued)

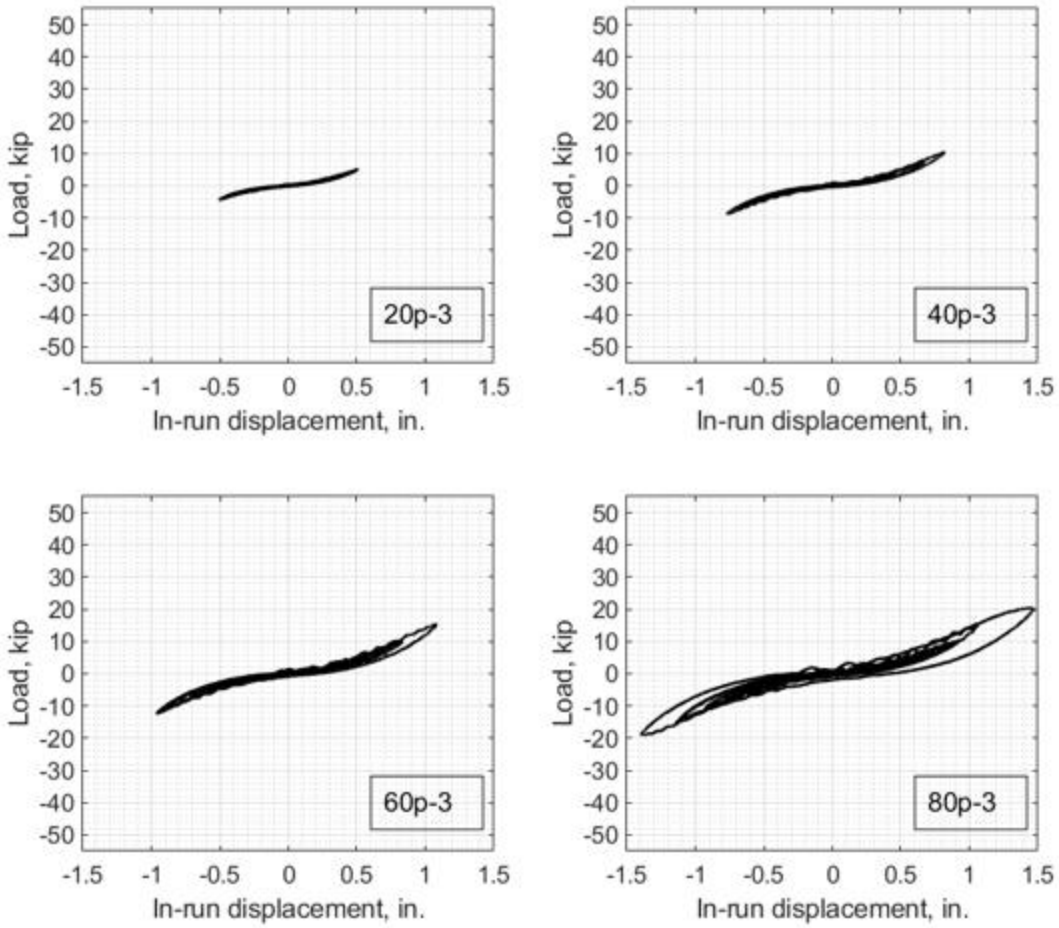

Figure D-101: Force-Drift response in Series F1-C-1PB (continued)[1]

[1] 1PB infill mostly removed prior to Run 20p-3. See Section 3.1.3

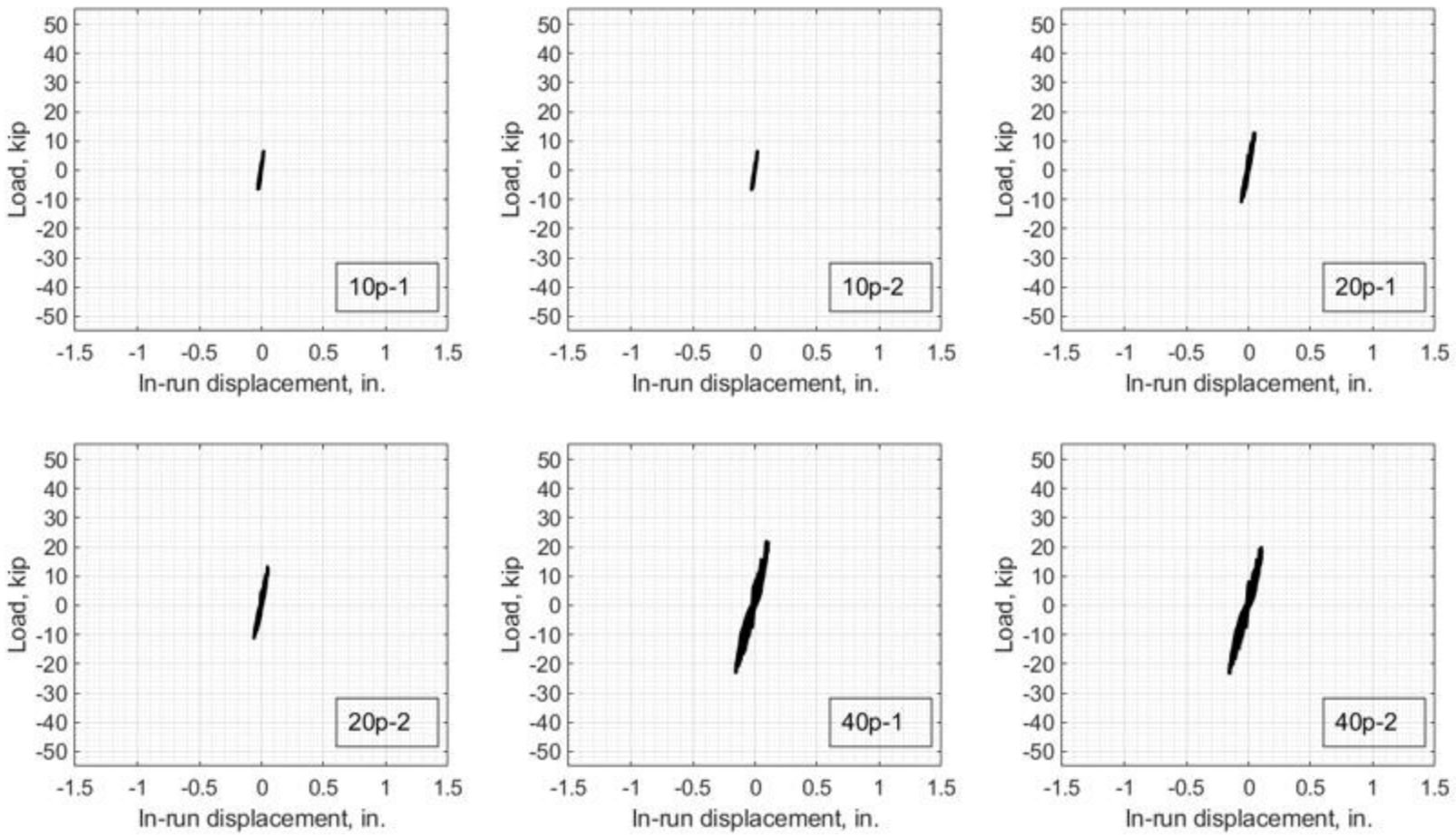

Figure D-102: Force-Drift response in Series F2-R-C-4PB

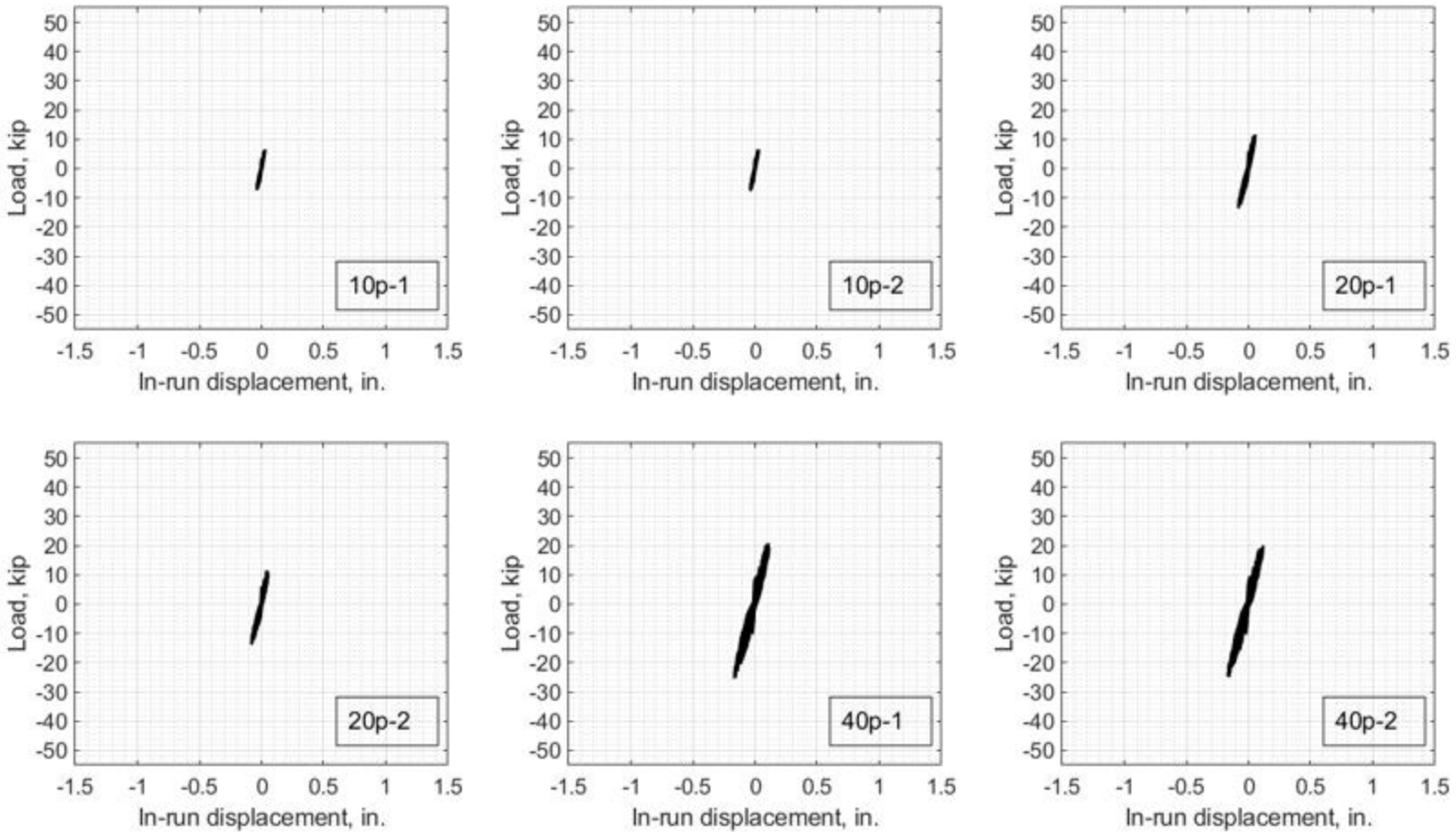

Figure D-102: Force-Drift response in Series F2-R-C-4PB

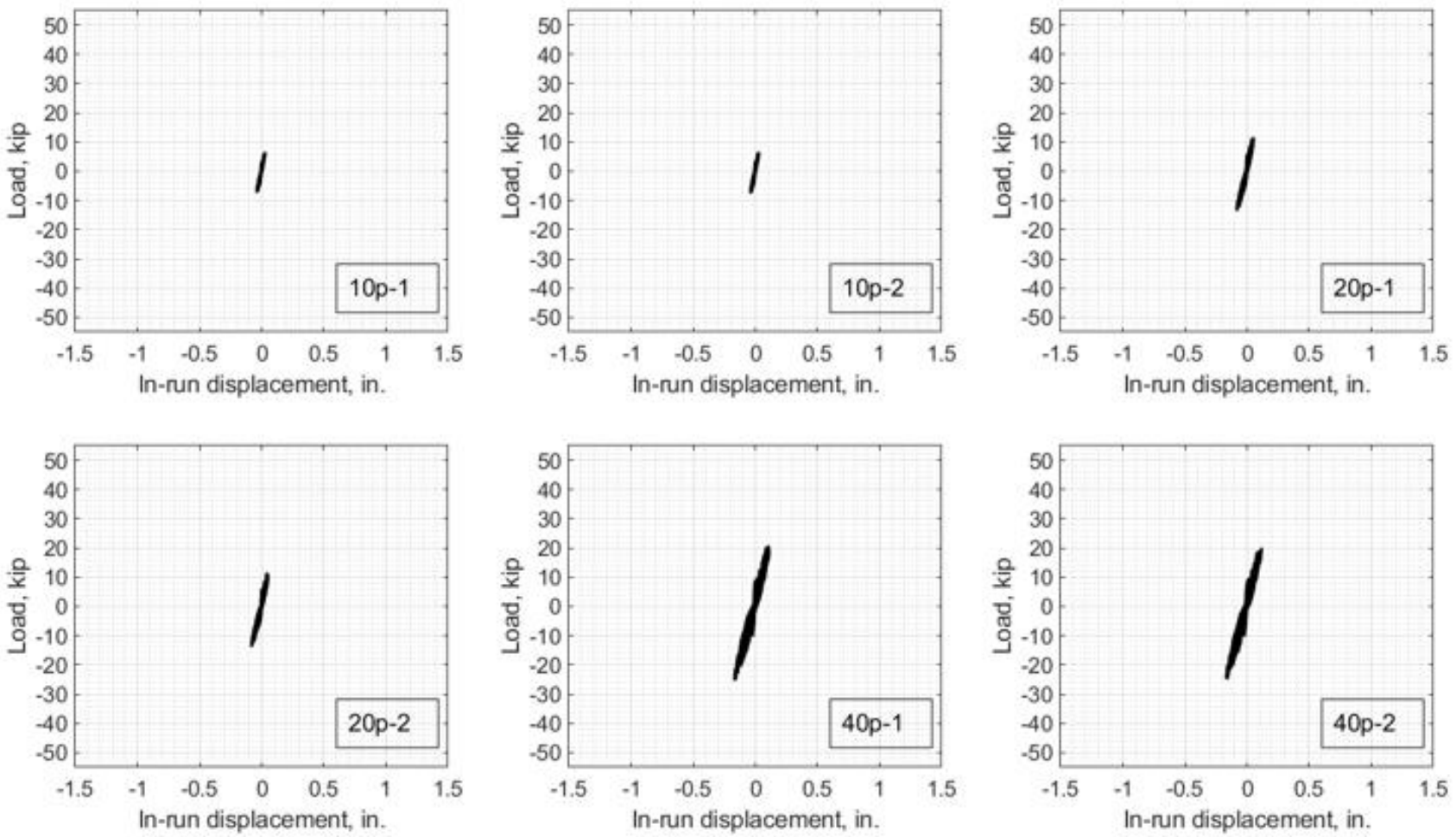

Figure D-103: Force-Drift response in Series F2-R-C-2PB

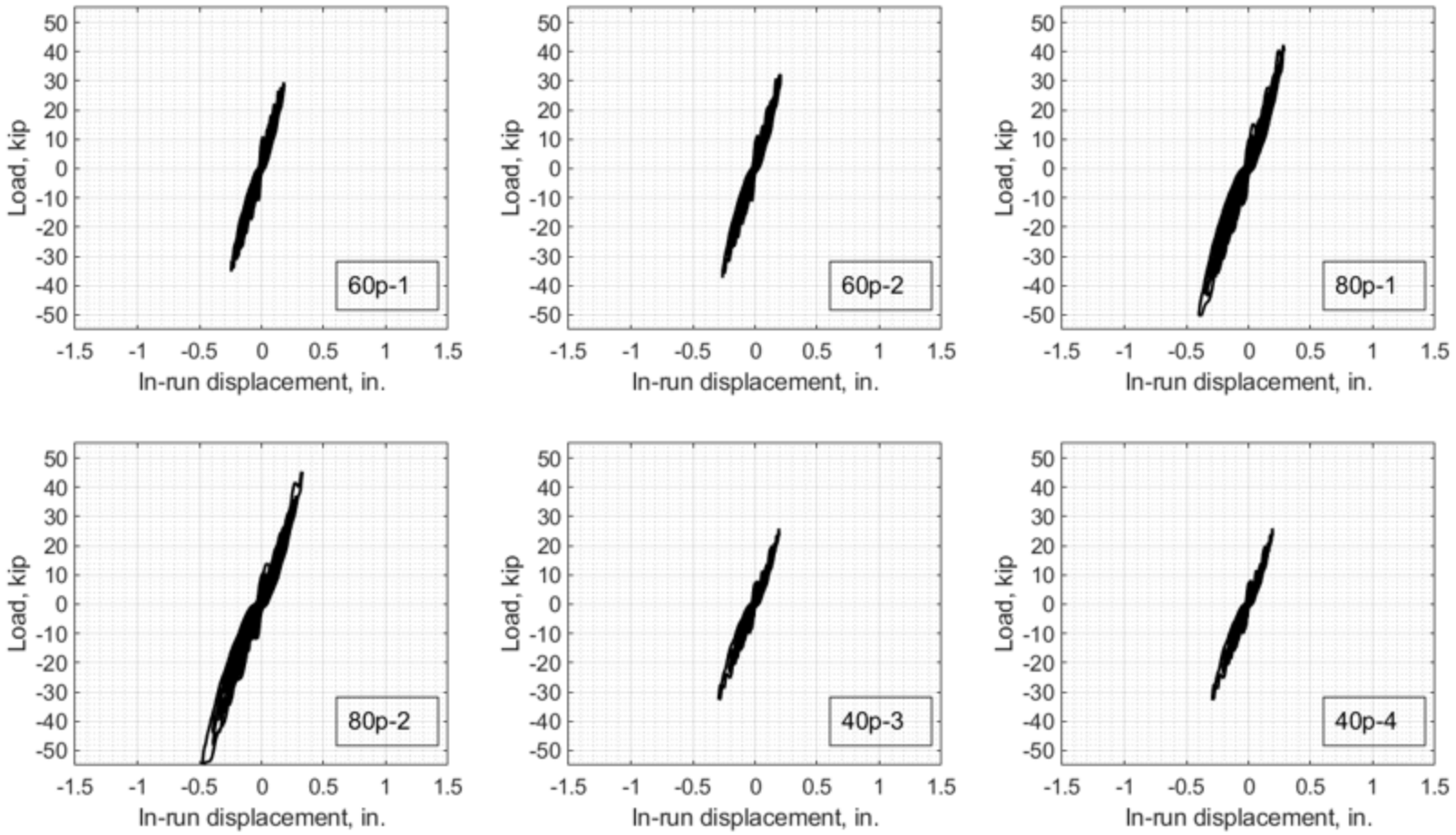

Figure D-103: Force-Drift response in Series F2-R-C-2PB (continued)

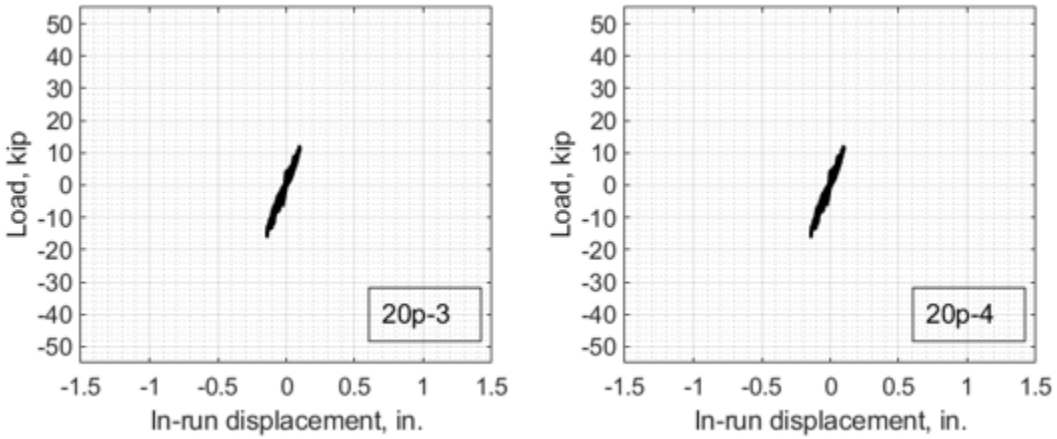

Figure D-103: Force-Drift response in Series F2-R-C-2PB (continued)

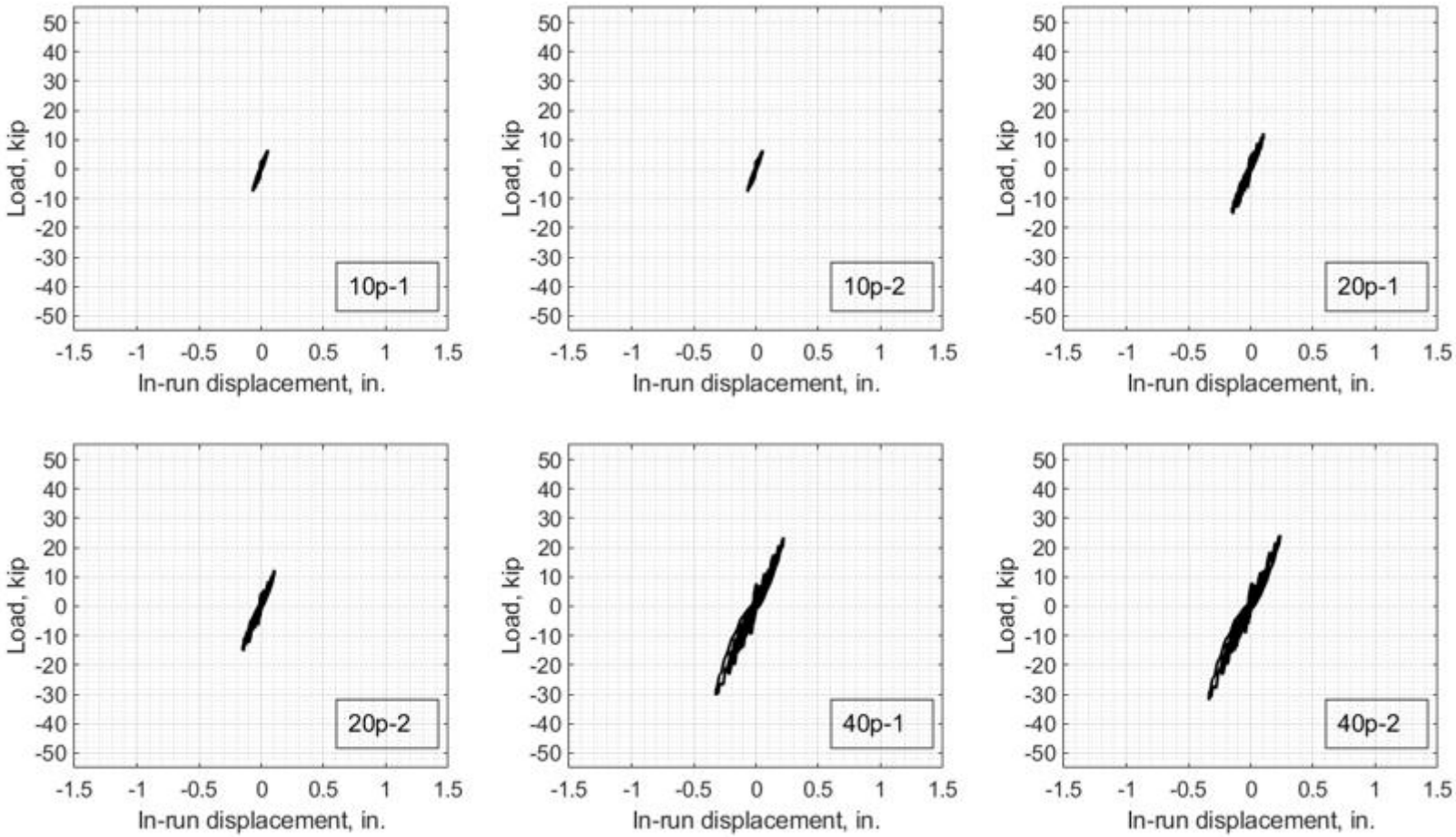

Figure D-104: Force-Drift response in Series F2-R-C-1PB

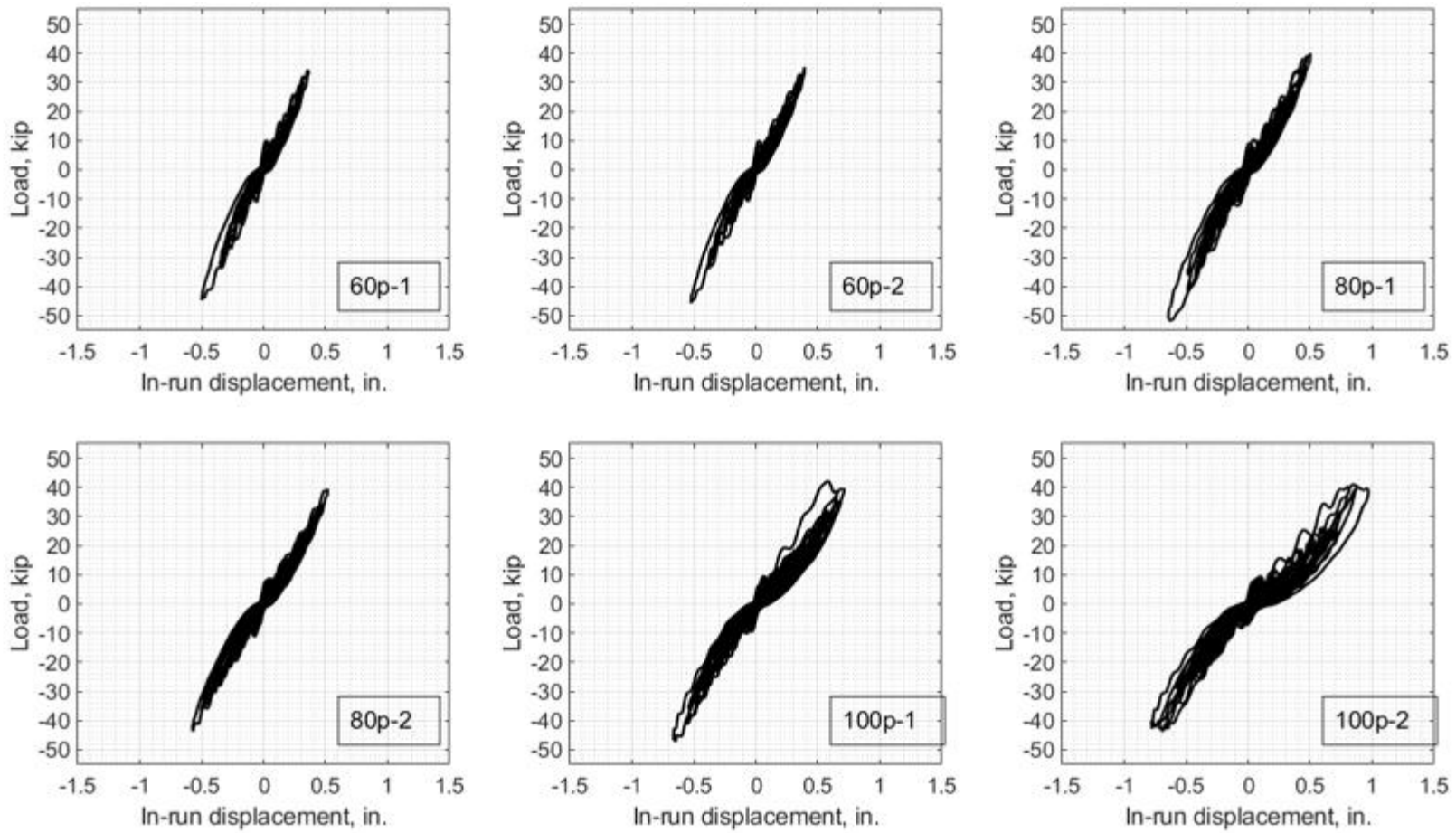

Figure D-104: Force-Drift response in Series F2-R-C-1PB (continued)

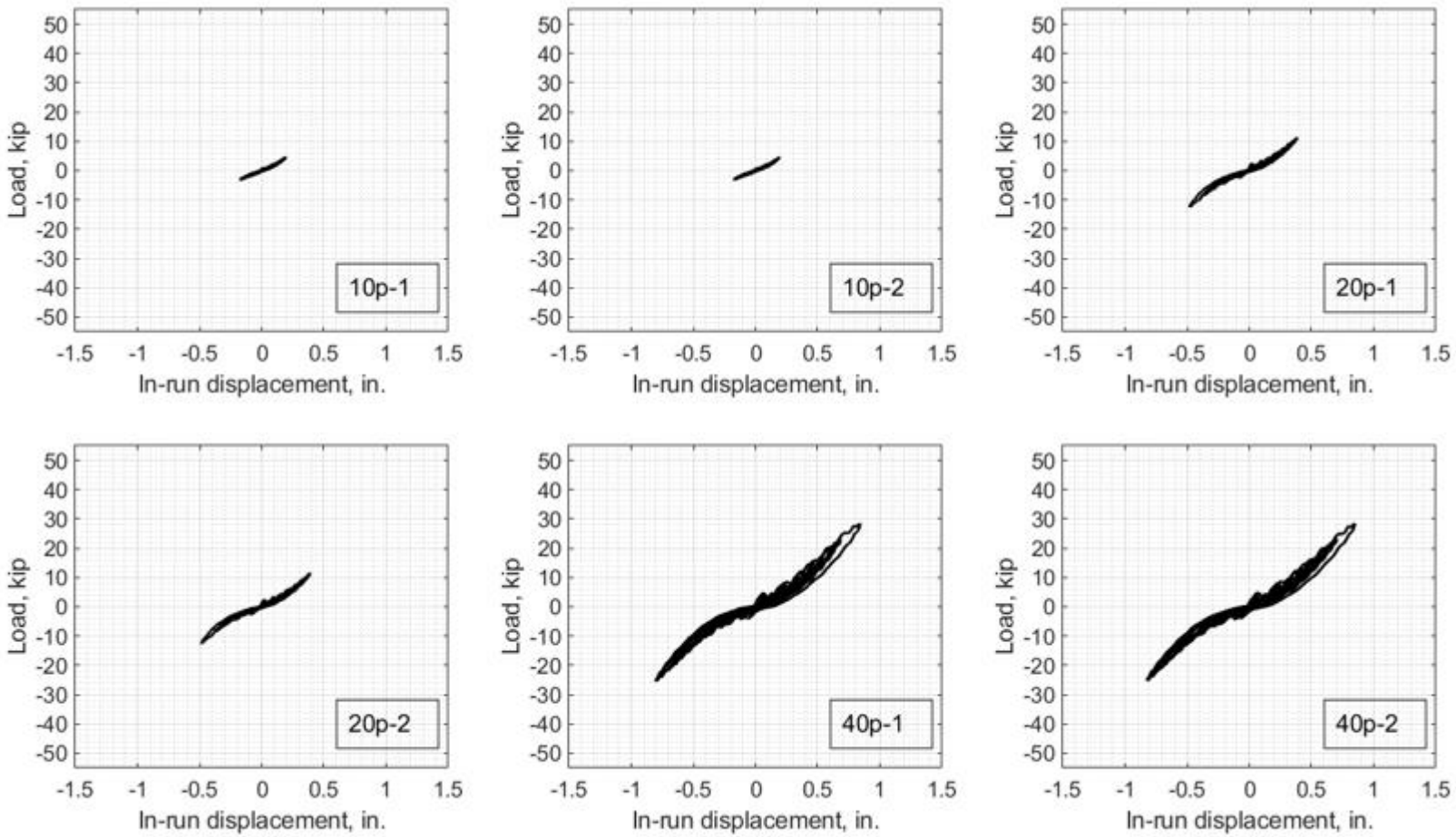

Figure D-105: Force-Drift response in Series F2-R-C

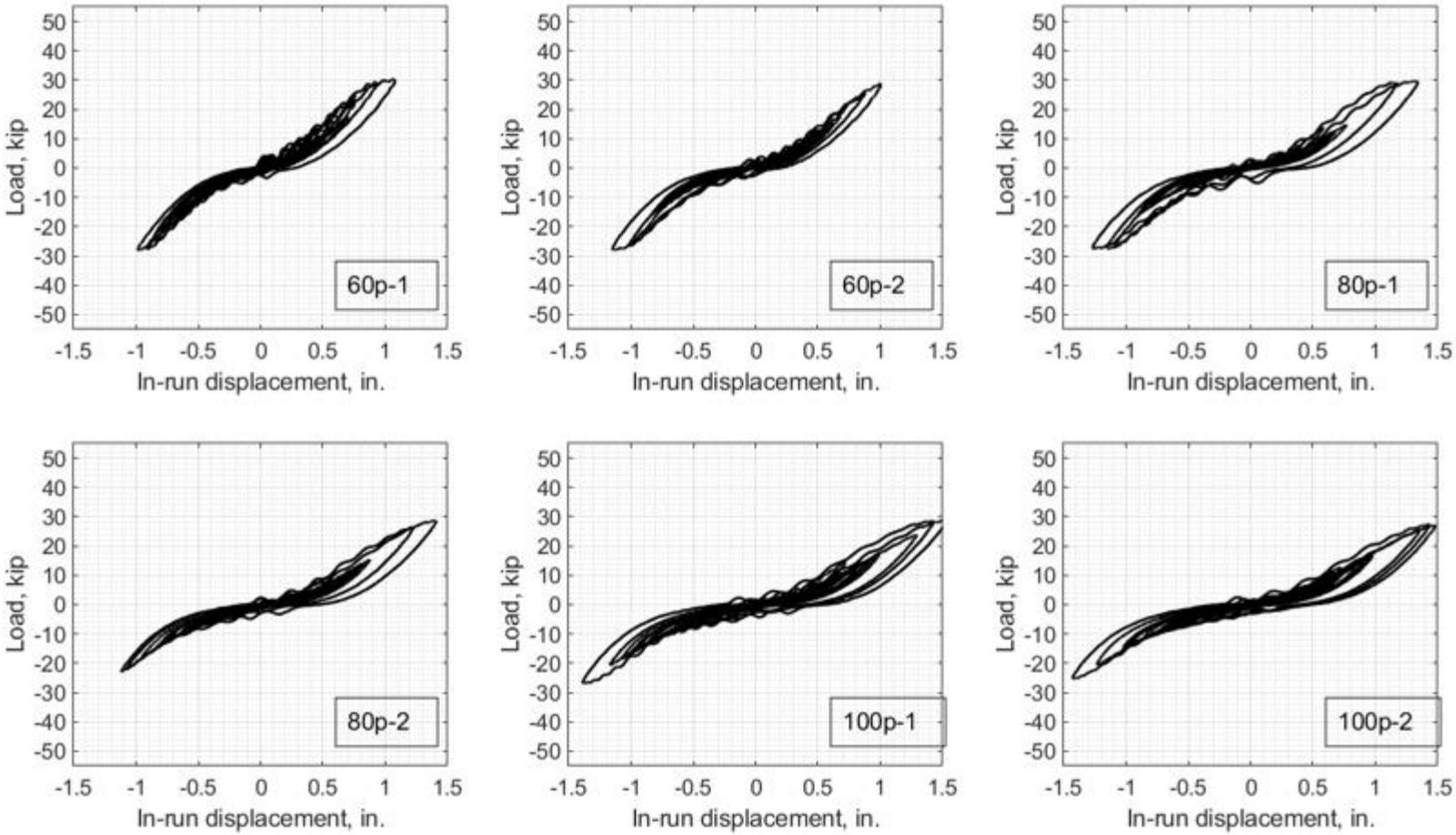

Figure D-105: Force-Drift response in Series F2-R-C (continued)

APPENDIX F: PERMISSION FOR REPRODUCTION OF DATA FROM J. MONICAL

*"*You have my permission to reproduce any data reported in my thesis."

-J. Monical in an email correspondence with C. Kerby and Dr. A. Irfanoglu on December 8th, 2021.

VITA

Charles Skehan Kerby was born in Wheaton, Illinois, USA on May 4th, 1999. He completed his Bachelor of Civil Engineering with an emphasis in Structural Engineering between August of 2017 and December of 2020, advised by Dr. Santiago Pujol and Dr. Ayhan Irfanoglu. He completed his Master of Civil Engineering in May of 2022, advised by Dr. Ayhan Irfanoglu.